INELASTIC BEHAVIOR AND SEISMIC COLLAPSE PREVENTION PERFORMANCE OF LOW-DUCTILITY STEEL BRACED FRAMES

BY

JOSHUA G. SIZEMORE

DISSERTATION

Submitted in partial fulfillment of the requirements
for the degree of Doctor of Philosophy in Civil Engineering
in the Graduate College of the
University of Illinois at Urbana-Champaign, 2017

Urbana, Illinois

Doctoral Committee:

Associate Professor Larry A. Fahnestock, Chair, Director of Research
Professor Daniel P. Abrams
Professor James M. LaFave
Professor Robert Tremblay, Polytechnique Montréal
Professor of Practice Eric Hines, Tufts University

ABSTRACT

Seismic-force-resisting systems (SFRSs) in areas of low and moderate seismicity such as the east coast of the United States have minimal ductility. Unlike high-ductility systems, whose design encompasses extensive seismic detailing and proportioning requirements to provide said ductility, the analogous requirements for low-ductility steel SFRSs are minimal, and in some instances nonexistent. Ordinary concentrically-braced frames (OCBFs) have requirements that are intended to provide a small level of ductility, and steel SFRSs designed with a response modification factor $R = 3$ have no specific seismic requirements. Rather than relying on ductility for post-elastic performance, these systems—that have received almost no research attention—must prevent collapse through other means that are not explicitly defined or considered in the design process. Reserve capacity, or additional lateral force resisting capacity following incipience of inelastic and often brittle behavior within the SFRS, has been shown through post-earthquake reconnaissance to be the probable mechanism by which low-ductility concentrically braced frames (CBFs) provide collapse prevention. Aside from these anecdotal cases, however, the inelastic behavior and seismic collapse prevention performance of low-ductility CBFs remain untested and unsubstantiated, and these topics are not yet understood at a fundamental level to the extent of high-ductility systems.

In this dissertation, the inelastic behavior and seismic collapse prevention performance of low-ductility CBFs are examined through a combination of numerical simulations and full-scale experimental testing. Sources of reserve capacity are systematically identified and evaluated through numerical simulations. The impact of common design choices, such as system type and system configuration, on reserve capacity is evaluated through full-scale tests of an $R = 3$ CBF in the chevron configuration and an OCBF ($R = 3.25$) in the split-x

configuration. Test results and numerical simulations indicate that the chevron configuration is more suitable for providing reserve capacity, and that while some of the minor seismic detailing requirements of the OCBF provision improve performance, others are detrimental and lead to uneconomical designs.

The knowledge gained from the initial numerical simulations and full-scale experimental testing inspired the development of a new low-ductility system for use in areas of low and moderate seismicity which provides collapse prevention through primary system ductility and intentional reserve capacity mechanisms: the R = 4 OCBF. In a reliability-based performance assessment this new system shows an improvement in behavior over the two primary low-ductility CBF SFRSs—the R = 3 CBF and the OCBF (R = 3.25)—while also minimizing design costs and complexity. This R = 4 OCBF concept is proposed for consideration in the upcoming 2022 AISC *Seismic Provisions*.

ACKNOWLEDGEMENTS

I would like to thank my advisor, Dr. Larry Fahnestock, for providing me with the opportunity to join his steel behavior research group at the University of Illinois and his project team on low-ductility braced frames. Dr. Fahnestock was instrumental in providing me with the foundation to expand my knowledge on the design and behavior of steel structures over the past 5 years. I always felt that I had his full support, and I am very grateful for that.

I would also like to thank the others members of the project team, including Dr. Eric Hines, Dr. Robert Tremblay, Ali Davaran, Cameron Bradley, Jessalyn Nelson, and Thierry Beland. I always knew I was going to learn something new in each conference call with these researchers. Without the collaborative efforts of this team, the research behind this dissertation would not have been possible.

One of the major aspects of this project was a full-scale testing program at Lehigh University. I would like to thank both the University of Illinois for providing me with the accommodations to support my temporary move to Bethlehem Pennsylvania to help with the test set-up and planning, as well as Catherine Somers and other involved staff members of the Business Office for jumping through the necessary bureaucratic hoops to make my move seamless and effortless.

Speaking of the full-scale testing, it would not have been possible without the help from Lehigh faculty members, staff members, and technicians including but not limited to Dr. Richard Sause, Dr. James Ricles, Peter Bryan, Gary Novak, Thomas Marullo, Todd Anthony, Carl Bowman, Darrick Fritchman, and Jeffrey Sampson. I am also thankful for the support provided by Sanders Park through the NEES undergraduate REU program in the preparation of the test units, and by the other REU students who chipped in along the way.

After the full-scale testing at Lehigh, I was tasked with performing coupon tests at the University of Illinois Newmark Lab. I would like to thank Darold Marrow for his help with fabrication of the tensile coupons, Charles Cook for providing me with the necessary laboratory training, and Don Marrow for teaching me how to run the machinery needed to perform the coupon tests. I would also like to thank undergraduate student Teng Li for his help with the coupon testing.

I would like to thank the faculty members who have agreed to serve on my doctoral committee for their extremely helpful feedback on this manuscript and the associating defense presentation – Dr. Larry Fahnestock, Dr. Daniel Abrams, Dr. James LaFave, Dr. Robert Tremblay, and Dr. Eric Hines.

I would like to thank office colleagues Jie Luo and Dan Borello for helping me with *OpenSees* related issues, and I would like to thank Chris Stoakes for sharing his *OpenSees* model with me—it was instrumental in helping me learn how to develop my own models.

Finally, I would like to thank my family and friends for all the love and support they have provided during my life. To my parents, Glenn and Mary Sizemore, as I would not be where I am today without them. And to my wife, Shyvonne Sizemore, for always being there for me and believing in me. Her unequivocal love and unwavering support has been a tremendous asset when dealing with the inevitable trials and tribulations of pursuing a PhD.

This material is based upon work supported by the National Science Foundation Graduate Research Fellowship (NSF GRFP) under Grant No. DGE - 1144245 as well as NSF Grant No. CMMI-1207976: “Reserve Capacity in New and Existing Low-Ductility Steel Braced Frames”. Additional funding was provided by the American Institute of Steel Construction (AISC). Testing was made possible by the Network for Earthquake Engineering

Simulation sponsored NEES@Lehigh location. Wide flange and brace members for the test units were provided by Nucor and Atlas Tube, respectively. Any opinion, findings, and conclusions or recommendations expressed in this material are those of the authors(s) and do not necessarily reflect the views of those acknowledged here.

TABLE OF CONTENTS

CHAPTER 1

INTRODUCTION

Seismic structural design is typically conducted using a ductile design philosophy. This philosophy, employed primarily in areas of high seismicity such as the west coast of the United States, underlies high-ductility seismic force resisting systems (SFRSs), including widely used steel SFRSs such as special moment frames (SMFs) and special concentrically-braced frames (SCBFs). The ability of these systems to prevent collapse of a building during a seismic event through inelastic ductile behavior is well documented and has been studied extensively over the past three decades. In contrast, in areas of low and moderate seismicity such as the east coast of the United States (Figure 1.1), low-ductility SFRSs are used. Unlike high-ductility systems, whose design encompasses extensive seismic detailing and proportioning requirements to provide said ductility, the analogous requirements for low-ductility steel SFRSs are minimal, and in some instances nonexistent. Ordinary concentrically-braced frames (OCBFs) have requirements that are intended to provide a small level of ductility, and steel SFRSs designed with a response modification factor $R = 3$ have no specific seismic requirements. Rather than relying on ductility for post-elastic performance, these systems—that have received almost no research attention—must prevent collapse through other means that are not explicitly defined or considered in the design process.

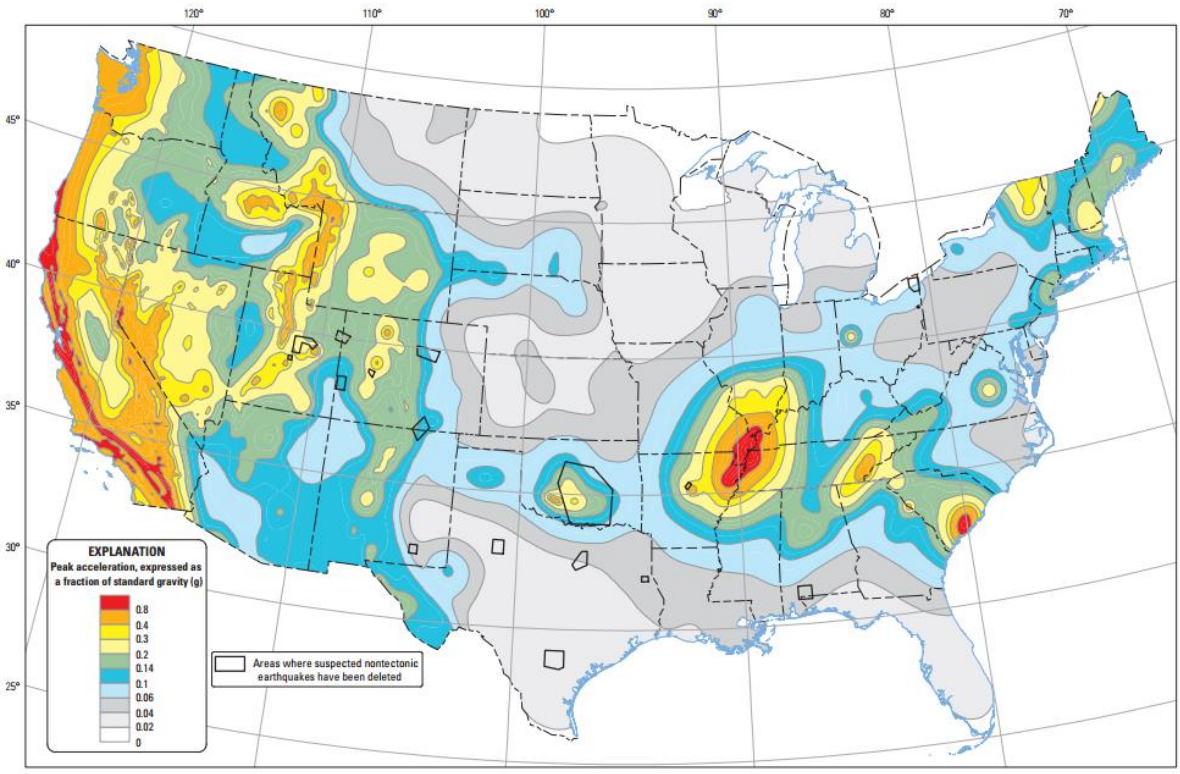

Figure 1.1 – 2014 National Seismic Hazard Map for continental U.S. – PGA, 2% probability of exceedance in 50 years. (Peterson et al., 2014).

1.1 SEISMIC FORCE RESISTING SYSTEMS

In general, although a higher *R*-value results in lower seismic lateral loads, it comes with the caveat of increased construction costs that are associated with more sophisticated seismic detailing and proportioning (capacity design) requirements. In low and moderate seismic regions—where lateral loads associated with expected seismic demands are already relatively low—wind can govern the lateral force resisting system (LFRS) design of taller buildings and negate the benefits of using a higher *R*-value to reduce design forces. Engineers avoid using a SCBF in these regions as doing so would result in all the added costs associated with its extensive seismic detailing and proportioning requirements without the decreased cost associated its reduction in seismic demands. For low and moderate seismic design, while the

OCBF is certainly more appealing than the SCBF, a third choice exists that is even more appealing for designers—the "*R* = 3" SFRS (Table 1.1).

Table 1.1 – Primary steel CBF SFRSs (ASCE, 2013)

Name	*R*	Seismic Detailing	Capacity Design	Permissible Regions	
				Low/Moderate	High
SCBF	6	Yes	Yes	Yes	Yes
OCBF	3.25	Yes	Yes[a]	Yes	Yes[b]
"*R* = 3"	3	No	No	Yes	No

[a] Partial, ad-hoc capacity design approach

[b] With height restrictions in Seismic Design Categories D and E.

1.1.1 The "*R* = 3" Seismic Force Resisting System

The "*R* = 3" SFRS was originally introduced in the commentary of the 1997 AISC *Seismic Provisions* (AISC, 1997, *Table I-C4-1*) to acknowledge the importance of seismic safety in moderate seismic regions without the burden of prescriptive detailing requirements. When designing an *R* = 3 steel SFRS an engineer must only satisfy the universal design requirements of AISC Standard 360–10 (AISC 360–10): *Specification for Structural Steel Buildings* (AISC, 2010b), which apply to all structural steel designs in the U.S. Considering the lack of seismic detailing requirements in its design, the *R* = 3 SFRS is understandably allowed only in low and moderate seismic regions (Table 1.1). To serve as a comparison with OCBF, which could be viewed as a competitor to the *R* = 3 SFRS in low and moderate seismic regions where each are permissible, the focal point of this dissertation as it pertains to *R* = 3 SFRSs is on CBFs. While the CBF is a popular choice for an *R* = 3 design, a unique distinction of this SFRS is that it can theoretically take on an infinite number of shapes, sizes, and configurations. Given the tradeoff of the seismic detailing requirements associated with the

OCBF for only a small reduction (0.25/3.00 = 8%) in design base shear, the popularity of R = 3 CBFs over OCBFs in low and moderate seismic regions is understandable.

1.2 COLLAPSE PREVENTION PERFORMANCE OF LOW-DUCTILITY SYSTEMS

The ability of fuse elements to provide ductility and improve collapse prevention performance is well understood thanks to decades of extensive research into high-ductility systems common of California and other high seismic regions. This is not the case for low-ductility systems, however, as despite frequent use across most of Midwest and Eastern North American, the fundamental behavior of these systems is not well understood, and certainly not to the extent of high-ductility systems.

Even the OCBF, which includes detailing and proportioning requirements for select members—such as local (b/t) and global (KL/r) slenderness limits for braces and the consideration of amplified seismic loads with a system overstrength factor (Ω_0 = 2) for select beams, columns, and brace connections (AISC, 2010b)—does not rigorously enforce the capacity design of any elements to ensure ductility is provided in the post-elastic range. By partially adopting and relaxing the requirements that enforce capacity design in the SCBF provisions, the OCBF provisions provide an ad-hoc capacity design approach rather than explicitly defining a mechanism. Thus, unlike the SCBF, both the OCBF and the R = 3 CBF rely on a range of contributors to collapse prevention rather than a specific source to justify their associated R-values. These possible contributors include but are not limited to: (1) inherent ductility, which may come from beams, columns, braces, or connections when these elements aren't explicitly detailed to undergo inelastic demands; (2) inherent overstrength, which may come from material overstrength, load and resistance factors, or as a consequence of discrete member sizes increasing the elastic capacity beyond what is required; and (3)

reserve capacity, which is defined as additional lateral force resisting capacity that is observed after a brittle limit state to the SFRS (Figure 1.2).

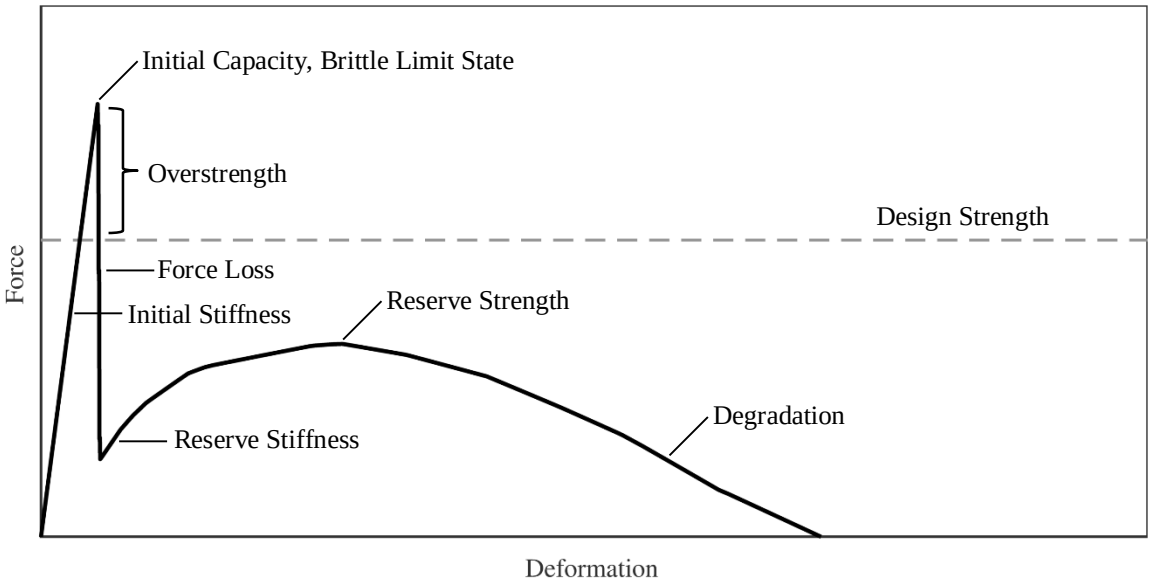

Figure 1.2 – Idealization of reserve capacity.

1.2.1 Reserve Capacity

Reserve capacity is viewed as the most important contributor towards collapse prevention in low-ductility systems, which are expected to experience one or more brittle limit states after a short period of initial ductility in the post-elastic range. Thus, developing a thorough fundamental understanding of reserve capacity is an essential first step towards providing more efficient and safer structures in low and moderate seismic regions. Despite the heavy implicit reliance that low-ductility design places on reserve capacity, its importance was unknown until recently. Specific research interest into reserve capacity was sparked in part by the performance of structural steel buildings during major earthquake events throughout the past few decades in Northridge (1994), Kobe (1995), Chile (2010), and Christchurch (2011), among others. Structural inspections following these earthquakes revealed that many older

nonductile or low-ductility steel-framed buildings did not collapse despite experiencing multiple brittle fractures to connections throughout their SFRSs (Tremblay et al., 1995; Tremblay et al., 1996; Nakashima et al., 1998; Saatcioglu et al., 2013; Tremblay et al., 2003; Clifton et al., 2011). These observations supported the notion that steel SFRSs have additional lateral force resisting capacity following brittle member or connection fractures (reserve capacity), despite it not being explicitly considered in design. Anecdotal cases such as these reinforce the thought that the OCBF and R = 3 are practical SFRSs for low and moderate seismic design. One counter-point to this claim was identified from the aftermath of the 1985 Mexico City earthquake, in which a 21-story steel building collapsed onto a neighboring 14-story building (Osteraas and Krawinkler, 1989; Ger et al., 1993); however, this was a unique case driven by local buckling of slender built up column sections which led to disproportionate collapse. Although future building codes addressed the issue of slender columns and a similar collapse has not occurred since, this collapse serves as an important reminder that while reserve capacity may help prevent collapse, engineers cannot and should not always rely on its ability to do so without carefully considering it in the design process. In recent years, the structural engineering community has started a more thorough investigation of reserve capacity, particularly in the case of low-ductility systems where it has a heightened importance. This research also has applications in high-ductility systems, which may experience brittle limit states at large drift levels and shift from a reliance on ductility to reserve capacity. An engineer can design a system with any combination of high or low amounts of ductility or reserve capacity if the implications of these decisions are considered when the system is detailed and proportioned.

1.3 OVERVIEW OF RESEARCH

1.3.1 Research Need

Investigations following previous significant seismic events have revealed that steel structures inherently possess additional lateral force resisting capacity following damage to their SFRS beyond what is assumed in design. These contributors to collapse prevention performance in low-ductility steel systems, e.g. reserve capacity, are not as well understood as sources of collapse prevention performance in high-ductility systems, e.g. ductility. Given the strong implicit reliance low-ductility systems have on reserve capacity, the need for a thorough examination of it and its sources is clear. The prevalence of low-ductility systems throughout the United States further compounds this need

Reserve capacity in low-ductility CBFs was recently investigated through numerical simulations (Rai and Goel 2003; Hines et al. 2009; Stoakes, 2012), and these initial studies provided a basic demonstration of reserve capacity and its contribution to collapse resistance. However, these studies looked exclusively at CBF behavior for chevron bracing configurations, and did not comprehensively study the effects of different system types (i.e. R = 3 vs. OCBF). Through better understanding of the inelastic behavior of low-ductility CBFs, building codes and provisions may be improved by explicit acknowledgment and consideration of reserve capacity during the design process.

1.3.2 Collaborative Research Program

To investigate the inelastic behavior of low-ductility CBFs, a comprehensive research program was launched under the National Science Foundation Grant No. CMMI-1207976: "Reserve Capacity in New and Existing Low-Ductility Steel Braced Frames" (Beland et al., 2014; Bradley et al., 2014; Davaran et al., 2014; Nelson et al., 2014; Sizemore el al., 2014;

Nelson, 2014; Bradley, 2016; Bradley et al., 2016; Sizemore et al., 2016). The research program included faculty and graduate students from the University of Illinois, Tufts University, and Polytechnique Montréal. Faculty and graduate students from Polytechnique Montréal researched sources of reserve capacity within low-ductility CBFs at the component level through experimental studies on angle capacity (Nelson et al., 2014 Beland et al., 2014; Beland, 2016), beam-column connection capacity (Beland et al., 2014), and behavior of brace-gusset connections following weld fracture (Davaran et al., 2014). Faculty and graduate students at the University of Illinois and Tufts University placed a heightened emphasis on overall system-level behavior of low-ductility CBFs through experimental studies on full-scale frame tests at Lehigh University. While the design, construction, detailing, and testing of these full-scale CBFs was a collaborative effort, Tufts University graduate student Cameron Bradley had a larger focus on the design and construction of the test units. A thorough documentation of the design, construction and testing of the test units – including shop drawings, member design calculations and methodical experimental observations – may be found in his thesis (Bradley, 2016).

1.3.3 Research Objectives

This research program had two fundamental research objectives. First, identify sources of reserve capacity in low-ductility steel CBFs and quantify their effectiveness. Second, determine cost-effective solutions for providing and increasing reserve capacity in low-ductility steel CBFs as a design strategy.

1.3.4 Research Scope

The first objective—identifying sources of reserve capacity in low-ductility steel CBFs and quantifying their effectiveness—was accomplished through experimental testing and

numerical simulations. The experimental component included a series of full-scale frame tests at Lehigh University on a 2-story R = 3 chevron CBF and a 2-story R = 3.25 split-x OCBF. The experimental tests revealed key differences in frame behavior that were influenced by differences in system configuration (e.g. chevron or split-x) and system type (e.g. R = 3 or R = 3.25 OCBF). Observations from these tests and subsequent material characterization tests were essential for calibration of a sophisticated numerical frame model developed in *OpenSees*. Component-level testing of beam-column connections and brace-gusset connections performed in a parallel study at Polytechnique Montréal were used to calibrate this model. The effectiveness of various reserve capacity sources was learned through comparative studies of *OpenSees* models with variations to member sizes, connection details, and modeling assumptions. These numerical simulations included static pushover and incremental dynamic analyses.

The second objective—determining cost-effective methods for providing and increasing reserve capacity in low-ductility steel CBFs as a design strategy—was accomplished through numerical simulations using knowledge from the experimental testing. First, static cyclic numerical simulations were performed on typical 3-story R = 3 CBF and R = 3.25 OCBF designs in both chevron and split-x configurations. The purpose of these simulations was to investigate observations made during the experimental tests regarding potential mechanisms and classes of behavior associated with system type and system configuration. The findings of these simulations were used to classify various seismic detailing and proportioning requirements for the current R = 3.25 OCBF design as either advantageous or disadvantageous from both the perspective of reserve capacity as well as overall collapse prevention performance. Following these classifications, a new SFRS was developed for low

and moderate seismic regions whose design process involves implicit consideration of reserve capacity: the R = 4 OCBF. The viability of this new SFRS was studied alongside the two current low-ductility SFRS alternatives—the R = 3 CBF and R = 3.25 OCBF—through incremental dynamic analyses and a reliability-based performance assessment.

1.4 ORGANIZATION OF THIS DISSERTATION

This dissertation describes the procedure used for investigation of the inelastic behavior and collapse prevention performance of low-ductility steel CBFs. It includes nine chapters:

- Chapter 1: Introduction

  A summary of the current seismic design methodology in the U.S. is provided. The concept of seismic hazard is presented to highlight defined areas of higher and lower seismicity in the U.S. and explain the rationale behind different seismic design requirements in these areas. Three steel building frame SFRSs are presented: the SCBF, which is associated with high seismic design, and the OCBF and R = 3 CBF, which are associated with low and moderate seismic design. The concept of reserve capacity and its heightened importance in low-ductility systems is introduced. An overview of the research is given, including the research need, program, objectives, and scope.

- Chapter 2: Literature Review

  Information on reserve capacity in steel structures is consolidated and divided into four categories: (1) behavior of steel structures during seismic events; (2) experimental and numerical component studies; (3) system-level numerical simulations; and (4) large scale experimental tests.

- Chapter 3: Reserve Capacity Component Study

The prototype building—that serves as the basis for the experimental frame testing program—is defined. A numerical model was created in OpenSees to investigate the reserve capacity of this prototype 3-story building with a chevron R = 3 CBF for its SFRS. A combination of static pushover analyses and dynamic analyses was used to assess the impact of modeling assumptions and design enhancements for components previously identified as contributors to reserve capacity.

- Chapter 4: Full-Scale Experimental Frame Tests

  Two experimental tests were conducted on full-scale 2-story steel SFRSs: one designed with braces in the chevron configuration using the "R = 3" classification, and one designed with braces in the split-x configuration using the OCBF (R = 3.25) classification. A demand-to-capacity ratio prediction method is presented and compared with the observed results from the two test units. Behavioral assessments are provided in the context of the influence that the two variables which defined the test units—system type and system configuration—had on both reserve capacity as well as ductility.

- Chapter 5: Numerical Building Model

  A numerical building model was constructed using OpenSees so that rigorous investigation into the reserve capacity of low-ductility steel CBFs could begin. The building model incorporates nonlinear brace behavior, beam and column degradation after the formation of plastic hinges, fiber discretized elements for beam-column connections, and brace-gusset weld fracture. Several techniques that were developed to mitigate convergence issues experienced during the use

of this complex and highly nonlinear model are presented. The effectiveness of the model was verified by simulating the previous experimental frame tests (Chapter 4).

- Chapter 6: Cyclic Static Parametric Study of 3-Story Frames

  The calibrated OpenSees model from Chapter 5 was used to evaluate the relative influence that the two design parameters (system type and system configuration) had on limit state progression and reserve capacity through numerical simulations of 12 unique 3-story frames. The consequence of slight variations to member sizes is presented in this chapter, as each building was designed twice: once using the approximate fundamental period (Ta), and once using the calculated fundamental period (Tc = 1.6Ta). The large variability of brace-gusset welded connection capacity is discussed, and additional frame designs are simulated with the assumption of amplified weld capacities of up to 80%, which was the largest observed overstrength for these connections in the previous experimental frame tests (Chapter 4).

- Chapter 7: The R = 4 OCBF

  A new SFRS is proposed for use in regions of low and moderate seismicity, the R = 4 OCBF. The proposed R = 4 OCBF is intended to replace the current R = 3.25 OCBF, which is the less desirable of the two current alternatives for low-ductility design (R = 3 CBF, R = 3.25 OCBF). While the R = 3 CBF is now the more popular of the two systems due to its lower costs and design simplicity, the sources of reserve capacity that develop and aid in collapse of this system are not documented. Thus, the intent of the R = 4 OCBF is to provide a cost-

effective alternative to the R = 3 CBF but with the added benefit of detailing requirements which are based on the notion of reserve capacity and ductility. The intention is for this safer and more robust R = 4 OCBF system to become the de-facto standard for low and moderate seismic design.

- Chapter 8: Performance Assessment of Low-Ductility CBFs

  A comprehensive performance assessment of low-ductility CBFs was conducted using a sophisticated OpenSees building model and dynamic numerical simulations. The assessment was conducted on a matrix of 18 case study buildings which varied by number of stories (3, 6, and 9), system configuration (chevron, split-x), and system type (R = 3 CBF, current R = 3.25 OCBF, proposed R = 4 OCBF). A series of incremental dynamic analyses (IDAs) was performed on each case study building, and patterns were identified regarding the collapse scale factors depending on the three variables that defined the test matrix (system type, system configuration, number of stories). The IDA results were used within the FEMA P695 framework (FEMA, 2009) to create adjusted fragility curves and assess collapse prevention performance.

- Chapter 9: Conclusions, Recommendations, and Future Work

  Conclusions from the research are presented. A recommendation is provided to adopt the proposed R = 4 OCBF in the upcoming 2022 AISC Seismic Provisions. Suggested avenues for future research are discussed, such as: (1) improving numerical models; (2) further full-scale and component-level testing; (3) refining the proposed R = 4 OCBF provision; (4) further numerical

simulations; (5) incorporating reserve capacity in high seismic design; and (6) using reserve capacity during other low-probability hazards.

CHAPTER 2

LITERATURE REVIEW

A comprehensive review of literature was performed to provide proper context and to focus the subsequent experimental testing and numerical simulations so that they would be of most value to the structural engineering community. Pertinent literature on reserve capacity was divided into four categories: (1) behavior of steel structures during seismic events; (2) experimental and numerical steel connection studies; (3) system-level braced frame numerical simulations; and (4) large-scale braced frame experimental tests. A large part of the information presented here was extracted from studies and reports where reserve capacity was not the primary focus, and in some instances not discussed at all.

2.1 SOURCES OF RESERVE CAPACITY

This chapter reveals and discusses sources of reserve capacity. Reserve capacity has been observed in actual seismic response of steel structures, experimental laboratory tests, and numerical simulations. A braced frame schematic in Figure 2.1 identifies notable sources of reserve capacity: rotation and flexural capacity of connections, yielding and flexural capacity of beams and columns, and brace reengagement in compression following connection fracture.

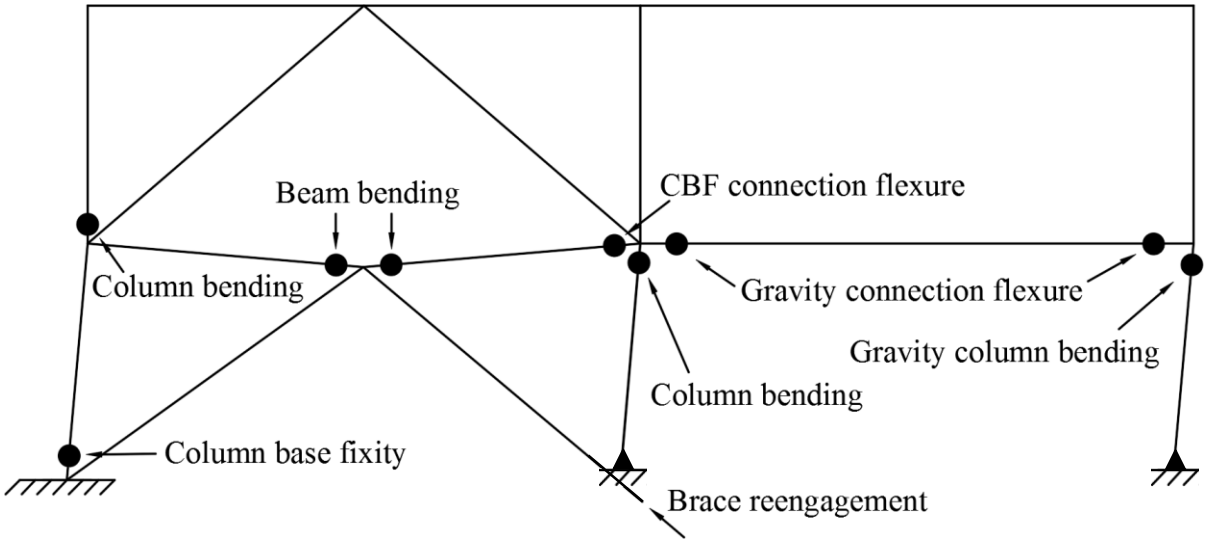

Figure 2.1 – Sources of reserve capacity.

2.2 BEHAVIOR OF STEEL STRUCTURES DURING SEISMIC EVENTS

Field investigations after large seismic events can provide evidence about structural behavior and reveal unexpected structural failures that become useful for updating structural design codes. Over the last few decades, several major earthquakes have caused significant damage to steel building frame systems. Studying and developing an understanding of structural steel building behavior during these earthquakes—particularly with regards to brittle failure types and their locations—allows for conclusions to be drawn as to how reserve capacity contributed to structural performance and prevented collapse.

2.2.1 1985 Mexico City Earthquake

The 1985 Mexico City Earthquake resulted in severe damage or collapse in 12 steel frame buildings, many of which were constructed over three decades prior to the event (Hanson and Martin, 1987). In general, the performance of the then-modern steel structures was exceptional, which highlighted the effectiveness of the many robust updates made to the Mexico building codes following earthquakes in 1957 and 1979. One major exception existed

in the case of the Pino Suárez building complex, which consisted of five high-rise steel buildings with V- and X-braced CBFs for their seismic force resisting systems (SFRSs). During the earthquake, one of the complex's 22-story high-rise buildings collapsed onto a neighboring 15-story building. Collapse was attributed to large overturning demands that caused the steel plate built-up box section columns to buckle locally before the braces within the SFRS could buckle (Osteraas and Krawinkler, 1989; Ger et al., 1993). This undesirable performance was recognized by the U.S. structural engineering community and requirements for increased axial force in column design were implemented in the 1988 Uniform Building Code (Diebold et al., 2008). The collapse of the Pino Suárez building provided a real-world example that supported the general idea that column buckling could lead to disproportionate collapse. Despite this, the ability of reserve capacity to prevent collapse when a severe limit state occurs should not be overlooked: two buildings within the complex experienced analogous local-buckling associated fractures and did not collapse (Osteraas and Krawinkler, 1989).

2.2.2 1994 Northridge Earthquake

In the aftermath of the 1994 Northridge Earthquake, an extensive reconnaissance effort was launched to assess the damage to building structures (Bertero et al., 1994; Blakeborough et al., 1997; Ghosh, 1994; Hall et al., 1994; Ross and Mahin, 1994; Tremblay et al., 1995; Youssef et al., 1995). In the San Fernando Valley region, 184 buildings were reported as destroyed (less than 0.1% of total building stock), while over 5,500 were reported as damaged (Blakeborough et al., 1997). One of the more significant findings from this field investigation was that no steel building collapsed, an especially interesting discovery considering that many of these steel buildings experienced undesirable brittle limit states within their SFRS.

In steel buildings, the most systematic damage occurred in moment resisting frames (MRFs) (Ross and Mahin, 1994; Tremblay et al., 1995; Youssef et al., 1995). The limit state most observed in these structures was brittle failure of the beam-column moment connections. This was a troubling discovery considering that the primary function of a beam-column connection within a MRF is to develop the plastic moment capacity of the attached beam ($M_{p,beam}$) which may then yield and provide system ductility. Hundreds of steel MRFs experienced this undesirable limit state during the Northridge Earthquake, neutralizing the effectiveness of the SFRS. These connections, which included full-penetration welds on both upper and lower flanges and bolted web shear tabs, often experienced weld fracture in the bottom flange (Tremblay et al., 1995).

For steel structures that used a CBF as their SFRS, the predominant limit state observed was brace buckling (Tremblay et al., 1995). While this is an accepted limit state for CBFs, some of the braces also experienced detrimental local buckling. Local buckling is undesirable because it accelerates the accumulation of low-cycle fatigue damage and eventual fracture of braces at their midspan; this brittle limit state decreases overall structural ductility and places a heightened demand on the reserve system of beams, columns, and beam-connections within the SFRS. The observation that none of the steel structures with CBFs collapsed was a sign that the reserve strength from these sources was sufficient. To confirm this claim, Rai and Goel (2003) performed a computational study on a building that was damaged during the Northridge Earthquake, and found that the building's gravity columns had adequate lateral force resisting strength to prevent collapse following multiple brace fractures within a story. In addition to brace buckling, other brittle limit states observed within CBFs during this earthquake included fractures of brace-gusset connections, cracking of base plates, and failure of anchor bolts at

column bases due to uplift demands (Tremblay et al., 1995). The Earthquake Engineering Research Institute (EERI) reconnaissance report noted that many of the base plate failures were started by weld fractures and were a result of large overturning forces (Krawinkler et al., 1996).

Beyond the observation that none of the steel structures collapsed, and that no loss of life was associated with the damaged steel buildings, the occurrence of unexpected brittle behavior and the uncertainty associated with collapse prevention under a more severe earthquake motivated a major investigation. The U.S. Federal Emergency Management Agency (FEMA) started a 6-year program (the SAC Joint Venture) with the intent of improving modern seismic design in consideration of the lessons learned from the Northridge Earthquake, particularly in regards to connections of MRFs (Mahin et al., 2002). Research conducted as part of the SAC Joint Venture identified the concept of reserve capacity, particularly with respect to contribution of gravity connections to lateral resistance (Liu and Astaneh-Asl, 2000; Liu and Astaneh-Asl, 2004). The lack of steel building collapses despite the large amount of fractures and overall damage sustained was a sign that reserve capacity played a major role during this earthquake.

2.2.3 1995 Kobe Earthquake

Occurring exactly one calendar year after the Northridge Earthquake, the 1995 Kobe Earthquake caused significantly more damage to buildings and homes, and resulted in a larger death toll. Over 100,000 buildings and homes collapsed, and 400,000 were damaged (UNCRD, 1995; Chandler, A. (Ed.), 1997). Many of these collapses were associated with traditional low-rise timber frame homes, however, which accounted for over 80% of the building stock (Chandler, A. (Ed.), 1997). In preliminary reconnaissance by the Architectural Institute of Japan (AIJ), over 4,500 engineered buildings were reported damaged, with just over 1,000

reported as collapsed or damaged beyond repair (Nakashima M. and Bruneau, M. (Eds.), 1995). Of these 4,500, over 1,000 were steel buildings, of which 10% (100) collapsed and another 30% (300) experienced severe damage (Nakashima et al., 1998). The number of steel structure collapses was surprising considering that zero collapses occurred in the Northridge Earthquake. Of the steel buildings that experienced damage, about 70% used MRFs in each direction for their SFRS while the remaining 30% used CBFs in at least one direction (Nakashima, 1995).

Damage to MRFs in the Kobe Earthquake was like those in Northridge, and consisted primarily of welded beam-column moment connection fractures (Tremblay et al., 1996). Unlike Northridge MRFs, in which the beam-column connections fractured before developing $M_{p,beam}$, the full-penetration welded beam-column connections in Kobe's modern MRFs often fully developed $M_{p,beam}$, as indicated through frequent observation of beam yielding. In contrast, Kobe's older MRFs used fillet welds that fractured before the beams could yield as intended. Later it was discovered that many of these fillet welds were undersized. Many of the surveyed MRFs that collapsed used these weaker fillet welds, while only three MRFs that used full penetration welds collapsed (AIJ, 1995).

Damage to CBFs in the Kobe Earthquake varied, though the severity of damage was higher in older buildings that used small rods and flat bars for bracing members (Nakashima et al., 1998). Brittle fracture at bolt holes was observed in the bolted brace connections used in these older CBFs, a similar limit state to the fractured brace-gusset connections of Northridge CBFs (Tremblay et al., 1996). Other limit states observed within CBFs included but were not limited to brace-gusset weld fracture, local brace buckling and low-cycle fatigue fracture, and fracture of gusset-column and gusset-beam welds (Tremblay et al., 1996; Nakashima et al.,

1998). Like Northridge, limit states within the braces changed the primary functionality of the CBF SFRS and placed an increased demand on beams and columns through frame action and column continuity. The primary source of reserve capacity that was believed to have helped prevent collapse of CBFs in the Kobe Earthquake was the fully rigid beam-column connections within the SFRS, which is typical of Japanese seismic design practices (Tremblay et al., 1996). Inspectors noted that severe yielding occurred within the beams of many of these CBFs, a sign that the moment-connected beam-column connections were enough to develop $M_{p,\,beam}$ within the braced frames and contributed to a beneficial reserve capacity mechanism (Tremblay et al., 1996). Not all damage types were beneficial from a reserve capacity perspective, however, as local buckling and brittle fracture in columns was also observed (Chandler, A. (Ed.), 1997)—which was previously identified as being one of the predominant sources for collapse of the Pino Suárez building in the 1985 Mexico City Earthquake (Osteraas and Krawinkler, 1989; Ger et al., 1993).

Of the 59 steel buildings that collapsed in the Kobe earthquake and had an identifiable SFRS, 49 used a MRF, while only 3 used a CBF and the remaining 7 used a combination of both (AIJ, 1995; Tremblay et al., 1996). Considering the discrepancy in the number of collapses observed amongst system types and their associated limit states, CBFs in Kobe had significantly more reserve capacity than MRFs. The heightened reserve capacity in CBFs was attributed to their rigid beam-column that allowed the beams and columns within the SFRS to act as a backup MRF system following damage to the CBF.

2.2.4 2010 Chile Earthquake

Due to the high cost of steel relative to other construction materials in Chile, very few buildings used steel SFRSs (Saatcioglu et al., 2013). Despite this, the seismic behavior of a

select few steel SFRSs that were found in industrial facilities are relevant to reserve capacity (Tremblay et al., 2013).

Brace buckling occurred in many of the frames investigated by Tremblay et al. (2013), though, unlike Northridge and Kobe, no fractures were observed in the plastic hinge region. Instead, brace failures all occurred at the connections. For one braced frame investigated, the brace-gusset connections comprised side plates bolted to the braces that were welded to gusset plates via transfer plates. During the earthquake, failure occurred at the welds between the side plates and the transfer plates, but remarkably, this fractured connection still transferred loads in compression through bearing on the columns following weld fracture (Figure 2.2a). This reserve capacity mechanism, called "brace reengagement" (Figure 2.1), was also photographed following the Kobe Earthquake (Figure 2.2b). Brace reengagement uniquely has the same reserve capacity source (braces) as its primary mechanism for resisting lateral forces. An experimental study on brace reengagement is presented in Section 2.3.3 (Davaran et al., 2014).

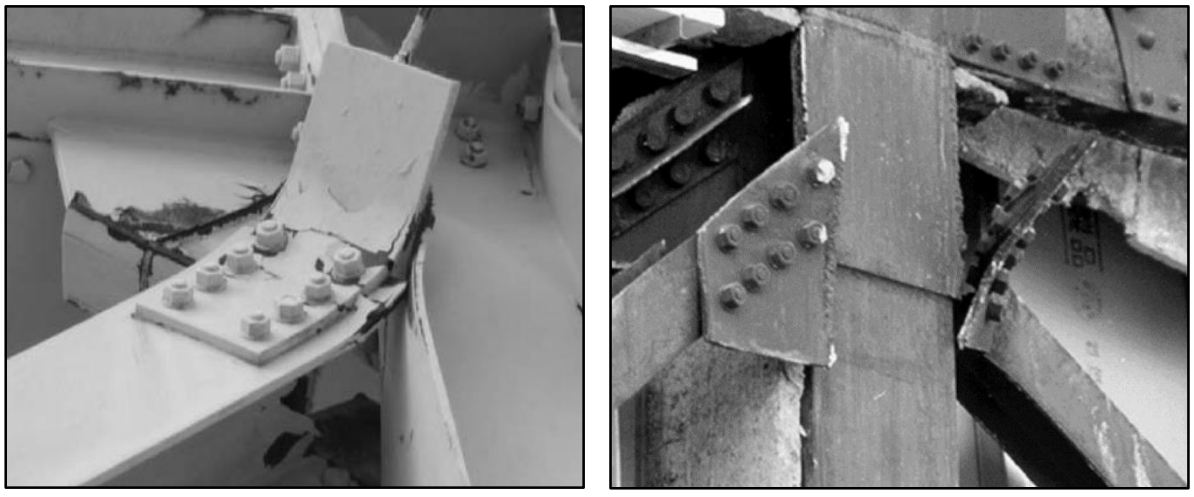

(a) (b)

Figure 2.2 – Brace reengagement observed during: (a) the 2010 Chile Earthquake (modified from Tremblay et al., 2013); and (b) the 1995 Kobe Earthquake (modified from Di Sarno and Elnashai, 2009).

2.2.5 2011 Christchurch Earthquake

A preliminary damage assessment of building stock following the 2011 Christchurch Earthquake found that 1,933 of 3,621 building checked within Christchurch's central business district had been labeled as collapsed or in need of demolition, while 826 had been labeled as in need of significant repair (Kam et al., 2011). Of the 3,621 buildings checked, 62% of unreinforced masonry buildings were labeled as collapsed or in need of demolition, while 14%, 16%, and 19% of timber, reinforced masonry, and reinforced concrete buildings, respectively, were labeled similarly. Only 7% of steel buildings were flagged for demolition, which was a sign they performed better than buildings primarily composed of other materials during this earthquake (Smyrou et al., 2011).

Field investigations of steel buildings following the Christchurch Earthquake were performed by Clifton et al. (2011), and the lessons learned from the event were summarized by MacRae et al. (2015). Of the steel buildings examined, SFRSs included CBFs, MRFs, and eccentrically braced frames (EBFs). In general, the steel structures performed well and avoided collapse despite experiencing undesirable limit states such as fractures of links in EBFs and brace-gusset connections in CBFs. In a hospital parking garage which was investigated, six EBFs were used at each level and in each primary direction; this redundancy contributed to reserve capacity following link fractures in one of the six EBFs as demand was shifted to the remaining five EBFs. Although not a direct comparison, the beneficial concept of redundant SFRSs is loosely related to the notion of dual-systems, in which reserve capacity is often provided by a flexible backup SFRS (i.e. MRF) after damage to a stiff primary SFRS (i.e. CBF).

2.2.6 The Influence of Reserve Capacity on Structural Performance

Site investigations following the Mexico City, Northridge, Kobe, Chile, and Christchurch Earthquakes revealed a variety of unexpected brittle behaviors. Although engineers have a sense of confidence in how their buildings will behave in an earthquake, structural behavior is often far more complicated. Unanticipated limit states can and will occur as shown through the summaries of historic earthquakes in this section. Despite the various degrees of design code sophistication in these countries, each earthquake resulted in brittle failures or undesirable damage within the steel SFRSs. In the wake of these unanticipated and unsatisfactory limit states, many beneficial aspects of reserve capacity were elicited and aided with collapse prevention. Various sources of reserve capacity such as beam-column connection capacity, brace reengagement, and column continuity were believed to have helped prevent collapse of these structures. While SFRS damage from these earthquakes informed the refinement of modern seismic design, engineers should consider the effect reserve capacity had on collapse prevention performance and seek ways to enhance its effectiveness so that unexpected limit states will be less likely to result in building collapse in the future.

2.3 EXPERIMENTAL AND COMPUTATIONAL CONNECTION STUDIES

This section gives an overview of relevant research studies which investigated specific sources of reserve capacity related to connections: (1) beam-column connections that are part of the gravity framing system (gravity connections); (2) braced frame beam-column-gusset connections (CBF connections); and (3) brace reengagement.

2.3.1 Gravity Connections

Over the past few decades, several experimental studies have focused on quantifying the stiffness, strength, and ductility of the connections found in gravity framing systems (gravity connections). These connections are typically composed of plates and angles bolted and/or welded to a beam web, and they are assumed to have no lateral force resisting flexural capacity in design. As the Northridge Earthquake revealed, these connections have significant flexural stiffness and give system-wide reserve capacity to help prevent collapse.

Some of the first full-scale cyclic tests on gravity connections were conducted by Astaneh et al. (1989) to investigate the hysteretic moment-rotation behavior of six double web angle (DWA) connections that were welded to the beam web and bolted to the column flange (welded-bolted). Although half of the tests used older and now-dated ribbed bolts, the others used 19 mm. [3/4 in.] diameter A325 bolts that are still commonly used today. The connection tests with A325 bolts consisted of 2L3x3x3/8 angles and used 6.4 mm. [1/4 in.] fillet welds with 4–6 rows of bolts. These DWA connections with 4, 5, and 6 rows of bolts developed ultimate moment capacities ($M_{p,conn}$) of 68 kN-m [50 kip-ft], 122 kN-m [90 kip-ft], and 176 kN-m [130 kip-ft], respectively, and were accompanied by a clear trend of increasing stiffness with number of bolt rows. The connections with 5 and 6 rows of bolts were attached to an S24x80 beam with $M_{p,beam}$ = 830 kN-m [612 kip-ft], and thus developed 0.15–0.20$M_{p,beam}$. Failure modes consisted of bolt fracture and angle fracture near the fillet, at ultimate rotations

of 0.03–0.05%. Moment rotation behavior for the specimens with 4 and 6 rows of bolts are provided in Figure 2.3.

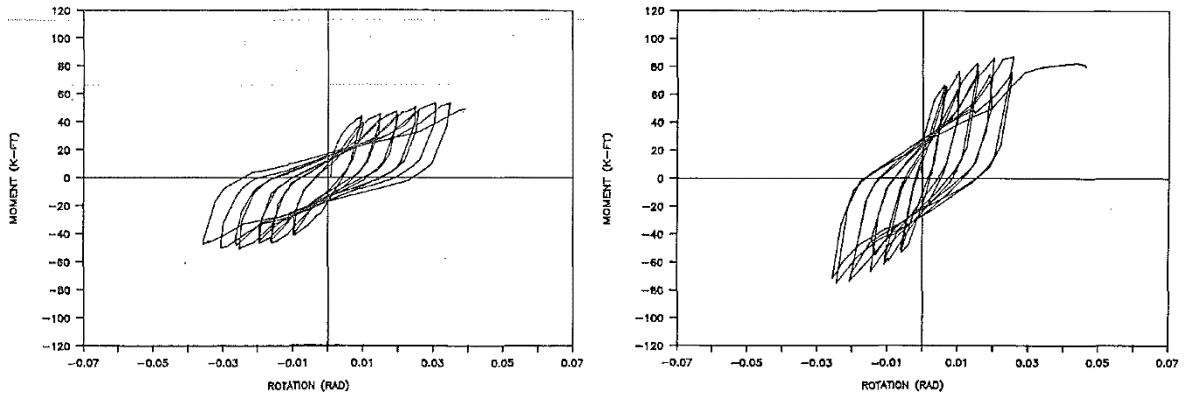

(a) (b)

Figure 2.3 – Moment-rotation behavior for 2L3x3x3/8 angles with 19 mm. [3/4 in.] A325 bolts and 6.4 mm. [1/4 in.] fillet welds attached to an S24x80 beam: (a) 4 rows of bots; and (b) 6 rows of bolts (Astaneh et al., 1989).

Liu and Astaneh-Asl (2000) expanded the study on gravity connections by considering the influence a concrete slab had on their flexural stiffness, strength, and ductility. The authors theorized that the composite action of the attached floor slab would provide a significant increase in flexural capacity and cause these connections—which are often idealized as pins —to behave like partially-restrained connections. They found that bare steel shear tabs developed 0.15–0.20$M_{p,beam}$ while sustaining ductile behavior through drifts of up to 0.15% (Figure 2.4a). When a concrete slab was added, the connection strength increased to 0.30–0.45$M_{p,beam}$ (Figure 2.4b). This additional strength was not sustainable, as crushing of the slab typically occurred at drifts of 0.04% and resulted in loss of the beneficial composite action. Of all configurations, a supplemental seat angle provided the biggest improvement to performance, increasing the connection capacity to 0.70$M_{p,beam}$ for drifts of up to 0.09%.

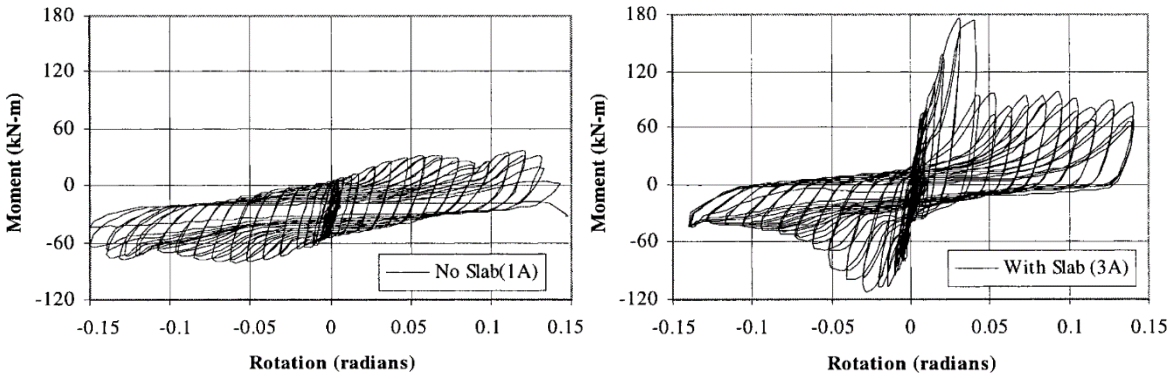

(a) (b)

Figure 2.4 – Moment-rotation for simple shear tab connections: (a) without slab; and (b) with slab (Liu and Astaneh et al., 2000).

The ability of gravity connections to provide flexural capacity was further investigated by Abolmaali et al (2003) through cyclic tests of 20 DWA connections to a W16x45 beam with varying number of bolts, weld thickness, angle height, and angle thickness. Twelve connections were welded-bolted and the remaining 8 were bolted-bolted. The 12 welded-bolted DWA connection suite reached an average moment capacity of $0.33M_{p,beam}$ and average ultimate rotation of 0.03–0.04%. The 8 bolted-bolted DWA connection suite reached an average moment capacity of $0.11M_{p,beam}$ and average ultimate rotation of 0.05%. The increased flexibility and decreased capacity of the bolted-bolted connections was attributed to bolt slip and elongation of bolt holes.

Inspired by the Northridge Earthquake and as a part of the SAC Joint Venture (Mahin et al., 2002), Liu and Astaneh-Asl (2004) continued their research program from 2000 and further studied gravity connections. In these later studies, the authors considered factors such as number of bolts in the shear tab, type of concrete, use of slab reinforcement, presence of a column web cavity, and whether the connection was made to the column flange or column web. The authors provided a method for calculating the moment capacity of shear tab connections.

2.3.2 Concentrically-Braced Frame Connections

Beam-column connections in braced bays (CBF connections) may also provide reserve capacity. Unlike gravity connections, these connections often include both a beam-column component and a gusset plate component (gusset-column), that latter of which gives a significant increase in flexural capacity. Despite this, the moment capacity of CBF connections and their ability to resist lateral demands are typically ignored in design. One of the best demonstrations of the ability for CBF connections to lend reserve capacity was the Kobe Earthquake (Section 2.2.3), where rigid CBF connections helped prevent collapse following brace fracture.

One of the first experimental studies focused specifically on cyclic flexural behavior of CBF connections was conducted by Stoakes and Fahnestock (2010). The authors compared the flexural hysteresis of a baseline double angle beam-gusset-column connection with seven other configurations, which included end plates, double angles with seat angles, complete-joint-penetration welds, and modified bolt layouts. They found that an end plate connection provided in increase in flexural strength over a typical DWA connection, but bolt fracture led to sudden loss of capacity. An increase in angle thickness had a large impact on negative moment strength, while the inclusion of a seat angle had a large impact on positive moment strength. Although all the modifications studied showed improvements over the baseline DWA connection detail, the DWA configuration with a supplemental seat angle provided the best balance of strength and deformation capacity, developing $1.00M_{p,beam}$ at drifts of up to 0.05%. This constituted a 50% increase in capacity over the connection without a seat angle (Figure 2.5). Observations from this experimental study assisted with the development of numerical

spring models that captured the moment-rotation hysteresis of typical CBF connections (Stoakes and Fahnestock, 2012).

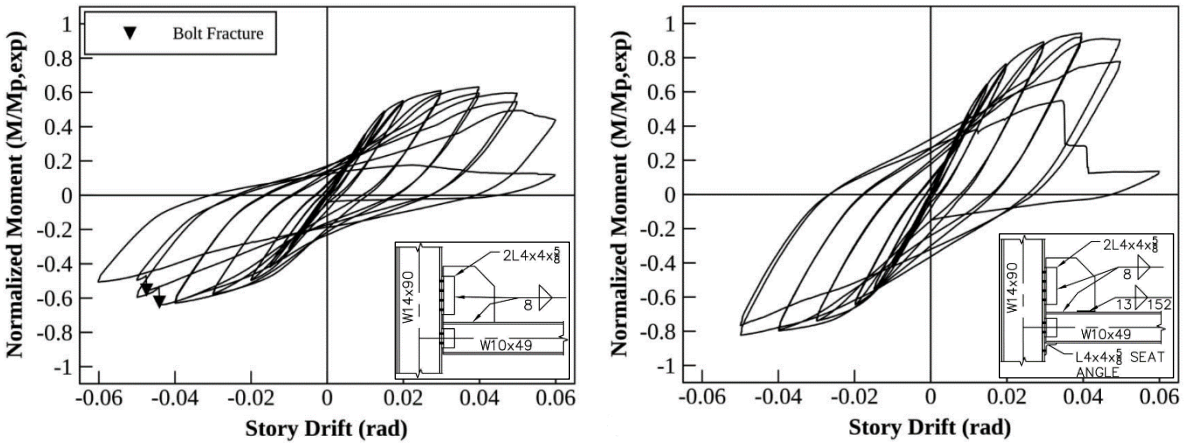

(a) (b)

Figure 2.5 – Moment-rotation hysteresis for CBF double web angle connection: (a) without seat angle; and (b) with seat angle (Modified from Stoakes and Fahnestock, 2010).

2.3.3 Brace Reengagement

Brace reengagement is a new topic in reserve capacity for seismic collapse prevention that was observed in select CBFs that were damaged in the Kobe and Chile Earthquakes. The first and only study to date with an exclusive focus on brace reengagement was performed by Davaran et al. (2014). The authors studied the behavior of four typical and two atypical chevron brace-gusset welded connections. Following weld fracture or net section rupture, the braces reengaged in compression when the interior of the HSS slot contacted the gusset plate. For slender gusset plates, the failure modes were asymmetrical, leading to buckling in the connection. Brace reengagement had capacities that ranged from 100% to 200% of the bearing capacity of the damaged connection, calculated from the steel ultimate stress acting over the bearing area, and with a significant reduction in stiffness.

2.4 SYSTEM-LEVEL BRACED FRAME NUMERICAL SIMULATIONS

System-level braced frame numerical simulations offer insight into the impact of reserve capacity mechanisms on global structural response.

2.4.1 Influence of Gravity Connections

A system-level static pushover (SPO) analysis considering the impact of beam-column connections was performed by Callister and Pekelnicky (2011) on an existing 2-story low-ductility CBF in California. The authors modeled brace connection fracture and considered partially-restrained gravity connections using the procedures developed by Liu and Astaneh-Asl (2004). In their SPO analysis, brace connection fracture occurred and was associated with a large drop in base shear (Figure 2.6). Following this, the reserve system of partially-restrained gravity connections was activated and base shear increased at a decreased stiffness, eventually passing the original elastic capacity. The authors concluded that gravity connections have enough strength, ductility, and stiffness to act as a backup lateral system to a non-ductile CBF. This study estimated potential reserve capacity in existing structures to find if seismic retrofit was needed.

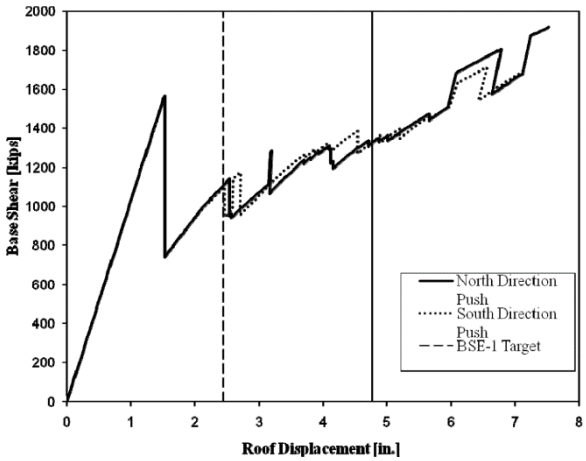

Figure 2.6 – Pushover of 2-story low-ductility CBF (Callister and Pekelnicky, 2011).

Hines et al. (2009) showed that beam-column connections may be used to enhance reserve capacity at the system level by performing numerical simulations of 3-, 6-, 9-, and 12-story CBFs with *R*-values of 2, 3, and 4 (R2, R3, R4 – Figures 2.7) and without any seismic detailing or proportioning requirements. A fourth configuration was a CBF designed to resist wind load only, coupled with a MRF reserve system (WRS – Figures 2.7). The authors found that moment connecting a part of the gravity framing for a CBF building increased collapse capacity (Figure 2.7) and reduced story shear on the primary lateral force resisting system (LFRS). Moment connecting the gravity frame part of a CBF requires extensive detailing, but the authors noted that the cost of such a configuration is typically four times lower than the cost associated with using moment frames as the primary LFRS. Another significant revelation from this study was that designing for a higher design base shear (lower *R*-value) did not always enhance collapse prevention performance. As select fragility curves from this study show, the 3-story $R = 4$ model outperformed both $R = 2$ and $R = 3$ counterparts (Figure 2.7a)

and the fragility curves of the 6-story R = 2, 3, and 4 models were indistinguishable from one another (Figure 2.7b).

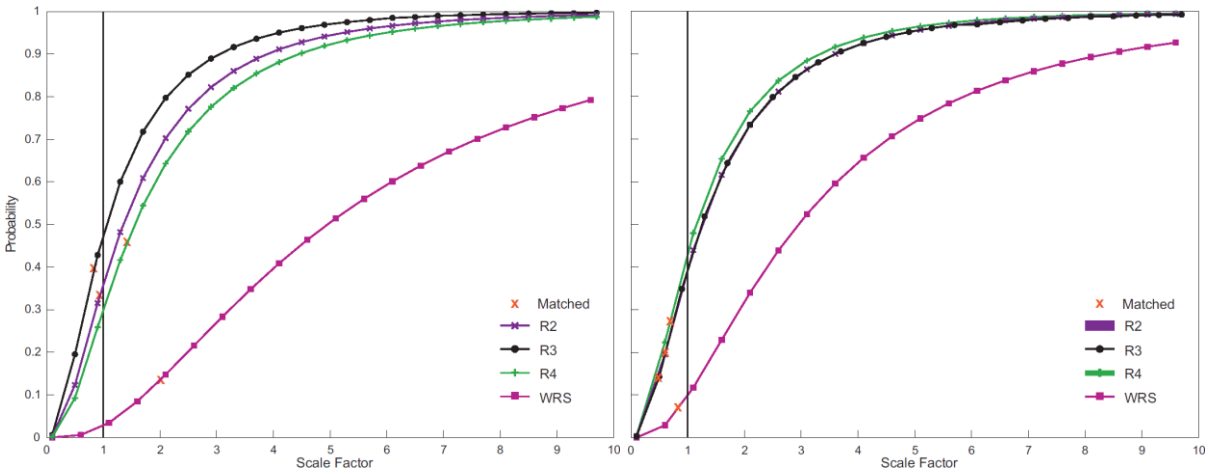

(a) (b)

Figure 2.7 – Performance of low-ductility chevron braced frame building models: (a) 3-story buildings; and (b) 6-story buildings. (Modified from Hines et al., 2009).

2.4.2 Influence of Gravity Columns and Column Base Fixity

The influence that base fixity and column continuity have on reserve capacity of CBF SFRSs was investigated by Tremblay and Stiemer (1994). The authors found that the bending moments induced in a building's columns during an earthquake depended on the differential story drifts of adjacent stories, and thus *P-Δ* effects were mitigated through the avoidance of large drift concentrations within a single story (soft-story collapse mechanism). Moreover, if the columns in a multistory frame were continuous over more than one story, any difference in story drift between two adjacent stories was resisted through column bending, and this reserve capacity source delayed collapse. The authors found that many failures occurred in the first story, and this problem was alleviated by increasing the column base fixity.

Further research on the influence of gravity column contribution was studied by Rai and Goel (2003) through SPO analyses on a representative 4-story chevron CBF from the Northridge Earthquake. The authors found that the building's overall base shear and stiffness dropped abruptly following brace buckling and subsequent fracture, yet the building continued to resist additional base shear following these fractures as the gravity columns began to resist upwards of 30% of the story shear (Figure 2.8). This result suggested that gravity columns could provide a significant reserve capacity in a building following brace buckling or fracture within a CBF SFRS. The authors concluded that the use of nonductile bracing contributed to the vulnerability of this structure, and thus a recommendation was provided to upgrade the structure to a Special Concentrically Braced Frame (SCBF).

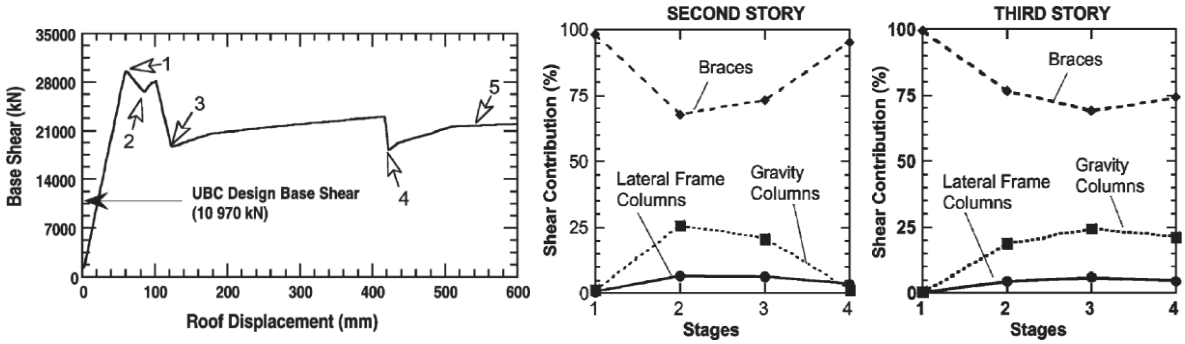

Figure 2.8 – Pushover of a 4-story low-ductility Northridge CBF showing the shear development in gravity columns (modified from Rai and Goel, 2003).

The influence of column stiffness was studied by MacRae et al. (2004) through SPO and dynamic analyses on CBFs with continuous columns. The study showed that if no flexural column stiffness was provided (i.e. from the use of continuous columns) a soft story mechanism and large story drifts would result from a design level earthquake. The authors found that story drift concentration decreased as the column stiffnesses increased. Along with

their findings, the authors provided a procedure for estimating drift concentrations and column moment demand in frames with continuous columns.

The notion of increasing base fixity to improve collapse prevention performance of CBFs was studied by Ji et al. (2009) through comparison of two distinct models: one gravity column bases fixed and one with gravity columns bases pinned. Continuous columns were considered in each model. Like Tremblay and Stiemer (1994), the author discovered that fixed base gravity columns were more effective at reducing drift concentration in the first story than pinned base gravity columns. Additionally, in multi-story CBFs with pinned beam-to-column connections, the author found that drift was prone to concentrate in the first story. This research revealed that a 6-story CBF with a few gravity columns could achieve collapse prevention under a Maximum Considered Earthquake (MCE) level ground motion.

2.4.3 Influence of Beams and Connections in Braced Bays

Rai and Goel (2003) observed that an imbalance in brace forces resulting from buckling or fracture in one brace could cause bending in the floor beams. The resulting mechanism of beam and column hinging within the SFRS (Figure 2.9) was viewed as detrimental, and in placing a strong emphasis on brace ductility and load redistribution, they recommended switching the system type to a SCBF with a 2-story X (split-x) bracing configuration to avoid yielding the beam. The ability of beams and columns within the SFRS to provide reserve capacity through frame action is discussed further in a summary of recent experimental testing of steel CBFs in Section 2.5.2.

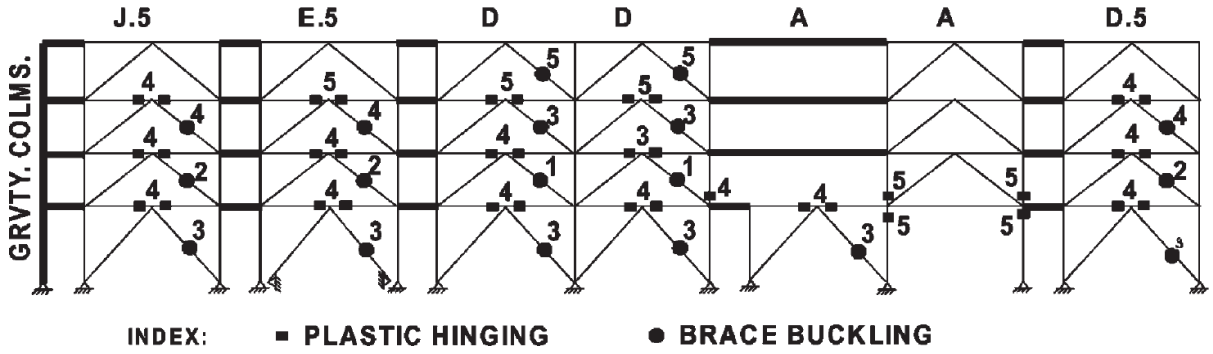

Figure 2.9 – Plastic hinges in the SFRS from a pushover analysis (Rai and Goel, 2003).

When the CBF connection spring model (Stoakes and Fahnestock, 2012) developed from experimental testing by Stoakes and Fahnestock (2010) was incorporated in building models (Stoakes, 2012), collapse prevention performance was significantly improved over the baseline case that assumed pinned CBF connections. The amount of reserve capacity provided by the CBF connections increased with beam depth (Figure 2.10).

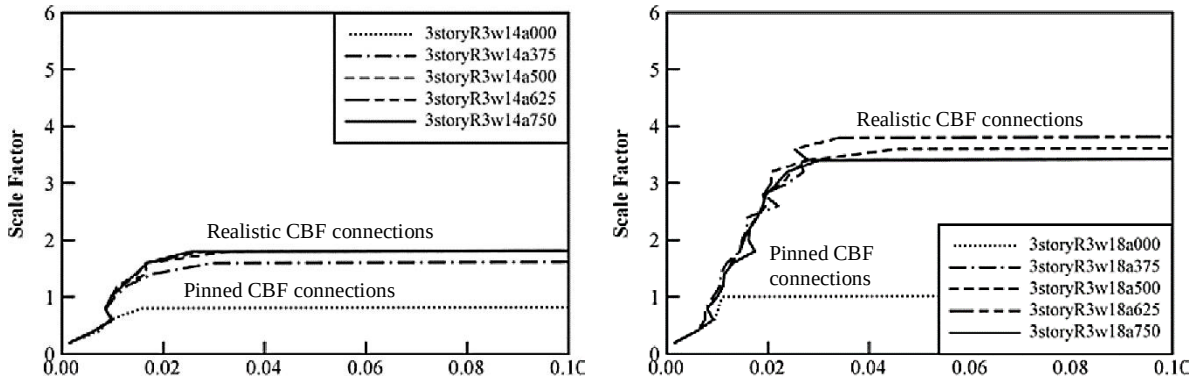

(a) (b)

Figure 2.10 – Impact of modeling realistic CBF connections on collapse prevention performance: (a) W14 beams in CBF; (b) W18 beams in CBF (modified from Stoakes, 2012).

Stoakes found that $M_{p,beam}$ significantly affected available reserve capacity and resulting collapse prevention performance. Flexural behavior at the midspan of beams within the CBFs simulated was observed following brace-gusset weld fracture within a given story, which caused the remaining story to behave similarly to a long-link EBF (Stoakes, 2012). The combined benefit of the provided beam flexural reserve strength through this mechanism and more exact CBF connection behavior was revealed in the collapse assessments performed by Stoakes. (Figure 2.11) As shown by Figure 2.11, all 3-story building models with W14 beams had a greater than 10% probability of collapse (Figure 2.11a), while all but one of the 3-story building models with W18 beams had less than a 10% probability of collapse, except for the pinned CBF connection case (Figure 2.11b).

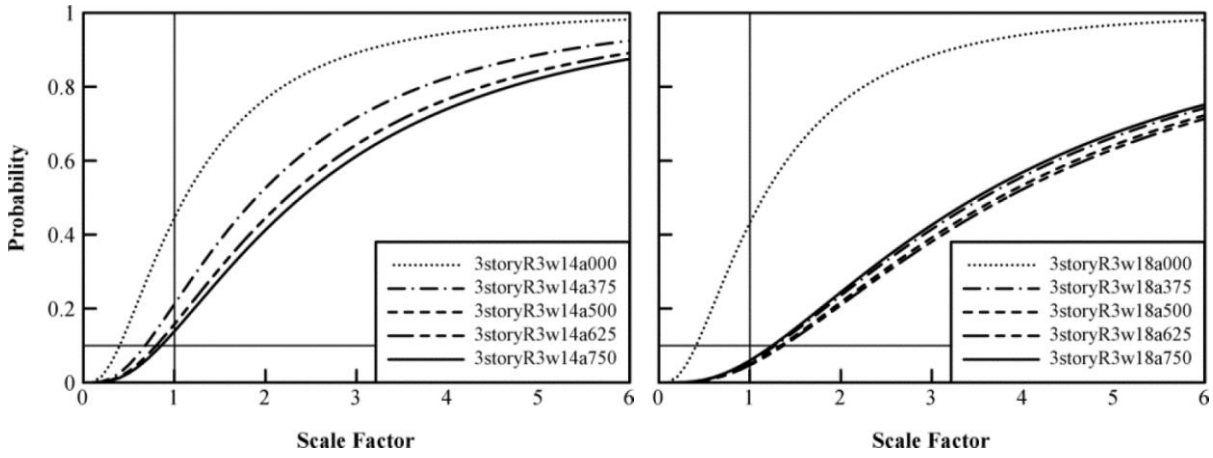

(a) (b)

Figure 2.11 – Collapse prevention performance of 3-story chevron braced frame building models: (a) with W14 beams; and (b) with W18 beams. (Modified from Stoakes, 2012).

2.5 LARGE SCALE EXPERIMENTAL BRACED FRAME TESTS

This section summarizes relevant tests of low-ductility CBFs that have been performed in the past few decades, and presents information about the evolution of high-ductility design

provisions to highlight the significantly larger volume of testing performed on high-ductility CBFs during this time.

2.5.1 US-Japan Cooperative Tests

In 1979 the *U.S. Japan Cooperative Earthquake Research Program Utilizing Large-Scale Testing Facilities* (UJ-CERP) was started with the purpose of improving seismic safety and design practices in both countries. One of the primary components of this collaborate effort was a first-of-its-kind testing program of large-scale steel CBFs and associated small-scale frame tests. Acknowledging the difficulty in replicating connection sizes in small-scale frame tests in combination with the knowledge that connection behavior can significantly influence reserve capacity, the observations presented here are exclusively from the large-scale or half-scale tests.

In 1983, as a part of the UJ-CERP, a full-scale 2-by-2 bay 6-story building using a chevron CBF as its primary SFRS was designed consistent with the then-current U.S. Uniform Building Code (UBC, 1979) and Japanese codes. The building was constructed and tested at the Large Size Structures Laboratory of the Building Research Institute (BRI) in Tuskuba, Japan (Foutch et al., 1987; Roeder et al., 1987; Yamanouchi et al., 1989). Consistent with Japanese practice, a moment connection was provided at every beam-column joint. Thus, the building's SFRS was a dual system, composed of a single stiff CBF with several flexible MRFs. A floor plan and elevation view of the building are shown in Figure 2.12.

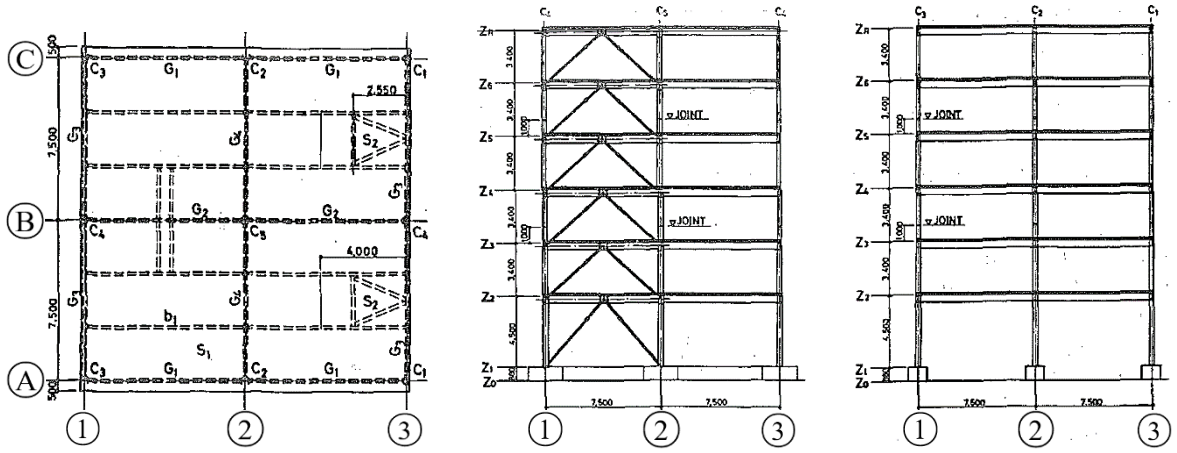

Figure 2.12 – UJ-CERP 6-story steel building: (a) floor plan; (b) elevation line [B]; and (c) elevation lines [A] and [C] (modified from Foutch et al., 1987).

When subjected to a scaled ground motion with peak acceleration of 0.51g, the building's CBF experienced significant amounts of brace buckling. While only minor brace buckling was observed in Stories 1, 4, and 5, one Story 3 brace ruptured completely, while both Story 2 braces experienced partial tearing of over half their section at mid-length where a hinge had formed. The test was stopped shortly after significant brace damage accumulation in Stories 2 and 3 to limit damage for later tests. Although the full sequence of limit states was not tested, valuable reserve capacity observations were still extractable from the results. For example, the viability of a reserve dual system created by moment-connecting beam-column connections was confirmed. While the braces carried 80% of the total shear in the elastic range (20% carried by the MRFs), the shear contribution dropped to only 40% after the Story 2 and 3 brace tearing and fractures occurred, with the MRFs carrying the other 60% of the lateral load. This beneficial dual-system behavior was further confirmed several years later by the excellent performance of steel CBF buildings in the 1995 Kobe Earthquake, where rigid beam-column connections were employed. Reserve capacity was also provided through frame action

associated with beam and column bending from within the CBF in Stories 2 and 3 where brittle limit states were observed (Figure 2.13).

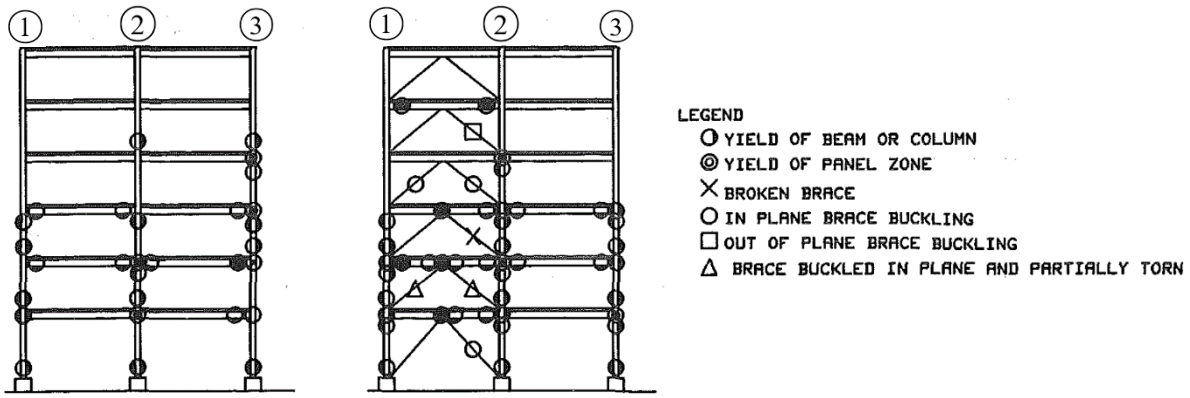

(a) (b)

Figure 2.13 – UJ-CERP 6-story steel building, observed damage in: (a) MRFs: elevation lines [A] and [C]; and (b) CBF: elevation line [B] (modified from Foutch et al., 1987).

Another part of the UJ-CERP included 6 half-scale tests performed at the CBI (Fukuta et al., 1989). The test set-up consisted of a 2-bay 3-story chevron CBF, which was designed to mimic the lower three stories of the primary SFRS (Figure 2.12b) from the full-scale 6-story prototype building. The purpose of these tests was to further study the lower three stories of the 6-story building prototype, where significant inelastic behavior was observed in the full-scale dynamic tests. All frames had identical geometry and loading profiles, while the member sizes and the inclusion or exclusion of a concrete slab were the primary variables that distinguished the 6 tests. Like the large-scale tests, these half-scale tests revealed that the braces carried 80% of the shear in the elastic range, but carried only 50% of the shear in the post-buckling range as demand shifted to the beams and columns via frame action associated with column bending and midspan beam bending (long-link EBF mechanism). The ability of the concrete slab to lend reserve capacity through composite action is displayed through comparison of the results from test frames No. 1 and No. 3 from the study. Frame No. 1 and

No. 3 had identical beam, column, and brace sizes, but frame No. 1 had a concrete slab while Frame No. 3 did not. Although both frames experienced Story 1 brace buckling at similar base shears, the reserve capacity of Frame No. 1 (400–450 kN [90–101 kips] – Figure 2.14a) was noticeably higher than that of Frame No. 3 (325 – 375 kN [73 –84 kips] – Figure 2.14b). This was a result of the increase in plastic moment capacity provided by the composite slab (2.5 times that of the bare steel beam in Frame No. 3).

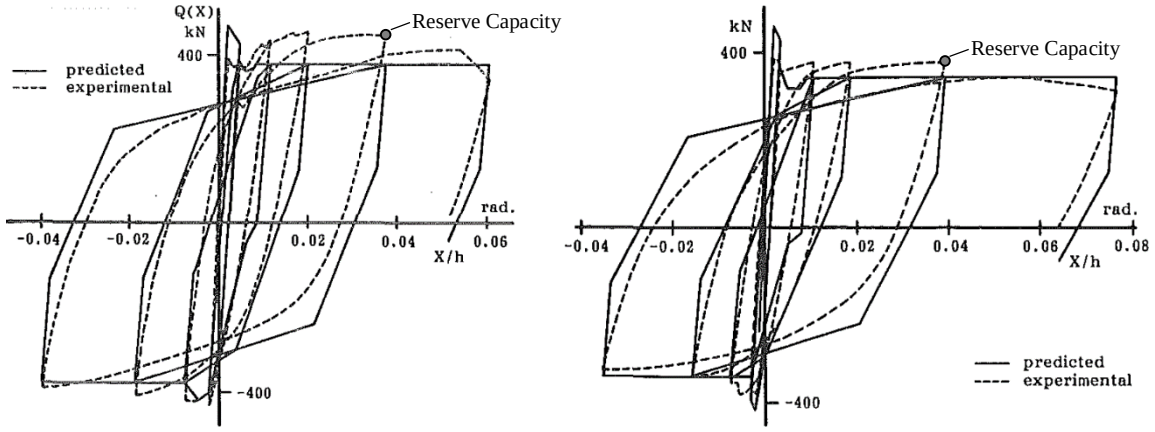

Figure 2.14 – UJ-CERP half-scale 3-story steel CBF, first story shear vs. drift: (a) Frame No. 1 with concrete slab; and (b) Frame No. 3 without concrete slab (modified from Fukuta et al., 1989).

Observations from the UJ-CERP on the then-modern CBF behavior preceded development of what is now known as the SCBF, which was introduced in the 1997 edition of the AISC *Seismic Provisions*, AISC 341–97 (AISC, 1997). The intent of the SCBF was to prevent the detrimental behavioral aspects associated with older nonductile CBFs that pre-dated the capacity design principles of high-ductility systems introduced in the 1990 edition of the AISC *Seismic Provisions*, AISC 341–90 (AISC, 1990). Local brace buckling and brace fracture due to low-cycle fatigue were addressed through local (b/t) and global (KL/r) brace slenderness limits. Brace connection fractures were addressed through enforcement of brace-

gusset connections to develop the expected yield strength of braces. The long-link EBF mechanism that was observed in the UJ-CERP tests was eliminated through requirements for beams to develop the moment induced from a force imbalance created under the desired mechanism of the system, i.e. when the compression brace is at its reduced buckling capacity and the tension brace is at its yield capacity.

2.5.2 Non-seismic Concentrically-Braced Frame Tests

Until recently, most of large-scale frame testing efforts focused on the SCBF SFRS and the Buckling-Restrained Braced Frame (BRBF) SFRS, which was introduced in 2005 as an alternative CBF for high seismic regions. While these tests were valuable for assessing the performance of modern high-ductility SFRSs, they tell little about the performance of existing CBFs in high-seismic regions that were designed prior to the beginning of modern high-ductility design. Specifically, it is unclear if these structures need seismic retrofitting to bring them in line with current high-ductility system requirements. In recognition of this, a research program was launched at the University of Washington to assess the behavior of these so-called non-seismic concentrically braced frames (NCBFs), which were designed prior to the inception of the AISC *Seismic Provisions* (Sen, 2015; Sen et al., 2015; Sen et al., 2016). The NCBF is like the modern $R = 3$ system used in low and moderate seismic regions today, which is also designed without any seismic detailing requirements. One defining characteristic of beams within NCBFs and $R = 3$ CBFs is that they can be expected to yield in flexure following brace buckling or brace-gusset weld fracture due to the absence of a capacity design requirements in their design.

To assess the viability of these beams, dubbed weak beams by Sen et al. (2016), several 2-story single bay CBFs were tested, including one typical NCBF (Specimen 1) and one SCBF

with a “weak” first story beam that is typical of a NCBF (Specimen 4). While both frames experienced brace buckling in the first story, HSS braces in Specimen 1 experienced significant concentrations of local buckling and fractured at very small drifts, which agrees with the observations of the NCBF buildings in California after the 1994 Northridge Earthquake. Beam yielding occurred following brace buckling in both Specimens 1 and 4 and contributed to reserve capacity via frame action. Severe local buckling of Specimen 1’s slender HSS7x7x1/4 braces (b/t = 27.0) resulted in a lower system reserve capacity than Specimen 4, which had HSS5x5x3/8 braces (b/t = 11.3) adhering to SCBF brace local slenderness limits (b/t < 13.2 for F_y = 91.0 MPa [50 ksi]).

2.6 SUMMARY OF LITERATURE REVIEW

2.6.1 Overview

In the seismic case studies presented, it was clear that reserve capacity had a significant influence on the collapse prevention of steel structures. This was true for structures designed with some notion of reserve capacity in mind, such as the Japanese CBFs with moment-connected beam-column connections that were exercised in the Kobe Earthquake. It was also true for structures not seismically detailed, such as NCBFs that avoided collapse in the Northridge Earthquake. Based on the performance of steel-framed buildings during these recent historic earthquakes, several sources of reserve capacity were identified: (1) beam-column connections that are part of the gravity framing system (gravity connections); (2) gravity columns and column base fixity; (3) braced frame beam-column gusset connections (CBF connections); (4) brace reengagement; and (5) beam and column bending. Throughout the past two decades, experimental and computational studies on these reserve capacity sources

illustrated how reserve capacity is attainable from components otherwise assumed to provide no lateral force resistance in design. In addition to these component studies, several large-scale frame tests were conducted and reserve capacity was observed following brace fracture or brace-gusset connection fracture by frame action associated with beam and column bending within the SFRS.

In reviewing the research described above, three primary conclusions were derived: (1) reserve capacity can assist with collapse prevention, as observed in several steel-framed buildings in recent major seismic events throughout the world; (2) there are several sources of reserve capacity, and many studies that have been conducted or are underway seek to quantify these sources; and (3) although many large-scale experimental test programs have investigated the performance of high-ductility systems, there has been limited testing of low-ductility systems.

2.6.2 Research Implications

Given these observations and conclusions, two primary tasks were identified to advance research efforts in reserve capacity: (1) conduct a large-scale experimental test program on low-ductility CBFs to bring knowledge of these systems more in line with the fundamental understanding of high-ductility CBFs; and (2) develop a sophisticated nonlinear model which incorporates the various components of reserve capacity to further the understanding of how reserve capacity contributes to the collapse prevention performance of low-ductility CBFs.

CHAPTER 3

RESERVE CAPACITY COMPONENT STUDY

The literature gives a good starting point for showing potential sources of reserve capacity and inferring their impacts on seismic performance within a typical low-ductility steel concentrically braced frame (CBF). However, there has not yet been a comprehensive investigation of how these reserve capacity sources affect the collapse prevention performance of a typical low-ductility steel CBF. To fill this void, a prototypical low-ductility building was designed and simulated numerically with a nonlinear frame model incorporating observed reserve capacity sources from the literature. This investigation had two primary thrusts. First, quantify the influence that modeling assumptions made by engineers can have on measured reserve capacity and collapse prevention performance in numerical models. Assumptions investigated in this regard are the decisions to model beam-column connections as pins or to accurately capture their flexural behavior (in braced bays and gravity bays) and whether to model column bases as pinned or fixed (in both braced bays and gravity bays). Second, the influence that various members and components within a building can have on reserve capacity and collapse prevention performance are evaluated by making small changes to connection details (e.g. adding top and seat angles to beam-column connections) and member sizes (e.g. increasing beam or column flexural capacity). These results are then compared with the results from analogous tests of a model with no enhancements. In doing so, the relative efficiency of various reserve capacity sources is studied.

3.1 DEVELOPMENT OF PROTOTYPE BUILDING

To set up the context for this study, a 3-story office building was designed for Boston, Massachusetts—a moderate seismic region with Seismic Design Category (SDC) B. The building was designed for local (Massachusetts State Building Code, 2010) and national building codes (International Code Council, 2009) using the Load and Resistance Factor Design (LRFD) methodology. Typical for moderate seismic regions such as Boston, the $R = 3$ provision was invoked for seismic force resisting system (SFRS), and thus only the AISC *Specification* (AISC 360–10; AISC, 2010b) was needed for design, and not the AISC *Seismic Provisions* (AISC 341–10; AISC, 2010a).

The building uses a rectangular floor plan that was loosely adapted from the SAC Joint Venture 9-story building (Krawinkler, 2000) with dimensions of 45.7 m. [150 ft.] by 53.3 m. [175 ft.] (5 bays at 9.1 m. [30 ft.] by 5 bays at 10.7 m. [35 ft.]). These dimensions, along with 4.6 m. [15 ft.] story heights, were chosen to fit the constraints imposed by the associated set-up of the large-scale testing program (Chapter 4). In addition to the primary beams and girders along the column lines, filler floor beams were spaced at 3.0 m. [10 ft.] on center. The 3-story prototype building includes two interior chevron CBFs in each direction using strong-axis columns for four braced bays in the building. When this prototype building floorplan was adapted for 6- and 9-story models in Chapter 8, a total of eight braced bays were needed in the building (4 in each direction) to decrease overturning effects. The overall column orientation in plan was chosen so there was a balance of columns oriented along their strong or weak axis in either direction. A floor plan of 3-story building and an elevation for one of the 10.7 m. [35 ft.] bay chevron CBFs is shown in Figure 3.1. All frames considered in this study have a 10.7

m. [35 ft.] bay width, which corresponds to secondary beams in the braced bays rather than girders.

Members were designed based on the 2005 edition of ASCE 7 (ASCE 7–05, 2005) to

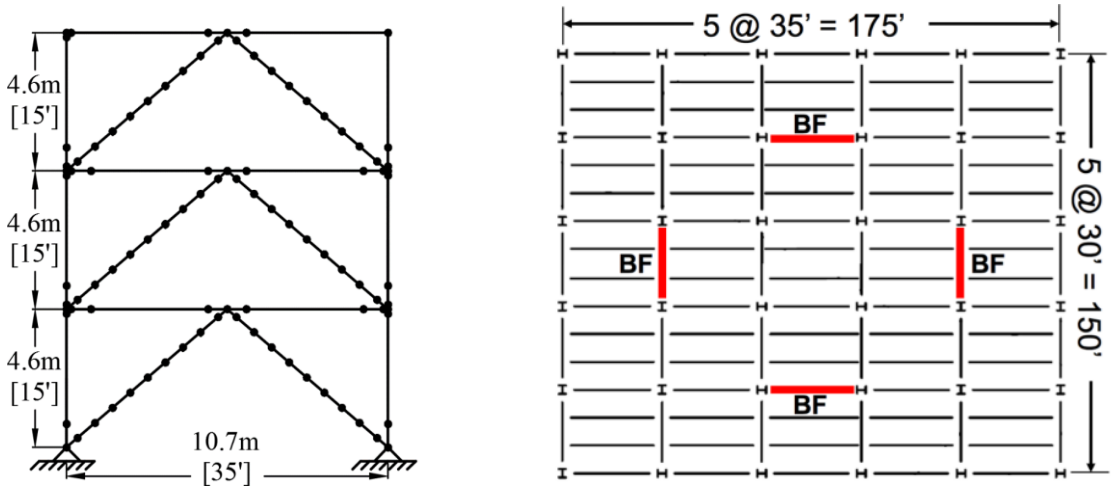

(a) (b)

Figure 3.1 – Prototype building: (a) elevation of 10.7 m. [35 ft.] bay; and (b) building floor plan showing two braced frames (BF) in each principal direction.

keep consistency with the referenced version of the Massachusetts State Building Code (2010). A simplified eigenvalue analysis produced a fundamental period for the building of 0.70 s., but in keeping with the simplicity of the R = 3 provision, the seismic design base shear, V = 1,495 kN [336 kips], was calculated using the approximate period $T_a = C_t h_n^x = (0.0488)(13.7\text{m.})^{0.75}$ = 0.347 s (ASCE 7–10, *Equation 12.8-7*). The floor weight in each building was 11,254 kN [2,530 kips] and the roof weight was 6,005 kN [1,350 kips], giving a total building weight (in kips) of 28.5 MN [6,400 kips]. The equivalent lateral force (ELF) procedure from ASCE 7–05 was used to determine seismic demands at each level, which governed over wind for this building. Pertinent load combinations used for member design include (1) 1.4D; (2) 1.2D + 1.6L + 0.5L_r; (3) 1.2D + 1.6L + 0.5S; (4) 1.2D + 1.6W + 0.5L + 0.5L_r; (5) 1.2D + 1.6W + 0.5L

+ 0.5S; (6) 1.2D + 1.0E + 0.5L + 0.2S. Gravity loads summarized in Table 3.1. Girders and beams that were a part of the gravity framing system were designed for composite action. More information of the design of this building is provided by Bradley (2016).

Table 3.1 – Summary of gravity loads used for design

Class.	Dead (kPa) [psf]	Live[a] (kPa) [psf]	Snow (kPa) [psf]
Roof	1.44 [30]	1.44 [30]	[28]
Floor	3.59 [75]	3.11 [65]	-

[a] Live load reduction used where applicable per ASCE 7–10.

3.2 NUMERICAL FRAME MODEL AND VARIATIONS

A baseline R = 3 design and associated numerical model, referred to as "R3-3-Baseline", was established to serve as a reference for assessing the impact that modeling choices and enhancing design parameters had on reserve capacity. An elevation of the numerical model—which was constructed using the *OpenSees* simulation platform (McKenna, 1997)—is provided in Figure 3.2.

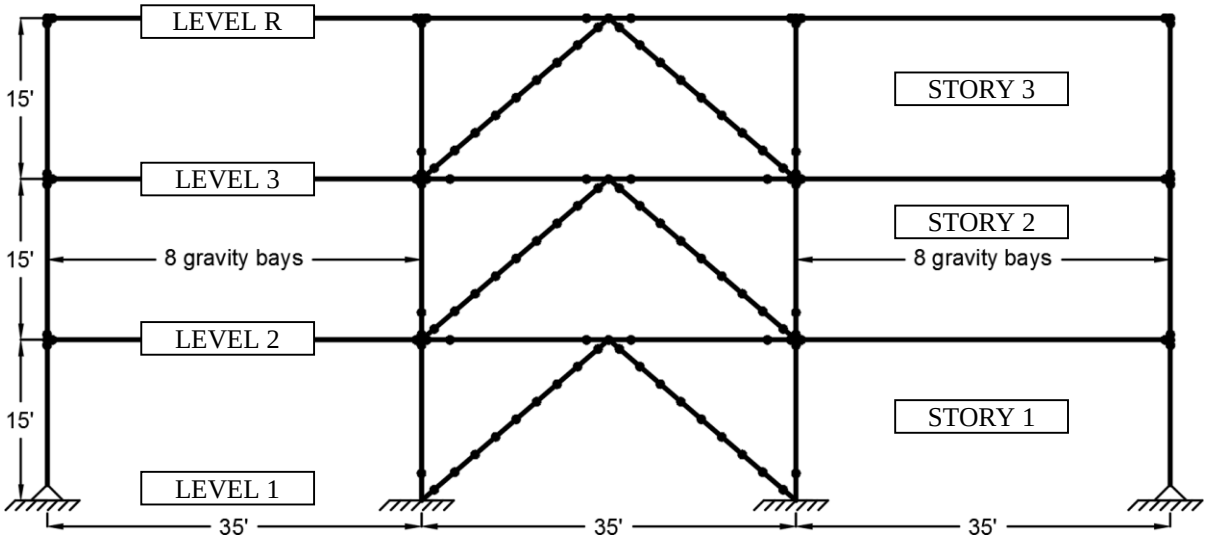

Figure 3.2 – Generalized elevation of 3-story OpenSees model.

A detailed discussion of this numerical model and its components is provided in Chapter 5. For the purposes of the relative comparisons made in this chapter, important aspects of the baseline numerical model are:

1. Beam-column connections. Gravity and CBF connections were explicitly modeled using fiber elements to simulate their estimated flexural capacity (Section 5.1.5). Gravity connections were 2L4x4x1/4s and CBF connections were two pairs of 2L4x4x1/2s (Figure 3.3).

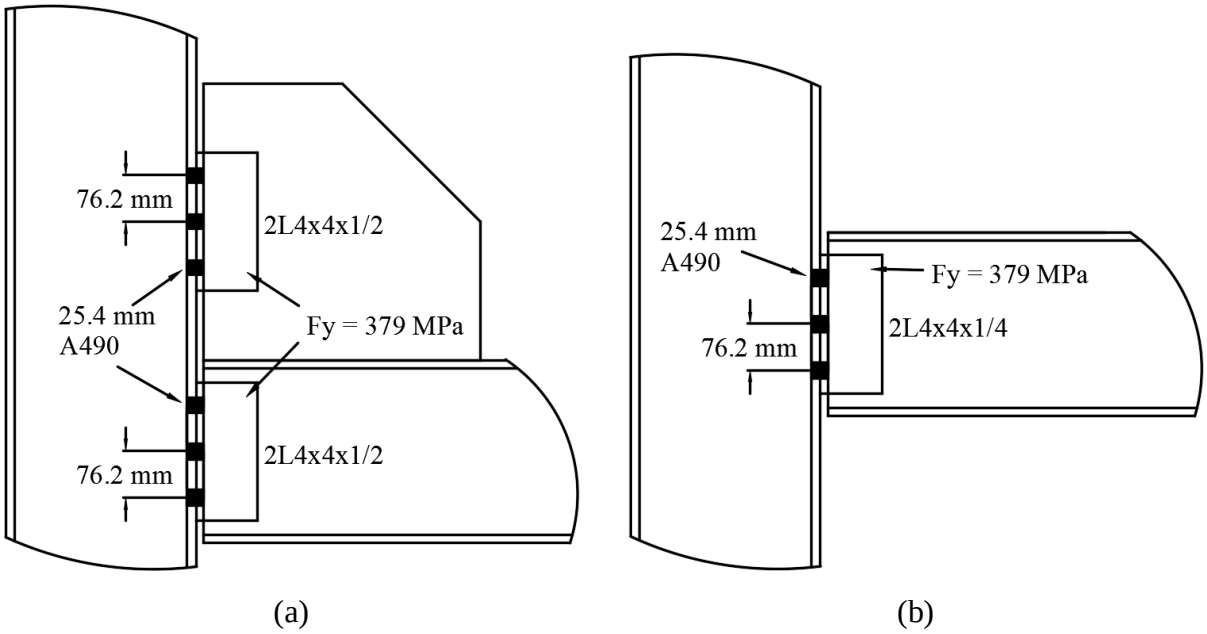

(a) (b)

Figure 3.3 – Typical connections used in prototype building model: (a) CBF connection; and (b) Gravity connection.

2. Columns and column bases. All columns were modeled as continuous over the height of the building. The base boundary condition for gravity framing columns was pinned, while the base boundary condition for braced bay columns was fixed.

3. Gravity loading. The expected gravity loading during a seismic event was considered per recommendation of Pacific Earthquake Engineering Research Center and Applied Technology Council (PEER/ATC 72–1): *Modeling and acceptance criteria for seismic design and analysis of tall buildings* (PEER/ATC, 2010), or 100% dead load and 20% live load (1.0D + 0.2L). Gravity loading within the braced bay was applied to the beams as uniformly distributed load, while gravity loading within the gravity bays was applied as point loads at the beam-column intersections.
4. Brace reengagement. Due to the highly variable nature of the brace-gusset weld interface (Davaran et al., 2014), braces were not considered to reengage in compression following connection fracture in the baseline model; once a brace-gusset weld fractured, the brace was no longer allowed to transfer force in either tension or compression.
5. Member sizes and connection capacities. Member and connection details for the baseline design are given in Table 3.2 and Table 3.3, for the braced bay and gravity bays, respectively.

Table 3.2 – Baseline 3-story prototype building: R = 3 chevron CBF

Story/Level	Beam	Column	Brace	Weld[a] (kN) [kips]
R	W12x26	—	—	—
3	W12x40	W12x53	HSS9x1/4	1,455 [327]
2	W12x40	W12x53	HSS8x1/4	1,188 [267]
1	—	W12x53	HSS6x1/4	539 [119]

[a] Brace-gusset welded connection.

Table 3.3 – Baseline 3-story prototype building: gravity framing system

Story/Level	Interior Beam	Perimeter Beam	Interior Column	Perimeter Column	Corner Column
R	W12x53	W12x58	—	—	—
3	W16x31	W18x35	W12x50	W12x40	W12x40
2	W16x31	W18x35	W12x50	W12x40	W12x40
1	—	—	W12x50	W12x40	W12x40

The impact of various parameters on reserve capacity was studied through variations made to the baseline model. Connection behavior, member sizes, and fixities were the parameters that were adjusted in the creation of supplemental building models. Some of these changes were classified as modeling assumptions (e.g. fixities) while others were structural enhancements (e.g. increased member sizes). A summary of these changes and associated model names is given in Table 3.4. Unless described in the "Notes" section of Table 3.4, all other components and details of the model variations were identical to those of the baseline model, R3-3-Baseline. All building models used the same 3-story office building and floorplan (Figure 3.1) with an SFRS that incorporated an R = 3 chevron CBF.

Table 3.4 – Summary of 3-story prototype building model variations

Building Model	Notes
R3-3-Baseline	Baseline model as described above.
R3-3-BC-Pin	Beam-column connections in all bays modeled as pins.
R3-3-GBC-Pin	Beam-column connections in gravity bays modeled as pins.
R3-3-BC-Enh	Top and seat angles added to beam-column connections in all bays.
R3-3-Base-Pin	All column bases modeled as pins.
R3-3-Base-Fix	All column bases modeled as fixed.
R3-3-BrRe–100	Brace reengagement in compression, 100% of bearing capacity.
R3-3-BrRe-200	Brace reengagement in compression, 200% of bearing capacity.
R3-3-Weld-50	Brace-gusset weld capacities increased by 50%.
R3-3-Col-50	Column flexural capacities increased by 50%.
R3-3-Beam-50	Beam flexural capacities increased by 50%.

3.3 STATIC PUSHOVER ANALYSES

A series of static pushover (SPO) analyses were performed on the baseline prototype building (R3-3-Baseline) and its variations to quantify basic characteristics of the reserve system. The seismic demands were idealized as a lateral load distribution using the equivalent lateral force (ELF) procedure from ASCE 7–05. The SPO results of the baseline model, R3-3-Baseline, are shown in Figure 3.4 through the relationship between base shear (V_B) and roof drift (δ_R/h).

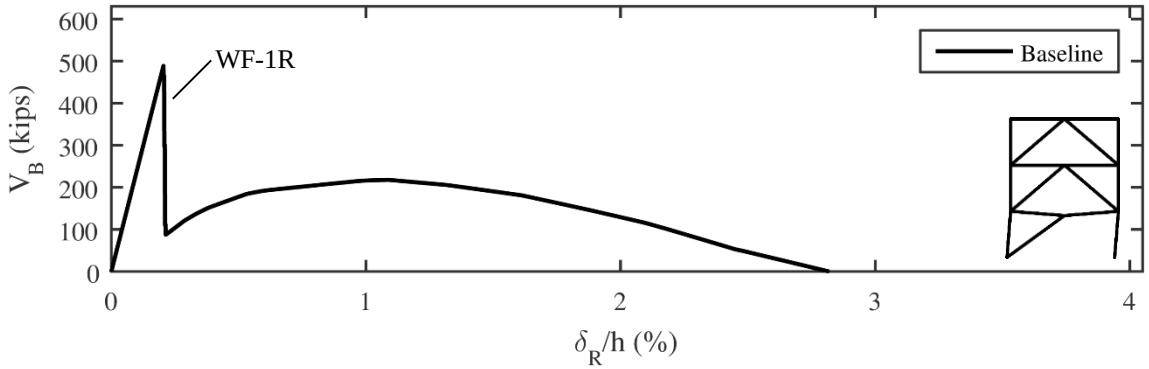

Figure 3.4 – Pushover analysis results of baseline building model, R3-3-Baseline.

The primary limit state observed in R3-3-Baseline was weld fracture at the brace-gusset interface in the Story 1 compression brace (WF-1R), which resulted in a sudden and large drop in V_B, from 2,225 kN [500 kips] to 445 kN [100 kips] (Figure 3.4). After weld fracture, Story 1 behaved like an eccentrically braced frame (EBF), as the half of the Level 2 beam corresponding to the side of the fractured brace underwent significant flexural deformations like those common of long "flexural links" found in EBFs (long-link EBF mechanism). The Level 2 beam was not capable of fully developing the imbalanced vertical force delivered by the remaining tension brace, and thus yielded at midspan, which capped the mechanism's available reserve strength. In addition to the reserve capacity provided by the yielding beam within the CBF, reserve capacity was also provided by the gravity framing beam-column connections (gravity connections), braced bay beam-column-gusset connections (CBF connections), and column bending within both the braced bay gravity bays. A deformed shape schematic and associating moment diagram for the reserve capacity mechanism observed in R3-3-Baseline is shown in Figure 3.5. Plastic hinge locations are marked on the deformed shape diagram using solid circles. Due to the added section modulus provided by the gusset plates within the CBF, plastic hinges formed at the interface of the beams and columns where the gusset plates ended. Only one gravity bay is shown in these schematics for clarity, though

there are 16 gravity bays within the actual model. As Figures 3.3 and 3.4 show, Story 1 is critical and governs the behavior of the structure, which reaches a peak reserve capacity of V_B = 975 kN [220 kips – 65% V].

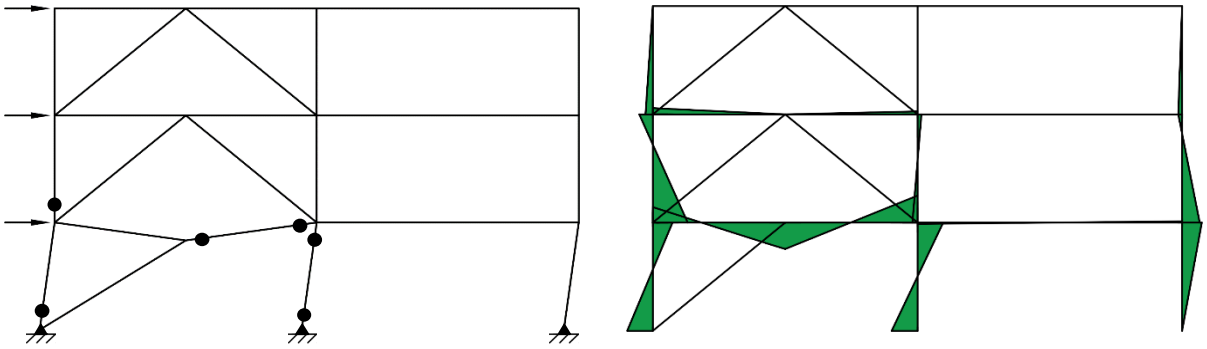

(a) (b)

Figure 3.5 – Deformed shape and moment diagram for R3-3-Baseline.

3.3.1 Influence of Beam-Column Connections

From the SPO results of R3-3-Baseline, the CBF connections appeared to contribute significantly more reserve capacity than the gravity connections, as the gravity frame beams experienced only minor amounts of bending (Figure 3.5). To confirm this observation, the influence of beam-column connections was isolated by subjecting R3-3-BC-Pin, R3-3-GBC-Pin, and R3-3-BC-Enh to the same SPO analysis as R3-3-Baseline. In R3-3-BC-Pin, all the beam-column connections within the building were replaced with pins. In R3-3-GBC-Pin, the beam-column connections within the braced bay (CBF connections) were untouched, while all gravity connections were replaced with pins. In R3-3-GB-Enh, a supplemental seat angle was included with all CBF connections, and supplemental top and seat angles were included with all gravity connections (Figure 3.6).

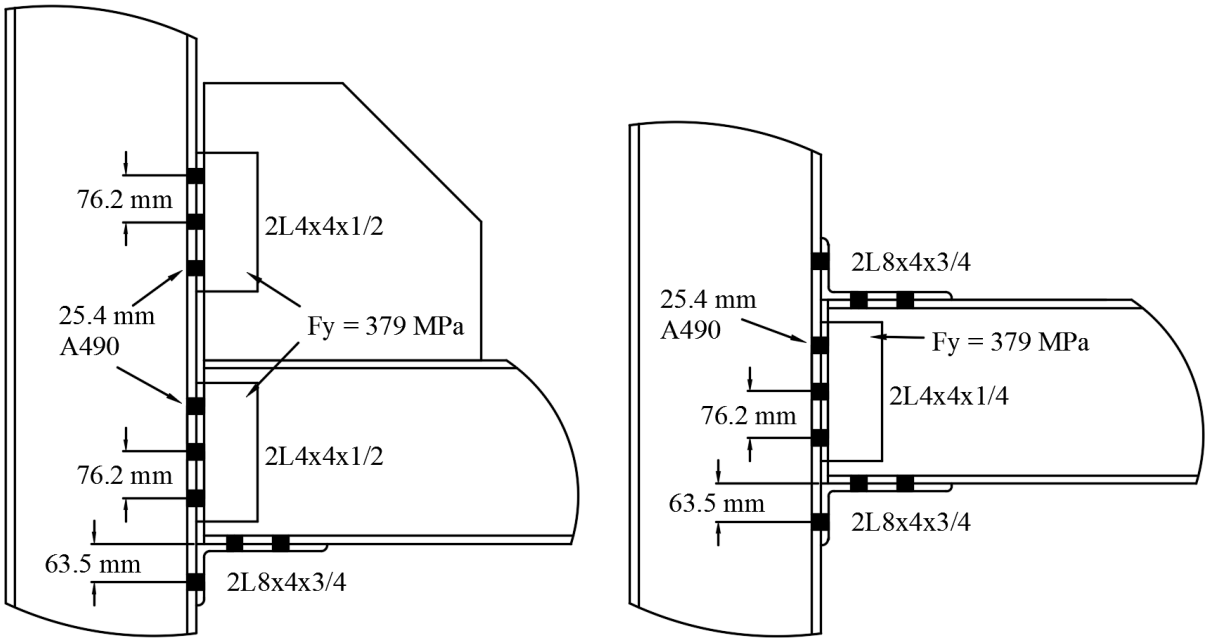

(a) (b)

Figure 3.6 – Typical enhanced connections used in prototype building model: (a) Enhanced CBF connection; and (b) Enhanced gravity connection.

The primary limit state observed in the SPO analyses of these three building models was identical to the baseline model: weld fracture at the brace-gusset interface in the Story 1 compression brace (Figure 3.5). However, the post-elastic behavior (reserve capacity) was different in each of these building models, as the SPO curves in Figure 3.7 show. When all beam-column connections were modeled as pins (R3-3-BC-Pin), there was an appreciable difference in reserve capacity as the peak V_B achieved following weld fracture was 755 kN [170 kips – 51% V], a decrease of 23% (220 kN [50 kips – 14% V]) from the baseline model, R3-3-Baseline (Figure 3.7a). When only the gravity connections were modeled as pins (R3-3-GC-Pin), the difference in reserve capacity was negligible, with peak V_B capping at 910 kN [205 kips – 61% V], a decrease of only 7% (65 kN [15 kips – 4% V]) from R3-3-Baseline (Figure 3.7b). Thus, for this building and set of SPO results, the gravity connections in all 16 gravity framing bays provided 65 kN [15 kips – 4% V] of reserve capacity, while the CBF

connections within the single braced bay provided the remaining 155 kN [35 kips – 10% *V*] of reserve capacity. Considering the large flexural demands that the long-link EBF mechanism placed on CBF connections (Figure 3.5), and their inherently larger flexural capacity (Figure 3.3), this difference in reserve capacity contribution was reasonable. When the beam-column connections were "enhanced" in model R3-3-BC-Enh, the resulting reserve capacity was 1,110 kN [250 kips – 74% *V*], an increase of 14% (135 kN [30 kips – 9% *V*]) over R3-3-Baseline (Figure 3.7c). Although their significance appears minor here, later dynamic simulations reveal the ability of gravity connections to lend large amounts of reserve stiffness and strength.

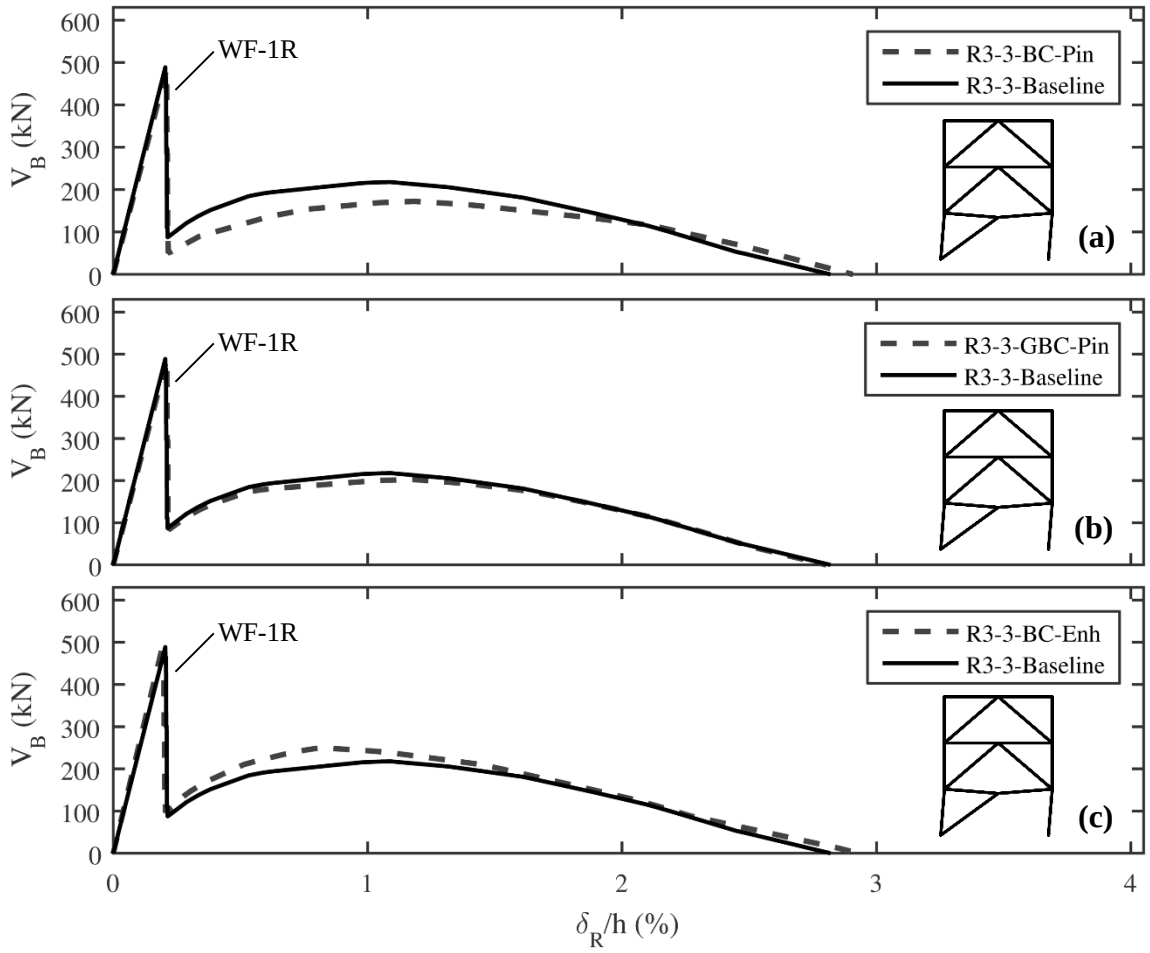

Figure 3.7 – Pushover analysis results for building model variations with emphasis on beam-column connections: (a) R3-3-BC-Pin; (b) R3-3-GBC-Pin; and (c) R3-3-BC-Enh.

Comparisons of the SPO results for building models R3-3-BC-Pin and R3-3-GBC-Pin with R3-3-Baseline revealed the significant influence that assuming pinned beam-column connections—a common modeling assumption—can have on reserve capacity. As Figure 3.6 shows, beam-column connections may safely be modeled as pins if finding the peak elastic strength of a structure is a modeler's sole concern. Conversely, if post-elastic behavior is of concern, effort should be made to model the flexural capacity of beam-column connections. Unlike R3-3-BC-Pin and R3-3-GBC-Pin, which simply investigated modeling assumptions, R3-3-BC-Enh investigated a potential for increasing reserve capacity in a new or existing building.

3.3.2 Influence of Base Fixity

The SPO results of R3-3-Baseline revealed that the assumption of fixed column bases within the CBF allowed large moments to develop at the base (Figure 3.5). The assumption of fixed column bases within CBFs is reasonable considering that these bases typically use extended base plates with many anchor bolts to accommodate the gusset plate. CBF column base flexural capacity may be further increased if designed for uplift under wind and seismic loading. Nevertheless, column bases within braced bays are often modeled conservatively by assuming a pinned condition. The impact that considering column bases within CBFs as pins can have on reserve capacity is investigated through building model R3-3-Base-Pin. The full range of behavior resulting from column base fixity was investigated through investigation of a second building model, R3-3-Base-Fix, where all column bases—even those in the gravity bays—were modeled as fixed. Like the other building models shown thus far, the primary limit state observed in the SPO analyses of building models R3-3-Base-Pin and R3-3-Base-Fix was Story 1 brace-gusset weld fracture (Figure 3.8). Following this limit state, behavior of the R3-

3-Base-Pin model continued like that of R3-3-Baseline model, but with a reduced reserve capacity that peaked at 710 kN [160 kips – 48% *V*], a decrease of 27% (265 kN [60 kips – 18% *V*]) from R3-3-Baseline (Figure 3.8a).

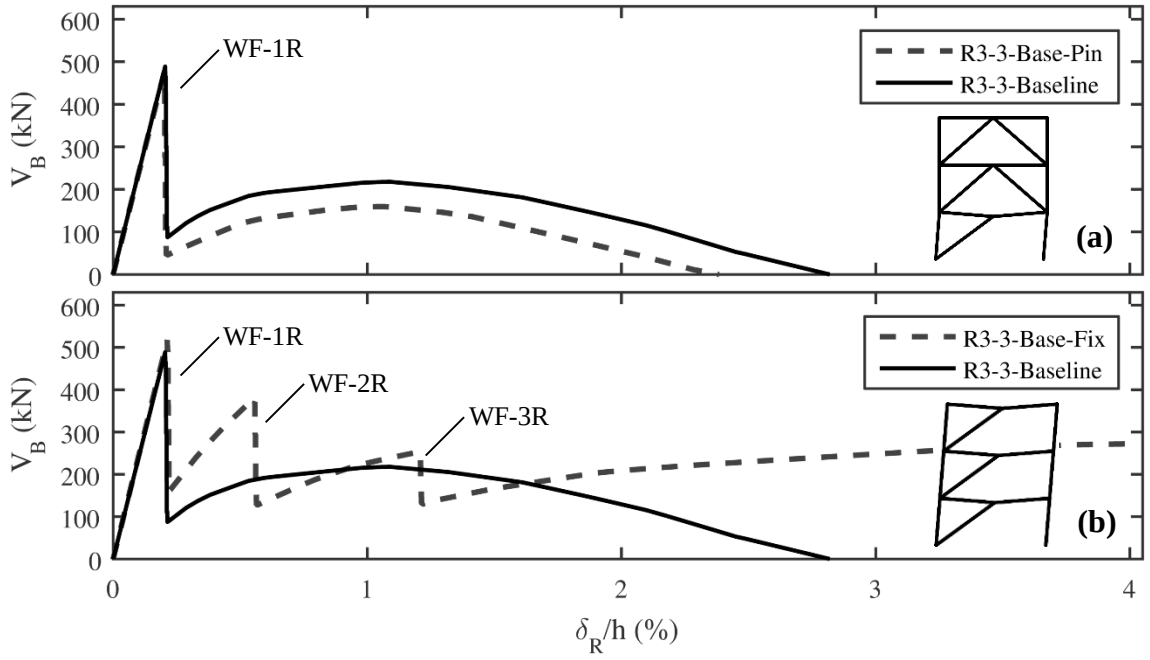

Figure 3.8 – Pushover analysis results for building model variations with emphasis on column base fixity: (a) R3-3-Base-Pin; and (b) R3-3-Base-Fix.

After Story 1 weld fracture in building model R3-3-Base-Fix, post-elastic stiffness and strength continued to increase until Story 2 and Story 3 brace-gusset weld fractures occurred (Figure 3.8a). This finding was an important distinction from the other model results presented up to this point, as it highlighted the potential for limit states in upper stories following a Story 1 limit state if the reserve stiffness and strength are sufficient. The development of additional weld fractures should not necessarily be viewed negatively, however, as this allowed for the development of long-link EBF mechanisms within all three stories of the SFRS rather than only Story 1 (Figure 3.9). Although this building model achieved a favorable reserve capacity, strict conditions are needed to provide fixed bases for gravity columns. While it may be

appropriate to model column bases within CBFs as fixed, gravity bays column bases are inherently more flexible given that they are not designed for uplift and their base plates are much smaller. In other words, significant amounts of added detailing are necessary to achieve the idealized fixed conditions at gravity bay column bases assumed in this model, and they would not be economical. Given that actual column bases will be neither pinned nor fixed but somewhere in between, these SPO results bracket the two extreme cases and give an understanding of the range of potential behavior. Recent research on the rotational stiffness and failure mechanisms of column bases (Kanvinde et al., 2012; Jones, 2016) gives a basis for realistic column base models, but these models were not considered in the present explorative study.

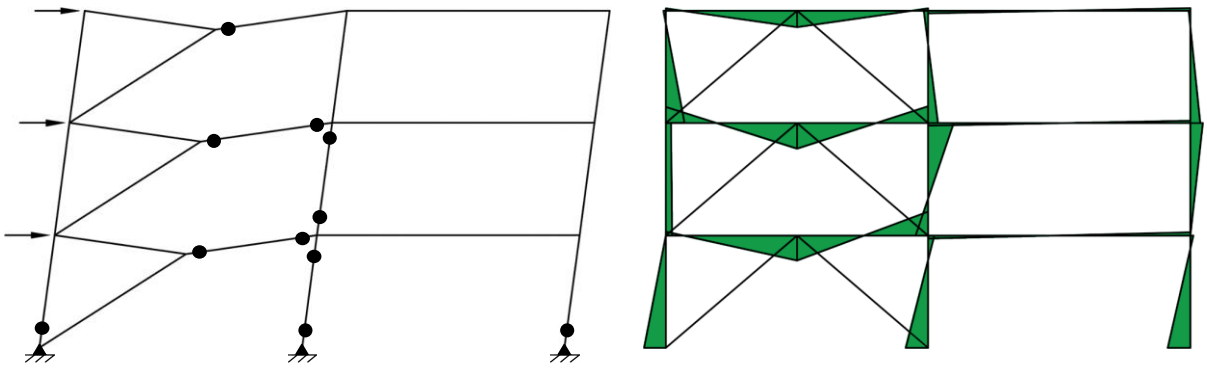

(a) (b)

Figure 3.9 – Deformed shape and moment diagram for R3-3-Base-Fix.

3.3.3 Influence of Brace Reengagement

Brace reengagement is an unknown and highly variable source of reserve capacity. Reengagement in compression following connection fracture has been observed in several major seismic events (Section 2.1), though only one laboratory test has been conducted thus far to quantify its effects (Davaran et al., 2014). Tests by Davaran et al. (2014) provided

intentionally favorable conditions to increase the likelihood of brace reengagement and yet it was still difficult to produce such a mechanism in a consistent fashion. Brace reengagement was not considered in the baseline model due to the difficulty of quantifying the capacity of such a mechanism and its reliability. Two SPO analyses were conducted on building models R3-3-BrRe–100 and R3-3-BrRe-200 to investigate the potential influence that brace reengagement might have on reserve capacity. Brace reengagement was simulated by providing an additional element to the brace-gusset interface following brace-gusset weld fracture during the SPO analysis. The element was modeled assuming an asymmetrical compression-only bilinear elastic material with an elastic stiffness equal to 1% of the original brace stiffness in compression. The brace reengagement strength in compression was capped at a percentage of the bearing capacity, calculated from $R_t F_u t_{HSS} t_{brace}$, or 135 kN [30 kips], for $R_{t,A1085}$ = 1.15, $F_{u,A1085}$ = 450 MPa [65 ksi], t_{HSS} = 19 mm. [3/4 in.], and t_{brace} = 6.4 mm. [1/4 in.]. In the two building models R3-3-BrRe–100 and R3-3-BrRe-200, brace reengagement strength was capped at 100% of the bearing capacity and 200% of the bearing capacity, respectively, which characterizes the range of strengths observed by Davaran et al. (2014). Reengagement strengths greater than 100% of the calculated bearing capacity are achievable due to growth of the bearing surface from the gusset plate cutting through the brace. A simplified schematic of how brace reengagement was modeled and how it appears globally is shown in Figures 3.10 and 3.11, respectively. Note the “detachment” condition in Figure 3.11c—the condition when the detached brace is pulled away from the gusset plate following brace-gusset weld fracture and transfers no force—is not applicable to the SPO analyses but is relevant for subsequent dynamic simulations (Section 3.3).

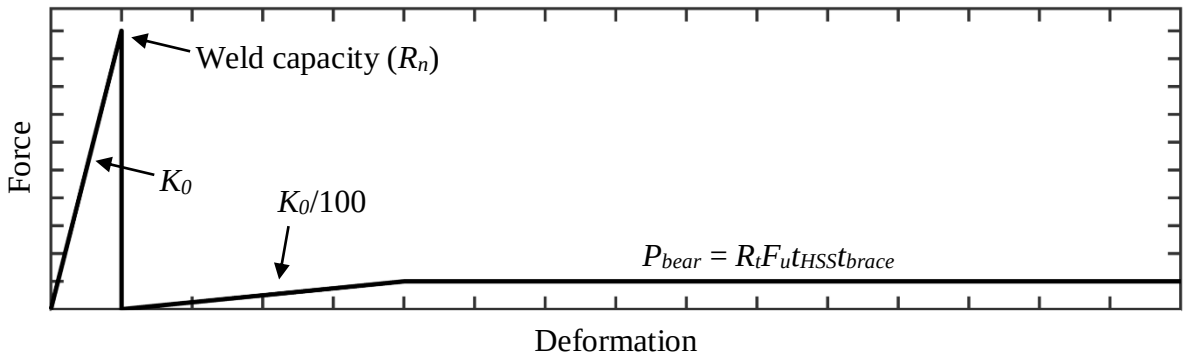

Figure 3.10 – Brace-gusset interface behavior: weld fracture followed by brace reengagement in compression, bearing on gusset plate.

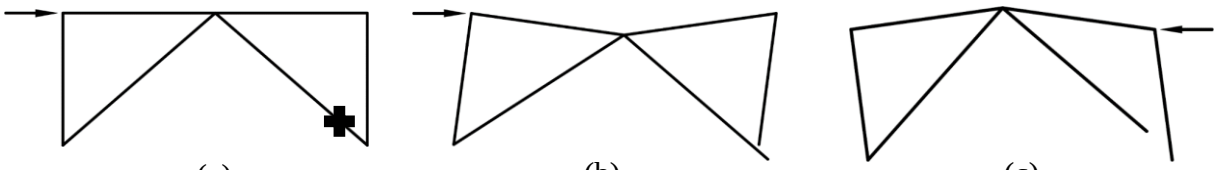

Figure 3.11 – Chevron frame brace-gusset interface behavior: (a) weld fracture; (b) brace reengagement on gusset plate in compression; (c) brace detachment – no force transferred.

The SPO results for these two building models are shown in Figure 3.12. In R3-3-BrRe–100, the brace reengagement mechanism illustrated in Figure 3.11b occurred in the Story 1 brace-gusset interface following weld fracture and resulted in a 20% (200 kN [45 kips – 13% *V*]) increase in reserve capacity over the baseline building model to 1,180 kN [265 kips – 79% *V*] (Figure 3.12a). In R3-3-BrRe-200, brace reengagement resulted in sufficient post-elastic stiffness and strength to cause brace-gusset weld fractures in Stories 2 and 3 (Figure 3.12b), which were followed by brace reengagement in these connections (Figure 3.13) Although there is significant variability involved with brace reengagement stiffness and strength, this limited study shows the potential reserve strength which brace reengagement can provide. Although not observed in the cases presented here, the extreme effect for this mechanism appears to be the point in which reengagement stiffness and strength causes story shears to reach levels high enough to fracture a weld in the tension brace. If this happens, the frame can lose the beneficial long-link EBF mechanism (Figure 3.5), resulting in a decrease in reserve capacity.

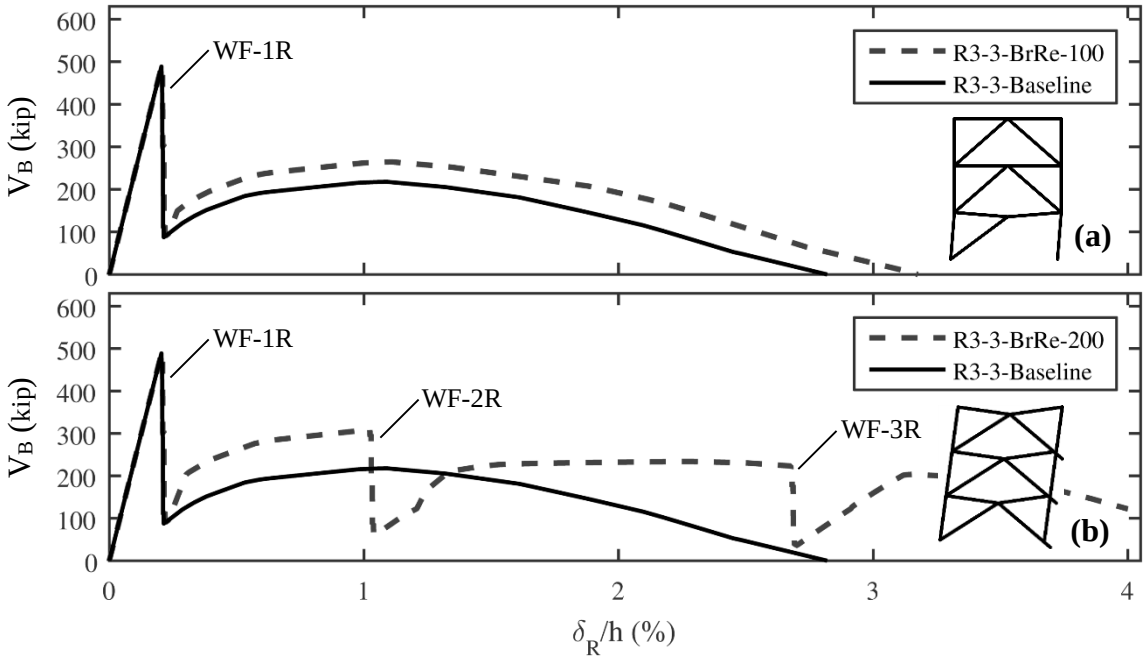

Figure 3.12 – Pushover analysis results for building model variations with emphasis on brace reengagement: (a) R3-3-BrRe-100; and (b) R3-3-BrRe-200.

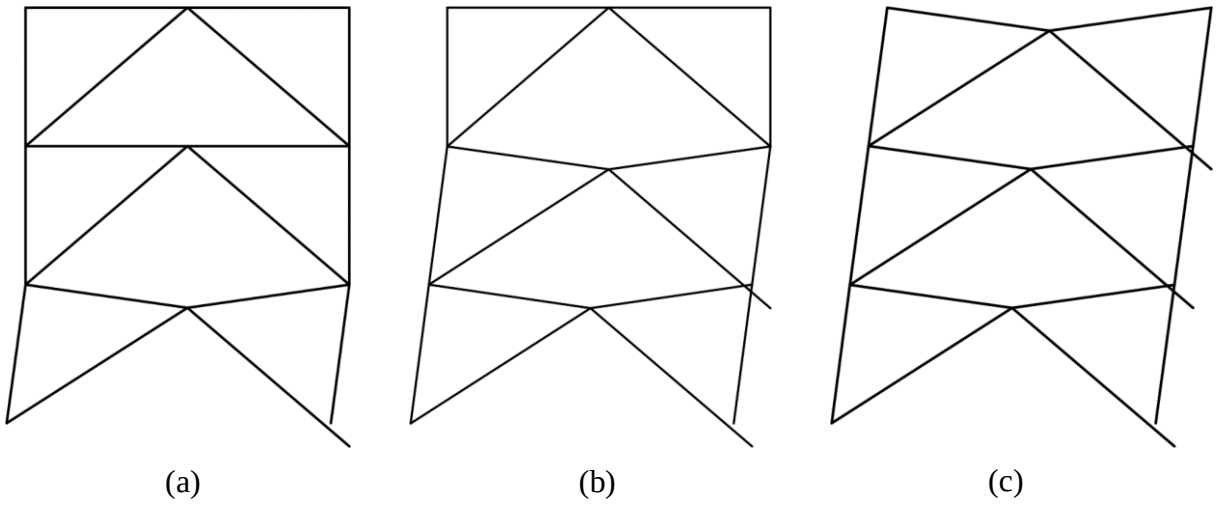

Figure 3.13 – Sequence of limit states for R3-3-BrRe-200. (a) Story 1 weld fracture (WF-1R) and brace reengagement; (b) WF-2R and brace reengagement; and (c) WF-3R and brace reengagement.

3.3.4 Influence of Member and Connection Sizes

The final variations to the baseline building model investigated in the SPO analyses were beam sizes, column sizes, and brace-gusset weld capacities. Given the significant amount of frame action within the SFRS that occurred following brace-gusset weld fracture (Figure 3.5), it was clear that beam and column flexural capacities could have a significant influence on the reserve capacity provided by this mechanism. The influence of beam and column flexural capacity was studied in building models R3-3-Beam-50 and R3-3-Col-50, in which beam and column sizes within the SFRS, respectively, were increased to sections with 50% larger flexural capacities than those required by design. The SPO results for R3-3-Beam-50 shown in Figure 3.14a reveal that a 50% increase in beam flexural capacity provided a peak reserve capacity of 1,110 kN [250 kips – 74% *V*], which was a 14% increase (135 kN [30 kips – 9% *V*]) over the baseline model. In R3-3-Col-50 (Figure 3.14b), post-elastic stiffness and strength following Story 1 brace-gusset weld fracture was enough to induce later limit states in Stories 2 and 3 (Figure 3.15). In building models R3-3-Beam-50 and R3-3-Col-50, reserve capacity was increased over R3-3-Baseline with only modest changes. In R3-3-Beam-50, for example, W14x53 floor beams provided a 50% larger flexural capacity than the required W12x40 floor beams, with only a 20% increase in weight. In R3-3-Col-50, W12x79 columns provided a 50% larger flexural capacity than the required W12x53 columns, for a 50% increase in weight. Given that designers typically try to keep column depth consistent over the height of the building, the required increase in weight to provide a similar increase in flexural capacity will be larger than in beams, where depths are increased to provide economical increases in section modulus.

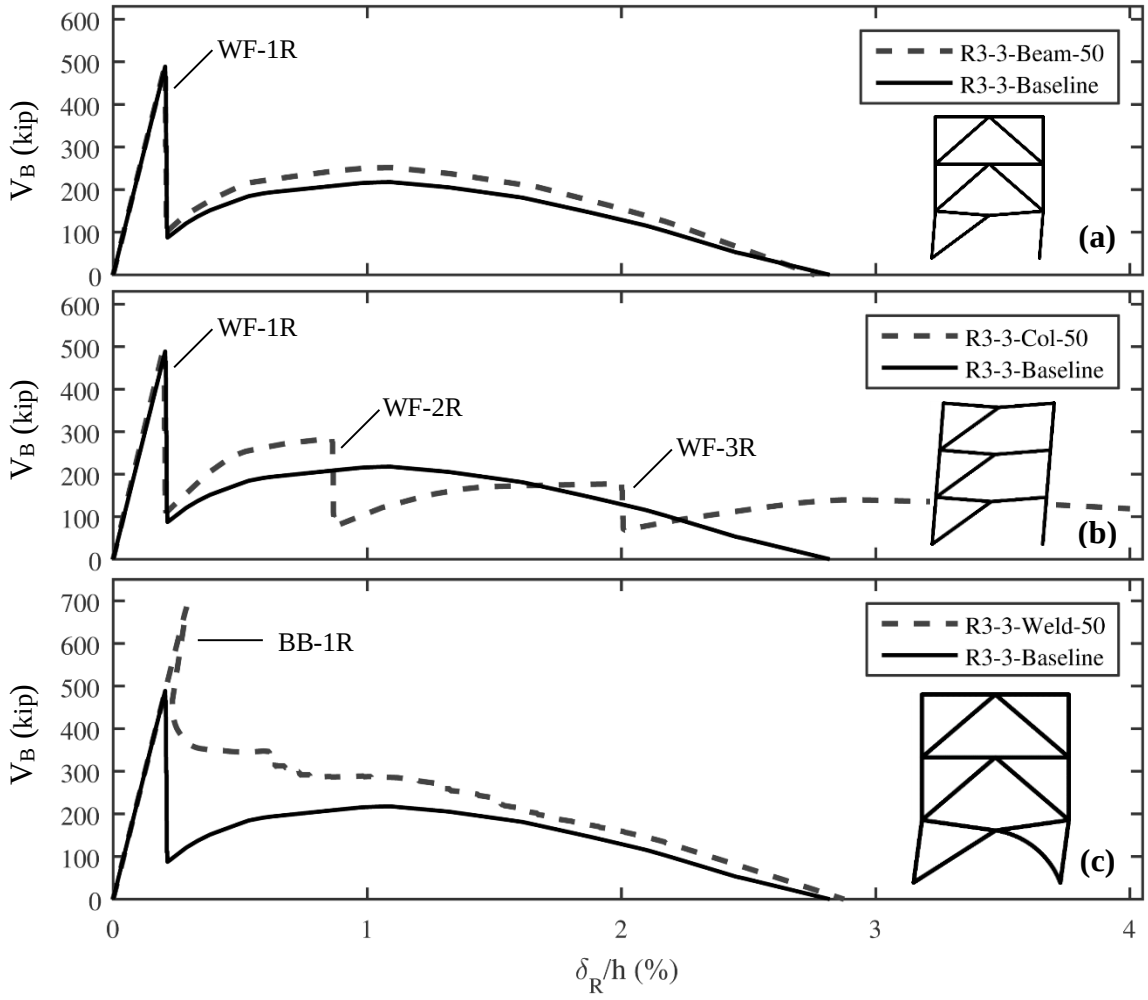

Figure 3.14 – Pushover analysis results for building model variations with emphasis on member and connection sizes: (a) R3-3-Beam-50; (b) R3-3-Col-50; and (c) R3-3-Weld-50.

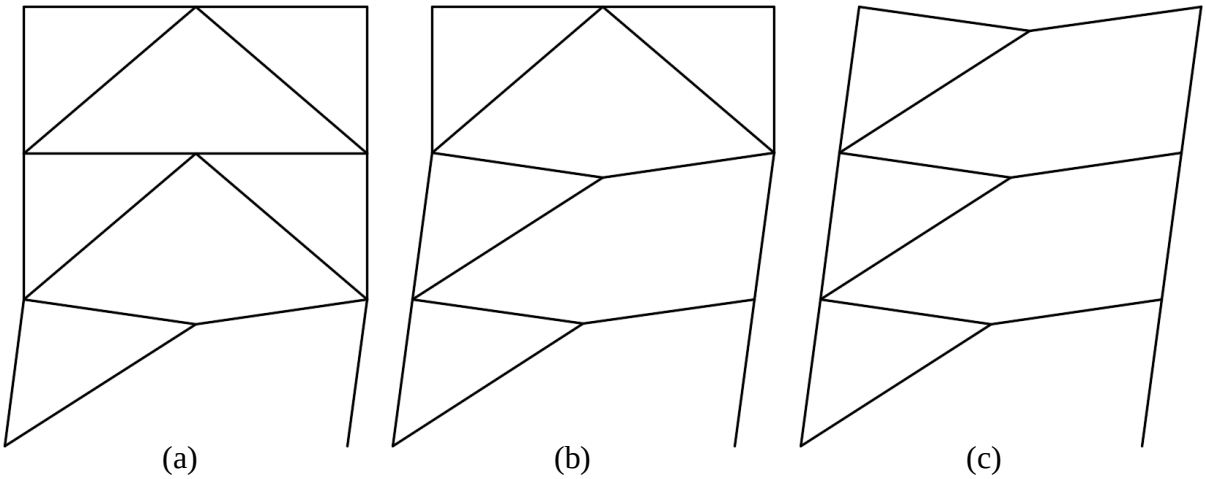

Figure 3.15 – Sequence of limit states for R3-3-Col-50. (a) Story 1 weld fracture (WF-1R); (b) WF-2R; and (c) WF-3R.

When weld capacities were assumed 50% larger than those required by design in R3-3-Weld-50, the brace-gusset connection capacities became larger than the brace buckling capacities, which increased the initial strength of the frame from 2,225 kN [500 kips] to 3,025 kN [680 kips]. This caused a shift in the initial limit state to Story 1 brace buckling, indicated by BB-1R in Figure 3.14c. The strength drop associated with this event was not as severe because the buckling Story 1 brace still carried force—albeit with decreasing capacity—compared to R3-3-Baseline in which the brace carried no force following brace-gusset weld fracture. As drift concentrates in Story 1 and localized plastic strain concentrates in the brace midspan hinge, the fiber element model degrades to represent localized low-cycle fatigue-related damage, starting at δ_R/h = 0.60% (Figure 3.14c). As fatigue damage accumulated and the brace's compressive strength approached zero, marginalizing the impact of increasing weld strength by 50% on reserve capacity.

3.4 DYNAMIC ANALYSES

Dynamic analyses expand the insight provided by the static analyses by considering ground motion input, higher mode effects and cyclic degradation. The baseline prototype building and some of its more realistic variations were subjected to a suite of 15 ground motions (GMs) developed by Hines et al. (2009). The baseline suite consisted of 14 synthetic Site Class B records (Sorabella, 2006; Hines et al., 2009). The GM selection process for low-ductility systems differs from that used for ductile systems due to the large shifts of period expected in a typical low-ductility system response. Due to the brittle mechanisms typical of R = 3 CBFs, the undamaged fundamental period of the associated building does not heavily govern its response in a seismic event. For example, a brace-gusset weld fracture or analogous brittle limit state within the SFRS significantly decreases the stiffness of the building and thus

increases its period, potentially protecting it from the more energetic short-period ranges of a given GM. This contrasts with the behavior of high-ductility systems, which are governed by first mode response and are not as susceptible abrupt shifts in period throughout a seismic event. In acknowledgement of this, the average of the GM suite (14 synthetic motions) was scaled to match the IBC 2006 MCE for Site Class B, rather than the typical process of scaling the individual GMs to the target design spectrum. Allowing the Site Class B response spectrum values to range from 0.5 to 2.0 times the uniform hazard spectrum points of the U.S. Geological Survey (USGS) data created a wider scatter of potential seismic events and thus allowed for a more thorough exploration of low-ductility CBF behavior (Hines et al., 2010).

In the scaling procedure used by Sorabella (2006), the 14 GMs described above exhibited, on average, spectral accelerations lower than the USGS Site Class D spectrum for $T > 2.0$, a period range that is important for low-ductility braced frames experiencing significant brittle limit states. Thus, one other artificial GM was developed (Hines et al., 2009) to match the Site Class D MCE as best possible with a heightened emphasis on the $T > 2.0$s period range. The total set of 15 GMs was used to examine detailed aspects of nonlinear building behavior and capture global trends related to collapse through incremental dynamic analysis. Response spectra for the 15 GMs and the suite average are plotted in Figure 3.16 along with the Site Class D MCE for Boston using 2008 U.S. Geological Survey data (USGS, 2013). More information about the GM suite and its development may be found in Sorabella (2006), Hines et al. (2009), and Hines et al. (2010).

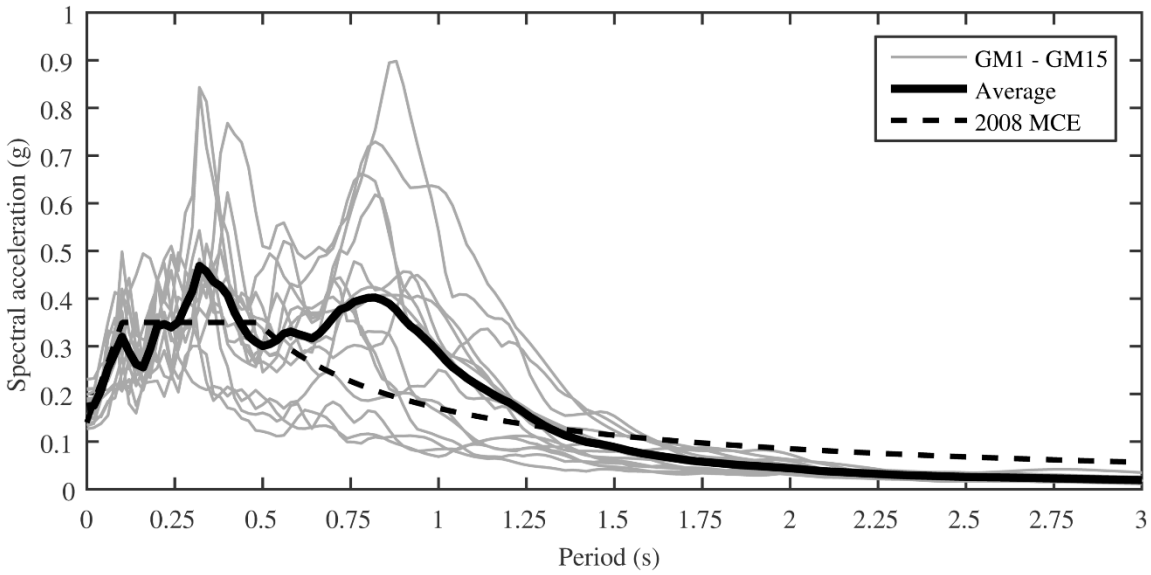

Figure 3.16 – Ground motion suite response spectra.

3.4.1 Single Record Dynamic Analyses

A few single-record dynamic analyses are presented to give a more thorough examination of limit-state sequences that the prototype building models experienced under dynamic loading. The most common limit states observed under the 15 GMs were the same as those observed from the SPO analyses: fracture of compression brace-gusset welds followed by midspan flexural beam yielding (long-link EBF mechanism). Unlike the SPO analyses, where limit states were isolated within Story 1 due to the constant load pattern, limit states in multiple stories were common in dynamic analyses because of higher mode effects. Ground motions were scaled relative to the MCE, which has an associated scale factor, SF, of 1.0. Collapse of the building models was defined by the instance where drifts exceeded 10% within any story ($\delta/h > 0.10\%$), as recommended by Vamvatsikos and Cornell (2002). The 3-story prototype buildings studied here often became globally unstable following the accumulation of δ/h = 3–5% within any story, and thus δ/h quickly diverged to over 10% shortly thereafter.

For each single record analysis presented, the sequence of limit states is labeled on the plots of V_B and illustrated schematically.

The first single record comparison presented is between building models R3-3-BC-Pin (all beam-column connections pinned) and R3-3-GBC-Pin (only gravity connections pinned) in Figure 3.17. Base shear (V_B) and roof drift (δ_R/h) are shown for the two building models, which were subjected to GM1 with SF = 0.6, or 60% of the MCE. Behavior exhibited prior to the first limit state within both building models was identical since the frame action behavior provided from the beams and columns was dwarfed by the lateral force resisting capacity of the braces in this elastic stage. Under this scaled GM both building models experience weld fractures in all three stories in quick succession (Figure 3.17), which significantly increased the flexibility of the building and significantly decreased their strength. In R3-3-BC-Pin, where all beam-column connections are modeled as perfectly pinned, this leads to the eventual development of δ_1/h_1 = 10%, marking collapse of the building. In R3-3-GBC-Pin, collapse is prevented because of the added strength and stiffness provided by modeling the more realistic beam-column behavior of the CBF connections rather than considering them as pins.

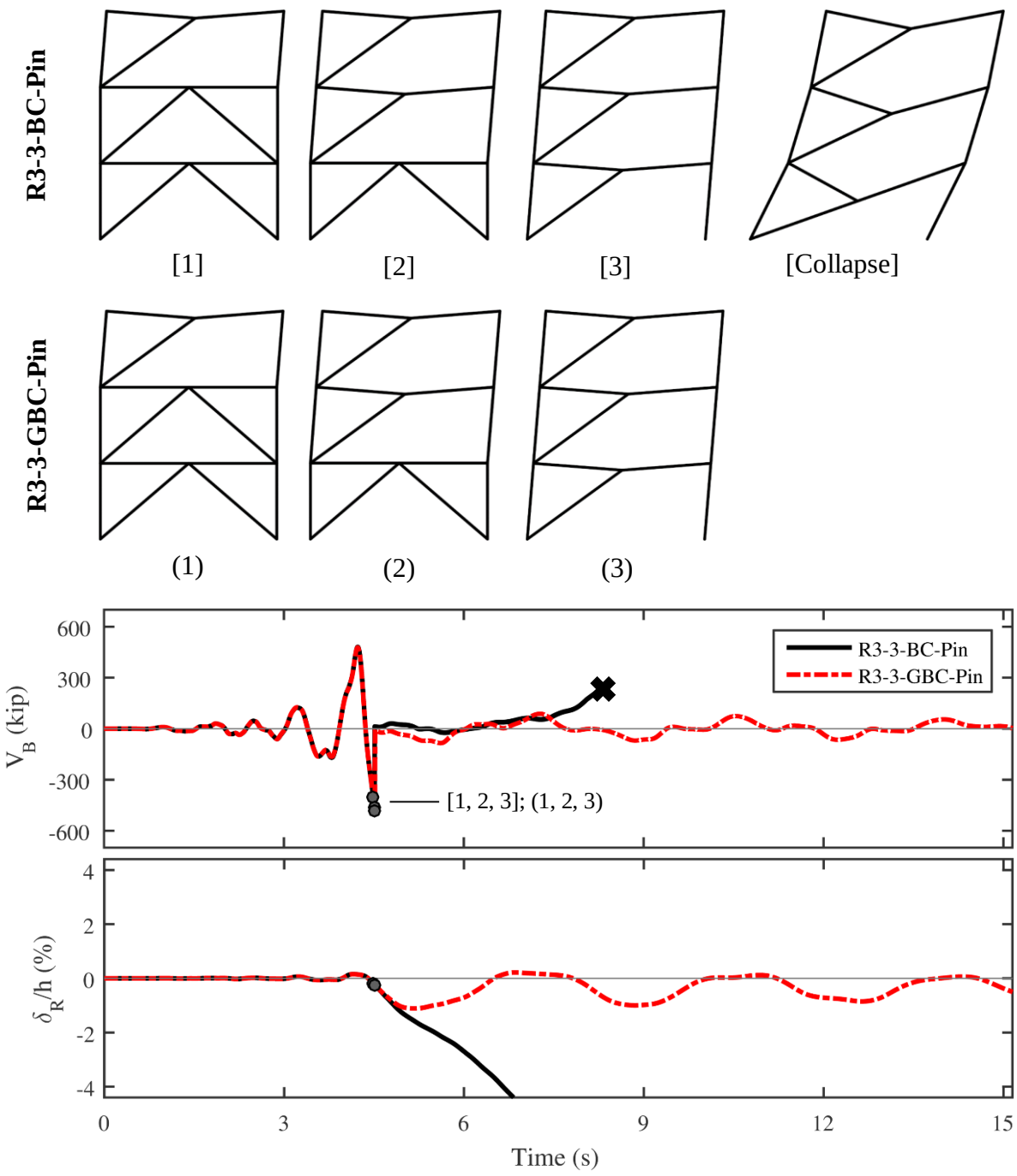

Figure 3.17 – Dynamic response of building models R3-3-BC-Pin and R3-3-GBC-Pin for GM1 with *SF* = 0.6.

In the next comparison, R3-3-GBC-Pin (pinned gravity connections) was continually subjected to increasingly larger scaled GM1 time histories until collapse was observed, at *SF* = 1.6. The baseline building model, R3-3-Baseline (actual gravity connection behavior) was then subjected to this scaled GM, and the comparison between these two building models is shown in Figure 3.18. Like the comparison between R3-3-BC-Pin and R3-3-GBC-Pin at a lower SF, these two building models behaved identically in the elastic range and experienced limit states at similar times and locations. The post-elastic behavior of the two models under this scaled ground motion did vary, however, as collapse was prevented in R3-3-Baseline but not in R3-3-GBC-Pin. Thus, although the flexural capacity provided by the CBF connections alone in R3-3-GBC-Pin was not enough to prevent collapse, collapse was prevented when the more realistic behavior of the gravity connections was modeled in R3-3-Baseline, rather than considering these connections as pins.

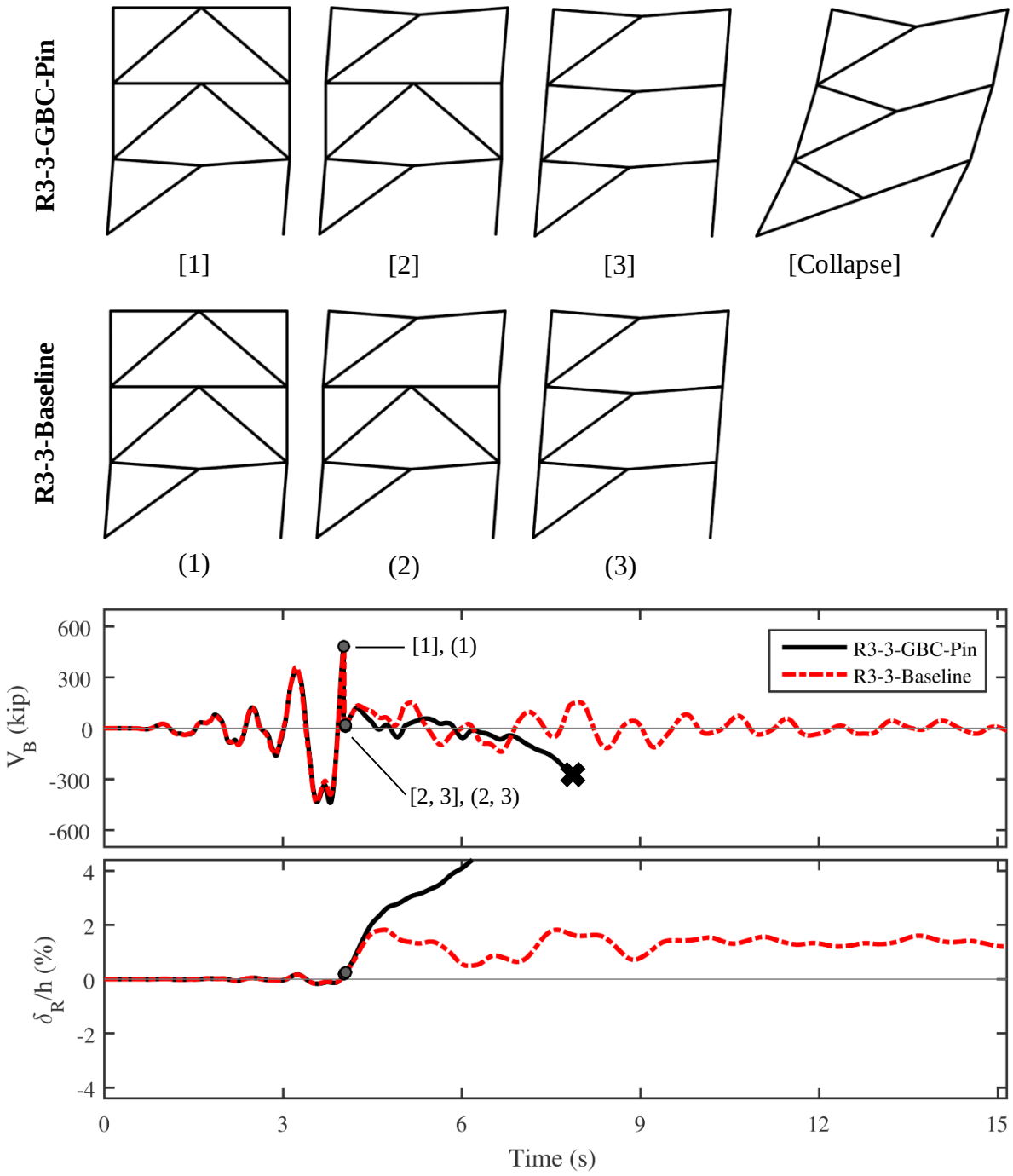

Figure 3.18 – Dynamic response of building models R3-3-GBC-Pin and R3-3-Baseline for GM1 with *SF* = 1.6.

When R3-3-Baseline was subjected to increasingly larger scaled GM1 time histories, collapse was observed at *SF* = 4.8, or three times the SF that caused collapse in R3-3-GBC-Pin. Thus for this GM, correctly modeling the flexural behavior of gravity connections significantly increased the collapse prevention performance. This observation was different from an earlier comparison between these same building models, as the gravity connections did not appear to have a noteworthy influence on reserve capacity in the SPO analyses (Figure 3.7). Gravity connection contribution was magnified in this dynamic simulation due to higher mode effects and redistribution of story shears, which were not captured in the SPO analyses. Additionally, brace-gusset weld fracture only occurred in Story 1 in the SPO analyses of these two models, and thus the upper two stories acted as a rigid body with zero beam and column bending. Conversely, in the dynamic analysis, weld fractures in multiple stories activated beam and column bending throughout the entire height of the building, increasing the effectiveness of the gravity connections.

The influence that adding top and seat angles to all beam-column connections (R3-3-BC-Enh) had on collapse prevention performance for GM1 at *SF* = 4.8 is highlighted in Figure 3.19. Unlike the earlier two comparisons, the addition of top and seat angles had an appreciable influence on the stiffness of the gravity framing system relative to the braced frame, which altered the sequence of limit states and behavior in the elastic range. Due to the increased stiffness of the gravity bays in R3-3-BC-Enh, the gravity columns took larger shear demands in the elastic region. Thus, the first brace-gusset weld fracture observed in R3-3-BC-Enh occurred at t = 3.09 s., slightly later than the first brace-gusset weld fracture in R3-3-Baseline (t = 2.18 s.). Although the limit states occurred at different times, eventually brace-gusset weld fracture occurred within each story in both building models. While the “as-designed” beam-

column connections in R3-3-Baseline were insufficient to overcome the *P-Δ* effects following these limit states and prevent collapse, this was not the case for R3-3-BC-Enh. In this model, the assumed addition of top and seat angles resulted in enough reserve stiffness and strength to prevent the development of a soft-story collapse mechanism (Figured 3.19).

The ability for brace reengagement to lend reserve capacity and prevent collapse in dynamic simulations is shown in Figure 3.20, for GM5 with SF = 2.4. For this scaled GM, R3-3-Baseline experienced brace-gusset weld fractures early in the time history but collapsed significantly later, at around t = 36 s. This behavior was compared with R3-3-BrRe–100, where brace reengagement equivalent to 100% of the bearing capacity (133 kN [30 kips]) was assumed. The effect of this small brace reengagement strength on V_B was not noticeable, though there was a noticeable effect on δ_R/h. While drifts began to rapidly diverge after t = 30 sec in R3-3-Baseline, this was not the case for R3-3-BrRe-100, as the stiffness provided from brace reengagement prevented collapse.

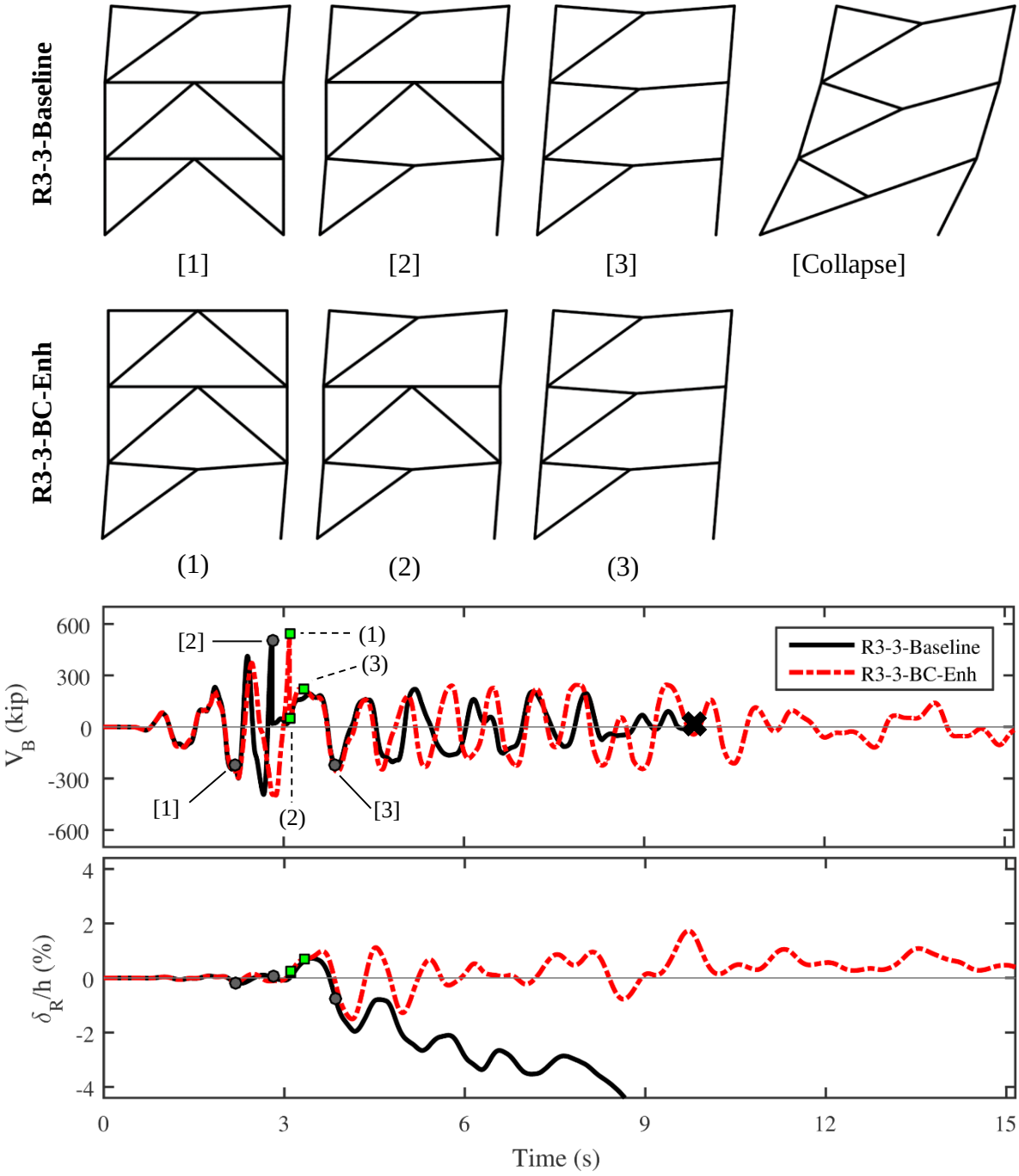

Figure 3.19 – Dynamic response of building models R3-3-Baseline and R3-3-BC-Enh for GM1 with *SF* = 4.8.

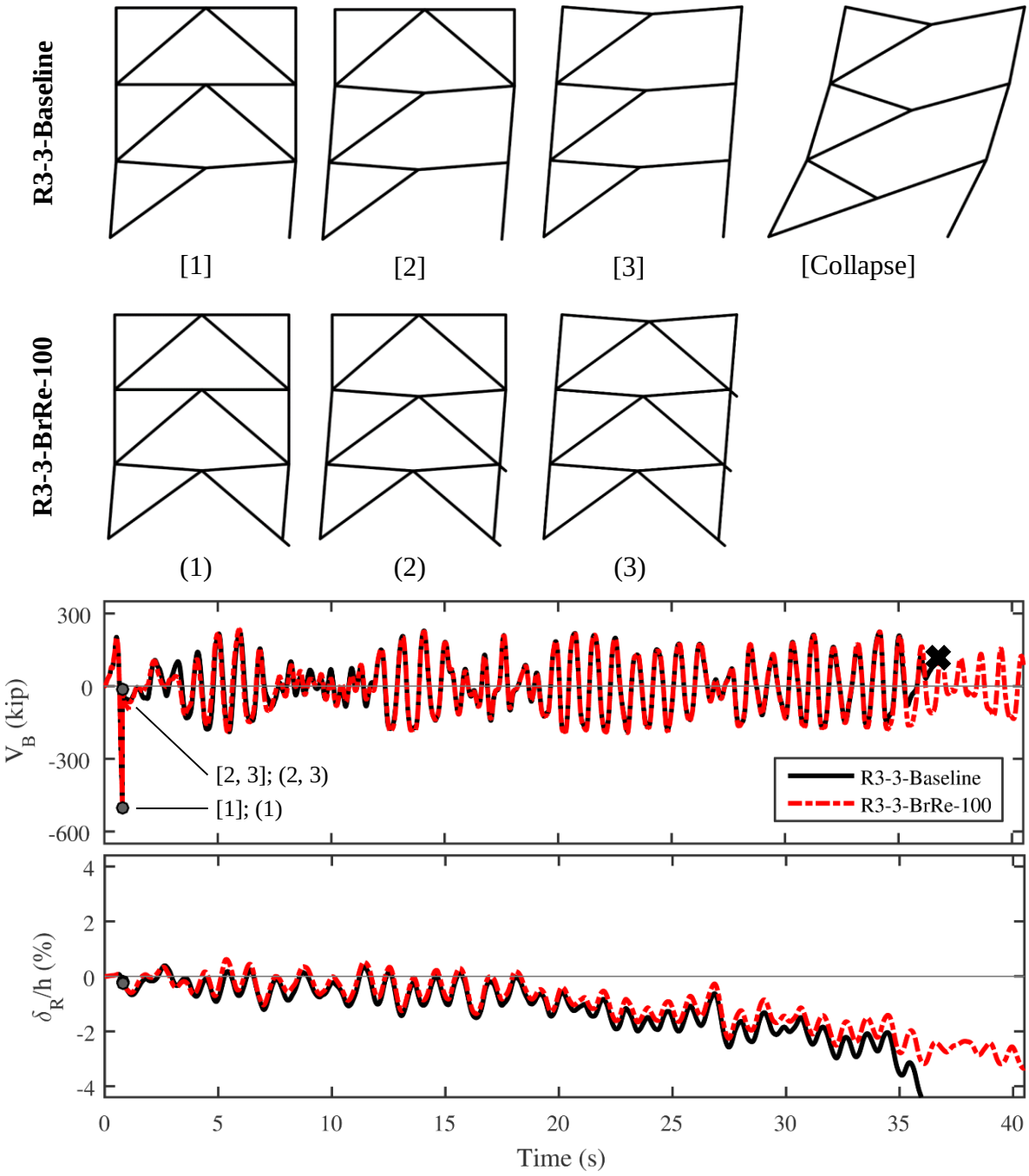

Figure 3.20 – Dynamic response of building models R3-3-Baseline and R3-3-BrRe-100 for GM5 with *SF* = 2.4.

Altering modeling assumptions more accurately represent the real building or incorporating structural enhancements that improve reserve capacity will not always improve collapse prevention performance for every GM, as Figure 3.19 reveals. Certain changes to modeling assumptions can alter the sequence of limit states and change the entire behavior of the building. In some cases, such as the example shown in Figure 3.21, these changes may be detrimental. In this figure, the results for GM10 with SF = 2.6 are presented for R3-3-Baseline, in which the braced bay columns are modeled as fixed, and R3-3-Base-Pin, in which the braced bay columns are modeled as pins. In both models, weld fractures in both Stories 1 and 3 occur around t = 10 s. Following this, the reserve capacity in R3-3-Baseline was visibly larger due to the added stiffness and strength provided by bending at the base of the braced bay columns (Figure 3.21). This added reserve capacity was detrimental, however, and caused a Story 2 brace-gusset weld fracture at t = 18 s. Following this limit state, the building did not have the necessary reserve capacity to prevent collapse. In R3-3-Base-Pin, the decreased stiffness after weld fractures in Stories 1 and 3 protected the building from further damage, and no weld fracture occurred in Story 2. This decreased stiffness continued to protect the building from the more energetic period ranges of this GM, and collapse was avoided.

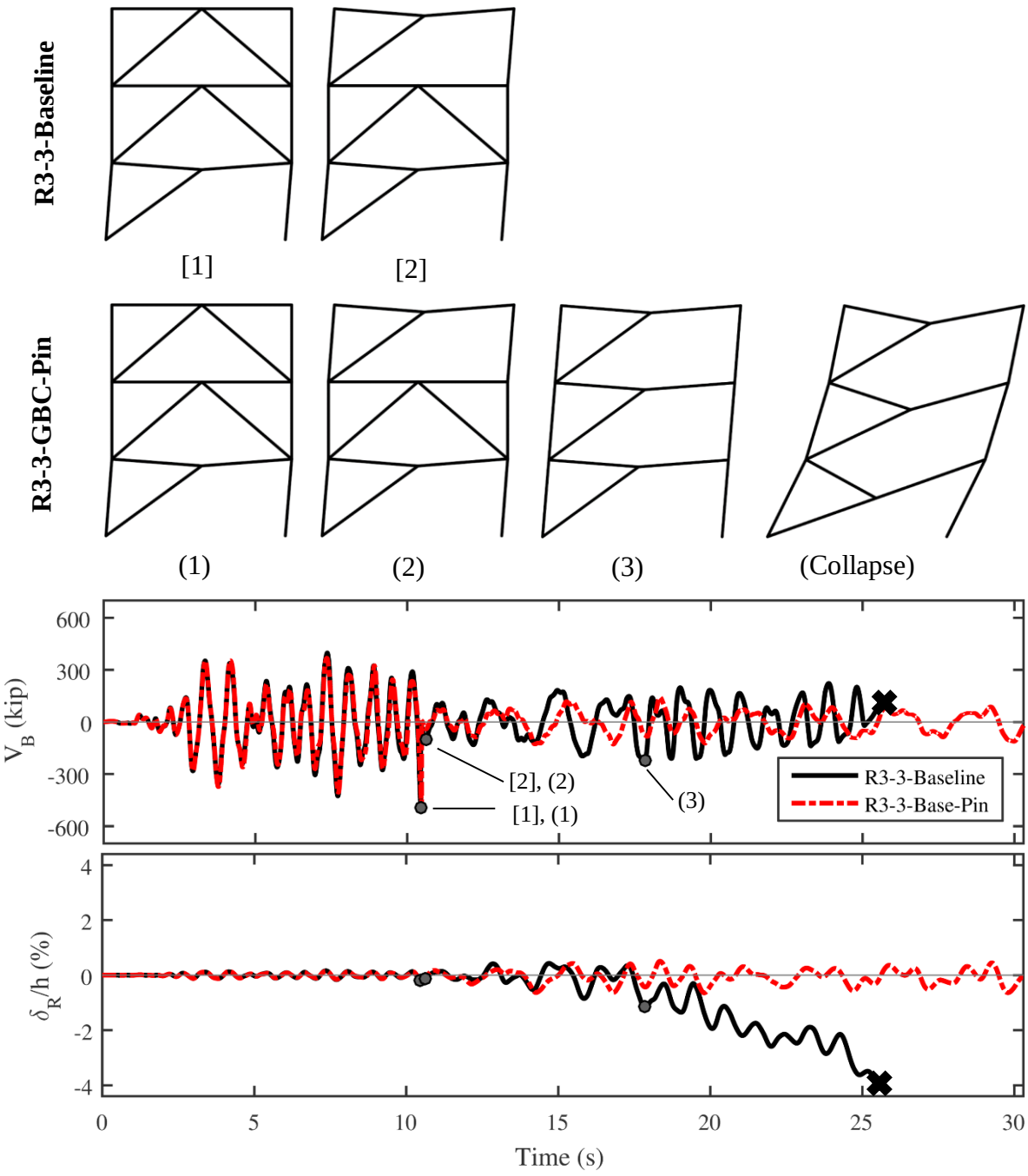

Figure 3.21 – Dynamic response of building models R3-3-Baseline and R3-3-Base-Pin for GM10 with *SF* = 2.6.

3.4.2 Incremental Dynamic Analyses

Further dynamic simulations were performed by scaling up each GM incrementally by a SF increment of 0.2, and starting from $SF = 0.2$. Once building collapse was identified for a given GM, no further SF*s* were tested for that GM. Thus, the phenomenon of structural resurrection—which is when a building experiences collapse at some SFs only to reappear as non-collapsing at a higher SF—was not investigated (Vamvatsikos and Cornell, 2002). The first SF corresponding to collapse of building models for each of the 15 GMs is shown in Table 3.5, for building models R3-3-Baseline, R3-3-GBC-Pin, R3-3-BC-Pin, R3-3-BC-Enh, R3-3-Beam-50, and R3-3-Col-50. In addition, the multi-record incremental dynamic analyses (IDAs) are summarized in Figure 3.22 as a series of 16%, 50% (median), and 84% fractile curves for the building models. IDA curves were created by recording the largest δ/h within a building model at each SF and for every GM. Median, 16%, and 84% fractiles are calculated until collapse occurs in 50% (8 of 15), 84% (13 of 15), and 16% (3 of 15) of GMs, respectively, at which point the calculated values yield infinity, which is identifiable by flat line regions of the plots. For example, in building R3-3-Col-50, at $SF = 1.0$ the third largest (3 of 15, 16%) largest δ/h was 1%, the eighth (8 of 15, 50%) was 1.5%, and the thirteenth (13 of 15, 84%) was 2% (Figure 3.22f). The individual IDAs for these six building models (all 15 GMs), are shown in Appendix A. One defining characteristic of these plots, is *weaving*, which is defined as points on an IDA curve where the structure appears to be headed towards collapse, only to then display lower drift levels as SFs are further increased. This behavior was previously observed in similar nonlinear models of low-ductility CBFs (Hines et al., 2009; Stoakes, 2012) and is a result of the strong dependence of the sequence of limit states on structural behavior, which is not typical of high-ductility systems.

Table 3.5 – Lowest scale factor (*SF*) corresponding with building collapse

Building Model "R3-3-"	Ground Motion															Avg. *SF*
	1	2	3	4	5	6	7	8	9	10	11	12	13	14	15	
Baseline	4.8	5.4	3.8	3.6	2.4	2.0	4.8	3.4	3.6	2.6	3.0	3.4	3.6	2.0	3.8	3.5
GBC-Pin	1.6	3.4	3.2	1.8	2.0	1.4	3.4	1.8	3.4	1.6	2.0	2.0	2.4	1.4	3.0	2.3
BC-Pin	0.6	0.8	1.4	0.4	1.6	1.4	2.4	0.8	0.2	0.6	1.2	1.0	1.4	0.4	1.0	1.0
BC-Enh	8.8	6.6	5.8	4.2	4.2	5.0	5.8	4.6	5.2	5.2	3.6	3.6	4.8	4.2	7.0	5.2
Beam-50	5.2	6.6	6.2	4.0	3.2	2.8	4.8	4.0	3.6	3.2	3.8	3.8	5.0	2.6	7.0	4.4
Col-50	4.6	8.8	4.0	3.8	2.4	2.0	5.0	4.2	2.8	2.6	3.0	3.6	4.4	2.4	7.4	4.1

As shown in Table 3.5, the most conservative building model, R3-3-BC-Pin, experienced collapse at an average SF of 1.0, or the MCE. Collapse was observed at or below this level for a majority (8 of 15) of GMs in this model. This is additionally identifiable in Figure 3.16c by the flat line region at $SF = 0.8$, which was the largest SF in which this building model avoided collapse in over half of the GMs. When realistic flexural behavior was considered for CBF connections in R3-3-GBC-Pin, the average SF at collapse increased to 2.3, with zero collapses occurring for the MCE or lower. When realistic flexural behavior was considered for the gravity connections as well (R3-3-Baseline) the average SF at collapse further increased to 3.5. Finally, when top and seat angles were added to all beam-column connections, the average SF at collapse increased to 5.2. The hierarchy of average SF at failure for these four building models agrees with results from the SPO analyses and the individual single record cases presented, which confirm that beam-column connection behavior significantly influences reserve capacity and collapse prevention performance. When beam and column flexural capacities were increased by 50% in R3-3-Beam-50 and R3-3-Col-50, respectively, reserve capacity was also noticeably increased and the average SF at collapse increased to 4.4 and 4.1.

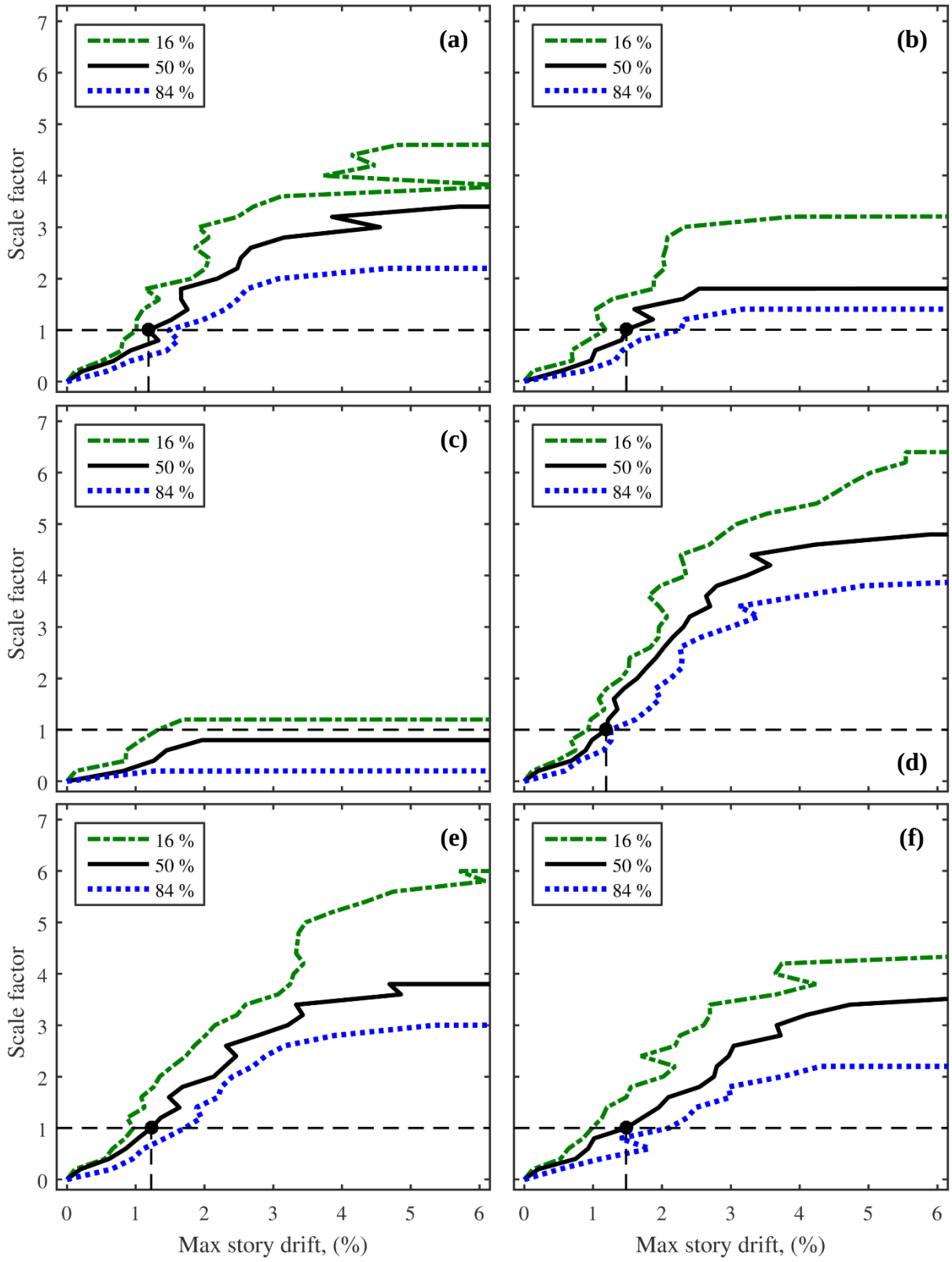

Figure 3.22 – Incremental dynamic analyses of three story prototype chevron frame baseline building model and variations: (a) R3-3-Baseline; (b) R3-3-GBC-Pin; (c) R3-3-BC-Pin; (d) R3-3-BC-Enh; (e) R3-3-Beam-50; and (f) R3-3-Col-50.

3.5 SUMMARY OF RESERVE CAPACITY COMPONENT STUDY

A numerical model was created in *OpenSees* to investigate the reserve capacity of a prototype 3-story building with an R = 3 chevron CBF as its SFRS. A combination of SPO analyses and dynamic analyses was used to assess the impact of varying modeling assumptions or potential enhancements for components that had been identified either experimentally in previous research or anecdotally in post-earthquake reconnaissance as contributors to reserve capacity. The investigated modeling assumptions included beam-column connections (actual behavior vs. pinned) and base fixity (pinned vs. fixed). The investigated enhancements included the addition of top and seat angles to beam-column connections, the increase of column and beam flexural capacity, and the increase of brace-gusset weld capacity. The phenomenon of brace reengagement was also investigated, with varying degrees of reengagement strength. Together, these modeling changes allowed for a comprehensive investigation of various sources of reserve capacity within a typical low-ductility CBF and allowed for the development of some initial conclusions regarding the relative efficiency of each reserve capacity source.

Beam-column connections, including both CBF connections and gravity connections, were found to have a significant effect on reserve capacity, and increased the required GM intensity for building collapse when they were explicitly modeled to capture their expected behavior rather than assuming a pinned condition. When top and seat angles were added to these connections, the reserve capacity and collapse prevention performance of the building was improved. Base fixity affected reserve capacity by opposing the P-Δ effects generated by gravity loads and providing the ability for additional column hinges to form at the base. Reserve capacity was also increased when brace reengagement was considered, and the

stiffness provided from reengagement delayed soft-story collapse mechanisms. Increases in column and beam sizes promoted additional reserve capacity through amplification of the available strength from the frame action mechanisms that developed following brace-gusset weld fracture. This study provided an improved understanding of the ability for various components within a building to contribute to reserve capacity, and provided an important transition between the literature review and the experimental tests that followed. Specifically, the significant amounts of reserve capacity provided by the braced bay columns through frame action as well as the braced bay beams through the long-link EBF mechanism motivated further study into investigating system types other than $R = 3$ and system configurations other than chevron. Multiple new potential areas for exploration arose from this study, including the potential for developing the long-link EBF mechanism in a split-x configuration and the effect of the seismic detailing and proportioning requirements of the alternate low-ductility SFRS—the $R = 3.25$ OCBF. A full-scale testing program was developed with the goal of answering these and other similar questions.

CHAPTER 4

FULL-SCALE EXPERIMENTAL FRAME TESTS

To evaluate limit states and damage progression in low-ductility braced frames, and to physically observe and quantify some of the sources of reserve capacity, two full-scale tests were conducted at Lehigh University's Advanced Technology for Large Structural Systems (ATLSS) facility, which was at the time an experimental facility (NEES@Lehigh) in the George E. Brown, Jr. Network for Earthquake Engineering Simulation. The experimental specimens were concentrically braced frames (CBFs) taken from the 3-story prototype building defined in Chapter 3. The purpose of the tests was to explore both connection and overall frame behavior of the low-ductility CBFs in the post-elastic range. These tests were used to update and refine existing numerical models so that a larger suite of low-ductility CBFs could be more accurately studied. The goal of this study was to assess the relationship between system type, system configuration, and individual system components in the context of reserve capacity.

The design of the test units and loading system was a collaborative effort between faculty and graduate students from the University of Illinois and Tufts University. As discussed in Section 1.5.2, Tufts University graduate student Cameron Bradley had a larger emphasis on the design and construction of the test units. Comprehensive pre-test information including member design calculations, detailed instrumentation plans, shop drawings, and more are discussed in his thesis (Bradley, 2016).

4.1 FRAME DESIGNS[1]

Several constraints at ATLSS dictated aspects of the final design of the two test units (Figure 4.1). A full-scale frame was selected for testing, primarily because connection accuracy would be difficult to maintain, and less-common member sizes would be harder to procure at reduced scale; however, this meant that the full 3-story prototype could not be tested due to lab height restrictions. A 2-story frame was taken from the existing 3-story prototype rather than creating a new 2-story prototype to compare experimental results with the numerical study. Two different seismic force resisting systems (SFRSs) were developed for the prototype building using a seismic weight of 28.5 MN [6,400 kips] for the entire building. The test units were 2-story CBFs based on SFRS designs for the 3-story prototype building per forces specified in ASCE 7–05 (ASCE, 2005). Considering precise damage and failure mechanisms for low-ductility CBFs had not been shown experimentally prior to these tests, the two test units were designed to expose a broad range of mechanisms. Consistent with this goal, the two frames were designed per distinct and contrasting approaches that are representative of current practice in moderate seismic regions. The first approach, embodied in the $R = 3$ provision, aims to relieve the designer of seismic detailing considerations. The $R = 3$ frame was designed in the chevron configuration, which is often favored for coordinating doors and passageways within an architectural program. In keeping with the simplicity of the $R = 3$ provision, this frame was proportioned using a design base shear, V, which was calculated using the approximate period $T_a = C_t h_n^x = (0.02)(45 \text{ ft.})^{0.75} = 0.347$ s. (ASCE 7–10, *Equation 12.8-7*). In contrast to the $R = 3$ approach, the second frame was designed per a more thoughtful approach

[1] Section 4.1 (only, not the subsections) has been adapted from an accepted journal manuscript with slight modifications: Sizemore, J., Fahnestock, L., Hines, E., and Bradley, C. (2016). Parametric Study of Low-Ductility Concentrically-Braced Frames under Cyclic Static Loading." *Journal of Structural Engineering.*

that is widely recognized to reflect a higher standard of care in moderate seismic regions, an ordinary concentrically braced frame (OCBF) in the split-x configuration. An OCBF includes local slenderness (b/t) limits for braces, and requires consideration of amplified seismic loads with a system overstrength factor ($\Omega_0 = 2$) for connection and column design, while a split-x configuration provides a multi-story load path through tension and compression braces. For the OCBF design, a provision in ASCE 7–10 was used that allows a designer to increase the building period to $1.6T_a$ (for $S_{D1} = 0.15$) when calculating V if it is lower than the analytically calculated period found from an eigenvalue analysis or similar procedure. For the OCBF, the period obtained from an eigenvalue analysis using the mass of the prototype building (Bradley, 2016) was 0.635 s., so the calculated design period (T_c) used to determine V was $1.6T_a = 0.555$ s., which resulted in a significantly lower base shear (V = 858 kN [193 kips]) than the $R = 3$ design (V = 1,490 kN [335 kips]). Schematic elevations of the test units with member sizes and boundary conditions are shown in Figure 4.1. To provide boundary conditions that are more exact for the two stories that were tested, the columns were extended slightly past the Level 3 beams so that a gusset plate for a partial Story 3 brace connection could be included.

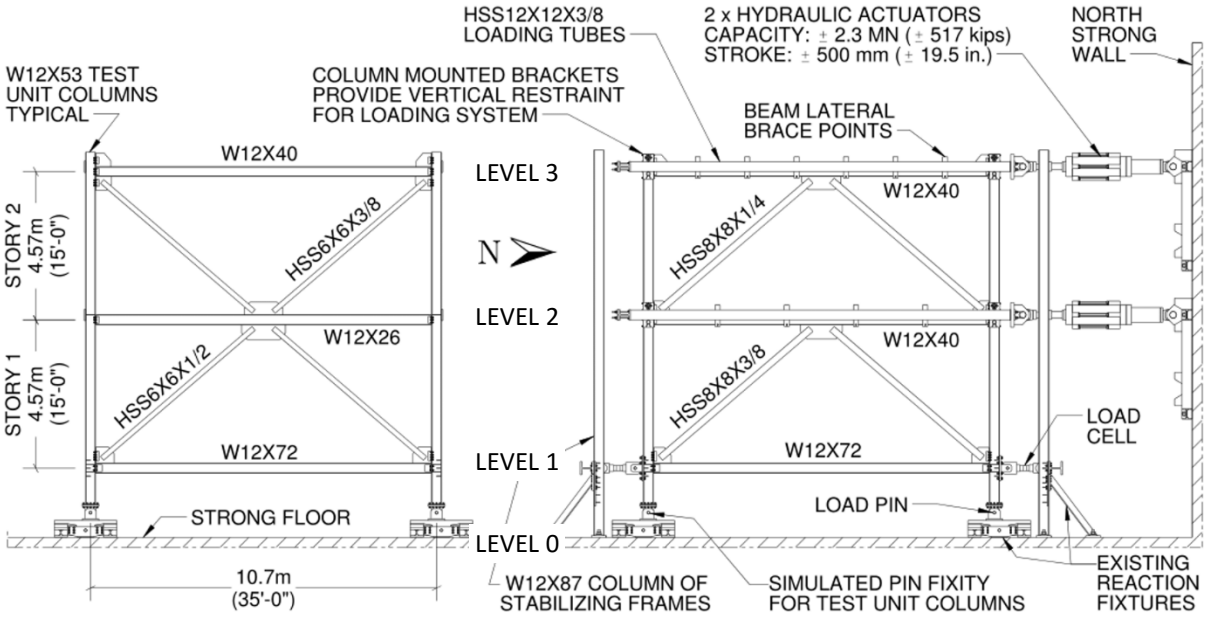

Figure 4.1 – Experimental test unit elevation: split-x OCBF (left) and chevron $R = 3$ (right). Modified from original drawing by Cameron Bradley (2016).

4.1.1 Loading System and Loading Protocol

A simple test procedure allowed for easier identification and isolation of reserve capacity. Each frame was loaded quasi-statically with two 2,300 kN [517 kips] actuators, with total stroke of 1.0 m. [39 in.] (±500 mm. [19.5 in.]), as shown in Figure 4.1. The chosen scheme loaded the frame in direct bearing at the floor levels through a rounded plate section that was welded to a W-section stub, which was bolted to the actuators. The rounded plates passed load into the test frame through bearing on plates welded to the test frames (Figure 4.2). The frame was loaded using the equivalent lateral force (ELF) static load distribution (ASCE, 2013) based on the story heights and masses from the 3-story prototype building. Because only two stories from the 3-story prototype were tested, the equivalent loads from Levels 3 and 4 (roof) were lumped together at Level 3, resulting in a load ratio from the Level 3 to Level 2 of 3.42:1. Thus, when the Level 3 actuator was at 342 kN, the Level 2 actuator was at 100 kN. Throughout the test, displacement control was essential as the primary control mode since numerical

simulations and general knowledge of behavior for these systems led to the expectation of force drops associated with brittle limit states. Placing both actuators in force control is not possible since after a brittle limit state decreased the lateral capacity of the test unit, the force protocol would continually try to achieve the current target force level, resulting in sudden and large increases in displacement. In the severe case, were the target force limit unachievable regardless of displacement, the frame would continue to be pushed as far as the actuators would allow unless manual intervention stopped the dangerous behavior. Thus, the actuator control scheme employed displacement control of the Level 3 actuator throughout the tests. To keep the force ratio as intended while providing a safe testing procedure, the Level 2 actuator was slaved in force control to be 22.6% of the Level 3 actuator.

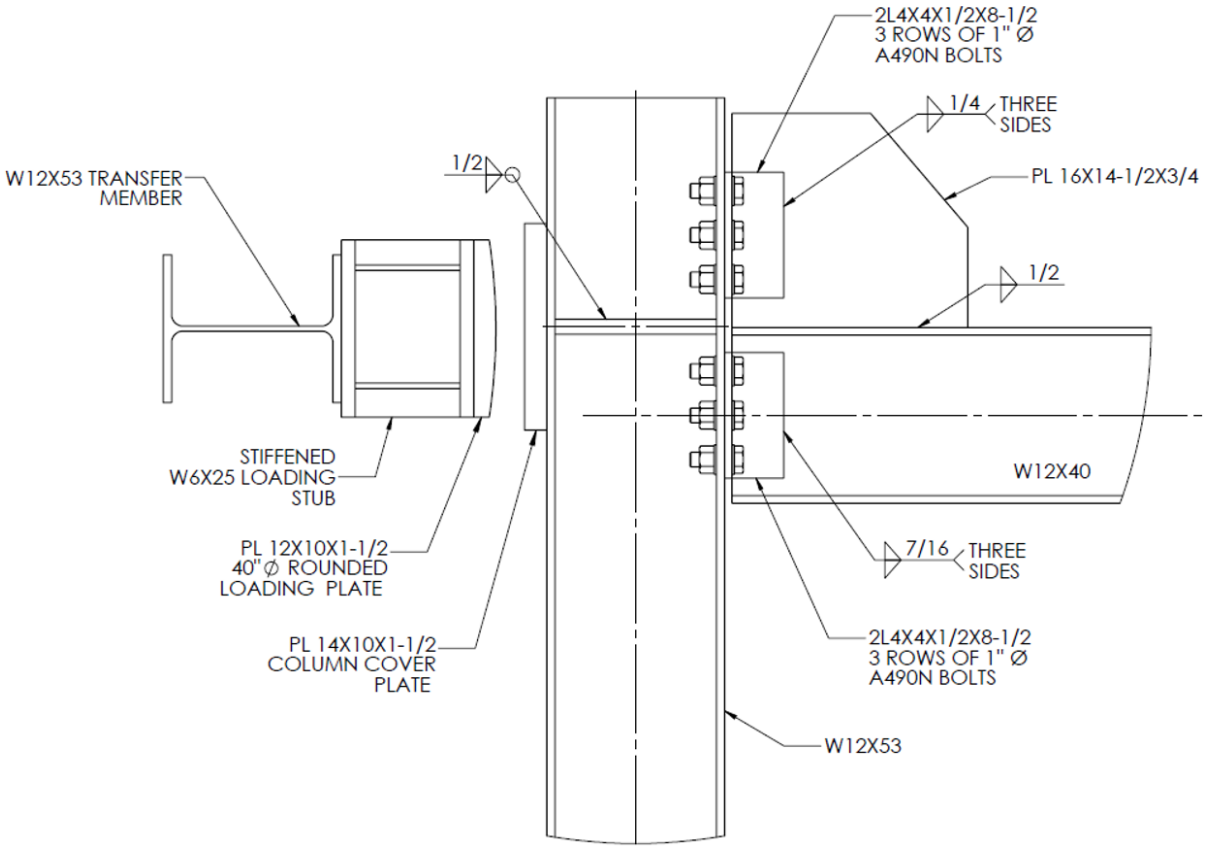

Figure 4.2 – Mechanism for load transfer into the test frames. Modified from original drawing by Cameron Bradley (2016).

Due to limitations of the testing facility and a lack of compatibility between common gravity load application methods (which typically involve a positive attachment to the test unit) and the selected method for applying lateral loads (no positive attachment – bearing only), gravity loading was not applied during the testing.

4.1.2 Test Frame Materials and Connections

To provide a consistent and simplified design, all gusset plates were cut from a 19 mm. [3/4 in.] thick steel plate and all double web angle connections other than the ground beam connection were made using 4x4x1/2 angles. The double web angle connections were welded to the beams and bolted to the columns using 19 mm. [3/4 in.] diameter A490N bolts. Brace-gusset connections were designed with a 6 mm. [1/4 in.] weld, but per standard construction practices, an 8 mm. [5/16 in.] weld was specified for these brace-gusset connections to account for the 1 mm. [1/16 in.] gap between the gusset plate and the brace slots. All connections were designed using the uniform force method and prying action was considered.

Members were made from their common material grades as summarized in the AISC *Steel Construction Manual* (AISC, 2011), except for braces, which were made from A1085 steel (ASTM, 2015) rather than the typical A500 steel for square hollow sections. There are two main differences between A1085 steel and A500 steel. First, tighter tolerances on wall thickness allows A1085tubes to be designed using properties based on the nominal wall thickness, whereas A500 tubes must be designed with a wall thickness equal to 93% of the nominal thickness. Second, tighter material tolerances: A1085 steel has both a minimum (345 MPa [50 ksi]) and maximum (480 MPa [70 ksi]) specified yield stress (F_y), while A500 steel has only a minimum specified yield stress, F_y = 320 MPa [46 ksi]. Mill report data sheets provided for beams, column, and braces, listed the measured yield ($F_{y,mill}$) and tensile capacities

($F_{u,mill}$) for the materials used. Following the tests, tensile coupons were cut from member drops and tested to obtain member-based stress-strain properties for later numerical modeling considerations. A summary of the material properties for test unit members from the mill reports (mill) and coupon tests (cpn) is given in Table 4.1. The reported values for W shapes were averaged from coupons taken from the webs (3) and the flanges (2 per flange – 4 total). Refer to Appendix B for a discussion of the coupon testing program and associated stress-strain curves for each member.

Table 4.1 – Material properties for test unit members

Member	Section	ASTM Material	$F_{y,mill}$ (MPa [ksi])	$F_{u,mill}$ (MPa [ksi])	$F_{y,cpn}$ (MPa [ksi])	$F_{u,cpn}$ (MPa [ksi])
Frame 1: R = 3 Chevron						
S. Column	W12x53	A992	393 [57]	217 [75]	365 [53]	496 [72]
N. Column	W12x53	A992	372 [54]	496 [72]	352 [51]	476 [69]
L3 Beam	W12x40	A992	400 [58]	496 [72]	352 [51]	476 [69]
L2 Beam	W12x40	A992	379 [55]	490 [71]	365 [53]	490 [71]
S2 Brace	HSS8x8x1/4	A1085	407 [59]	503 [73]	365 [53]	448 [65]
S1 Brace	HSS8x8x3/8	A1085	421 [61]	531 [77]	421 [61]	496 [72]
Frame 2: R = 3.25 OCBF Split-x						
Both Columns	W12x53	A992	372 [54]	510 [74]	372 [54]	503 [73]
L3 Beam	W12x40	A992	-	-	365 [53]	483 [70]
L2 Beam	W12x26	A992	379 [55]	469 [68]	352 [51]	448 [65]
S2 Brace	HSS6x6x3/8	A1085	400 [58]	524 [76]	428 [62]	496 [72]
S1 Brace	HSS6x6x1/2	A1085	393 [57]	469 [68]	400 [58]	448 [65]

4.1.3 Test Instrumentation

Both test units were heavily instrumented to capture internal (member) and external (reaction) forces, local deformation (connection rotations), and global displacements. A partial

schematic of the instrumentation plan is shown in Figure 4.3, on an elevation of the split-x test unit. Four strain gages were placed individually at each of the locations (which were expected to remain nominally elastic) labeled on Figure 4.3 to allow for the calculation of moments and axial forces from the combined group of strain readings at the section. Two groups of strain gages were placed between each connection region within an element to allow for the calculation of the moment gradient (shear) between the adjacent instrumented sections. String potentiometers (string pots) were provided to measure beam vertical displacement during the long-link eccentrically braced frame (EBF) mechanism, as well as to capture brace longitudinal deformation, both during buckling and brace reengagement. Rotation meters (inclinometers) were provided at the beam midspan to measure the long-link EBF rotation, and at the beam-column intersections to measure connection rotation. Temposonics were provided at each level to measure the overall frame displacement and interstory drifts (δ/h). Linear Variable Displacement Transducers (LVDTs) were provided above and below the gusset plates to measure connection rotation and at the load cells (Level 1) to measure differential displacement of the ground links and the stabilizing frame (not shown). A comprehensive description of the instrumentation plan, data channels, and camera setup is provided by Bradley (2016).

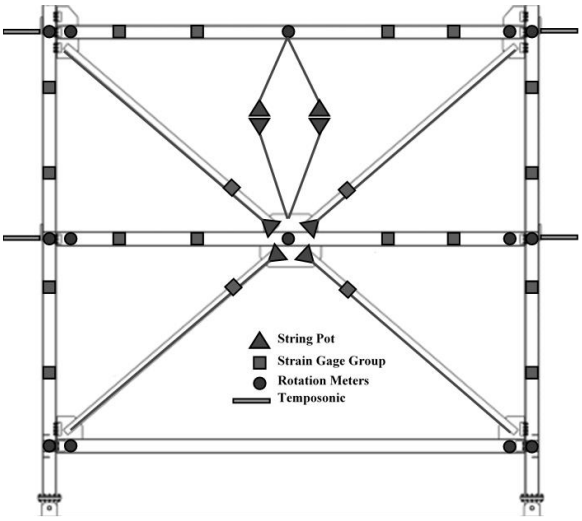

Figure 4.3 – Simplified instrumentation plan. Modified from original drawing by Cameron Bradley (2016). A detailed instrumentation plan is provided in Bradley (2016).

4.2 FRAME TEST PREDICTIONS

Prediction of the limit state sequences for the test units were developed using demand-to-capacity ratios (DCRs). Capacities were computed for brace members and brace-gusset weld groups using mill data (Table 4.1) and nominal weld capacities with an assumed overstrength factor of 10% ($1.1R_n$). A 6.1 m. [20 ft.] effective length was considered in calculation of brace buckling capacities, which corresponds to the end-to-end length of the braces (7.0 m. [23 ft.] workpoint-to-workpoint length). Demands were approximated using assumed story shears associated with the 3.42:1 experimental loading protocol. The DCRs were calculated assuming a static pushover in the North direction. The process for determining the expected base shear, V_B, and associated limit state at the onset of inelastic behavior involved a four step process. First, anticipated member demands were calculated from statics as if the design base shear, V, were applied to frame. Second, the design level DCR values were calculated by dividing the expected member demands by their capacity (Table 4.2). Third, the primary limit state was identified in the member or connection that had the highest DCR,

DCR_{max}. Fourth, a prediction for the base shear, V_B, associated with this limit state was calculated by V/DCR_{max}. As shown in Table 4.2, the R = 3 chevron CBF was expected to experience Story 2 North brace buckling at V_B = 1,490/0.63 = 2,365 kN [525 kips], while the R = 3.25 split-x OCBF was expected to experience Story 1 North brace buckling at V_B = 858/0.63 = 1,360 kN [305 kips].

Table 4.2 – Demand-to-capacity ratios at $V_B = V$ for the two test units (forces in kN)

Member	R = 3.25 split-x: V = 858 kN			R = 3 chevron: V = 1,490 kN		
	Capacities	Demand	DCR	Capacities	Demand	DCR
Story 2 North Brace	1,984[c] 1,525[b]	383	0.193[c] 0.251[b]	-1,210[a] -1,272[b]	-761	**0.629[a]** 0.598[b]
Story 2 South Brace	-805[a] -1,525[b]	-495	0.614[a] 0.324[b]	1,535[c] 1,272[b]	761	0.496[c] 0.598[b]
Story 1 North Brace	–974[a] -1,997[b]	-614	**0.630[a]** 0.307[b]	-1,753[a] -1,597[b]	-966	0.551[a] 0.605[b]
Story 1 South Brace	2,415[c] 1,997[b]	502	0.208[c] 0.251[b]	2,589[c] 1,597[b]	966	0.373[c] 0.605[b]
$V_{B,e}$	858/0.630 = **1,362kN (1.59*V*)**			1,490/0.629 = **2,369kN (1.59*V*)**		

[a] buckling capacity; [b] brace-gusset weld capacity; [c] brace net section rupture capacity

DCR analysis of the R = 3 test unit revealed three potential limit states all within a small margin of expected V_B: Story 2 North brace buckling (DCR = 0.629, V_B = 2,365 kN [525 kips]), Story 1 brace-gusset weld fracture (DCR = 0.605, V_B = 2,460 kN [555 kips]), and Story 2 North brace-gusset weld fracture (DCR = 0.598, V_B = 2,490 kN [560 kips]). Considering the many potential uncertainties in weld capacity (throat size, length, material overstrength), any of the three limit states were conceivable in the test. The DCR analysis was supplemented with a series of numerical simulations in *OpenSees*, which confirmed that the frame behavior was highly sensitive to the brace-gusset weld sizes and estimated overstrength. For example, when a 10% overstrength was assumed for weld capacities, the numerical model predicted Story 2 brace buckling at V_B = 2,530 kN [570 kips] (Figure 4.4a); but when no overstrength was assumed for welds, the model predicted Story 1 North brace-gusset weld fracture at V_B = 2,340 kN [525 kips] (Figure 4.4b). When brace-gusset weld fracture occurred in the *OpenSees* model a secondary artificial limit state of brace-gusset weld fracture in the remaining Story 1 brace was imposed at δ/h = 3%. This limit was loosely based on testing of a 2-story nonductile concentrically braced frame (NCBF) with composite slab by Sen et al. (2016), in which connection failure in the remaining brace following development of the long-link EBF mechanism occurred at δ/h = 1%.

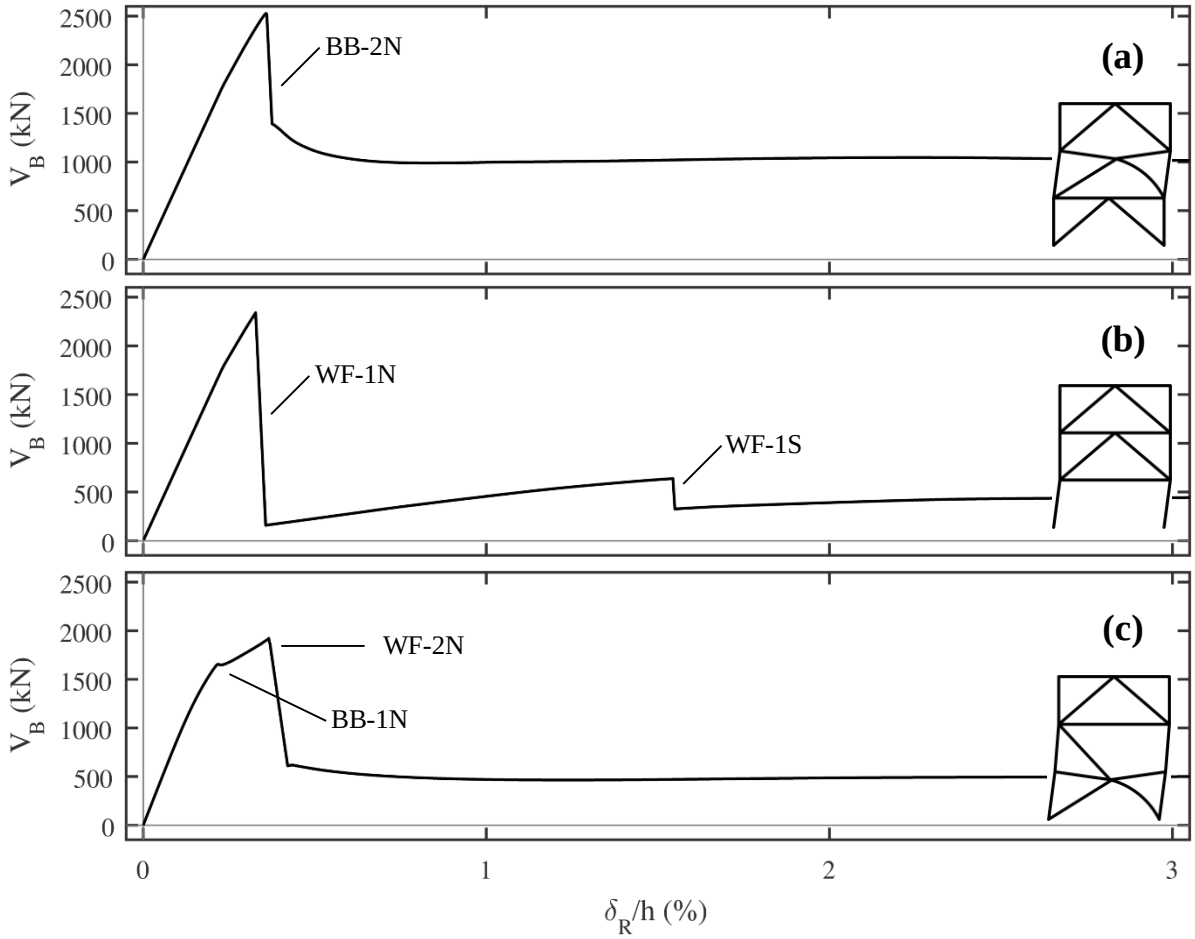

Figure 4.4 – OpenSees numerical model predictions of experimental test behavior: (a) R = 3 chevron CBF with assumed brace-gusset weld overstrength of 10%; (b) R = 3 chevron CBF with no assumed brace-gusset weld overstrength; and (c) R = 3.25 split-x OCBF.

Although the DCR analysis for the OCBF revealed less sensitivity to assumed weld overstrength, there were still two limit states within a small margin of V_B: Story 1 North brace buckling (DCR = 0.630, V_B = 1,360 kN [305 kips]) and Story 2 South brace buckling (DCR = 0.614, V_B = 1,395 kN [315 kips]). A scenario in which the Story 2 South brace buckled instead of the Story 1 North brace was easily conceivable, considering variations in effective buckling length, yield strength, and imperfections. A simple pushover of the OCBF in *OpenSees* revealed an expected limit state sequence of Story 1 South brace buckling at V_B = 1,615 kN

[365 kips] followed by Story 2 North brace-gusset weld fracture at V_B = 1,920 kN [430 kips] (Figure 4.4c), which agreed with the hand-calculated results of the DCR analysis.

4.3 TEST 1: *R* = 3 CHEVRON CBF

Due to the lack of seismic detailing requirements for R = 3 frames, the chevron CBF was expected to experience brittle limit states with minor or no ductility. The observations from the R = 3 chevron CBF test unit are presented in this section.

4.3.1 Test Summary

An overview photo of the R = 3 chevron test unit and test set-up with actuators is shown in Figure 4.5. The test unit was whitewashed with a coating of a water and lime mixture to reveal lines that show the development of local yielding and plastic hinge formation. A summary of the loading history for the frame is given in Table 4.3. The test was defined by four distinct phases (Phases I–IV). Each phase corresponded to a switch in the load pattern that was driven by constraints imposed by the frame's unexpected behavior.

The frame remained elastic throughout the first six cycles (up to roof drifts, δ_R/h = ±0.30%, or ±27.4 mm. [1.08 in.] displacement at Level 3). When pushing the frame North to a target displacement of 32.0 mm. [1.26 in.] in the seventh cycle, buckling occurred at mid-height of the Story 2 North brace (Figures 4.6 and 4.7 [1]). Due to the high local slenderness ratios of the Story 2 braces (b/t = 28.8, Figure 4.7), the buckling limit state was brittle and resulted in a sudden drop in V_B from 2,000 kN [450 kips] to 670 kN [150 kips]. This caused the frame to move forward past the target roof drift of δ_R/h = 0.35% to 0.45%. Upon cycling the frame back to zero load, permanent deformation—both local and global—was visible in the buckled brace (Figure 4.8). Significant flaking of whitewash was clear at the brace mid-

span, which was a sign that it had yielded and buckled locally in the same cycle in which it buckled globally. As the photos of the braces (Figure 4.8) and plots of their hysteresis (Figure 4.7) show, the braces nearly experienced local buckling and global buckling simultaneously. Yielding and buckling of the braces was localized to an area equivalent to the brace's section width (b = 200 mm. [8 in.] – Figure 4.8b).

Figure 4.5 – Overview of R = 3 chevron CBF, stabilizing frame, and actuators.

Table 4.3 – R = 3 Chevron Frame Loading History

Cycle	Target δ_R/h	Summary
Phase I: Standard Loading Protocol		
I.1	± 0.05%	Elastic behavior
I.2	± 0.10%	
I.3	± 0.15%	
I.4	± 0.20%	
I.5	± 0.25%	
I.6	± 0.30%	
I.7	+ 0.35%	Story 2 North brace buckling [1]
I.7	- 0.35%	Story 2 South brace buckling [2]
Phase II: Attempt to damage Story 1		
II.1	N/A	Did not induce Story 1 limit state
Phase III: Resume Standard Loading Protocol		
III.1	± 0.50%	Soft Story 2, Story 1 undamaged
III.2	± 1.00%	Drift limited by reaction frame
III.3-35	± 1.00%	33 Fatigue cycles on buckled braces
Phase IV: Damage lower story and observe EBF behavior		
IV.1	N/A	≈ 50 mm. [2 in.] weld removed from tension brace
IV.2	N/A	≈ 100 mm. [4 in.] weld removed
IV.3	N/A	≈ 150 mm. [6 in.] weld removed
IV.4	N/A	≈ 225 mm. [9 in.] weld removed – weld fracture
IV.5	δ_1/h_1 = ± 0.50%	Brace reengagement in compression
IV.6	δ_1/h_1 = ± 1.00	
IV.7	δ_1/h_1 = ± 1.50%	
IV.8	δ_1/h_1 = ± 2.00%	
IV.9	δ_1/h_1 = + 3.00%	Brace slip out of plane off gusset plate
IV.10	δ_1/h_1 = + 6.00%	End of test

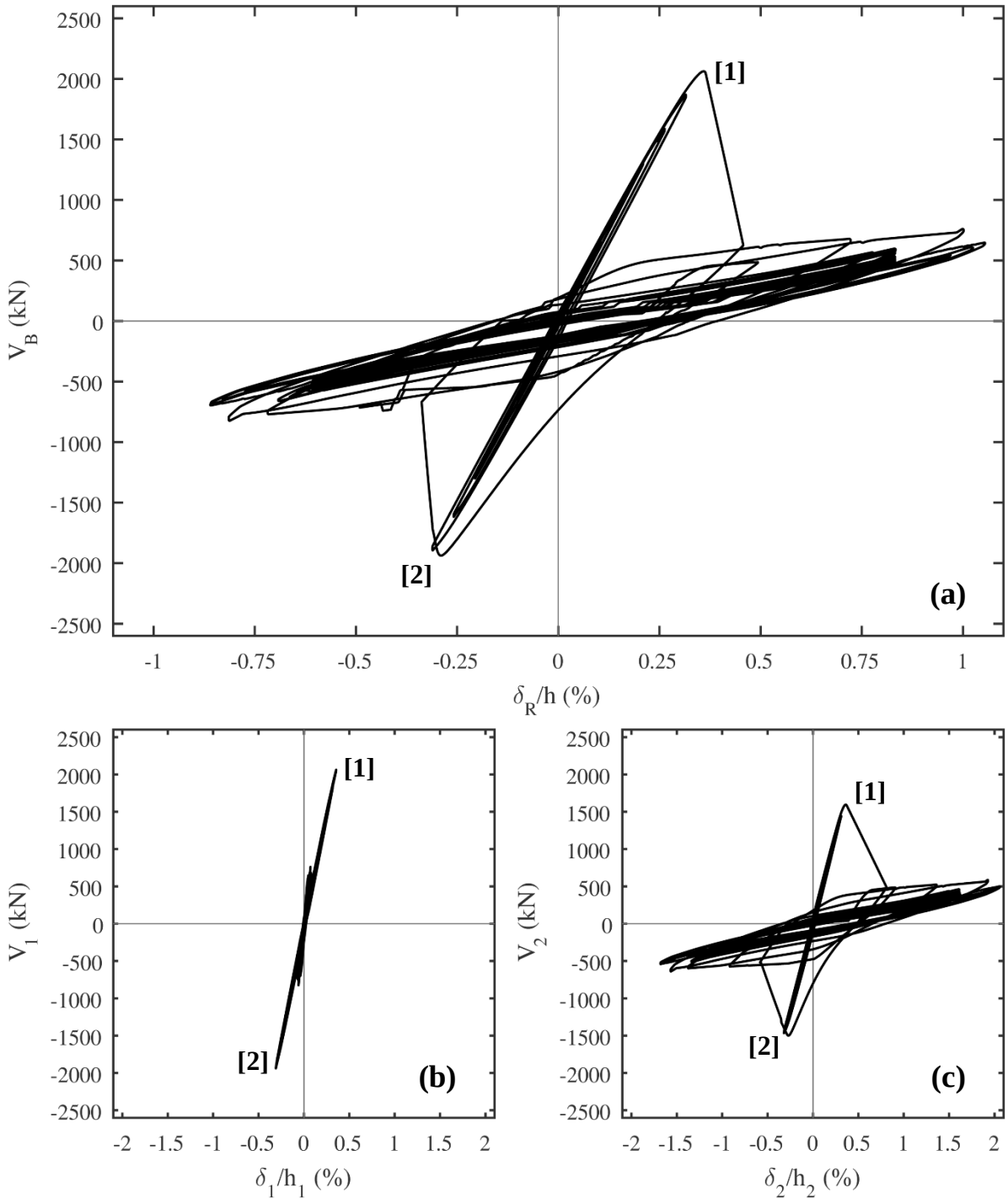

Figure 4.6 – Overall behavior, R = 3 chevron CBF Phase I and III. (a) Base shear vs. roof drift; (b) Story 1 shear vs. drift; and (c) Story 2 shear vs. drift. Indicators: [1] Story 2 North brace buckling; and [2] Story 2 South brace buckling.

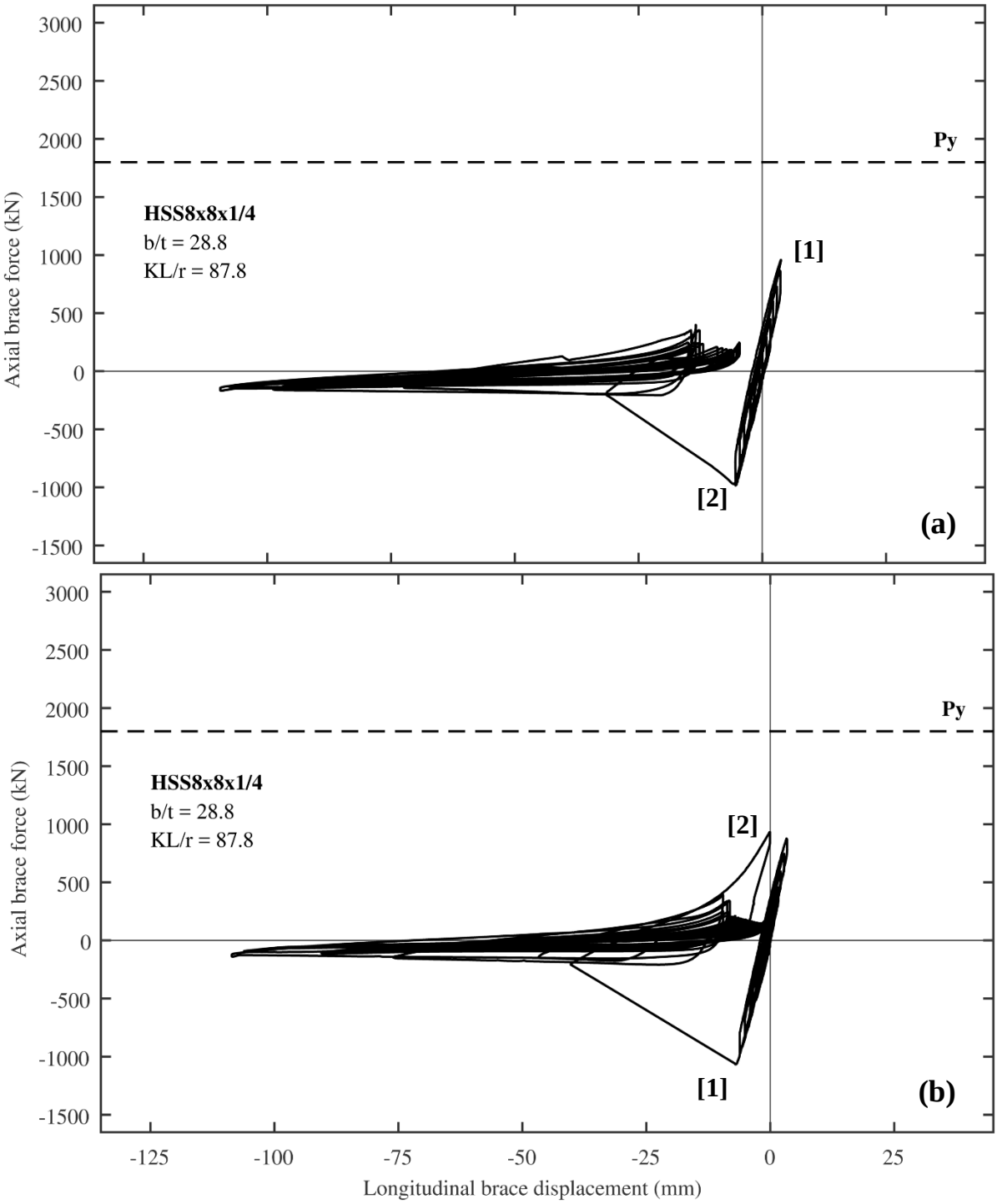

Figure 4.7 – Brace force-displacement behavior, *R* = 3 chevron CBF Phase I & III. (a) Story 2 South brace; and (b) Story 1 North brace: [1] Story 2 North brace. Indicators: [1] Story 2 North brace buckling; and [2] Story 2 South brace buckling.

(a) (b)

Figure 4.8 – R = 3 chevron frame brace buckling; (a) initial buckling; and (b) end of test.

Upon reloading the frame and pushing towards the next target displacement (δ_R/h = -0.35%), the overall stiffness of the frame increased as the buckled brace was pulled in tension, but remained noticeably smaller than the elastic range (Figure 4.6). In this half-cycle, the Story 2 South brace experienced buckling like the North brace had in the half-cycle prior (Figures 4.6 and 4.7 [2]). Buckling occurred at a δ_R/h = -0.30% and V_B = -2,000 kN [-450 kips]. Like the previous limit state, this brittle brace buckling caused V_B to decrease to -670 kN [-150 kips] and an increase in δ_R/h to the target of -0.35%, ending the cycle.

The brace force vs. displacement plots (Figure 4.8) show that both North and South braces buckled at around the same load, followed by large drops in stiffness and strength. Brace forces were estimated using the applied loads, the reaction forces measured in the load cells at the base, and the beam and column strain gages (Fig. 4.3). Estimated values for the two HSS8x8x1/4 Story 2 braces indicate that they buckled at around 1,100 kN [250 kips] (Figure 4.7).

Once buckling occurred in both Story 2 braces, it became clear that a soft-story mechanism had developed in Story 2, as the story stiffness had decreased 96% from 110

kN/mm [625 kips/in] to 4.4 kN/mm [25 kips/in] (Figure 4.6c). Due to the large stiffness reduction in Story 2, the 3.42:1 load ratio could no longer pass enough shear into Story 1 to exercise it sufficiently. Thus, the standard loading protocol was paused and other options were considered to exercise Story 1, beginning Phase II (Table 4.3).

The loading pattern was shifted so that the Level 2 actuator delivered all the force to the system and the Level 3 actuator was set to a force control with a target value of 0 kN. In this configuration, the Level 2 actuator was brought near its capacity of 2,300 kN [520 kips] to induce a limit state in Story 1. The adjustment of the loading protocol was not necessarily viewed as a realistic condition representing earthquake demand, but it was intended to obtain the most information from the test specimen.

Brace force vs. deformation plots (Figure 4.9) for Phase II revealed that both the Story 1 tension brace and compression brace each developed axial demands around 1,535 kN [345 kips], below the expected brace-gusset weld capacity of 1,600 kN [360 kips] and the expected brace buckling capacity of 1,750 kN [395 kips]. Shortly before reaching the capacity of the Level 2 actuator, the Level 2 beam and column began to crush locally under the high loads (Figure 4.10), and an attempt was made to apply more load into the frame via the Level 3 actuator. Given the weakened Story 2, the Level 3 actuator could only deliver an additional 500 kN [112 kips] of lateral load, which when combined with the Level 2 actuator load of 2,000 kN [450 kips], created a Story 1 shear, V_1, of 2,500 kN [562 kips] as shown in the plots of Figure 4.11. Although this story shear resulted in brace demands just shy of the expected weld capacities, given the previously established high degree of uncertainty in their capacity there was no guarantee that weld fracture would occur at the demands expected. Thus, it was decided to unload the frame and prevent further localized Level 2 beam crushing. Other than

localized damage resulting from introducing large compressive forces into the beam, the frame remained un-damaged. Upon unloading, a residual 0.2% increase in δ_R/h was realized due to the localized crushing at the South end of the Level 2 beam (Figure 4.11). This displacement is not shown in the presentation of later results since it was viewed as an artificial limit state not representative of the intended test. There were no perceivable effects of this permanent beam deformation throughout the rest of the test.

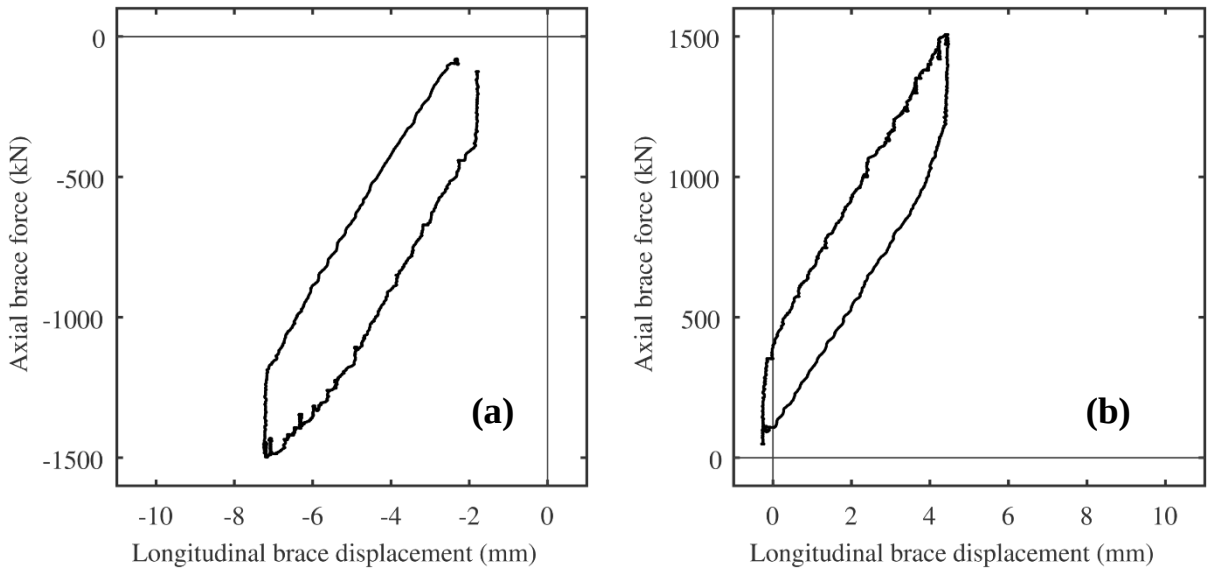

Figure 4.9 – Brace force-displacement behavior, R = 3 chevron CBF Phase II. (a) Story 1 North brace; and (b) Story 1 South brace.

(a) (b)

Figure 4.10 – R = 3 chevron frame Level 2 beam crushing and buckling while attempting to exercise Story 1.

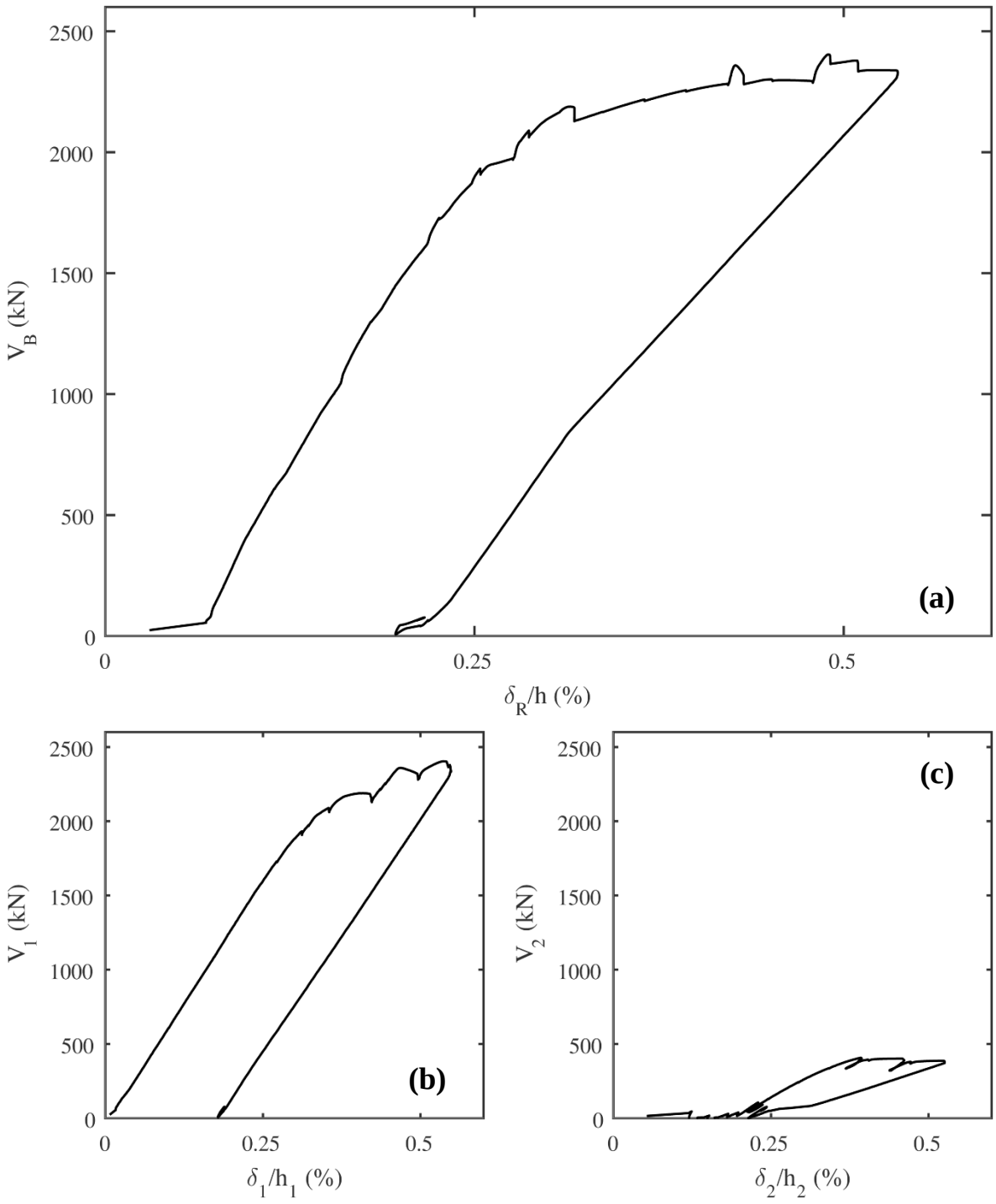

Figure 4.11 – Overall behavior, *R* = 3 chevron CBF Phase II. (a) Base shear vs. roof drift; (b) Story 1 shear vs. drift; and (c) Story 2 shear vs. drift.

Since the Phase II protocol of loading the frame entirely through the Level 2 actuator was not successful in generating a limit state in Story 1, it was decided to return to the original loading protocol in Phase III to fracture one of the buckled braces in tension. In this phase, Story 2 drifts (δ_2/h_2) reached maximums of -1.50% and +2.00% before cycles needed to be stopped as the braces had buckled over 300 mm. [12 in.] out of plane and were beginning to bear on the red reaction frame (Figure 4.5). The frame was subjected to over 35 fatigue cycles under the 3.42:1 force ratio, causing the braces to degrade significantly to a point where only a single tube face remained (Figure 4.8b). Due to the constraint of the red reaction frame, the researchers were unable to push the frame to sufficiently large enough drifts to fracture either of the braces at their midspan. The buckling braces pulled down on the Level 3 beam as the frame was cycled, causing a permanent deformation of 75 mm. [3 in.] (Figure 4.12) as measured by string pots (Figure 4.3) and providing reserve capacity through the long-link EBF mechanism.

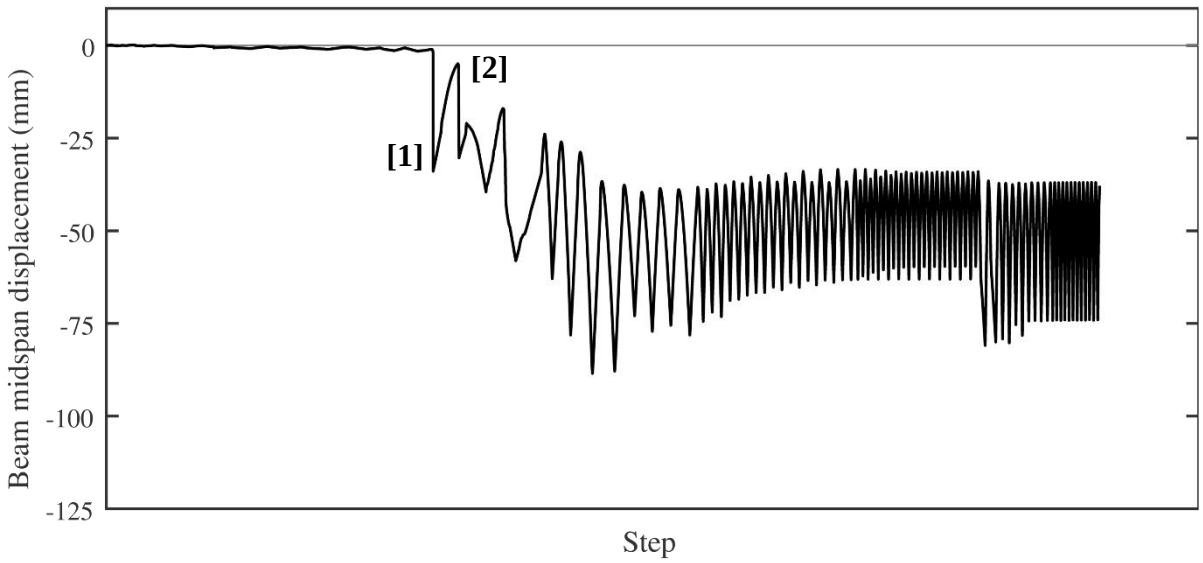

Figure 4.12 – Level 3 beam midspan vertical displacement, R = 3 chevron CBF Phase I & III. Indicators: [1] Story 2 North brace buckling; and [2] Story 2 South brace buckling.

Since both braces were still intact, the beam midspan vertical displacement was negative (downwards). If one of the braces had fractured completely in tension, then positive beam vertical displacement could have occurred, and thus a long-link EBF mechanism more like the one presented in the Chapter 3 component-level reserve capacity study could have occurred. Nevertheless, the ability for the beam to deflect vertically in both directions might not be as pertinent, as the Story 2 shear (V_2) plot in Figure 4.13 shows. The "Braces" label on this figure shows the balanced shear component carried by the braces, i.e. if the compression brace carried 40 kN of shear and the tension brace carried 30 kN of shear the "Braces" component was 30 + 30 = 60 kN of shear. Frame action provided by the EBF behavior (beam bending) was calculated from the force imbalance in the tension and compression braces, or 40 – 30 = 10 kN in the example. Frame action provided by the columns was calculated under the assumed condition that the columns took the rest of the shear not carried by the braces, and strain gage data supported this. For clarity, only the half-cycles in the North direction are

included in Figure 4.13, though the South direction half-cycles revealed a similar trend. As the plots show, the braces carried 90% of V_2 in the elastic range while the other 10% was carried by frame action. Following brace buckling, the reserve capacity provided by frame action was robust, and continued to increase as the braces were further degraded from low-cycle fatigue. At the end of Phase III, only 30% of V_2 was carried by the braces, while the remaining 50% and 20% were carried by frame action of the columns and beam, respectively. The reserve strength of the system under this mechanism was 500 kN [112 kips], and persisted for over 35 cycles. Eventually, after no perceivable change in behavior for multiple cycles at the drift limits, the researchers decided to conclude Phase III and revisit options for exercising the still-elastic Story 1. The frame behavior during this phase is appended to plots of frame and brace behavior in Figures 4.6 and 4.7, with the behavior from Phase II removed.

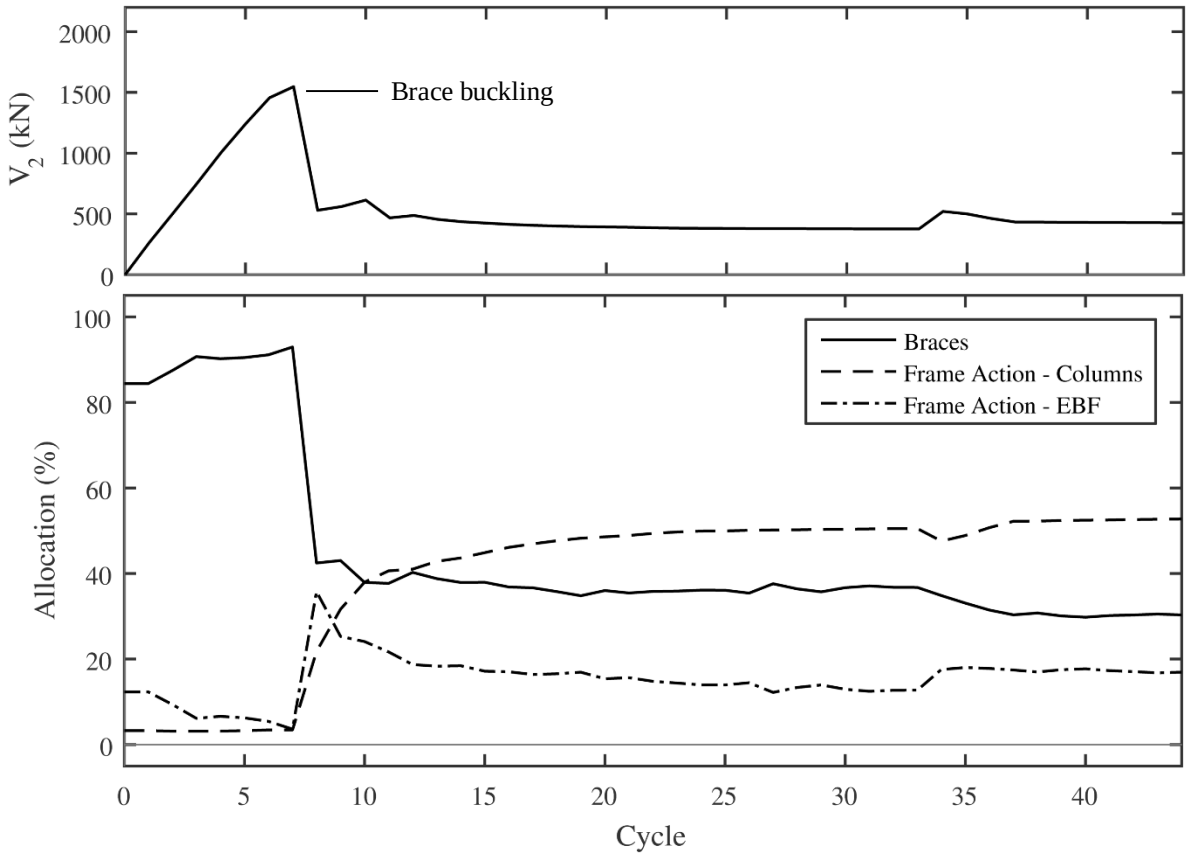

Figure 4.13 – Story 2 shear and its allocation, R = 3 chevron CBF Phase I & III.

In a final effort to exercise Story 1, a plan was made to remove portions of the Story 1 brace-gusset welds by grinding them off (Phase IV – Table 4.3). Each of the four welds in the Story 1 South brace-gusset weld group were grinded off approximately 50 mm. [2 in.] at a time, and the frame was loaded from the Level 2 actuat1or only. In this phase, load was applied through the North side of the frame to reduce demands on the weakened South end of the Level 2 beam from Phase II. After a 4th attempt of weld grinding which reduced the weld lengths down to 50 mm. [2 in.] from their original length of 275 mm. [11 in.], a brace-gusset weld fracture occurred at a V_B = 1,560 kN [350 kips] and an axial force of 1,200 kN [270 kips] in the weakened connection. What this says about the weld's true capacity is uncertain, as it was too difficult to measure how much weld had been removed from the connection. The weld that

had filled into the gap was hard to reach or remove completely with a grinding wheel. As expected, the brittle nature of the weld fracture resulted in a large instantaneous drop in V_1 (and thus V_B) to 0 kN (Figure 4.14).

After weld fracture was induced, the frame was cycled in increments of $\delta_1/h_1 = 0.5\%$, from the Level 2 actuator. In the North direction, the fractured brace was pulled in tension, and was only capable of transferring miniscule amounts force through friction with remaining pieces of weld on the gusset plate (Figure 4.15). In the South direction, the frame remarkably kept the entirety of its original stiffness, as the fractured brace reengaged onto the gusset plate and gave a mechanism for transferring load in compression (Figure 4.16). As the brace continued to bear on the gusset plate, the slot length grew from the gusset plate cutting through the brace (Figure 4.17), and further increased the theoretical capacity of the fractured brace in compression. Large unloading stiffnesses were a result of the brace sliding in friction and bearing on small amounts of fractured weld that stayed attached to the brace and gusset plate. As displacements were increased further, significant beam deformation occurred as the frame exhibited long-link EBF behavior (Figures 4.14). A plot of the vertical midspan displacement for the Level 2 beam, which exhibited EBF behavior, is provided in Figure 4.18. When pushing the frame to the North, the remaining brace was placed into compression and the beam had a positive vertical displacement at its midspan. When pushing the frame to the South, the remaining brace was placed into tension and pulled down on the beam, resulting in a negative vertical displacement.

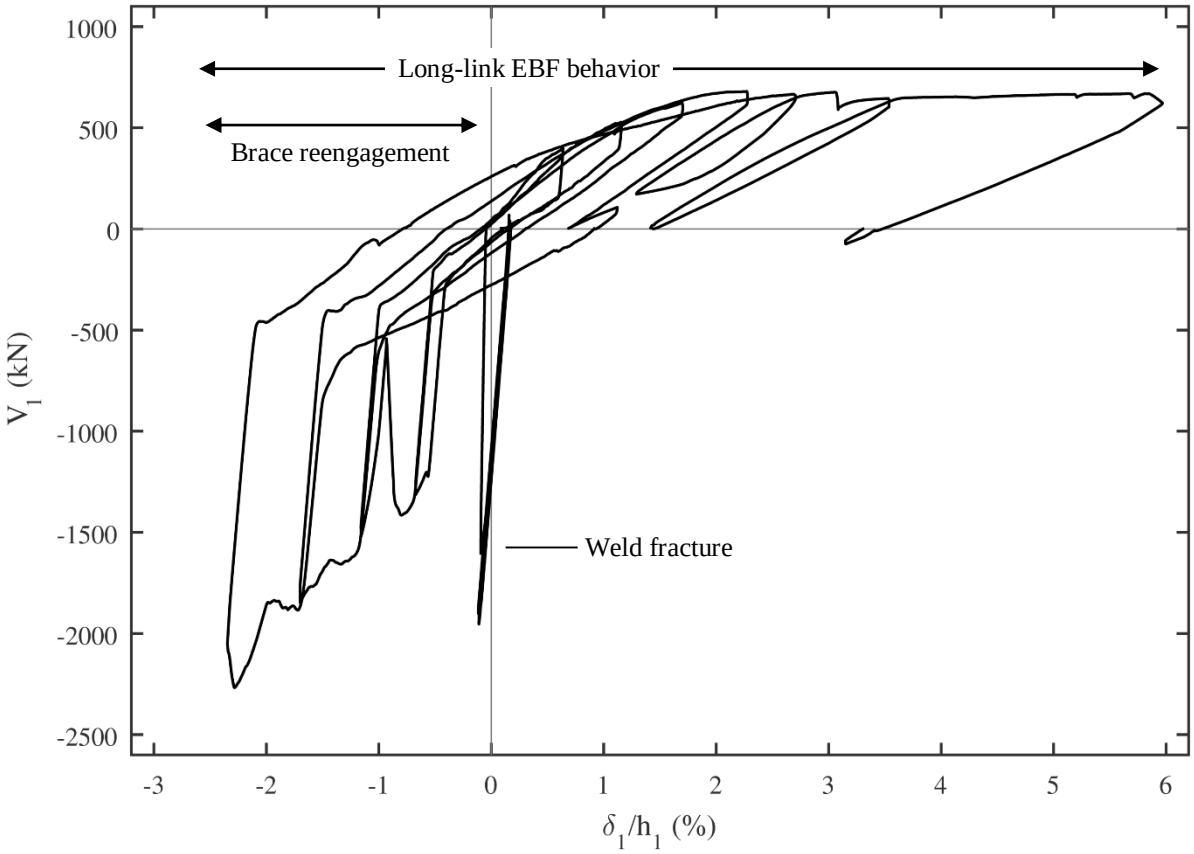

Figure 4.14 – Story 1 shear vs. drift, *R* = 3 chevron CBF Phase IV.

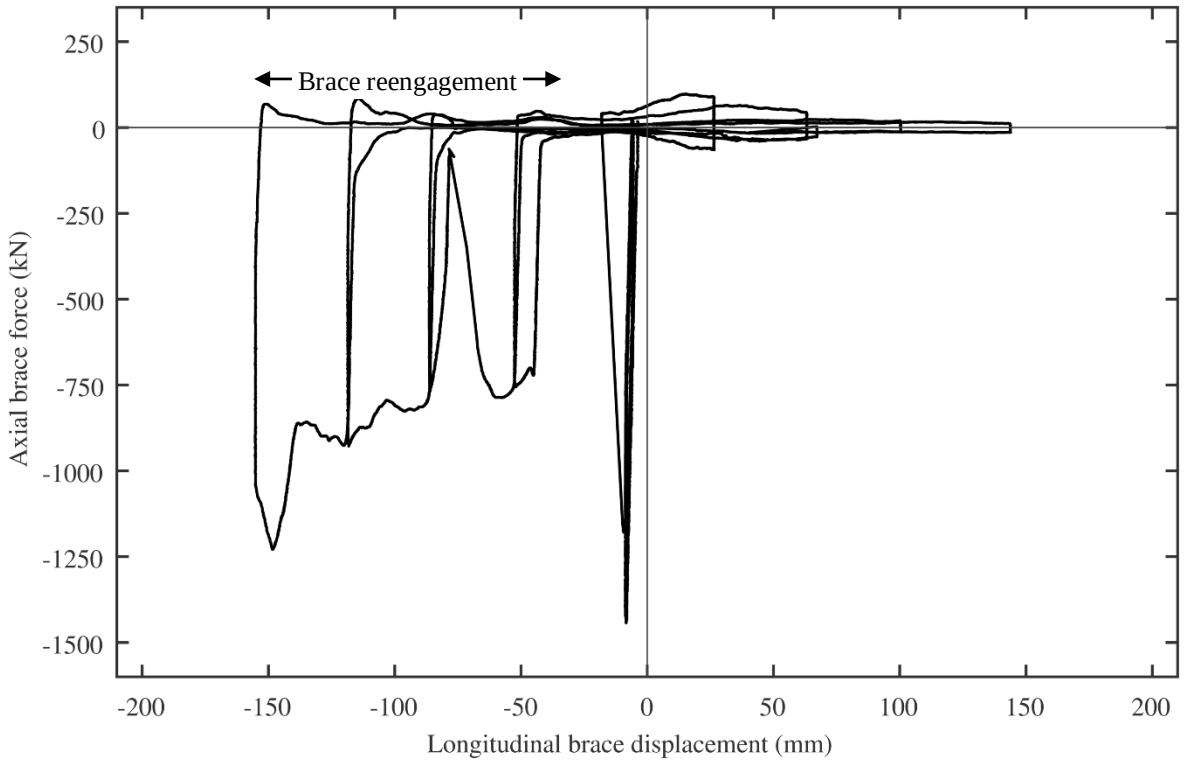

Figure 4.15 – Story 1 South brace reengagement behavior, *R* = 3 chevron CBF Phase IV.

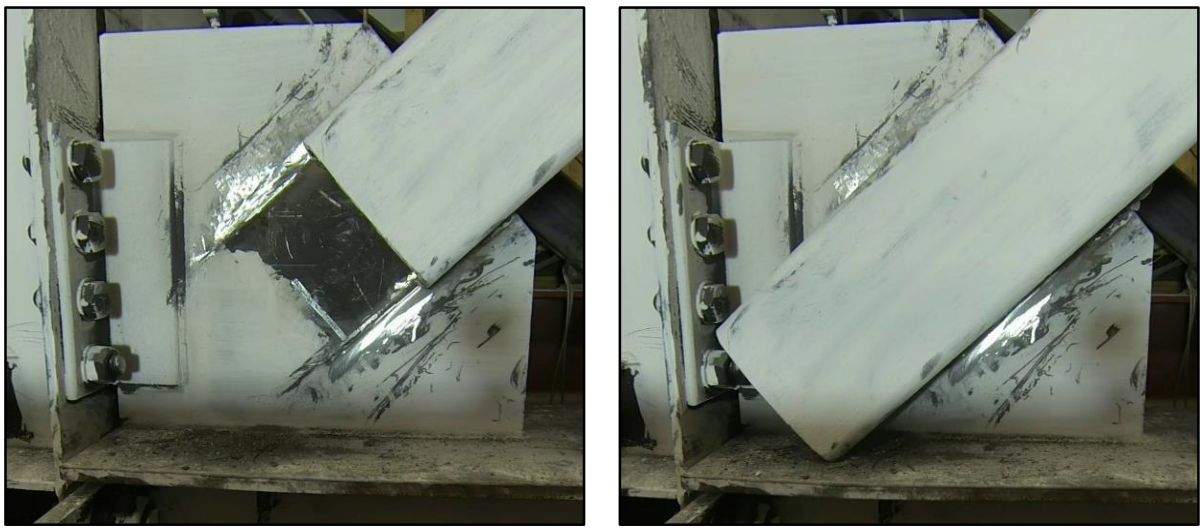

(a) (b)

Figure 4.16 – Story 1 South brace lower connection, *R* = 3 chevron CBF Phase IV: (a) brace detachment; and (b) brace reengagement.

Figure 4.17 – Story 1 South brace lower connection HSS slot, *R* = 3 chevron CBF Phase IV. The effective thickness of the slot has increased to five times its original thickness due to bearing on the gusset plate.

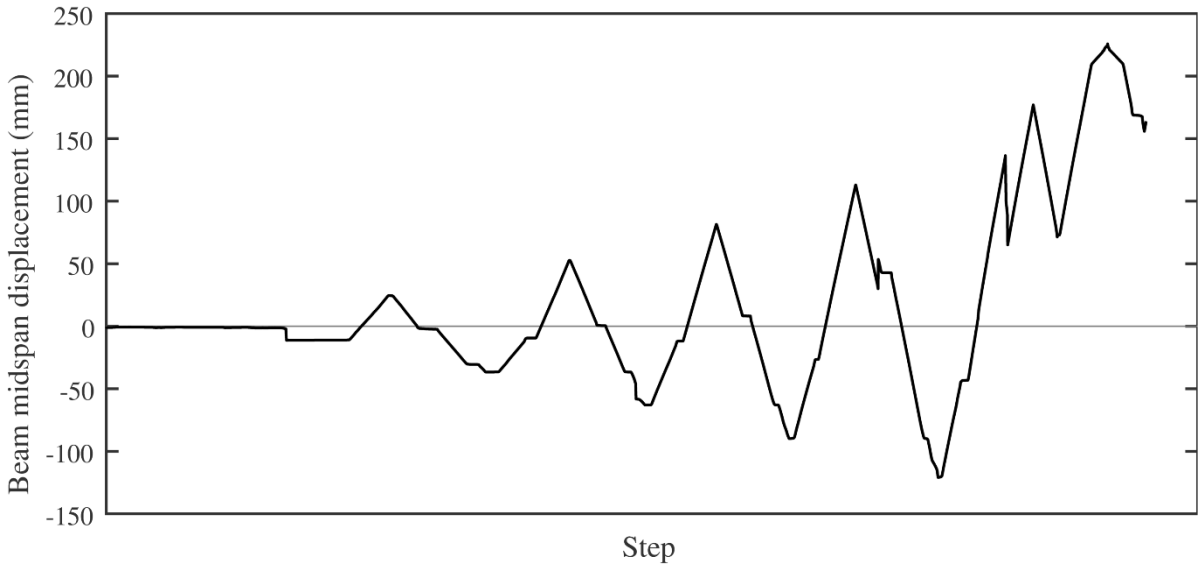

Figure 4.18 – Level 2 beam midspan vertical displacement, R = 3 chevron CBF Phase IV.

Schematic elevations are provided to show the deflected shapes, applied loads, and approximated reactions of the frame during periods of when the brace reengaged in compression (Figure 4.19a) and in the other direction when the frame drew much of its strength from the long-link EBF mechanism (Figure 4.19b). A residual downwards displacement of 50 mm. [2 in.] was visible in the Level 3 beam due to prior pull-down from the buckling of the Story 2 braces in Phase III. Larger amounts of shear were taken by the columns as drift increased, causing them to yield (Figure 4.20). When Story 1 was pushed to δ_1/h_1 = +3.0%, the brace slipped suddenly off the gusset plate and out of plane, preventing any possibility of brace reengagement. Despite this, the frame kept its EBF-like behavior, with a reserve capacity plateau of 670 kN [150 kips] as beam yielding occurred outside the gusset plate regions at the beam midspan. To end the test, the frame was pushed North to the largest distance the actuators allowed, resulting in δ_1/h_1 = 6%. EBF behavior persisted during this final half-cycle, and the remaining brace's connection did not experience fracture at any point during the test.

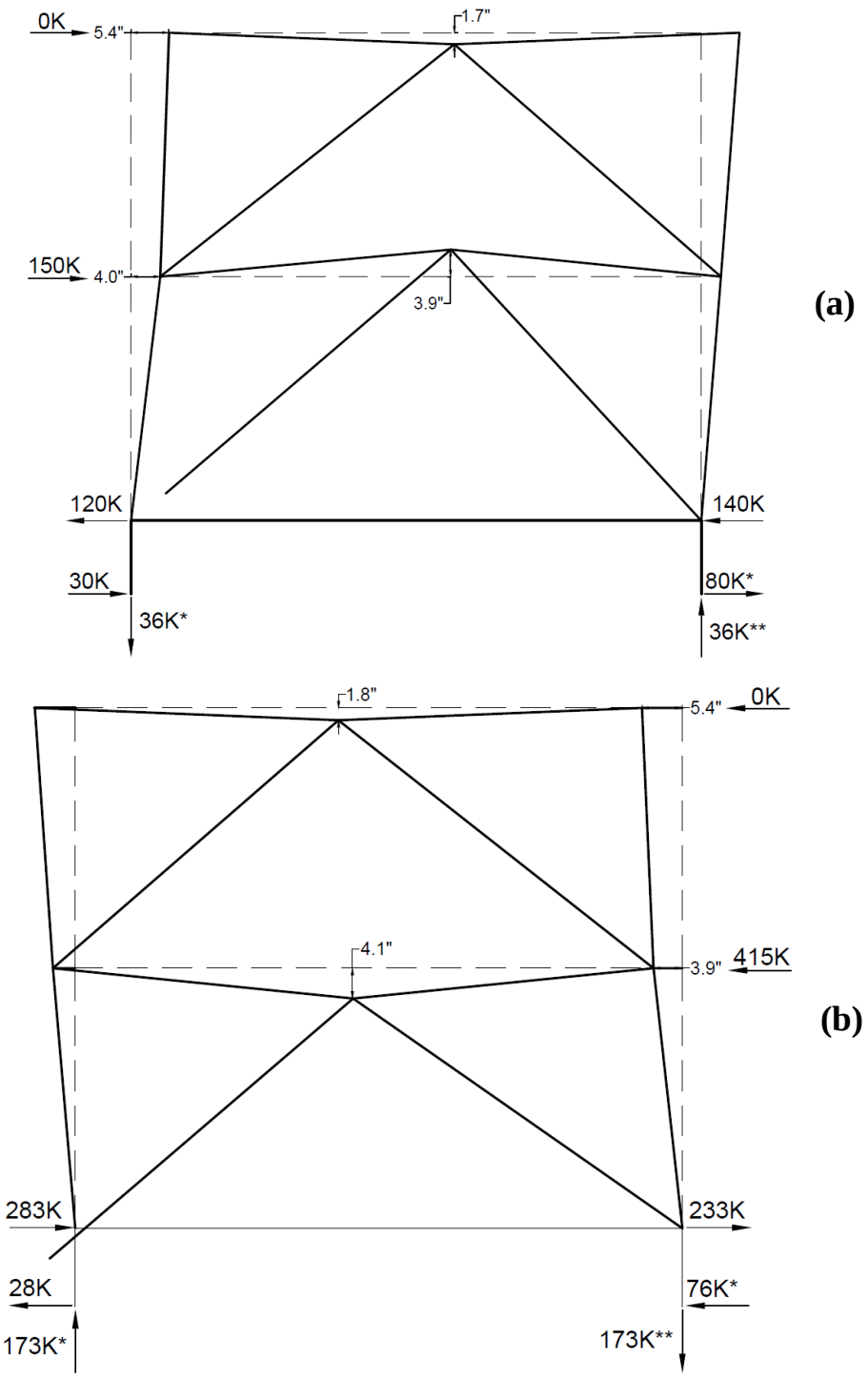

Figure 4.19 – Deformed configuration and reserve capacity at peak cycles following weld fracture, *R* = 3 chevron CBF Phase IV. (a) brace detachment; and (b) brace reengagement.

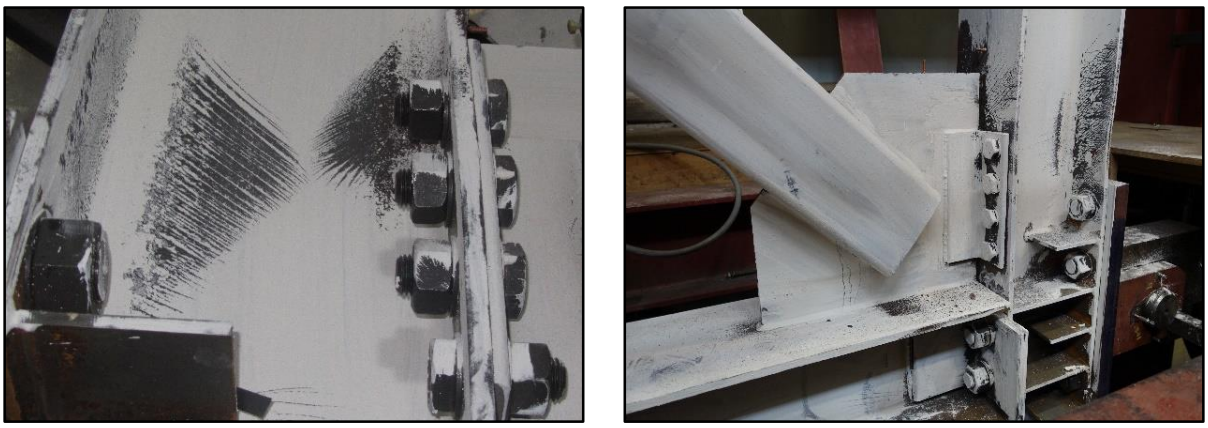

(a) (b)

Figure 4.20 – Lower Story 1 column (Level 1) plastic hinging, R = 3 chevron CBF Phase IV: (a) South column; and (b) North column.

4.3.2 Conclusions

The R = 3 chevron frame showed significant overstrength, reaching a V_B = 2,000 kN [450 kips] under the standard loading protocol, compared to the design load of 1,495 kN [336 kips], for an observed overstrength of 1.34. Although the failure mode of Story 2 brace buckling was consistent with one of the three expected results from simple *OpenSees* models and DCR analyses, the violently brittle nature of local and global brace buckling occurring simultaneously was unexpected, as the *OpenSees* model did not capture local brace buckling. Still, the brittle nature of the brace buckling from this test is consistent with the ideology of the low-ductility R = 3 systems. Brace buckling was associated with a large and sudden drop in V_B, but the frame kept a capacity of 450 kN [100 kips] up to δ_2/h_2 = 2%, highlighting the reserve capacity delivered by frame action and beam-column connections following brace buckling. The Phase IV test revealed that when weld fracture did occur, the strength in bearing was not capped by $2t_{HSS}t_{PL}F_{u,exp}$ because the bearing surface grew as the gusset plate cut through the brace (Figure 4.17). Another interesting observation from this test was the durability and longevity of the EBF-like behavior following weld fracture. Before these tests were conducted,

it was assumed that the remaining brace would experience a weld fracture at around δ/h = 1–3% based on tests by Sen et al. (2016). However, this mechanism withstood δ/h = 6% in this test, which suggested that the long-link EBF could provide more reserve capacity than previously expected.

4.4 TEST 2: *R* = 3.25 SPLIT-X OCBF

Unlike the R = 3 SFRS, the R = 3.25 OCBF provisions has seismic detailing and proportioning requirements which aim to offer limited inelastic deformation capacity in members and connections. Due to the lack of any true capacity design methodology within the OCBF provisions, this test unit was expected to experience a brittle limit state in one of its brace-gusset weld connections as shown in Section 4.2. The observations from the R = 3.25 split-x OCBF test unit are provided in this section.

4.4.1 Test Summary

Unlike the first test, the standard loading protocol was used throughout the entire duration of the second test, with only a slight modification. Based on preliminary stiffness checks performed on each frame by elastic loading of up to 178 kN [40 kips], there was concern that the frame could reach a buckling limit state at a small drift increment and some of the finer details during the transition from the ductile region to the brittle region would be missed. Thus instead of beginning with 0.05% increments in δ_R/h, 0.025% increments were used up to δ_R/h = 0.10%. At this point, the originally proposed 0.05% drift increments were resumed. Like the R = 3 chevron frame, a summary of the loading history is presented in Table 4.4, and an overview photo of the test frame is shown in Figure 4.21.

Table 4.4 – R = 3.25 Split-x OCBF Loading History

Cycle	Target δ_R/h	[Figure Label], Summary
1	± 0.025%	Elastic behavior
2	± 0.05%	
3	± 0.075%	
4	± 0.10%	
5	± 0.15%	[1] Yield lines forming in beam (Fig. 4.22a)
6	± 0.20%	
7	± 0.25%	
8	+ 0.30%	[2] Story 2 South brace buckling (Figs. 4.23, 4.24, 4.25a)
8	- 0.30%	[3] Story 1 South brace buckling (Figs. 4.23, 4.24, 4.25b)
9	± 0.35%	
10	± 0.40%	Yielding in Level 3 South brace gusset plate (Fig. 4.26b)
11	± 0.45%	
12	± 0.50%	
13	± 0.75%	
14	+ 1.00%	Slight tearing of gusset-beam weld (Fig. 4.22b)
14	- 1.00%	Yielding of brace welds and net section (Fig. 4.27a)
15	± 1.25%	Bolt slips – no drop in load. Local yielding.
16	± 1.50%	[4] Weld fracture in Story 2 North brace (Fig. 4.27b)
17	± 2.00%	[5] Fracture in lower Level 2 gusset-beam weld (Fig. 4.30)
18	± 3.00%	Began to interfere with reaction frame, end of test

Figure 4.21 – Overview of R = 3.25 split-x OCBF, stabilizing frame, and actuators.

When pushing the frame to δ_R/h = 0.15% for the first time and at V_B = 1060 kN [240 kips], yield lines began to form at the Level 2 beam mid-span, at the center of the "X" in the bracing configuration (Figure 4.22a, Figures 4.23 and 4.24 – [1]). During the frame design, this region was labeled as potentially susceptible to localized limit states. Due to the indeterminacy of this complex connection region, several statically admissible stress fields were evaluated. The need for local reinforcement (stiffeners) was unclear since different assumptions about internal forces led to different conclusions. Owing to the desire to design an efficient frame at the bare minimum, stiffeners at this location were omitted in the final design. In the end, this decision was reasonable since the local yielding and buckling that developed did not have any observable detrimental effects on the overall system response; instead, the local yielding of this region contributed to overall system ductility at larger drift levels and was viewed as beneficial.

(a) (b)

Figure 4.22 – Yielding at the Level 2 beam midspan, R = 3.25 split-x OCBF.

The yield lines at the Level 2 beam mid-span continued to develop as drift increased, but did not appear to have a large impact on the global frame performance until the frame was pushed to δ_R/h = 0.30%. Although this localized region had undergone large amounts of yielding, the frame remained otherwise elastic during this period of the test. The damage at this location developed due to high shear in the panel zone region (Fortney and Thornton, 2015), with some yield lines appearing at 60-degree angles, others appearing at 30-degree angles, and some parallel to the beam flange. By the end of the test, the location had yielded sufficiently to flake off the entirety of the white wash on this region (Figure 4.22b). In addition to the visible indicators from the whitewash, the beam experienced modest amounts of web deformations as well, with the formation of multiple "waves" along the beam web perpendicular to the beam section and along the length of the yielded region.

When pushing to a target Story 2 displacement of 27.4 mm, [1.08 in.], or δ_R/h = 0.30%, brace buckling occurred in the Story 2 South brace at V_B = 1,845 kN [415 kips] (Figures 4.23 and 4.24 – [2]). Upon reversing the direction of load and cycling to a target Story 2 displacement of -27.4 mm. [-1.08 in.], or δ_R/h = 0.30%, brace buckling occurred in the Story 1 South brace at a V_B = -1,925 kN [-433 kips] (Figures 4.22 and 4.23 – [3]). Owing mostly to the

limiting b/t requirements for OCBFs of $0.64\sqrt{(E/F_y)}$ (AISC, 2010a – $b/t \leq 15.4$ for $F_{y,A1085}$ = 345 MPa [50 ksi] and E = 200 GPa [29,000 ksi]), the buckling behavior of these braces was more ductile than those in the R = 3 chevron CBF. For further comparative purposes, a summary of the slenderness ratios between the braces of the two frames is provided in Table 4.5. Photos of the buckled braces (Figure 4.25) show that the yielding was much more distributed in these braces than in the thin-walled R = 3 braces, as whitewash flaking indicated that the plastic hinge length (L_{ph}) was spread over four times the brace width ($L_{ph} > 4b$).

Table 4.5 – Summary of brace slenderness ratios used in the test units

Frame	Story	Section	b/t [a]	KL/r [b]
R = 3 chevron CBF	1	HSS8x8x3/8	18.1	89.3
R = 3 chevron CBF	2	HSS8x8x1/4	28.8	87.6
R = 3.25 split-x OCBF	1	HSS6x6x1/2	8.4	125
R = 3.25 split-x OCBF	2	HSS6x6x3/8	12.8	122

[a] May not exceed 15.4 for A1085 steel OCBF braces (AISC, 2010a).

[b] May not exceed 96.3 for A1085 steel OCBF braces in chevron or "V" configurations (AISC, 2010a).

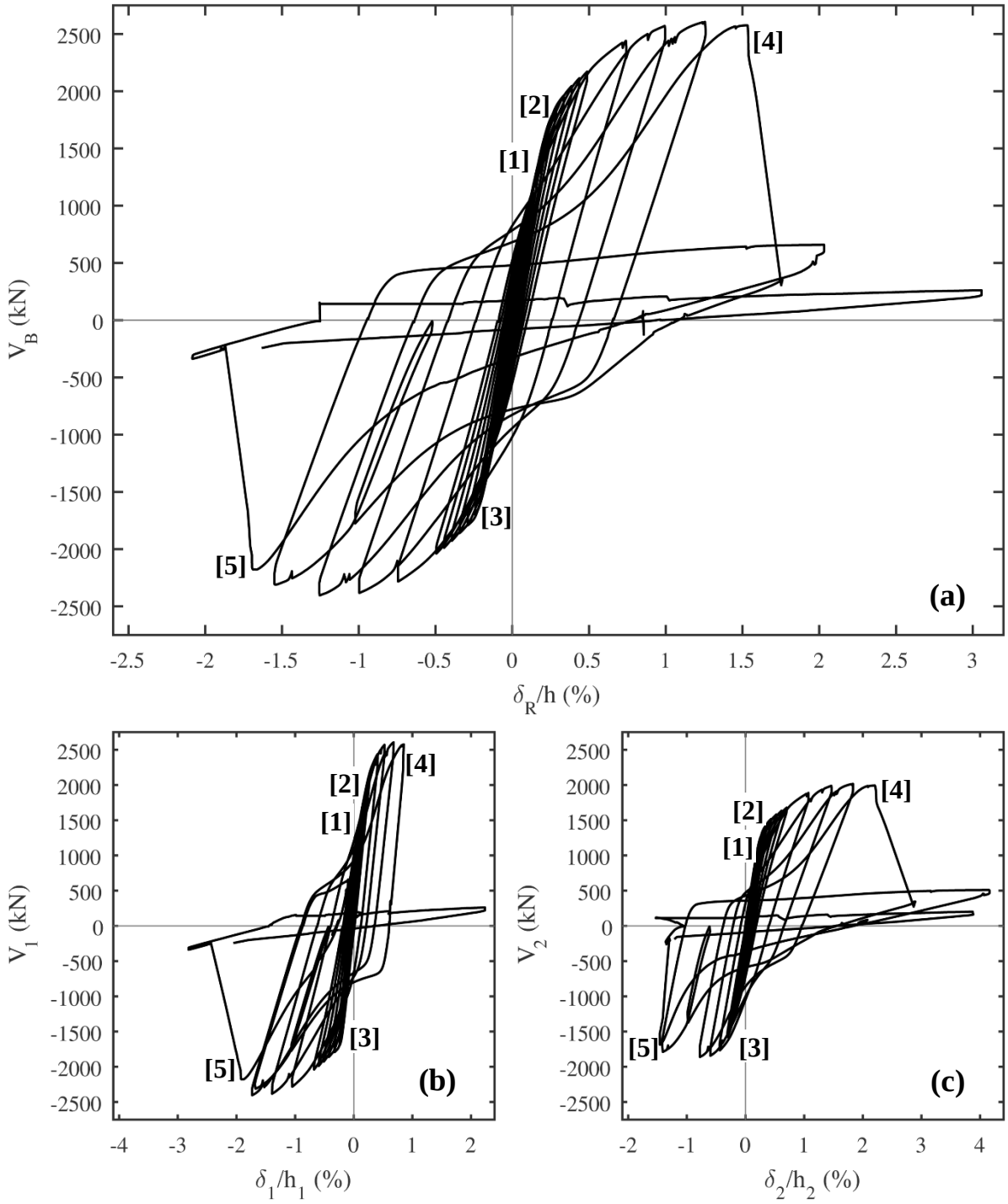

Figure 4.23 – Overall behavior, R = 3.25 split-x OCBF. (a) Base shear vs. roof drift; (b) Story 1 shear vs. drift; and (c) Story 2 shear vs. drift. Indicators: [1] Formation of yield lines on Level 2 beam; [2] Story 2 South brace buckling; [3] Story 1 South brace buckling; [4] Story 2 North brace-gusset weld fracture; and [5] Level 2 lower beam-gusset weld fracture.

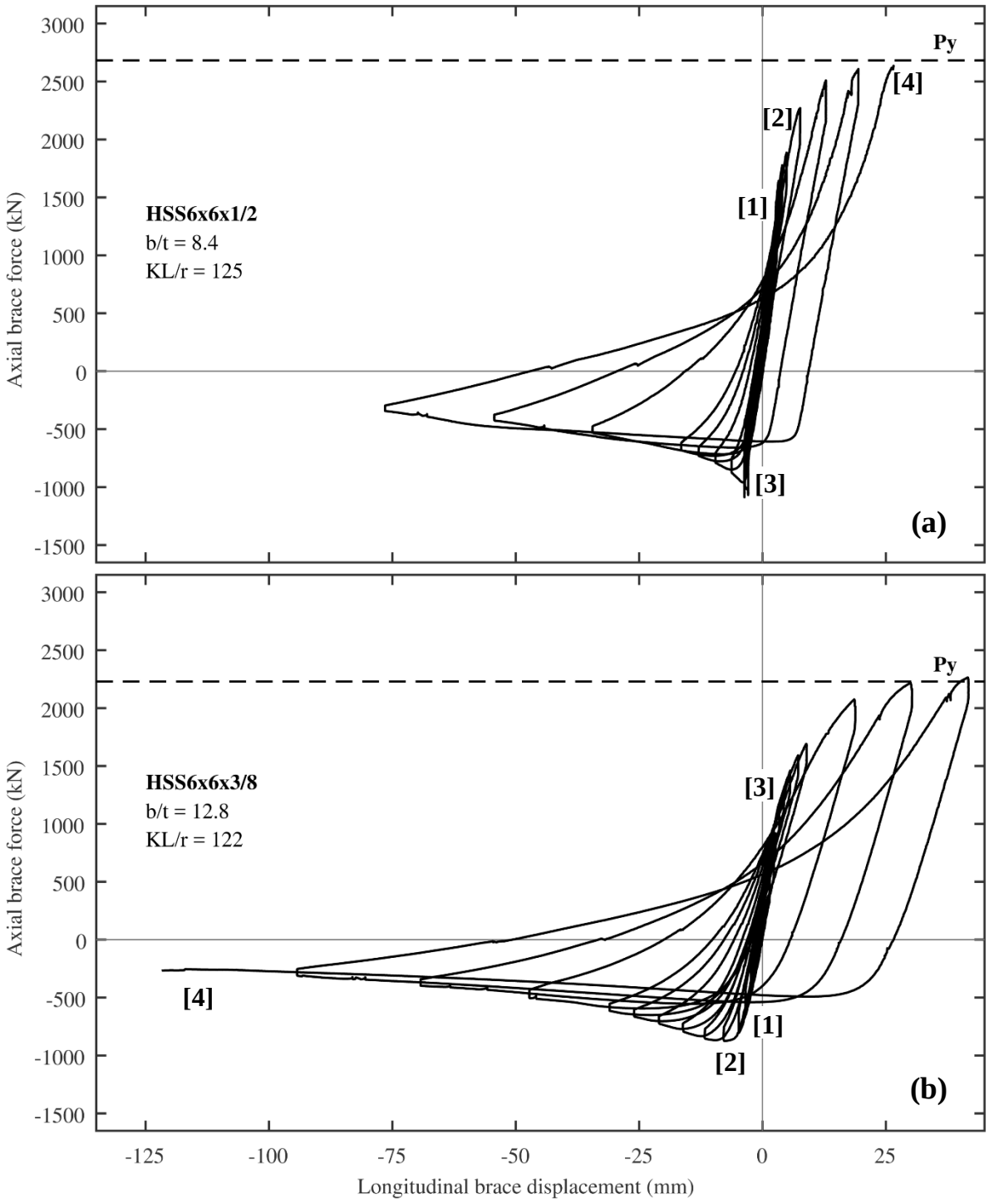

Figure 4.24 – Brace force vs. displacement behavior, *R* = 3.25 split-x OCBF. (a) Story 1 South brace; and (b) Story 2 North brace. Indicators: [1] Formation of yield lines on Level 2 beam; [2] Story 2 South brace buckling; [3] Story 1 South brace buckling; [4] Story 2 North brace-gusset weld fracture.

(a) (b)

Figure 4.25 – Buckling braces, R = 3.25 split-x OCBF. (a) Story 2 South brace; and (b) Story 1 South brace with hinge region spread over 4 times the brace depth.

As previously discussed, strain gage data was used to estimate forces in the members. These member forces were then used in conjunction with measured applied forces and reaction forces to develop consistent internal equilibrium. After brace buckling, the brace gages were no longer useful to determine the brace forces directly due to inelastic behavior in the braces, so the force in the braces was calculated using equilibrium in both the x- and y-directions from the brace-beam-column intersections at the corners of the 2-story X. The brace force vs. deformation plots (Figure 4.24) show that the Story 2 South brace buckled at an axial load of 855 kN [192 kips] compared to the predicted capacity of 805 kN [181 kips], and the Story 1 South brace buckled at 945 kN [213 kips] compared to the predicted capacity of 975 kN [219 kips] (Table 4.2). Although these capacities seem to agree with the predicted values, the

asymmetrical limit states were unexpected, as conventional wisdom and models suggested that brace buckling would occur in the same story when cycling in opposite directions given identical section sizes and source materials for the bracing members within a given story. For instance, when the Story 2 South brace buckled at 855 kN [192 kips] when pushing North, the Story 1 North brace along the compression diagonal was carrying 1,060 kN [238 kips]—a force 10% higher than the Story 1 South brace buckled at on the following cycle. One hypothesis as to why this occurred was that the softening and yielding of the Level 2 beam coupled with buckling of the Story 2 South brace and gusset plate bending altered the effective lengths of the bracing members such that the Story 1 South brace became the critical components when cycling in the opposite direction.

After brace buckling occurred in each story, drift increments were set to 0.25% to help better understand the behavior of the asymmetric multi-story mechanism that developed. At δ_R/h = 1.0%, slight tearing became visible in the gusset-beam welds at the center of the "X" in both stories (Figure 4.22b)—but this tearing did not appear to appreciably affect the overall behavior of the frame or the individual stories. Overall frame stiffness gradually decreased after brace buckling, but strength continued to grow as demand shifted from the buckling braces to the tension braces. In the δ_R/h = 1.25% drift cycle, a few "pops" were heard which were attributed to bolt slip in the beam-to-column connections, but did not appear to influence the overall system behavior. In the same cycle, significant yielding was observed in both corner and center gusset plates, coupled with out-of-plane permanent deformation in the gusset plates from brace buckling. Yielding also occurred at the beam ends because of the combined bending stresses and large applied axial loads from the actuators (Figure 4.26a). In addition to yielding in the gusset plates, yielding was also clearly visible on the brace-gusset welds in Story 2

(Figure 4.27a), as well as at the net section of the Level 3 North brace-gusset connection (Figure 4.26b).

(a) (b)

Figure 4.26 – Localized yielding following brace buckling, R = 3.25 split-x OCBF. (a) Level 2 beam South end; and (b) Level 3 beam and gusset plate, South end.

In the next cycle to δ_R/h = 1.50%, a combined limit state of weld fracture and net section rupture occurred (Figure 4.27b) as the Story 2 North brace was pulled in tension to 2,325 kN [523 kips] (Figure 4.28). This brittle fracture resulted in a drop of force to 0 kN, and a sudden increase in δ_R/h from 1.50% to 1.75%. Given the expected weld strength calculated from $1.1R_n$ was only 1,525 kN [343 kips], these brace-gusset welds appeared to have significant higher capacity than expected, with an overstrength of $1.67R_n$. When considering that geometric conditions and rounding led the actual weld size (267 mm. [10.5 in.]) to be slightly larger than what was needed to meet the required connection capacity (250 mm. [9.83 in.], Rn = 1,300 kN [292 kips]), the "true" weld overstrength was closer to $1.8R_n$. The combined limit state was even higher than the expected net section rupture capacity of 1,984 kN [446 kips], and was close to the rupture capacity of 2,520 kN [567 kips] calculated by ignoring the shear lag reduction factor, U, and instead using the net area, A_n.

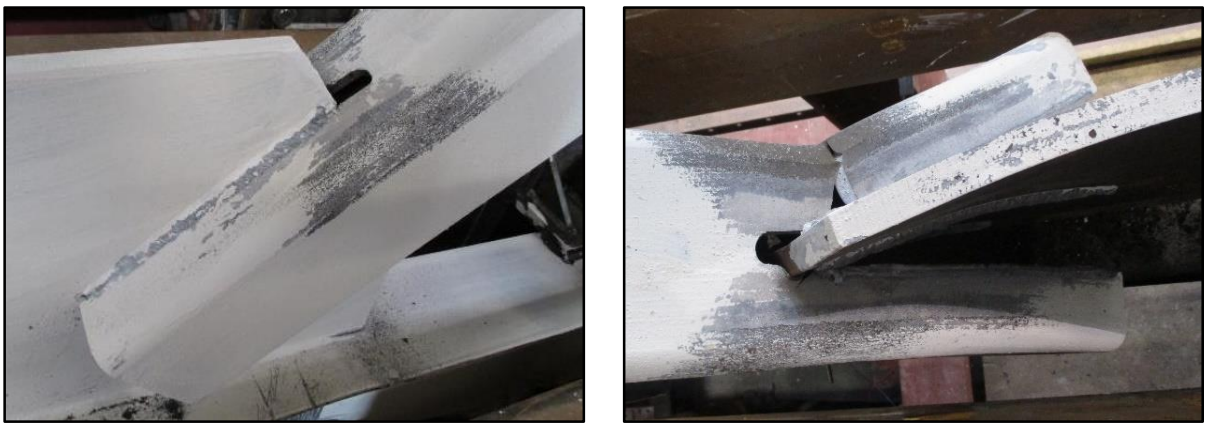

(a) (b)

Figure 4.27 – Story 2 North brace-gusset connection behavior, *R* = 3.25 split-x OCBF: (a) Yielding at weld and net section; and (b) Combined net section rupture and weld fracture.

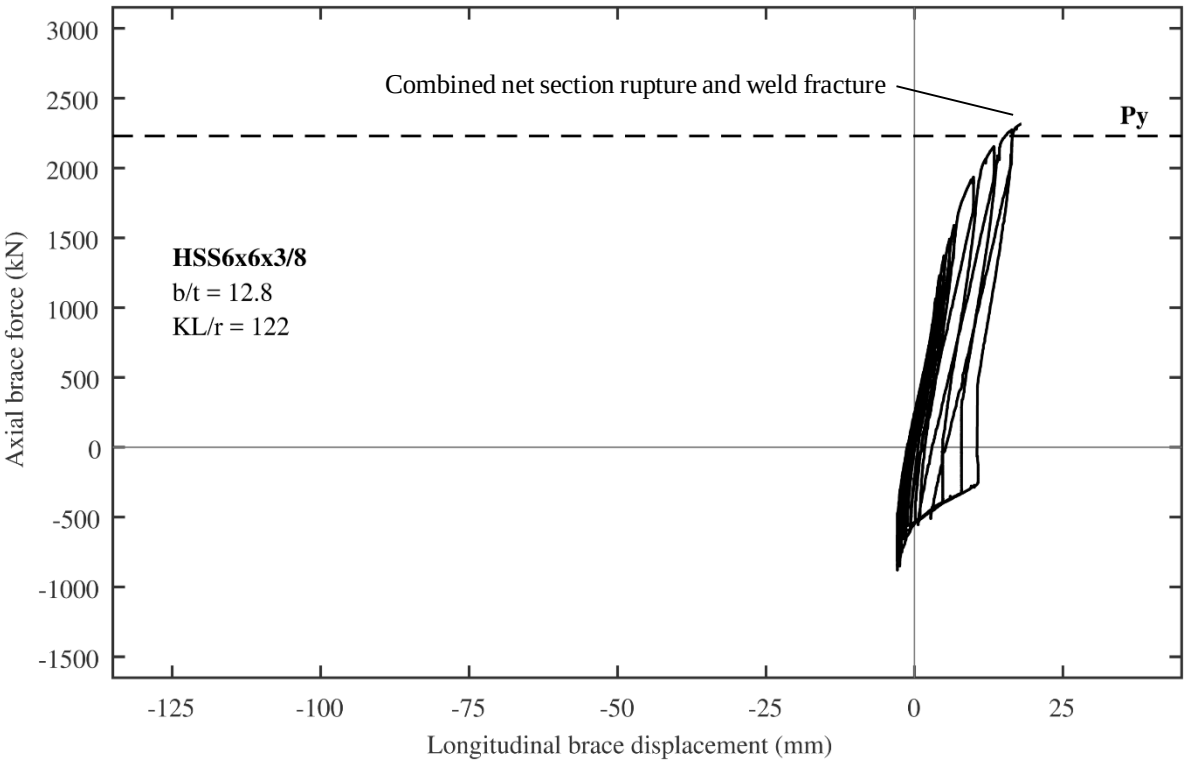

Figure 4.28 – Story 2 North brace behavior prior to weld fracture, *R* = 3.25 split-x OCBF.

Drift increments were once again increased following this brittle limit state, this time to 0.5%, to accelerate the rest of the test. In the next half cycle, when pushing to δ_R/h = -1.50%, the frame experienced only a small drop in stiffness, due to the X-configuration load path which allowed the remaining Story 2 South brace which had previously buckled in North-pushing half-cycles to carry most of V_2 through tension. Story 2 was understandably less stiff when the frame was pushed to δ_R/h = 2.0%, owing to most of the force now being transferred through the buckled Story 2 South brace. The frame still had some reserve capacity in this direction, carrying V_2 equal to 500 kN [113 kips], with over 70% distributed to the columns via frame action (Figure 4.29). Due to the split-x configuration, a long-link EBF-mechanism could not form, which reduced the potential for more reserve capacity. Upon cycling the frame back to δ_R/h = -2.0%, the increased stiffness in the negative direction was realized once again as the buckled Story 2 South brace carried load in tension. At the end of this cycle however, the lower Level 2 beam-gusset weld completely fractured at the beam mid-span (Figure 4.23 – [5]), which resulted in a significant drop in frame stiffness and capacity as Story 2 became detached from Story 1 other than by the columns (Figure 4.30).

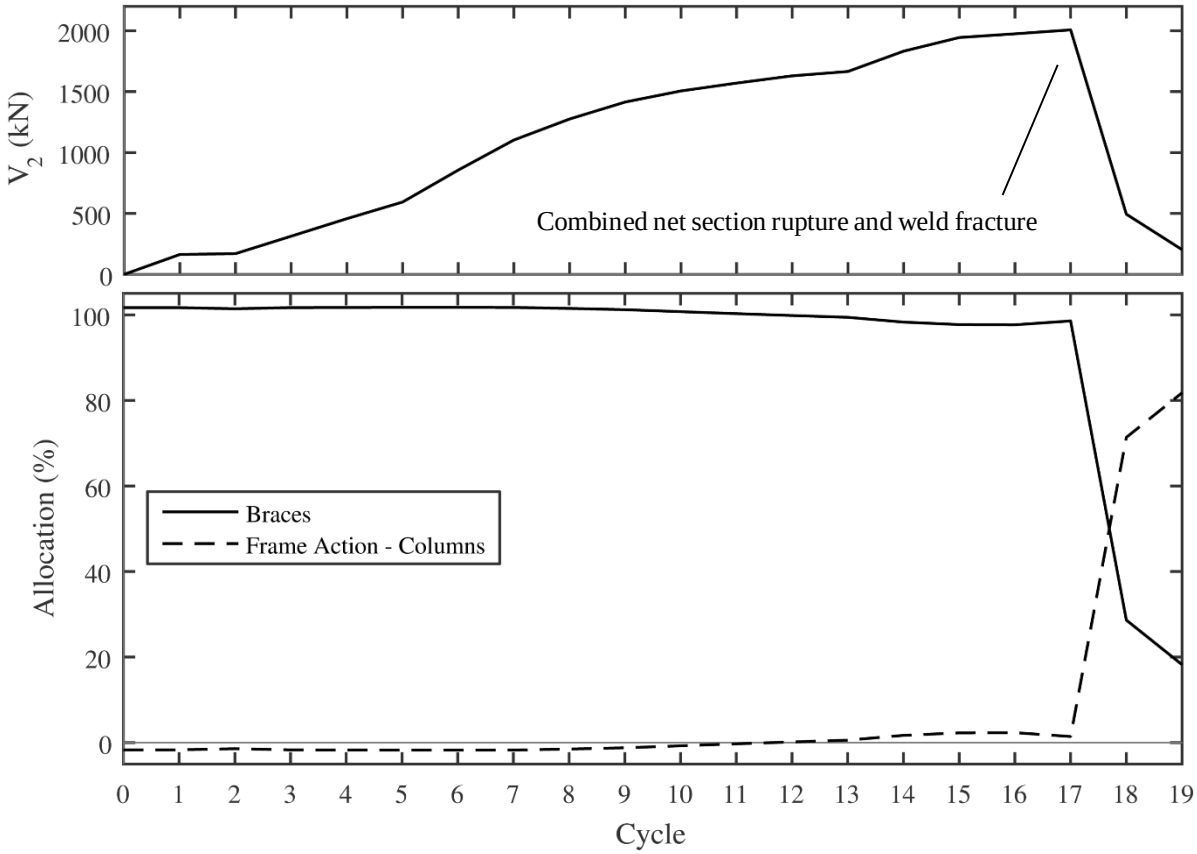

Figure 4.29 – Story 2 shear and its allocation, *R* = 3.25 split-x OCBF – North half-cycles.

Figure 4.30 – Level 2 beam bottom beam-gusset weld fracture, *R* = 3.25 split-x OCBF.

As the frame was pushed further, the Story 1 braces and brace-gusset connection swung out-of-plane behind the Level 2 beam, allowing it to deflect upwards vertically. One final cycle was completed before the end of the test, as the frame was pushed North to δ_R/h = 3.0%. As there was no longer a load path for the Story 2 compression brace to transfer load into the Story 1 braces, the reserve capacity in this direction was significantly decreased to V_2 = 335 kN [75 kips], with 80% resisted by the columns. Significant yielding became visible in the base of the Story 1 columns (Figure 4.31) as the detached Story 1 braces resulted in the entirety of V_1 being transferred into the base through column shear.

(a) (b)

Figure 4.31 – Lower Story 2 column (Level 1) plastic hinging, R = 3.25 split-x OCBF: (a) South column; and (b) North column.

4.4.2 Conclusions

The R = 3.25 split-x OCBF was significantly more ductile than the R = 3 chevron CBF, which confirmed the value of seismic detailing. Unlike the R = 3 chevron, the R = 3.25 split-x OCBF had a significant overstrength, reaching a V_B = 2,560 kN [580 kips] under the specified loading protocol, compared to its design shear V of 860 kN [193 kips], for an observed overstrength of 3.00. The limit state of tensile brace-gusset weld fracture was consistent with

predictions that tensile weld fracture would occur after brace buckling. However, the weld capacity was far greater than expected, with an overstrength of $1.7R_n$. The R = 3.25 split-x OCBF had modest reserve capacity after weld fracture, but it was not as robust as the R = 3 chevron CBF. This was primarily due to the frame action that developed in the chevron configuration.

4.5 COMPARISON OF TEST OBSERVATIONS

Although designed as a part of the same prototype building and for the same seismic hazard, these two test frames behaved very differently. The difference in the behavior of the two frames can be described in part by the two fundamental differences in their designs: system type and system configuration. System type is defined by the seismic force reduction factor, R, and the associated seismic detailing and proportioning requirements for a class of SFRS, such as the R = 3 CBF or R = 3.25 OCBF. System configuration, on the other hand, is defined by the bracing geometry, such as chevron or split-x. Throughout the tests, system type appeared to have a large influence on ductility, while system configuration appeared to have a large influence on reserve capacity.

4.5.1 System Type

The distinction between R = 3 and OCBF had a significant influence on the ductility of the two test units. This was a result of seismic detailing and proportioning considerations, which are required for OCBFs and not considered for R = 3 SFRSs. One of the seismic detailing requirements for OCBFs is b/t limits for braces, and the effects of adopting these limits are visible in comparing the photos of the buckled braces (Figure 4.8 – R = 3 braces, Figure 4.25 – OCBF braces) and plots of axial force and deformation (Figure 4.7 – R = 3 braces, Figure

4.24 – OCBF braces). As the brace photos show, the stocky walls of the OCBF braces ($b/t \leq$ 15.4) allowed for plastic hinging to develop over a region equivalent to four times the width of the section, with no localized limit states or tearing. The behavior of the R = 3 braces was noticeably different, as significant amounts of localized buckling and tearing occurred at the immediate onset of global brace buckling. In addition, the plastic hinge region of these braces was significantly concentrated, over a region equivalent to the width of the section. The effects of local brace buckling are clear in the plots of axial brace behavior, which reveal that the R = 3 braces experienced a significant drop in capacity following brace buckling, as opposed to the OCBF braces which had a more gradual decrease in capacity.

One seismic proportioning requirement for OCBFs is that the brace-gusset connections are designed for the amplified seismic load, using the system overstrength factor Ω_0 = 2.0. Because of this provision, the brace-gusset welds in the OCBF were sufficiently larger than the brace buckling capacities, allowing for a significant period of ductility in the post-elastic range prior to weld fracture (Figure 4.23). This is a contrast to typical proportioning of welds and braces in R = 3 CBFs, in which brace-gusset welds may have expected capacities quite like brace buckling capacities (Table 4.1) since they are designed for the same governing load combinations.

4.5.2 System Configuration

The choice between a chevron and split-x configuration had a significant influence on the reserve capacity and associated mechanisms of the two test units. While the split-x frame appeared to lend itself towards a more beneficial ductile behavior, it had less reserve capacity than the chevron frame. Chevron frames inherently allow for development of a long-link EBF mechanism after brace-gusset weld fracture, while a split-x brace layout inherently restricts

brace reengagement and long-link EBF behavior. For example, once a brace-gusset weld fractured in the split-x test unit, the remaining braces still provided a two-story load path and restrained beam bending, which is necessary for brace reengagement. The split-x frame kept most of its stiffness following a single brace-gusset weld fracture, which increased the likelihood of a second brace-gusset weld fracture or analogous brittle limit state, as seen in the split-x OCBF test unit.

The lack of gravity loading on the test units had an influence on the result of both test units. Both the elastic capacity and reserve capacity of the test units were artificially increased because of the omission of gravity loads. Were gravity loading included, it is likely that the initial limit states would have occurred earlier, and likewise, the reserve strength would decrease because of a part of the flexural capacity of the plastic hinges that formed now being allocated to gravity demands rather than exclusively to lateral effects as was the case in the experimental tests. It is hypothesized that the influence of gravity loading would have been more significant in the split-x test unit, as the configuration transfers more gravity loads through braces. Although gravity load was not included in these tests, later building models did include gravity load on the braced frames, so broader conclusions related to low-ductility braced frame system behavior do incorporate the influence of gravity load.

4.6 SUMMARY OF FULL-SCALE EXPERIMENTAL FRAME TESTS

Two experimental tests were conducted on full-scale 2-story steel SFRSs: one designed with braces in the chevron configuration using the "R = 3" classification, and one designed with braces in the split-x configuration using the OCBF (R = 3.25) classification. While the R = 3 chevron CBF had poor ductility and significant reserve capacity, the R = 3.25 split-x OCBF had significant ductility and poor reserve capacity. Both system type and system configuration

played an important role in the system behavior for the two test units, and these tests provided insight into the influence that system type and system configuration have on both reserve capacity and collapse prevention performance.

The full-scale tests revealed the wide range of uncertainty inherent within these systems, from the brace buckling capacity, to the brace-gusset connection capacity, to the ductility and robustness of column and beam bending contributions to frame action mechanisms. Although reserve capacity is not explicitly considered within design practice in low and moderate seismic regions, these tests offered a foundation for exploration into ways in which reserve capacity might be incorporated into future design codes and standards. However, these tests are only two data points among a countless number of low-ductility SFRSs, and thus, care should be made not to generalize these tests as representative of all chevron frames, split-x frames, R = 3 CBFs, or OCBFs. In Chapter 6, numerical simulations with models calibrated based on these tests (Chapter 5) are conducted to expand the experimental test matrix through cyclic static analyses. In addition, the modeling framework developed based on these tests was used to investigate a wider range of R = 3 and R = 3.25 (OCBF) split-x and chevron systems, for buildings with 3-, 6-, and 9-stories using dynamic analyses (Chapter 8).

CHAPTER 5

NUMERICAL BUILDING MODEL

Test data from the full-scale experimental study provided the basis for calibration of numerical building models using the *OpenSees* simulation platform (McKenna, 1997). Previously, only R = 3 chevron concentrically (CBFs) had been investigated using numerical models (Hines et al., 2009; Stoakes, 2012), except for a simple 3-story R = 3.25 split-x OCBF model which was created earlier in the research program to aid with predictions for the associated full-scale test unit. However, neither numerical study was linked to experimental data, since there was none at the time. The reserve capacity component study in Chapter 3 for the R = 3 chevron CBF provided a good introduction to modeling low-ductility frames and buildings within *OpenSees*, and after verifying and calibrating the models using the test data in Chapter 4, the models provided a solid basis to expand the study of reserve capacity through more comprehensive and sophisticated numerical simulations. This chapter begins with a description of the components that were included in the numerical model, discusses the difficulty of achieving convergence with nonlinear models of low-ductility systems, and ends with the verification study, which consisted of replicating the full-scale tests numerically.

5.1 MODEL DETAILS

In this section, the various components needed to build the *OpenSees* model are discussed in detail; this includes model definition and boundary conditions, members (beams, columns, and braces), connections (gusset plates, gusset plate connections and beam-column connections), damping, loads and masses.

5.1.1 Model Definition and Boundary Conditions

The *OpenSees* building model was constructed in 2-dimensions (2D), using 3 degrees of freedom (DOFs) at each node (Δ_x, Δ_y, θ_z). In *OpenSees*, these 3 DOF correspond to directions 1, 2, and 6, respectively. Modeling the building in 2D allowed for significant reduction in computational cost, as the number of DOFs per node was reduced by half (6 to 3). One caveat of making this simplification was that the ability to consider global building torsional effects (in plan) was lost, which could be significant in instances where only one braced experiences damage while another braced bay on the opposite end of the building remains elastic. By modeling a building with two braced bays in each direction in 2D, for example, the assumption is that following a limit state within one seismic force resisting system (SFRS), demand would quickly shift to the other, still-elastic SFRS. This was assumed to have caused an analogous limit state within that braced bay, given identical designs of the two SFRSs. Thus, the global torsional effects were assumed minimal, and a model incorporating them was viewed as beyond the scope of the current research.

The symmetrical floorplan of the building allowed for modeling only half of the building in cases where there were two SFRSs in each direction (e.g. 3-story porotypes in this study), and only quarter of the building in the cases where there were four SFRSs in each direction (e.g. 6- and 9-story prototypes in this study). The decision to model only a part of the building further reduced computational costs. Gravity columns were connected to one another and to the braced frame at each level with a rigid diaphragm constraint to carry *P-Δ* forces into the SFRS, and they were distributed evenly on both sides of the SFRS to account for the actual location of the SFRS within the building.

Modeling in 2D instead of 3D required an additional adjustment that was a deviation from actual behavior of the braces. In an SFRS within a real building, brace buckling will of HSS tube sections typically occurs out-of-plane (Δ_z) due to the orientation of gusset plates. To address this numerically, the gusset plate within the SFRS was modeled as if it were rotated 90-degrees about its primary axis, so that the weak-axis for the braces fell within the Δ_x and Δ_y DOFs, placing it within the bounds of a 2D model and providing the ability to capture buckling. Others have shown with numerical simulations in *OpenSees* that this simplification will not compromise the accuracy of the results either locally (brace behavior) or globally, as shown in Figure 5.1 (Terzic, 2013).

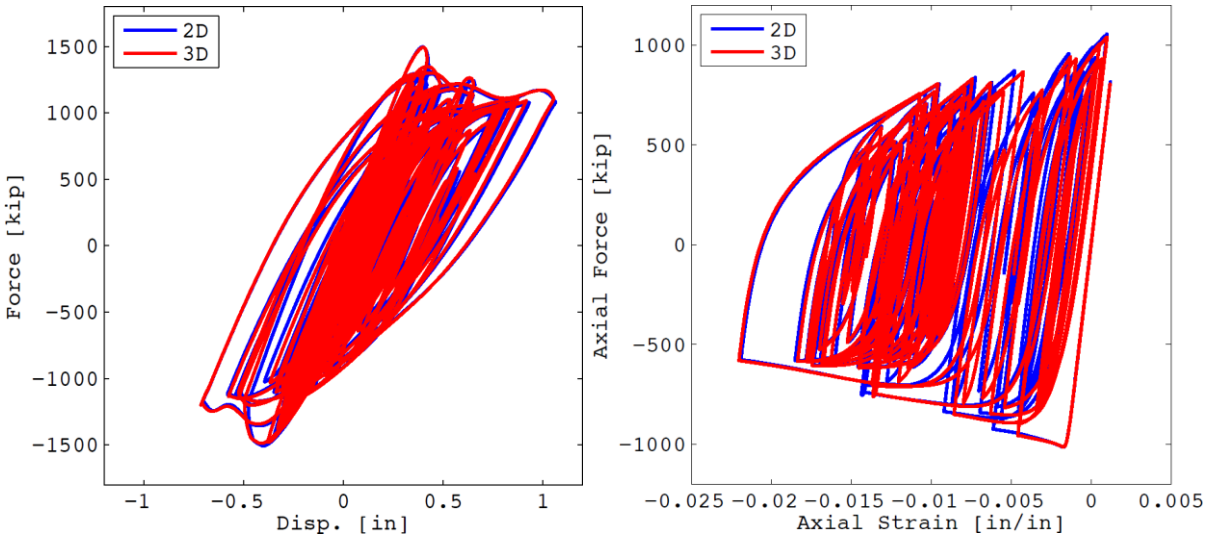

(a) (b)

Figure 5.1 – Artificially rotating gusset plates to appropriately consider and model brace buckling in 2D. Effects on (a) global behavior; and (b) local brace behavior (Terzic, 2013).

The final consideration for basic model definition was the base boundary conditions. For reasons previously discussed in Chapter 3, base boundary conditions for columns within the SFRS were modeled as fixed, while column bases within the gravity framing system were modeled as pinned. These assumptions carried through into future models, with a few

exceptions, for example in the numerical verification study of the full-scale tests at Lehigh, in which laboratory column bases were real pins.

5.1.2 Beams and Columns

When modeling beams and columns in consideration of nonlinear behavior, there are two primary options: (1) distributed plasticity models; and (2) concentrated plasticity models (Figure 5.2). Each option has strengths and weaknesses, and the choice between the two often comes down to the modeler's goal.

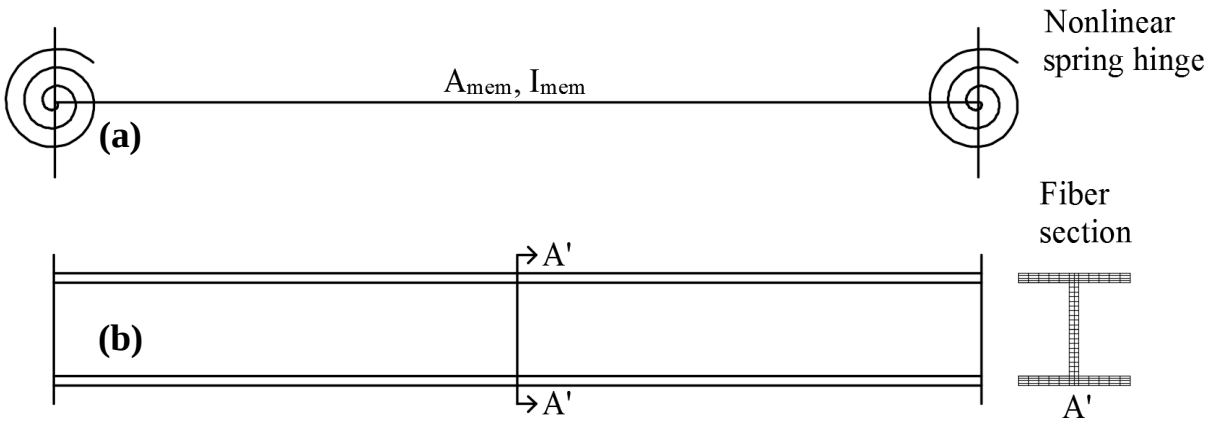

Figure 5.2 – Methods for nonlinear modeling of frame members: (a) concentrated plasticity; and (b) distributed plasticity.

Distributed plasticity models (Figure 5.2b) incorporate force-based elements (FBE) or displacement-based elements (DBE) which allow the spread of plasticity along the element. The FBE approach relies on an exact equilibrium solution between element and section forces, and uses the principal of virtual forces to formulate compatibility between section and element deformations, while the DBE approach involves interpolation of section deformations from an approximate displacement field and uses the principal of virtual displacements to form the element equilibrium relationship (Terzic, 2011). Both element types allow for the development

of yielding at any location along the element, and thus are especially useful when the plastic hinge locations for a member are unknown or can vary based on loading conditions. In addition, these distributed plasticity models often include explicit consideration of the element's cross-section through fiber discretization, which can capture the interaction between axial and flexural forces (*P-M* interaction). One of the primary caveats of distributed plasticity models is that there are no comprehensive methods for including the effects of cyclic deterioration, which has a critical influence on structural performance at large drifts. In addition, these models are computationally expensive, requiring multiple inelastic beam-column elements along the length of the actual member. The members are sensitive to the discretization of the finite element mesh used, which can lead to convergence issues in trying to keep section-wide equilibrium for large building models. Inelastic elements can also have a negative effect when considering structural damping, which is discussed in Section 5.1.6.

Concentrated (or lumped) plasticity models (Figure 5.2a) incorporate elastic elements that are connected by zero-length rotational spring elements at the ends that represent the element's nonlinear behavior. One of the strengths of concentrated plasticity models is their simplicity and reduced computational cost: a beam or column may be modeled using a single elastic element with springs at each end. These models are phenomenological, and require the moment-rotation (M-θ) relationship expected at the plastic hinge rather than the engineering stress-strain relationship. Spring properties can be determined in a variety of manners, such as: (1) M-θ hysteresis curves from test data; (2) empirical equations calibrated to test data such as those provided by Lignos and Krawinkler (2010); or (3) procedures outlined in ASCE 41: *Seismic Evaluation and Retrofit of Existing Buildings* (ASCE, 2014). One of the limitations of concentrated plasticity models is that they do not capture *P-M* interaction, which can lead to

an unconservative representation for column behavior in taller buildings unless measures are taken to artificially reduce the moment of the columns in anticipation of expected axial demands (PEER/ATC, 2010).

Due to the strong importance of member deterioration on structural performance, the concentrated plasticity model was selected for beam and column elements in this research. The modified Ibarra-Medina-Krawinkler (IMK) deterioration material model (Ibarra et al., 2005; Lignos and Krawinkler, 2009) was used for the springs at the member ends, which was recently adopted by PEER/ATC 72–1: *Modeling Criteria for Seismic Design* (PEER/ATC, 2010). Input parameters that define the M-θ response for beam and column springs in the numerical models are shown in Figure 5.3. These parameters are:

1. Elastic Stiffness (K_e): Double-curvature was assumed, giving $K_e = 6EI/L$.
2. Yield Moment and Rotation (M_y and θ_y): Calculated using expected yield strength (R_yF_y). The preferred A992 steel material was assumed for beam and column members, giving $F_{y,exp}$ = (1.1)(345 MPa) = 380 MPa [55 ksi].
3. Capped Moment and Rotation (M_c and θ_c): A ratio of M_c/M_y = 1.1 is recommended by PEER/ATC 72–1 based on observations of Lignos and Krawinkler (2010), giving $M_c = (1.1)(F_{y,exp})(S_x)$.
4. Plastic Rotation (θ_p), Post-capping Plastic Rotation (θ_{pc}), Deterioration Parameter (Λ): Calculated using empirical equations derived by Lignos and Krawinkler (2010) through calibration with a test database of over 100 steel W-sections (mostly beams), with inputs of h/t_w, $b_f/2t_f$, and L/d.
5. Residual Strength Ratio ($\kappa = M_r/M_y$): A ratio of 0.4 was assumed per recommendation by PEER/ATC 72–1 and Lignos and Krawinkler (2010).

6. Ultimate Rotation Capacity (θ_u): This rotation marks the onset of ductile tearing. Earlier research studies have shown that steel frame structures usually collapse before ductile tearing occurs (Ibarra et al., 2005; Lignos and Krawinkler, 2009). Thus, θ_u was set to a large value (0.5) to prevent the onset of ductile tearing.
7. Stiffness Amplification Parameter (n): A value of 10 was assumed per the recommendations of Ibarra and Krawinkler (2005), which involved amplifying the elastic stiffness of the rotational spring such that it was 10 times larger than that of the elastic beam element. This amplification ensures that all deformation was forced into the plastic hinge spring as intended, while minimizing numerical instability problems. To correct for this adjustment in the elastic beam and column members and keep the same overall element stiffness, the moment of inertia of the elastic beam and column elements was multiplied by $(1 + n)/n$ (Ibarra and Krawinkler, 2005). A similar adjustment $(1 + n)$ was made to the deterioration parameter (Λ) per the recommendation of Ibarra and Krawinkler (2005).

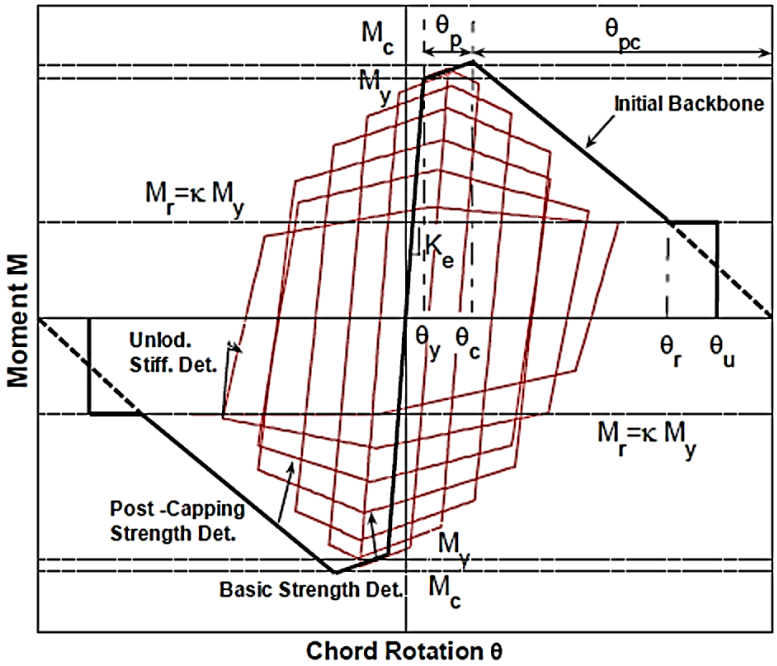

Figure 5.3 – Modified Ibarra-Medina-Krawinkler (IMK) deterioration model that was used for beam and column springs in building models (from Lignos and Krawinkler, 2011).

One of the main caveats of the concentrated plasticity model is the inability to capture the effects of *P-M* interaction. This leads to unconservative assumptions in the available moment capacity (M_p) of columns, where axial effects from gravity loads will often be large. To counter this detrimental effect, M_p of columns within all building models was reduced through *P-M* interaction by the expected gravity load at each level. The use of concentrated plasticity models in columns was still unconservative within braced bay columns due to the development of lateral-load overturning forces, which in combination with gravity load effects may increase the rate of cyclic deterioration and further decrease the plastic moment capacity. However, in absence of any available data for the moment-rotation behavior of columns, the empirical equations from Lignos and Krawinkler (2010) can serve as a reasonable upper-bound (PEER/ATC, 2010) after making the reduction in moment capacity in consideration of gravity demands.

Given the effort to provide a balance of column orientation through the prototype buildings in each direction, about half of the gravity columns within each building model were oriented about their weak axis (Figure 5.4). No test data was available for weak-axis gravity columns, and the beam test data was all from strong-axis behavior, so the modified IMK model could not be adopted rigorously as was done for the strong axis columns. In consideration of *P-M* interaction, the moment capacity of these columns was reduced by the expected gravity demands. The IMK spring model was still used for these weak-axis columns, but with several simplifications: cyclic deterioration was not considered, and θ_p = 10% was assumed.

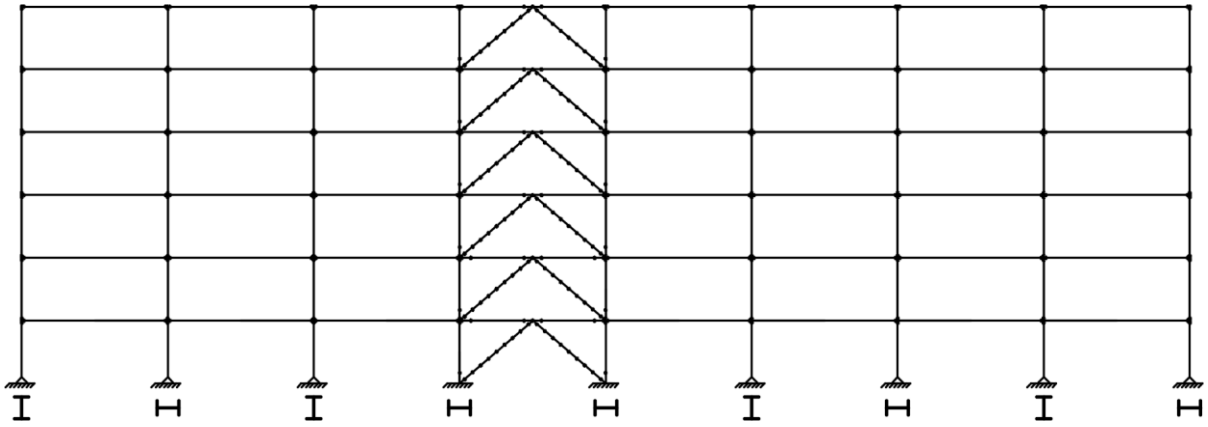

Figure 5.4 – Column orientation in model of 6-story building, which uses four braced bays in each direction. Using symmetry, only one quarter of the building (9 columns and 1 braced bay) is modeled.

5.1.3 Braces

Due to the importance of properly modeling brace buckling and considering both *P-δ* effects and *P-M* interaction, inelastic displacement based elements (DBEs) with distributed plasticity were used for the braces. Per recommendations from recent research (Karamanci, 2013; Karamanci and Lignos, 2014), a fiber section discretization was used with ten fibers along the width of the cross-section and four fibers through the HSS wall thickness. 8 DBEs

were used for each brace, and the Gauss-Lobatto quadrature rule was employed with five integration points per element. Only the physical brace itself (end-to-end) was modeled using these elements. The corotational geometric transformation was invoked in *OpenSees* for brace elements to portray *P-δ* effects.

The *Steel02* model from the *OpenSees* material library was selected to represent the cyclic behavior of the braces. This material model was applied to each of the fiber elements used to discretize the brace cross-section. The *Steel02* model uses the Menegotto-Pinto relationship (Menegotto and Pinto, 1973), with primary inputs of yield strength (F_y), elastic stiffness (E_0), and kinematic strain-hardening ratio (b). The transition between the elastic and plastic branch is defined by three empirical parameters (R_0, cR_1, and cR_2). The material additionally allows for the consideration of isotropic hardening through parameters a_1 to a_4. For all braces used in building models a strain-hardening ratio of 0.1% (b = 0.001) was assumed, and values of 22.0, 0.925, and 0.250 were used for R_0, cR_1, and cR_2, respectively, per the recommendation of Karamanci and Lignos (2014). A plot of the hysteretic material behavior using these parameters, and with E_0 = 200 GPa [29,000 ksi.] and the expected yield strength for ASTM A1085 braces, $F_{y,exp} = R_y F_y = (1.25)(345) = 431$ MPa [62.5 ksi] is shown in Figure 5.5.

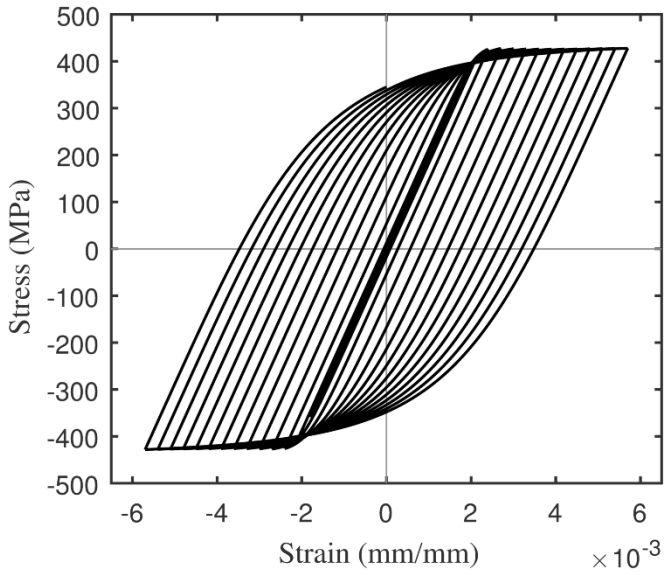

Figure 5.5 – Stress-strain behavior of *Steel02* material used for modeling of ASTM A1085 braces in building models.

Post-buckling brace strength degradation from low-cycle fatigue was modeled using the *Fatigue* material (Uriz, 2005), which returns a stress of zero in a fiber after it has accumulated enough strain per a control parameter, ε_0. This parameter was calculated using an empirical equation which was proposed by Karamanci and Lignos (2014) following calibration of experimental data for 65 different square steel tube braces from multiple tests worldwide. Local slenderness values of braces in this database ranged from $4.20 \leq b/t \leq 30.4$, which defined the range of applicable section geometries for the equation.

To capture brace buckling numerically, an initial out-of-straightness must be specified. Karamanci and Lignos found that a brace mid-length imperfection of $L/1000$ was adequate to capture global buckling, and this imperfection coincides with the largest permissible for nominally straight compression members in the AISC *Code of Standard Practice for Steel Buildings and Bridges* (AISC, 2010c). However, modeling an imperfection of $L/1000$ does not always provide a match between predicted and experimentally observed response (D'Aniello

et al., 2015). In some cases, initial imperfections as large as $L/100$ are required to match numerical buckling loads with experimentally observed behavior. D'Aniello et al. (2015) also noted that the initial imperfections do not have a significant influence on cyclic behavior following the onset of global buckling—only the initial buckling load. Due to the emphasis on post-elastic response, the code-specified largest allowable value of $L/1000$ was assumed consistently for all braces in building models.

5.1.4 Gusset Plates and Brace-Gusset Connections

Brace-gusset connections were modeled using spring elements consisting of both translational and rotational components, and were located at the physical ends of the HSS braces. The remaining section from the end of the brace to the beam-column-brace workpoint was modeled using a rigid link with area and moment of inertia equal to 10 times the associated properties of the braces. The rotational spring component captures gusset plate rotational stiffness and moment capacity (Hsiao et al., 2012). As mentioned in Section 5.1.1, the gusset plate spring were artificially rotated 90-degrees to allow brace buckling to occur within the plane of the frame. Thus, the rotational spring component acts in *OpenSees* direction 6, or θ_z. The spring was modeled using the *Steel02* material model, with inputs of $M_{y,gp}$ and K_{gp}. Hsiao et al. (2012) proposed calculating the yield capacity of the gusset plate using the Whitmore width (W_w). For these models, W_w was approximated from a projection of 45-degree angles from the face of the brace at the end of the gusset plate to the physical end of the brace (Figure 5.6a), and assumed that the brace-gusset fillet weld extended to the edge of the gusset plate. This gives a gusset plate moment capacity, $M_{y,gp}$, of $W_w t^2 F_{y,gp}/6$, where t is the gusset plate thickness and $F_{y,gp}$ is the expected yield stress of the gusset plate material. All gusset plates used in numerical building models were 19 mm. [3/4 in.] thick and made from the preferred

plate material, A36 steel, with $F_{y,exp}$ = (1.5)(248 MPa) = 372 MPa [54 ksi]. The rotational stiffness, K_{gp}, was calculated using an equation proposed by Hsiao et al. (2012). The equation is based on gusset plate geometry of the gusset plate and was previously verified by a finite element study (Yoo, 2006): $K_{gp} = EW_w t^3/(12L_{avg})$, where E is Young's Modulus and L_{avg} is an average of three lengths measured perpendicular from the Whitmore cross-section to the nearest beam or column face (Figure 5.6a). A typical M-θ hysteresis for the gusset plate spring of a select brace-gusset connection from the numerical building model is shown in Figure 5.6b.

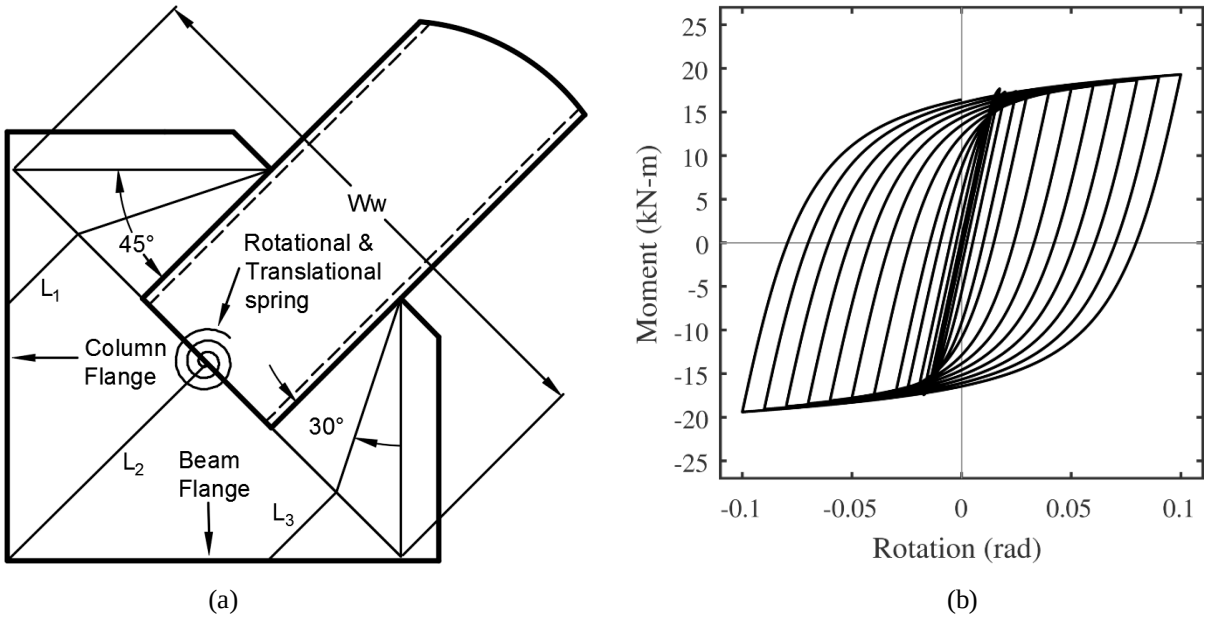

(a) (b)

Figure 5.6 – OpenSees gusset plate model used in numerical simulations: (a) Definition of variables used to calculate moment capacity and stiffness; (b) typical M-θ hysteresis.

The translational spring component (Figure 5.6a) models weld fracture, and consisted of an elastic spring with stiffness equal to E_{steel}. After the defined weld capacity, R_n = (1/0.75)1.392Dl (AISC, 2010b), was reached within the translational spring, weld fracture was modeled by removal of both the translational and rotational gusset plate spring. Accounting for the realistic condition in which one of the two brace-gusset welds at the brace ends will

always be larger than the other, weld fracture was only modeled in one end of the braces, at the corner brace-gusset connection. To achieve convergence after removal of this spring, a new spring was put in its place with very low stiffness, $1.0e^{-8}E_{steel}$. A similar flexible spring was placed into the direction perpendicular to the weld spring following brace-gusset weld fracture to simulate the ability for the brace to slide up and down the gusset plate, and in the rotational direction (direction 6), to help with numerical convergence. In general, the effect of brace reengagement was not considered in these numerical models, though brace reengagement was needed to correctly model the behavior of the R = 3.25 split-x OCBF test unit, as shown in Section 5.3. When applicable, brace reengagement was modeled by following the same procedure as described above, except the translational weld spring was replaced with an elastic-plastic element following weld fracture with stiffness equal to the assumed reengagement stiffness and strength capped by the assumed bearing capacity (Section 3.3.3).

5.1.5 Beam-Column Connections

Beam-column connections were modeled using a fiber section with one fiber at each bolt line for double angle connections both with and without gusset plates. This connection model includes hysteretic angle behavior, angle bearing behavior in compression, and captures the beam flange bearing on the column flange at large drifts following bolt failure. The hysteretic properties of the angle that are implemented in this connection model may be determined from test data, such as from angle pull tests. In lieu of test data, a simple nonlinear model was constructed in collaboration with Thierry Beland, a graduate student from Polytechnique Montréal to give a method for estimating the force-deformation relationship of an angle section. The basis for the creation of the nonlinear angle and connection models was the aggregation of test data from over 100 angle pull tests conducted at Polytechnique Montréal

(Beland et al., 2014; Nelson et al., 2014; Beland, 2016). Once the hysteretic properties were obtained, the full material for use in *OpenSees* was constructed (Figure 5.7a), which consisted of:

1. A *Hysteretic* material containing the angle's force-deformation behavior.
2. A *minMax* material wrapped around the hysteretic material. This material specifies the largest deformation limit the angle can achieve, after which the hysteretic material assumes a force of 0.
3. An *ElasticNoTension* material placed in parallel with the previous materials and modeled the contact between the angles and the column flange.
4. An *Elastic* flexible spring placed in parallel with the previous three materials and provided numerical stability following angle failure.

After defining the material properties for a unit slice of angle, the entire angle section was constructed. The section was built by "stacking" unit angle slices to create a representative angle connection at a corresponding location on a frame using fiber layers. The number of fiber layers was defined by the number of bolt rows for the angle connection, and the area of each layer was defined by the number of unit angle strips included within each fiber (tributary bolt row area). The centroids of the lower and upper bolt rows within each angle were defined to locate the angle in its proper local configuration respective to the depth of the beam or gusset plate that it connected. A schematic of the section configuration for a double angle connection is shown in Figure 5.7b. Modeling beam-column connections explicitly using the procedure based on the actual section properties and geometry allowed for easy extension into a variety of configurations. For example, a CBF connection was modeled with two regions, one for the beam-column angle component and one for the gusset-column component. A top and seat

angle may be modeled in this framework by placing a single fiber layer above or below the beam flange, respectively, with area equal to the width of the angle used.

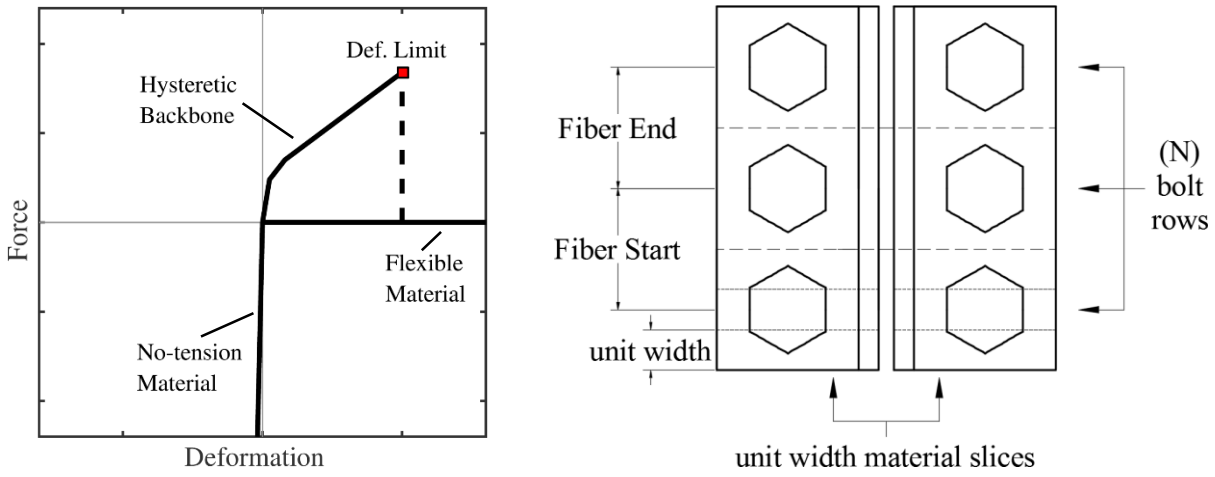

Figure 5.7 – OpenSees beam-column connection model: (a) material behavior for input as unit width slices at the (b) section level within a connection.

The angle connection itself was modeled as a *zeroLengthSection* element with the section property defined previously as an aggregation of all angle fiber layers. The element was placed such that it connected two coincident nodes corresponding to the location where the beam met the column flange (length = 0). For modeling the angle as part of a beam-column connection, additional "gap" fibers were added to the section at the edges of the upper and lower beam flange. These fibers included an elastic gap material with large elastic stiffness and gap equal to the clear distance between the beam flange and the column flange (typically 12.7 mm. [1/2 in.]), and accounted for the possibility of the beam bearing on the column after significant angle degradation or failure at multiple bolt rows with a connection. A representative figure of an element as it exists in the numerical building model is shown in Figure 5.8 for a typical CBF connection and Figure 5.9 for a typical gravity connection. Also

shown in these figures are the rigid links which are used at all gusset plate regions and beam column intersections, as well as the typical locations of the modified IMK springs used to model beam and column M-θ behavior.

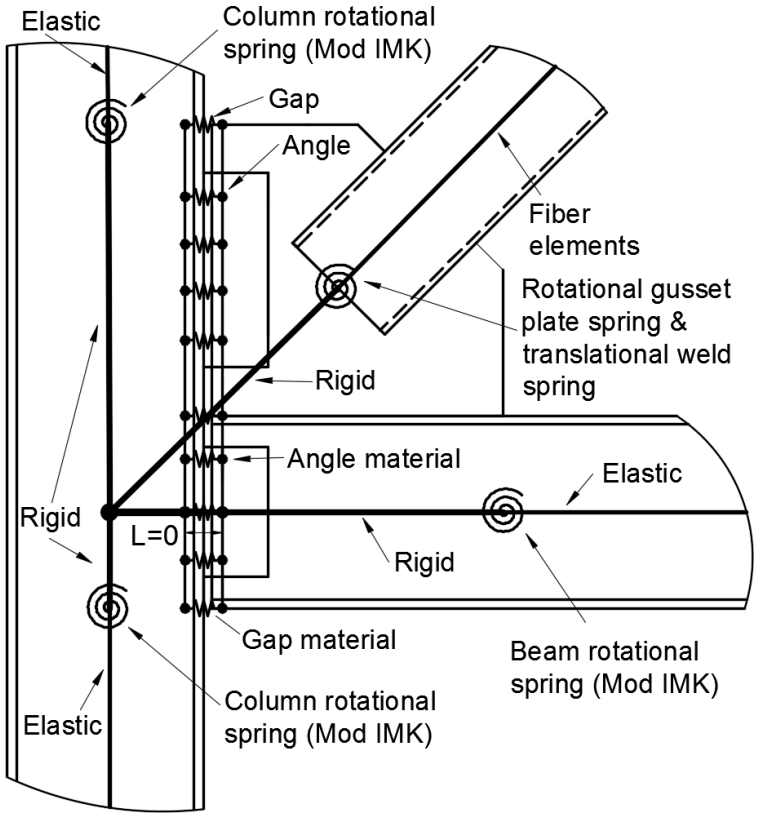

Figure 5.8 – OpenSees discretization for CBF connection.

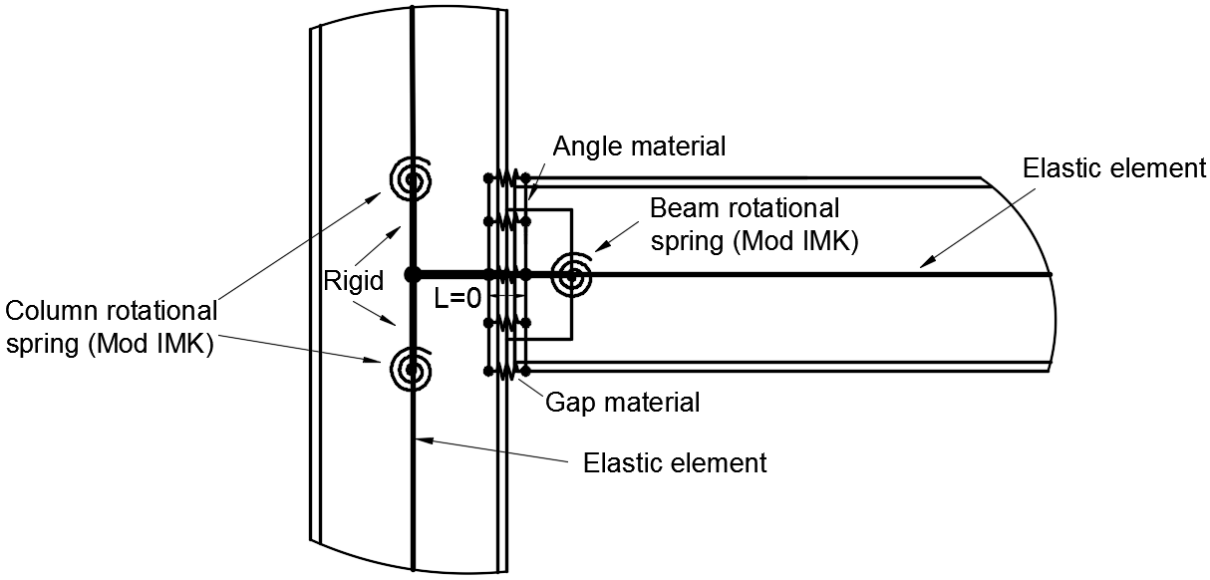

Figure 5.9 – OpenSees discretization for gravity connections and beam-column connections within odd-numbered levels of split-x SFRSs.

The adequacy of the connection model was verified by simulating results from a connection test program performed by Abolmaali et al. (2003). Force-deformation properties of the angle sections used within the connection were estimated using a nonlinear angle model built in *OpenSees*. After obtaining these properties, the connection model was built and the cyclic tests were replicated for the beam-column connections. This validation study is presented in Figure 5.10, for two double-web angle connections that were tested by Abolmaali et al. (2003), which were bolted to the column flange and welded to the beam web.

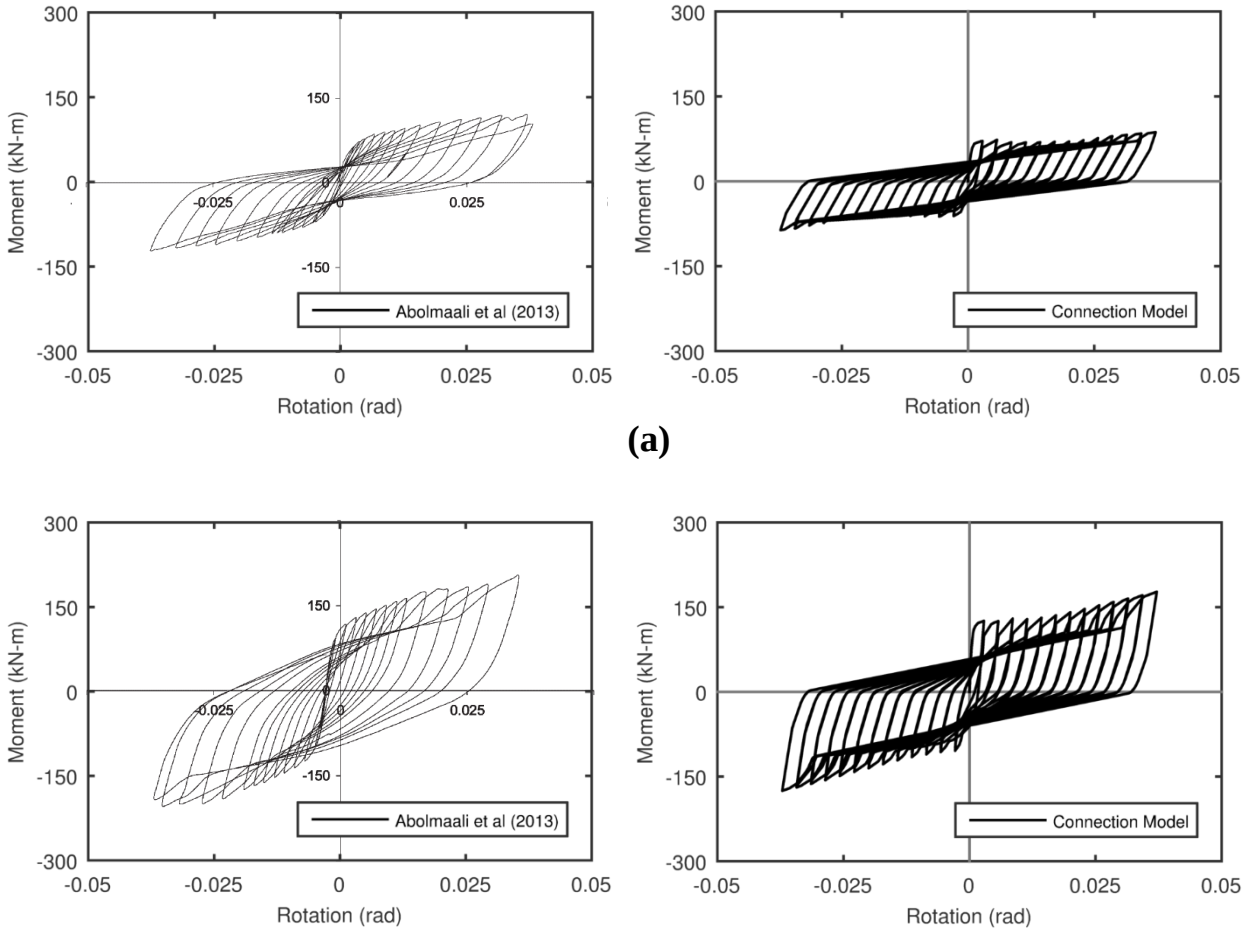

Figure 5.10 – Connection model validation – select tests from Abolmaali et al. (2003): (a) Test BW2 – 2L3x3x1/2 in. with 4 rows of 19 mm. [3/4 in.] diameter bolts and column gage, g_c = 89 mm. [3.5 in.]; (b) Test BW8 – 2L6x6x1/2 in. with 6 rows of 22 mm. [7/8 in.] diameters bolts and column gage, g_c = 140 mm. [5.5 in.].

5.1.6 Damping

Rayleigh damping, which involves a linear combination of mass and stiffness damping, was used to construct the damping matrix in the *OpenSees* building models. A critical damping ratio of 0.02 ($\zeta = 2\%$) was used in all building models, per the recommendations of PEER/ATC 72–1 for steel systems with less than 30 stories (PEER/ATC, 2010). This damping ratio was assumed in the first and third modes of each structure (Leger and Dussault, 1992, Zareian and

Medina, 2010). As suggested by Zareian and Medina (2010), the stiffness proportional damping term was only assigned to the elastic beam and column elements within the building models, while the mass proportional damping term was applied only to the frame nodes that had mass. This was carried out by invoking the *region* command within *OpenSees*, which allowed the creation of element and node subgroups to which damping could be applied, rather than applying damping to the entire building model. Due to the earlier stiffness modification made to the beam and column springs, the stiffness-proportional damping term applied to the elastic beam and column elements was multiplied by $(1 + n)/n$, or 1.1 for $n = 10$, as explained in Ibarra and Krawinkler (2005) and Zareian and Medina (2010). Applying damping to elements that are expected to behave nonlinearly—such as braces and all springs within the model—can cause large fictitious damping forces when the building begins to experience inelastic behavior. These undesirable increases in damping can range from a few percent to several hundred percent (Charney, 2008), and can consequently overestimate the collapse capacity of buildings by a factor of about 2.5, as shown by Karamanci and Lignos (2014).

5.1.7 Loads and Masses

Masses were assigned to the building model at each level, and were concentrated at the central node within the SFRS (Figure 5.11). For a building model with 2 SFRSs in each direction, only half of the gravity bays and one SFRS were modeled, thus only half of the entire building mass was included. In building models with 4 SFRSs in each direction, one quarter of the entire building mass was considered in conjunction with modeling only one quarter of the building. Gravity loads were applied at each level, and were equivalent to $1.0D + 0.2L$ per the recommendations of PEER/ATC 72–1 (PEER/ATC, 2010). The gravity loads within the gravity bays were applied as point loads onto the column, and the gravity loads carried by the

girders framing into the SFRS (Figure 3.1b) were applied as point loads based on tributary area. Gravity loads along the beams within the SFRS were applied as distributed loads (Figure 5.11). Gravity loading was applied prior to dynamic analyses and held constant throughout the simulated seismic event. Rigid elements were used to connect the gravity columns to one another and apply *P-Δ* effects to the SFRS.

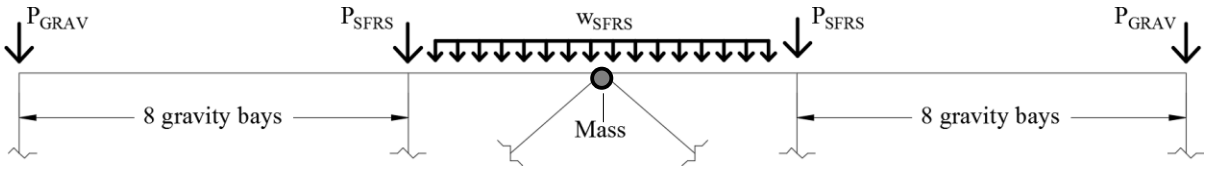

Figure 5.11 – *OpenSees* elevation with locations of gravity loads and mass. Roof shown.

5.2 ACHEIVING CONVERGENCE

As shown in Section 5.1, the numerical building models are complex, and employ the latest practices for considering nonlinear behavior and strength degradation, which are paramount for correctly assessing the performance of steel structures. Nonlinear behavior was included in many of the building model components, such as: (1) brace-gusset rotational springs; (2) fiber discretized brace sections with inelastic DBE elements; (3) beam and column rotational modified IMK springs; and (4) fiber discretized beam-column connections. Structural degradation was considered in many ways, such as: (1) beam and column rotational modified IMK springs; (2) low-cycle fatigue of brace elements using the *Fatigue* material; and (3) brace-gusset weld fracture through removal of translational weld elements once a specified force level was reached.

Separately, each of these sources can create distinct challenges that make obtaining model convergence difficult. When combined within one numerical model, the difficulty in reaching convergence is significantly amplified. Further complicating this issue is the fact that

solving nonlinear systems for large building models is inherently complex. Multiple solutions or solution paths often exist, while only one is representative of realistic behavior and is thus the desired or "correct" path. In an ideal scenario, a single set of analysis parameters would give convergence for all nonlinear building models. This was not the case, however, and the solution algorithm often had to be adjusted during an analysis to find convergence. Several techniques were devised to aid with obtaining numerical convergence in *OpenSees* models throughout the research project.

5.2.1 Problem Definition for Dynamic and Static Simulations

For both dynamic and static simulations, the *UmfPack* command was used in *OpenSees* to construct the system of equations for factoring and solving (Davis, 2004). This system was found to offer the best efficiency with respect to computational time. The *RCM* command was used to number the degrees of freedom, which uses reverse Cuthill-McKee scheme to order the matrix equations (Cuthill and McKee, 1969). The *Plain* command was used to enforce constraints.

5.2.2 Convergence Techniques for Dynamic Simulations

When performing dynamic simulations, a solution loop was created to employ different techniques for reaching convergence if the primary technique failed. The primary solution technique used in dynamic analyses was the *EnergyIncr* convergence test, with a tolerance (*tol*) of $1.0e^{-6}$ and 10 iterations (*iter*). The *Newmark* integration method was used, with recommended parameters $\gamma = 0.5$ and $\beta = 0.25$ for the average acceleration method (Newmark, 1959). The primary solution algorithm used was the *Newton* method. A time step, *dt*, of 0.005 seconds was used in all dynamic simulations for consistency with the available acceleration data. Often throughout the analysis, these parameters did not lead to convergence, and thus a

solution loop was created. A generalized version of the approach used for reaching convergence in dynamic simulations is outlined below.

while $T < T_{end}$,

Try primary solution scheme.

if *Convergence* = No,

Try decreasing time step, i.e. *dt*/10 or *dt*/50.

if *Convergence* = No,

Try alternate solution algorithms, such as *ModifiedNewton*, *KrylovNewton*, *SecantNewton*, "-*initial*" variations of the above, "-*initialThenCurrent*" variations of the above, and *NewtonLineSearch*.

if *Convergence* = No,

Try increasing the number of iterations, i.e. *iter* = 50, 100, 250, 2000.

if *Convergence* = No,

Try changing the convergence test, i.e. to *NormDispIncr*.

if *Convergence* = No,

Try relaxing the tolerance, i.e. *tol* = $1.0e^{-3}$

Effort was made to try all other combinations of time step, algorithm, convergence test, and number of iterations, prior to relaxing the tolerance, to limit the possibility of converging to an incorrect solution. In addition, relaxing the tolerance can have a compounding effect that requires relaxing the tolerance again in later analysis steps. When cycling through alternate solution algorithms, *NewtonLineSearch* was tried last. This algorithm was often found to give the best chance of reaching convergence, but at the highest likelihood of converging to an incorrect solution.

5.2.3 Convergence Techniques for Static Simulations

Techniques used to reach convergence in models during static pushover simulations were mostly the same as those used for dynamic simulations, but with a few key differences. In static pushover simulations, a control node was specified in the integration scheme, which was *DisplacementControl*. The *DisplacementControl* method tries to move the control node specified by a target displacement increment under the defined loading pattern. In general, the control node was specified to be one of the top column node within the SFRS, however, when numerical convergence issues arose, the control node was temporarily switched mid-analysis to lower stories. This was particularly useful for cases in which brace-gusset weld fracture occurred and created a soft first story, while the still-elastic upper stories tended to "snap back" or unload elastically. Changing the control node was also useful in aiding with convergence of pushover analyses when brace-buckling was starting, as switching the control node to the midspan of the buckling brace temporarily gave a smoother transition to the post-buckled configuration.

5.2.4 Localized Methods for Obtaining Convergence

In addition to the global approaches used to obtain convergence, other considerations were made at the local level to aid with convergence. Within the DBE that made up the brace members, the default number of iterations and tolerances in *OpenSees* to satisfy local element compatibility are 10 and $1.0e^{-12}$, respectively. To speed up the analyses and reduce the number of iterations needed globally to achieve convergence during brace buckling, the local tolerance limit for the braces was relaxed to $1.0e^{-8}$. Another common technique for dealing with convergence issues within brace members is to adjust the number of integration points (5), number of elements (8), and discretization of the fiber mesh (10 by 4). However, due to the

reliance of the empirical *Fatigue* material model on these specific values, which were derived in a calibration study by Karamanci and Lignos (2014), these properties were not altered.

A final localized source of convergence problems comes from the consideration of brace-gusset weld fracture. As discussed in Section 5.1.4, brace-gusset weld fracture was simulated through removal of the brace-gusset spring after axial demands reached the specified weld capacity. Following this, local convergence was ensured by providing a ramp of decreasing stiffness "dummy" elements. For example, after the original brace-gusset weld with stiffness = $1.0E_{steel}$ was removed, it was replaced with an element that has stiffness = $1.0e^{-1}E_{steel}$, and a solution step was performed with a very short time step ($dt/100$). After successful convergence was reached following the methods outlined in Section 5.2.1, the $1.0e^{-1}E_{steel}$ element was removed and replaced with an element with stiffness = $1.0e^{-2}E_{steel}$, and the process was repeated as necessary until the final stiffness of the brace-gusset interface was $1.0e^{-8}E_{steel}$.

5.3 MODEL VERIFICATION[2]

The numerical building model was next verified through simulation of the full-scale experimental tests from Chapter 4. Prior to system simulations, the brace behavior was calibrated to match what was seen in the tests due to the important role the braces placed in both test units. To calibrate the brace model against experimental behavior, an isolated model of a representative brace from each test unit was axially displaced under the measured experimental displacement history (Figure 5.12). To capture the experimental buckling loads within these brace models, initial imperfections of $L/250$, $L/400$, and $L/500$, were needed for the HSS8x8x1/4 (Story 2 – R = 3 chevron), HSS6x6x3/8 (Story 2 – split-x OCBF), and

[2] Section 5.3 has been adapted from an accepted journal manuscript with slight modifications: Sizemore, J., Fahnestock, L., Hines, E., and Bradley, C. (2016). Parametric Study of Low-Ductility Concentrically-Braced Frames under Cyclic Static Loading." *Journal of Structural Engineering*.

HSS6x6x1/2 (Story 1 – split-x OCBF) braces, respectively, where *L* was the actual end-to-end length of the brace (6.1 m. [20 ft.]). These imperfections agree with the observation made by Goggins and Salawdeh (2012) that stockier braces typically needed lower initial imperfections for correct modeling, while less compact specimens (such as the HSS8x8x1/4 braces in the *R* = 3 chevron CBF) needed larger initial imperfections.

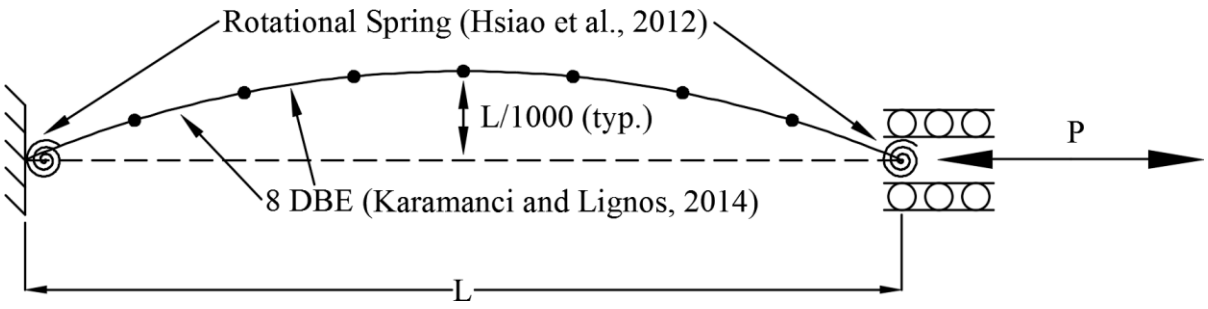

Figure 5.12 – Schematic of *OpenSees* brace buckling simulations.

The comparison plots from this validation study are shown for the *R* = 3 chevron CBF buckling braces in Figures 5.13a and 5.13b and the *R* = 3.25 split-x OCBF buckling braces in Figures 5.13c and 5.13d. During the frame tests, buckling occurred in the upper story HSS8x8x1/4 braces of the *R* = 3 CBF, and both an upper (HSS6x6x3/8) and lower (HSS6x6x1/2) brace in the OCBF. The OCBF braces did not experience local buckling or evidence of fatigue-related damage during the test, and the empirical *Fatigue* parameters calculated from the equation proposed by Karamanci and Lignos (2014) produced behavior that agreed with this result. On the other hand, HSS8x8x1/4 braces in the *R* = 3 CBF experienced significant degradation associated with local buckling both at the onset of global buckling and then subsequently throughout the rest of the test. For these braces, despite having a local slenderness (*b*/*t* = 28.8) within the applicable range of the empirical equation, the calculated ε_0 of 0.0297 (Karamanci and Lignos, 2014) was significantly larger than the ε_0

parameter (0.0175) needed to best match the behavior of the HSS8x8x1/4 braces tested in the lab. Even though ε_0 of 0.0175 captured the buckling strength and post-buckling behavior, the sudden large initial degradation that resulted from local buckling at the immediate onset of global buckling was not captured. This was expected since the existing low-cycle fatigue brace models—which are based on accumulation of damage over multiple cycles—are not intended to model local-buckling induced degradation damage and sudden loss of strength that occur in high *b*/*t* tubes. Isotropic hardening for these cold-rolled A1085 braces was captured through use of the following *Steel02* parameters definitions: $a_{1,3} = 0.01$; $a_{2,4} = 1.0$. This is a slight deviation from the recommended values of Karamanci and Lignos for hot-rolled braces: $a_{1,3} = 0.03$; $a_{2,4} = 1.0$ (Karamanci and Lignos, 2014) and cold-rolled braces: $a_{1,3} = 0.01$; $a_{2,4} = 1.0$ (Karamanci and Lignos, 2013). These fitted values ($a_{1,3} = 0.01$; $a_{2,4} = 1.0$) were adopted for use in future numerical simulations.

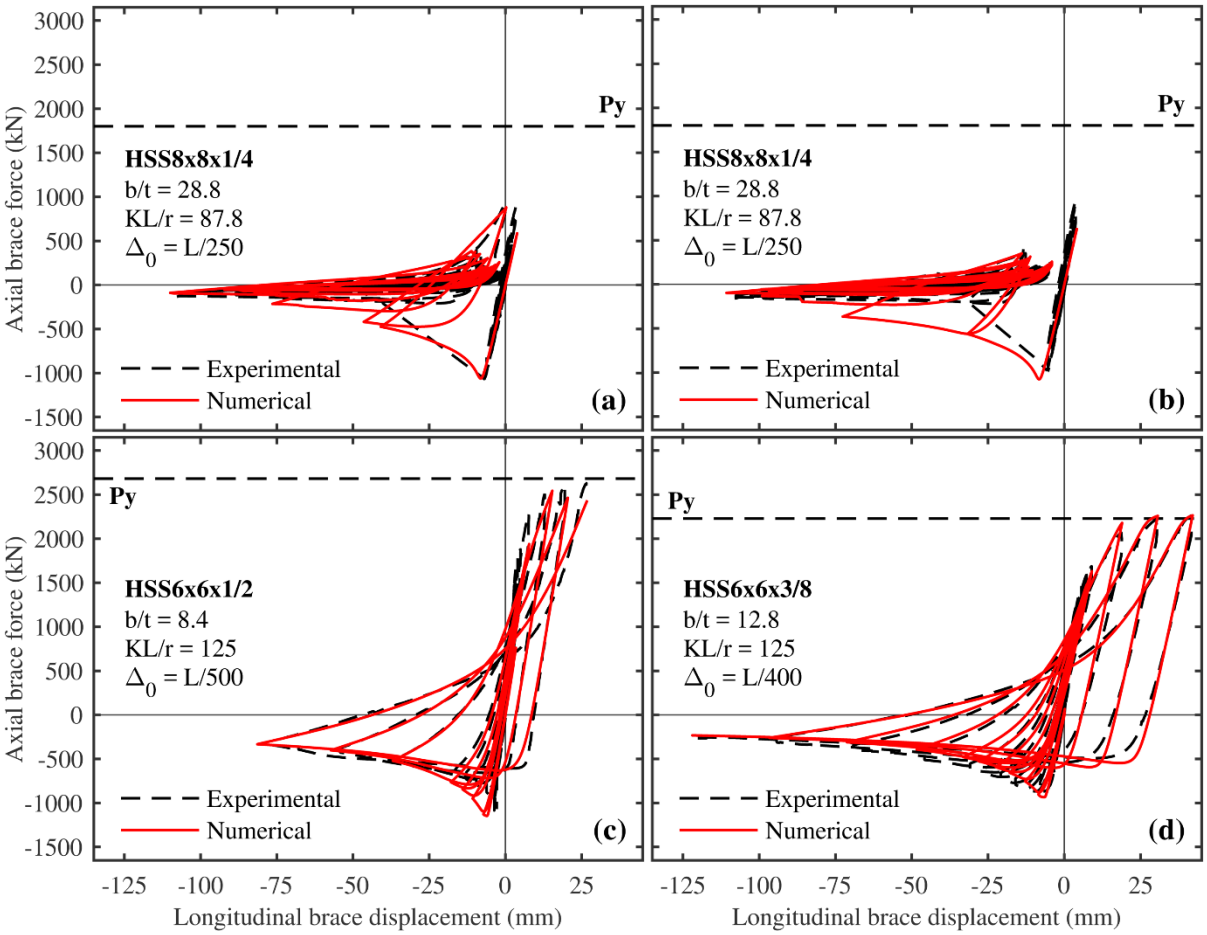

Figure 5.13 – Numerical validation of test unit brace behavior: (a-b) chevron R = 3 story 2 braces; (c) split-x OCBF story 1 brace; (d) split-x OCBF story 2 brace.

5.3.1 Numerical Simulation of Full-Scale Tests

After brace model calibration was performed as described above, the two full-scale tests were conducted numerically. The numerical models replicated the geometry, loading and boundary conditions from the laboratory. The column base fixtures were modeled as true pins, and the ground links—which in the lab were stiff pin-ended load cell assemblies attached collinearly to a W12x72 beam at Level 1 (Figure 5.14a)—were modeled using an elastic spring with a gap at zero displacement. An elastic spring stiffness of 250 kN/mm [1,425 kip/in] was found to give the best match with the overall frame behavior, compared to 1,000 kN/mm [5,700

kip/in] as measured by the Linear Variable Displacement Transducers (LDVTs) and the load cell readings at the ground links (Figure 5.14b). This deviation was rationalized in consideration that one of the load cell pin LVDTs malfunctioned during each test. In addition, the column base pin was not perfectly restrained in the x-direction, though it was modeled as a perfect pin due to a lack of instrumentation to measure any small movements at the base. In other words, the reduction in modeled vs. measured stiffness of the load cell pin acted to offset the increase in modeled vs. actual stiffness of the column bases to give a match between the experimental frame stiffness and simulated frame stiffness.

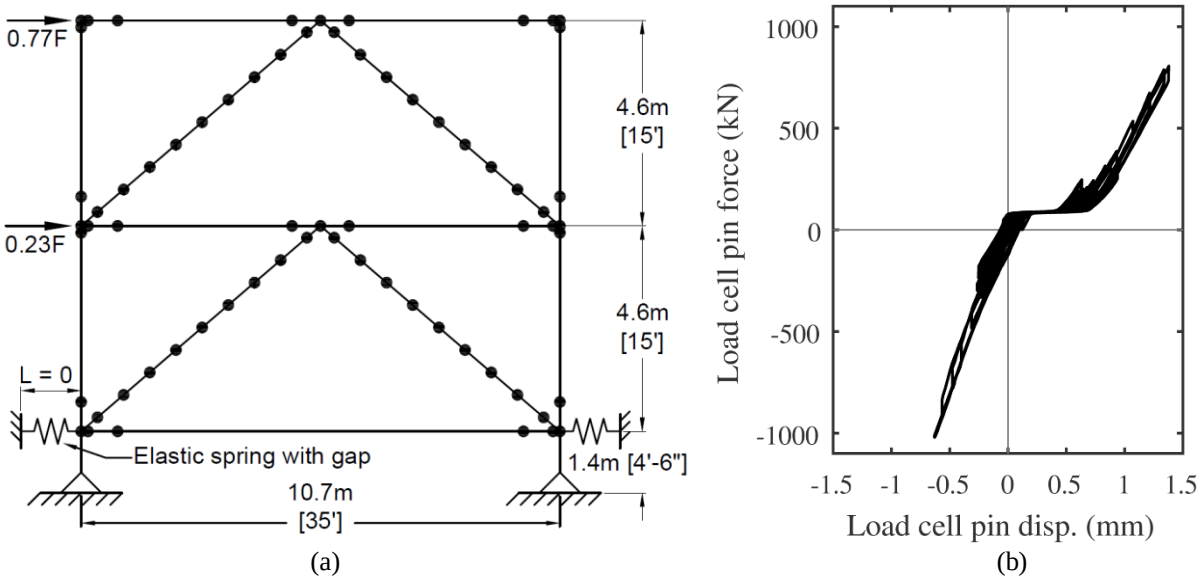

Figure 5.14 – OpenSees numerical model for full-scale frame tests: (a) chevron R = 3 test unit elevation with elastic gap springs for load cell pins; (b) measured load cell behavior.

As discussed in Chapter 4, the primary events in the R = 3 chevron CBF test were Story 2 North brace buckling [1], followed by Story 2 South brace buckling [2]. In this test, local buckling occurred at the onset of global brace buckling, which resulted in a sudden and immediate loss of system strength. Although global buckling capacity was captured in the numerical models, several more cycles were needed for the *Fatigue* material to accumulate

damage and degrade the strength of the braces to an amount comparable to what occurred instantly in the experiment (Figure 5.15). As with the isolated brace model, this mismatch highlights the inability of existing empirical *Fatigue*-based brace models to represent sudden strength loss due to local buckling behavior that occurs in tubes with high b/t ratios. Although the *Fatigue*-based brace model did not capture the initial sudden strength loss associated with combined global–local buckling, it still adequately captured the overall brace behavior in the post-buckling regime. After significant brace buckling occurred, the frame was cycled back and forth within the range of ±1% total frame drift (δ_R/h). Throughout these cycles, the frame model captured the reduced system strength and stiffness associated with the degraded brace buckling behavior in combination with beam and column bending. After the braces buckled, the frame action contribution to lateral resistance increased while the brace contribution decreased. This behavior is captured by the *OpenSees* model, and is a combination of three components: (1) Story 2 column bending; (2) Level 3 beam bending; and (3) Level 3 beam-column connection rotational capacity. The *OpenSees* model also correctly captured the relative story stiffnesses following brace buckling, as the story shear vs. drift plots in Figures 5.15b and 5.15c show.

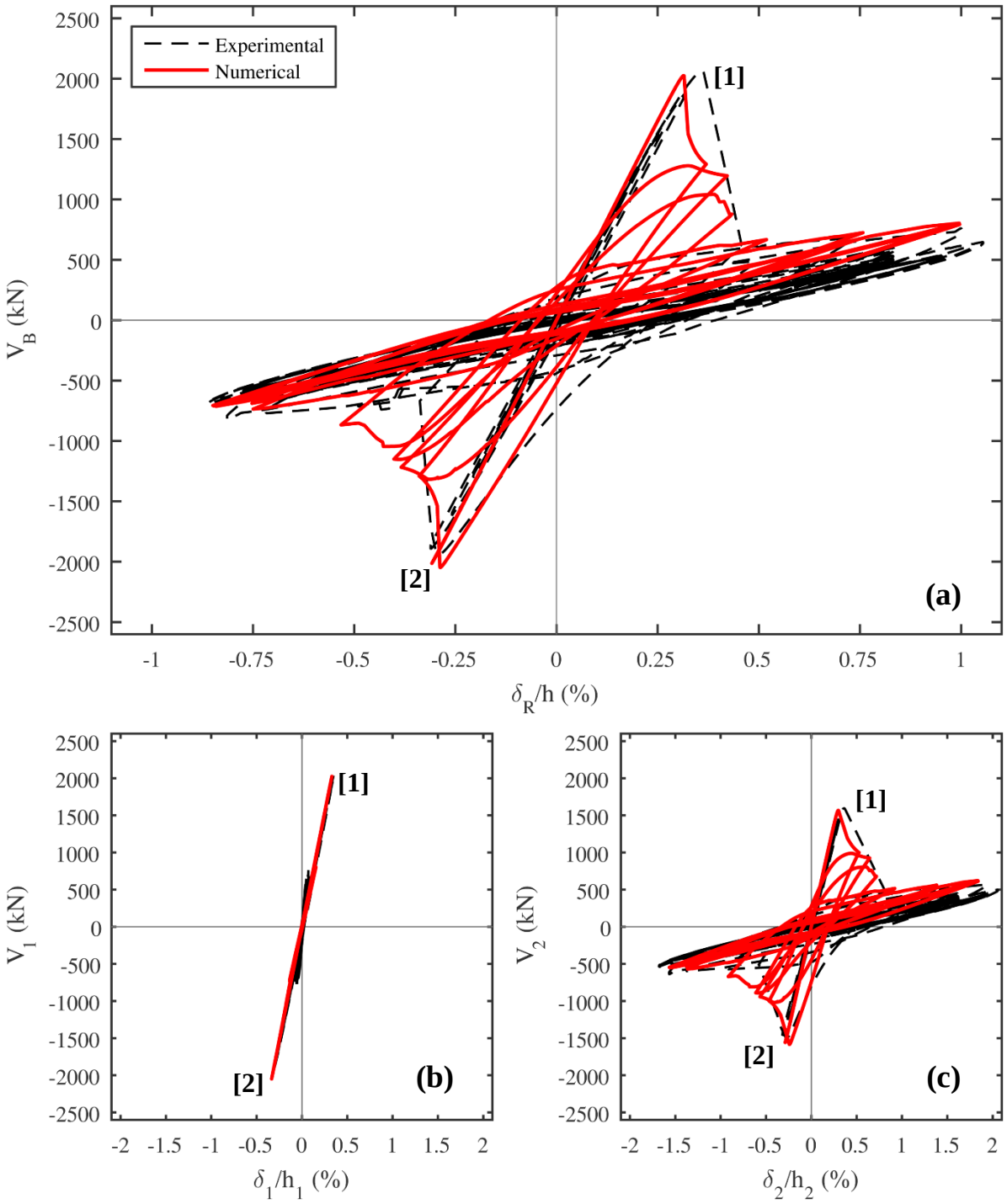

Figure 5.15 – Overall behavior, R = 3 chevron CBF Phase I and III: comparison with numerical simulation. (a) Base shear vs. roof drift; (b) Story 1 shear vs. drift; and (c) Story 2 shear vs. drift. Indicators: [1] Story 2 North brace buckling; and [2] Story 2 South brace buckling.

Limit state progression in the R = 3.25 split-x OCBF test was more complex, as yielding occurred in several locations and led to a more balanced distribution of energy dissipation across both stories. As Figure 5.16 shows, the *OpenSees* model correctly captured several of the observed limit states from the experimental test. Story 2 South brace buckling was captured as seen in the experiment when pushing the frame North to δ_R/h = 0.35% (Figure 5.16 – [1]). When cycling back to δ_R/h = -0.35%, brace buckling occurred in the Story 1 South brace [2]. The initial imperfections were slightly adjusted in the numerical model to replicate the asymmetrical buckling pattern that was seen in the test (Rather than L/400, which was used for the Story 2 South brace, L/500 was used in the Story 2 North brace). Although not predictable, this type of small difference in brace out-of-straightness is realistic considering the combination of variability in member initial imperfections prior to installation and the additional out-of-straightness induced during erection. The next major event that occurred following brace buckling was a combined weld fracture and net-section rupture of the brace-gusset connection in the Story 2 North brace [3]. To reproduce the weld fracture numerically at the observed drift level, brace-gusset weld strength of $1.8R_n$, where R_n is the nominal weld strength (AISC, 2010c) was needed. Although partially attributable to material overstrength, most of the overstrength was attributed to the increased weld throat thickness needed to fill the gap between the HSS and the gusset plate. As shown in Section 4.4, this combined material and geometrical overstrength was seen in the test unit, in which the measured weld capacity exceeded the design-required R_n by as much as 80%.

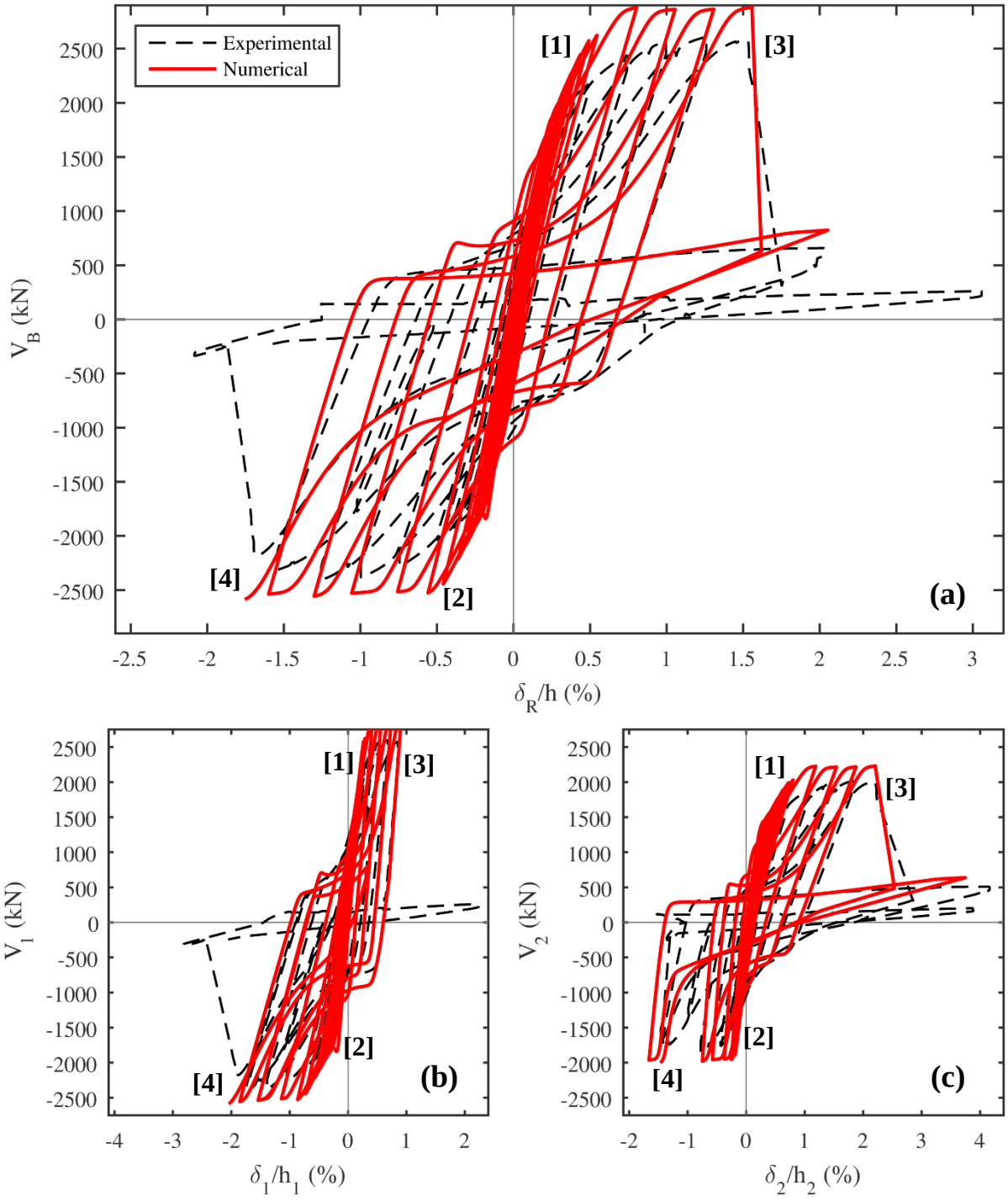

Figure 5.16 – Overall behavior, R = 3.25 chevron OCBF: comparison with numerical simulation. (a) Base shear vs. roof drift; (b) Story 1 shear vs. drift; and (c) Story 2 shear vs. drift. Indicators: [1] Story 2 South brace buckling; [2] Story 1 South brace buckling; [3] Story 2 North brace-gusset weld fracture; and [4] Lower Level 2 beam-gusset weld fracture.

Brace reengagement in compression was modeled with a largest resistance equal to 180 kN [40 kips], and was calculated from the product of the interface area, $2t_g t_{HSS}$, with the measured tensile strength of the HSS braces, $F_{u,m}$ = 495 MPa [72 ksi]. The reengagement stiffness was assumed equal to 0.1% of the original interface stiffness. Although reengagement stiffness and strength were not directly measured in the CBF tests, these values agree with values observed in earlier brace reengagement studies (Davaran et al, 2014). The last significant limit state in the OCBF test, lower Level 2 beam-gusset weld fracture [4], was not considered in the numerical model due to the complex flow of stresses in this region, which could not be captured within the concentrated plasticity elastic element framework used in the present study. Thus, the localized yielding that occurred in the Level 2 beam panel zone was also not captured by the numerical model, which resulted in a slightly less pronounced post-elastic softening than was observed experimentally (Figure 5.16).

5.4 SUMMARY OF NUMERICAL BUILDING MODEL

A numerical frame model was constructed using *OpenSees* so that a rigorous investigation into reserve capacity of low-ductility steel CBFs could start. The frame model incorporated nonlinear brace behavior, beam and column degradation after the formation of plastic hinges, and brace-gusset weld fracture. Several techniques were derived for dealing with the many convergence issues experienced during the use of this complex and highly nonlinear model. The effectiveness of the model was verified by simulating the experimental frame tests that were conducted at Lehigh University (Chapter 4). After some slight modifications to the modeling criteria, such as weld overstrength and brace imperfections, the numerical frame model was effective in capturing the overall behavior of both test units, including brace buckling with degradation and connection failure (brace-gusset weld fracture).

The verification study also revealed limitations of current modeling techniques, such as the inability to accurately predict the effects of coupled global–local buckling and rapid strength degradation in locally slender (large b/t) braces used in $R = 3$ frames. Regardless, the experimental results gave a valuable point of reference for establishing and calibrating the numerical models that were used for the later simulations to broaden the impact of the experimental program.

CHAPTER 6[3]

CYCLIC STATIC PARAMETRIC STUDY OF 3-STORY FRAMES

After confirming adequate behavior of the numerical modeling framework through calibration with the full-scale frame tests, a cyclic static parametric study was conducted to expand the insight provided by the tests. The primary goals were to: (1) identify reserve capacity characteristics; (2) identify practical reserve capacity mechanisms; and (3) distinguish the influence of system type (R = 3 CBF or OCBF) and system configuration (chevron or split-x). In agreement with the experimental tests, gravity framing and gravity loads were not considered since the goal of this part of the research was to evaluate overall response and reserve capacity in low-ductility CBFs (Figure 6.1). CBF geometry was consistent with the

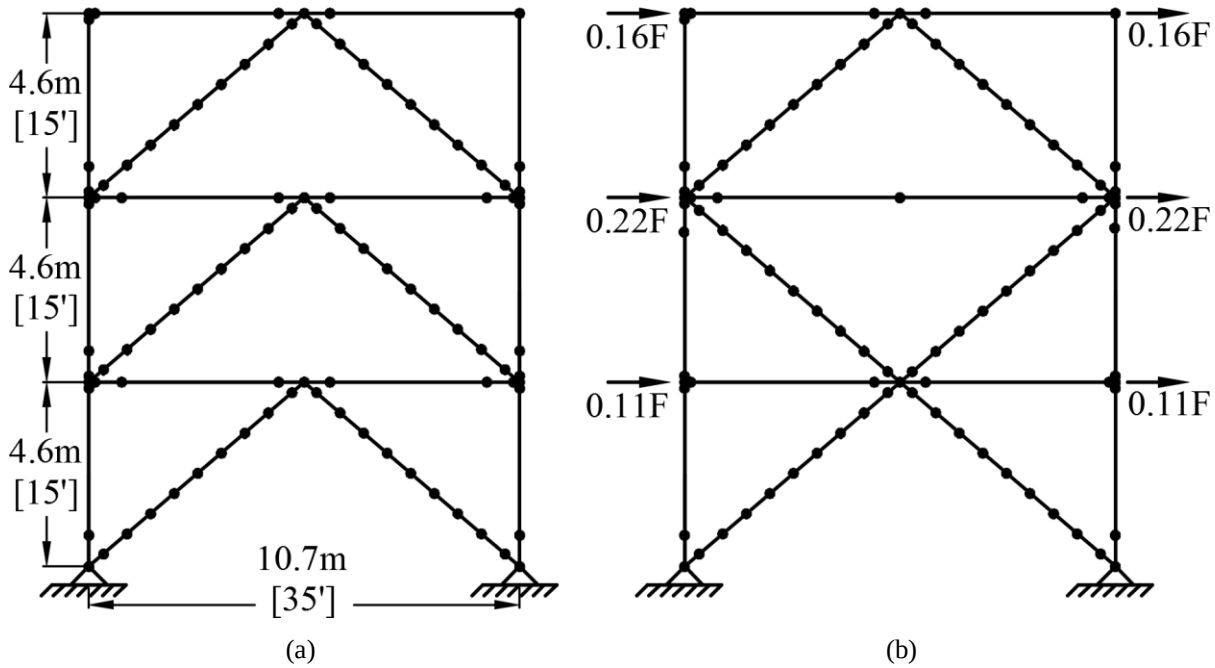

Figure 6.1 – Schematic elevations of frame configurations for parametric numerical simulations in OpenSees: (a) chevron; (b) split-x.

[3] This chapter in its entirety is included from an accepted journal manuscript with slight modifications: Sizemore, J., Fahnestock, L., Hines, E., and Bradley, C. (2016). Parametric Study of Low-Ductility Concentrically-Braced Frames under Cyclic Static Loading." *Journal of Structural Engineering*.

prototype and used 4.6 m. [15 ft.] story heights and a 10.7 m. [35 ft.] bay width. These prototype frames were simulated using the full 3-story height (Figure 6.1) and pinned column base boundary conditions were used.

6.1 FRAME DESIGNS

In addition to system type and system configuration, the period used for calculation of design base shear, V, was also varied (approximate period, T_a, or calculated period, T_c) as a method to extend the primary test matrix to eight valid frame designs rather than four. The labeling scheme for each frame is *Type-Configuration-Period*. For example, the model frame designs that portray the experimental study test units are R3-CHEV-Ta and OCBF-SX-Tc, which indicates an R = 3 CBF in chevron configuration designed with base shear determined using T_a (0.347s) and an OCBF in split-x configuration designed with base shear determined using T_c. For all frames studied, the calculated building periods using the mass of the corresponding prototype building (Bradley, 2016) exceeded the upper limit C_uT_a (C_u = 1.6) imposed by ASCE 7–10 (ASCE, 2013). Thus, this upper limit, $T_c = C_uT_a$ = 0.555s, governed the design of the OCBFs.

A summary of the designs for the eight prototype frames is presented in Tables 6.1 and 6.2. Weld capacities in Table 6.2 were calculated per the AISC *Specification* Equation 8-2a (AISC, 2010b) assuming a 480 kPa [70 ksi] weld, length (l) and throat size (d). The nominal weld capacity, R_n, was conservatively assumed for this baseline parametric study, as there is not an accepted value for weld overstrength reported in the literature. Acknowledging that significant weld overstrength is possible based on the full-scale experimental tests (Chapter 4) and prior brace tests (Davaran et al, 2014), the test matrix was expanded by assuming the largest observed overstrength for the brace-gusset welded connections, $1.8R_n$. This variation

enabled alternate practical mechanisms that were not observed in the eight primary frame designs. Of these additional model frames, the results for two chevron frames (R3-CHEV-Ta*, OCBF-CHEV-TC*), and two split-x frames (R3-SX-Tc*, OCBF-SX-Tc*), are included in Figures 6.2 and 6.3, respectively. The differences in weld capacity between these frames and their primary counterparts are listed in Table 6.2.

Table 6.1 – Frame designs for numerical simulations – member sizes

Frame Designation	Story 1 Braces (HSS) [b/t][a]	Story 2 Braces (HSS) [b/t][a]	Story 3 Braces (HSS) [b/t][a]	Level 2 Beam	Level 3 Beam	Roof Beam	Columns
R3-CHEV-Ta	9x9x1/4 [32.8]	8x8x1/4 [28.8]	6x6x1/4 [20.8]	W12x40	W12x40	W12x26	W12x53
R3-SX-Ta	9x9x1/4 [32.8]	8x8x1/4 [28.8]	6x6x1/4 [20.8]	W12x26	W18x40	W12x26	W12x53
OCBF-CHEV-Tc	8x8x1/2 [12.4]	8x8x1/2 [12.4]	8x8x1/2 [12.4]	W30x116	W30x99	W12x26	W12x53
OCBF-SX-Tc	6x6x1/2 [8.40]	6x6x3/8 [12.8]	8x8x1/2 [12.4]	W12x26	W18x40	W12x26	W12x53
R3-CHEV-Tc	8x8x1/4 [28.8]	7x7x1/4 [24.8]	6x6x3/16 [28.7]	W12x35	W12x30	W12x26	W12x53
R3-SX-Tc	8x8x1/4 [28.8]	7x7x1/4 [24.8]	6x6x3/16 [28.7]	W12x26	W18x40	W12x26	W12x53
OCBF-CHEV-Ta	8x8x1/2 [12.4]	8x8x1/2 [12.4]	8x8x1/2 [12.4]	W40x167	W36x135	W21x62	W12x65
OCBF-SX-Ta	7x7x1/2 [10.4]	7x7x1/2 [10.4]	8x8x1/2 [12.4]	W12x26	W18x40	W21x62	W12x65

[a] For OCBFs, b/t must not exceed $0.64\sqrt{(E/F_y)} = 15.4$ for $F_y = 50$ ksi (AISC, 2010a)

Table 6.2 – Frame designs for numerical simulations – brace-gusset weld sizes

Frame Designations	Story 1 (mm)	kN	Story 2 (mm)	kN	Story 3 (mm)	kN
R3-CHEV-Ta & R3-SX-Ta	l = 4x279, d = 6.4	1470	l = 4x229, d = 6.4	1200	l = 4x152, d = 4.8	601
R3-CHEV-Tc & R3-SX-Tc	l = 4x203, d = 6.4	1070	l = 4x203, d = 4.8	800	l = 4x152, d = 3.2	400
OCBF-CHEV-Ta & OCBF-SX-Ta	l = 4x330, d = 9.5	2580	l = 4x305, d = 7.9	1980	l = 4x203, d = 6.4	1070
OCBF-CHEV-Tc & OCBF-SX-Tc	l = 4x330, d = 6.4	1710	l = 4x254, d = 6.4	1330	l = 4x203, d = 4.8	801
R3-SX-Tc* (Story 2 welds = $1.8R_n$)	l = 4x203, d = 6.4	1070	l = 4x203, d = 4.8	***1440***	l = 4x152, d = 3.2	400
R3-CHEV-Ta* (Welds = $1.8R_n$)	l = 4x279, d = 6.4	***2650***	l = 4x229, d = 6.4	***2180***	l = 4x152, d = 4.8	***1090***
OCBF-CHEV-Tc* (Welds = $1.8R_n$)	l = 4x330, d = 6.4	***3090***	l = 4x254, d = 6.4	***2380***	l = 4x203, d = 4.8	***1450***
OCBF-SX-Tc* (Welds = $1.8R_n$)	l = 4x330, d = 6.4	***3090***	l = 4x254, d = 6.4	***2380***	l = 4x203, d = 4.8	***1450***

6.2 OVERVIEW OF FRAME RESPONSE

Each frame was loaded statically with a lateral load profile defined using the equivalent lateral force (ELF) procedure from ASCE 7–10 (Figure 6.1). Frames were subjected to a cyclic analysis with frame (roof) drift, δ_R/h, increments of 0.05% up to 0.50% drift, followed by 0.10% drift increments up to 1.0% drift, and finally 0.25% drift increments up to δ_R/h = 2.0%. Overall response plots for the eight primary frame designs are included in Figures 6.2 and 6.3, for frames using the chevron bracing configuration and the split-x bracing configuration, respectively. Figures 6.2 and 6.3 show the relationship between base shear (V_B) and frame drift (δ_R/h), the mechanism, the system type (R = 3 or OCBF), the design period (T_a or T_c), the design base shear (V), the weld capacity (R_n), the maximum achieved base shear, $V_{B,m}$, and the base shear at ±2.5% story drift, $V_{B,\Delta a}$. This drift level is consistent with the allowable story drift $\Delta_a = 0.025h_s$ from ASCE 7–10, and is a suitable point for comparing reserve capacity between frames. $V_{B,\Delta a}$ is displayed on the plots of overall behavior with a square indicator. The degree of reserve capacity was influenced by the type of mechanism that formed, as reflected by the moment diagrams in Figure 6.4. Unlike the experimental test units, in which brace buckling occurred, brace-gusset weld fracture was the dominant limit state in analyses of the primary frames, due to the assumption of nominal weld capacity, R_n, which resulted in brace-gusset weld fracture occurring before the braces could buckle in all frames other than split-x OCBFs.

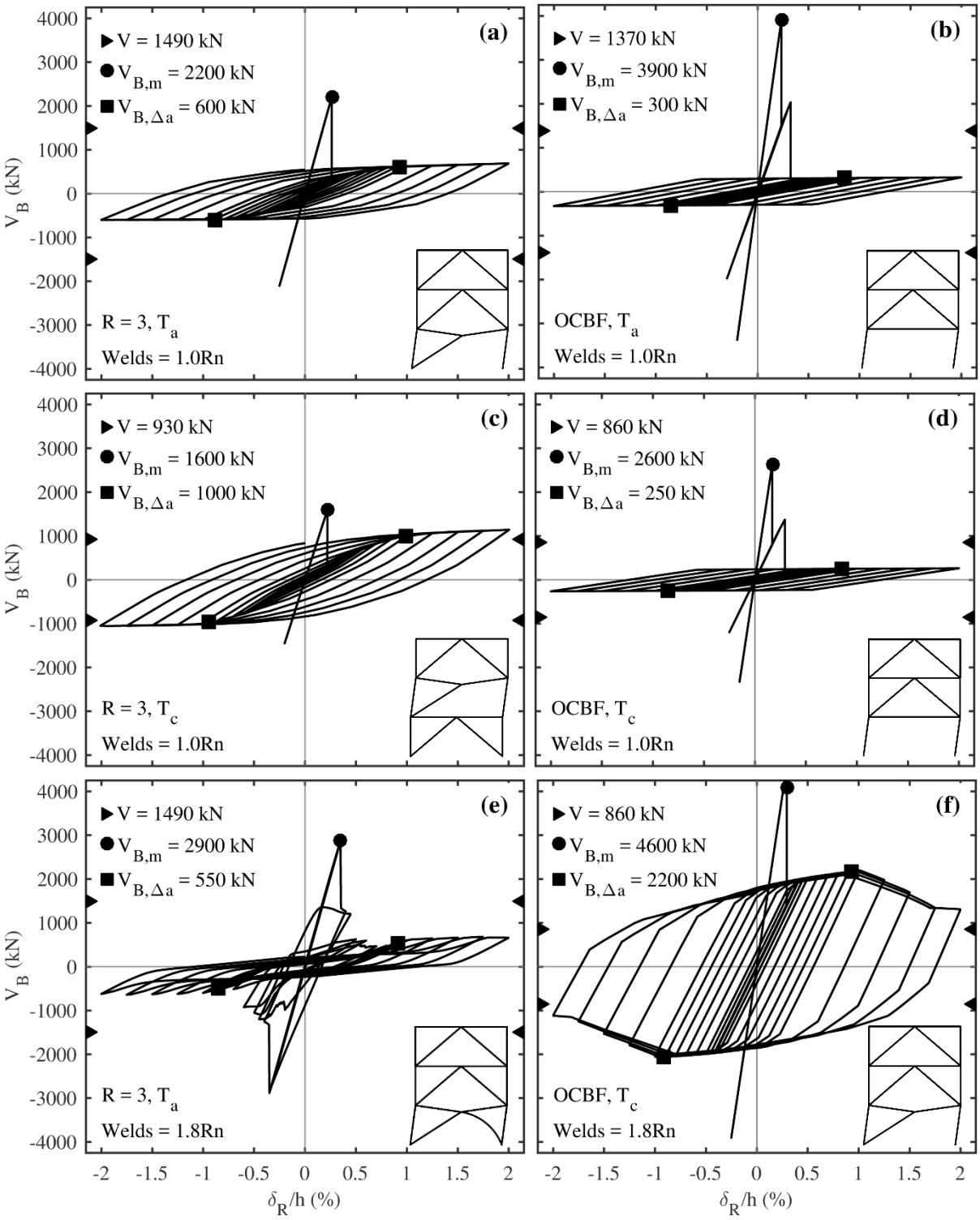

Figure 6.2 – Cyclic behavior of frames in the chevron configuration: (a) R3-CHEV-Ta; (b) OCBF-CHEV-Ta; (c) R3-CHEV-Tc; (d) OCBF-CHEV-Tc; (e) R3-CHEV-Ta*; (f) OCBF-CHEV-Tc*.

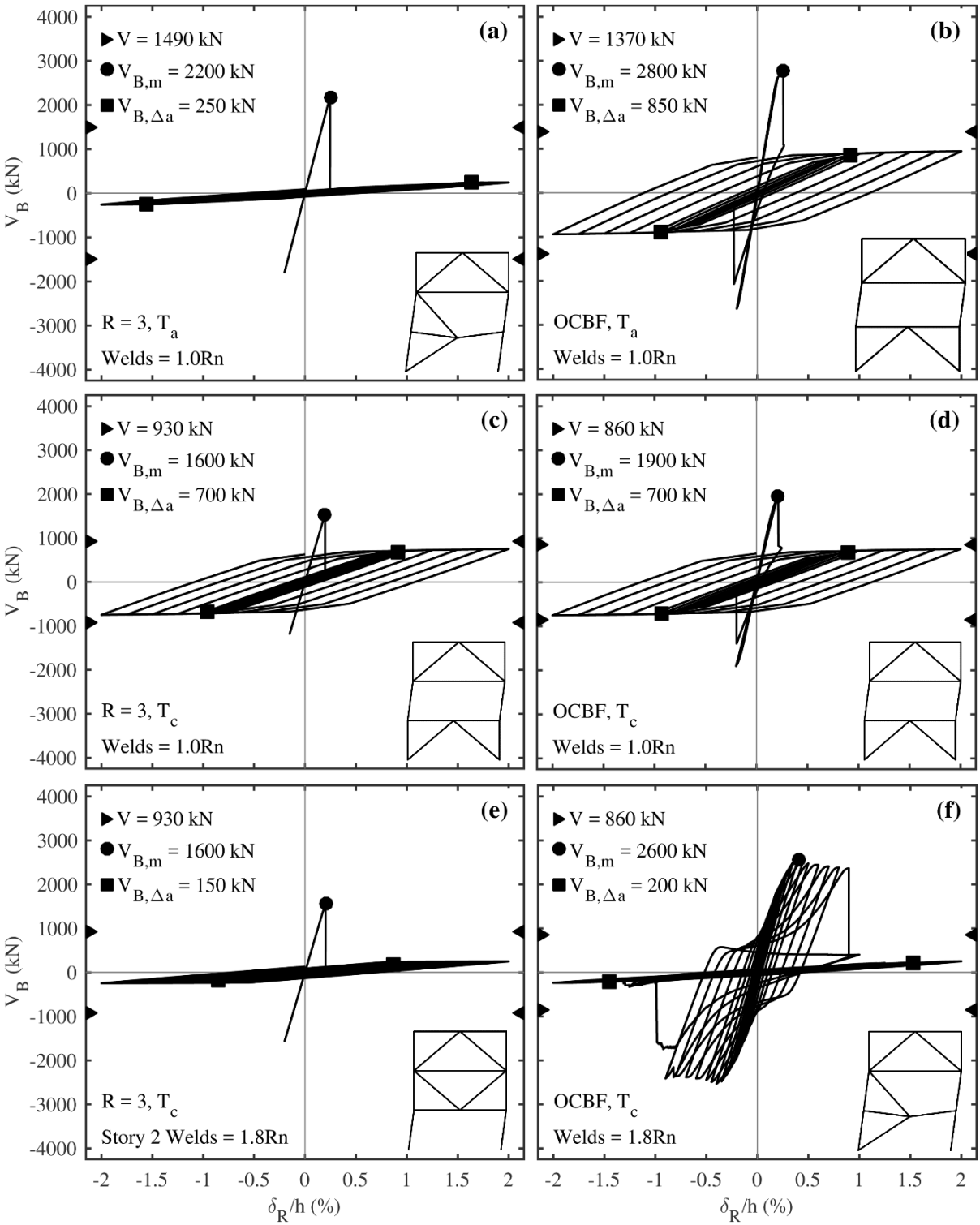

Figure 6.3 – Cyclic behavior of frames in the split-x configuration: (a) R3-SX-Ta; (b) OCBF-SX-Ta; (c) R3-SX-Tc; (d) OCBF-SX-Tc; (e) R3-SX-Ta*; (f) OCBF-SX-Tc*.

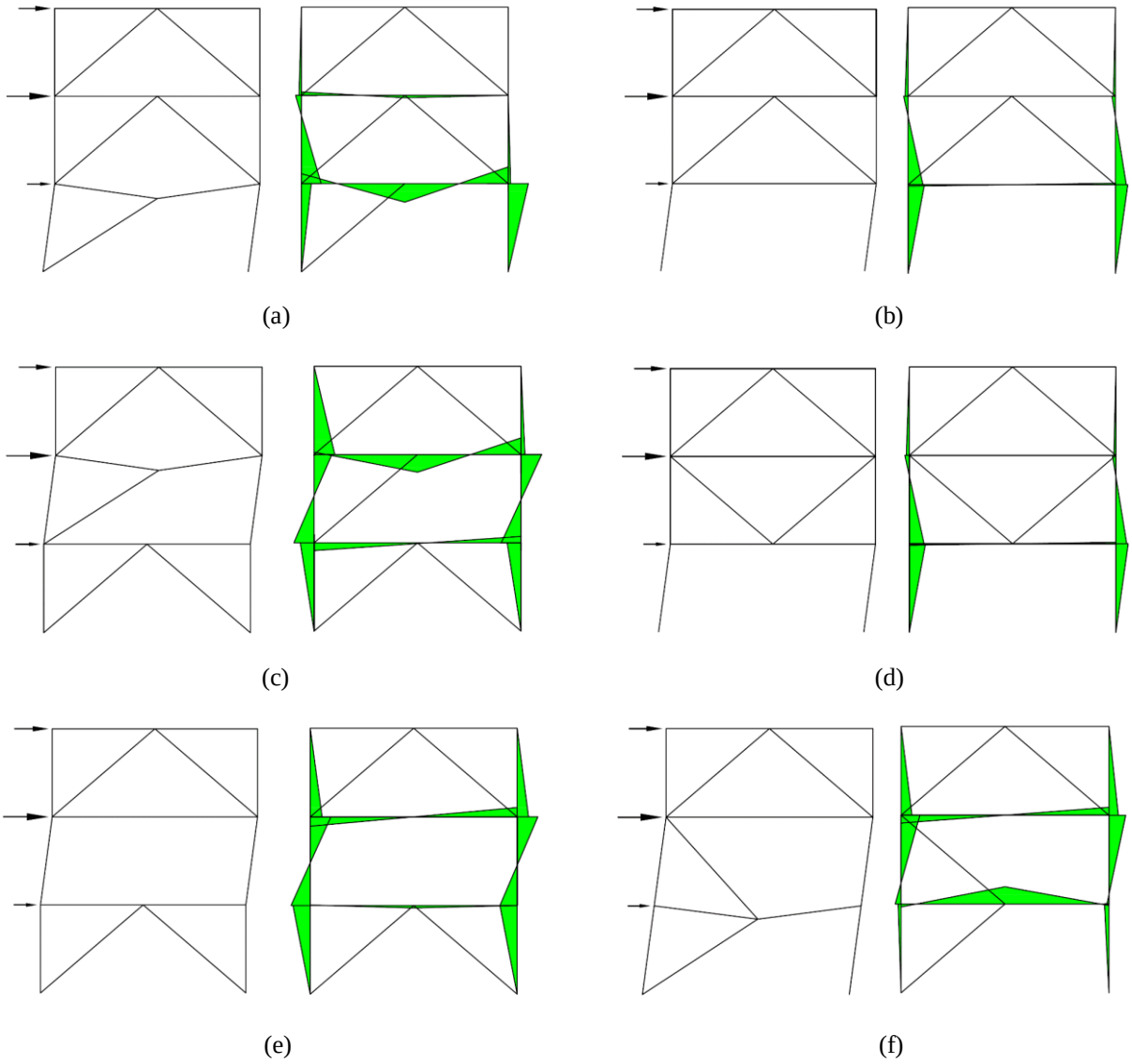

Figure 6.4 – Schematic deformed shapes and associated moment diagrams for the six mechanisms observed in the prototype frame study: (a) chevron first-story single brace; (b) chevron first-story double brace; (c) chevron second-story single brace; (d) split-x first-story double brace; (e) split-x second-story double brace; (f) split-x two-story.

6.2.1 Influence of System Configuration

System configuration (chevron vs. split-x) significantly influenced the progression of limit states as illustrated in Figures 6.2–6.4. In the chevron configuration, the first limit state was a fracture of the brace-gusset welded connection, which occurred, in either the first or second story in primary chevron designs but never both the first and second story (Figure 6.2).

After this limit state occurred, a mechanism developed that provided reserve capacity through column bending in addition to beam bending at the midspan (long-link EBF mechanism) of the damaged story. With one brace incapable of transmitting force, the remaining brace applied vertical load on the beam at its midspan as the frames were cycled. This force imbalance mobilized beam flexure (Figure 6.4a, 6.4c) which contributed to reserve capacity. The longevity and robustness of this mechanism was dependent on the flexural capacity of the beam, and thus was influenced by the system type. When this mechanism occurred in the second story (Figure 6.4c), reserve capacity was significantly increased (1,000 kN [225 kips] – 108% *V*) due to column reverse curvature. For the secondary R = 3 chevron frame, R3-CHEV-Ta*, the brace-gusset welds were assumed to have capacities of $1.8R_n$, which resulted in brace buckling occurring rather than brace-gusset weld fracture. A counterintuitive result is observed when comparing the first story mechanism of this frame (Figure 6.2e) with the first story mechanism of the primary frame R3-CHEV-Ta (Figure 6.2a): the reserve capacity was lower in the frame with larger weld strengths, R3-CHEV-Ta*. In secondary frame R3-CHEV-Ta*, after brace buckling occurred in one brace, the story stiffness was mostly retained when cycling in the other direction, which resulted in brace buckling of the other brace within the same story. After multiple cycles, both braces significantly degraded due to their high b/t ratios, which limited their ability to develop the beam midspan bending mechanism. Thus, this behavior was a hybrid of the mechanisms in Figure 6.4a and Figure 6.4b, as beam midspan bending occurred but needed increasingly larger drifts to develop the beam's moment capacity due to brace strength degradation.

When the braces were in a split-x configuration, the co-diagonal pairs of braces that made up the "X" acted as two-story continuous tension ties and compression struts. After weld

fracture occurred whilst the frame was cycled in one direction, the story in which the weld fracture occurred became a soft story, but only in the same direction. In the opposite direction, the frame kept most of its stiffness and strength, as the remaining brace within the story carried nearly the entirety of the story shear through tension. This phenomenon continued until a second weld fracture occurred, in either the remaining brace within the previously damaged story (Figure 6.4d, 6.4e), or in the brace of the adjacent story along the tension strut within the "X" configuration in that direction (Figure 6.4f). In the case where weld fracture occurred in multiple braces within the same story (most common amongst frames studied), a single story mechanism developed, and reserve capacity was governed by column bending. For the split-x frames studied, reserve capacity from column bending was significantly lower for mechanisms that occurred in the first story (Figure 6.3e, 150 kN [34 kips] – 16% *V*) than for mechanisms that occurred in the second story (Figure 6.3b, 850kN [191 kips] – 62% *V*; Figure 6.3c, 700kN [157 kips] – 81% *V*; Figure 6.3d, 700kN [157 kips] – 75% *V*). In the case where failures occurred on both stories that made up the split-x, a multi-story mechanism was formed (Figure 6.4f). Although beam bending was no longer restricted in this multi-story mechanism, the overall loss in frame stiffness resulting from two soft stories diminished the reserve capacity to a point where the benefits from beam bending were not relevant (Figure 6.3a, 250 kN [56 kips] – 17% *V*; Figure 6.3f, 700kN [157 kips] – 23% *V*).

6.2.2 Influence of System Type

Variations in detailing and proportioning associated with system type appreciably affected overall behavior, as seen in Figures 6.2 and 6.3. The OCBF provisions place an upper limit on *b*/*t* ratios for braces (AISC, 2010b), in addition to an upper-bound on the *KL*/*r* ratio for braces in "V' and "inverted-V" orientations (i.e. all braces in chevron configuration and

the upper story braces in split-x frames with odd number of stories). The $R = 3$ design approach has no such provisions, allowing for braces with significantly higher b/t ratios—making them more prone to local buckling and associated degradation. Although the effect of local buckling on overall behavior was clear from the experimental brace response plots (Figures 5.13, 5.15, and 5.16), it did not appear in the primary simulations because the assumed weld capacity, R_n, was lower than brace buckling capacities. This was not the case in the secondary frame model, R3-CHEV-Ta*, with large weld overstrength ($1.8R_n$). Because of this overstrength, brace buckling occurred, and was quickly followed by degradation due to the high local slenderness of the HSS9x9x1/4 braces ($b/t = 32.8$).

In addition to changes in brace slenderness, system type also significantly influenced the sizes of beams, especially in the chevron frames. In the OCBF chevrons, the beams were designed for an unbalanced midspan force per the 2010 AISC *Seismic Provisions* (AISC 341–10, 2010b), and thus were significantly larger than the beams found in the $R = 3$ chevron frames. Counterintuitively, these larger OCBF beams provided a less desirable mechanism from a reserve capacity perspective. The stronger beams can deliver enough axial force to fracture the brace-gusset weld connection in the remaining brace of chevron frames, which had already lost one brace due to brace-gusset weld fracture. After this occurred, neither brace was capable of transferring force within the weakened story, and thus the beneficial beam midspan bending mechanism (long-link EBF) was eliminated. The mechanism that followed was pure column bending, with noticeably smaller reserve capacity (Figures 6.2b, 6.2d, and 6.4b). In the $R = 3$ chevron frames, this secondary limit state was avoided as the beams were not large enough to deliver the force needed to fracture the brace-gusset connection in the remaining brace, allowing for the persistence of the favorable mechanism in Figures 6.4a and 6.4c. This

juxtaposition agrees with the conclusion made by Sen et al. (2015) regarding chevron braced frames: "good performance may be achieved using shallower, lighter beams [beams in R = 3 frames, for example] than permitted by the current *Seismic Provisions*." Thus, the current AISC *Seismic Provisions* (AISC 341–10) encourage beam sizes that may be counterproductive from a reserve capacity perspective. The behavior of secondary frame model OCBF-CHEV-Tc* further demonstrates the relationship between beam size and weld capacity as it applies to the robustness and longevity of the beam midspan bending mechanism. Unlike primary frame model OCBF-CHEV-Tc (Figure 6.2d), in which both braces within Story 1 experienced brace-gusset weld fracture, in secondary frame model OCBF-CHEV-Tc* the weld overstrength assumption ($1.8R_n$) resulted in a favorable relationship between beam size and weld strength: the beam was incapable of developing the necessary axial force to fracture the brace-gusset weld in the remaining brace (Figure 6.2f). As with the R = 3 chevron frames, avoiding brace-gusset weld fracture in the remaining brace resulted in a favorable reserve mechanism, with the deeper OCBF beam contributing significantly to the reserve strength up until it reached its plastic rotation capacity at δ_R/h = 1%, at which point the benefits began to slowly diminish due to the postcapping plastic degraded behavior. This beneficial response could be considered in design. For example, after one brace has become detached due to a brace-gusset weld fracture, the vertical force component, P, transferred into the remaining brace in the beam midspan bending mechanism may be approximated by $P = 8M_p/2L$, where L is the clear half beam span measured between the face of the gusset plates. Thus, the second brace-gusset weld fracture may be prevented if the following inequality is true: Assuming the beam ends are fixed, $R_n > 8M_p/(2L\sin\theta)$, where θ is the brace inclination angle with respect to the horizontal. As the OCBF chevron results have shown, preventing brace-gusset weld fracture in the remaining

brace of a story can provide significantly higher reserve strength (Figure 6.2f, 2,200 kN [495 kips] – 256% V) compared to cases where weld fracture occurs in both braces (Figure 6.2b, 300 kN [67 kips] – 22% V, Figure 6.2d, 250 kN [56 kips] – 29 % V).

The OCBF provisions additionally require that diagonal brace connections are designed using the amplified seismic load, based on the system overstrength, $\Omega_0 = 2$. Although there are a few exceptions to this criterion (AISC, 2010b), diagonal brace connection capacities in OCBFs can be expected to be larger than connection capacities in a comparable $R = 3$ CBF, in which there are no requirements to amplify seismic loads for connection design. Because brace-gusset weld fracture was a predominant limit state in all eight primary frames, the elastic capacities of the OCBFs were all larger than their $R = 3$ counterparts due to the increased weld capacity. In the $R = 3$ split-x CBFs, the weld capacity was smaller than the brace buckling capacity, so compression brace-gusset weld fracture occurred immediately after tension brace-gusset weld fracture within the same cycle. In the $R = 3.25$ split-x OCBFs, however, the weld capacity was smaller than the brace buckling capacity, which restricted weld fracture to occur in the tension braces only.

Contrary to the experimental $R = 3.25$ split-x OCBF test unit, in which large amounts of ductility due to brace yielding and buckling occurred prior to the initial weld fracture (Figure 5.16), weld fracture occurred in all primary split-x OCBFs prior to any similar amount of ductility associated with brace inelasticity (Figures 6.3b, 6.3d). This is due to the assumption that brace-gusset weld capacities in the eight primary parametric study frames were equal to R_n, or lower than the yield strengths of the braces. In the secondary frame model OCBF-SX-Tc*, welds were assigned a large overstrength, $1.8R_n$, which gave them capacities larger than the yield strengths of the braces. Thus, multiple cycles occurred in which Story 1 compressive

brace buckling and Story 2 tension brace yielding acted to provide significant ductility (Figure 6.3f). This period of ductility was sustained until tensile weld fracture occurred in a Story 2 brace at δ_R/h = 0.9%. When cycling the frame back in the other direction, the Story 1 brace that had undergone significant buckling in the prior cycle experienced complete degradation due to low-cycle fatigue, resulting in a multi-story mechanism with unfavorable reserve capacity (200 kN [45 kips] – 23% V).

Finally, the OCBF provisions also require that columns be designed using the amplified seismic load with Ω_0 = 2. This led to slightly larger columns in some of the OCBFs, which promoted a small increase in reserve capacity most noticeable in frames that developed mechanisms governed by pure column bending. This benefit was effectively doubled in the frames that experienced second-story mechanisms, as these mechanisms provided double curvature column bending due to the first-story backspan, thus requiring two column plastic hinges in each column for a mechanism (Figures 6.4b, 6.4d).

6.3 SUMMARY OF PARAMETRIC FRAME STATIC CYCLIC SIMULATIONS

The calibrated modeling framework was used to evaluate the relative influences of two design parameters (system type and system configuration) on limit state progression and reserve capacity through numerical simulations of twelve 3-story frames.

System configuration (chevron vs split-x) influenced the type of mechanism that formed, which in turn affected reserve capacity. The chevron configuration out-performed the split-x in this regard since it mobilized both column bending and beam bending. Furthermore, while unfavorable multi-story mechanisms were avoided in all six chevron frame simulations, two-story mechanisms occurred in 2 of 6 split-x frame simulations and the split-x test unit (Section 4.4). This is a scenario where a larger beam, enhanced beam-column connections in

the middle of the split-x, larger columns, or fixed column bases may be implemented to enhance reserve capacity.

System type (R = 3 CBF vs OCBF) influenced ductility in the case of split-x frames: when weld strength exceeded brace yield capacity, appreciable ductility was observed prior to fracture of the brace-gusset welded connections. This beneficial effect was more likely to occur in OCBFs than in R = 3 frames, as the OCBF design provisions dictated that the welds be designed for the amplified seismic load with Ω_0 = 2. For the frames studied numerically, however, this ductility was only achieved in an OCBF split-x frame when weld capacity was $1.8R_n$, a value that agreed with experimental observations from the OCBF split-x test unit. Thus, a split-x OCBF will not necessarily behave in a ductile manner prior to connection fracture, because this ductile performance depends on the actual weld capacity.

System type also influenced the behavior of chevron frames, but affected reserve capacity more so than it did ductility. For the primary frames studied, the deeper beams found in the chevron OCBFs were strong enough to carry the brace unbalanced force and fracture the remaining brace-gusset weld after an earlier brace-gusset weld fracture within a story. This resulted in an unfavorable mechanism governed by column bending. When evaluating sources of reserve capacity, designers should consider that brace-gusset welds can be capacity designed to develop the axial force delivered to the brace when full plastic capacity of the beam is developed in the damaged story.

Development of a backspan for column bending increased reserve capacity significantly by doubling the number of plastic hinges required per column to form a mechanism. This was true for all frames studied regardless of system type of configuration. For the frames studied, this occurred when a second-story mechanism developed rather than a

first-story or multi-story mechanism. In an actual building, this behavior may also be seen in a first-story mechanism if there is a sufficiently tall basement level, or if enough fixity is provided at the base of the SFRS. Both the soft story columns and the column backspans could be compromised by inadequate column splices, however, if the relationship between these splices and an expected reserve system is not considered.

The building period, *T*, and the *R*-factor are both in the denominator of the ASCE 7–10 equivalent lateral force equation for base shear. Therefore, the amplification of T_a by 1.6 affects the OCBF base shear as much as using an *R*-factor of 3.25*1.6 = 5.2. This variation in design force sharply contrasts with the fine distinction drawn by ASCE 7–10 between $R = 3$ systems and OCBF systems for which $R = 3.25$ (ASCE, 2013). As this variation suggests, and as this study has found, the design base shear itself is less relevant for building collapse prevention than the damage mechanisms and reserve systems that form in the post-elastic range.

CHAPTER 7

THE *R* = 4 OCBF

In review of conclusions from the numerical static cyclic analyses and the full-scale experimental tests, many beneficial aspects of frame behavior were identified as components of a seismic force resisting system (SFRS) that provide adequate collapse prevention through primary system ductility and reserve capacity. In addition, several areas within the current OCBF provisions were identified as detrimental in respect to reserve capacity while additionally causing the system to be uneconomical compared to the R = 3 SFRS, which is the more popular of the two systems within low and moderate seismic regions. Thus, a new SFRS was proposed for low and moderate seismic regions which incorporated the beneficial aspects of frame behavior that were previously identified during the research program, such as formation of the long-link EBF mechanism (common in R = 3 CBFs studied) and ductile brace buckling (common in OCBFs studied). This new SFRS, dubbed the R = 4 OCBF, is proposed to replace the existing R = 3.25 OCBF in the upcoming 2022 edition of the AISC *Seismic Provisions* (AISC 341) for use in low and moderate seismic regions.

In contemplation of a new system, altering the OCBF SFRS or the R = 3 SFRS were both considered as options. The rationale for proposing to change the OCBF provisions was rooted in the fact that the R = 3 SFRS operates independently of AISC 341–10 and is found solely within ASCE 7–10. Its definition inherently exempts it from any seismic detailing provisions, and thus any attempt to "improve" the R = 3 system by providing seismic detailing requirements within AISC 341 through use of reserve capacity would go against the core nature of the system.

The difficulty in making changes to the R = 3 system is not confined to the bureaucratic details of where a proposed improvement to the R = 3 system would be located (ASCE 7, AISC 341, a combination of the 2). Another issue created by the R = 3 system's lack of seismic provisions is that the design possibilities for an R = 3 system are endless. For example, a designer could design an R = 3 eccentrically braced frame, an R = 3 moment frame, or any combinations of conceivable system configurations. The reality than an R = 3 frame can take on any number of system configurations is one of the main sources of uncertainty in trying to assess its viability as an adequate SFRS. As the experimental tests (Section 4.5.2) and the numerical static cyclic analyses (Section 6.2.2) have shown, system configuration has a significant influence on reserve capacity. Thus, while the studies on R = 3 CBFs as a part of this research program—both numerically and experimentally—captured the most commonly used R = 3 configurations, they only represent a small sample of R = 3 SFRS designs. In consideration of the above, it was not possible to make broad definitive statements as to the viability of an R = 3 system; thus, it was concluded that "improving" the R = 3 system was not possible without a complete revamping of its entire philosophy.

7.1 JUSTIFICATION FOR R = 4 AND ECONOMIC CONSIDERATIONS

In creation of a proposal for an improved OCBF, the combination of enhanced seismic performance and economy was critical. The ideal OCBF system would incorporate seismic detailing and proportioning requirements to provide measurable and definable performance characteristics, while matching or beating an equivalent R = 3 system in cost. As mentioned, the R = 3 system is the preferred system in low and moderate seismic regions, and a large contributor to this is the relative cost between it and the R = 3.25 OCBF.

Using a 3-story structure for example, the large weight discrepancy between typical R = 3 CBF and OCBF with chevron and split-x bracing configurations is given in Table 7.1. The R = 3 designs were created assuming the approximate fundamental period (T_a), while the R = 3.25 OCBF designs were created assuming the calculated fundamental period, $1.6T_a$. Thus, the design base shear (V) for the R = 3 system was (1.6/1)(3.25/3) = 1.73 times larger than the R = 3.25 system. Despite this discrepancy, both 3-story R = 3 SFRSs were lighter than their R = 3.25 OCBF counterparts, so it should come as no surprise that engineers and designers are attracted to the R = 3 SFRS. Acknowledging that cost is one of the primary factors in choice of an SFRS between practical alternatives, any improvements to the OCBF system, regardless of their robustness or efficiency in providing reserve capacity for collapse prevention performance, would be for naught if designers continue to simply choose the R = 3 system over the new OCBF system. The primary goal is that designers adopt and use this safer and more robust SFRS. The R = 4 OCBF avoids collapse through primary system ductility and intentional reserve capacity mechanisms that have a lower strength than the initial CBF system strength but have significant deformation capacity. This is a contrast to the R = 3 SFRS, which cannot be rigorously evaluated due to the lack of constraints on its design.

Table 7.1 – 3-story SFRS member sizes and weight

SFRS	Beams 10.7 m. [35 ft.]	Columns 13.7 m. [45 ft.]	Braces 7.0 m. [23 ft.]	Weight (Tonnes)
R = 3 chevron	W12x40 W12x40 W12x26	W12x53	HSS9x9x1/4 HSS8x8x1/4 HSS5x5x5/16	5.39
OCBF chevron	W30x116 W30x90 W12x26	W12x53	HSS8x8x1/2 HSS8x8x1/2 HSS8x8x1/2	8.90 (165% of R = 3)
R = 3 split-x	W12x26 W18x40 W12x26	W12x53	HSS9x9x5/16 HSS8x8x1/4 HSS5x5x5/16	5.38
OCBF split-x	W12x26 W18x40 W12x26	W12x53	HSS7x7x1/2 HSS6x6x1/2 HSS8x8x1/2	6.25 (116% of R = 3)

Considering that economy is one of the critical components of a potential OCBF design (due to the ability for a designer to fall back on the R = 3 SFRS in low and moderate seismic regions), the proposed new version of the OCBF was assigned a trial R-value of 4. One of the conclusions from the numerical cyclic frame study was that the R-value did not have a large influence on the structural behavior, which was instead driven by a combination of seismic detailing and proportioning requirements and system configuration. A value of R = 4 serves as an appealing identifier for the new OCBF provisions for design engineers, as it inherently allows them to proportion their SFRS for design forces 33% lower than the current R = 3 system, which is a large change from the current 8% reduction that the R = 3.25 OCBF system provides. The change from R = 3.25 to R = 4 is not drastic, as it is still far below the current R-value for a SCBF (R = 6), and the OCBF itself has had an R-value of 5 in the past, as recent as

the 2002 AISC *Seismic Provisions* (AISC 341–02, 2002). The decrease from $R = 5$ to $R = 3.25$ occurred with the release of ASCE 7–05 and AISC 341–05 (ASCE, 2005; AISC, 2005). The rationale for this decrease is loosely inferred from commentary of ASCE 7–05 regarding structures in areas in high seismicity (SDC D, E, and F), which appears to have been adapted by some systems intended for low and moderate seismic design. The commentary states:

> **C12.3.4 Redundancy.** This standard introduces a revised redundancy factor for structures in Seismic Design Categories D, E, and F to quantify redundancy. The value of this factor is either 1.0 or 1.3. This factor has an effect of reducing the *R* factor for less redundant structures thereby increasing the seismic demand. The factor is specified in recognition of the need to address the issue of redundancy in the design. The National Earthquake Hazards Reduction Program (NEHRP) Commentary Section 5.2.4 explains that this new revised requirement is "intended to quantify the importance of redundancy." The NEHRP Commentary points out that "many non-redundant structures have been designed in the past using values of *R* that were intended for use in designing structures with higher levels of redundancy." In other words, the use of the *R* factor in the design has led to slant in design in the wrong direction. The NEHRP Commentary indicates that the source of the revised factor is Technical Subcommittee 2 of the NEHRP Provisions.

The proposed increase from $R = 3.25$ to $R = 4$ does not oppose the language above, as the intention is to incorporate beneficial aspects of reserve capacity into the design process to improve the behavior and provide “redundancy” beyond what is included in the $R = 3.25$ OCBF design, as will be discussed later in this section. In its current state, the OCBF system has arguably enough redundancy through its seismic detailing and proportioning requirements to justify an *R*-value that is more than 8% (3.25/3.0) larger than the $R = 3$ system. The rationale for the current OCBF *R*-value of 3.25 is unclear when viewed alongside the $R = 3$ system. In addition, an *R*-value with three significant figures implies a degree of precise calibration that does not exist, so adopting an OCBF *R*-value with one significant figure brings this system in line with other SFRS.

7.2 RECOMMENDATIONS FOR THE *R* = 4 OCBF AND THEIR JUSTIFICATION

Simply increasing the *R*-value is not enough to improve the economy of the OCBF sufficiently to compete with the *R* = 3 system. As shown in Table 7.1, the seismic detailing and indirect capacity design requirements of the OCBF increase member sizes and the weight of the SFRS. Thus, these requirements are effectively negating the larger *R*-value and resulting in a system that is both heavier than the alternative *R* = 3 system and, in some cases, more difficult to construct due to constraints imposed by these requirements.

In this section, seismic detailing requirements from the current OCBF provisions in AISC 341–10 (AISC, 2010a) are investigated case-by-case with the knowledge gained from the experimental tests and companion cyclic numerical simulations and assessed with respect to their effectiveness at providing collapse prevention through a combination of primary system ductility and reserve capacity. The proportioning requirements that are discussed include those for column strength, beam strength, beam-column connection strength, and brace-gusset connection strength, while the detailing requirements discussed include brace local (*b*/*t*) and global (*KL*/*r*) slenderness limits. The then-current *R* = 3.25 OCBF provision (AISC, 2010a), current 2016 *R* = 3.25 OCBF provisions, and the proposed 2022 *R* = 4 OCBF provision are included in Appendix C.

7.2.1 Column Strength

One of the seismic proportioning requirements in current *R* = 3.25 OCBF design is column strength. As the seismic provisions below show (AISC, 2010a), columns within *R* = 3.25 OCBFs must be designed for the amplified seismic load, which is defined in ASCE 7–10 based on the system overstrength factor, Ω_0 = 2.0 (ASCE, 2013):

4a. Required Strength

The required strength of columns in the SFRS shall be determined from the following:

(1) The load effect resulting from the analysis requirements for the applicable system per Sections E, F, G and H.

Exception: Section D1.4a need not apply to Sections G1, H1 or H4.

(2) The compressive axial strength and tensile strength as determined using the load combinations stipulated in the applicable building code including the ***amplified seismic load***. It is permitted to neglect applied moments in this determination unless the moment results from a load applied to the column between points of lateral support. The required axial compressive strength and tensile strength need not exceed either of the following:

(a) The maximum load transferred to the column by the system, including the effects of material overstrength and strain hardening in those members where yielding is expected.

(b) The forces corresponding to the resistance of the foundation to overturning uplift.

In the research conducted thus far, the flexural capacity of columns was shown in several instances to be an important contributor to reserve capacity. In Chapter 3, the reserve capacity component study revealed that an increase in column flexural capacity by 50% within the SFRS provided a significant increase in reserve strength and stiffness under a static pushover analysis, and increased the average scale factor at failure in an incremental dynamic analysis by 17% (from 3.5 to 4.1). In addition, both experimental full-scale tests and the subsequent companion numerical simulations revealed that column bending from frame action was an important contributor to reserve capacity, as the columns carried over 50% of the story shear following brace buckling in the $R = 3$ chevron experimental test. Based on these findings, the column overstrength factor is viewed as favorable from a reserve capacity and overall performance perspective, as it will increase the flexural capacity of columns and improve their ability to lend reserve capacity through frame action. Thus, column overstrength is to remain

a component of the proposed R = 4 OCBF system despite the slight weight increase associated with this proportioning requirement.

7.2.2 Beam Strength

Another major component of the seismic proportioning requirements in the current R = 3.25 OCBF provisions is the condition to design beams in V and inverted-V configurations (not split-x) for the force imbalance created from a limit state involving one buckled brace and one tension brace at a demand typically defined by the amplified seismic load condition with Ω_0 = 2.0. Additionally, beams in these configurations must pass a design check under factored gravity loading conditions assuming the braces provide no support to dead and live loads, i.e. $M = wL^2/8$ for uniformly distributed gravity load:

> **4a. V-Braced and Inverted V-Braced Frames**
>
> Beams in V-type and inverted V-type OCBF shall be continuous at brace connections away from the beam-column connection and shall satisfy the following requirements:
>
> (1) The required strength shall be determined based on the load combinations of the applicable building code ***assuming that the braces provide no support of dead and live loads.*** For load combinations that include earthquake effects, the seismic load effect, E, on the member shall be determined as follows:
>
> (i) The forces in braces in tension shall be assumed to be the least of the following:
>
> (a) The expected yield strength of the brace in tension, $R_y F_y A_g$
>
> (b) ***The load effect based upon the amplified seismic load***
>
> (c) The maximum force that can be developed by the system
>
> (ii) ***The forces in braces in compression shall be assumed to be equal to*** $\boldsymbol{0.3P_n}$.
>
> (2) As a minimum, one set of lateral braces is required at the point of intersection of the braces, unless the member has sufficient out-of-plane strength and stiffness to ensure stability between adjacent brace points.

Designing beams in V and inverted-V configurations for a force imbalance has a significant effect on the weight of the SFRS, as Table 7.1 shows. Compounding this issue was

the discovery throughout this research program that the force-imbalance design—that leads to increased structural weight—does not necessarily lead to better seismic performance. In fact, the opposite was observed in the numerical simulations of OCBF chevrons (Chapter 6) as these frames (Figure 6.2b, 6.2d) had worse reserve capacity than their $R = 3$ counterpart (Figure 6.2a, 6.2c).

The requirement for designing beams in V and inverted-V (chevron) configurations in consideration of a force imbalance was first introduced in AISC 341–97 (AISC, 1997) for special concentrically braced frames (SCBFs) based on observations from the 1979 UJ-CERP tests (Section 2.5.1) in which flexural beam bending at midspan occurred rather than the desired mechanism of brace yielding. The implementation of the force-imbalance design requirement in combination with the capacity design requirement for brace-gusset welds in AISC 341–97 supported the development of a favorable mechanism consisting of compression brace buckling and tension brace yielding. In AISC 341–05, an analogous force imbalance requirement was adopted for beams in V and inverted-V configurations within OCBFs, with one major caveat: a capacity design was not enforced for the brace-gusset connections (AISC, 2005). Thus, a brittle limit state such as brace-gusset weld fracture may be expected in tension braces within these frames rather than brace yielding. The impact of this subtle distinction on the mechanism that forms following compression brace buckling (or, in the case of the OCBF chevrons simulated in Chapter 6, compression brace-gusset weld fracture) is significant. Rather than the tension brace yielding to provide a ductile mechanism equivalent of SCBFs, the tension brace-gusset weld has the potential to fracture. Thus, the detrimental influence of the force-imbalance designed beam is clear: the remaining brace can experience brace-gusset weld fracture when it is pulled into tension due to the beam's ability to develop the force imbalance

created in this remaining brace. The result is a story in which both braces have experienced fractures in their connections, rendering them incapable of providing any contribution to lateral force resistance. When this is compared to the behavior of an R = 3 CBF, in which the beam is not designed for any force imbalance and is thus able to yield following loss of one brace due to brace-gusset weld fracture, the benefit of the beam bending (long-link EBF) mechanism is clear. Typical limit state sequence for these various SFRSs and their associated mechanisms are shown in Figure 7.1a-c, for the SCBF, current R = 3.25 OCBF, and R = 3 CBF, respectively.

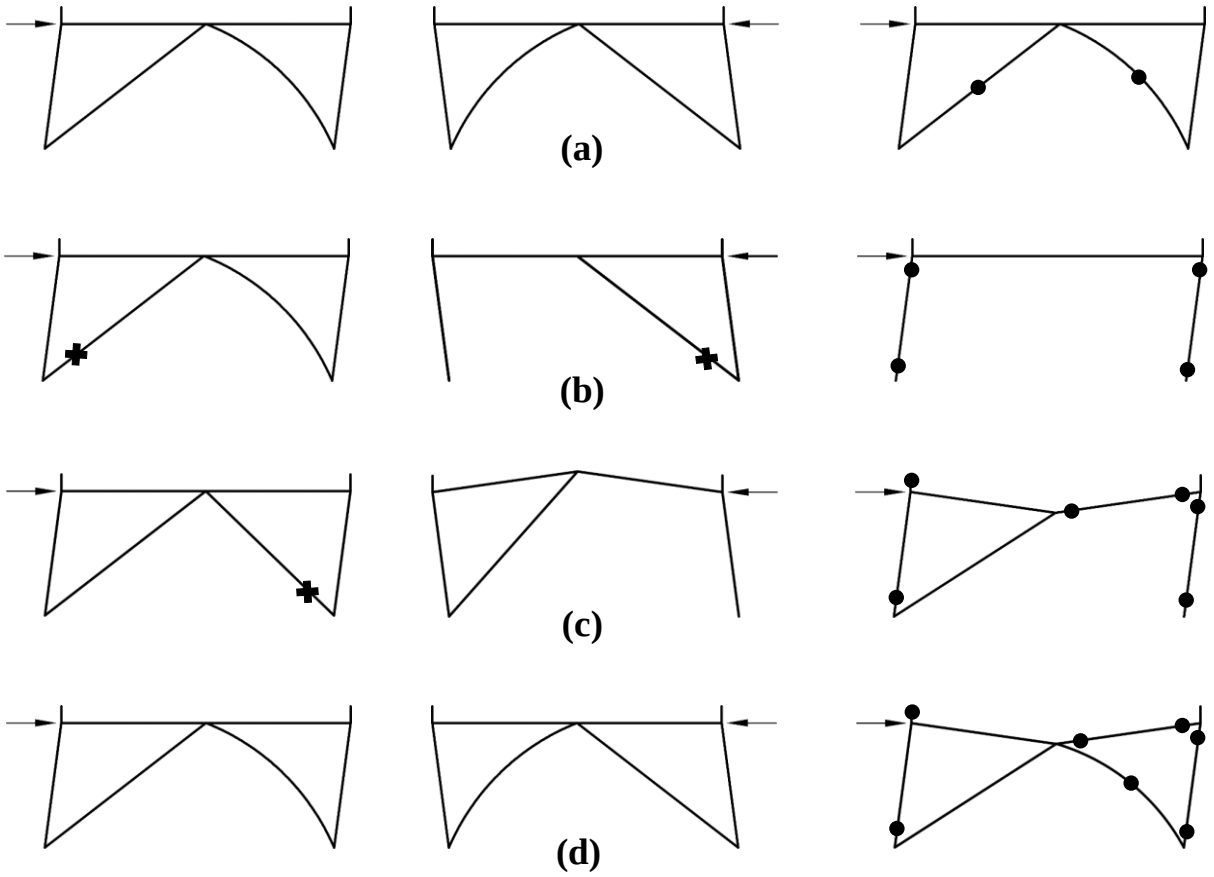

Figure 7.1 – Expected progression of limit states in chevron frames designed as: (a) SCBF; (b) current R = 3.25 OCBF; (c) R = 3; and (d) proposed R = 4 OCBF.

The benefit of the long-link EBF mechanism was shown in the experimental test of the R = 3 chevron CBF and subsequent companion static cyclic simulations. In contrast, the behavior of a non EBF-based mechanism, i.e. one driven by column bending only, was also shown in several instances throughout the research project, such as in the final cycles of the R = 3.25 split-x OCBF and the static cyclic simulations of OCBF chevrons in Chapter 6. Considering the detrimental effects that designing beams in OCBFs for a force imbalance can have on reserve capacity (e.g. prevent the development of a long-link EBF mechanism – Figure 6.2b and 6.2d), and economy (significantly increasing beam weights – Table 7.1), it was clear that a change was needed to this requirement in the proposed R = 4 OCBF system.

One could define methods for providing a "balanced" beam size that offers large amounts of reserve capacity through the long-link EBF mechanism but does not cause fracture of the remaining brace-gusset weld (Sizemore et al., 2016). The danger of these methods, however, is rooted in the large amounts of uncertainty in weld capacity and beam capacity. These uncertainties may lead to fracture in both braces within a story even if the designer's intention is to provide a "balanced" beam that yields following loss of a single brace. These sources of beam overstrength include: (1) material overstrength within the beam; (2) strain hardening within the beam; (3) formation of plastic hinges outside the gusset plate regions which effectively reduce the beam span and increase its capacity; (4) the assumed end-condition of the beam-column connection; and most significantly (5) composite action. As was shown in the UJ-CERP tests (Fukuta et al., 1989), composite action increased the beam strength to over 2.5 times its bare steel moment capacity ($2.5M_{p,beam}$). When these sources of beam overstrength are considered, a beam with $M_{p,beam,exp}$ 3–4 times higher than what it was designed for is conceivable.

The force imbalance requirement was removed entirely in the proposed R = 4 OCBF system. Several reasons led to this decision:

1. The uncertainties in a beam's true moment capacity. This increases the difficulty of intentionally providing a "balanced" beam that is larger than what is required from simply gravity demands alone but that is not too large such that it can fracture both brace-gusset welds within a story.
2. The risk-reward concept. Providing a method for designing a "balanced" beam comes with an inherent risk (discussed in [1]), which is not justifiable based on the reward (reserve capacity gained). This is most clearly shown from the numerical simulations in Chapter 6, in which an R = 3 chevron with a "weak" W12x40 beam had a larger reserve capacity than an OCBF chevron with a "strong" W30x116 beam. Since both frames had identical column sizes, and both formed a first story mechanism, the 300 kN [67 kips] of additional reserve capacity in the R = 3 chevron CBF is entirely attributable to the bending of the "weak" W12x40 beam at its midspan. In other words, even a small beam may provide significant reserve capacity after formation of an EBF-mechanism.
3. Economy. By dropping the force imbalance requirement from the beams entirely, a large part that drives up the weight of OCBF chevrons is removed, making them more competitive with R = 3 chevrons CBFs.
4. Simplicity. Dropping the force imbalance requirement from beams within OCBFs significantly decreases the complexity of the design process, making them more competitive with R = 3 chevrons.

A schematic for the typical mechanism which is expected to form in chevron frames designed with this proposed R = 4 OCBF provision is included in Figure 7.1d.

A few other changes to beam design are proposed in addition to removing the force imbalance requirement for the proposed R = 4 OCBF. Currently, OCBF beams in V- and inverted-V configurations must be designed for gravity demands assuming that the braces do not provide any support. In the R = 4 OCBF, this requirement is extended to all beam members. This change primarily affects the beams in split-x braced frames that are intersected above and below by braces, which were previously not required to span for gravity on their own. By designing these beams to span their full length for gravity the reserve capacity of split-x OCBFs is increased when a two-story mechanism is formed, such as those observed in the numerical cyclic simulations (6.3a, 6.3f, 6.4f). Although this change increases the minimum required beam weights in every other level of R = 4 split-x frames, many designers already design all beams within a structure to span on their own for gravity in consideration of construction or rehabilitation scenarios where braces may not be attached.

The removal of the force imbalance requirement for beams in combination with the expectation and reliance on flexural beam yielding to provide reserve strength puts a heightened importance on the ability of beams to resist local limit states. Thus, in the R = 4 OCBF proposal it is required that, like braces, all beams satisfy the requirements within the AISC *Seismic Provisions* for *moderately ductile members*, with C_a = 1.0 (AISC 341–10, *Table D1.1*). The result of this requirement is that all beam members must have b/t less than $0.38\sqrt{(E/F_y)}$, or 9.15, and h/t_w less than $1.49\sqrt{(E/F_y)}$, or 35.8, for $F_{y,A992}$ = 345 MPa [50 ksi]. This eliminates all beam sections designated with an “f” (does not pass flange requirement—flange is noncompact or slender in flexure) or with a “c” (does not pass web requirement—

web is slender in compression) in Table 1.1 of the AISC *Steel Construction Manual* (AISC, 2011). These added seismic detailing requirements are critical in ensuring that a beam reaches its plastic moment capacity and provides a robust long-link EBF mechanism, rather than experiencing any local buckling limit states under combined axial and flexure demands.

7.2.3 Beam-Column Connections

Although the current R = 3.25 OCBF provisions do not specify any proportioning requirements for the flexural capacity of beam-column connections, the reliance on frame action to lend reserve capacity and assist with performance in the proposed R = 4 OCBF dictates consideration of the flexural capacity of these connections. In the long-link EBF mechanism, for example, the peak reserve capacity is governed by the limit state of two plastic hinges developing: one at the beam midspan and one at either of the beam ends. Thus, the effectiveness of this mechanism is related to the flexural capacity of the beam-column CBF connections. If the beam-column connection's flexural capacity exceeds $1.0M_{p,beam}$, then the mechanism described above has the potential to form. Otherwise, as the flexural capacity of the beam-column connections relative to the beam flexural capacity decreases, the effectiveness of the potential EBF mechanism is reduced and the potential for a limit state within the beam-column connection is increased.

In acknowledgement of the above, a proportioning requirement was added to the R = 4 proposal to ensure a moderate amount of beam-column connection flexural capacity, $0.5M_{p,beam}$. However, a designer will only need to check this requirement when using a beam-column connection that does not have a gusset plate. As shown from the research of Stoakes (Stoakes and Fahnestock, 2011; Stoakes and Fahnestock, 2012; Stoakes, 2012), typical double web angle beam-column-gusset connections can provide about $0.48–0.63M_{p,beam}$, without any

added detailing considerations. For standard double web angle beam-column connections without a gusset plate, such as those on every other level within a split-x frame, a designer could consider adding a top- and seat-angle to increase the connection's flexural capacity at little incremental cost.

The necessity for beam-column connection flexural capacity is especially critical in the split-x configuration, where many detrimental limit state sequences were identified in the previous numerical simulations (Chapter 6). Although no specific mechanism is targeted for the split-x configuration, this requirement is intended to provide compensation if previously identified detrimental mechanisms occur. For example, when weld failures occur in two braces within a given level; the weakened bay essentially becomes a moment frame, of which the reserve strength is highly dependent on the flexural capacity of the beam-column connections. If weld failures occur in two (or three) braces within adjacent levels that make up the "X", a two-story mechanism can form, which creates a double-height moment bay with even less capacity than the previously discussed mechanism, although it is also highly dependent on beam-column flexural capacity for strength and stiffness.

7.2.4 Brace-Gusset Connection Strength

Another of the seismic proportioning requirements in the existing R = 3.25 OCBF provisions involves brace-gusset connection strength. As noted in AISC 341–10, the diagonal brace (brace-gusset) connections within OCBFs must be designed for the amplified seismic load, based on Ω_0 = 2.0, like the requirement for columns (AISC, 2010a):

6a. Diagonal Brace Connections

The required strength of *diagonal brace* connections is the load effect based upon the ***amplified seismic load***.

Exception: The required strength of the brace connection need not exceed the following:

(1) In tension, the expected yield strength of the brace multiplied by 1.0 (LRFD) or divided by 1.5 (ASD), as appropriate. The expected yield strength shall be determined as $R_yF_yA_g$.

(2) In compression, the expected brace strength in compression multiplied by 1.0 (LRFD) or divided by 1.5 (ASD), as appropriate. The expected brace strength in compression is permitted to be taken as the lesser of $R_yF_yA_g$ and $1.14F_{cre}A_g$ where F_{cre} is determined from *Specification* Chapter E using the equations for F_{cr} except that the *expected yield stress* R_yF_y is used in lieu of F_y. The brace length used for the determination of F_{cre} shall not exceed the distance from brace end to brace end.

The component study in Chapter 3 revealed that an increase in brace-gusset weld capacity by 50% changed the limit state from brace-gusset weld fracture to brace buckling, which gave a temporary increase in reserve system stiffness and strength. Based on the research conducted thus far, brace buckling is viewed as preferable over weld fracture—given the braces are stocky enough (small b/t) to protect themselves from local buckling and low-cycle fatigue related fractures at low drifts—due to the smoother transition it provides into the inelastic region which reduces velocities during a seismic event. The development of brace buckling is especially beneficial in the split-x configuration, as shown in the R = 3.25 split-x OCBF experimental test, in which significant amounts of ductility (±1.5% frame drift – Figure 4.23) were provided prior to the occurrence of brace-gusset weld fracture. This was also observed in the numerical simulation of an R = 3.25 split-x OCBF that assumed a weld overstrength of 80%, or $1.8R_n$ (Figure 6.3f). The influence of weld strength is clear when comparing the two previously discussed results with the results in Figures 6.3b and 6.3d. In these simulations, weld strength was only slightly larger than the brace buckling capacity, resulting in a significant decrease in ductility. Based on these observations, the diagonal brace

connection overstrength factor (Ω_0 = 2.0) is viewed as favorable from a ductility and overall performance perspective, and thus is retained in the proposed R = 4 OCBF. Based on the significant improvements in behavior observed when the weld strength was larger than the brace yield capacity (Figure 4.23, Figure 6.3f), an argument could be made to capacity design brace-gusset welds within split-x OCBFs, which was a design requirement for all OCBFs in the 2002 *Seismic Provisions* (AISC 341–02, 2002). However, to simplify the design of the OCBF, this criterion was not included in the proposed R = 4 OCBF system. Even without an explicit capacity design approach, some inherent weld overstrength is expected, which could push the weld capacity above the brace yield capacity as was observed in the experimental test of the R = 3.25 split-x OCBF.

7.2.5 Brace Local Slenderness Limits

Local slenderness (b/t) limits are one of the seismic detailing requirements in current R = 3.25 OCBF design. As specified in AISC 341–10, all braces within OCBFs must adhere to the detailing requirements for *moderately ductile members*, which, for rectangular HSS sections, is equal to $0.64\sqrt{(E/F_y)}$, or 15.4 for ASTM A1085 braces (F_y = 345 MPa [50 ksi]).

> **5a. Basic Requirements**
>
> Braces shall satisfy the requirements of Section D1.1 for *moderately ductile members*. [$0.64\sqrt{(E/F_y)}$ for walls of rectangular HSS, Table D1.1]

The effect b/t limits can have on structural response was observed in the full-scale frame tests (Chapter 4). In the R = 3 frame test, the slender HSS8x8x1/4 braces (b/t = 28.8) experienced a brittle limit state that consisted of local buckling and global buckling simultaneously which resulted in a significant drop in frame capacity (Figure 4.6). Throughout the rest of the test, the braces continued to degrade significantly, until most of the section had

torn apart at the brace midspan. In the OCBF test, the stocky HSS6x6x3/8 (b/t = 12.8) and HSS6x6x1/2 (b/t = 8.4) braces experienced ductile behavior, with spread plasticity at the hinge location. Additionally, these braces did not experience local buckling or tearing from low-cycle fatigue despite achieving story drifts of over 3%. Based on these observations, the b/t limit is viewed as favorable due to its contribution to overall system ductility, and should remain a part of the proposed R = 4 OCBF system. One potential caveat of the b/t limit is the reduction in available members for design selection, which can in some cases result in a brace that has a strength that is upwards of 60% larger than is needed in design in one extreme case. A list of the ASTM A1085 braces that pass the OCBF b/t limit along with their design strengths for a length of 7.0 m. [23 ft.]—which corresponds to the prototype building studied in this research program—is provided in Table 7.2 in order of increasing compressive strength, φP_n. For brevity, only brace sizes HSS4x4 and larger are shown, as all sizes HSS3.5x3.5 and below have permissible b/t ratios. Of the 79 ASTM A1085 brace sections size HSS4x4 and larger, only 28 have an acceptable b/t ($\leq$ 15.4). In Table 7.3, uneconomical sections (sections that have a φP_n lower than that of a lighter section), are removed, as designers will in most cases not use these sections if their priority for member selection is to choose the lightest possible section that meets b/t requirements while providing the required design strength.

Table 7.2 – Permissible braces for OCBF, HSS4x4 and larger

Section [HSS]	Weight [N/m]	b/t	φP_n (L = 7.0 m) [kN]
4x4x1/4	178	12.8	108
4x4x5/16	216	9.58	126
4x4x3/8	252	7.47	141
4.5x4.5x1/4	203	14.8	160
4x4x1/2	316	4.4	162
4.5x4.5x5/16	247	11.2	188
4.5x4.5x3/8	289	8.8	212
4.5x4.5x1/2	365	5.4	246
5x5x5/16	278	12.8	265
5x5x3/8	326	10.1	300
5x5x1/2	415	6.4	357
5.5x5.5x5/16	309	14.4	363
5.5x5.5x3/8	364	11.5	414
6x6x3/8	401	12.8	547
6x6x1/2	514	8.4	663
6x6x5/8	617	6	756
7x7x1/2	614	10.4	1094
7x7x5/8	741	7.6	1277
8x8x1/2	713	12.4	1566
8x8x5/8	865	9.2	1850
9x9x1/2	812	14.4	2046
9x9x5/8	989	10.8	2446
10x10x5/8	1114	12.4	3042
10x10x3/4	1306	9.73	3518
12x12x3/4	1604	12.4	4937
14x14x3/4	1902	15.1	6316
14x14x7/8	2183	12.4	7206
16x16x7/8	2530	14.7	8807

Table 7.3 – Economical braces for OCBF, HSS4x4 and larger

Section [HSS]	Weight [N/m]	b/t	φP_n (L = 7.0 m.) [kN]	$\Delta\ \varphi P_n$ [kN]
4x4x1/4	178	12.8	108	-
4.5x4.5x1/4	203	14.8	160	52
4.5x4.5x5/16	247	11.2	188	28
5x5x5/16	278	12.8	265	77
5.5x5.5x5/16	309	14.4	363	98
6x6x3/8	401	12.8	547	184
6x6x1/2	514	8.4	663	116
7x7x1/2	614	10.4	1094	431
8x8x1/2	713	12.4	1566	471
9x9x1/2	812	14.4	2046	480
9x9x5/8	989	10.8	2446	400
10x10x5/8	1114	12.4	3042	596
10x10x3/4	1306	9.73	3518	476
12x12x3/4	1604	12.4	4937	1419
14x14x3/4	1902	15.1	6316	1379
14x14x7/8	2183	12.4	7206	890
16x16x7/8	2530	14.7	8807	1601

As Table 7.3 shows, the “steps” of economical braces is relatively smooth for 7.0 m. [23 ft.] braces with required capacities less than 663 kN [149 kips], or HSS6x6x1/2 braces and lower. However, after this section, there is a large increase in the capacity of the next lightest member, an HSS7x7x1/2. For example, if a designer had to provide a 7.0 m. [23 ft.] brace capable of resisting an axial demand of 670 kN [151 kips], the lightest section they could provide would be a HSS7x7x1/2, with φP_n = 1094 kN [246 kips], which is 424 kN [95 kips]

more capacity than required, for an equivalent overstrength, $\varphi P_n/P_{req}$, of 1.63. The distinction of overstrength is important considering the benefits of brace buckling over weld capacity. Since weld size is more or less provided via a continuum, these large steps in brace size can lead to circumstances where achieving weld fracture prior to the occurrence of brace buckling is significantly more likely. This is especially true when considering other aspects that can contribute to an increase in brace buckling capacity, such as the difference between the true brace length and the designed brace length, the stiffness of the gusset plate connection, the initial imperfection of the brace, and the brace material overstrength.

For this specific example, if the b/t limit was instead a mere 0.1 higher (15.5) then an HSS7x7x3/8 would have been acceptable, which has φP_n = 885 kN [199 kips] ($\varphi P_n/P_{req}$ = 1.32). If the b/t limit was 20.0, then an HSS7x7x5/16 would have been acceptable, which has φP_n = 760 kN [171 kips] ($\varphi P_n/P_{req}$ = 1.13).

From a historical perspective, the local slenderness limit in AISC 341–97 and AISC 341–02 (AISC, 1997 and 2002) simply required that braces be either compact or noncompact, but not slender, $b/t \leq 1.40\sqrt{(E/F_y)}$, per the LRFD specification. The current limit was adopted in AISC 341–05 based on observations from the 1994 Northridge Earthquake (Lawson, 2010). A more rigorous investigation into b/t limits and their influence on brace ductility, particularly for braces with $15.4 < b/t \leq 20.0$ for example, is needed before a suggestion for relaxing the tolerance on b/t limits for OCBF braces can be made. For this reason, the current b/t limit of $0.64\sqrt{(E/F_y)}$ is retained for the proposed R = 4 OCBF, with the acknowledgement that it is an area for potential future improvement as described in this section.

7.2.6 Brace Global Slenderness Limits

In addition to local slenderness (b/t) limits, global slenderness (KL/r) limits are another seismic detailing requirement associated with current R = 3.25 OCBF design, for braces in V- and inverted-V configurations (AISC, 2010a):

> **5b. Slenderness**
> Braces in V or inverted-V configurations shall have $KL/r \leq 4\sqrt{(E/F_y)}$.

These KL/r requirements equate to an upper bound of 100.4 for ASTM A500 braces (F_y = 317 MPa [46 ksi]) and 96.3 for the newest ASTM A1085 braces (F_y = 345 MPa [50 ksi]), which is a much tighter restriction than the global slenderness limits for all braces within SCBFs, $KL/r \leq 200$ (AISC, 2010a). An explanation for the stark difference in these KL/r requirements is hinted at by the distinction that this tighter limit of $KL/r \leq 4\sqrt{(E/F_y)}$ [e.g. 100.4] only applies to braces within V- and inverted-V configurations (not split-x). In other words, the limit aims to decrease the imbalanced force imposed by the braces onto the beam and adjoining elements in current R = 3.25 OCBF design. This works in theory because as KL/r decreases, the ratio between the tensile capacity of a brace and its buckling capacity, P_y/P_n, decreases accordingly. The justification for the tighter KL/r limit is given in the commentary of AISC 341–05, in discussion of SCBFs (AISC, 2005):

C13.2a. Slenderness

The slenderness (KL/r) limit has been raised to 200 for SCBF. Research has shown that frames with slender braces designed for compression strength behave well due to the overstrength inherent in their tension capacity (Tremblay, 2000). For braces with overall slenderness greater than $4\sqrt{(E/F_y)}$, the overstrength factor of 2.0 in SEI/ASCE 7 is not adequate to account for the effect of this overstrength on adjoining members, so such slender braces are only permitted in frames in which the columns are designed with explicit consideration of brace overstrength, rather than with the overstrength factor in the amplified seismic load. Tang and Goel (1989) and Goel and Lee (1992) showed that the postbuckling cyclic fracture life of bracing members generally increases with an increase in slenderness ratio. An upper limit is provided to maintain a reasonable level of compressive strength.

Even though a lower KL/r does in fact reduce the inherent tension overstrength, the discussion and rationale given above as it pertains to current R = 3.25 OCBF design is confusing considering the design of typical R = 3.25 OCBF chevrons throughout this research project. In those designs, the load combinations including the amplified seismic load (based on Ω_0 = 2.0) was the governing check in the force-imbalance design for OCBF chevron beams, meaning that the minimized tension overstrength did not accomplish its desired effect. This was driven by the combined effect of the tighter KL/r requirement in conjunction with the b/t requirements, which apply to all braces within OCBFs. For the 7.0 m. [23 ft.] braces used in prototype buildings designed and tested numerically in this project, Table 7.4 presents a list of all applicable brace sections in OCBF chevrons, i.e. those with both $KL/r \leq 100.4$ (for L = 7.0 m. [23 ft.]) and $b/t \leq 15.4$.

Table 7.4 – Permissible braces for R = 3.25 OCBF Chevron, L = 7.0 m

Section [HSS]	Weight [N/m]	b/t	KL/r	φP_n (L = 7.0 m) [kN]
8x8x1/2	713	12.4	91.4	1566
8x8x5/8	865	9.2	92.9	1850
9x9x1/2	812	14.4	80.5	2046
9x9x5/8	989	10.8	81.7	2446
10x10x5/8	1114	12.4	72.8	3042
12x12x3/4	1306	9.73	74.2	3518
14x14x3/4	1604	12.4	60.8	4937
14x14x7/8	1902	15.1	51.5	6316
16x16x7/8	2183	12.4	52.2	7206

Even without dropping the uneconomical HSS8x8x5/8 section from Table 7.4, a problem develops when the strict KL/r limit for braces in V and inverted-V configurations is applied in combination with the b/t limit. Specifically, the lightest section that passes both limits for braces with L = 7.0 m. [23 ft.] is an HSS8x8x1/2, with φP_n = 1,566 kN [352 kips]. In a 3-story OCBF chevron such as "OCBF-CHEV-Tc" listed in Table 6.1, the required strength for the Story 1 braces was 649 kN [153 kips], or over two times less than the capacity provided by the HSS8x8x1/2 braces ($\varphi P_n/P_{br,req}$ = 2.4). Of course, this situation is further worsened for the upper stories, and in taller buildings, as the member demands decrease but the smallest applicable section is still an HSS8x8x1/2. In the extreme case investigated, the Story 9 braces for a 9-story OCBF chevron building had an overstrength ($\varphi P_n/P_{br,req}$) equal to 16.5 (see Chapter 8).

In summary, while the intention of the strict KL/r requirement for OCBF braces in V and inverted-V configurations was to minimize the force imbalance, it had the opposite effect

for the buildings studied with 10.7 m. [35 ft.] bays and 7.0 m. [23 ft.] brace length. The *KL*/*r* limits caused brace sizes to be 2.4–16.5 times larger than what was required by design, which in turn increased the force-imbalance on the beams. This problem was further complicated by the relationship with the requirement to design the brace-gusset connections for load combinations in consideration of the amplified seismic demand, with $\Omega_0 = 2.0$. In other words, the efforts to increase the likelihood of ductile brace buckling instead of brittle brace-gusset weld fracture were negated by the *KL*/*r*-driven oversized braces, leading to a near-certainty in the formation of a connection-based limit state prior to brace buckling ($\varphi R_n/P_{br,req} = 2.0$ vs. $\varphi P_n/P_{req} = 2.4–16.5$).

In consideration of the above, the proposed *KL*/*r* limit for all braces in the new $R = 4$ OCBF system is 200 (the current limit for SCBFs). The rationale given in the AISC 341–05 commentary (AISC, 2005) regarding braces with high *KL*/*r* limits placing increased demands on adjoining members is of no concern to the $R = 4$ OCBF, as the primary intention of this system is to offer reserve capacity through beam and column bending (frame action) following brace buckling or brace-gusset weld fracture. The relaxation of *KL*/*r* to 200 additionally allows designers to select from more brace sections, which mitigates the problem of unnecessarily large braces (Table 7.4). Previous research (Tang and Goel, 1989; Goel and Lee, 1992) has shown that the postbuckling cyclic fracture life of bracing members increases with an increase in *KL*/*r* (AISC, 2005), and prolonging the ductile range of brace behavior is certainly a beneficial aspect of frame performance.

Based on the proposed $R = 4$ OCBF provisions, which require designing braces for the standard load combinations while designing the brace-gusset welds for the amplified seismic load effect ($\Omega = 2.0$), one would expect brace buckling to be the dominant limit state in all

stories within an R = 4 SFRS. However, due to the many sources of brace overstrength induced by the design process (finite number of brace sections, actual brace length compared to design length. To this end, a small study was conducted to assess the implication of weld fracture vs. brace buckling on the long-link EBF response that this system relied on for reserve strength. A single bay, single story model with pin-ended beams was used for this purpose, with the same geometry as the test frames studied thus far (10.7 m. [35 ft.] bay width, 4.6 m. [15 ft.] bay height, 7.0 m. [23 ft.] braces) Beam size was W14x48, and column size was W12x53. Three different brace sizes were selected: two that meet the R = 4 b/t criteria (HSS7x7x1/2, HSS6x6x3/8), and one that is more typical of an R = 3 CBF (HSS9x9x1/4). Weld capacity was adjusted up and down when necessary to shift the limit state from brace buckling to weld fracture. The results of this study (Figure 7.2) reveal that for braces typical of an R = 4 OCBF, a long-link EBF that forms because of brace buckling (and features only downwards beam deflection in both directions) produces response equal to or better than the response of a long-link EBF that forms because of weld fracture. Conversely, for braces with a large b/t (disallowed by both the proposed R = 4 OCBF current R = 3.25 OCBF provisions) such as the HSS9x9x1/4, low cycle fatigue degradation occurs at earlier story drift levels (Figure 7.2c), creating a pinches hysteresis that has less ductility than the case of brace-gusset weld fracture (Figure 7.2d). Thus, so long as braces with low b/t ratios are provided, the hysteretic response of a long-link EBF mechanism with buckling braces is shown to be equal to or better than a long-link EBF mechanism with brace-gusset weld fracture, for the system shown and for the given modelling assumptions. This conclusion is highly sensitive to the post-buckling degradation rate of braces, which, while included for the braces studied, comes from an empirical equation, and does not include the impact of local brace buckling.

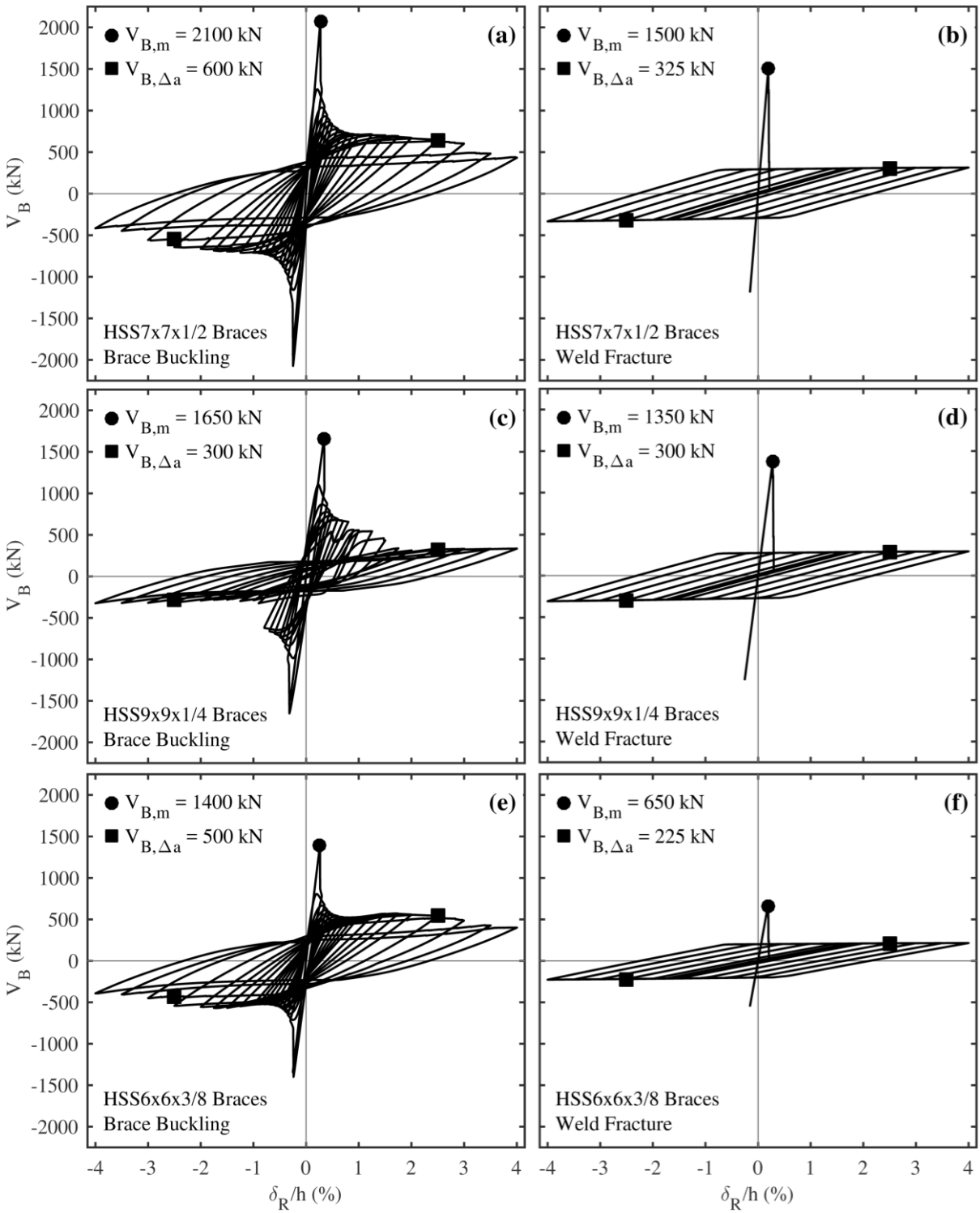

Figure 7.2 – Cyclic behavior of chevron frames: influence of brace size and limit state on long-link EBF response.

7.3 SAMPLE STATIC CYCLIC RESPONSE OF *R* = 4 OCBF

For an initial comparison between the proposed *R* = 4 OCBF and the current *R* = 3.25 OCBF, a static cyclic numerical simulation was performed as a companion study to those in Chapter 6. To highlight the most significant change in the *R* = 4 OCBF and current *R* = 3.25 OCBF design provisions, a 3-story chevron configuration was selected for this study. Thus, the effect of the relaxed of *KL*/*r* limits and removal of the force-imbalance design requirement were shown.

The designs for the two comparison frames, a 3-story *R* = 4 chevron OCBF (R4-CHEV-3), and a 3-story *R* = 3.25 chevron OCBF (OCBF-CHEV-3), are given in Table 7.5. The economical improvements were clear, as the SFRS weight for the *R* = 4 OCBF was only 65% (5.76/8.90) of the weight of the current *R* = 3.25 OCBF. The shift in weight is dominated by the relaxation in *KL*/*r* requirements and the removal of the force-imbalance requirement for beams, rather than by the 23% increase in *R*-value from 3.25 to 4.

Table 7.5 – Comparison of 3-story chevron: *R* = 4 OCBF and current OCBF

Frame Designation	Story 1 Braces (HSS)	Story 2 Braces (HSS)	Story 3 Braces (HSS)	Level 2 Beam	Level 3 Beam	Roof Beam	Columns	SFRS Weight (Tonnes)
OCBF-CHEV-3	8x8x1/2	8x8x1/2	8x8x1/2	W30x116	W30x90	W12x26	W12x53	8.90
R4-CHEV-3	6x6x3/8	6x6x3/8	5x5x5/16	W14x48	W14x48	W10x33	W12x53	5.76

The behavior of these two systems during static cyclic analyses, which were performed using the protocol described in Chapter 6, is shown in Figure 7.3. As described in Chapter 6, frame OCBF-CHEV-3 had both poor reserve capacity and poor ductility. The first limit state was Story 1 compression brace-gusset weld fracture, which was followed by Story 1 tension

brace-gusset weld fracture due to the large W30x116 Level 2 beam, which was designed per the force-imbalance procedure. This sequence of limit states created an unfavorable mechanism driven purely by column bending, with no reserve capacity provided by the excessively large beam. In the more economical R4-CHEV-3, the first limit states were Story 1 North brace buckling when pushing to positive drifts followed by Story 1 South brace buckling when pushing to negative drifts. Due to the lighter W14x48 Level 2 beam, the ductile brace buckling formed a mechanism that involved frame action from column bending and beam bending through long-link EBF behavior. Consequently, frame R4-CHEV-3 achieved a peak reserve capacity four times larger than frame OCBF-CHEV-3 (1000 kN [225 kips] vs. 250 kN [56 kips]). Pinching of the hysteresis to 500 kN [112 kips] within later stages of the R4-CHEV-3 response is a result of brace degradation from low-cycle fatigue damage. To further show the benefits of the proposed R = 4 OCBF over the current R = 3.25 OCBF, an approximate "performance rating" was calculated by dividing the measured reserve capacity by the weight of the SFRS in tonnes. For the current R = 3.25 OCBF, the rating was (250)/(8.90) = 28.08; and for the proposed R = 4 OCBF, the rating was (1000)/(5.76) = 173.6. Thus, the relative performance rating of the R = 4 OCBF was (173.6/28.08) = 6.2 times that of the current R = 3.25 OCBF for this example.

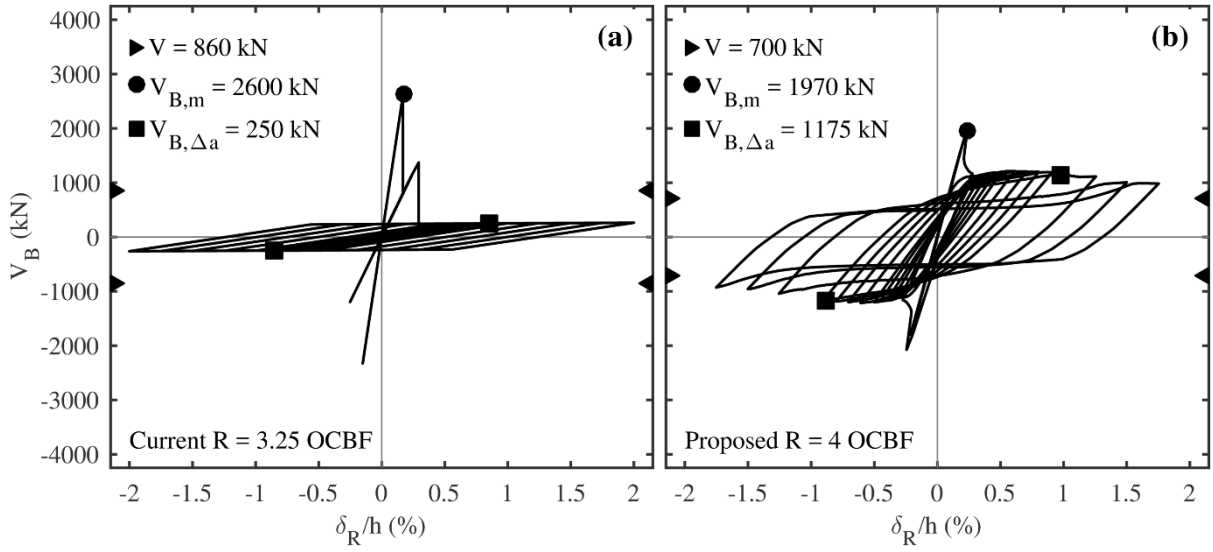

Figure 7.3 – Cyclic behavior of OCBF chevron frames designed with: (a) current R = 3.25 OCBF provisions; and (b) proposed R = 4 OCBF provisions.

7.4 SUMMARY OF *R* = 4 OCBF

Given the inability to systematically assess the performance of R = 3 SFRSs, in addition to the observed flaws in the current provisions for the R = 3.25 OCBF SFRSs, a new SFRS was proposed for use in regions of low and moderate seismicity, the R = 4 OCBF. The goal of the R = 4 OCBF is to give a cost-effective alternative to the R = 3 SFRS but with the added benefit of detailing and proportioning requirements which are based on the notion of reserve capacity and ductility. The result is a more reliable system than the R = 3 SFRS and R = 3.25 OCBF. As shown in Chapter 8, these existing systems can in some cases achieve adequate seismic collapse prevention performance, but this collapse prevention does not have a fundamental link to the design process and the sources of reserve capacity that develop are not well documented.

The intended behavior of the R = 4 SFRS is to prevent collapse through a combination of primary system ductility and reserve capacity, which are provided through a careful choice of seismic detailing requirements.

- Reserve Capacity:
  - Design columns for amplified seismic force, with Ω_0 = 2.0.
  - Beams must span full length under gravity without considering brace support.
  - Modest beam-column connection flexural capacity, $M_{p,conn} \geq 0.50 M_{p,beam}$.
  - Web (h/t_w) and flange ($b_f/2t_f$) slenderness limits for beams.
- Primary System Ductility:
  - Design brace-gusset connections for amplified seismic force, with Ω_0 = 2.0.
  - Local ($b/t < 0.64\sqrt{E/F_y}$) and global ($KL/r \leq 200$) slenderness limits for braces.

The full proposal for the R = 4 OCBF as it would appear in the 2022 AISC *Seismic Provisions* is given in Appendix C. The seismic detailing and proportioning requirements of the R = 4 OCBF give robust collapse prevention performance through capitalization of the significant reserve capacity provided by the long-link EBF behavior. The long-link EBF behavior involves midspan beam bending within the SFRS and occurs following the development of ductile brace buckling or brace-gusset weld fracture. This design approach is a stark contrast with the R = 3 and current R = 3.25 OCBF SFRS design frameworks, in which a mechanistic approach is not considered.

The next step in the research was to assess the performance of the proposed R = 4 OCBF, and this was done through a comparison of its behavior with the current alternative systems used in low and moderate seismic regions, the R = 3 CBF and R = 3.25 OCBF. A brief introduction to this process was presented in the previous section, where the proposed R = 4

chevron OCBF was shown to display higher reserve capacity than the current R = 3.25 chevron OCBF, with the added benefit of a 35% reduction in SFRS weight (Table 7.5, Figure 7.2). In the following chapter, this investigation was extended using dynamic analyses, and a full performance investigation was used to assess the viability of the proposed R = 4 OCBF in the context of the current R = 3.25 OCBF and R = 3 SFRSs.

CHAPTER 8

PERFORMANCE ASSESSMENT OF LOW-DUCTILITY CONCENTRICALLY-BRACED FRAMES

In the previous chapters, the impact of system type and system configuration on collapse prevention performance was investigated through static cyclic numerical simulations. The simulations were performed using *OpenSees* models, which were verified through calibration with full-scale test results (Chapter 5). These simulations offered a basic understanding of the types of mechanisms which can form for a given system configuration and type, and motivated the proposal for a modified ordinary concentrically-braced frame, the R = 4 OCBF system presented in Chapter 7. To comprehensively assess the performance of the three low-ductility CBF systems (R = 3, current R = 3.25 OCBF, proposed R = 4 OCBF), a series of dynamic simulations was conducted. A set of 18 case study buildings was designed with the plan configuration used previously in this research program (Figure 3.1b). Parameters used to define the case study buildings were: (1) system configuration: chevron or split-x; (2) system type: R = 3, current R = 3.25 OCBF, proposed R = 4 OCBF; and (3) number of stories: 3, 6, and 9. Following development of the building designs and their respective numerical models, a series of incremental dynamic analyses (IDAs) were conducted using the 15 ground motions (GMs) developed by Hines et al., 2009 (Section 3.1) for Boston, Massachusetts. Dynamic behavior was first evaluated by studying response for individual earthquake records to assess the collapse prevention performance of the different mechanisms that formed for a given system configuration and type. Finally, the IDA results were used within a reliability-based performance assessment framework (FEMA P695 – FEMA, 2009) to draw overall

conclusions on the viability of different seismic force resisting system (SFRS) types and configurations.

8.1 BUILDING DESIGNS

Eighteen baseline case study building designs were created for the performance assessment. Three variables—system type, system configuration, and number of stories—defined the matrix of options used to distinguish each building design. There were three considerations for system type: R = 3 SFRS [R3], current R = 3.25 OCBF [OC], and proposed R = 4 OCBF [R4]; two considerations for system configuration: chevron [CH], split-x [SX]; and three considerations for number of stories: 3-story [3], 6-story [6], and 9-story [9]. These abbreviations were used to label the case study buildings for easier identification in the format of *SystemType-SystemConfiguration-No.Stories*. For example, the 6-story building designed using the proposed R = 4 OCBF provision with braces in the chevron configuration was labeled R4-CH-6.

In the spirit of keeping consistency with the full-scale frame tests and previous numerical simulations, all designs were based on the same 5-by-5 bay office building in Boston (Section 3.1). In the 3-story buildings, two braced bays were included in each direction, and thus half of the building was modeled in *OpenSees*. In the 6- and 9-story buildings, four braced bays were needed in each direction to minimize overturning effects, and thus one quarter of the building was modeled in *OpenSees*. Also for consistency, all R = 3 SFRSs were designed using the approximate fundamental period, T_a, while the current and proposed OCBF SFRSs were designed using the calculated fundamental period, which was capped based on the ASCE 7 framework at $T_c = 1.6T_a$. Gravity loading (Live Load, Dead Load, and Snow Load) was identical throughout all case study buildings, and consistent with the previous 3-story prototype

building used in this research program (Table 3.1). Like the previous frame studies and simulations, all buildings were studied in the direction of their 10.7 m. [35 ft.] wide bays, which have beams rather than girders. All other modeling assumptions are identical to those introduced and discussed in Chapter 5.

8.1.1 SFRS Members

Summaries of the SFRS member sizes for the 3-, 6-, and 9-story buildings are given in Tables 8.1, 8.2, and 8.3, respectively. In addition to beam, column, and brace sizes, the design base shear (V) and SFRS weight (W_{SFRS}) in tonnes (t) for a single braced bay are also included in these tables. Design base shear (V) for the R = 3 frames was larger than the OCBFs because of the different design period used (T_a vs. $T_c = 1.6T_a$). In this regard, the R = 3 SFRS may be thought of as having an effective R-value of 3/1.6 = 1.8 for a more direct comparison between member sizes in the case study buildings.

Table 8.1 – SFRS members: 3-story case study buildings

Member	R3-CH-3	OC-CH-3	R4-CH-3	R3-SX-3	OC-SX-3	R4-SX-3
Story 1 Brace [HSS]	9x9x1/4	8x8x1/2	6x6x3/8	9x9x5/16	7x7x1/2	6x6x5/8
Story 2 Brace [HSS]	8x8x1/4	8x8x1/2	6x6x3/8	9x9x1/4	6x6x1/2	6x6x3/8
Story 3 Brace [HSS]	6x6x1/4	8x8x1/2	5x5x5/16	6x6x1/4	8x8x1/2	5x5x5/16
Story 1–3 Columns [W]	12x53	12x53	12x53	12x53	12x53	12x53
Level 2 Beam [W]	12x40	30x116	14x48	12x26	12x26	14x48
Level 3 Beam [W]	12x40	30x90	14x48	18x40	18x40	14x48
Level R Beam [W]	12x26	12x26	10x33	12x26	12x26	10x33
V [kN]: 1/2 building	1490	860	700	1490	860	700
W_{SFRS} [t]	5.39	8.9	5.76	5.38	6.26	6.07

Table 8.2 – SFRS members: 6-story case study buildings

Member	R3-CH-6	OC-CH-6	R4-CH-6	R3-SX-6	OC-SX-6	R4-SX-6
Story 1 Brace [HSS]	8x8x1/4	8x8x1/2	6x6x3/8	9x9x1/4	7x7x1/2	6x6x1/2
Story 2 Brace [HSS]	8x8x1/4	8x8x1/2	5.5x5.5x3/8	8x8x1/4	6x6x1/2	6x6x3/8
Story 3 Brace [HSS]	8x8x1/4	8x8x1/2	5.5x5.5x5/16	8x8x1/4	6x6x3/8	6x6x3/8
Story 4 Brace [HSS]	7x7x1/4	8x8x1/2	5.5x5.5x5/16	7x7x1/4	5.5x5.5x5/16	5.5x5.5x5/16
Story 5 Brace [HSS]	6x6x1/4	8x8x1/2	5x5x5/16	6x6x1/4	5.5x5.5x5/16	5x5x5/16
Story 6 Brace [HSS]	5x5x3/16	8x8x1/2	4x4x1/4	5x5x3/16	4x4x1/4	4x4x1/4
Story 1–2 Columns [W]	12x96	12x96	12x87	12x87	12x96	12x87
Story 3–4 Columns [W]	12x58	12x58	12x58	12x58	12x58	12x53
Story 5–6 Columns [W]	12x40	12x40	12x40	12x40	12x40	12x40
Level 2 Beam [W]	12x35	12x26	14x48	12x26	12x26	14x48
Level 3 Beam [W]	12x35	18x40	14x48	18x40	18x40	14x48
Level 4 Beam [W]	12x35	12x26	14x48	12x26	12x26	14x48
Level 5 Beam [W]	12x26	18x40	14x48	18x40	18x40	14x48
Level 6 Beam [W]	12x26	12x26	14x48	12x26	12x26	14x48
Level R Beam [W]	12x26	14x22	10x33	14x22	14x22	10x33
V [kN]: 1/4 building	970	560	455	970	560	455
W_{SFRS} [t]	10.91	16.7	11.92	10.69	11.46	12.35

Table 8.3 – SFRS members: 9-story case study buildings

Member	R3-CH-9	OC-CH-9	R4-CH-9	R3-SX-9	OC-SX-9	R4-SX-9
Story 1 Brace [HSS]	8x8x1/4	8x8x1/2	6x6x5/8	9x9x1/4	7x7x1/2	7x7x1/2
Story 2 Brace [HSS]	8x8x1/4	8x8x1/2	6x6x1/2	9x9x1/4	7x7x1/2	7x7x1/2
Story 3 Brace [HSS]	8x8x1/4	8x8x1/2	6x6x1/2	9x9x1/4	7x7x1/2	6x6x5/8
Story 4 Brace [HSS]	8x8x1/4	8x8x1/2	6x6x3/8	8x8x1/4	6x6x1/2	6x6x1/2
Story 5 Brace [HSS]	8x8x1/4	8x8x1/2	6x6x3/8	8x8x1/4	6x6x1/2	6x6x1/2
Story 6 Brace [HSS]	7x7x1/4	8x8x1/2	5.5x5.5x3/8	7x7x1/4	6x6x3/8	6x6x3/8
Story 7 Brace [HSS]	7x7x1/4	8x8x1/2	5.5x5.5x3/16	7x7x1/4	5.5x5.5x3/8	5.5x5.5x3/8
Story 8 Brace [HSS]	6x6x1/4	8x8x1/2	5x5x5/16	6x6x3/16	5x5x5/16	5x5x5/16
Story 9 Brace [HSS]	4.5x4.5x3/16	8x8x1/2	4x4x1/4	4.5x4.5x3/16	8x8x1/2	4x4x1/4
Story 1–2 Columns [W]	12x152	12x152	12x152	12x152	12x152	12x152
Story 3–4 Columns [W]	12x120	12x120	12x106	12x106	12x106	12x106
Story 5–6 Columns [W]	12x65	12x72	12x65	12x65	12x65	12x65
Story 7–9 Columns [W]	12x50	12x50	12x50	12x50	12x50	12x50
Level 2 Beam [W]	12x40	30x90	14x48	12x26	12x26	14x48
Level 3 Beam [W]	12x40	30x90	14x48	18x40	18x40	14x48
Level 4 Beam [W]	12x40	27x84	14x48	12x26	12x26	14x48
Level 5 Beam [W]	12x35	27x84	14x48	18x40	18x40	14x48
Level 6 Beam [W]	12x35	24x76	14x48	12x26	12x26	14x48
Level 7 Beam [W]	12x30	21x62	14x48	18x40	18x40	14x48
Level 8 Beam [W]	12x26	18x40	14x48	12x26	12x26	14x48
Level 9 Beam [W]	12x26	18x40	14x48	18x40	18x40	14x48
Level R Beam [W]	12x26	12x26	10x33	12x26	12x26	10x33
V [kN]: 1/4 building	1100	635	515	1100	635	515
W_{SFRS} [t]	20.19	29.98	22.51	19.8	21.85	23.35

Braces were designed with A1085 steel, assuming a buckling length equal to the workpoint-to-workpoint length of 7.0 m. [23 ft.]. In addition to the local (b/t) and global (KL/r) slenderness limits associated with the OCBF designs, slender brace sections in compression were avoided in R = 3 designs for consistency with the design approach of the full-scale R = 3 test frame (Chapter 4).

Columns within the SFRSs were designed for load combinations in consideration of reduced live loads. A column splice was provided every two stories, apart from the 3-story buildings and upper three stories of the 9-story buildings, in which a continuous column over 3-stories was provided to decrease the number of splices. Additionally, a common nominal column depth was kept over the height of the building (W12s). This decision was consistent with typical design practices, and helps to decrease the complexity of column splice detailing met when large jumps in section sizes are made.

Beams within SFRSs were designed to span their full length under gravity demands only where specifically required in the applicable building codes (in V- and inverted-V configurations for the current R = 3.25 OCBF, in all beams for the proposed R = 4 OCBF). Reduced live loads were used in the design of members for load combinations that consisted of purely gravity demands. Typical of standard design procedures, all beams within the SFRSs were designed as bare steel, i.e. without consideration of composite action.

8.1.2 Brace-Gusset Connections

Summaries of the brace-gusset welded connection sizes for the 3-, 6-, and 9-story buildings are given in Tables 8.4, 8.5, and 8.6, respectively. To keep gusset plate sizes comparable throughout the 18 case study buildings, all fillet weld lengths were kept under 380 mm. [15 in.]. Increments of 12.7 mm. [1/2 in.] were used for the weld lengths. Fillet weld sizes

ranged from 3.2 mm. [1/8 in.] to 6.4 mm. [1/4 in.]. At minimum, a weld with length (l) equal to the brace width (b) was specified even if the demand did not require such a length.

Table 8.4 – Brace-gusset welds: 3-story case study building

Story		R3-CH-3	OC-CH-3	R4-CH-3	R3-SX-3	OC-SX-3	R4-SX-3
1	l (mm) [a]	279	330	267	318	368	305
	d (mm)	6.4	6.4	6.4	6.4	6.4	6.4
	R_n (kN)	1450	1715	1385	1650	1915	1585
2	l (mm) [a]	229	254	279	241	279	305
	d (mm)	6.4	6.4	4.8	6.4	6.4	4.8
	R_n (kN)	1190	1585	1090	1255	1455	1190
3	l (mm) [a]	203	229	191	203	229	191
	d (mm)	3.2	3.2	3.2	3.2	3.2	3.2
	R_n (kN)	530	595	495	530	595	495

[a] Weld lengths for strength calculations are four times (4x) the lengths shown, which is for a single face of the four face brace-gusset interface.

Table 8.5 – Brace-gusset welds: 6-story case study building

Story	Prop.	R3-CH-6	OC-CH-6	R4-CH-6	R3-SX-6	OC-SX-6	R4-SX-6
1	l (mm) [a]	267	305	241	254	279	241
	d (mm)	4.8	4.8	4.8	6.4	6.4	6.4
	R_n (kN)	1040	1190	940	1320	1455	1255
2	l (mm) [a]	254	279	229	279	241	279
	d (mm)	4.8	4.8	4.8	4.8	6.4	4.8
	R_n (kN)	990	1090	890	1090	1255	1090
3	l (mm) [a]	229	254	216	267	292	241
	d (mm)	4.8	4.8	4.8	4.8	4.8	4.8
	R_n (kN)	890	990	840	1040	1140	940
4	l (mm) [a]	279	305	254	292	216	267
	d (mm)	3.2	3.2	3.2	3.2	4.8	3.2
	R_n (kN)	725	790	660	760	840	1040
5	l (mm) [a]	205	229	191	205	229	191
	d (mm)	3.2	3.2	3.2	3.2	3.2	3.2
	R_n (kN)	530	595	495	530	595	495
6	l (mm) [a]	127	205	102	127	102	102
	d (mm)	3.2	3.2	3.2	3.2	3.2	3.2
	R_n (kN)	330	530	265	330	265	265

[a] Weld lengths for strength calculations are four times (4x) the lengths shown, which is for a single face of the four face brace-gusset interface.

Table 8.6 – Brace-gusset welds: 9-story case study building

Story	Prop.	R3-CH-9	OC-CH-9	R4-CH-9	R3-SX-9	OC-SX-9	R4-SX-9
1	l (mm) [a]	305	254	279	279	330	279
	d (mm)	4.8	6.4	4.8	6.4	6.4	6.4
	R_n (kN)	1190	1320	1090	1455	1715	1455
2	l (mm) [a]	292	241	267	241	292	254
	d (mm)	4.8	6.4	4.8	6.4	6.4	6.4
	R_n (kN)	1140	1255	1040	1255	1520	1320
3	l (mm) [a]	279	241	254	241	279	241
	d (mm)	4.8	6.4	4.8	6.4	6.4	6.4
	R_n (kN)	1090	1255	990	1255	1455	1255
4	l (mm) [a]	254	292	241	279	241	279
	d (mm)	4.8	4.8	4.8	4.8	6.4	4.8
	R_n (kN)	990	1140	940	1090	1255	1090
5	l (mm) [a]	229	267	216	279	241	279
	d (mm)	4.8	4.8	4.8	4.8	6.4	4.8
	R_n (kN)	890	1040	840	1090	1255	1090
6	l (mm) [a]	292	229	279	216	254	216
	d (mm)	3.2	4.8	3.2	4.8	4.8	4.8
	R_n (kN)	760	890	725	840	990	840
7	l (mm) [a]	241	267	229	267	292	254
	d (mm)	3.2	3.2	3.2	3.2	3.2	3.2
	R_n (kN)	625	695	595	695	760	660
8	l (mm) [a]	165	203	165	165	178	152
	d (mm)	3.2	3.2	3.2	3.2	3.2	3.2
	R_n (kN)	430	530	430	430	460	395
9	l (mm) [a]	114	203	114	114	203	114
	d (mm)	3.2	3.2	3.2	3.2	3.2	3.2
	R_n (kN)	295	530	295	295	530	295

[a] Weld lengths for strength calculations are four times (4x) the lengths shown, which is for a single face of the four face brace-gusset interface.

8.1.3 Gravity Framing Members

Beams within gravity bays were designed for composite action, and in consideration of reduced live load effects. The gravity framing beam members were unchanged from those designed by Bradley (2016) since the gravity loading conditions assumed in this study were unchanged. Gravity beam sizes for all case study buildings studied are presented in Table 8.7.

Table 8.7 – Gravity frame beams, all case study buildings

Perimeter	Perimeter, Roof	Interior	Interior, Roof
W18x35	W12x58	W16x31	W12x53

Columns within gravity bays were designed for reduced live load effects and with the same column splice locations used for the columns within the SFRS. Gravity loading on columns was adjusted based on location within the building and associated tributary area. Interior, perimeter, and corner columns had tributary areas of 97.5 m^2 [1,050 ft^2], 51.8 m^2 [557.5 ft^2], and 27.5 m^2 [296 ft^2], respectively. Summaries of gravity column sizes for 3-, 6-, and 9-story buildings are given in Tables 8.8, 8.9, and 8.10, respectively.

Table 8.8 – Gravity frame columns: 3-story case study buildings

Interior Story 1–3 [W]	12x50
Perimeter Story 1–3 [W]	12x40
Corner Story 1–3 [W]	12x40

Table 8.9 – Gravity frame columns: 6-story case study buildings

Interior Story 1–2 [W]	12x79
Interior Story 3–4 [W]	12x53
Interior Story 5–6 [W]	12x40
Perimeter Story 1–2 [W]	12x53
Perimeter Story 3–4 [W]	12x40
Perimeter Story 5–6 [W]	12x40
Corner Story 1–2 [W]	12x40
Corner Story 3–4 [W]	12x40
Corner Story 5–6 [W]	12x40

Table 8.10 – Gravity frame columns: 9-story case study buildings

Interior Story 1–2 [W]	12x120
Interior Story 3–4 [W]	12x87
Interior Story 5–6 [W]	12x65
Interior Story 7–9 [W]	12x50
Perimeter Story 1–2 [W]	12x65
Perimeter Story 3–4 [W]	12x53
Perimeter Story 5–6 [W]	12x50
Perimeter Story 7–9 [W]	12x40
Corner Story 1–2 [W]	12x50
Corner Story 3–4 [W]	12x40
Corner Story 5–6 [W]	12x40
Corner Story 7–9 [W]	12x40

8.1.4 Beam-Column Connections

Beam-column connections consisted of bolted-welded ASTM A572 Grade 50 Steel double web angles ($F_{y,exp}$ = 379 MPa [55 ksi]). Bolts in all connections were spaced at 12.7 mm. [1/2 in.]. Within the gravity bays, these connections only needed to resist gravity loads, and thus a 2L4x4x1/4 connection with 3 rows of 25.4 mm. [1.0 in.] diameter A490 bolts was sufficient. The contribution of gravity connections was not considered in the baseline case study buildings presented in this chapter (all gravity connections were modeled as pins). This assumption allowed for isolation of the collapse prevention performance of the individual SFRSs themselves without gravity framing contribution, and was appropriate given that gravity framing contribution was not considered in the lateral design of the buildings.

Prying action was considered in the design of beam-column connections. To meet the varying connection demands, a 2L4x4x1/2 connection with 3 rows of 25.4 mm. [1.0 in.] diameter A490 bolts was provided, centered over the depth of the beam. An additional 2L4x4x1/2 connection with 3 rows of 25.4 mm. [1.0 in.] diameter A490 bolts was provided for all gusset-column connections, centered over the depth of the gusset plate. All beam-column connections were assumed to have a 63.5 mm. [2.5 in.] angle-to-column bolt gage (g_c) to minimize the g_c/t ratio, which comes within 6 mm. [1/4 in.] of the workable column gage for all considered combinations of beam and column sizes. Angle and connection tests at Polytechnique Montréal (Beland et al., 2014; Nelson et al., 2014) revealed that the flexural capacity of a connection was inversely proportional to the g_c/t ratio of its angles, and thus g_c/t was minimized with the intent of maximizing the flexural capacity of these connections.

Beam-column connections were modeled using the fiber discretization approach introduced in Chapter 5. The moment-rotation hysteresis for typical beam-column connections

included in the case study buildings within this chapter are shown in Figure 8.1. For R = 4 split-x beam-column connections (Figure 8.1c), top and seat angles were included to meet the $0.50M_{p,beam}$ requirement in the proposed R = 4 provision (Section 7.2.5). Top and seat angles were L8x4x3/4s with a single row of 25.4 mm. [1.0 in.] diameter A490 bolts and a width of 152.4 mm. [6 in.]. As shown in Figure 8.1c, these connections had a moment capacity, $M_{p,conn}$ = 347 kN-m [256 kip-ft], which was 87% of the moment capacity of the W14x48 beams used in the R = 4 frames (φM_p = 399 kN-m [294 kip-ft]), and was thus acceptable per the proposed R = 4 provision. The split-x connection used in R = 3 and current R = 3.25 OCBF buildings (Figure 8.1b) had $M_{p,conn}$ = 56.0 kN-m [41.3 kip-ft], and thus with $M_{p,conn} = 0.14M_{p,beam}$ did not pass the R = 4 requirement ($M_{p,conn} = 0.5M_{p,beam}$).

As shown in Figure 8.1a, the moment capacity of the typical CBF chevron exceeded the moment capacity of the W14x48 beams used in the R = 4 frames, easily meeting the $0.50M_{p,beam}$ requirement ($M_{p,conn}$ = 509 kN-m [375 kip-ft] = $1.28M_{p,beam}$). The significantly larger moment capacity of these connections compared to those tested by Stoakes (2012) was partially attributable to a combination of the smaller 63.5 mm. [2.5 in.] column gage and 25.4 mm. [1.0 in.] diameter bolts (Stoakes used 19.0 mm. [3/4 in.] bolts). Additionally, certain connection limit states observed by Stoakes were not modeled in the current connection framework, such as beam-gusset weld fracture. Finally, although fracture at individual bolt lines was captured in the connection model, structural deterioration prior to this limit states was not. Together, these assumptions and limitations increased $M_{p,conn}$ beyond what was observed by Stoakes ($0.65M_{p,beam}$).

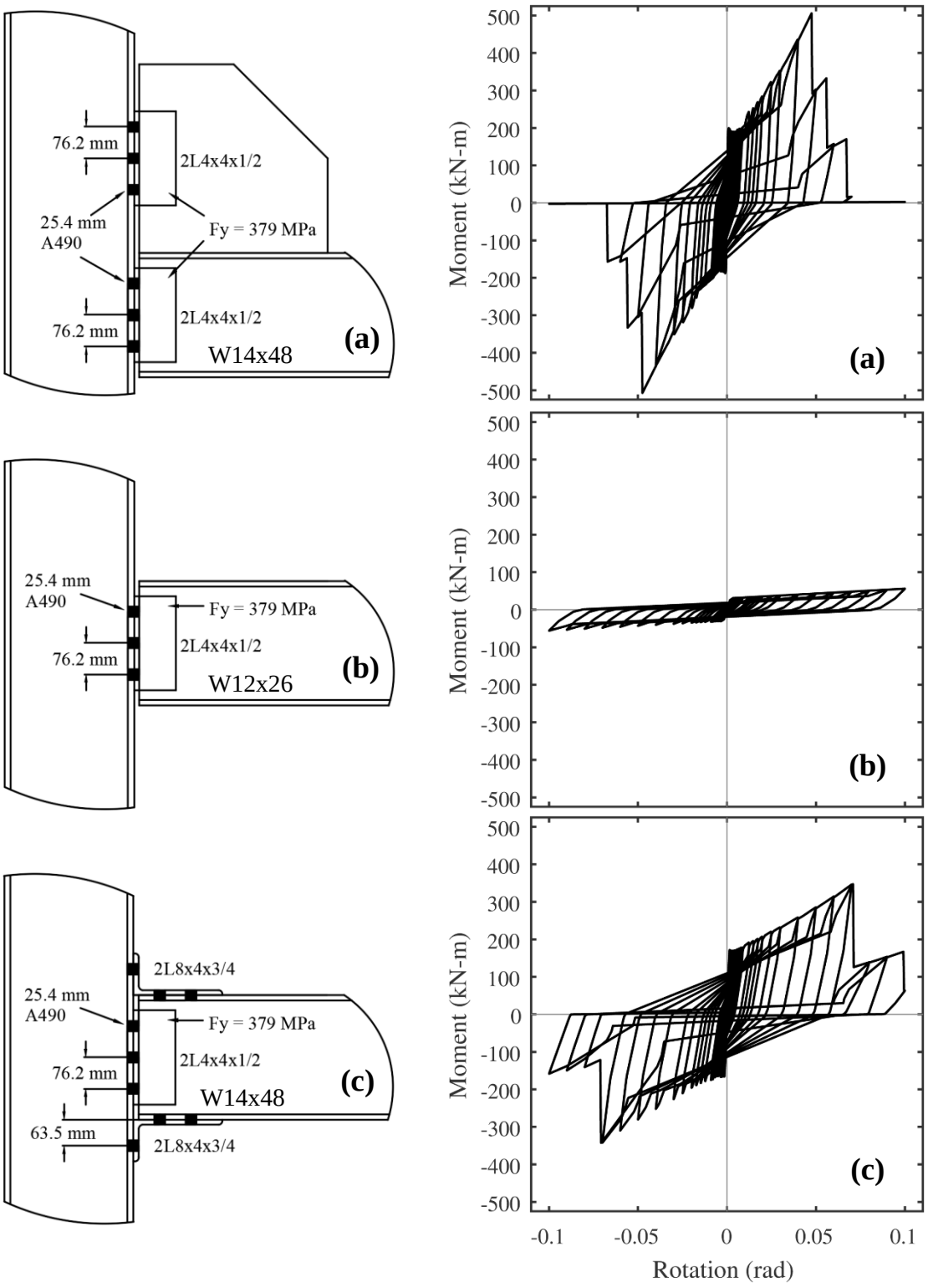

Figure 8.1 – Moment-rotation hysteresis for typical connections in case study buildings: (a) chevron connection; (b) split-x connection without gusset plates; (c) split-x connection without gusset plates in proposed R = 4 frames.

8.1.5 Mass and Fundamental Periods

The structural mass of each case study building for implementation in *OpenSees* was calculated from a combination of dead loads, partitions, and the building façade using the assumptions of Bradley (2016). The floor weight in each building was 11,254 kN [2,530 kips] and the roof weight of 6,005 kN [1,350 kips] was artificially adjusted by ±45 kN [10 kips] in acknowledgement of potential variations in equipment loads. These adjustments created total building weights (in kips) of 28.5 MN [6,400 kips], 62.3 MN [14,000 kips], and 96.1 MN [21,600 kips], for the 3-, 6-, and 9-story buildings, respectively. The symmetry of the building's floor plan was used to reduce the complexity and computational cost of the *OpenSees* simulation. Only half of the 3-story building was modeled (weight = 14.2 MN [3,200 kips]), and only a quarter of the 6-story (weight = 15.6 MN [3,500 kips]) and 9-story (weight = 24.0 MN [5,400 kips]) buildings were modeled.

The weights were converted to masses and applied to the *OpenSees* building models at each level at the center of the SFRS (Section 5.1.7). Prior to beginning the dynamic analyses for the performance assessment, an eigenvalue analysis was performed in *OpenSees* to calculate the fundamental period of each case study building. These building periods are presented alongside their respective design periods (T_a for R = 3 frames, $T_c = 1.6T_a$ for OCBFs) in Table 8.11. Relevant modeling assumptions used for structural period determination include: (1) actual beam-column connections within braced bays; (2) pinned connections within braced bays; (3) rigid gusset plate regions and beam-column intersecting regions; and (4) rigid diaphragm in gravity bays. Although this collection of assumptions decreased the *OpenSees* period below the design period of $1.6T_a$ for two of the R = 3.25 OCBFs (OC-CH-3, OC-CH-

6), the periods obtained from a less sophisticated analysis, of the type more commonly used in design practice, still exceeded $1.6T_a$, justifying the use of $T_c = 1.6T_a$ for these frames.

Table 8.11 – Fundamental periods of case study buildings

Building Designation	*OpenSees* period (s)	Design period (s)
R3-CH-3	0.700	0.347
OC-CH-3	0.527	0.556
R4-CH-3	0.695	0.556
R3-SX-3	0.662	0.347
OC-SX-3	0.613	0.556
R4-SX-3	0.642	0.556
R3-CH-6	1.161	0.584
OC-CH-6	0.902	0.935
R4-CH-6	1.164	0.935
R3-SX-6	1.146	0.584
OC-SX-6	1.074	0.935
R4-SX-6	1.124	0.935
R3-CH-9	1.831	0.792
OC-CH-9	1.487	1.267
R4-CH-9	1.725	1.267
R3-SX-9	1.796	0.792
OC-SX-9	1.674	1.267
R4-SX-9	1.674	1.267

The *OpenSees* eigenvalue analyses revealed that for SFRS designs that have mostly the same elements, the split-x configuration was slightly stiffer than the chevron configuration. The current R = 3.25 OCBF chevron buildings had the lowest periods among others with the same number of stories, a direct result of the force-imbalance design requirement and strict KL/r requirement increasing beam and brace sizes, respectively.

8.2 DYNAMIC SIMULATIONS

Following the design and modeling of the 18 case study buildings, a series of dynamic simulations was conducted to begin the performance assessment. Each building was subjected to the 15 ground motions (GMs) developed by Hines et al. (2009) which were previously introduced in Chapter 3. Based on the response spectra of the ground motion suite (Figure 3.16), it was clear that the highest energy portions of the time histories would have the largest impact on the stiffer 3-story buildings, which had periods that ranged from 0.527–0.700 s. The higher fundamental periods of the 6-story and 9-story buildings (0.902–1.831 s.) would protect them from these higher energy regions, with the caveat that these taller and more flexible buildings would be more susceptible to collapse driven from *P-Δ* effects.

8.2.1 Incremental Dynamic Analyses

Like the study in Chapter 3, incremental dynamic analyses (IDAs) were conducted per the method introduced by Vamvatsikos and Cornell (2002). Dynamic simulations on each case study building started with a scale factor (SF) of 0.2 (20% of the MCE) which was increased in increments of 0.2 until story drift, δ/h, exceeded 10% within any story during the simulation. The 16%, 50% (median), and 84% fractile IDA curves are plotted in Figures 8.2, 8.3, and 8.4, for the 3-, 6-, and 9-story case study buildings, respectively. The flat-line regions of the IDAs show the largest δ/h a case study building could achieve on average without collapsing. For example, the 3-story chevron frames collapsed on average (reached δ/h >10%) if δ/h > 3% was achieved throughout the time history. In other words, once 3% story drift was reached within these buildings, collapse quickly followed through a swift accumulation of drift in the soft story(s). The full suite of IDA results for the individual ground motions (GMs) is provided in Appendix A.

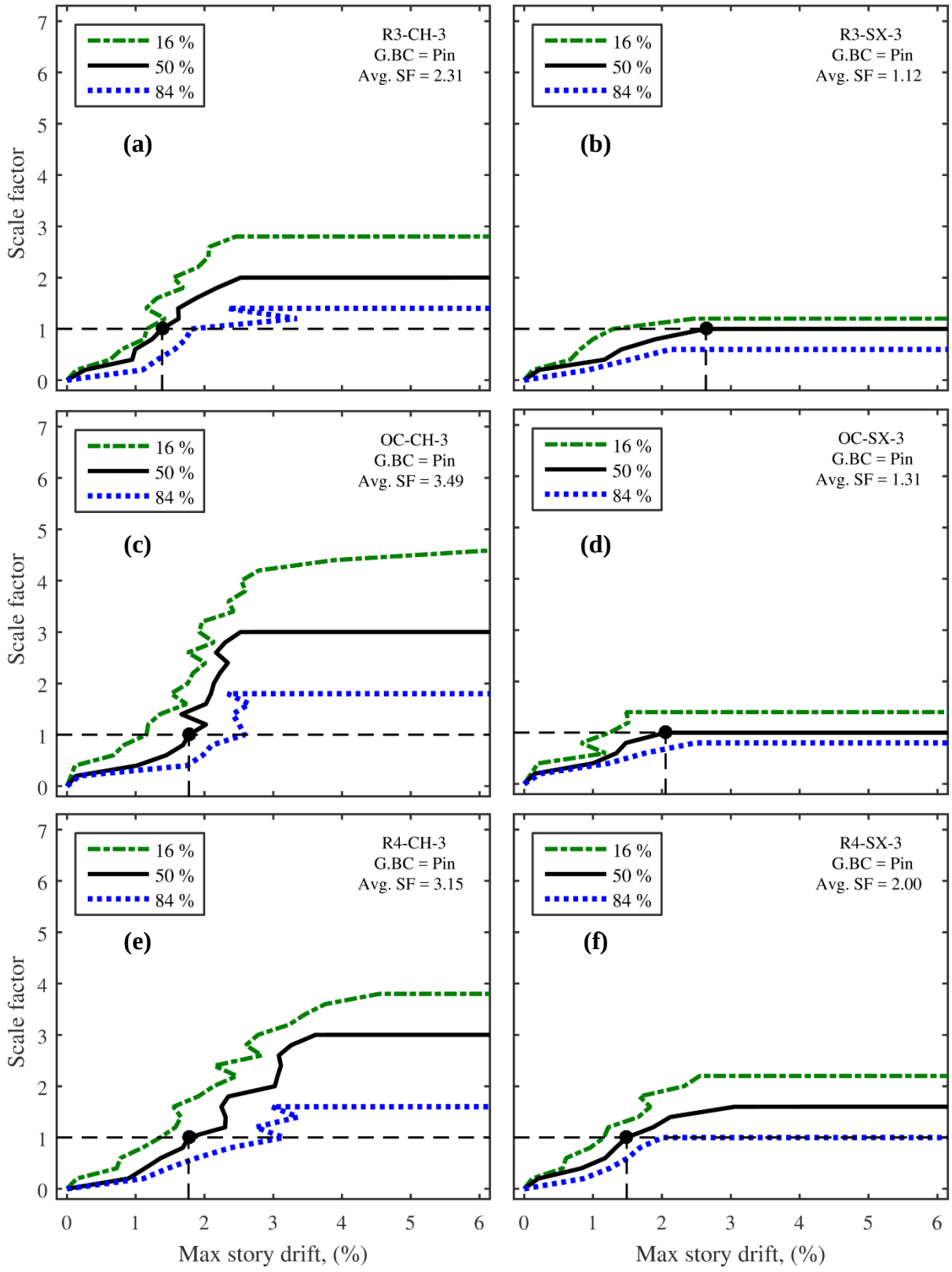

Figure 8.2 – Incremental dynamic analysis results for 3-story case study buildings: (a) R3-CH-3; (b) R3-SX-3; (c) OC-CH-3; (d) OC-SX-3; (e) R4-CH-3; and (f) R4-SX-3.

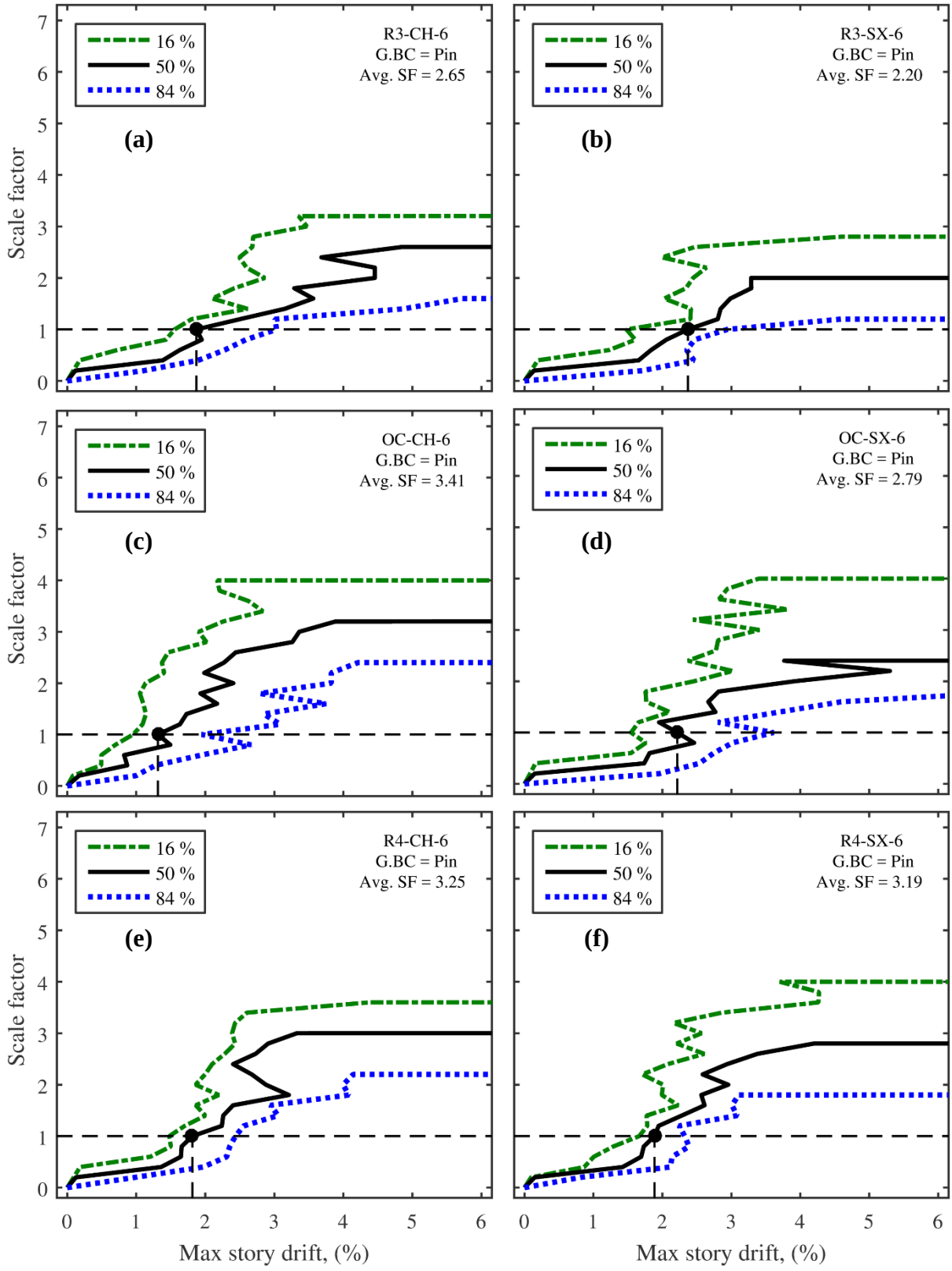

Figure 8.3 – Incremental dynamic analysis results for 6-story case study buildings: (a) R3-CH-6; (b) R3-SX-6; (c) OC-CH-6; (d) OC-SX-6; (e) R4-CH-6; and (f) R4-SX-6.

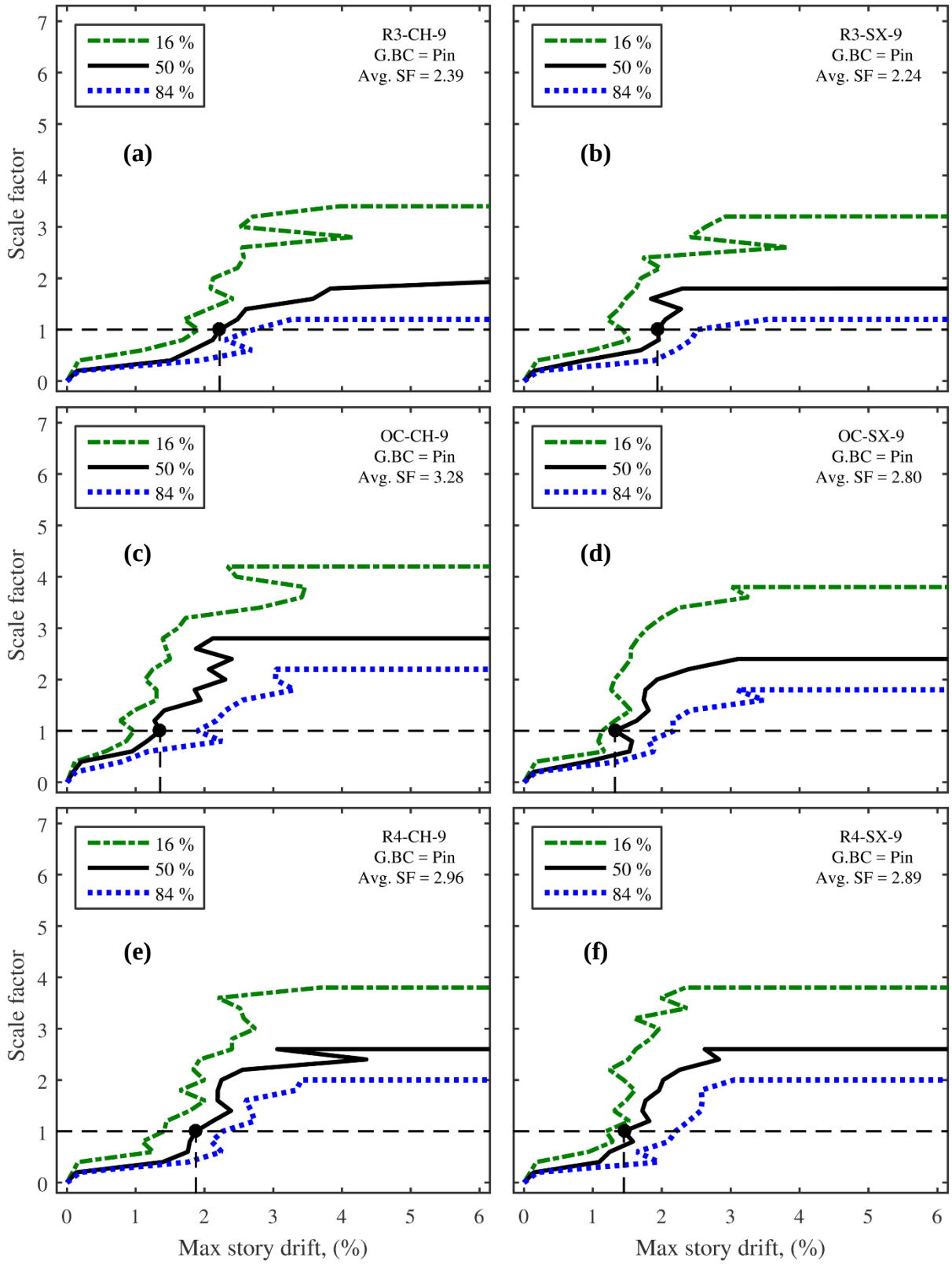

Figure 8.4 – Incremental dynamic analysis results for 9-story case study buildings: (a) R3-CH-9; (b) R3-SX-9; (c) OC-CH-9; (d) OC-SX-9; (e) R4-CH-9; and (f) R4-SX-9.

In addition to the plots, the IDA results are also summarized in Tables 8.12, 8.13, and 8.14 for the 3-, 6-, and 9-story buildings, respectively. These tables show the SF at collapse and the story that reached 10% drift to trigger said collapse for each GM. The average SF at failure and the most common story that reached 10% drift for these case study buildings, which did not consider the effects of gravity connections (G.BC = Pin), are also provided.

Table 8.12 – Summarized IDA results for 3-story case study buildings – Scale Factor at failure and story where drift first reached 10%

Building label and collapse identifiers		Ground Motion															Avg. SF / Mode Story
		1	2	3	4	5	6	7	8	9	10	11	12	13	14	15	
R3-CH-3	SF	2.2	2.8	2.6	3.4	2.2	1.0	3.0	1.8	3.8	2.8	1.6	2.0	1.8	1.2	2.4	2.31
	Story	1	1	2	1	3	3	2	1	2	1	3	1	2	2	1	1
OC-CH-3	SF	2.0	3.2	3.0	4.8	3.0	3.6	3.6	2.0	4.4	6.6	4.8	3.2	4.6	1.0	2.6	3.49
	Story	1	2	1	1	1	1	1	1	1	1	1	1	1	2	2	1
R4-CH-3	SF	3.0	5.2	4.0	3.4	1.6	1.4	4.0	2.8	3.4	3.2	3.0	2.8	3.6	1.8	4.0	3.15
	Story	3	2	1	1	1	1	2	2	1	2	2	1	3	1	1	1
R3-SX-3	SF	0.6	1.4	1.2	1.0	1.2	0.6	1.8	1.2	1.0	1.0	1.4	0.8	1.2	0.8	1.6	1.12
	Story	2	3	2	3	1	2	1	1	2	2	3	2	2	2	2	2
OC-SX-3	SF	1.2	1.8	1.4	1.4	1.0	1.0	2.4	0.8	1.0	1.2	1.6	1.6	1.2	0.6	1.4	1.31
	Story	2	2	1	2	2	2	1	2	1	3	2	2	2	3	2	2
R4-SX-3	SF	1.6	3.2	2.2	1.6	1.2	1.2	3.6	1.6	2.0	1.6	2.4	1.8	2.4	1.2	2.4	2.00
	Story	2	1	1	1	1	1	1	1	1	1	1	1	1	1	1	1
R4-SX-3-FIX	SF	3.8	3.8	3.0	2.0	1.6	1.2	3.8	2.2	2.0	2.0	2.0	2.6	2.2	1.8	3.2	2.48
	Story	1	1	1	1	1	1	1	1	1	1	1	1	1	1	1	1

Table 8.13 – Summarized IDA results for 6-story case study buildings – Scale Factor at failure and story where drift first reached 10%

Building label and collapse identifiers		Ground Motion															Avg. SF / Mode Story
		1	2	3	4	5	6	7	8	9	10	11	12	13	14	15	
R3-CH-6	SF	3.4	4.0	3.0	2.6	1.8	1.4	3.8	2.2	2.2	2.8	2.8	1.6	3.4	1.8	3.0	2.65
	Story	2	6	2	2	1	5	6	2	2	4	6	6	2	6	2	2
OC-CH-6	SF	3.6	4.8	4.2	2.8	3.0	2.0	5.0	2.6	3.4	3.8	3.6	3.2	3.8	2.4	3.0	3.41
	Story	1	1	1	1	1	1	1	1	2	1	4	2	1	1	1	1
R4-CH-6	SF	3.6	5.6	3.8	2.6	2.2	1.8	5.2	2.4	3.2	3.0	3.2	3.2	3.2	2.6	3.2	3.25
	Story	2	2	1	1	1	2	1	1	1	1	1	1	2	1	2	1
R3-SX-6	SF	1.6	3.0	2.2	2.0	1.0	1.8	2.6	1.4	3.0	2.8	3.8	2.8	2.2	1.2	1.6	2.20
	Story	2	1	1	2	2	1	1	1	1	1	1	1	2	2	2	1
OC-SX-6	SF	2.8	4.2	2.2	2.0	2.8	2.2	4.0	1.2	4.4	4.8	2.6	2.0	3.0	1.4	2.2	2.79
	Story	2	2	2	2	2	2	2	2	1	1	2	2	2	1	2	2
R4-SX-6	SF	4.8	6.8	3.0	2.0	2.6	2.0	4.2	1.6	3.4	2.8	3.2	3.4	3.2	2.4	2.4	3.19
	Story	1	1	1	1	1	1	1	2	1	1	1	1	2	1	1	1
R4-SX-6-FIX	SF	4.4	5.2	3.6	3.0	2.4	1.8	3.0	2.2	4.0	3.0	3.0	2.8	4.2	1.8	2.8	3.15
	Story	1	1	1	1	1	1	1	2	1	1	3	2	3	1	1	1

Table 8.14 – Summarized IDA results for 9-story case study buildings – Scale Factor at failure and story where drift first reached 10%

Building label and collapse identifiers		Ground Motion															Avg. SF / Mode Story
		1	2	3	4	5	6	7	8	9	10	11	12	13	14	15	
R3-CH-9	SF	3.6	3.6	1.4	2.2	1.2	2.4	3.4	1.8	1.6	3.2	1.4	2.0	1.6	2.8	3.6	2.39
	Story	2	4	8	2	8	2	9	9	2	1	9	2	2	2	2	2
OC-CH-9	SF	3.6	4.8	3.0	2.4	3.0	2.8	5.6	2.2	3.4	4.4	3.4	3.0	2.6	2.0	3.0	3.28
	Story	1	1	1	1	2	4	1	9	2	4	4	1	2	2	1	1
R4-CH-9	SF	3.0	4.6	2.4	2.4	2.4	2.4	5.2	1.6	2.2	4.0	3.2	2.8	3.0	1.8	3.4	2.96
	Story	4	4	4	2	2	4	2	1	4	3	3	3	2	4	2	4
R3-SX-9	SF	3.4	2.0	2.2	1.4	2.0	2.6	3.4	1.8	2.0	3.4	2.0	1.4	2.6	1.2	2.2	2.24
	Story	2	2	2	2	2	2	2	5	4	2	1	2	4	6	1	2
OC-SX-9	SF	4.4	4.0	1.8	2.0	2.0	3.0	3.4	2.2	5.0	2.4	3.2	2.8	2.6	1.2	2.0	2.80
	Story	2	2	2	2	2	2	2	8	1	2	2	1	2	4	2	2
R4-SX-9	SF	4.4	4.2	3.2	1.6	2.8	2.2	3.8	2.0	3.2	4.0	2.2	2.4	2.2	2.2	3.0	2.89
	Story	1	2	2	2	1	2	1	1	1	2	2	1	2	2	2	2
R4-SX-9-FIX	SF	3.2	4.0	3.4	2.8	2.8	2.2	4.0	1.8	2.4	2.4	4.0	3.2	3.0	2.2	3.2	2.97
	Story	2	1	2	1	1	1	2	1	2	2	1	1	1	1	2	1

As shown in Figure 8.1c, the moment capacity of the beam-column connections in proposed R = 4 split-x OCBF was equivalent to $0.87M_{p,beam}$. This preliminary study revealed that the behavior of the proposed R = 4 split-x OCBFs was not noticeably better than the current R = 3.25 split-x OCBFs when accounting for the relative weights of the SFRS. Thus, a second proposed R = 4 split-x OCBF design was created for each building height which assumed fixed beam-column connections within the braced bay ($M_{p,conn} > M_{p,beam,actual}$). This assumption allowed for consideration of the "best-case" proposed R = 4 split-x OCBF design, in which a connection capable of fully developing the plastic moment capacity of the beam is provided. These building models have "-FIX" appended to the end of their standard building labels, e.g. R4-SX-3-FIX.

For the 3-story case study buildings investigated, there was a noticeable trend of the chevron frames outperforming their split-x counterpart, regardless of system type. This difference was most severe for the 3-story current R = 3.25 OCBF buildings studied, in which the average SF at collapse for building OC-CH-3 was 3.49, while the average SF at collapse for the building OC-SX-3 was 1.31. In addition, OC-CH-3 experienced one collapse at the MCE (GM 14), while OC-SX-3 experienced five collapses at or below the MCE (GMs 5, 6, 8, 9, and 14).

Due to the modeling assumption of pinned gravity connections, all case study buildings relied on their SFRS to prevent collapse. The poor performance of the 3-story split-x case study buildings was partially attributable to this assumption. Given the lower natural period of these buildings (Table 8.11), there was increased importance on reserve capacity to prevent collapse during the more energetic ranges of the ground motions (Figure 3.16). Due to the lower reserve capacity in split-x SFRSs compared to their chevron counterpart, 3-story buildings that used a

split-x SFRS did not have adequate sources of reserve capacity to avoid collapse at SFs where chevrons buildings survived. Of the 3-story split-x case study buildings, the R = 3 displayed the worst behavior, collapsing at or below the MCE for 7 of 15 GMs (GMs 1, 4, 6, 9, 10, 12, 14), while the proposed R = 4 split-x OCBF displayed the best behavior and survived all GMs at the MCE.

Nearly all the chevron 3-story case study buildings avoided collapse at or below the MCE, with 2 observed collapses: one in building R3-CH-3 (GM 6), and one in building OC-CH-3 (GM14), with none in the proposed R = 4 OCBF building, R4-CH-3. Although R4-CH-3 avoided collapse at the MCE for every GM, the OC-CH-3 building had an average SF at collapse of 3.49 compared to 3.15 for R4-CH-3. This is only a part of the story, however, as the relative weights of the SFRSs for these two buildings are widely different (Table 8.1). A further discussion of building performance in consideration of weight of the SFRS, W_{SFRS}, is given in Section 8.3.3.

Collapse for the 3-story case study buildings was mostly triggered by the development of 10% drift within Story 1. Although the most common collapse-triggering story within 3-story split-x buildings was Story 2, a more thorough investigation revealed that while Story 2 did in fact reach 10% drift first during most GMs, the drift in Story 1 at collapse was often as high, between 9 and 10%. The development of large drifts that triggered collapse in stories other than Story 1 is a new observation that differs from what was observed by Stoakes (2012). However, unlike the constant 4.6 m. [15 ft.] story heights assumed throughout all case study buildings in this dissertation, Stoakes used case study buildings with a 5.5 m. [18 ft.] tall Story 1 and 4.0 m. [13 ft.] tall upper stories, a scenario that tends to cause development and isolation of drifts in the more flexible Story 1.

In the 6- and 9-story case study buildings, performance between chevron and split-x configurations was similar. Like the 3-story case study buildings, both chevron and split-x R = 3 buildings performed the worst of the SFRS alternatives for their respective building heights, which highlighted the benefits of seismic detailing and proportioning on collapse prevention performance. Another similarity across all building heights was the average collapse SF among current R = 3.25 OCBF chevrons and proposed R = 4 OCBF chevrons: buildings OC-CH-3, OC-CH-6, and OC-CH-9 all had slightly larger average collapse SFs (3.49, 3.41, and 3.28) than buildings R4-CH-3, R4-CH-6, and R4-CH-9 (3.15, 3.25, and 2.96). For split-x OCBFs, the trend was reversed, as buildings R4-SX-3, R4-SX-6, and R4-SX-9 achieved larger average collapse SFs (2.00, 3.19, and 2.89) than buildings OC-SX-3, OC-SX-6, and OC-SX-9 (1.31, 2.79, and 2.80).

Interestingly, the difference in behavior between R4-SX-3/6/9 buildings and R4-SX-3/6/9-FIX buildings was minor (Figure 8.3 and 8.4; Table 8.13 and 8.14). In other words, there appeared to be only a minimal effect in providing a fully rigid beam-column connection as opposed to one with finite stiffness and a flexural capacity of $0.87M_{p,beam}$ (Figure 8.1c). Furthermore, there was only a minimal difference in behavior between R4-SX-6/9 buildings and OC-SX-6/9 buildings, which suggested that providing a beam-column connection with $0.87M_{p,beam}$ (R4-SX buildings) as opposed to one with $0.14M_{p,beam}$ (OC-SX buildings) did not increase reserve capacity or collapse SF by the amount expected. Thus, the beam-column connection proportion requirements introduced by the proposed R = 4 OCBF provisions for split-x frames did not appear to have a measurable benefit on collapse prevention performance over the current R = 3.25 OCBF provisions, at least for the 6- and 9-story case study buildings

studied here. This observation is further analyzed through a reliability-based performance assessment (FEMA P695) in Section 8.3.

8.2.2 Single Record Investigations

To develop a more fundamental understanding of the underlying behavior that caused difference in the IDAs results among buildings studied, select case study buildings were compared against one another for a specific scaled GM. Four comparisons are presented, all for the 3-story case study buildings: (1) R3-CH-3 vs. R3-SX-3; (2) R4-CH-3 vs. R4-SX-3-FIX; (3) R4-CH-3 vs. OC-CH-3; and (4) R4-SX-3-FIX vs. OC-SX-3. The purpose of this investigation was to study the differences in mechanisms that formed in these various buildings, and how they differed from those discovered in the static cyclic simulations of Chapter 6.

The first comparison, R3-CH-3 vs. R3-SX-3 is shown in Figure 8.5 for GM14 with *SF* = 0.8. The behavior of the two case study buildings was identical for the first few seconds of the GM. Between t = 3 s. and 6 s., building R3-SX-3 began to carry a noticeably higher base shear, V_B, than R3-CH-3, which was attributable to its slightly larger brace sizes and associated larger stiffness. At around t = 7 s., R3-CH-3 experienced three limit states in quick succession—a common theme during these dynamic analyses. The sequence of limit states for building R3-CH-3 and the impact they had on V_B and roof drift (δ_R/h) are shown in Figure 8.6. The limit state sequence began with Story 3 North brace-gusset weld fracture, followed by Story 1 North brace-gusset weld fracture, and finally Story 2 North brace-gusset weld fracture. The only limit state that was associated with a significant drop in V_B, however, was Story 1 North brace-gusset weld fracture, which resulted in a significant period elongation. After each limit state, the SFRS within building R3-CH-3 began to develop long-link EBF mechanisms

at each level, as the W12x40 beams yielded at their midspan and offered enough reserve capacity to prevent collapse.

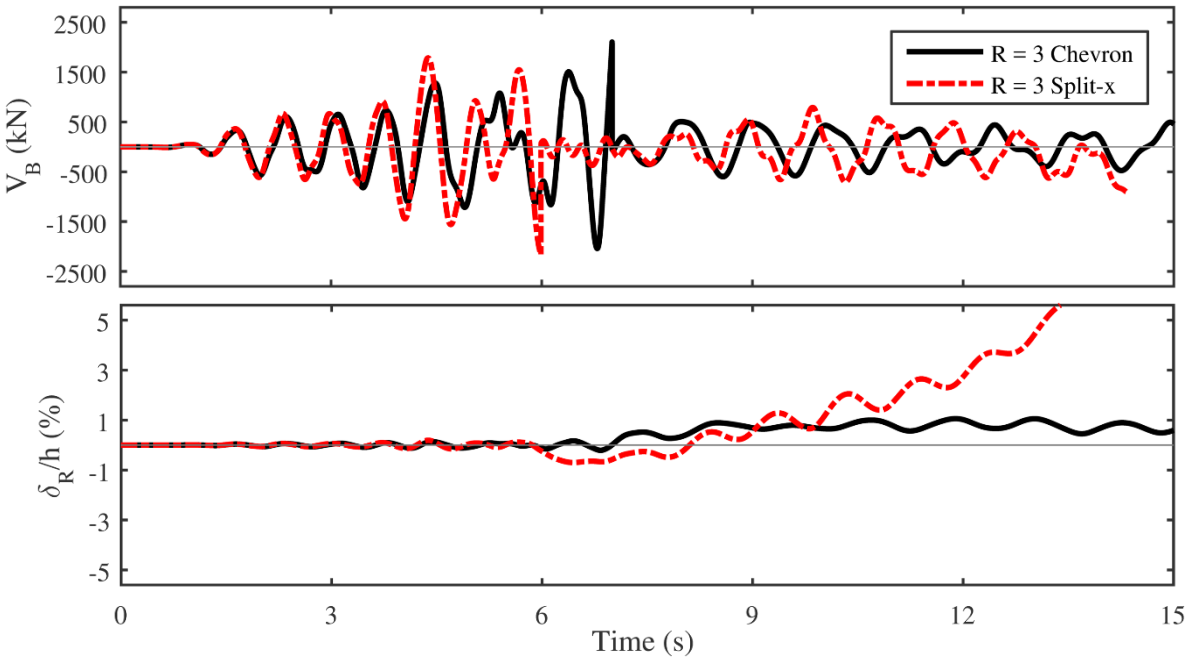

Figure 8.5 – Individual time history of R3-CH-3 and R3-SX-3 subjected to GM14 with *SF* = 0.8. (a) Base shear vs. time; and (b) Roof drift vs. time.

In building R3-SX-3, weld fracture occurred in all three stories under this scaled GM, and long-link EBF mechanisms formed at Level 2 and the roof level (Level R). Like what was seen in the static cyclic simulations (Chapter 6), the two-story mechanism at Level 2 (Figure 8.7 – [3]) had poor reserve strength. Following the development of this flexible two-story mechanism, the SFRS was incapable of offering enough reserve strength to prevent collapse, and drift concentrated and increased in both Story 1 and 2 until collapse occurred at t = 14.5 s. (Figure 8.7 – [4]). This comparative study illustrated clear differences between the mechanisms realized in dynamic simulations and static simulations of low-ductility buildings.

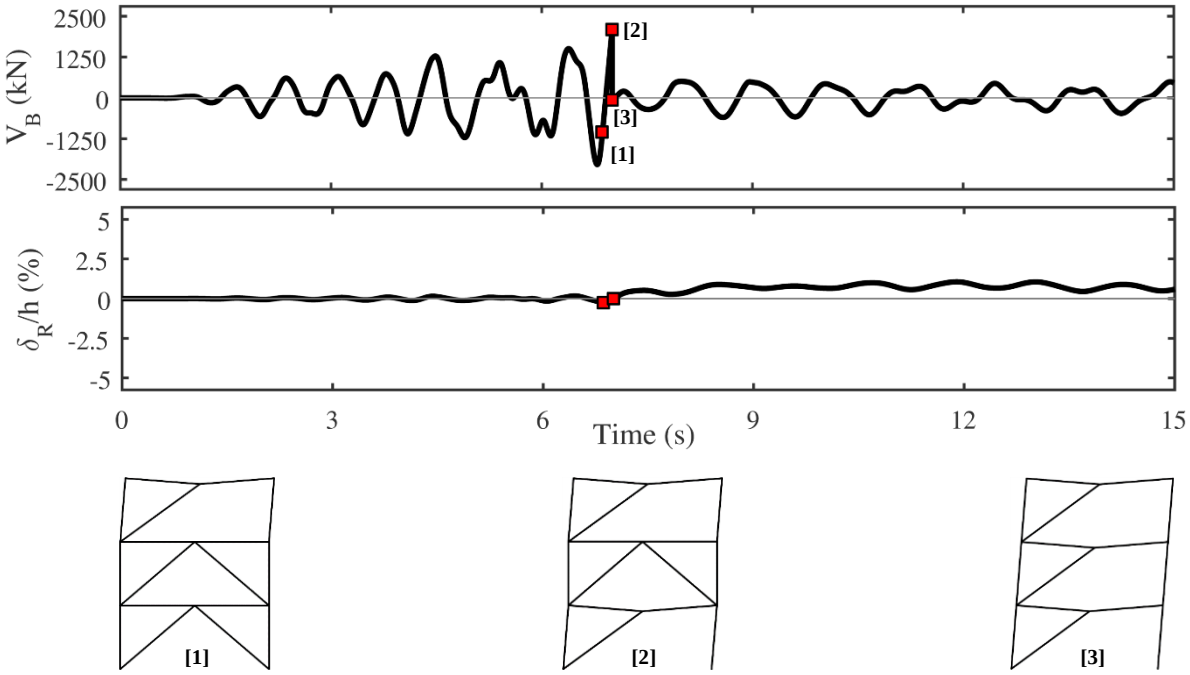

Figure 8.6 – Individual time history of R3-CH-3 subjected to GM14 with *SF* = 0.8. (a) Base shear vs. time; and (b) Roof drift vs. time. Indicators: [1] Story 3 North weld fracture; [2] Story 1 North weld fracture; and [3] Story 2 North weld fracture.

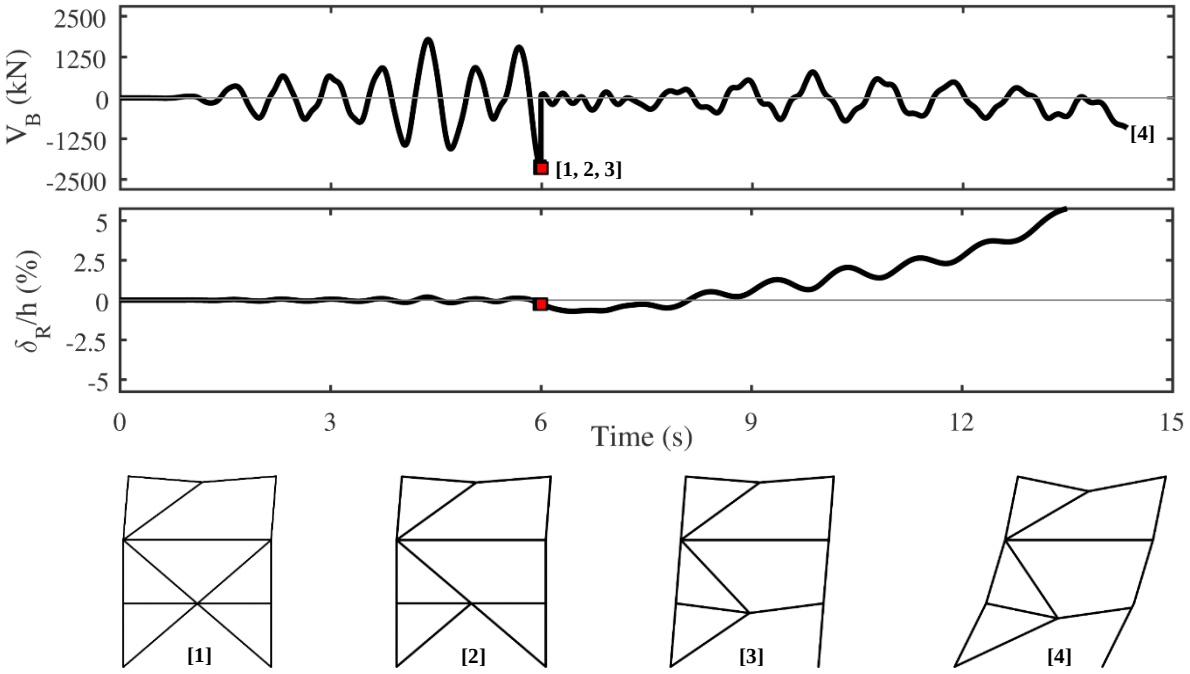

Figure 8.7 – Individual time history of R3-SX-3 subjected to GM14 with *SF* = 0.8. (a) Base shear vs. time; and (b) Roof drift vs. time. Indicators: [1] Story 3 North weld fracture; [2] Story 2 North weld fracture; [3] Story 1 North weld fracture; and [4] building collapse.

In the static cyclic simulations of Chapter 6, limit states were concentrated to one or two stories—a consequence of the assumed constant load profile. Dynamic simulations, conversely, gave an opportunity for the buildings to redistribute demands through the evolving inertial force profiles based on the changing story stiffnesses throughout a GM, resulting in limit states within multiple or all stories. This could be viewed as beneficial from a performance perspective so long as enough reserve capacity and ductility are available within each story to oppose the *P-Δ* effects and prevent collapse (Stoakes, 2012). The observation of limit states across multiple stories, and in some cases, all stories, was consistent for dynamic simulations of all case study buildings, including 6-story and 9-story buildings.

The second comparison, R4-CH-3 vs. R4-SX-3-FIX is shown in Figure 8.8 for GM2 with *SF* = 3.8. This comparison investigated the impact of system configuration on behavior, but from within the context of the proposed *R* = 4 OCBF design and its additional seismic detailing and proportioning requirements. The "-FIX" variant of the *R* = 4 system is selected for this study to assess the performance of a "best possible" *R* = 4 split-x OCBF which uses fixed beam-column connections compared to a typical *R* = 4 chevron OCBF which uses explicitly modelled connections (Figure 8.1a). As Figure 8.8 shows, R4-CH-3 survived the scaled GM while R4-SX-3-FIX collapsed. The trend of R4-SX-3-FIX collapsing at a SF that R4-CH-3 survived was true for 12 of the 15 GMs, and was true for all 15 GMs when comparing R4-CH-3 with the more realistic non "-FIX" version of R4-SX-3 with connection capacity shown in Figure 8.1b. The limit state sequences for R4-CH-3 and the R4-SX-3-FIX are shown in Figures 8.9 and 8.10, respectively, and show why many of the R4-SX-3-FIX buildings collapsed at lower *SFs* than their R4-CH-3 counterpart did.

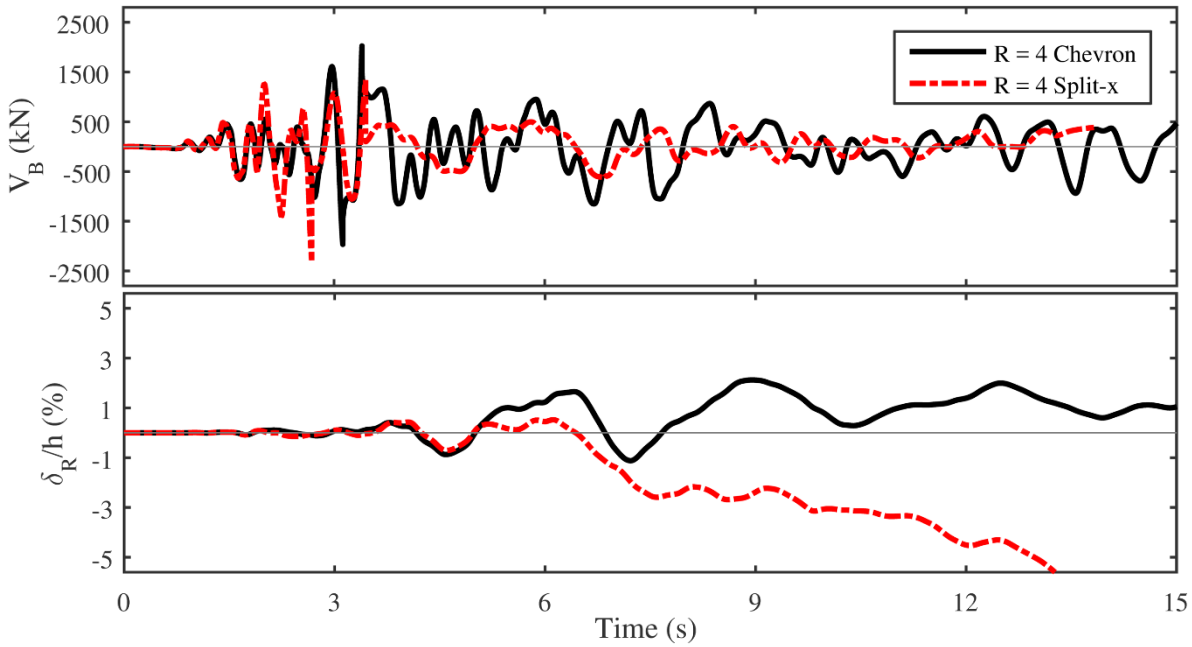

Figure 8.8 – Individual time history of R4-CH-3 and R4-SX-3-FIX subjected to GM2 with *SF* = 3.8. (a) Base shear vs. time; and (b) Roof drift vs. time.

As Figures 8.9 and 8.10 show, both buildings experienced limit states in all 3 stories during this scaled GM. One of the primary differences in the behavior of the two SFRSs was the avoidance of weld fracture in the Story 1 braces within building R4-CH-3. This was the case for Story 2 and 3 in the R4-CH-3 example presented in Figure 8.9, while Story 1 represents one of the

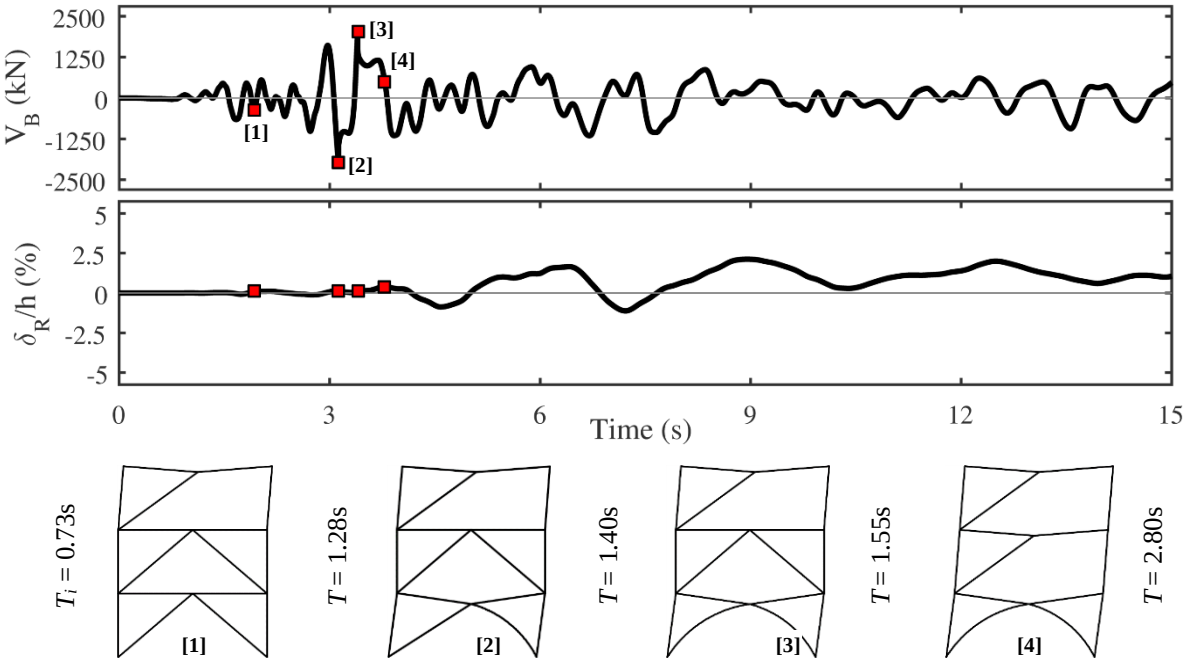

Figure 8.9 – Individual time history of R4-CH-3 subjected to GM2 with *SF* = 3.8. (a) Base shear vs. time; and (b) Roof drift vs. time. Indicators: [1] Story 3 North weld fracture; [2] Story 1 North brace buckling; [3] Story 1 South brace buckling; and [4] Story 2 North weld fracture.

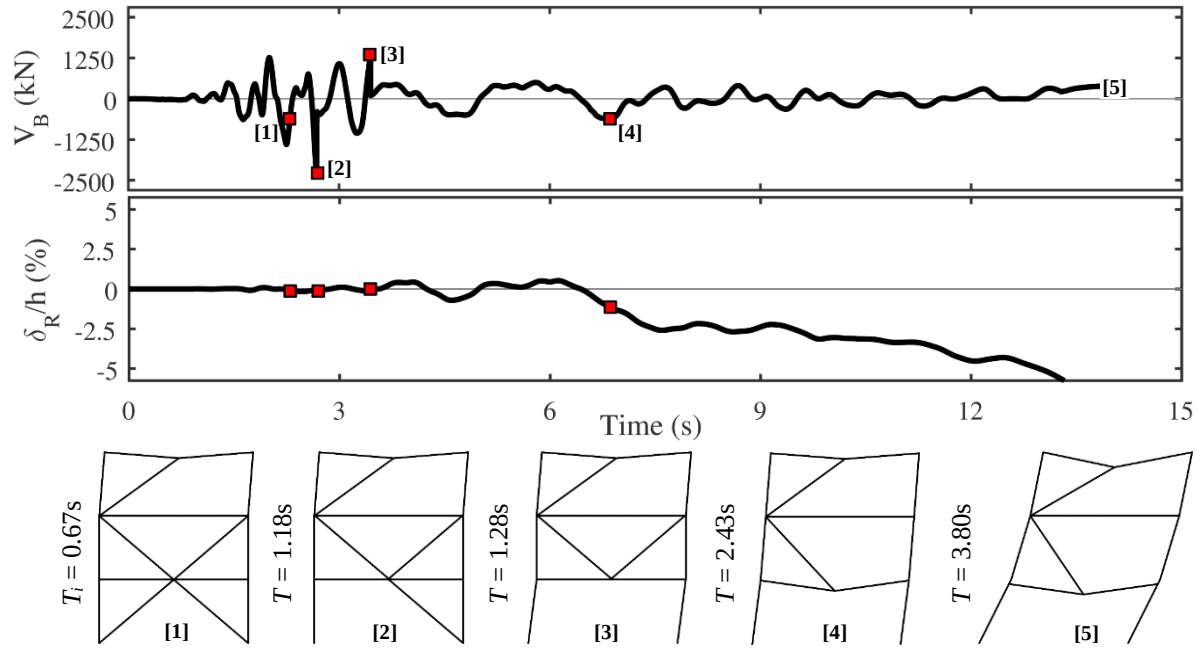

Figure 8.10 – Individual time history of R4-SX-3-FIX subjected to GM2 with *SF* = 3.8. (a) Base shear vs. time; and (b) Roof drift vs. time. Indicators: [1] Story 3 North weld fracture; [2] Story 1 South weld fracture; [3] Story 1 North weld fracture; [4] Story 2 North weld fracture; and [5] building collapse.

exceptions in which the brace buckling capacity was lower than brace-gusset weld capacity. This was not a choice made in the design process, and in reality it is unclear whether brace buckling or brace-gusset weld fracture will be the governing limit state within the proposed *R* = 4 OCBFs as a true capacity design is not performed. However, if weld overstrength is as large as in the full-scale experimental tests (Chapter 4—1.8R_n), it is significantly more likely that brace buckling will be the governing limit state over brace-gusset weld fracture in an actual building. In addition, no weld overstrength was assumed for these case study buildings (Weld capacity = 1.0R_n). The ductile brace buckling in Story 1 and long-link EBF mechanisms that formed in all three stories contribute to the reserve capacity of R4-CH-3, and collapse was avoided (Figure 8.9). Due to the slightly stronger beams in the R4-CH-3 than in R3-CH-3, the reserve capacity from the long-link EBF mechanism was larger at each level, and this is reflected in the collapse SFs for the two buildings, as R4-CH-3 surviving SFs larger than R3-CH-3 for 12 of 15 GMs.

Unlike building R4-CH-3, building R4-SX-3-FIX was unable to avoid collapse for this scaled GM following development of limit states in all three stories (Figure 8.10). The inability of R4-SX-3-FIX to avoid collapse was attributable to the detrimental two-story mechanism that formed (Figure 8.10 – [4]) in combination with brace-gusset weld fracture within both Story 1 braces (Figure 8.10 – [3]). The combined effect of these two limit states was that the SFRS lost a significant amount of stiffness. The change in building period associated with each limit state is shown in Figures 8.9 and 8.10 to illustrate this fact, as the final configuration of R4-SX-3-FIX had T = 3.80s (prior to collapse) while the final configuration of R4-CH-3 had T = 2.80s. In this case, the loss of stiffness was so high that even the fixed beam-column connections were incapable of providing enough reserve strength to overcome the *P-Δ* effects

on the flexible structure and prevent collapse. The schematics in Figures 8.9 and 8.10 show that even with the fixed beam-column connections, the capacity of the mechanism that forms within the split-x configuration could not achieve that of the chevron configuration. This is because the chevron configuration allowed for the formation of beam midspan hinges at every level, while the split-x restricts formation of midspan beam hinges to form at only every other level. The discovery that even fixed beam-column connections were not enough to bring the split-x configuration up to the performance level of the chevron configuration requires deeper exploration, and an alternative suggestion for improving the behavior of the $R = 4$ split-x OCBF is offered at the end of this chapter.

The impact of prescribing flexural strength to beam-column connections within split-x frames does help performance in some cases, as is shown by the third comparison, R4-SX-3-FIX vs. OC-SX-3. Behavior of these two case study buildings for GM9 at the MCE ($SF = 1.0$) is shown in Figure 8.11. For this comparison, both R4-SX-3-FIX and OC-SX-3 developed a similar sequence of limit states and an identical mechanism at around $t = 17$ s. comprising brace-gusset weld fractures in both Story 2 braces as well as Story 1 and 3 North braces. The difference in behavior of the two buildings following the development of this mechanism is attributable to the differences in their beam-column connections.

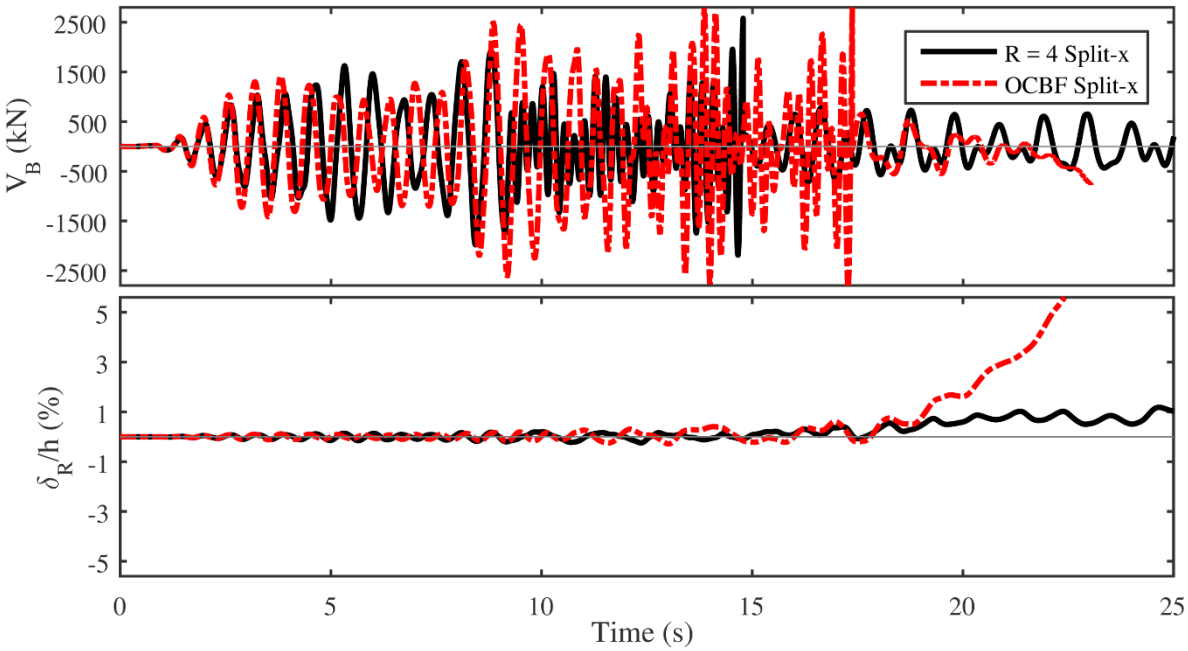

Figure 8.11 – Individual time history of R4-SX-3-FIX and OC-SX-3 subjected to GM9 with *SF* = 1.0. (a) Base shear vs. time; and (b) Roof drift vs. time.

In this scaled GM, the rigid beam-column connections within R4-SX-3-FIX offered enough flexural resistance to mobilize the two-story long-link EBF mechanism at Level 2 (Figure 8.12 – [3, 4]) and prevent collapse. When the same mechanism formed at Level 2 in OC-SX-3, the weaker beam-column connections in this building (Figure 8.1b, $M_{p,conn}$ = $0.14M_{p,beam}$) were unable to offer enough flexural strength or stiffness to oppose the flexible mechanism and prevent the concentration and accumulation of drifts in Story 1 and 2. Thus, drift continuously increased following the formation of this two-story mechanism (Figure 8.13 – [4]) until the building collapsed at t = 23 s. This case study suggested that, at least in some cases, there appears to be a benefit of the proposed R = 4 OCBF proportioning requirement for beam-column connections within split-x frames over the current R = 3.25 OCBF provisions, which do not specify a flexural capacity for these connections.

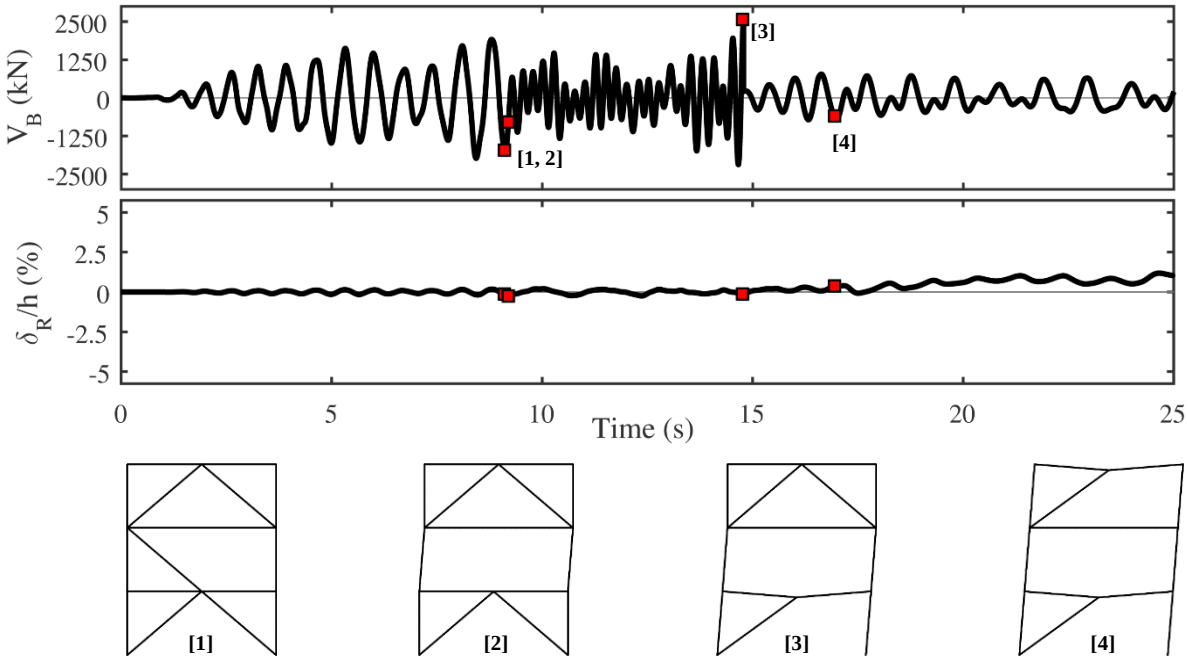

Figure 8.12 – Individual time history of R4-SX-3-FIX subjected to GM9 with *SF* = 1.0. (a) Base shear vs. time; and (b) Roof drift vs. time. Indicators: [1] Story 2 North weld fracture; [2] Story 2 South weld fracture; [3] Story 1 North weld fracture; and [4] Story 3 North weld fracture.

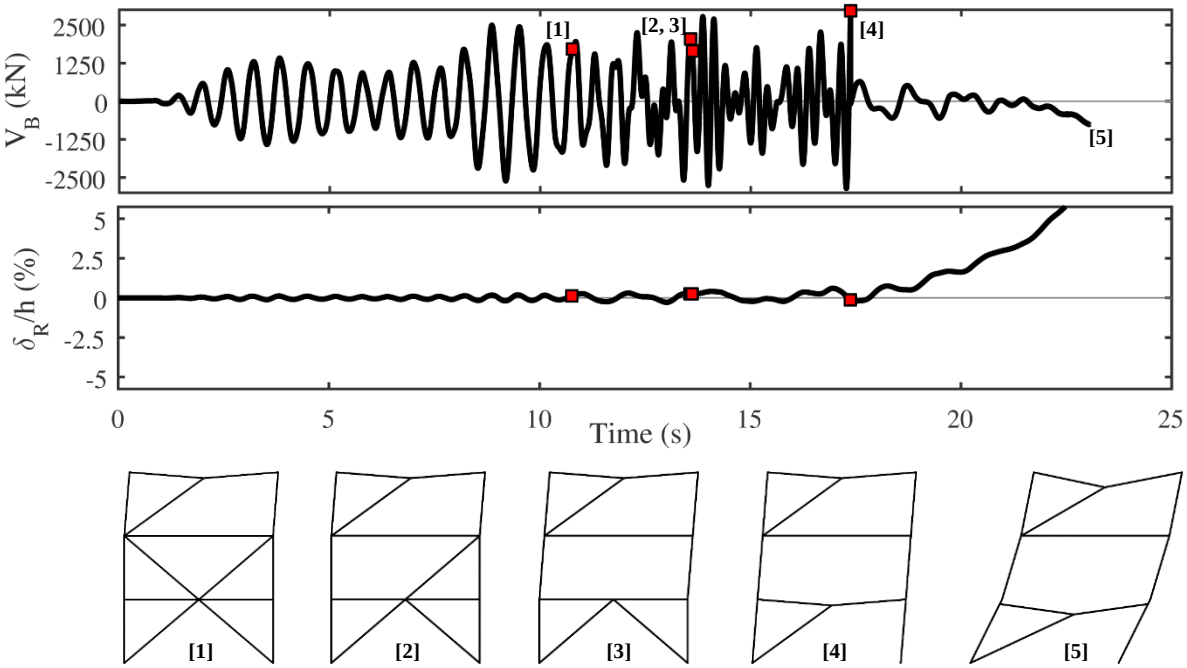

Figure 8.13 – Individual time history of OC-SX-3 subjected to GM9 with *SF* = 1.0. (a) Base shear vs. time; and (b) Roof drift vs. time. Indicators: [1] Story 3 North weld fracture; [2] Story 2 South weld fracture; [3] Story 2 North weld fracture; [4] Story 1 North weld fracture; and [5] building collapse.

The final comparison study assessed the viability and benefits of the proposed R = 4 OCBF provisions compared to the current R = 3.25 OCBF provisions for chevron configurations in the context of dynamic analyses. The benefits of the removal of the force-imbalance requirements and relaxation of KL/r requirements in the proposed R = 4 OCBF provisions were shown theoretically in Chapter 7, and are displayed in Figure 8.14 for GM14 with SF = 1.0 through a comparison of R4-CH-3 and OC-CH-3. As Figure 8.14 shows, R4-CH-3 and OC-CH-3 both experienced multiple limit states and accumulated increasingly large δ_R/h at around t = 7 s. However, in R4-CH-3 this increase in δ_R/h plateaued at 2.5%, while δ_R/h increased without bound in OC-CH-3, leading to collapse at t = 12.5 s. The individual limit state plots for R4-CH-3 (Figure 8.15) and OC-CH-3 (Figure 8.16) during this time history analysis reveal why R4-CH-3 avoided collapse, but OC-CH-3 did not.

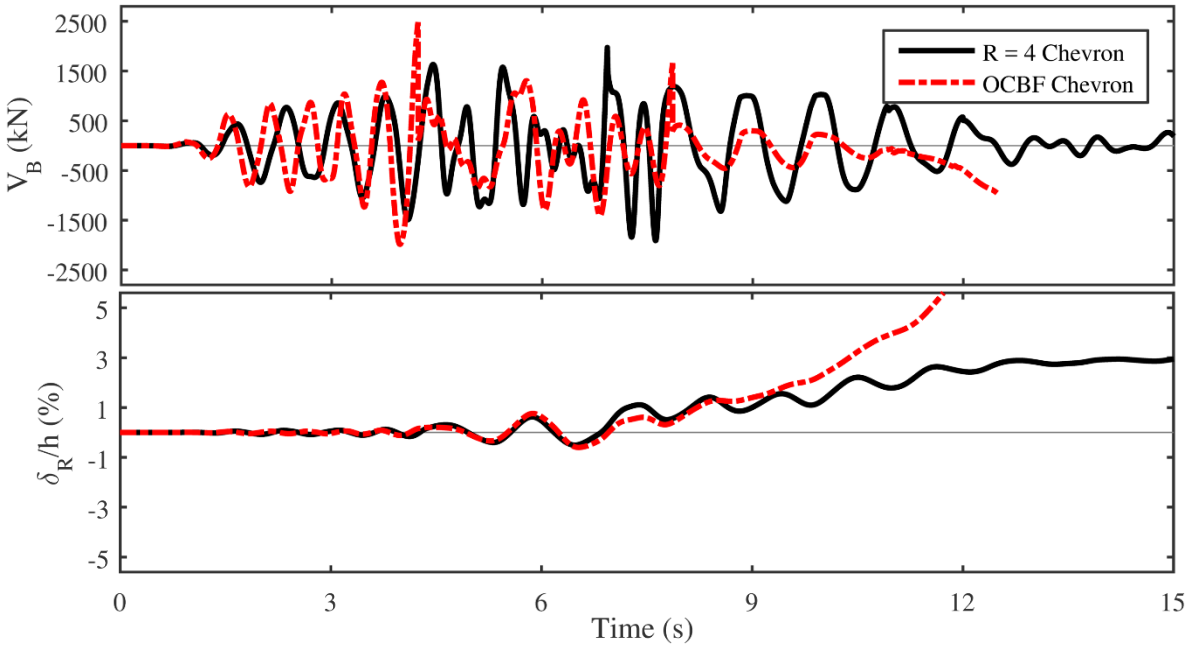

Figure 8.14 – Individual time history of R4-CH-3 and OC-CH-3 subjected to GM14 with SF = 1.0. (a) Base shear vs. time; and (b) Roof drift vs. time.

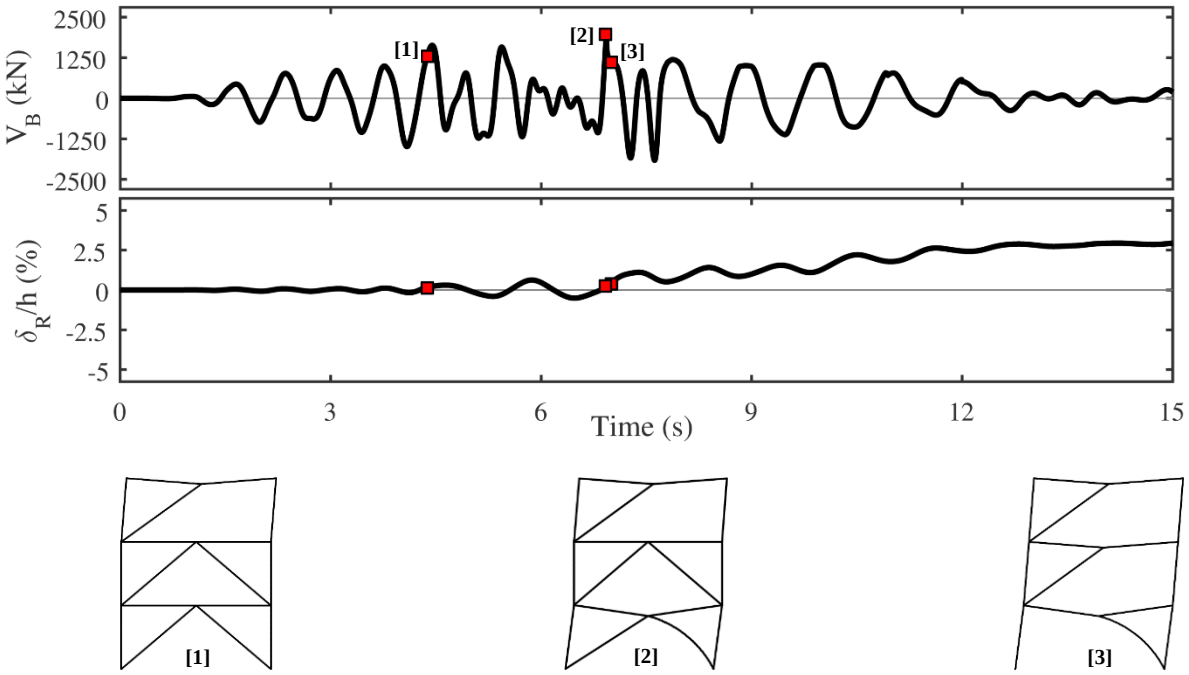

Figure 8.15 – Individual time history of R4-CH-3 subjected to GM14 with *SF* = 1.0. (a) Base shear vs. time; and (b) Roof drift vs. time. Indicators: [1] Story 3 North weld fracture; [2] Story 1 North brace buckling; and [3] Story 2 North weld fracture.

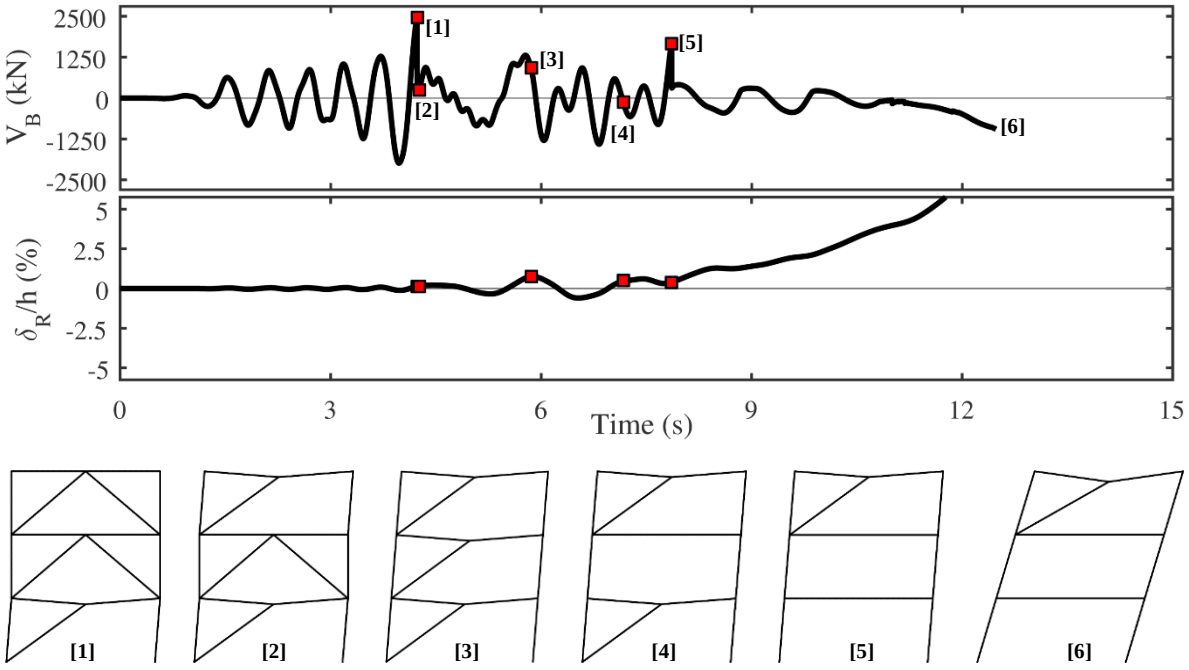

Figure 8.16 – Individual time history of OC-CH-3 subjected to GM14 with *SF* = 1.0. (a) Base shear vs. time; and (b) Roof drift vs. time. Indicators: [1] Story 1 North weld fracture; [2] Story 3 North weld fracture; [3] Story 2 North weld fracture; [4] Story 2 South weld fracture; [5] Story 1 South weld fracture; and [6] building collapse.

In R4-CH-3, a long-link EBF mechanism formed in all three stories and lent reserve capacity that contributed to collapse prevention. In OC-CH-3, however, the deep W30 Level 2 and 3 beams were strong enough to develop the weld capacity of the remaining brace following brace-gusset weld fracture within a single brace in their respective stories. Thus, the second brace within these stories experienced a brace-gusset weld fracture later in the time history, eliminating the potential for the formation of a long-link EBF mechanism and creating a soft-story mechanism with reserve capacity from column bending only. The beneficial result of removing the force-imbalance requirement for the design of beams within the proposed R = 4 OCBF provisions was shown through this example, and compliments the suggestions of Chapter 7 that formed the basis for the R = 4 OCBF proposal.

As the schematics of Figures 8.15 and 8.16 show, the potential reserve strength of R4-CH-3 is higher than that of OC-CH-3 because of the mechanisms that form. The strong beams of OC-CH-3 do not allow for the formation of midspan hinges in the first and second story beams, while the smaller beams within R4-CH-3 can develop plastic hinges and contribute to reserve capacity. Methods for calculating the reserve capacity of a typical low-ductility system such as those proposed by Stoakes (2012) allow for quick checks of lateral system strength for damaged chevron CBFs. For example, in a single bay single story chevron frame, assuming pinned beam-column connections and column bases, the reserve strength of an EBF mechanism is $2Mp_{col}/h + 2Mp_{beam}/h$. This is $2Mp_{beam}/h$ larger than a purely column bending mechanism (such as those that formed in the lower two stories of OC-CH-3 in this example), which has a reserve capacity of only $2Mp_{col}/h$. This difference is how R4-CH-3 avoids collapse when OC-CH-3 does not. More information on the calculation and approximation of reserve capacity for simple cases such as these are provided by Stoakes (2012) and Bradley (2016).

8.2.3 Summary of Dynamic Simulations

Dynamic simulations of the 18 case study buildings allowed for the consideration of many scenarios that the static cyclic simulations of Chapter 6 could not investigate. Specifically, the impact of stiffness changes on lateral inertia forces was on clear display in the single record investigations as most of the case study buildings investigated experienced limit states in each of story. This was a significant difference from the static cyclic simulations where limit states were concentrated to one or two stories due to use of a constant load profile. Thus, these simulations allowed for a proper investigation of 6- and 9-story buildings, whose behavior was often dominated by higher-mode effects as their IDA summaries show. The influence of higher-mode effects on these buildings is identifiable from the collapse story listings, which in the case of many 6- and 9-story buildings, was among the upper stories (Tables 8.13. and 8.14).

Because limit states often occurred in multiple stories, the dynamic simulations served as a useful tool for assessing the performance of various mechanisms that were initially discovered in Chapter 6 in the context of opposing the *P-Δ* effects introduced from the consideration of gravity loading. In general, the split-x configuration had poor performance in this regard for the 3-story buildings relative to buildings that used a chevron configuration. This disparity was mostly unidentifiable in the 6- and 9-story buildings, however, as the split-x and chevron buildings had comparable collapse SFs.

Performance of most 3-story buildings was worse than the performance of their 6- and 9-story counterparts. This was attributable to the reduced fundamental period of these structures, which made them more susceptible to the higher energy ranges of the GMs used in this study, which were below T = 1.0 s. In addition, the 3-story building models had twice as

many gravity bays per braced bay than the 6- and 9-story buildings, which created a stronger *P-Δ* effect without gravity connection contribution to offer relief.

Finally, the dynamic simulations allowed for a further investigation into the behavior of frames designed using the proposed R = 4 OCBF provision introduced in Chapter 7 in comparison to frames designed using the current R = 3.25 OCBF provisions. In general, the buildings designed with the proposed R = 4 OCBF provisions performed better than their current R = 3.25 OCBF counterparts. The R = 4 chevron OCBFs collapsed at slightly lower scale factors than their R = 3.25 OCBF counterpart, but did so while having significantly lower W_{SFRS} (Tables 8.1–8.3) and developing better mechanisms from a reserve capacity perspective (Figures 8.14–8.16). The R = 4 split-x OCBF buildings all experienced collapse at an average scale factor larger than their R = 3.25 split-x OCBF counterparts, and the collapse scale factor was further increased when fixed beam-column connections were assumed within the SFRS ("-FIX" variants).

8.3 COLLAPSE PREVENTION PERFORMANCE EVALUATION

The IDAs and single record investigations offer valuable insight into the relative behavior of three low-ductility SFRS alternatives for low and moderate seismic design: the R = 3 CBF, the current R = 3.25 OCBF, and the proposed R = 4 OCBF. Specifically, the single record investigations helped answer previously open questions on the spread of limit states throughout multiple stories of a low-ductility building during a seismic event. A secondary benefit of the IDAs was that they gave the necessary information to perform a comprehensive performance evaluation of the three low-ductility SFRS alternatives using the framework of FEMA P695: *Quantification of Building Seismic Performance Factors* (FEMA, 2009). The FEMA P695 document outlines a procedure for evaluating SFRSs and their collapse

prevention performance. Thus, the FEMA P695 procedure is useful in assessing the performance of the proposed R = 4 OCBF SFRS relative to its low-ductility alternatives, the R = 3 and R = 3.25 OCBF, neither of which have been rigorously investigated using nonlinear models as comprehensive as the ones presented in this dissertation. The FEMA P695 process is composed of three main parts: (1) development of initial fragility curves from IDA results; (2) identification and evaluation of uncertainty in the IDA results; and (3) development of adjusted fragility curves that incorporate the uncertainty, which are then used to evaluate performance based on an acceptable collapse margin ratio.

8.3.1 Initial Fragility Curves

The FEMA P695 performance assessment is based on the creation of initial fragility curves, which are lognormal cumulative distribution functions (CDFs) relating ground motion (GM) intensity (SFs) to the probability of collapse (Ibarra et al., 2002). The probability of collapse is calculated by counting the number of GMs that the building collapses under for a given *SF*. For example, if a building collapses at the MCE (*SF* = 1.0) for 5 of the 15 GMs, a discrete point is plotted at *SF* = 1.0, and collapse probability = 5/15 = 0.333. This procedure is continued until a building collapses in all 15 GMs for a given SF, i.e. collapse probability = 15/15 = 1.0. The discrete points are then fit with a lognormal CDF with properties μ and σ, which define the mean and standard deviation of the collapse SFs, respectively. Two example initial fragility curves are shown in Figure 8.17, for R3-CH-3 and OC-SX-3. As shown in Figure 8.17, R3-CH-3 experienced 1 collapse at the MCE, or p(Collapse) = 1/15 = 0.067, while OC-SX-3 experienced 5 collapses at the MCE, or p(Collapse) = 5/15 = 0.333. Per the FEMA P695 methodology, uncertainty must be considered before a more meaningful assessment of

collapse probability can be made. The initial fragility curves for all 18 case study buildings are included in Appendix A.

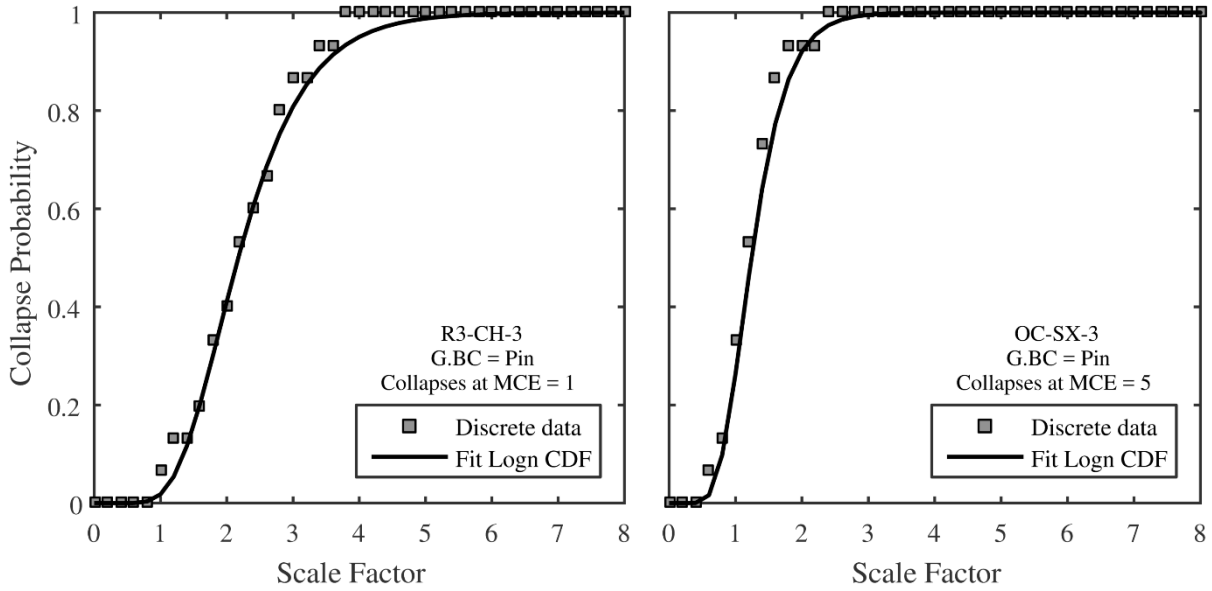

Figure 8.17 – Initial fragility curves for building (a) R3-CH-3; and (b) OC-SX-3 for use in FEMA P695 performance evaluation.

8.3.2 Total System Collapse Uncertainty

After creating initial fragility curves, the next step in the FEMA P695 process is to quantify various sources of uncertainty that affect the IDA results used to generate said curves. FEMA P695 defines four sources of uncertainty, β, which must be investigated during this process: (1) Record-to-Record Uncertainty — β_{RTR}; (2) Design Requirements Uncertainty — β_{DR}; (3) Test Data Uncertainty — β_{TD}; and (4) Modeling Uncertainty — β_{MDL}. The total system uncertainty, β_{TOT}, is calculated from the square root of the sum of squares of the four individual sources of uncertainty: $\beta_{TOT} = \sqrt{(\beta^2_{RTR} + \beta^2_{DR} + \beta^2_{TD} + \beta^2_{MDL})}$.

The first source of uncertainty, β_{RTR}, is due to variability in the response of the building models to different ground motions. Based on the recommendations of FEMA P695, a value of 0.40 was selected for β_{RTR} (FEMA, 2009):

> Based on available research and studies of example archetype evaluations using the Far-Field ground motion record set in Appendix A, a fixed value of β_{RTR} = 0.40 is assumed in the performance evaluation of systems with significant period elongation. Most systems, even those with limited ductile capacity, have significant period elongation before collapse, and are appropriately evaluated using this value.

Uncertainty in design requirements, β_{DR}, is related to the completeness and robustness of the design requirements in combination with the confidence in the basis of those requirements. The FEMA P695 document gives a matrix to help with the choice of β_{DR} based on a rating of "Low", "Medium", or "High" for these two parameters (robustness, confidence), which is shown in Figure 8.18. The choice of β_{DR} for the SFRSs studied in this chapter is shown in this figure and differed based on the system type.

Table 3-1 Quality Rating of Design Requirements

Completeness and Robustness	Confidence in Basis of Design Requirements		
	High	Medium	Low
High. Extensive safeguards against unanticipated failure modes. All important design and quality assurance issues are addressed.	(A) Superior β_{DR} = 0.10	(B) Good β_{DR} = 0.20	(C) Fair β_{DR} = 0.35
Medium. Reasonable safeguards against unanticipated failure modes. Most of the important design and quality assurance issues are addressed.	(B) Good β_{DR} = 0.20	(C) Fair β_{DR} = 0.35	(D) Poor β_{DR} = 0.50
Low. Questionable safeguards against unanticipated failure modes. Many important design and quality assurance issues are not addressed.	(C) Fair β_{DR} = 0.35	(D) Poor β_{DR} = 0.50	--

Proposed R = 4 OCBF & Current R = 3.25 OCBF

R = 3

Figure 8.18 – FEMA P695 table for selection of β_{DR} with selections for the SFRSs studied in this chapter (Modified from FEMA, 2009).

Although acceptable behavior of low-ductility buildings has been well documented from post-earthquake investigations (Section 2.1), one of the central themes of this dissertation

is the acknowledgement that the sources of this acceptable behavior are not well understood. Thus, the confidence in design requirements for these systems was labeled as "Medium", as opposed to a SCBF, which would have received a rating of "High" for this category. Further study of low-ductility systems, particularly the proposed R = 4 OCBF, may warrant an upgrade in this category to "High" in the future. As for the completeness and robustness characteristics, the R = 3 system was assigned the "Low" rating due to the lack of seismic detailing and proportioning involved in its design. Both the current R = 3.25 OCBF and proposed R = 4 OCBF were assigned a rating of "Medium" since their designs include some degree of seismic detailing and proportioning requirements. Like the confidence rating, further study of the proposed R = 4 OCBF may warrant an upgrade of this category to "High" in the future, but for now it was assumed at the same level as the current R = 3.25 OCBF to better compare the relative performance of the two systems using the FEMA P695 methodology. Given these selections, a value of β_{DR} = 0.50 was assigned to buildings which use an R = 3 SFRS and a value of β_{DR} = 0.35 was assigned to buildings which use either the current R = 3.25 OCBF or proposed R = 4 OCBF (Figure 8.18).

Uncertainty in test data, β_{TD}, is related to the completeness and robustness of the test data in combination with the confidence in the data itself. The completeness and robustness of the test data is related to how well the system behavior is understood, while the confidence in test data is related to the repeatability of the testing or the similarity with results from other testing programs. Like β_{DR}, FEMA P695 gives a matrix to help with the choice of β_{TD} based on a rating of "Low", "Medium", or "High" for these two parameters (robustness, confidence) which is shown in Figure 8.19. Based on the information gained from the experimental test program regarding behavior of the long-link EBF mechanism in chevron frames, detrimental

behavior of two-story mechanisms in split-x frames, and detrimental behavior of braces with high *b*/*t* ratios, a ranking of "Medium" was selected for the completeness and robustness

Table 3-2 Quality Rating of Test Data from an Experimental Investigation Program

Completeness and Robustness	Confidence in Test Results		
	High	Medium	Low
High. Material, component, connection, assembly, and system behavior well understood and accounted for. All, or nearly all, important testing issues addressed.	(A) Superior β_{TD} = 0.10	(B) Good β_{TD} = 0.20	(C) Fair β_{TD} = 0.35
Medium. Material, component, connection, assembly, and system behavior generally understood and accounted for. Most important testing issues addressed.	(B) Good β_{TD} = 0.20	(C) Fair β_{TD} = 0.35	(D) Poor β_{TD} = 0.50
Low. Material, component, connection, assembly, and system behavior fairly understood and accounted for. Several important testing issues not addressed.	(C) Fair β_{TD} = 0.35	(D) Poor β_{TD} = 0.50	--

Figure 8.19 – FEMA P695 table for selection of β_{TD} with the value assumed for the SFRSs studied in this chapter (Modified from FEMA, 2009).

criterion. Due to the limited number of test results (2 full-scale tests) and the lack of similar full-scale testing of low-ductility systems to compare the test data with, a rating of "Medium" was selected for the confidence in test results category, yielding β_{TD} = 0.35 for all case study buildings.

Like the earlier two sources of uncertainty, the final source, β_{MDL}, is also defined from a table in FEMA P695 based on a rating from "Low" to "High" for two categories: accuracy and robustness of models, and representation of collapse characteristics (Figure 8.20). For individual buildings, FEMA P695 recommends the choice of "High" for the representation of collapse characteristics, because the building configuration is a known quantity (FEMA, 2009). Thus, the only choice that was needed to determine β_{MDL} was the accuracy and robustness of the model. Based on the following definition of a "High" rating for model robustness in FEMA P695, this rating was selected, in acknowledgement that the nonlinear models used in this study incorporated the aspects mentioned (FEMA, 2009):

High. Nonlinear models directly simulate all predominate inelastic effects, from the onset of yielding through strength and stiffness degradation causing collapse. Models employ either concentrated hinges or distributed finite elements to provide spatial resolution appropriate for the proposed system. Computational solution algorithms are sufficiently robust to accurately track inelastic force redistribution, including cyclic loading and unloading, without convergence problems, up to the point of collapse.

Table 5-3 Quality Rating of Index Archetype Models

Representation of Collapse Characteristics	Accuracy and Robustness of Models		
	High	Medium	Low
High. Index models capture the full range of the archetype design space and structural behavioral effects that contribute to collapse.	(A) Superior $\beta_{MDL} = 0.10$	(B) Good $\beta_{MDL} = 0.20$	(C) Fair $\beta_{MDL} = 0.35$
Medium. Index models are generally comprehensive and representative of the design space and behavioral effects that contribute to collapse.	(B) Good $\beta_{MDL} = 0.20$	(C) Fair $\beta_{MDL} = 0.35$	(D) Poor $\beta_{MDL} = 0.50$
Low. Significant aspects of the design space and/or collapse behavior are not captured in the index models.	(C) Fair $\beta_{MDL} = 0.35$	(D) Poor $\beta_{MDL} = 0.50$	--

Figure 8.20 – FEMA P695 table for selection of β_{MDL} with the value assumed for the SFRSs studied in this chapter (Modified from FEMA, 2009).

Based on this choice, a value of β_{MDL} = 0.10 was obtained, thus completing the individual selections of uncertainty needed for determination of total system collapse uncertainty, β_{TOT}.

Using the determined values of β_{RTR} (0.4), β_{DR} (R = 3 — 0.5; OCBFs — 0.35), β_{TD} (0.35), and β_{MDL} (0.10), β_{TOT} was calculated from $\beta_{TOT} = \sqrt{(\beta^2_{RTR} + \beta^2_{DR} + \beta^2_{TD} + \beta^2_{MDL})}$, giving a value of β_{TOT} = 0.75 for R = 3 frames and β_{TOT} = 0.65 for current R = 3.25 and proposed R = 4 OCBFs. This was slightly lower than the uncertainty β_{TOT} = 0.80 assumed by Stoakes (2012) and Hines et al. (2009) for R = 3 frames, and was attributable to improvements in nonlinear models which reduced modeling uncertainty. A summary of the IDA uncertainty for the systems is given in Table 8.15. Per the definitions of the uncertainty components and the

assumptions made to select each value, total uncertainty only changed based on the SFRS type, and was unaffected by change in system configuration or story height in this study.

Table 8.15 – Summary of uncertainty for performance assessment

SFRS in Case Study Building	β_{RTR}	β_{DR}	β_{TD}	β_{MDL}	β_{TOT}
R = 3	0.4	0.5	0.35	0.10	0.75
Current R = 3.25 OCBF	0.4	0.35	0.35	0.10	0.65
Proposed R = 4 OCBF	0.4	0.35	0.35	0.10	0.65

8.3.3 Adjusted Fragility Curves

After β_{TOT} was determined, it was used to replace the standard deviation (σ) of the lognormal CDF in the initial fragility curves, which were fit to the collapse data, creating a new lognormal CDF with properties μ and β_{TOT}. Adjusting the fragility curves per the system uncertainty has a significant effect on the shape of the collapse distribution, and thus, the FEMA P695 collapse probability. The degree of this significance is shown through an example in Figure 8.21, in which the adjusted fragility curves of R4-SX-9 are presented with different choices for β_{TOT}: (a) initial fragility curve; (b) the assumed value for this study for OCBFs (0.65); and (c) the value used by Stoakes and Hines et al. in previous research (0.80). As shown in Figure 8.21a, when uncertainty was not considered, the probability of collapse or failure, *p(F)*, of the building at the MCE (SF = 1.0) is 0.01. When uncertainty was considered, the collapse probability at MCE increased to 0.07 for β_{TOT} = 0.65 (Figure 8.18b) and 0.11 for β_{TOT} = 0.80 (Figure 8.18c).

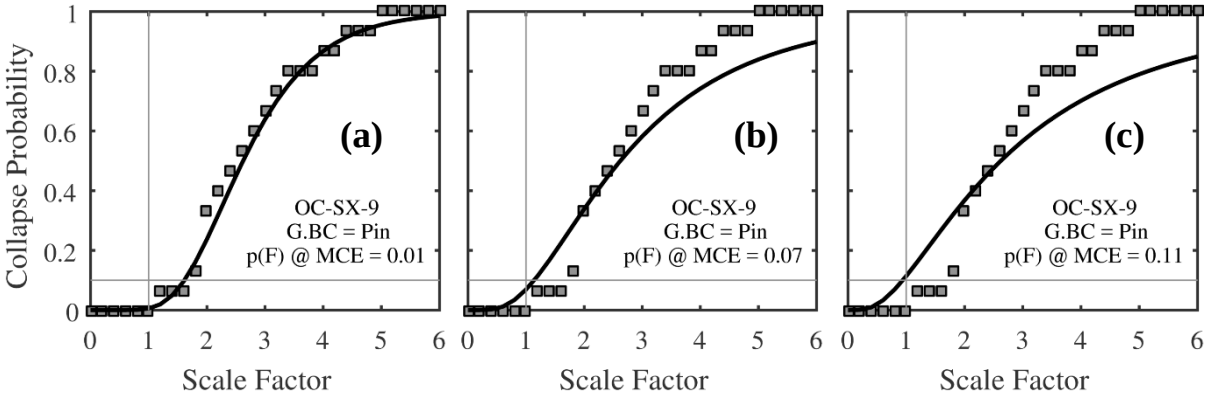

Figure 8.21 – The influence of β_{TOT} on performance assessment per FEMA P695. (a) No consideration of uncertainty; (b) β_{TOT} = 0.65; and (c) β_{TOT} = 0.80.

The probability of collapse at the MCE is the key attribute used in the FEMA P695 methodology to determine if a building has acceptable performance. Per the suggestions of FEMA P695, a building is considered to have acceptable performance if the probability of collapse for the MCE ground motion is less than or equal to 10%. In consideration of this 10% level recommended by FEMA P695, the relevance of the example presented in Figure 8.21 is further revealed: OC-SX-9 had acceptable performance (*p(F)* at MCE = 0.07 ≤ 0.10) with the chosen value β_{TOT} = 0.65, but would not have passed the FEMA P695 condition if β_{TOT} = 0.80 was assumed.

The adjusted fragility curves which incorporate β_{TOT} = 0.65 for case study buildings using OCBF SFRSs and β_{TOT} = 0.75 for case study buildings using *R* = 3 SFRSs are presented in Figures 8.22, 8.23, and 8.24, for 3-, 6-, and 9-story prototype buildings, respectively. Included on the plots is the probability of collapse at the MCE (*p(F)* at *SF* = 1.0) in addition to the adjusted collapse margin ratio (ACMR), or the collapse SF at *p(F)* = 0.50 (median). Note that ACMR is equal to collapse margin ratio (CMR) for this study since the GMs used were derived from the USGS uniform hazard spectrum and, thus, the spectral shape factor (SSF) from which ACMR = SSF x CMR can be taken as unity (Sorabella, 2006).

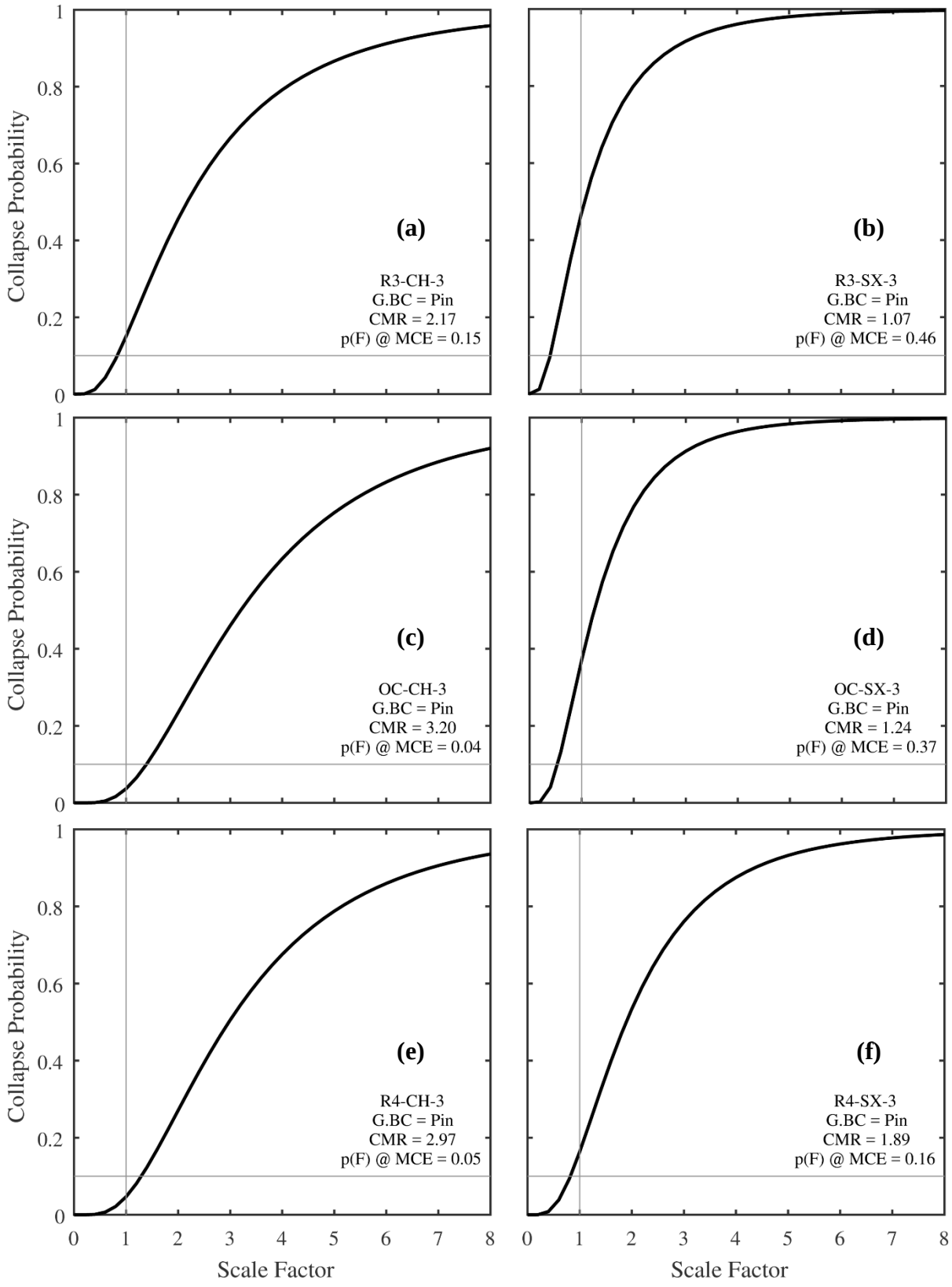

Figure 8.22 – Adjusted fragility curves for 3-story case study buildings (a) R3-CH-3; (b) R3-SX-3; (c) OC-CH-3; (d) OC-SX-3; (e) R4-CH-3; and (f) R4-SX-3.

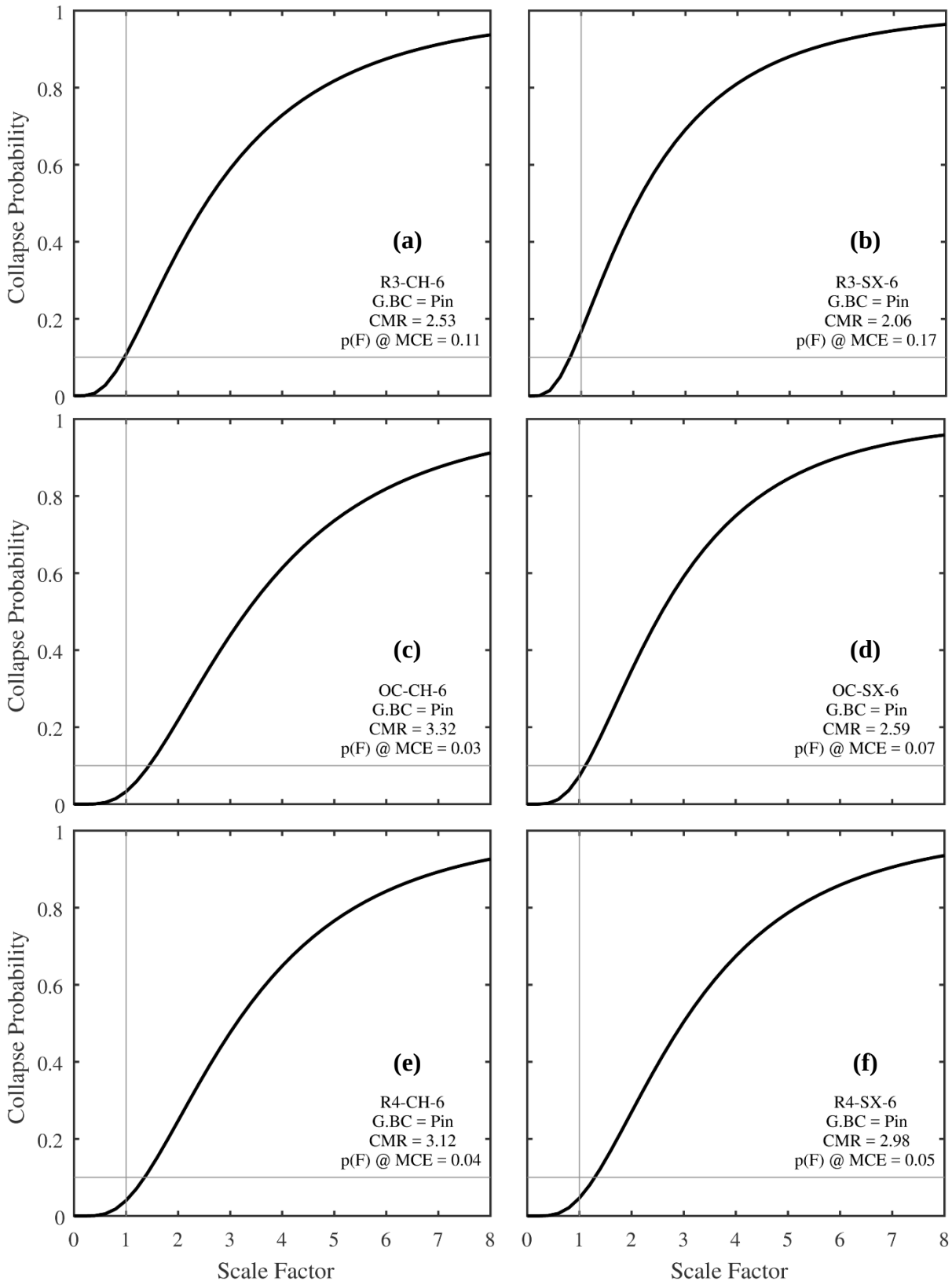

Figure 8.23 – Adjusted fragility curves for 6-story case study buildings (a) R3-CH-6; (b) R3-SX-6; (c) OC-CH-6; (d) OC-SX-6; (e) R4-CH-6; and (f) R4-SX-6.

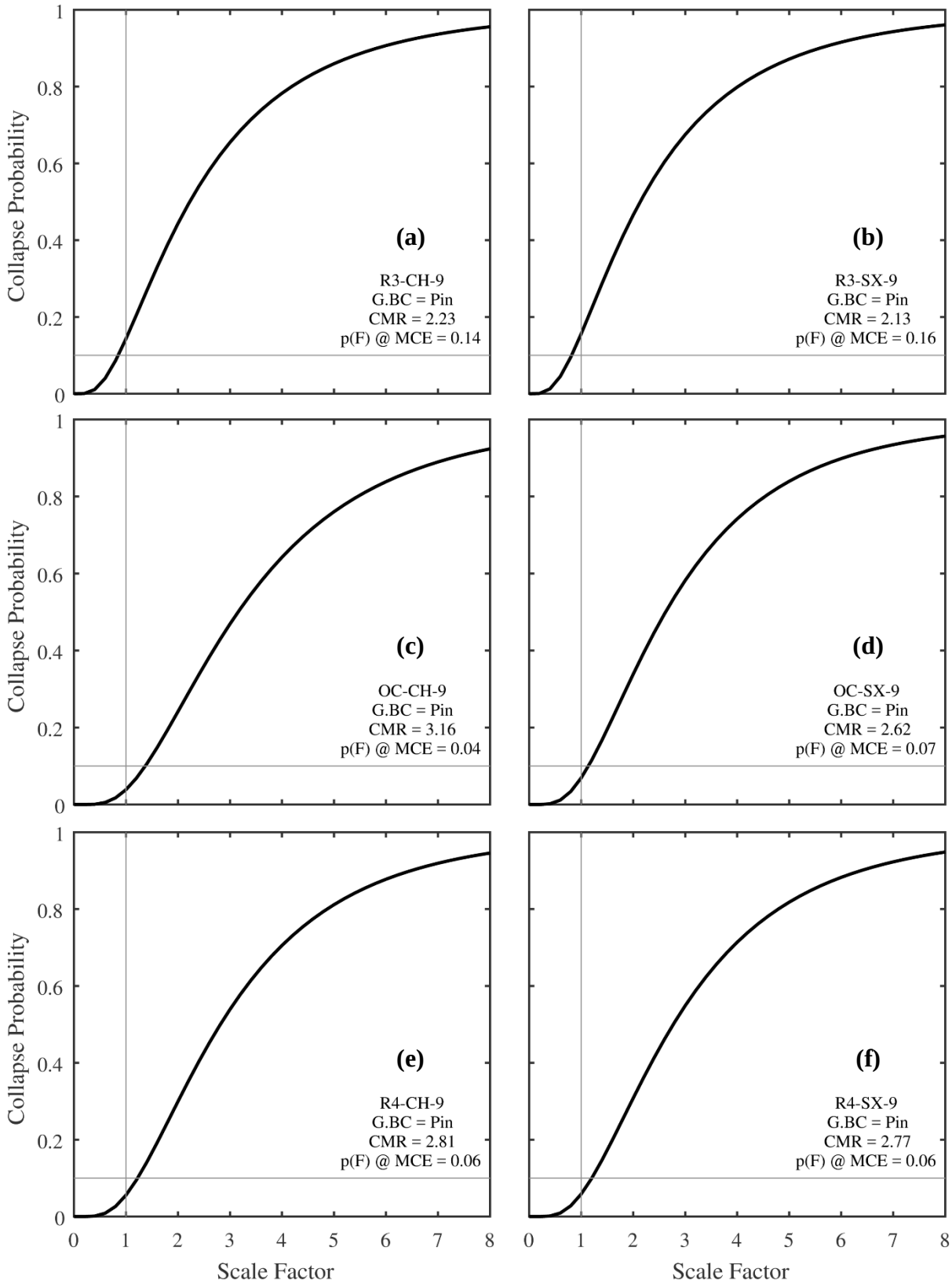

Figure 8.24 – Adjusted fragility curves for 9-story case study buildings (a) R3-CH-9; (b) R3-SX-9; (c) OC-CH-9; (d) OC-SX-9; (e) R4-CH-9; and (f) R4-SX-9.

In addition to the adjusted fragility curves, the performance evaluation results are summarized in Tables 8.16, 8.17, and 8.18, for 3-, 6-, and 9-story case study buildings, respectively. In addition to the ACMR and *p(F)* at the MCE ($p(F)_{,MCE}$), which are the primary outputs from the FEMA P695 investigation, the number of collapses at the MCE ($n_{collapse}$) and average scale factor at building collapse (SF_{avg}) are also presented from the IDA results. Finally, the SFRS weights (W_{SFRS}) are listed, along with a performance rating (S) which was developed as a simplistic metric to weight-normalize the performance results, calculated from $ACMR/W_{SFRS}$. Although this ratio does not have any specific scientific meaning, it does provide a measure that combines collapse stability and structural weight, and thus was useful for relative comparisons between different SFRSs. Within each table, values of S are standardized amongst all alternative buildings investigated with the same height to create a normalized performance rating, S_{norm}. An S_{norm} of 1.0 indicates an SFRS that provided the most efficient collapse prevention performance, e.g. high *ACMR*, low W_{SFRS}, while lower normalized performance ratings indicate a percent reduction in performance. A building with a $S_{norm} = 0.5$ for example could have achieved the same ACMR as a building with a normalized performance rating of 1.0, but with double the W_{SFRS}, and thus was only considered half as effective. Both variants of the R4-SX buildings are given in these tables (R4-SX-3/6/9 and R4-SX-3/6/9-FIX) to show the influence that providing fixed beam-column connections within the $R = 4$ split-x OCBF framework had on collapse prevention performance. The IDA plots and fragility curves for the "-FIX" variants of the R4-SX building models are included in Appendix A.

Table 8.16 – Summarized performance results for 3-story case study buildings

	W_{SFRS} (t)	$n_{collapse}$	SF_{avg}	$ACMR$	$p(F)_{,MCE}$	S	S_{norm}
R3-CH-3	5.39	1	2.31	2.17	0.15	0.403	0.781
OC-CH-3	8.90	1	3.49	3.20	0.04	0.360	0.697
R4-CH-3	5.76	0	3.15	2.97	0.05	0.516	1.000
R3-SX-3	5.38	7	1.12	1.07	0.46	0.199	0.386
OC-SX-3	6.26	5	1.31	1.24	0.37	0.198	0.384
R4-SX-3	6.07	0	2.00	1.89	0.16	0.311	0.604
R4-SX-3-FIX	6.07	0	2.48	2.35	0.09	0.387	0.751

Table 8.17 – Summarized performance results for 6-story case study buildings

	W_{SFRS} (t)	$n_{collapse}$	SF_{avg}	$ACMR$	$p(F)_{,MCE}$	S	S_{norm}
R3-CH-6	10.91	0	2.65	2.53	0.11	0.232	0.886
OC-CH-6	16.7	0	3.41	3.32	0.03	0.199	0.760
R4-CH-6	11.92	0	3.25	3.12	0.04	0.262	1.000
R3-SX-6	10.69	1	2.20	2.06	0.17	0.193	0.736
OC-SX-6	11.46	0	2.79	2.59	0.07	0.226	0.863
R4-SX-6	12.35	0	3.19	2.98	0.05	0.241	0.922
R4-SX-6-FIX	12.35	0	3.15	3.01	0.05	0.244	0.931

Table 8.18 – Summarized performance results for 9-story case study buildings

	W_{SFRS} (t)	$n_{collapse}$	SF_{avg}	$ACMR$	$p(F)_{,MCE}$	S	S_{norm}
R3-CH-9	20.19	0	2.39	2.23	0.14	0.110	0.885
OC-CH-9	29.98	0	3.28	3.16	0.04	0.105	0.844
R4-CH-9	22.51	0	2.96	2.81	0.06	0.125	1.000
R3-SX-9	19.8	0	2.24	2.13	0.16	0.108	0.862
OC-SX-9	21.85	0	2.80	2.62	0.07	0.120	0.961
R4-SX-9	23.35	0	2.89	2.77	0.06	0.119	0.950
R4-SX-9-FIX	23.35	0	2.97	2.90	0.05	0.124	0.995

As both the tables and figures show, the proposed R = 4 demonstrated acceptable collapse prevention performance for all building heights in both chevron and split-x configurations, except for building R4-SX-3 ($p(F)_{MCE}$ = 0.16). When fixed beam column connections were assumed within the SFRS in R4-SX-3-FIX, collapse was forestalled and the FEMA P695 requirement was satisfied. This was the only 3-story split-x building to pass FEMA P695.

In general, buildings that used the current R = 3.25 OCBF chevron configuration demonstrated the largest ACMRs. However, in consideration of the significantly larger W_{SFRS} in these buildings, their performance was less desirable. In the 3-story buildings for example, OC-CH-3 had $ACMR$ = 3.20 and W_{SFRS} = 8.90 t., giving it a performance rating, S = 0.360. Although building R4-CH-3 achieved an $ACMR$ of only 2.97, it had a significantly lower W_{SFRS} of 5.76 t., for S = 0.516. When these S-values were normalized in comparison to one another, R4-CH-3 was shown to have a 43% better performance (1.000/0.697) than OC-CH-3. A similar trend was seen for 6- and 9-story buildings, with R4-CH-6 achieving a 32% better performance (1.000/0.760) than OC-CH-6 and R4-CH-9 achieving an 18% better performance (1.000/0.844) than OC-CH-9. All 6- and 9-story OCBF variants passed the FEMA P695 10% limit for acceptable collapse prevention performance

For the 3-story buildings, a similar comparison of the proposed R = 4 split-x OCBF buildings and current R = 3.25 split-x OCBF buildings can be made. Building OC-SX-3 failed FEMA P695 with a $p(F)_{MCE}$ = 0.37, and while building R4-SX-3 also failed FEMA P695, it did so with $p(F)_{MCE}$ = 0.16, a relative decrease of over 50%. Furthermore, building R4-SX-3-FIX passed FEMA P695, albeit narrowly, with $p(F)_{MCE}$ = 0.09. Although the proposed R = 4 split-x OCBFs outperformed the current R = 3.25 split-x OCBFs for the 3-story buildings, it

took extreme circumstances (assumed fixed beam-column connections) to achieve acceptable collapse prevention performance. Thus, although the measures introduced by the proposed R = 4 split-x OCBF provisions gave an improvement in performance over the current R = 3.25 split-x OCBF design for the 3-story case study buildings, they did not give as robust collapse prevention performance as was seen for R = 4 chevron OCBFs. For the 6- and 9-story split-x buildings, the efforts introduced by the proposed R = 4 OCBF had only a marginal impact. Though the *ACMRs* for these R4-SX-6/9 buildings were slightly increased over the OC-SX-6/9 buildings, they were associated with a slightly larger W_{SFRS}, which mostly negated the relative gain in performance, S.

In addition to the 3-story buildings which used split-x frames, all buildings that used R = 3 SFRSs additionally demonstrated unacceptable performance per FEMA P695 (R3-CH-3: $p(F)_{,MCE}$ = 0.15, R3-SX-3: $p(F)_{,MCE}$ = 0.46, R3-CH-6: $p(F)_{,MCE}$ = 0.11, R3-SX-6: $p(F)_{,MCE}$ = 0.17, R3-CH-9: $p(F)_{,MCE}$ = 0.14, and R3-SX-9: $p(F)_{,MCE}$ = 0.16). Per definition of the R = 3 SFRS, there was no seismic detailing in these designs, and thus collapse prevention relied on inherent reserve capacity within the SFRS, such as through the long-link EBF mechanism within the chevron frames or column bending within the split-x frames. Based on these results, the R = 3 SFRS itself does not appear to have enough reserve strength to provide acceptable performance per the FEMA P695 definition. However, these results do not include the potential contribution of the gravity beam-column connections in collapse prevention. As was demonstrated in Chapter 3, gravity beam-column connections can provide a significant source of reserve capacity during dynamic simulations, and thus the gravity connection contribution is an important effect to evaluate for the R = 3 SFRS.

8.3.4 Performance Evaluation Considering Gravity Connection Contribution

Although the fragility curves in Section 8.3.3 give a useful means for isolating the influence that the SFRSs alone have on building collapse prevention performance, they do not fully recognize all sources of reserve capacity within the building. Furthermore, while the reserve capacity contribution of the gravity framing system is not explicitly considered in seismic design, its influence is implicitly relied upon for collapse prevention, especially in the R = 3 SFRS. The importance of the gravity framing system in buildings which incorporate an R = 3 SFRS was highlighted in the previous section in the discovery that none of the 6 buildings which used an R = 3 SFRS had an acceptable performance. In this section, a new set of FEMA P695 analyses is presented for the buildings which did not pass FEMA P695 with pinned gravity connections (G.BC = Pin), this time with actual gravity beam-column connection behavior (G.BC = Actual).

Gravity connections were significantly smaller than CBF connections since they were only designed to resist gravity loads. A typical detail and moment-rotation plot for the gravity connections, which include a 2L4x4x1/4 with 3 rows of 25.4 mm. [1.0 in.] diameter A490 bolts, is shown in Figure 8.25. What these connections lack in flexural strength relative to the more robust CBF connections, they partially make up for due to the larger quantity. In the 6-story case study building, for example, there are 7 columns within the gravity bay, which gives 14 locations for gravity connections. With one beam-column connection at every level, this amounts to a total of 14 x 7 = 98 gravity connections, compared to just 12 CBFs connections.

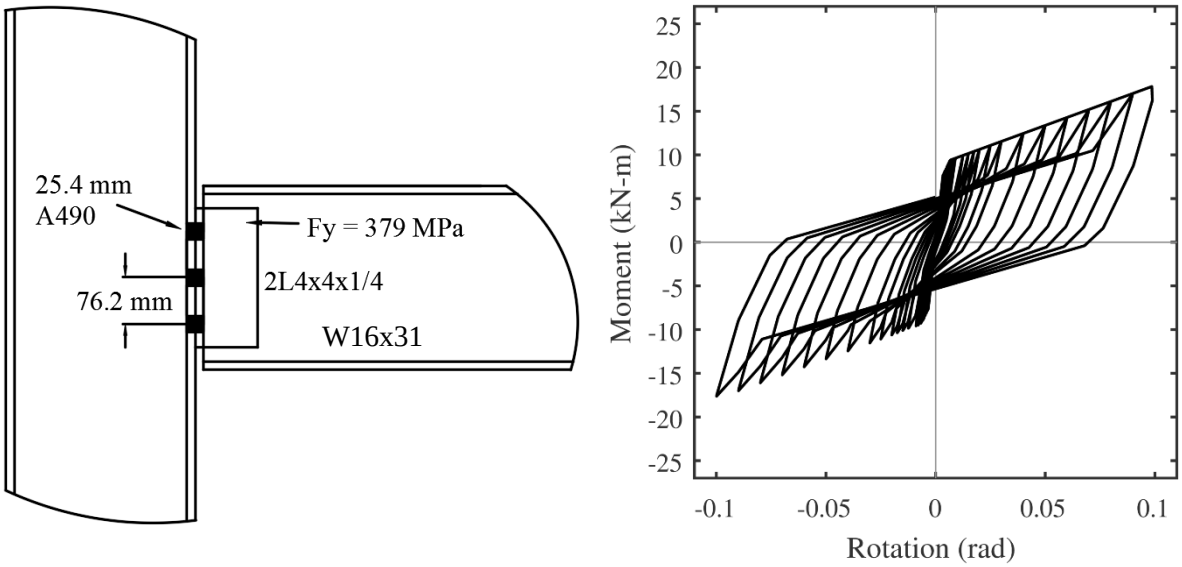

Figure 8.25 – Connection detail and moment-rotation hysteresis for gravity beam-column connections in case study buildings.

The adjusted fragility curves for the FEMA P695 analysis with explicit consideration of gravity connection contribution are presented in Figure 8.26 for buildings OC-SX-3 and R4-SX-3, and Figure 8.27 for all 6 R = 3 case study buildings. The buildings shown are those that did not pass FEMA P695 from the performance of their SFRS alone. A summary of the FEMA P695 results with gravity connections is given in Table 8.19, for a more direct comparison with the results from the previous P695 analyses of Section 8.3.3 which did not include gravity connection contribution.

Table 8.19 – Comparative performance for case study buildings that failed FEMA P695 without considering gravity framing

Building	G.BC Conn.	$n_{collapse}$	SF_{avg}	*ACMR*	$p(F)_{,MCE}$
OC-SX-3	Pinned	5	1.31	1.24	0.37
	Actual	0	3.19	2.95	0.05
R4-SX-3	Pinned	0	2.00	1.89	0.16
	Actual	0	3.59	3.38	0.03
R3-CH-3	Pinned	1	2.31	2.17	0.15
	Actual	0	4.11	3.87	0.04
R3-SX-3	Pinned	7	1.12	1.07	0.46
	Actual	0	3.25	2.95	0.07
R3-CH-6	Pinned	0	2.65	2.53	0.11
	Actual	0	3.95	3.70	0.04
R3-SX-6	Pinned	1	2.20	2.06	0.17
	Actual	0	3.07	2.90	0.08
R3-CH-9	Pinned	0	2.39	2.23	0.14
	Actual	0	3.33	3.12	0.06
R3-SX-9	Pinned	0	2.24	2.13	0.16
	Actual	0	2.84	2.73	0.09

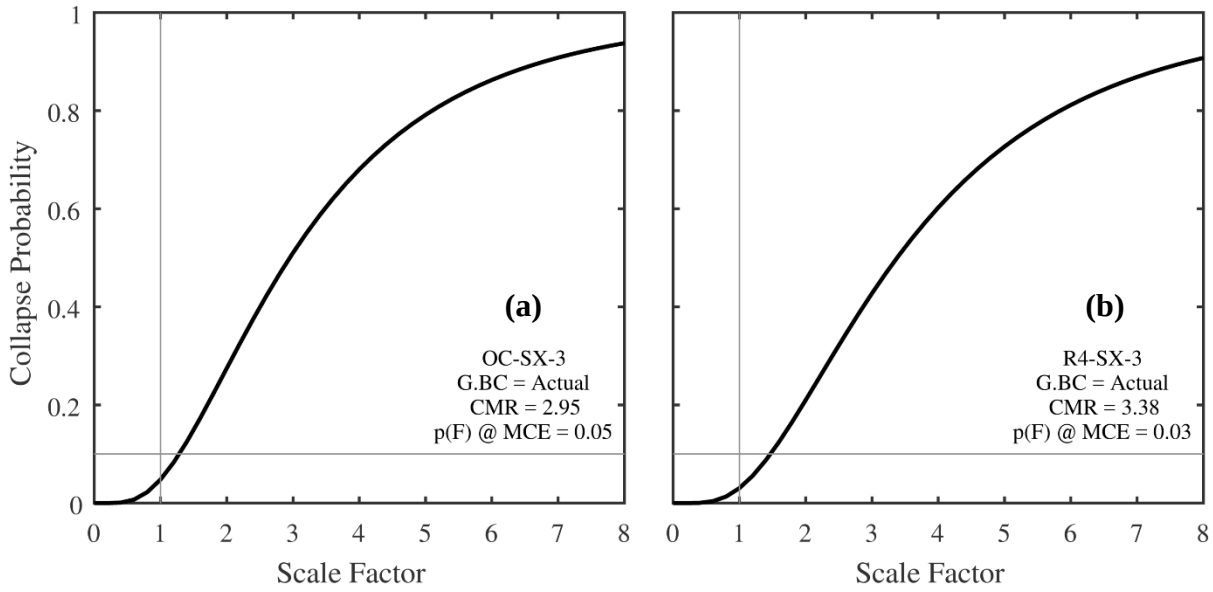

Figure 8.26 – Adjusted fragility curves that consider gravity connection contribution: (a) OC-SX-3; and (b) R4-SX-3.

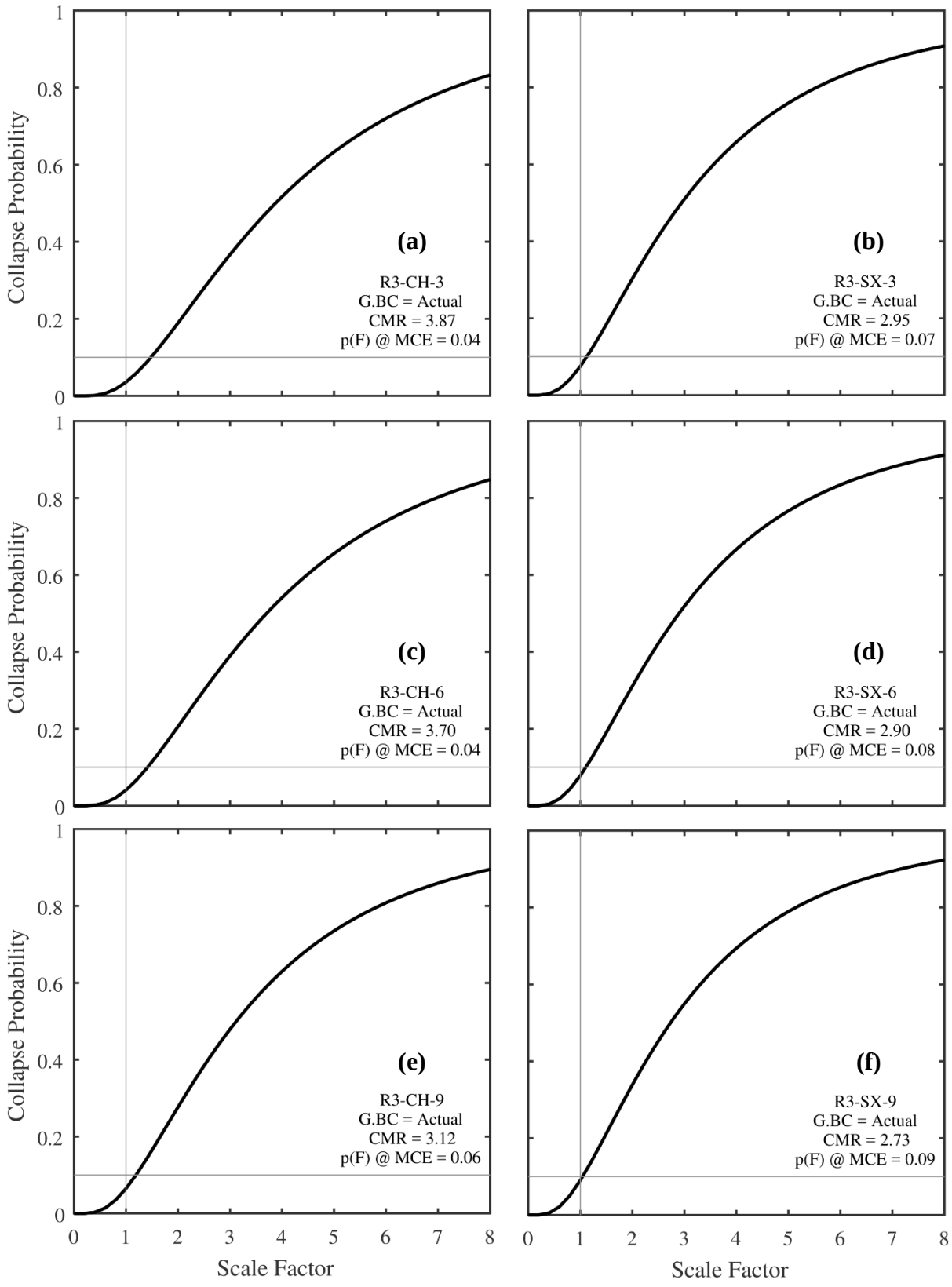

Figure 8.27 – Adjusted fragility curves that consider gravity connection contribution: (a) R3-CH-3; (b) R3-SX-3; (c) R3-CH-6; (d) R3-SX-6; (e) R3-CH-9; and (f) R3-SX-9.

As these new fragility curves show, the impact of gravity beam-column connection behavior was significant. When accurately modeling gravity beam-column connection behavior in buildings OC-SX-3 and R4-SX-3, collapse probability at the MCE decreased from 0.37 to 0.05 in OC-SX-3 and from 0.16 to 0.03 in R4-SX-3, putting both within the FEMA P695 acceptable limit of 10%. The same observation was made for all of the R = 3 case study buildings. As building height increased, the relative gain from including the flexural capacity of beam-column connections was marginalized, with largest gains in *ACMR* observed in the 3-story buildings and smallest gains observed in the 9-story buildings. Although the R3-SX-9 building narrowly passed FEMA P695 in this study, further modeling refinements within the gravity system could have further increased its performance, such as the accurate modeling of partially rigid column bases within gravity bays rather than pins. In summary, despite nearly half (8/18) of the case study buildings not passing the FEMA P695 requirements under the simplifying assumptions of zero gravity connection contribution, these failure cases were erased when a more exact portrayal of gravity beam-column connections was included in the numerical models. This observation further reinforces the notion that R = 3 systems can reach acceptable collapse prevention performance through reserve capacity from their gravity connections.

8.4 SUMMARY OF LOW-DUCTILITY CONCENTRICALLY-BRACED FRAME PERFORMANCE ASSESSMENT

A comprehensive performance assessment of low-ductility CBFs was conducted using a sophisticated *OpenSees* building model and dynamic numerical simulations. The assessment was conducted on a matrix of 18 case study buildings which varied by number of stories (3, 6,

and 9), system configuration (chevron, split-x), and system type (R = 3, current R = 3.25 OCBF, proposed R = 4 OCBF).

A series of incremental dynamic analyses was performed on each case study building, and conclusions were drawn based on the three variables that defined the test matrix (system type, system configuration, number of stories). Gravity framing contribution was ignored in the first assessment through modeling of pinned beam-column connections in the gravity bays. In general, the buildings that used a chevron configuration were found to survive the scaled ground motions at larger scale factors on average than their split-x counterparts. Additionally, all R = 3 systems collapsed at lower scale factors on average than their OCBF counterparts, which was indicative of the benefits offered by requiring some amount of seismic detailing and proportioning in design. The 3-story buildings collapsed at lower scale factors on average than their 6- and 9-story counterparts, which was indicative of the higher demands the selected ground motion suite placed on stiffer buildings, whose fundamental periods aligned more closely with the high-energy range of the ground motion suite. Of the 3-story case study buildings studied, collapse was identified at the MCE (SF = 1.0) in building R3-CH-3 for 1 ground motion, building R3-SX-3 for 7 ground motions, building OC-CH-3 for 1 ground motion, and building OC-SX-3 for 5 ground motions. Collapse at the MCE occurred in one 6-story case study building (R3-SX-6), and for only 1 ground motion. None of the 9-story case study buildings collapsed at the MCE.

As a supplement to the IDAs, response for individual ground motion records were studied for a more in-depth view of system behavior and limit state progression considering the influence of system configuration and system type. Specifically, these investigations provided valuable insights into the performance of the proposed R = 4 OCBF system—which

was introduced in Chapter 7—and allowed for a rigorous comparison of this new SFRS with current alternatives in low and moderate seismic regions (R = 3, current R = 3.25 OCBF). In these single record investigations, it was shown that buildings R3-CH-3 and R4-CH-3 avoided collapse under the same ground motion in which their split-x counterparts, R3-SX-3 and R4-SX-3-FIX, collapsed. Like what was seen in the static cyclic simulations of Chapter 6, the long-link EBF mechanism provided reserve capacity that contributed to collapse prevention of the buildings with chevron CBFs. Although the split-x frames formed a similar EBF mechanism at their roof level, the EBF behavior they formed at Level 2 was the detrimental "two-story" mechanism previously identified in the full-scale testing program (Chapter 4) and subsequent static cyclic numerical simulations (Chapter 6). This behavior appears to be entirely attributable to the configuration of the braces. In short, a chevron CBF has the potential to form a long-link EBF mechanism at every level, while a split-x CBF may only form a long-link EBF at every other level, which reduces its potential reserve capacity. As the single record comparison between buildings R4-CH-3 and OC-CH-3 revealed, the formation of the long-link EBF can be extremely beneficial. Collapse was prevented in R4-CH-3 under the same scaled ground motion in which OC-CH-3 failed, despite the R = 4 OCBF SFRS weighing only two-thirds that of the R = 3.25 OCBF SFRS. A final single record comparison between buildings R4-SX-3-FIX and OC-SX-3 demonstrated the potential of preventing collapse by providing increased flexural capacity in beam-column connections within split-x frames. Beam-column flexural capacity was especially critical at the levels where the long-link EBF has the potential to form. In split-x buildings without flexural strength proportioning requirements for their beam-column connections (R3-SX-3, OC-SX-3), the CBF connections

did not have enough strength and stiffness to oppose the flexibility of the two-story mechanisms that formed.

The IDA results were used within the FEMA P695 framework (FEMA, 2009) to create adjusted fragility curves and assess collapse prevention performance. Per the recommendation of FEMA P695, a collapse probability of less than or equal to 10% under the MCE (SF = 1.0) was considered as an acceptable level of performance. In this regard, 10 of the 18 case study buildings investigated achieved this acceptable performance level, while 8 did not (OC-SX-3, R4-SX-3, and all 6 R = 3 buildings). When normalizing the median collapse margin ratios of the buildings, it was discovered that for a given story height, the R = 4 chevron OCBF had the best performance, confirming the beneficial aspects of the newly proposed R = 4 OCBF provision in Chapter 7. Although the R = 4 split-x OCBFs achieved slightly larger *ACMRs* than their R = 3.25 split-x OCBF counterparts, the increase in SFRS weight associated with the adoption of the R = 4 provisions offset this marginal gain for the 6- and 9-story buildings. Thus, while the proposed R = 4 OCBF provision appeared to significantly improve the performance of chevron configuration CBFs, it did not have an appreciable effect on the performance of the split-x configuration CBFs. One avenue of future research to improve the behavior of R = 4 split-x OCBFs is to investigate the impact of preventing collapse through ductility, which the split-x configuration seems to naturally lend itself to, rather than reserve capacity, which the chevron configuration appears best suited for. In other words, rather than trying to provide seismic proportioning for beam-column connections to meet a required level of flexural capacity in the R = 4 split-x OCBF, a better approach might involve seismic detailing of the brace-gusset connections through a capacity design approach. Capacity designing the brace-gusset connections within a split-x frame such that weld fracture is avoided can result in a

significant increase in ductility, and help to avoid or delay the undesirable behavior associated with the two-story mechanism that was common in split-x frames studied.

As a supplement to the first FEMA P695 analyses performed without consideration of gravity beam-column connections, a second FEMA P695 analyses was conducted for the 8 case study buildings that did not pass the first FEMA P695 evaluation. Accurate portrayal of gravity connections resulted in acceptable performance (passed FEMA P695) within these 8 case study buildings that otherwise collapsed (did not pass FEMA P695) when gravity connections were modeled as pins.

CHAPTER 9

CONCLUSIONS, RECOMMENDATIONS, AND FUTURE WORK

Current U.S. seismic design provisions allow structures in areas of lower seismicity (e.g. Midwest and Eastern North America) to be designed with modest seismic requirements compared to the requirements that must be satisfied in areas of higher seismicity (e.g. Western North America). Because of the lessened seismic detailing and proportioning requirements in these areas of low or moderate seismicity, seismic force resisting systems (SFRSs) within these regions are classified as "low-ductility", in contrast to "high-ductility" systems common of areas of higher seismicity.

In a high-ductility system, rigorous proportioning (capacity design) and prescriptive detailing requirements are intended to enforce a favorable ductile mechanism using fuse elements, which are specific elements designed with the intention of undergoing significant inelastic demands during a large seismic event. The ability of fuse elements to give ductility and collapse prevention performance is well understood thanks to decades of extensive research into high-ductility systems common of California and other high seismic regions. This is not the case for low-ductility SFRSs, however, as despite their frequent use across most of Midwest and Eastern North American, the fundamental behavior of these systems is still not well understood, and certainly not to the extent of high-ductility systems.

9.1 SUMMARY OF RESEARCH NEED, OBJECTIVES, AND SCOPE

Given the prevalence of low-ductility steel structures in a large part of the U.S., there is a strong need to develop a more fundamental understanding of their inelastic behavior and overall collapse prevention performance. Structural investigations of low-ductility steel

structures following previous significant seismic events highlighted the fact that these structures inherently have additional lateral load resisting capacity, other than what is assumed in design (reserve capacity), following damage to their SFRS. Although these anecdotal cases serve to partially affirm the viability of low-ductility SFRSs, the contributors to collapse prevention performance in these structures (sources of reserve capacity) are not as well understood as sources of collapse prevention performance in high-ductility systems (energy dissipation from fuse element ductility).

Based on the established need, a two-part approach was established for the research objective. First, identify sources of reserve capacity in steel structures and quantify their effectiveness. Second, determine cost-effective solutions for providing and increasing reserve capacity in steel structures as a design strategy. This dissertation discussed the above process, and the various tasks that were performed to meet this established need made up the chapters of this document:

1. [Chapter 3]: Reserve Capacity Component Study – Numerical simulations were performed to quantify the effectiveness of various sources of reserve capacity identified through review of previous literature.
2. [Chapter 4]: Full-Scale Experimental Frame Tests – In acknowledgement of the lack of full-scale experimental test data for low-ductility SFRSs, two full-scale test units were designed: an R = 3 chevron CBF and an R = 3.25 split-x OCBF. These units were tested to assess the influence of two key design parameters on reserve capacity: system type and system configuration.

3. [Chapter 5]: Numerical Building Model – A sophisticated numerical building model was created to further study low-ductility SFRSs. This model was verified and updated based on observations and lessons learned from the full-scale testing program.
4. [Chapter 6]: Cyclic Static Parametric Study of 3-Story Frames – The numerical building models were used to expand the experimental test matrix and thoroughly investigate the relationship between the two system types (R = 3 CBF, R = 3.25 OCBF, and system configurations (chevron, split-x) which defined the full-scale test units.
5. [Chapter 7]: The R = 4 OCBF – A new low-ductility system was proposed for use in areas of low and moderate seismicity which uses beneficial aspects of reserve capacity identified in Chapters 3–6, the R = 4 OCBF.
6. [Chapter 8]: Performance Assessment of Low-Ductility CBFs – A comprehensive investigation on the influence of system type, system configuration, and number of stories, on reserve capacity was conducted in the context of a reliability-based performance assessment (FEMA P695) to study the viability of current low-ductility CBFs and the proposed R = 4 OCBF.

9.2 CONCLUSIONS

In this section, the overarching conclusions from the primary investigative chapters, Chapters 3–8 are summarized to show how the objectives of the research program were met. Conclusions that are more detailed are included within the final section of these chapters.

9.2.1 Conclusions from Chapter 3: Reserve Capacity Component Study

- Accurately modeling the flexural behavior of gravity connections was shown to marginally increase reserve capacity in static pushover (SPO) analyses. The beneficial impact of accurately modeling these connections was noticeably larger in dynamic analyses, highlighting a potential limitation of analyzing reserve capacity using pushovers only.
- The collapse scale factors (SFs) for the studied ground motion (GM) suite were significantly increased when top- and seat-angles were considered in addition to the typical double web angle detail. More economically efficient options for providing reserve capacity were discovered during this study (i.e. increase beam or column flexural capacity).
- Accurately modeling the flexural behavior of CBF connections was shown to improve performance. When pinned CBF connections were used, many of the building models failed under GMs scaled at the MCE or lower. When an effort was made to model the actual flexural behavior of these connections, the building survived all MCE-level GMs. Similar to Stoakes (2012), it is concluded that accurate modeling of these connections is critical for properly assessing the performance of low-ductility CBFs.
- Providing slightly larger beams and columns within the SFRS appears to be a simple and economical approach to providing an increase in reserve capacity without any additional detailing or construction costs.
- If brace reengagement occurs, the lateral force resisting capacity of chevron frames in the post-elastic range is increased following the fracture of a single brace-gusset weld. However, due to the inherently unreliable nature of this mechanism, further study is needed before it can be relied on to provide collapse prevention in the design phase.

9.2.2 Conclusions from Chapter 4: Full-Scale Experimental Tests

- Local slenderness (b/t) limits were observed to have contributed significantly to both local and overall system ductility. Braces within the OCBF test unit had a significantly more robust hysteresis following the initiation of global buckling. Braces within the R = 3 CBF test unit exhibited a detrimental coupled global–local buckling limit state and significant tearing at their midspan.
- The difference between actual weld strength, provided weld strength, and minimum weld strength required for design may vary greatly. Weld overstrengths as high as 80% were observed in the full-scale test experiments. The influence weld overstrength has on system performance is related to system type. From the test units, the ranked preference of brace limit states in order of most to least desirable appeared to be: (1) ductile brace buckling; (2) brace-gusset weld fracture; and (3) non-ductile brace buckling. Since controlled local slenderness was found to promote ductile brace buckling, weld overstrength may be welcomed in systems such as the OCBF. The opposite could be said for R = 3 frames, however: if the brace-gusset welds in these frames have an unanticipated overstrength, then the detrimental global–local coupled buckling limit state is more likely to occur instead of brace-gusset weld fracture, giving an equivalent loss in capacity while additionally eliminating any potential for brace reengagement.
- The long-link EBF mechanism in the chevron test unit was sustained for story drifts of up to 6%, suggesting there is a stronger potential for this mechanism to provide reserve capacity and at drifts larger than was previously thought.
- The two-story mechanism that formed within the split-x test unit was identified as a detrimental mechanism from a reserve capacity perspective.

- The split-x configuration appeared beneficial from a ductility perspective, accommodating redistribution of loads following brace buckling without a significant loss in system stiffness, and without any loss in strength.

9.2.3 Conclusions from Chapter 5: Numerical Building Model

- The ability for a sophisticated *OpenSees* model to accurately capture global behavior of low-ductility steel CBFs was demonstrated, given necessary measures are taken to help with model convergence following the occurrence of brittle limit states common of these systems.
- Limitations of current modeling techniques were identified, such as the ability to accurately predict the effects of coupled global–local buckling and rapid strength degradation in locally slender braces (high b/t) used in $R = 3$ frames.

9.2.4 Conclusions from Chapter 6: Cyclic Static Parametric Study of 3-Story Frames

- System configuration (chevron vs split-x) influenced the type of mechanism that formed, which in turn affected reserve capacity. The chevron configuration out-performed the split-x in this regard since it mobilized both column bending and beam bending.
- System type ($R = 3$ CBF vs OCBF) influenced ductility in the case of split-x frames. When weld strength exceeded brace yield capacity in OCBFs, appreciable ductility was observed prior to fracture of the brace-gusset welded connections.
- System type also influenced the behavior of chevron frames, but affected reserve capacity more so than it did ductility. For the primary frames studied, the deeper beams found in the chevron OCBFs were strong enough to carry the brace unbalanced force and fracture the remaining brace-gusset weld after an earlier brace-gusset weld fracture within the same

story. This resulted in an unfavorable mechanism driven by column bending as opposed to the more favorable long-link EBF mechanism seen in the R = 3 chevron CBFs.

- Independent of both system type and system configuration, development of a backspan for column bending, or needing two plastic hinges per column to form a mechanism, increased reserve capacity significantly.
- The design base shear itself was shown to be less relevant for building collapse prevention than the damage mechanisms and reserve systems that formed in the post-elastic range.

9.2.5 Conclusions from Chapter 7: The R = 4 OCBF

- In consideration of the full-scale test results from Chapter 4 and numerical simulation results of Chapter 6, several aspects of the current R = 3.25 OCBF provisions were identified as detrimental from a performance perspective, such as the KL/r limits and force-imbalance design requirements for braces in V- and inverted-V configurations. Together, these requirements significantly increase the weight of an OCBF SFRS relative to the alternative SFRS for low and moderate seismic regions, the R = 3 CBF. Additionally, these requirements increase beam flexural capacity relative to brace-gusset weld capacity, which reduces the potential for the favorable long-link EBF mechanism to form and increases the likelihood of a detrimental mechanism driven purely by column bending.
- Other aspects of the current R = 3.25 OCBF provisions were identified as beneficial from a performance perspective: (1) b/t proportioning limits; (2) requirement to design columns and brace-gusset welds for the system overstrength factor (Ω_0 = 2.0); and (3) the requirement to design beams to span their full length under gravity loads without considering brace support. As was shown in the full-scale testing, b/t limits can significantly influence brace buckling behavior, which in turn affects overall system

ductility. As was shown in the component-level reserve capacity study, a small increase in beam and column size can give a large increase in reserve capacity.

- Incorporating the beneficial aspects of the R = 3.25 OCBF and removing the detrimental aspects gave the basis for the proposed R = 4 OCBF, which was shown through a static cyclic simulation to have a larger reserve capacity than the current R = 3.25 OCBF, and with a significant reduction in weight.

9.2.6 Conclusions from Chapter 8: Performance Assessment of Low-Ductility CBFs

- The chevron configuration was found to survive scaled GMs at larger average SFs than their split-x counterparts, a reaffirmation of earlier findings throughout this research project.
- All R = 3 systems collapsed at lower average SFs than their OCBF counterparts, which is indicative of the potential benefit that is given from seismic detailing and proportioning.
- Most of the case study buildings experienced limit states in each of their stories, which may have been influenced by the equal story height design.
- In general, the buildings designed with the proposed R = 4 OCBF provisions performed better than their current R = 3.25 OCBF counterparts. The R = 4 chevron OCBFs collapsed at slightly lower SFs than their R = 3.25 OCBF counterpart, but did so while having significantly lower weight and while developing better mechanisms from a reserve capacity perspective. However, although the R = 4 split-x OCBFs achieved slightly larger collapse SFs that their R = 3.25 split-x OCBF counterparts, the increase in SFRS weight associated with the adoption of the R = 4 provisions offset this marginal gain for the taller 6- and 9-story buildings.

- Accurate portrayal of gravity connections provided sufficient reserve capacity to achieve acceptable performance (passed FEMA P695) within 8 case study buildings that otherwise collapsed (did not pass FEMA P695) when the gravity connections were modeled as pins. This was a reaffirmation of the findings from the component-level reserve capacity study, in which explicitly modeling gravity connections provided a significant increase in the observed collapse SFs.

9.3 ENGINEERING RECOMMENDATIONS

One of the primary tasks of this research project—and by association, this dissertation—was to determine cost-effective solutions for providing and increasing reserve capacity in steel structures as a design strategy. To this extent, the proposed R = 4 OCBF SFRS was shown to meet this criterion in the performance assessment of Chapter 8. Thus, the primary engineering recommendation from this dissertation is that the version of the R = 4 OCBF provision presented and discussed herein—or a slightly modified version of it within the same spirit—replace the current R = 3.25 OCBF provision in the upcoming 2022 edition of the AISC *Seismic Provisions*.

Particularly for chevron configurations, the R = 4 OCBF provision capitalizes on many of the beneficial aspects of reserve capacity observed through experimental testing and numerical simulations of this research project (e.g. long-link EBF behavior), and does so in an economical manner with minimal seismic detailing and proportioning requirements. The economy and simplicity of the R = 4 OCBF provision is critical as long as the R = 3 SFRS is an alternative for low and moderate design, since the R = 4 OCBF performed the best of the two SFRSs.

Although R = 4 OCBFs designed in a split-x configuration did not perform significantly better than their R = 3.25 OCBF counterparts, their performance was not decreased either. Thus the current recommendation is for adoption of the R = 4 provision as-is for systems in this configuration (and all other untested configurations) as well, but with the acknowledgement that there is potential for improvement in this area. One particularly promising idea of improving split-x performance is acknowledging what it is "good at" and what it is "bad at". For example, the split-x configuration appears to have a naturally lower "cap" to its peak reserve strength, as it may only form a long-link EBF mechanism at every other level, and doing so involves damage to two or more braces within each two-story X. At the same time, the split-x configuration appears to lend itself to favorable ductile mechanisms without significant loss of stiffness or strength so long as the brace-gusset connections are sufficiently strong enough to develop the tensile capacity of the braces and form a mechanism analogous to those typical of split-x SCBFs. In this light, a better way of posing the R = 4 OCBF provisions for split-x configurations and all other configurations that cannot form a long-link EBF mechanism at every story (e.g. single story X, single diagonal) is to focus on collapse prevention through ductility rather than through reserve capacity. In other words, rather than specifying a flexural capacity need for beam-column connections in these configurations, one could instead provide a specification for capacity designing the brace-gusset welds. It is believed that such a provision may offer significantly better collapse prevention performance with the bonus of significantly less detailing complexity (i.e. no need to design a beam-column connection to meet a specific flexural demand).

9.4 FUTURE WORK

9.4.1 Component-Level Sources of Reserve Capacity

- Further testing should be performed on brace-gusset connections like the small study by Davaran et al. (2014). The potential for significant reserve capacity from brace reengagement was demonstrated in numerical simulations, and affirmed from the full-scale R = 3 chevron CBF, though only after a clean weld fracture was initiated. Such a study should seek to find a range of potential reengagement strengths and stiffnesses such that future performance assessments can account for the reserve capacity from this phenomenon through a reliability-based framework. The study could also seek to find methods for adjusting typical brace-gusset connections to increase the likelihood of a beneficial brace reengagement mechanism occurring. An idea for such a connection detail is given in Appendix D.
- The range of behavior associated with a given brace local slenderness (b/t) should be investigated with the goal of providing a slight relaxation to the current b/t limits in SCBF and OCBF design such that the stock of available sections is not as limited.

9.4.2 Reserve Stiffness and Strength

- A strong emphasis was placed on reserve strength in this dissertation; however, reserve stiffness is also an important consideration in preventing collapse. A larger reserve stiffness influences the period of damaged structures and in turn can lead to increased seismic demands that need a large reserve strength to resist collapse. However, a small reserve stiffness may not be enough to resist the negative stiffness from P-Δ effects, which is equally if not more detrimental. Thus, the relationship between reserve strength and stiffness is important and the best design procedure would carefully balance both criteria

for collapse prevention. One such method might consist of defining a minimum reserve stiffness and an associated reserve strength to resist collapse based on that stiffness. A consideration of the needed reserve stiffness was studied by Stoakes (2012), but more work on this topic is needed before it can be integrated into the design process for low-ductility systems.

- Related to reserve stiffness, the reserve stiffness provided by the beam-column connections is of interest, since they are thought to provide a considerable boost to post-elastic stiffness but do not have a large impact on reserve strength.
- Similarly, future work could also investigate the minimum reserve strength required to achieve collapse prevention. An SDOF system study could help identify benchmark reserve strengths for designers to target in the design process. An initial study in this vein was conducted by Li and Fahnestock (2013).
- Simplified equations should be developed to show the potential reserve strength and stiffness for a given plastic mechanism.

9.4.3 Full-Scale Testing

- Full-scale testing should be performed to investigate the viability of the long-link EBF mechanism. The demands (axial, shear, and flexure) placed on the brace-gusset weld of the remaining brace is of extreme interest, as the mechanism is lost if this connection fails. An example test set-up could consist of a one-bay one-story chevron configuration frame but with only one brace. Potential variables for such a study include beam depth, weld size, and the inclusion or exclusion of a concrete slab (composite action).
- Along the theme of composite action, further full-scale testing of multi-story CBFs would benefit from the inclusion of a concrete slab to measure its influence on reserve capacity.

The influence of composite action is especially critical considering that a higher than expected beam strength was shown to detrimentally affect the response of the SFRS in this research.

9.4.4 Numerical Building Models

- If accurate portrayal of local brace behavior is critical for R = 3 frames, a new *OpenSees* material model must be developed that can capture the effects of local buckling.
- Adapt models to allow for the consideration of composite action.
- Adapt models to allow for the modeling of panel zones and their behavior.
- Include sophisticated methods for defining brace imperfection (Dicleli and Calik, 2008).
- Develop and calibrate spring(s) that can portray the semi-rigidity of gravity column bases.
- Extend beam-column-gusset connection modeling framework to consider other limit states such as beam-gusset weld fracture.
- Include the possibility of beam and column buckling
- Extend building models to look at cases where the braced frames include girders rather than secondary beams.

9.4.5 Ground Motion Selection

- Most ground motions used in this study included short and strong durations, which introduces potential limitations to the range of applicability of the results discusses in this dissertation. For example, a low-ductility system such as an R = 4 OCBF constructed on a softer and/or western site (e.g. Site Class E) would need greater reserve capacity as it would be subjected to significantly heightened demands and at large periods. As the current OCBF provisions allow for implementation in high seismic regions with some height

limitations, a study should investigate the performance of an R = 4 OCBF in comparison to the current R = 3.25 OCBF for applicable building heights in high seismic regions.

9.4.6 The R = 4 OCBF

- The idea of capacity designing brace-gusset welds for all frame configurations that cannot form a long-link EBF at every level should be considered and investigated.
- Concern must be raised as to the viability of the current R = 3 SFRS—particularly for configurations that cannot form a long-link EBF—to the extent of potentially banning certain configurations or otherwise removing the R = 3 provision entirely.
- If the R = 4 OCBF is to be allowed in higher seismic regions, a minimum reserve strength should be specified within the design procedure so that minimum energy dissipation capacity relative to the amount implicitly assumed by the R-factor used in design can be achieved. For example, in high-seismic areas a beam simply designed by gravity demands only may not be strong enough to prevent collapse under the high demands. However, such a design would also need to consider the detrimental impact of having a beam that is too strong, which can cause limit states in both attaching braces.

9.4.7 Numerical Simulations

- A collapse assessment should be performed on buildings designed similarly to those presented in Chapter 8 of this dissertation with the SCBF system type to compare the performance between low-ductility and high-ductility systems in the context of reserve capacity.

9.4.8 Beyond Seismic Design of Low-Ductility Steel Buildings

- The ability for reserve capacity to contribute to collapse prevention performance can be investigated under other hazards, such as disproportionate collapse from blast loading.
- The ability for reserve capacity to contribute to collapse prevention performance can be extended to other structure types (e.g. bridges), other materials (e.g. reinforced concrete), or in areas of high seismicity.

REFERENCES

Abolmaali, A., Kukreti, A. R., & Razavi, H. (2003). Hysteresis behavior of semi-rigid double web angle steel connections. *Journal of Constructional Steel Research, 59*(8), 1057–1082.

American Institute of Steel Construction. (AISC). (1990). *Seismic provisions for structural steel buildings – load and resistance factor design.* American Institute of Steel Construction.

American Institute of Steel Construction. (AISC). (1997). *Seismic provisions for structural steel buildings.* American Institute of Steel Construction.

American Institute of Steel Construction. (AISC). (2002). *Seismic provisions for structural steel buildings.* (ANSI/AISC 341–02). American Institute of Steel Construction.

American Institute of Steel Construction. (AISC). (2005). *Seismic provisions for structural steel buildings.* (ANSI/AISC 341–05). American Institute of Steel Construction.

American Institute of Steel Construction. (AISC). (2010a). *Seismic provisions for structural steel buildings.* (ANSI/AISC 341–10). American Institute of Steel Construction.

American Institute of Steel Construction. (AISC). (2010b). *Specification for structural steel buildings.* (ANSI/AISC 360–10). American Institute of Steel Construction.

American Institute of Steel Construction. (AISC). (2010c). *Code of Standard Practice for Steel Buildings and Bridges*. AISC 303–10. Chicago, IL.

American Institute of Steel Construction. (AISC). (2011). Steel Construction Manual. *Fourteenth Edition.* Chicago, IL.

American Society for Testing and Materials (ASTM). (2015). ASTM A1085 / A1085M-15, Standard Specification for Cold-Formed Welded Carbon Steel Hollow Structural Sections (HSS), ASTM International, West Conshohocken, PA, 2015, www.astm.org

American Society of Civil Engineers. (ASCE). (2005). *Minimum Design Loads for Buildings and Other Structures.* ASCE/SEI Standard 7–05. Reston, VA.

American Society of Civil Engineers. (ASCE). (2013). *Minimum Design Loads for Buildings and Other Structures.* ASCE/SEI Standard 7–10. Reston, VA.

American Society of Civil Engineers. (ASCE). (2014). *Seismic Evaluation and Retrofit of Existing Buildings.* ASCE/SEI Standard 41-13. Reston, VA.

Architectural Institute of Japan (AIJ). (1995). Performance of steel buildings during the 1995 Hyogoken-Nanbu earthquake. Architectural Institute of Japan, Tokyo, Japan. (In Japanese with English summary.)

Astaneh, A., Nader, M. N., & Malik, L. (1989). Cyclic behavior of double angle connections. *Journal of Structural Engineering, 115*(5), 1101-1118.

Beland, T., Bradley, C., Nelson, J., Davaran, A., Hines, E. M., Tremblay, R. & Fahnestock, L. A. (2014). Full-scale testing of beam-column connections with angles. *Proceedings, 2014 Structures Congress*. Boston, MA.

Bertero, V. V., Anderson, J. C., & Krawinkler, H. (1994). *Performance of steel building structures during the Northridge earthquake*. Earthquake Engineering Research Center, University of California.

Blakeborough, A., Merriman, P. A., & Williams, M. S. (1997). The Northridge, California earthquake of 17 January 1994: a field report by EEFIT. *Earthquake Engineering Field Investigation Team, London*.

Bradley, C., Sizemore, J., Nelson, J., Tremblay, R., Hines, E. M., & Fahnestock, L. A. (2014). Large-scale testing of low-ductility, concentrically-braced frames. *Proceedings, 2014 Structures Congress*. Boston, MA.

Bradley, C. (2016). Experimental investigation of post-elastic failure mechanisms in low-ductility braced frames and the implications for collapse performance. (M.S. thesis, Tufts University)

Bradley, C. R., Fahnestock, L. A., Hines, E. M., & Sizemore, J. G. (2016, accepted). Full-scale cyclic testing of low-ductility concentrically-braced frames. *Journal of Structural Engineering*

Building Seismic Safety Council. (BSSC). (1995). NEHRP recommended seismic provisions for new buildings, part 1: provisions. *FEMA Rept. No. 222A*.

Building Seismic Safety Council. (BSSC). (2015). NEHRP recommended seismic provisions for new buildings and other structures, part 1: provisions, part 2: commentary. *FEMA Rept. No. P-1050*, 1, 2015.

Callister, J. T., & Pekelnicky, R. G. (2011). Seismic evaluation of an existing low ductility braced frame building in California. In *Structures Congress 2011* (pp. 2756-2767). ASCE.

Chandler, A. (Ed.). (1997). *The Hyogo-ken Nanbu (Kobe) Earthquake of 17 January 1995: a field report by EEFIT*. Earthquake Engineering Field Investigation Team, The Institution of Structural Engineers.

Charney, F. A. (2008). Unintended consequences of modeling damping in structures. *Journal of structural engineering*, *134*(4), 581-592.

Clifton, C., Bruneau, M., MacRae, G., Leon, R., & Fussell, A. (2011). Steel structures damage from the Christchurch earthquake series of 2010 and 2011. *Bulletin of the New Zealand Society for Earthquake Engineering*, *44*(4), 297-318.

Cuthill, E., & McKee, J. (1969, August). Reducing the bandwidth of sparse symmetric matrices. *In Proceedings of the 1969 24th national conference* (pp. 157-172). ACM.

D'Aniello, M., La Manna Ambrosino, G., Portioli, F., & Landolfo, R. (2015). The influence of out- of-straightness imperfection in physical theory models of bracing members on seismic performance assessment of concentric braced structures. *The Structural Design of Tall and Special Buildings*, *24*(3), 176-197.

Davaran, A., Beland, T., Fahnestock, L. A., Hines, E. M., & Tremblay, R. (2014). Experimental behavior of low-ductility brace connection limit states. *Proceedings, 2014 Structures Congress*. Boston, MA.

Davis, T. A. (2004). Algorithm 832: UMFPACK V4. 3---an unsymmetric-pattern multifrontal method. *ACM Transactions on Mathematical Software (TOMS)*, *30*(2), 196-199.

Di Sarno, L., & Elnashai, A. S. (2009). Bracing systems for seismic retrofitting of steel frames. *Journal of Constructional Steel Research*, *65*(2), 452-465.

Dicleli, M., & Calik, E. E. (2008). Physical theory hysteretic model for steel braces. *Journal of structural engineering*, *134*(7), 1215-1228.

Diebold, J., Moore, K., Hale, T., & Mochizuki, G. (2008). SEAOC Blue Book: Seismic Design Recommendations 1959 to 2008. *In 14th World Conf. on Earthquake Engineering*, Beijing, China.

Elnashai, A. S., & Di Sarno, L. (2008). *Fundamentals of earthquake engineering* (p. 347). Chichester, UK: Wiley.

Federal Emergency Management Agency (FEMA). (2009). Quantification of Building Seismic Performance Factors.

Foutch, D. A., Goel, S. C., & Roeder, C. W. (1987). Seismic testing of full-scale steel building-Part I. *Journal of Structural Engineering*, *113*(11), 2111-2129.

Fortney, P. J., & Thornton, W. A. (2015). The Chevron Effect-Not an Isolated Problem. *Engineering Journal*, 52(2), 125-163.

Fukuta, T., Nishiyama, I., Yamanouchi, H., and Kato, B. (1989). "Seismic performance of steel frames with inverted V braces." *Journal of Structural Engineering*, *115*(8) 2016-2028.

Ger, J. F., Cheng, F. Y., & Lu, L. W. (1993). Collapse behavior of Pino Suárez building during 1985 Mexico City earthquake. *Journal of Structural Engineering*, *119*(3), 852-870.

Ghosh, S. K. (1994). Code implications of the Northridge earthquake of January 17, 1994. In *Proceedings, 6th US-Japan Workshop on the Improvement of Building Structural Design and Construction Practices* (pp. 15-5).

Goel, S. C., & Lee, S. (1992, April). A fracture criterion for concrete-filled tubular bracing members under cyclic loading. In *Proceedings of the 1992 ASCE Structures Congress* (pp. 922-925). ASCE.

Goggins J, Salawdeh S. (2012). Validation of nonlinear time history analysis models for single-storey concentrically braced frames using full-scale shake table tests. *Earthquake Engineering & Structural Dynamics*, DOI: 10.1002/eqe.2264.

Hanson, R. D., & Martin, H. W. (1987). Performance of steel structures in the September 19 and 20, 1985 Mexico earthquakes. *Earthquake spectra*, *3*(2), 329-346.

Hall, J. F., Holmes, W. T., & Somers, P. (1994). Northridge earthquake, January 17, 1994. *Preliminary reconnaissance report*.

Hines, E. M., Appel, M. E., & Cheever, P. J. (2009). Collapse performance of low-ductility chevron braced steel frames in moderate seismic regions. *Engineering Journal*, 46(3), 149.

Hines, E. M., Baise, L. G., & Swift, S. S. (2010). Ground-motion suite selection for eastern North America. *Journal of Structural Engineering*, *137*(3), 358-366.

Hsiao, P. C., Lehman, D. E., & Roeder, C. W. (2012). Improved analytical model for special concentrically braced frames. *Journal of Constructional Steel Research*, *73*, 80-94.

Ibarra, L., Medina, R., and Krawinkler, H. (2002). "Collapse assessment of deteriorating SDOF systems," *Proceedings*, 12th European Conference on Earthquake Engineering, London, Elsevier Science Ltd, paper #665.

Ibarra, L. F., & Krawinkler, H. (2005). *Global collapse of frame structures under seismic excitations*. Berkeley, CA: Pacific Earthquake Engineering Research Center.

Ibarra L.F., Medina R. A., and Krawinkler H. (2005). "Hysteretic models that incorporate strength and stiffness deterioration", *Earthquake Engineering and Structural Dynamics*, *34*(12), 1489-1511.

International Code Council (ICC). (2009). *International Building Code (IBC).* Country Club Hills, IL.

Ji, X., Kato, M., Wang, T., Hitaka, T., & Nakashima, M. (2009). Effect of gravity columns on mitigation of drift concentration for braced frames. *Journal of Constructional Steel Research*, *65*(12), 2148-2156.

Jones, T. A. (2016). Finite Element Modeling of Shallowly Embedded Connections to Characterize Rotational Stiffness. (Doctoral dissertation). Brigham Young University.

Kam, W. Y., Akguzel, U., & Pampanin, S. (2011). 4 Weeks On: Preliminary Reconnaissance Report from the Christchurch 22 Feb 2011 6.3 Mw Earthquake. Christchurch, New Zealand. *New Zealand Society for Earthquake Engineering Inc.*, 1-6.

Kanvinde, A. M., Grilli, D. A., & Zareian, F. (2011). Rotational stiffness of exposed column base connections: Experiments and analytical models. *Journal of Structural Engineering*, *138*(5), 549-560.

Karamanci, E., and Lignos, D. G. (2013). "Collapse assessment and performance-based evaluation techniques for concentrically braced frames designed in seismic regions." M.S. thesis, Dept. of Civil Engineering and Applied Mechanics, McGill Univ., Montreal, QC

Karamanci, E., & Lignos, D. G. (2014). Computational approach for collapse assessment of concentrically braced frames in seismic regions. *Journal of Structural Engineering*, 140(8), A4014019.

Kassis, D., & Tremblay, R. (2008). Brace fuse system for cost-effective design of low-rise steel buildings. In CSCE 2008 Annual Conference.

Krawinkler, H., Anderson, J., Bertero, V., Holmes, W., and Theil Jr., C. (1996). Steel Buildings. *Earthquake Spectra*: January 1996, Vol. 12, No. S1, pp. 25-47.

Krawinkler, H. (2000). State of the art report on systems performance of steel moment frames subject to earthquake ground shaking. *Report no. FEMA-355C, SAC Joint Venture.*

Lawson, J. W. (2010). A Solution to Seismic Bracing Restrictions. *Structure Magazine*, *17*(2), 14.

Léger, P., & Dussault, S. (1992). Seismic-energy dissipation in MDOF structures. *Journal of Structural Engineering*, *118*(5), 1251-1269.

Li, G. and Fahnestock, L.A. "Seismic Response of Single-Degree-of-Freedom Systems representing Low-Ductility Steel Concentrically-Braced Frames with Reserve Capacity," *Journal of Structural Engineering*, ASCE, 139 (2): 199-211, (2013).

Lignos, D. G., and Krawinkler, H. (2009). "Sidesway collapse of deteriorating structural systems under seismic excitations." *Rep. No. TB 172*, The John A. Blume Earthquake Engineering Center, Stanford Univ., Stanford, CA.

Lignos, D. G., & Krawinkler, H. (2010). Deterioration modeling of steel components in support of collapse prediction of steel moment frames under earthquake loading. *Journal of Structural Engineering*, *137*(11), 1291-1302.

Lignos, D. G., Krawinkler, H., & Whittaker, A. S. (2011). Prediction and validation of sidesway collapse of two scale models of a 4- story steel moment frame. *Earthquake Engineering & Structural Dynamics*, *40*(7), 807-825.

Liu, J., & Astaneh-Asl, A. (2000). Cyclic testing of simple connections including effects of slab. *Journal of Structural Engineering*, *126*(1), 32-39.

Liu, J., & Astaneh-Asl, A. (2004). Moment-rotation parameters for composite shear tab connections. *Journal of Structural Engineering*, *130*(9), 1371-1380.

MacRae, G. A., Kimura, Y., & Roeder, C. (2004). Effect of column stiffness on braced frame seismic behavior. *Journal of Structural Engineering*, *130*(3), 381-391.

MacRae, G., Clifton, G. C., Bruneau, M., Kanvinde, A., & Gardiner, S. (2015). Lessons from Steel Structures in Christchurch Earthquakes. *Behaviour of Steel Structures in Seismic Areas STESSA 2015*.

Mahin, S., Malley, J., & Hamburger, R. (2002). Overview of the FEMA/SAC program for reduction of earthquake hazards in steel moment frame structures. *Journal of Constructional Steel Research*, *58*(5), 511-528.

Massachusetts State Building Code. (2010). Massachusetts State Board of Building Regulations and Standards. (780 CMR), Eighth Edition. Boston, MA.

Menegotto, M., and Pinto, P. E. (1973). "Method of analysis for cyclically loaded reinforced concrete plane frames including changes in geometry and non-elastic behavior of elements under combined normal force and bending." *Proc., IABSE Symposium on Resistance and Ultimate Deformability of Structures Acted on by Well Defined Repeated Loads*, 15–22.

McKenna, F. (1997). Object oriented finite element programming frameworks for analysis, algorithms and parallel computing. (Ph.D. dissertation, Univ. of Calif. at Berkeley, CA).

Nakashima, M. (1995). Reconnaissance report on damage to steel buildings structures observed from the 1995 Hyogoken-Nanbu (Hanshin/Awaji) earthquake, Abridged English edition. *Steel Committee of Kinki Branch, the Architectural Institute of Japan (AIJ)*.

Nakashima, M. & Bruneau, M. (1995). 'English Edition of Preliminary Reconnaissance Report of the 1995 Hyogoken-Nanbu Earthquake,' The Architectural Institute of Japan, April 1995, 215pp.

Nakashima, M., Inoue, K., & Tada, M. (1998). Classification of damage to steel buildings observed in the 1995 Hyogoken-Nanbu earthquake. *Engineering Structures*, *20*(4), 271-281.

Nelson, J. (2014). Lateral system design philosophy within moderate seismic regions: Tozzer library case study and angle connection component test program. (M.S. Thesis, Tufts University).

Nelson, J., Bradley, C., Davaran, A., Beland, T., Hines, E. M., Fahnestock, L. A., & Tremblay, R. (2014). Cyclic experimental behavior of angles and applications for connection design and modeling. *Proceedings, 2014 Structures Congress*. Boston, MA.

Newmark, N. M. (1959). A method of computation for structural dynamics. In *Proc. ASCE* (Vol. 85, No. 3, pp. 67-94).

Osteraas, J., & Krawinkler, H. (1989). The Mexico earthquake of September 19, 1985-Behavior of steel buildings. *Earthquake Spectra*, *5*(1), 51-88.

Pacific Earthquake Engineering Research Center. Applied Technology Council. (PEER/ATC). (2010), *Modeling and Acceptance Criteria for Seismic Design and Analysis of Tall Buildings*. PEER/ATC 72-1 Report, Applied Technology Council, Redwood City, CA.

Petersen, M.D., Moschetti, M.P., Powers, P.M., Mueller, C.S., Haller, K.M., Frankel, A.D., Zeng, Yuehua, Rezaeian, Sanaz, Harmsen, S.C., Boyd, O.S., Field, Ned, Chen, Rui, Rukstales, K.S., Luco, Nico, Wheeler, R.L., Williams, R.A., and Olsen, A.H. (2014). Documentation for the 2014 update of the United States national seismic hazard maps: U.S. Geological Survey Open-File Report 2014–1091, 243 p., *http://dx.doi.org/10.3133/ofr20141091*.

Rai, D. C., & Goel, S. C. (2003). Seismic evaluation and upgrading of chevron braced frames. *Journal of Constructional Steel Research*, *59*(8), 971-994.

Roeder, C. W., Foutch, D. A., & Goel, S. C. (1987). Seismic testing of full-scale steel building-Part II. *Journal of Structural Engineering*, *113*(11), 2130-2145.

Ross, A. E., & Mahin, S. H. (1994). Steel moment resisting frames and the Northridge earthquake. In *Proceedings, 6th US-Japan Workshop on the Improvement of Building Structural Design and Construction Practices* (pp. 15-5).

Saatcioglu, M., Tremblay, R., Mitchell, D., Ghobarah, A., Palermo, D., Simpson, R., Adebar, P., Ventura, C., & Hong, H. (2013). Performance of steel buildings and nonstructural elements during the 27 February 2010 Maule (Chile) Earthquake 1. *Canadian Journal of Civil Engineering*, *40*(8), 722-734.

Sen, A. D. (2015). Seismic performance of chevron concentrically braced frames with weak beams (Doctoral dissertation).

Sen, A. D., Ballard, R., Sloat, D., Johnson, M., Roeder, C. W., Lehman, D. E., & Berman, J. W. (2015). Seismic Evaluation and Retrofit of Older Concentrically-Braced Frames. *In Improving the Seismic Performance of Existing Buildings and Other Structures 2015* (pp. 317-327).

Sen, A. D., Roeder, C. W., Berman, J. W., Lehman, D. E., Li, C. H., Wu, A. C., & Tsai, K. C. (2016). Experimental Investigation of Chevron Concentrically Braced Frames with Yielding Beams. *Journal of Structural Engineering*, 04016123.

Sizemore, J., Davaran, A., Fahnestock, L., Tremblay, R., and Hines, E. (2014) Seismic Behavior of Low-Ductility Concentrically-Braced Frames. *Proceedings, 2014 Structures Congress.* Boston, MA.

Sizemore, J., Fahnestock, L., Hines, E., and Bradley, C. (2016, accepted). Parametric Study of Low-Ductility Concentrically-Braced Frames under Cyclic Static Loading. *Journal of Structural Engineering*

Smyrou, E., Tasiopoulou, P., Bal, Ï. E., & Gazetas, G. (2011). Ground motions versus geotechnical and structural damage in the February 2011 Christchurch earthquake. *Seismological research letters*, *82*(6), 882-892.

Sorabella, S. (2006). Ground Motion Selection for Boston, Massachusetts. (Masters Thesis). Tufts University.

Stoakes, C. D., & Fahnestock, L. A. (2010). Cyclic flexural testing of concentrically braced frame beam-column connections. *Journal of Structural Engineering*, *137*(7), 739-747.

Stoakes, C. D., & Fahnestock, L. A. (2012). Cyclic flexural analysis and behavior of beam-column connections with gusset plates. *Journal of Constructional Steel Research*, *72*, 227-239.

Stoakes, C. (2012). Beam-column connection flexural behavior and seismic collapse performance of concentrically braced frames. (Doctoral dissertation). University of Illinois at Urbana-Champaign.

Tang, X., & Goel, S. C. (1989). Brace fractures and analysis of phase I structure. *Journal of Structural Engineering*, *115*(8), 1960-1976.

Terzic, V. (2011). Force-based Element vs. Displacement-based Element. *UC Berkeley, OpenSees, NEES, & NEEScomm.*

Terzic, V. (2013). Modeling SCB frames using beam-column elements. In *Discovering OpenSees seminar*.

Tremblay, R., & Stiemer, S. F. (1994). Backup stiffness for improving the stability of multi-storey braced frames under seismic loading. *Proceedings of the 1994 SSRC Annual Technical Session, Bethlehem, Pa*, 311-325.

Tremblay, R., Filiatrault, A., Timler, P., & Bruneau, M. (1995). Performance of steel structures during the 1994 Northridge earthquake. *Canadian Journal of Civil Engineering*, *22*(2), 338-360.

Tremblay, R., Filiatrault, A., Bruneau, M., Nakashima, M., Prion, H. G., & DeVall, R. (1996). Seismic design of steel buildings: lessons from the 1995 Hyogo-ken Nanbu earthquake. *Canadian Journal of Civil Engineering*, *23*(3), 727-756.

Tremblay, R. (2000), "Influence of Brace Slenderness on the Seismic Response of Concentrically Braced Steel Frames," *Behaviour of Steel Structures in Seismic Areas. Stessa 2000: Proceedings of the Third International Conference*, August 21–24, 2000,

F.M. Mazzolani and R. Tremblay, (eds.), pp. 527–534, Montreal, Canada. Tremblay, R., Mitchell, D., & Tinawi, R. (2013). Damage to industrial structures due to the 27 February 2010 Chile earthquake 1. *Canadian Journal of Civil Engineering*, *40*(8), 735-749.

United Nations Centre for Regional Development (UNCRD). (1995). Comprehensive Study of the Great Hanshin Earthquake, United Nations Centre for Regional Development (UNCRD), Nagoya, November 1995.

Uriz, P. (2005). Towards earthquake resistant design of concentrically braced steel structures. (Doctoral dissertation). Dept. of Civil and Environmental Engineering, Univ. of California, Berkeley, CA

Uniform Building Code (UBC). (1979). *Uniform Building Code Standards.* International Conference of Building Officials, 1979. Whittier, CA.

United States Geological Survey. (USGS). (2013). Design Maps Summary Report. Retrieved from http:// geohazards.usgs.gov/designmaps/us/application.php

Vamvatsikos D, Cornell CA (2002): Incremental dynamic analysis. *Earthquake Engineering & Structural Dynamics*, *31*(3), 491-514

Yamanouchi, H., Midorikawa, M., Nishiyama, I., & Watabe, M. (1989). Seismic behavior of full-scale concentrically braced steel building structure. *Journal of Structural Engineering*, *115*(8), 1917-1929.

Yoo, J. H. (2006). Analytical investigation on the seismic performance of special concentrically braced frames. (Doctoral dissertation). University of Washington, Seattle.

Youssef, N. F., Bonowitz, D., & Gross, J. L. (1995). *A survey of steel moment-resisting frame buildings affected by the 1994 Northridge earthquake*. US National Institute of Standards and Technology.

Zareian, F., & Medina, R. A. (2010). A practical method for proper modeling of structural damping in inelastic plane structural systems. *Computers & structures*, *88*(1), 45-53.

APPENDIX A

SUPPLEMENTAL DYNAMIC ANALYSES RESULTS

A.1 INDIVIDUAL GROUND MOTION IDA CURVES

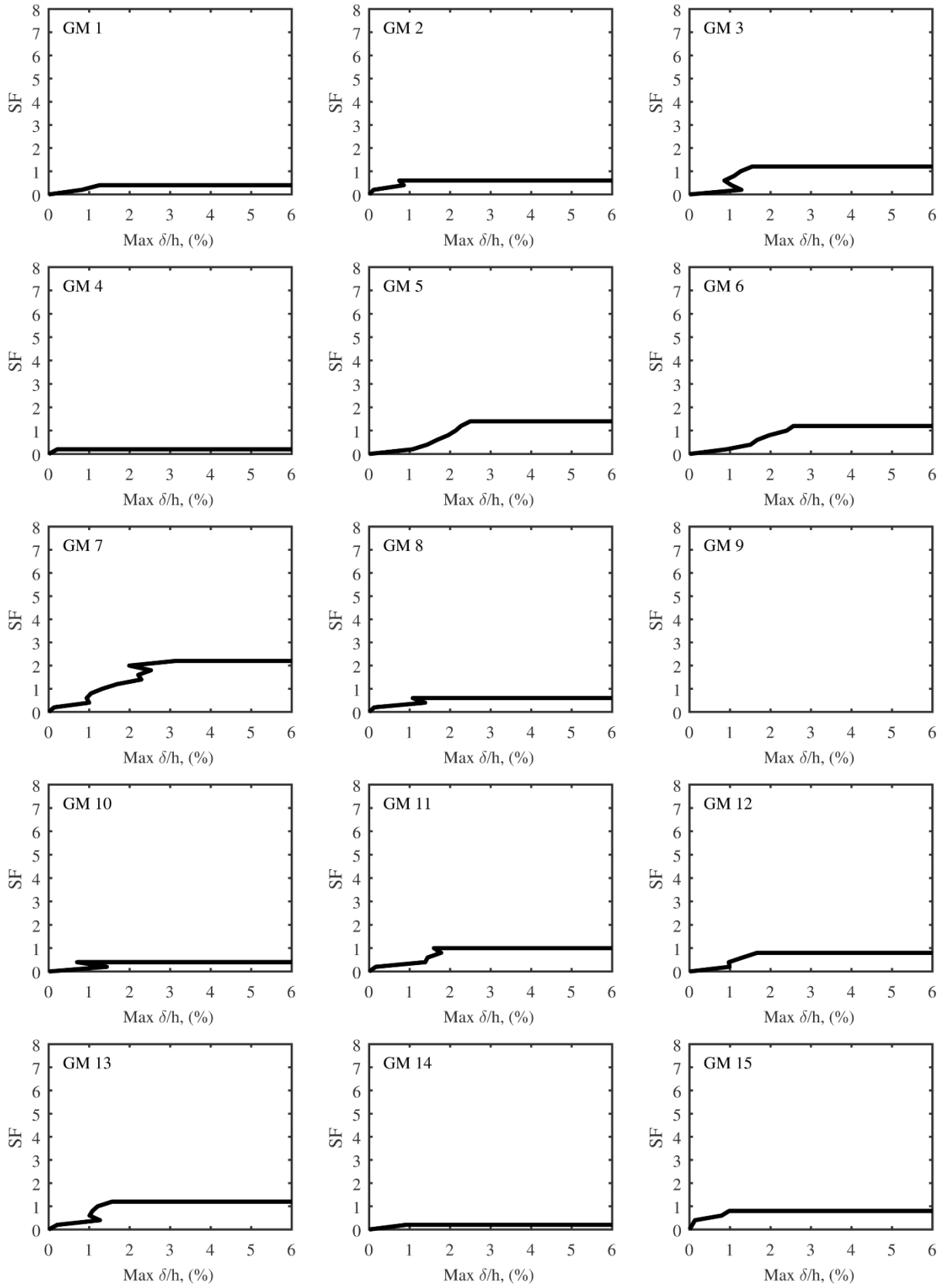

Figure A.1 – Individual IDA results for Ch. 3 prototype building R3-3-BC-Pin.

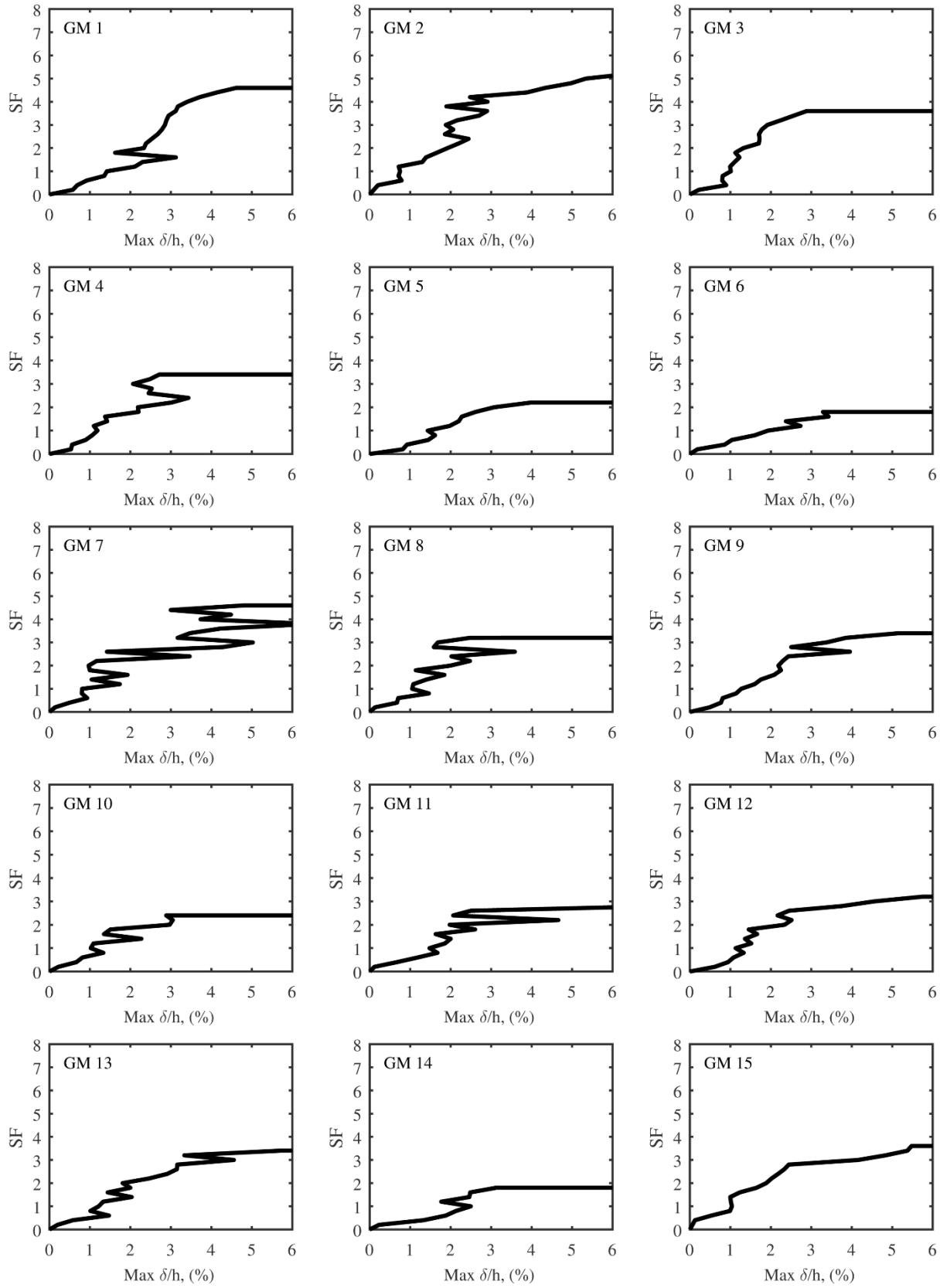

Figure A.2 – Individual IDA results for Ch. 3 prototype building R3-3-Baseline.

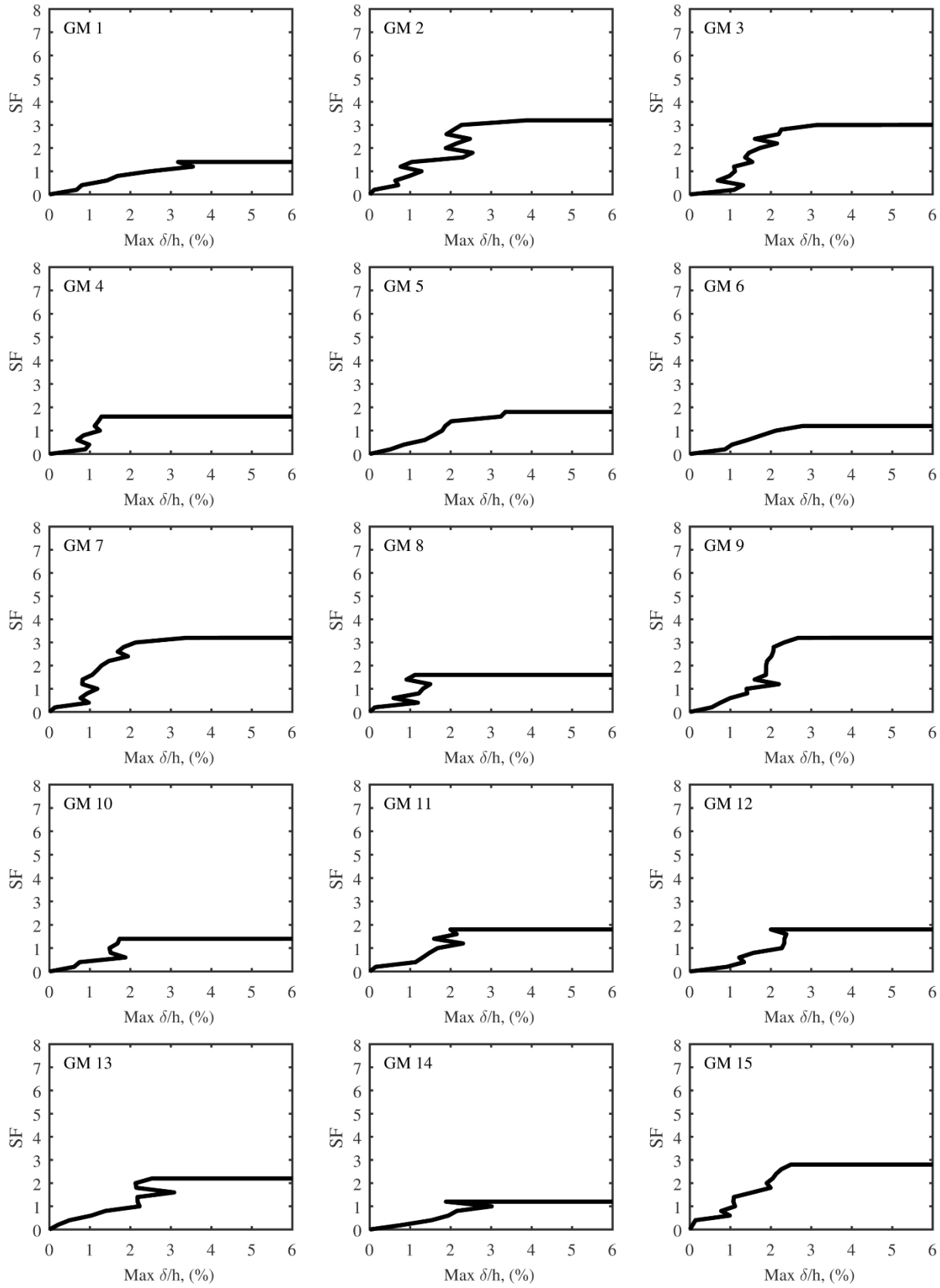

Figure A.3 – Individual IDA results for Ch. 3 prototype building R3-3-GBC-Pin.

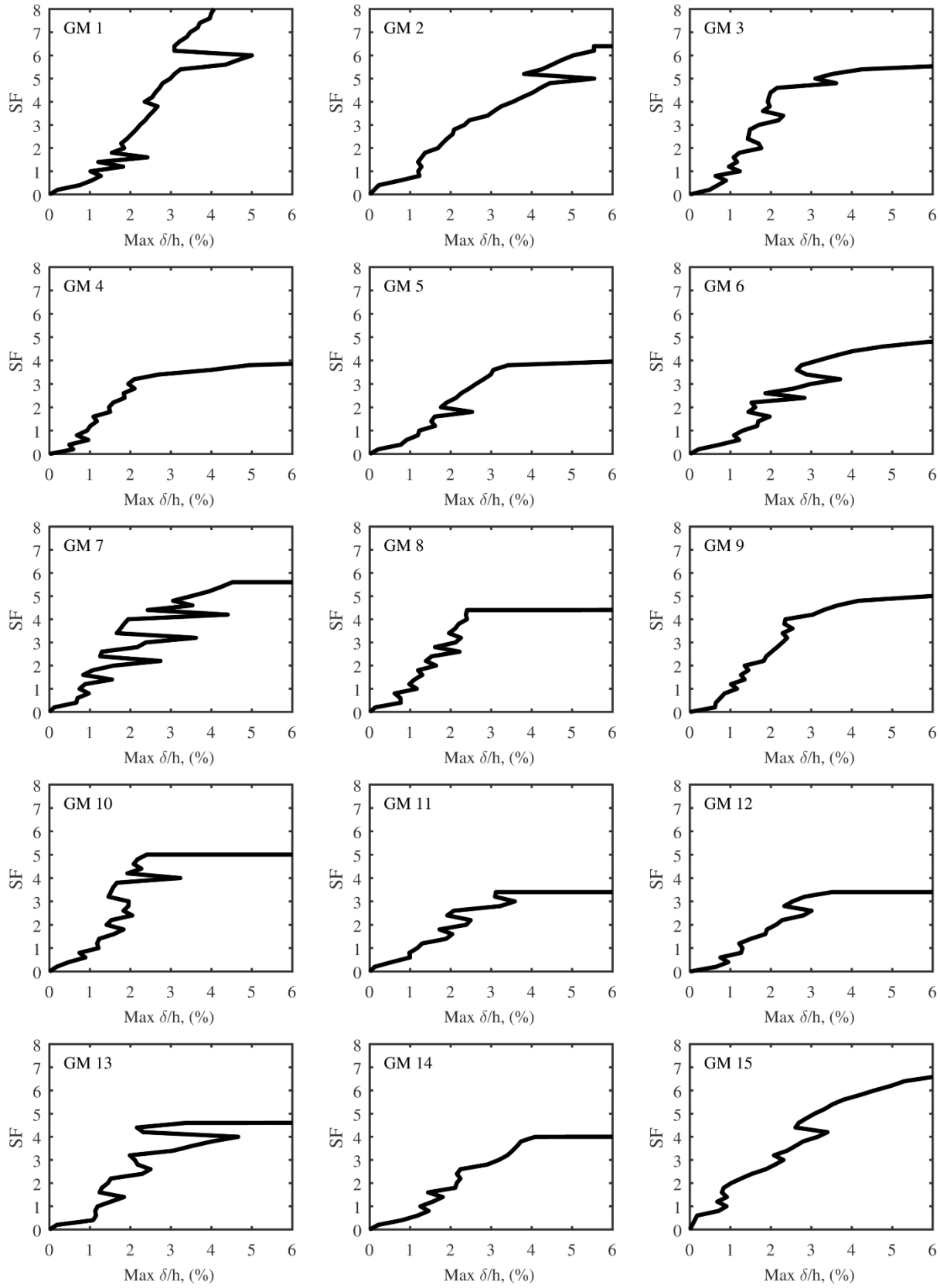

Figure A.4 – Individual IDA results for Ch. 3 prototype building R3-3-GBC-Pin.

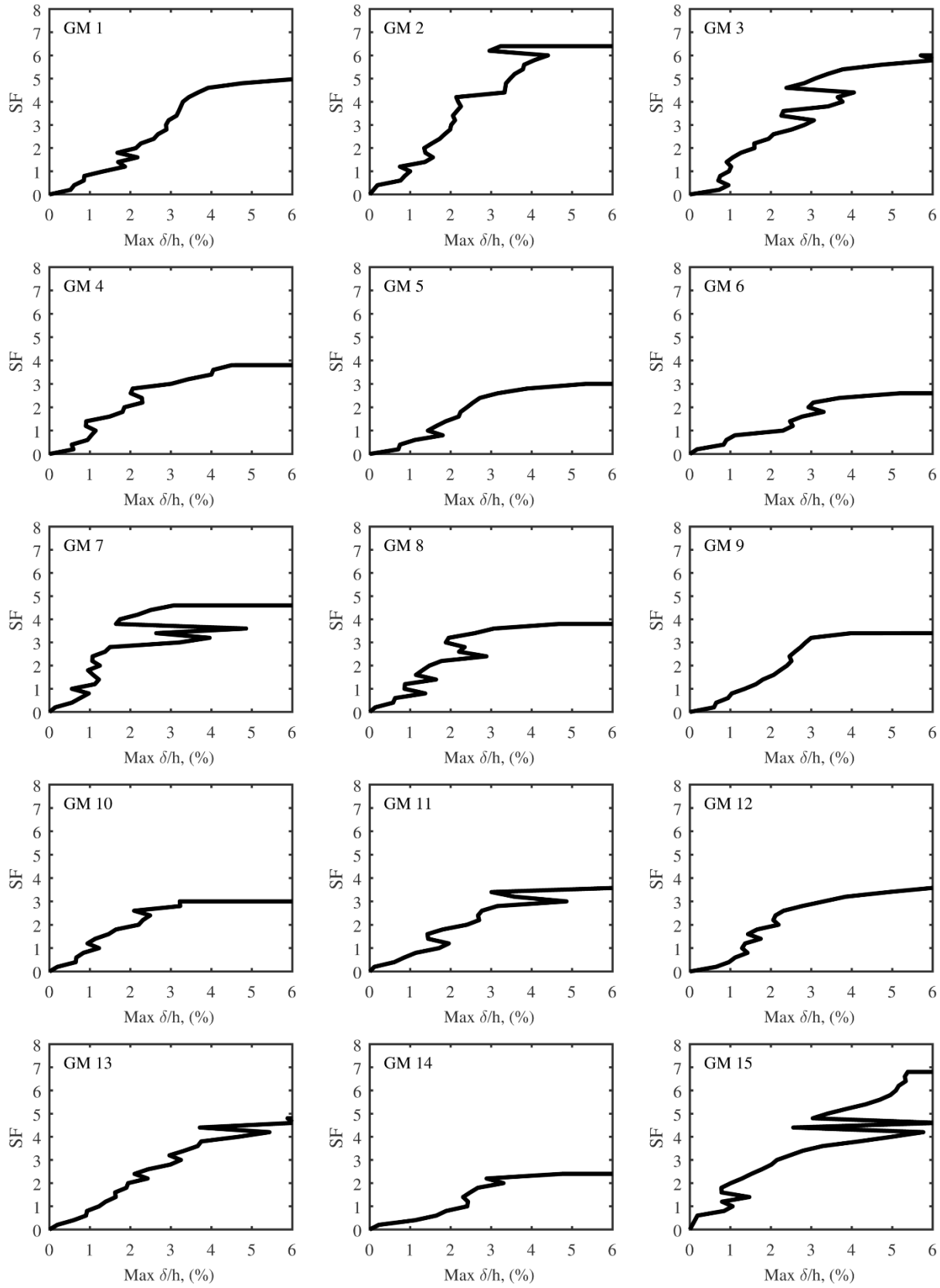

Figure A.5 – Individual IDA results for Ch. 3 prototype building R3-3-Beam-50.

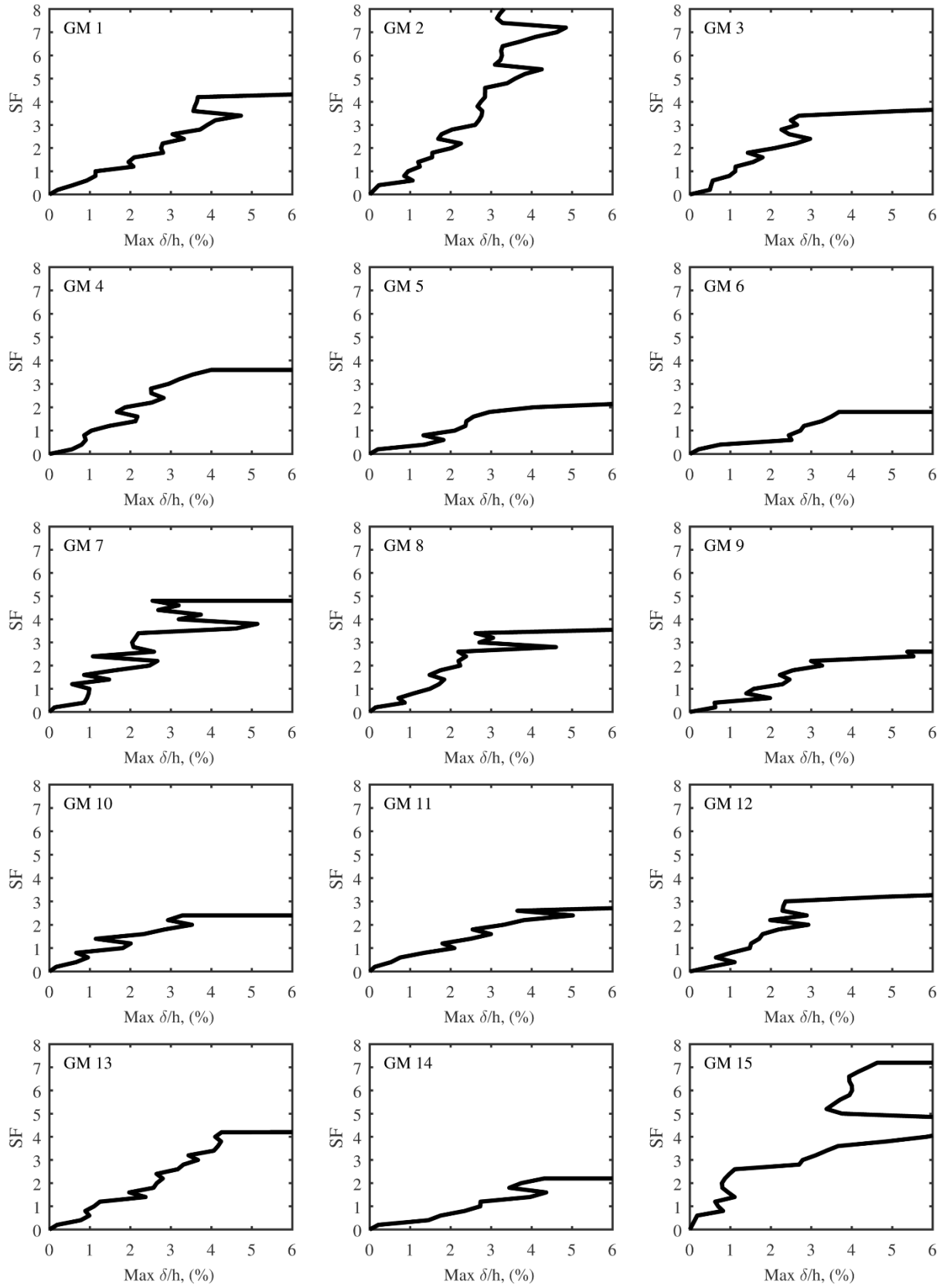

Figure A.6 – Individual IDA results for Ch. 3 prototype building R3-3-Col-50.

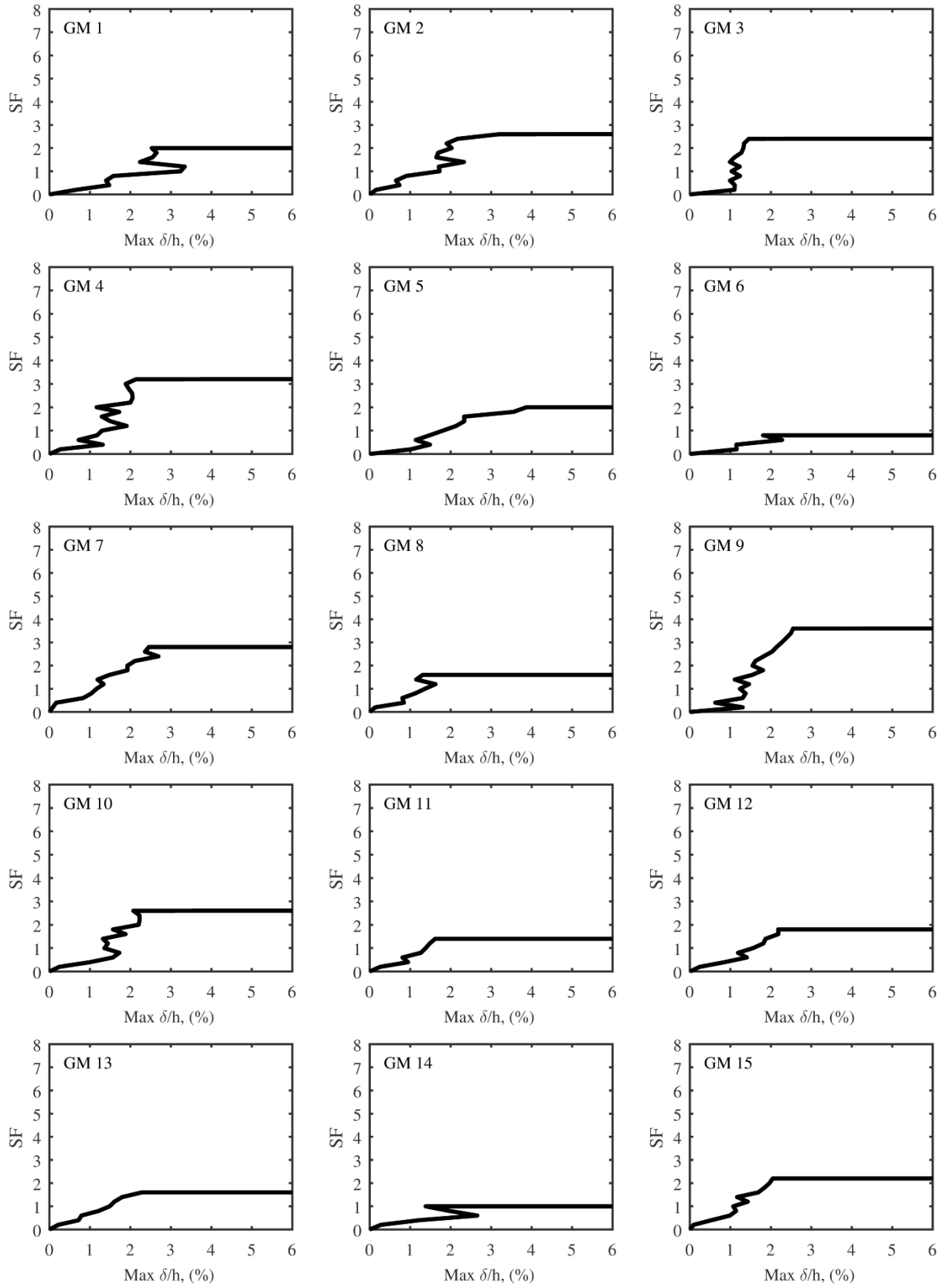

Figure A.7 – Individual IDA results for Ch. 8 building R3-CH-3 (Pinned GBC).

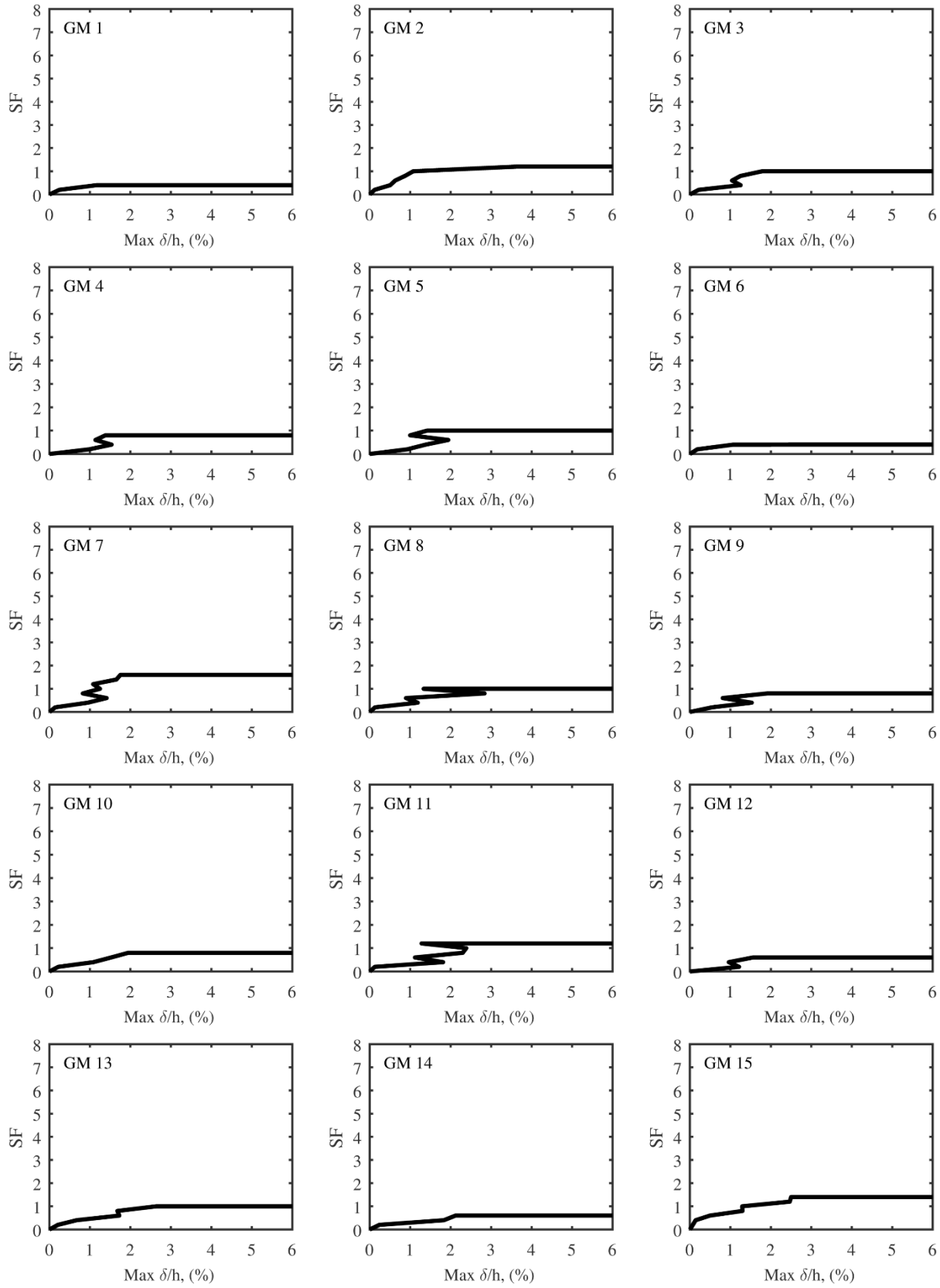

Figure A.8 – Individual IDA results for Ch. 8 building R3-SX-3 (Pinned GBC).

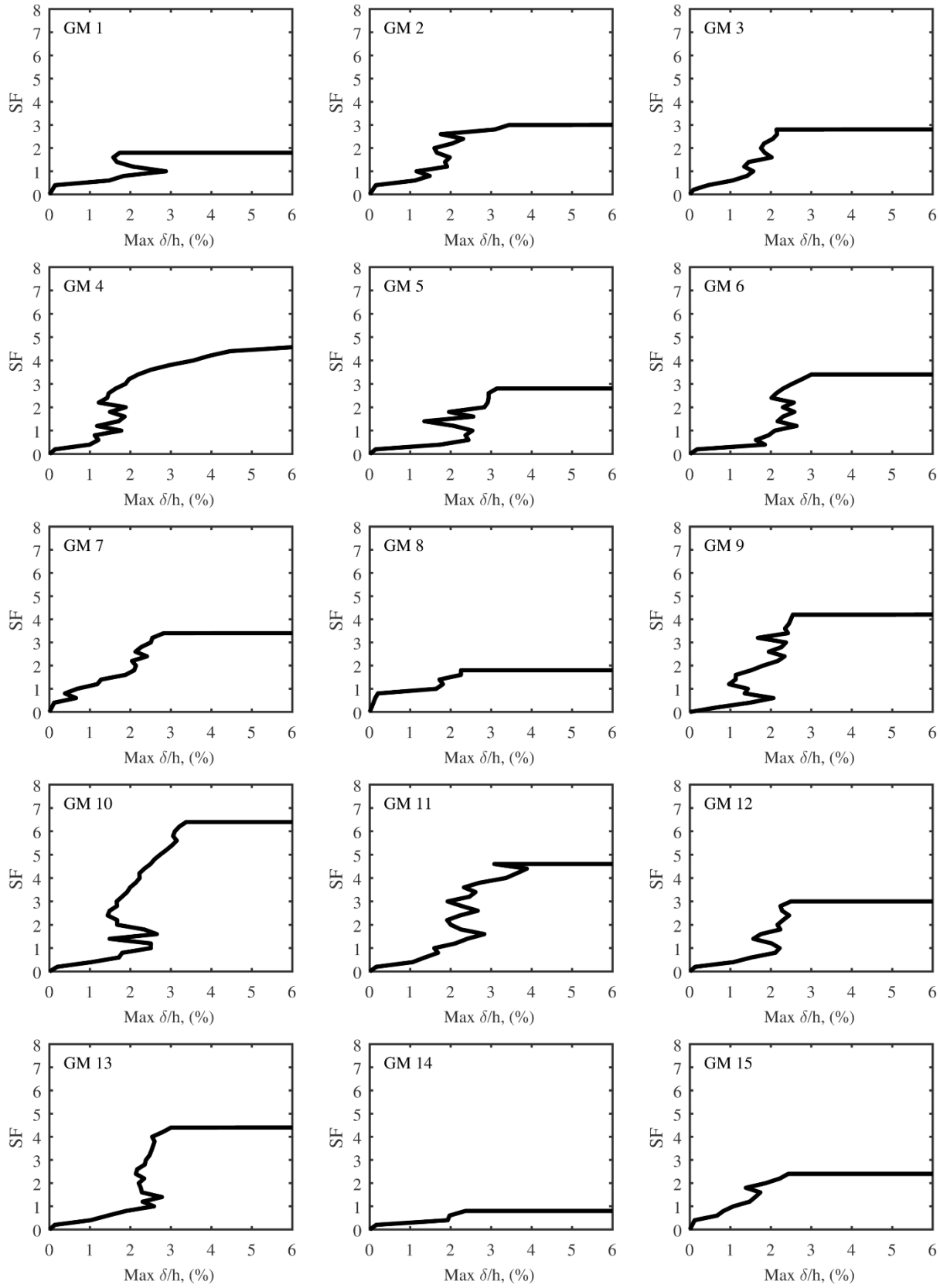

Figure A.9 – Individual IDA results for Ch. 8 building OC-CH-3 (Pinned GBC).

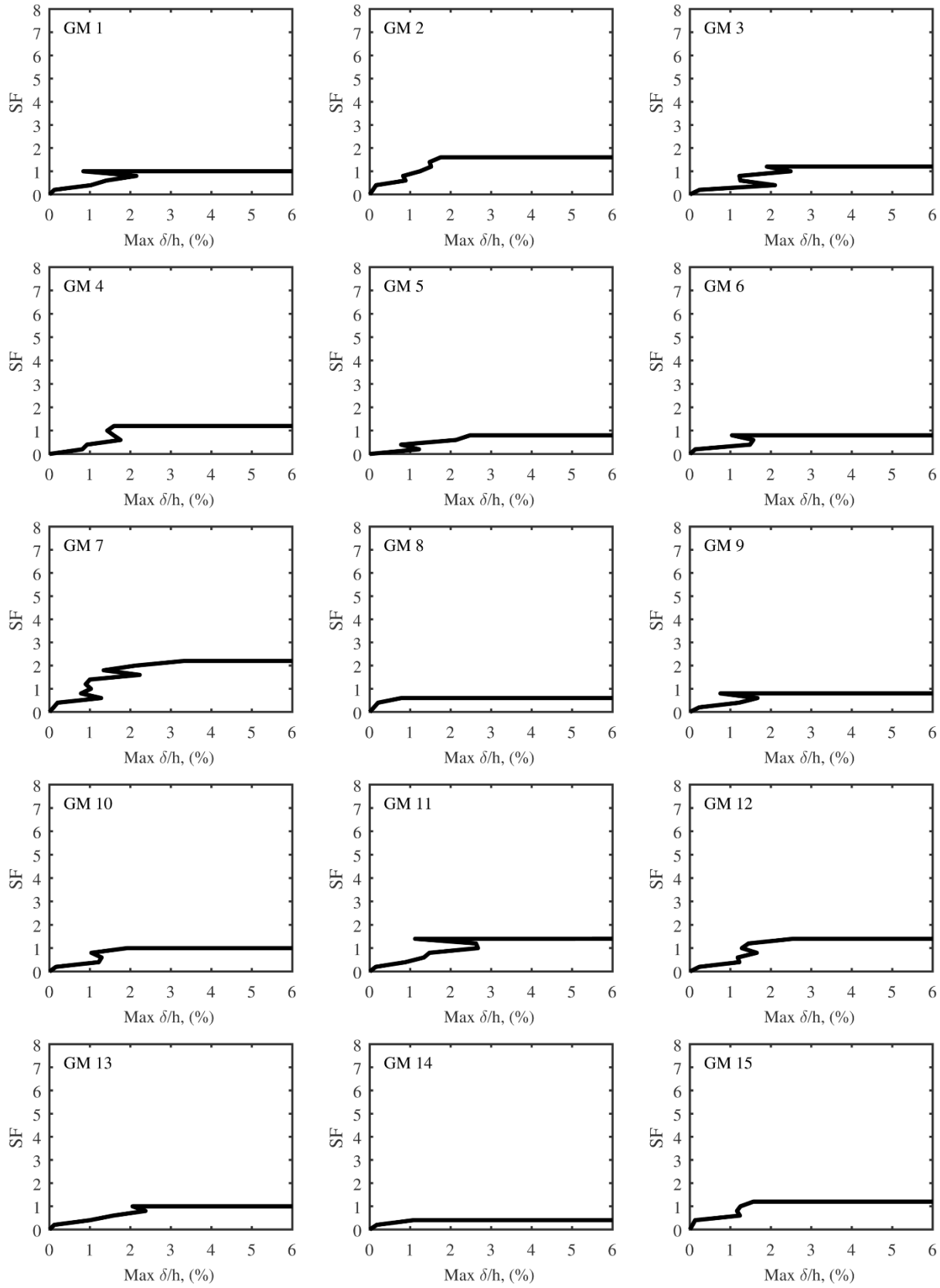

Figure A.10 – Individual IDA results for Ch. 8 building OC-SX-3 (Pinned GBC).

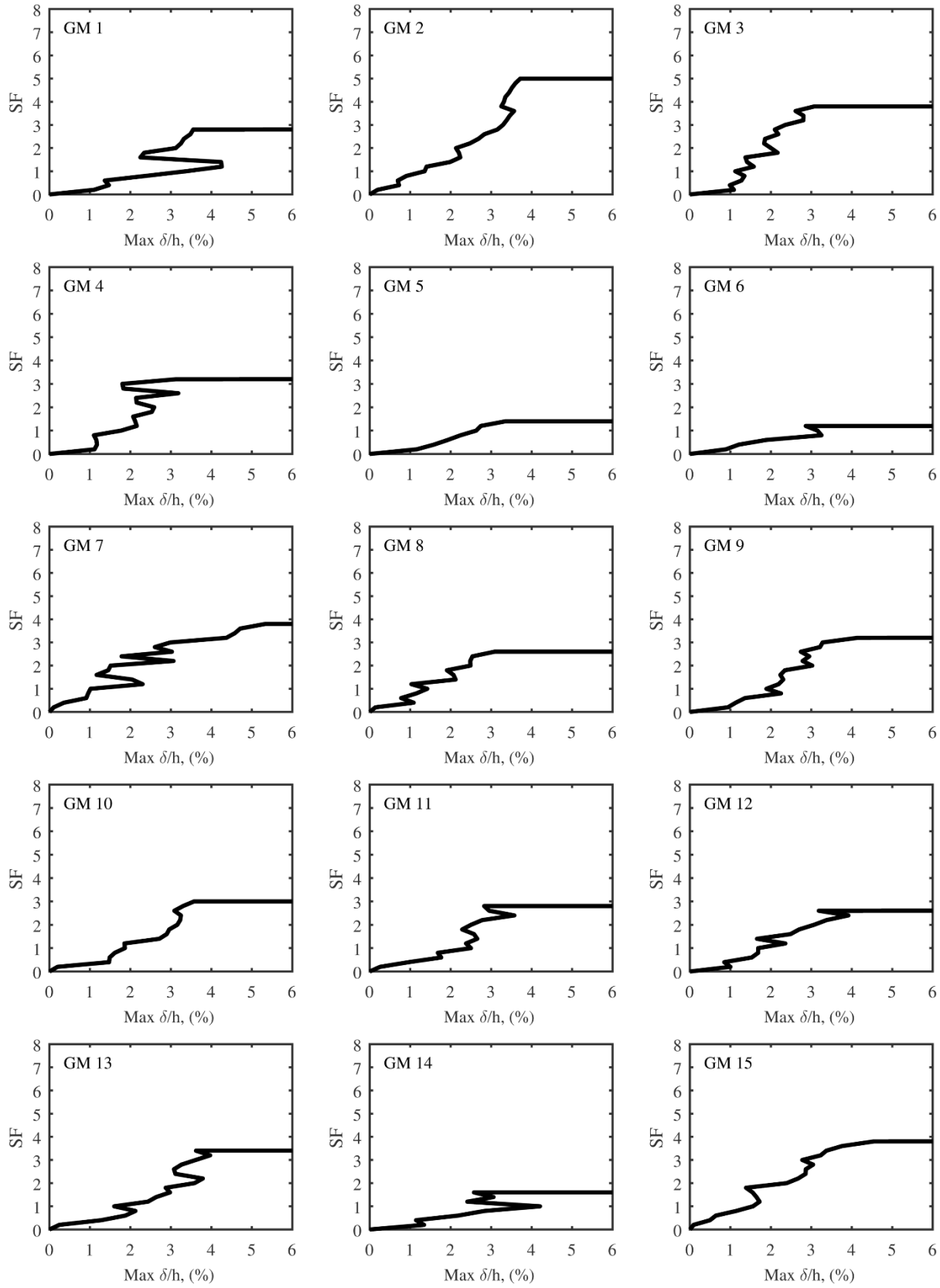

Figure A.11 – Individual IDA results for Ch. 8 building R4-CH-3 (Pinned GBC).

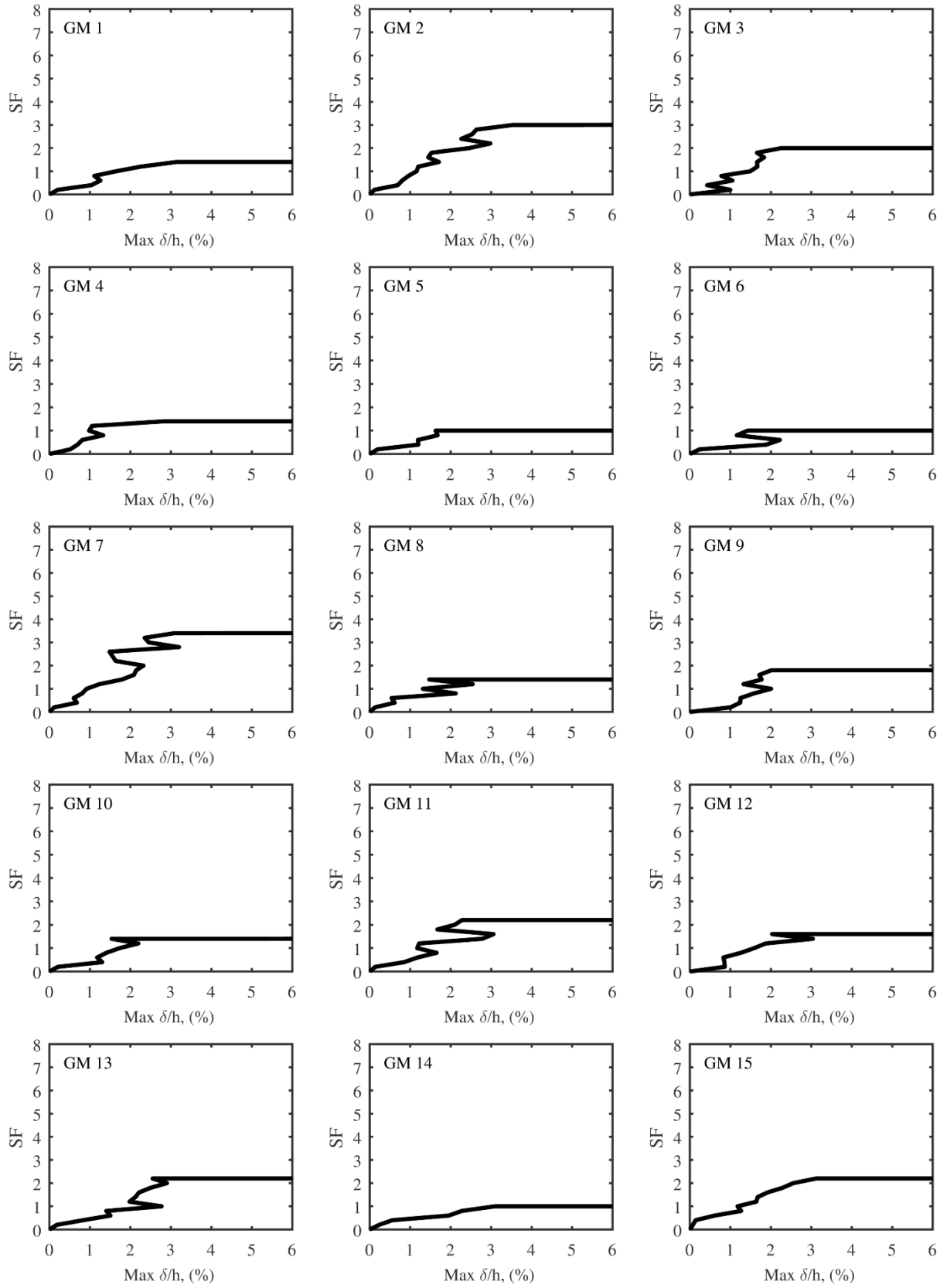

Figure A.12 – Individual IDA results for Ch. 8 building R4-SX-3 (Pinned GBC).

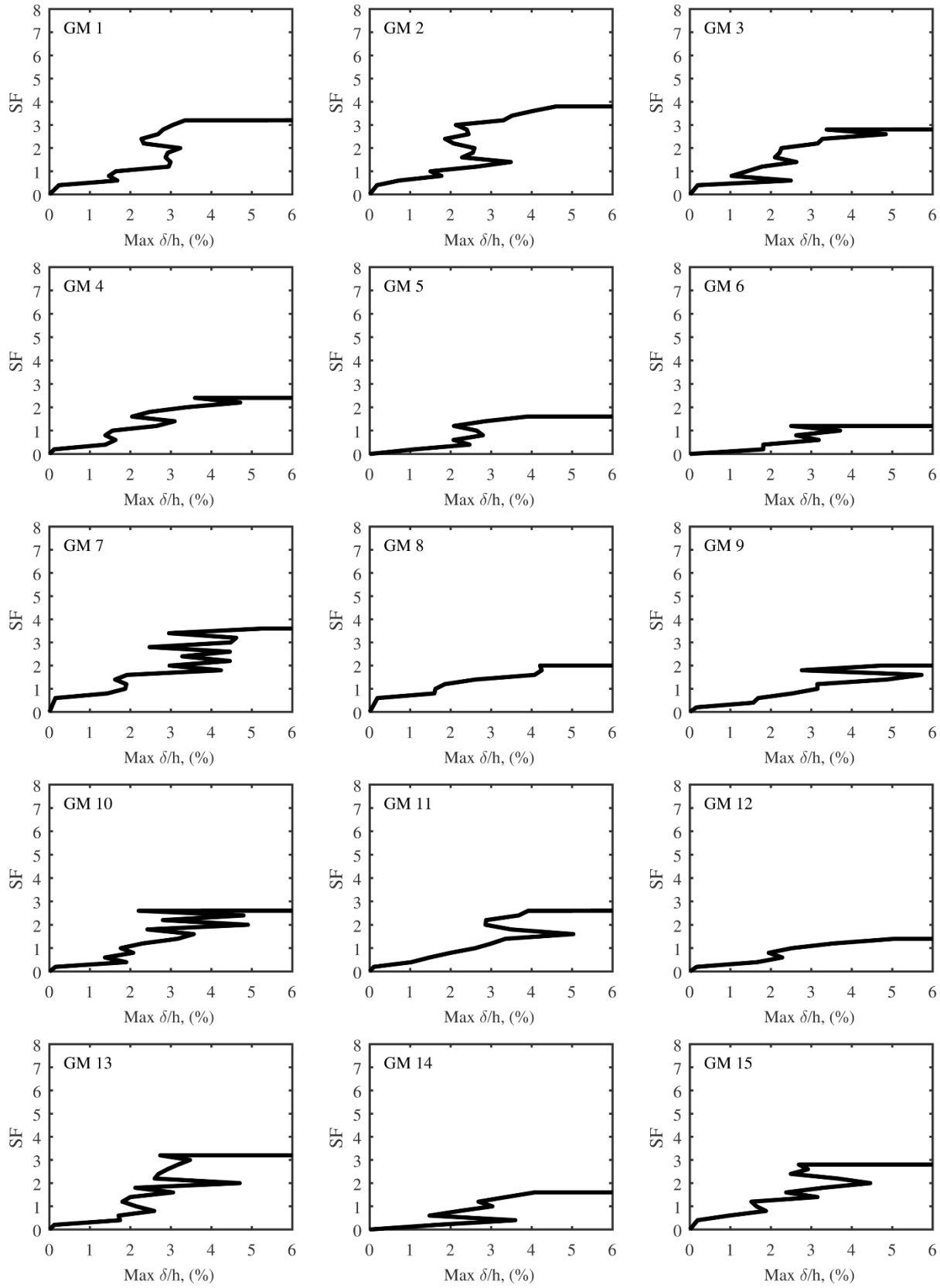

Figure A.13 – Individual IDA results for Ch. 8 building R3-CH-6 (Pinned GBC).

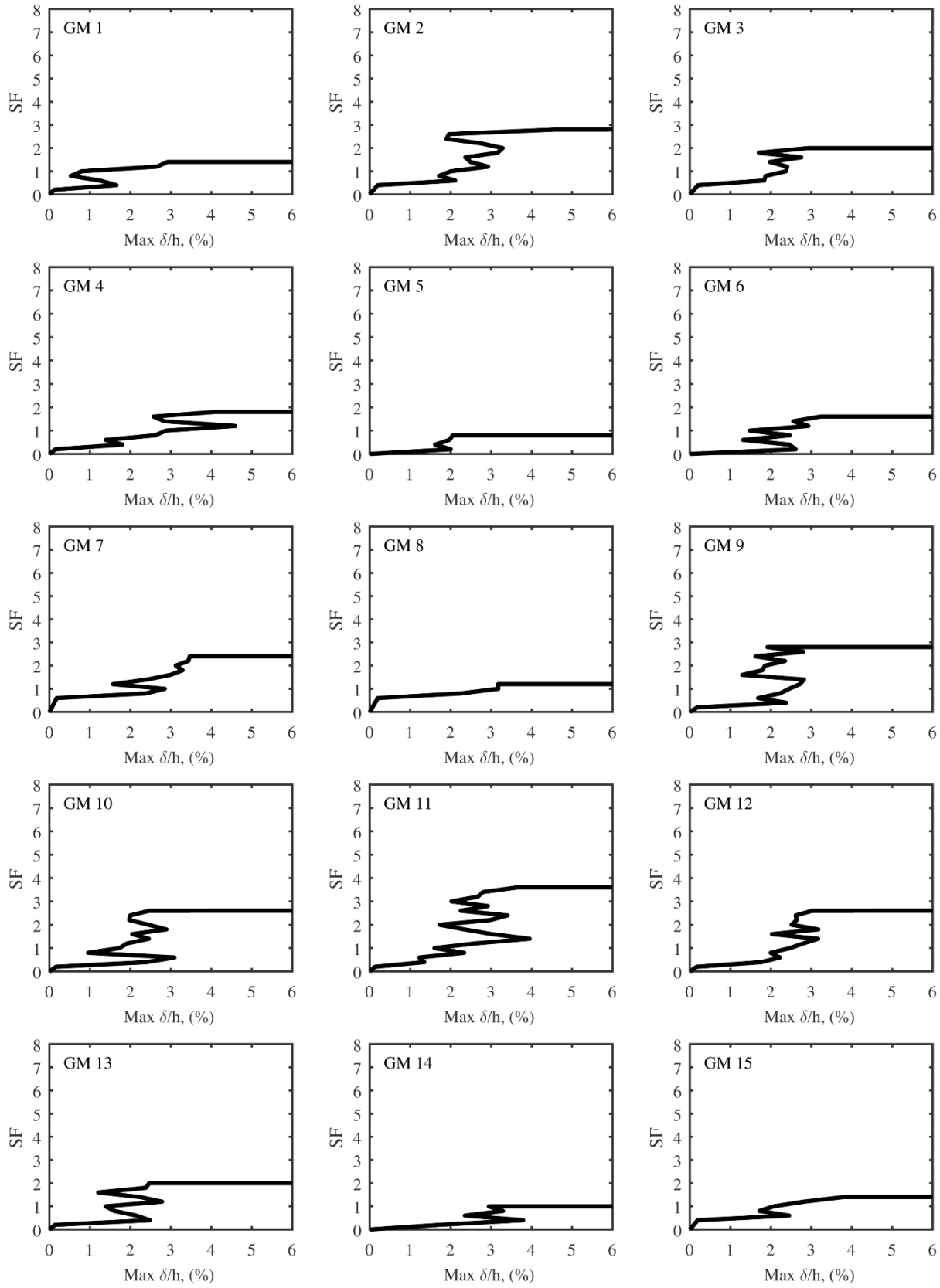

Figure A.14 – Individual IDA results for Ch. 8 building R3-SX-6 (Pinned GBC).

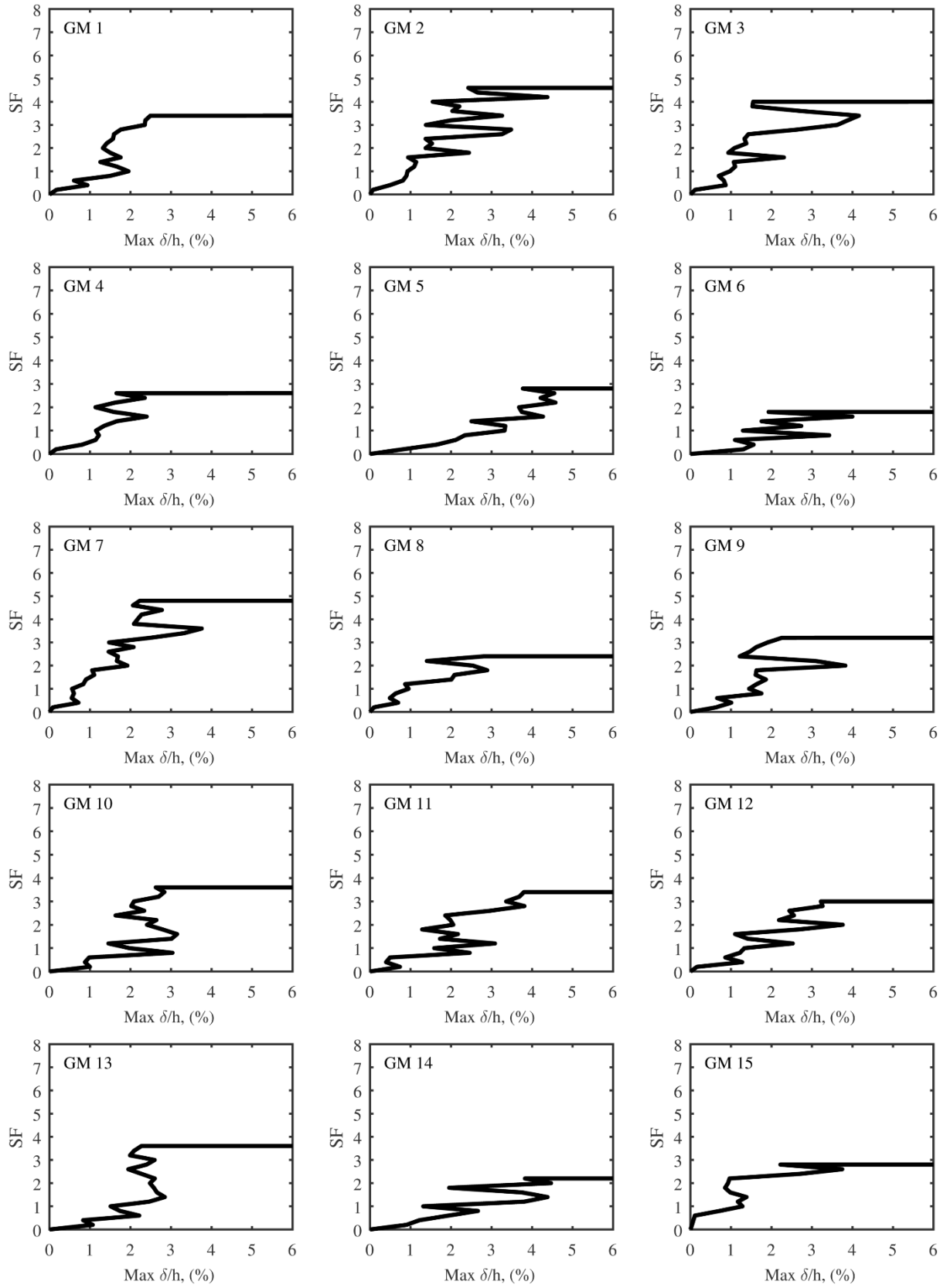

Figure A.15 – Individual IDA results for Ch. 8 building OC-CH-6 (Pinned GBC).

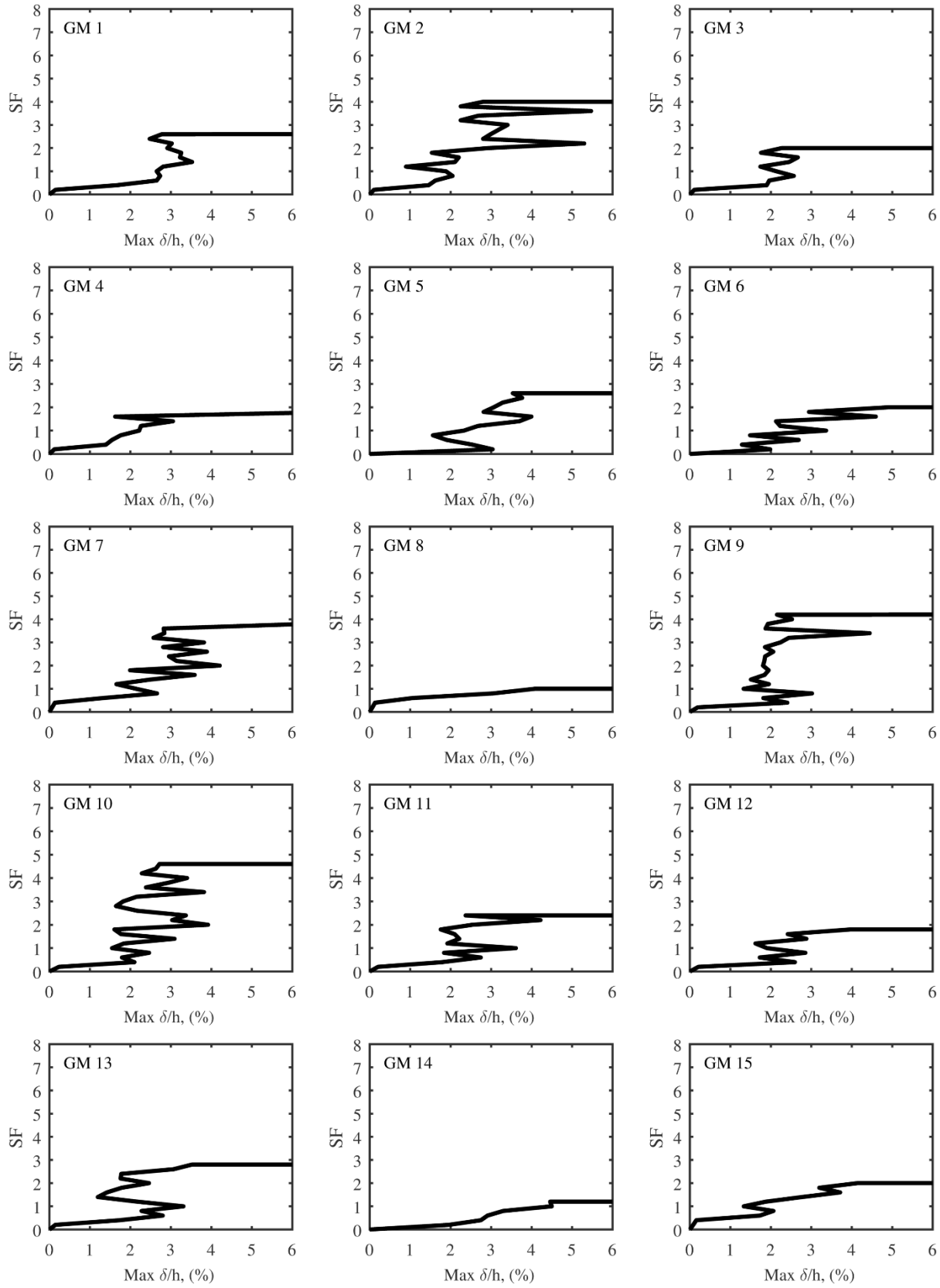

Figure A.16 – Individual IDA results for Ch. 8 building OC-SX-6 (Pinned GBC).

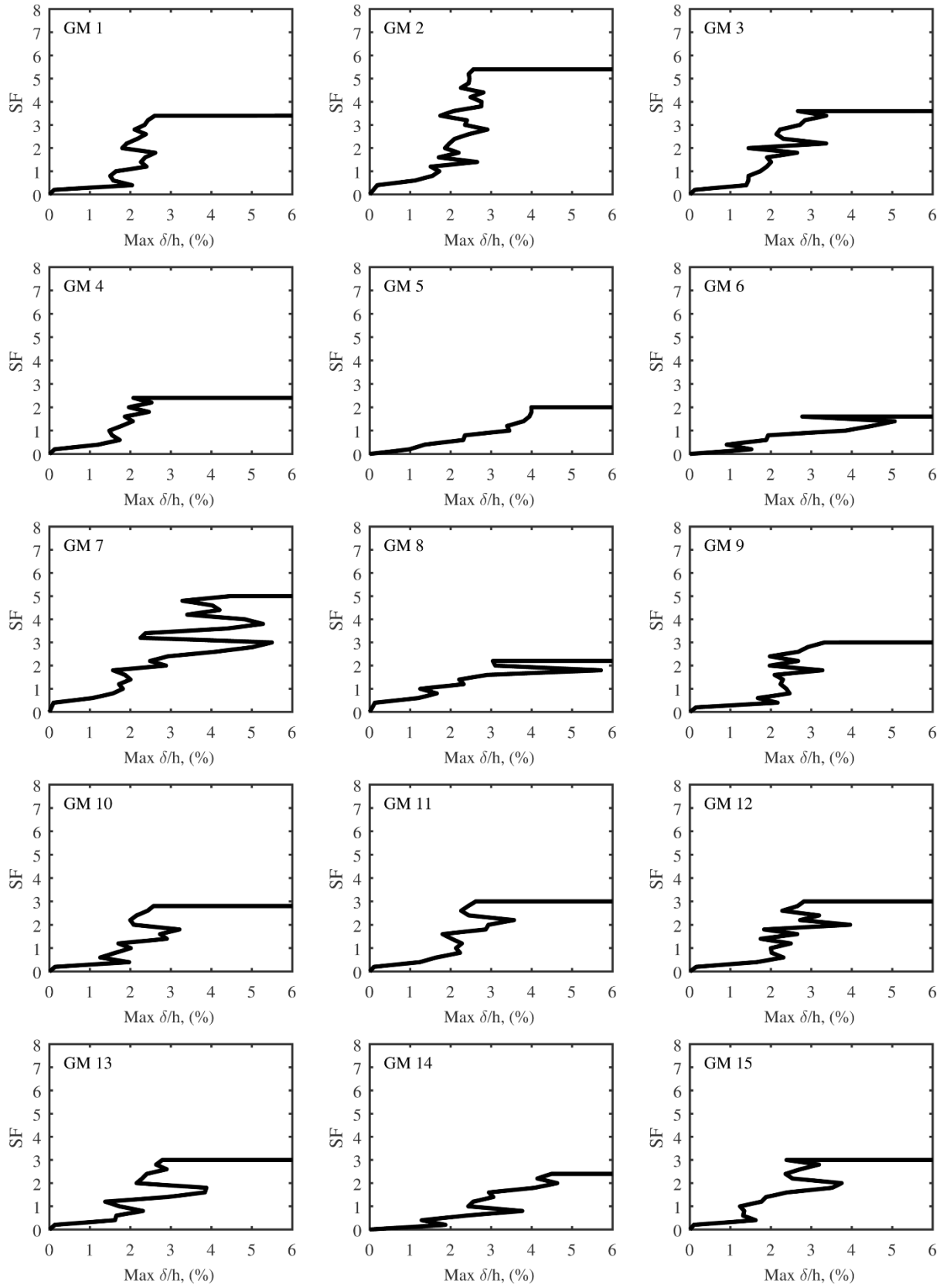

Figure A.17 – Individual IDA results for Ch. 8 building R4-CH-6 (Pinned GBC).

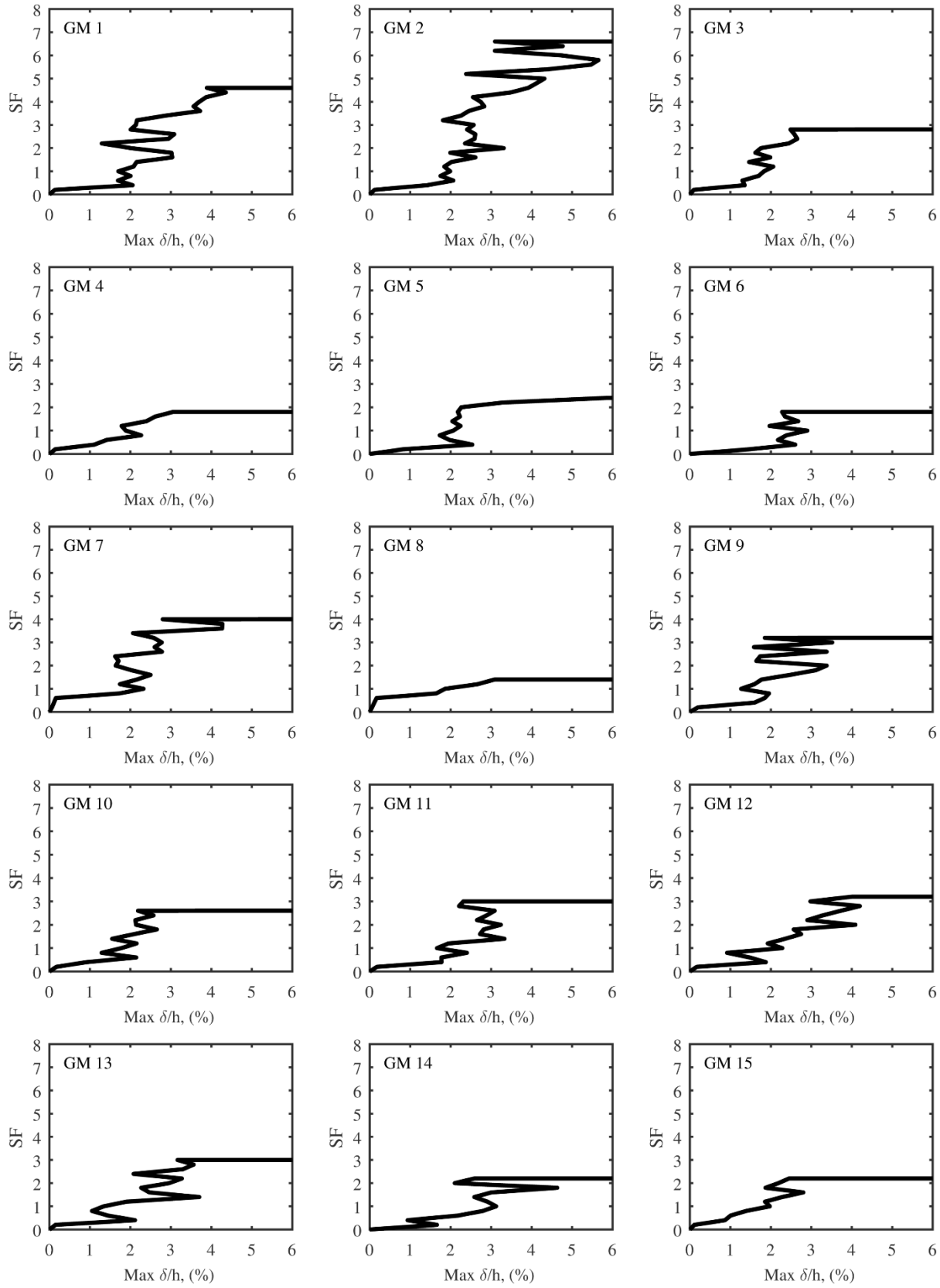

Figure A.18 – Individual IDA results for Ch. 8 building R4-SX-6 (Pinned GBC).

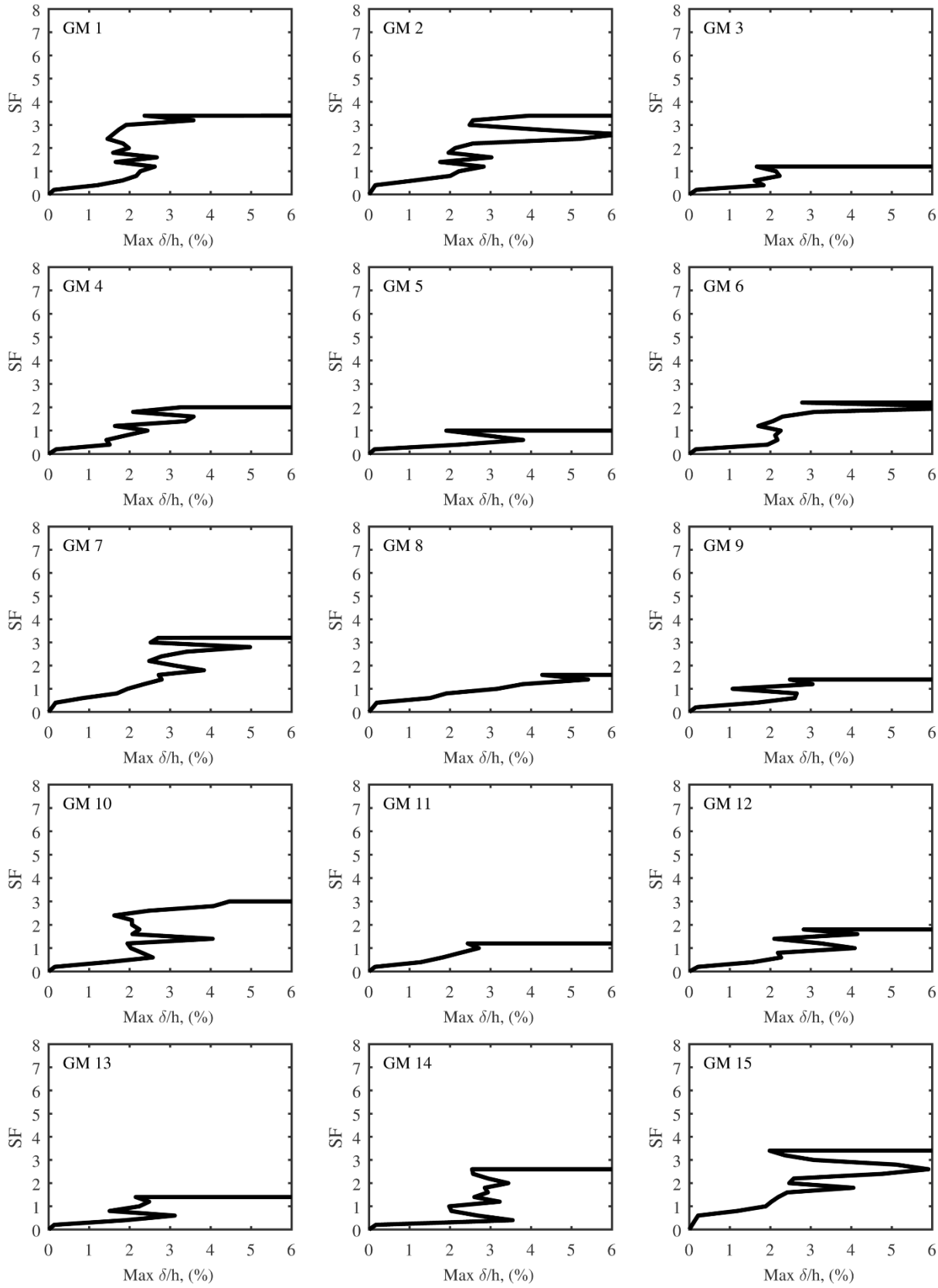

Figure A.19 – Individual IDA results for Ch. 8 building R3-CH-9 (Pinned GBC).

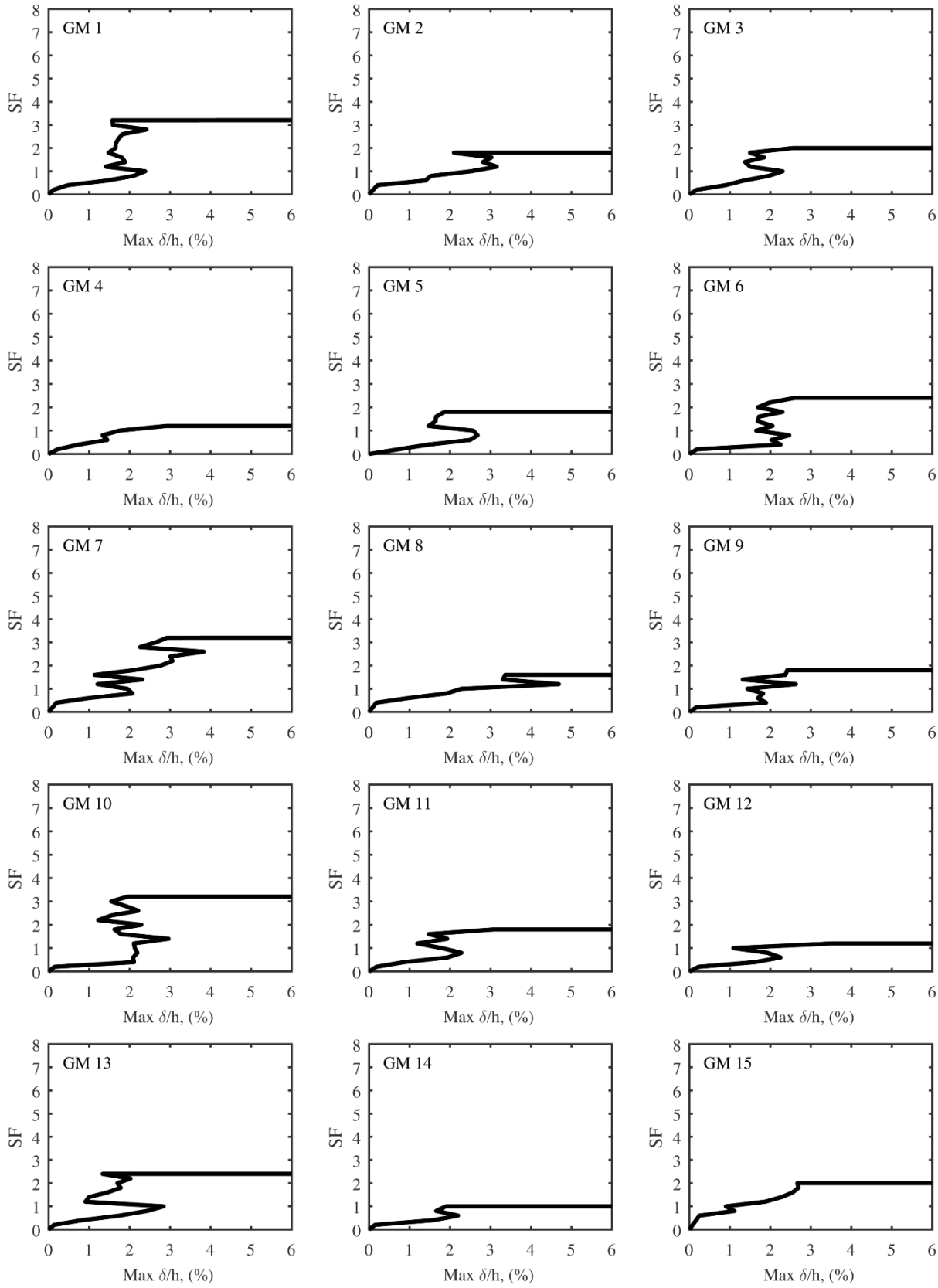

Figure A.20 – Individual IDA results for Ch. 8 building R3-SX-9 (Pinned GBC).

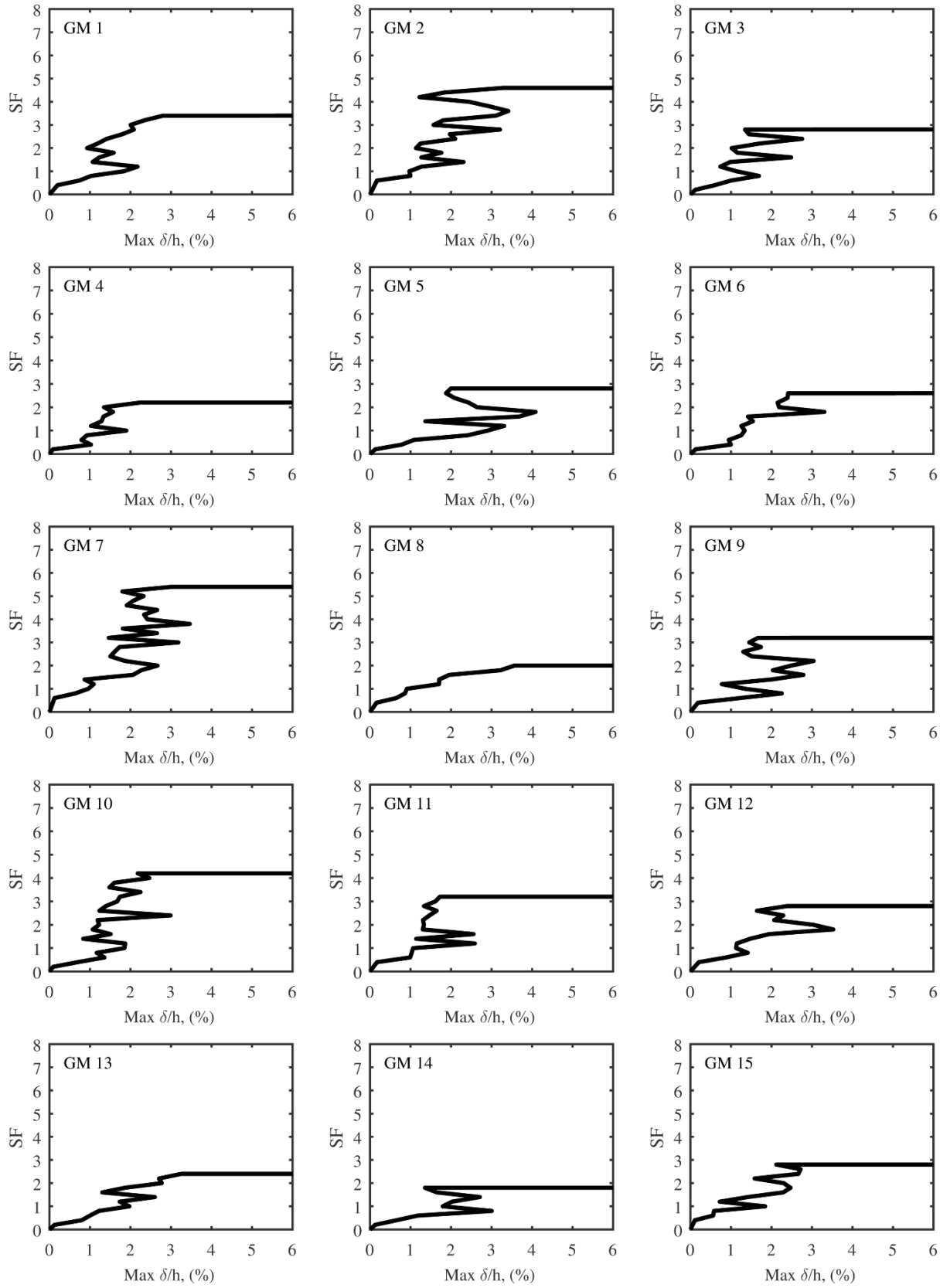

Figure A.21 – Individual IDA results for Ch. 8 building OC-CH-9 (Pinned GBC).

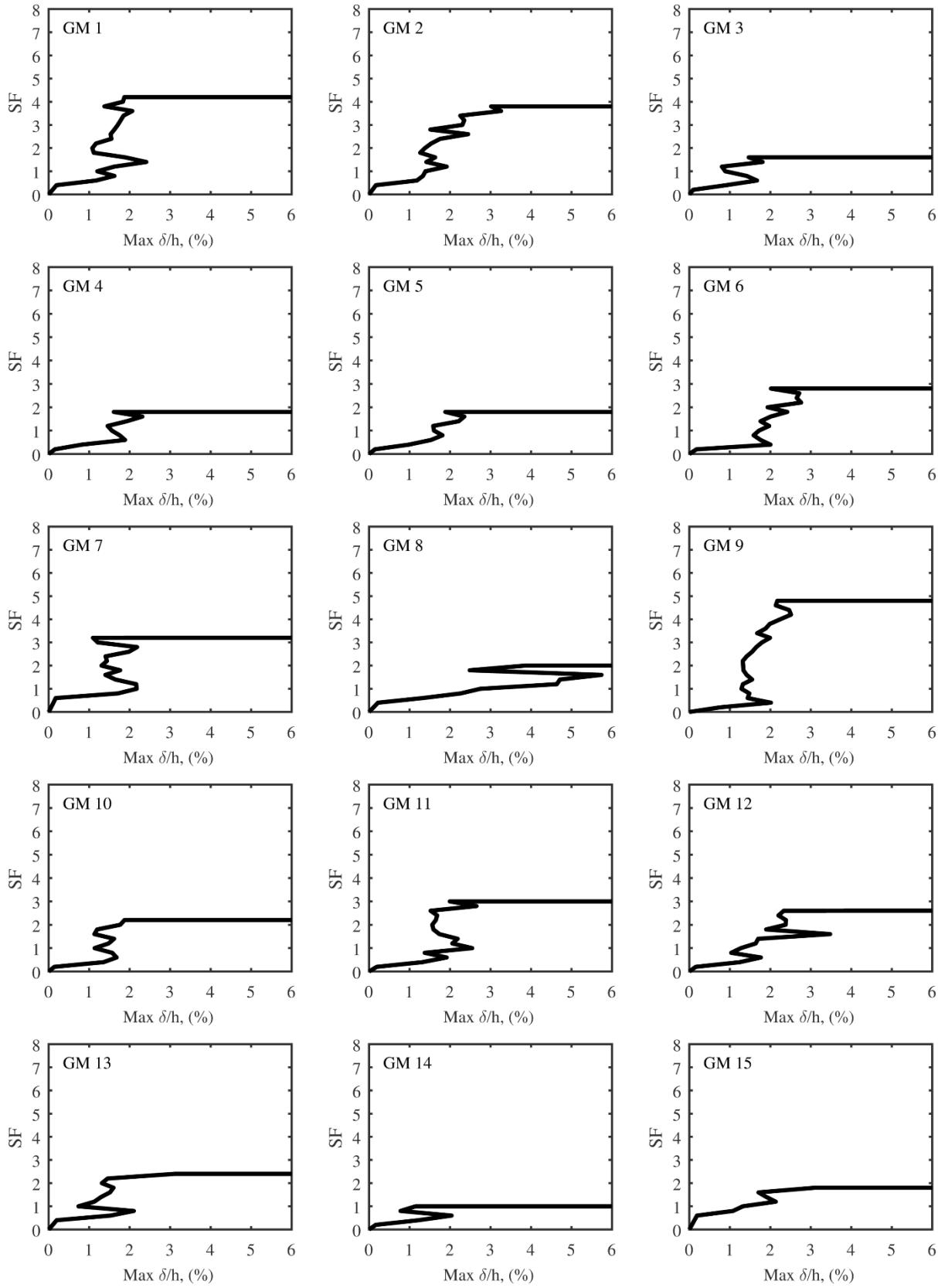

Figure A.22 – Individual IDA results for Ch. 8 building OC-SX-9 (Pinned GBC).

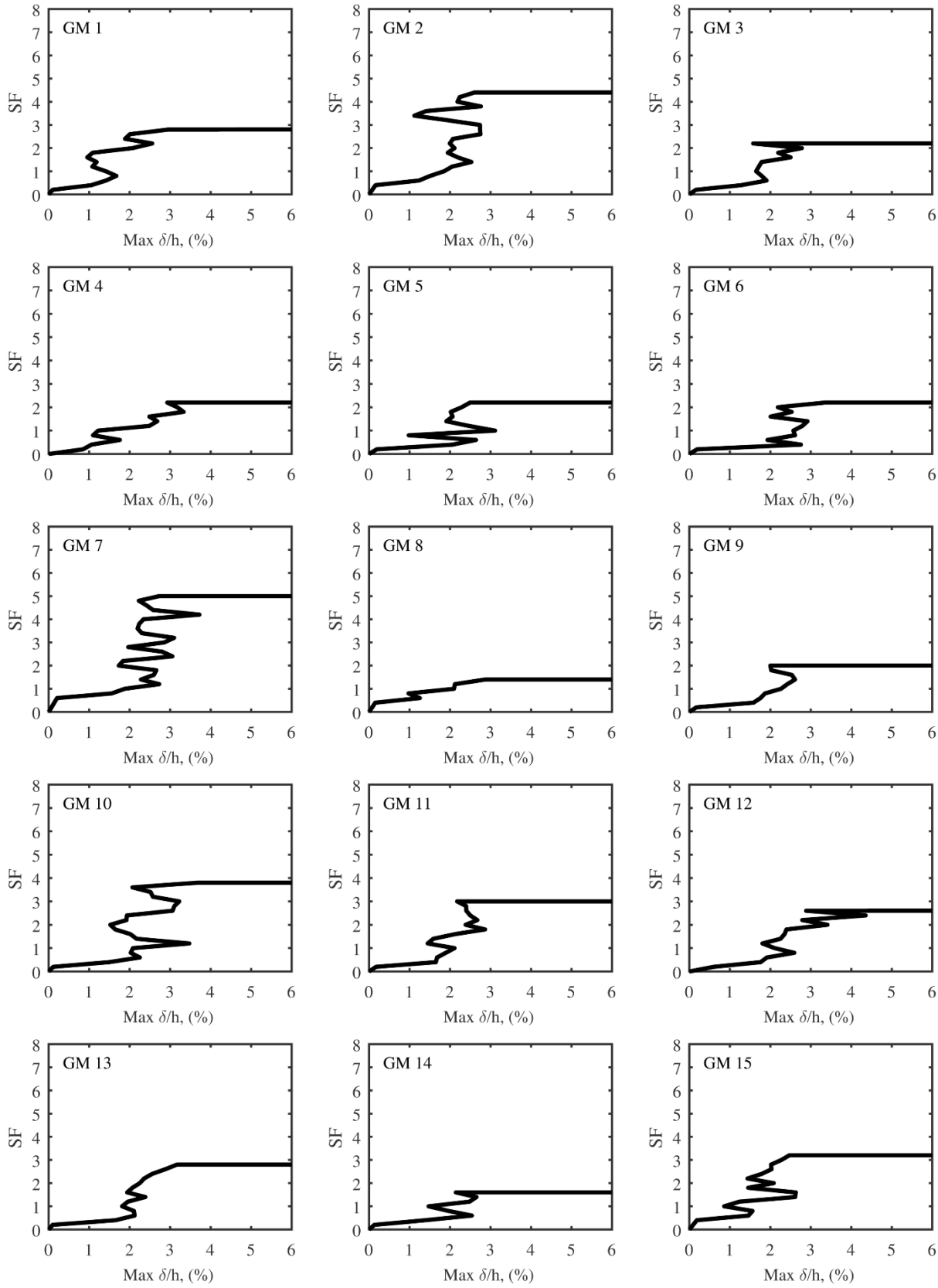

Figure A.23 – Individual IDA results for Ch. 8 building R4-CH-9 (Pinned GBC).

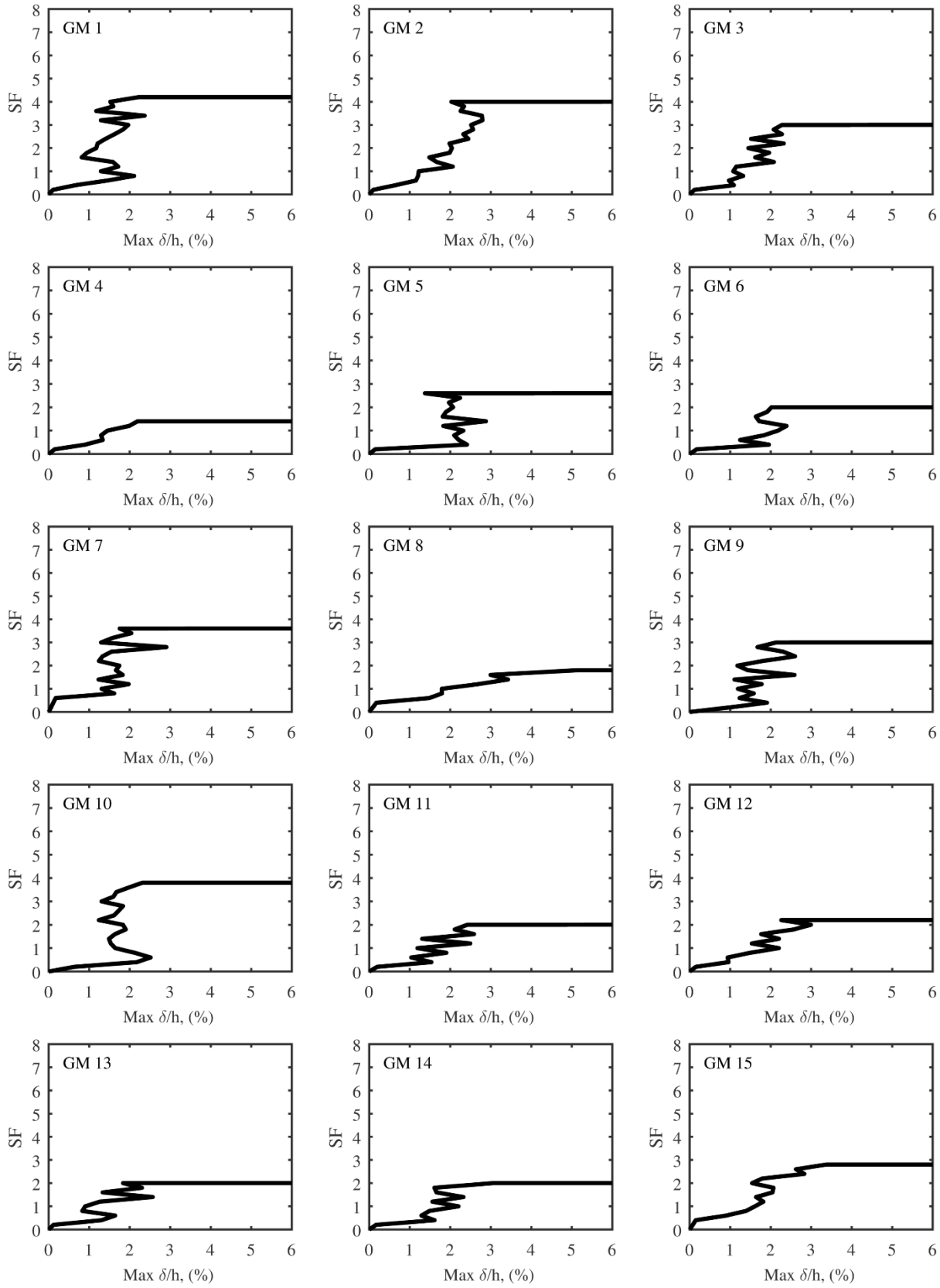

Figure A.24 – Individual IDA results for Ch. 8 building R4-CH-9 (Pinned GBC).

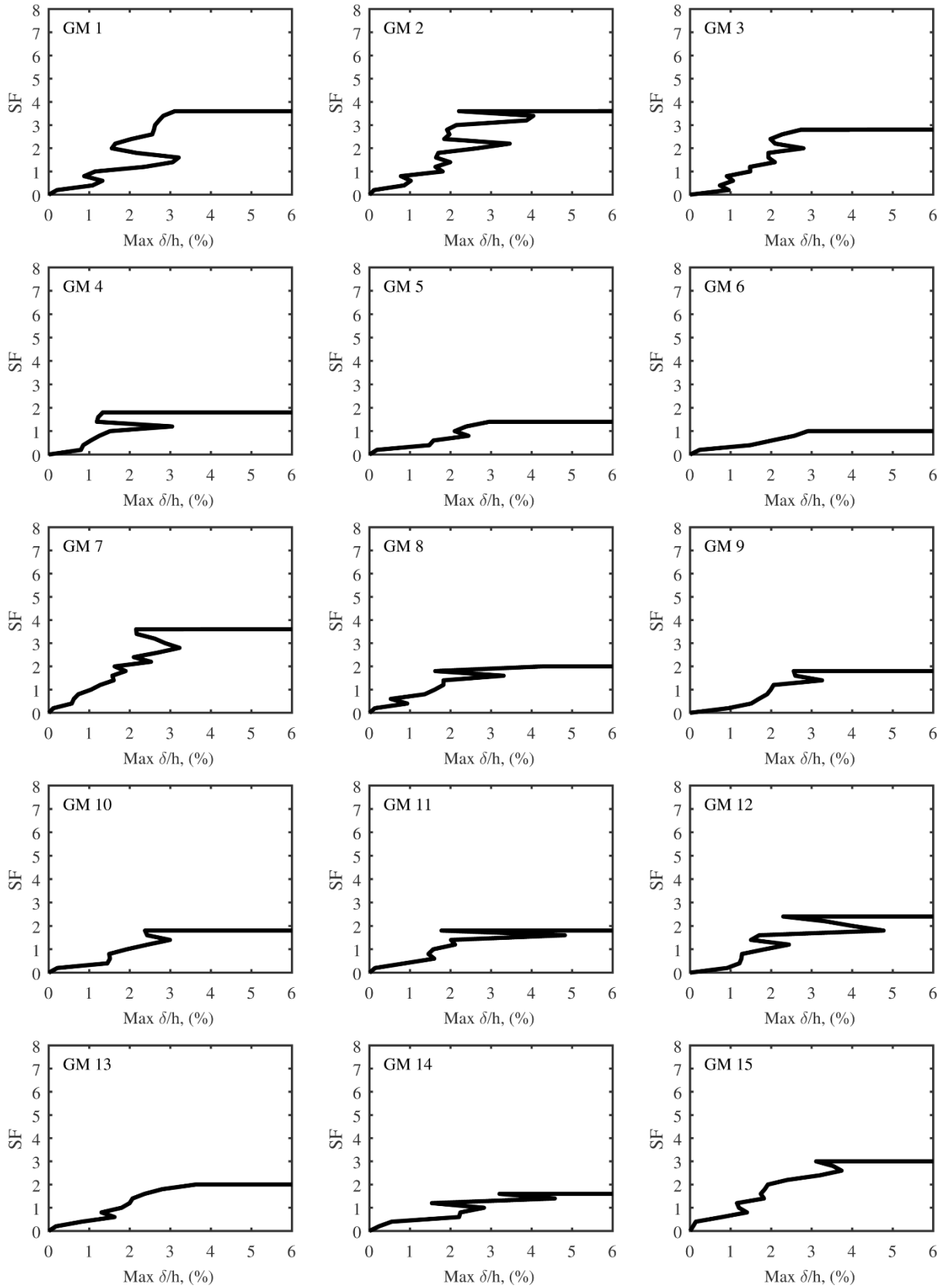

Figure A.25 – Individual IDA results for Ch. 8 building R4-SX-3-FIX (Pinned GBC).

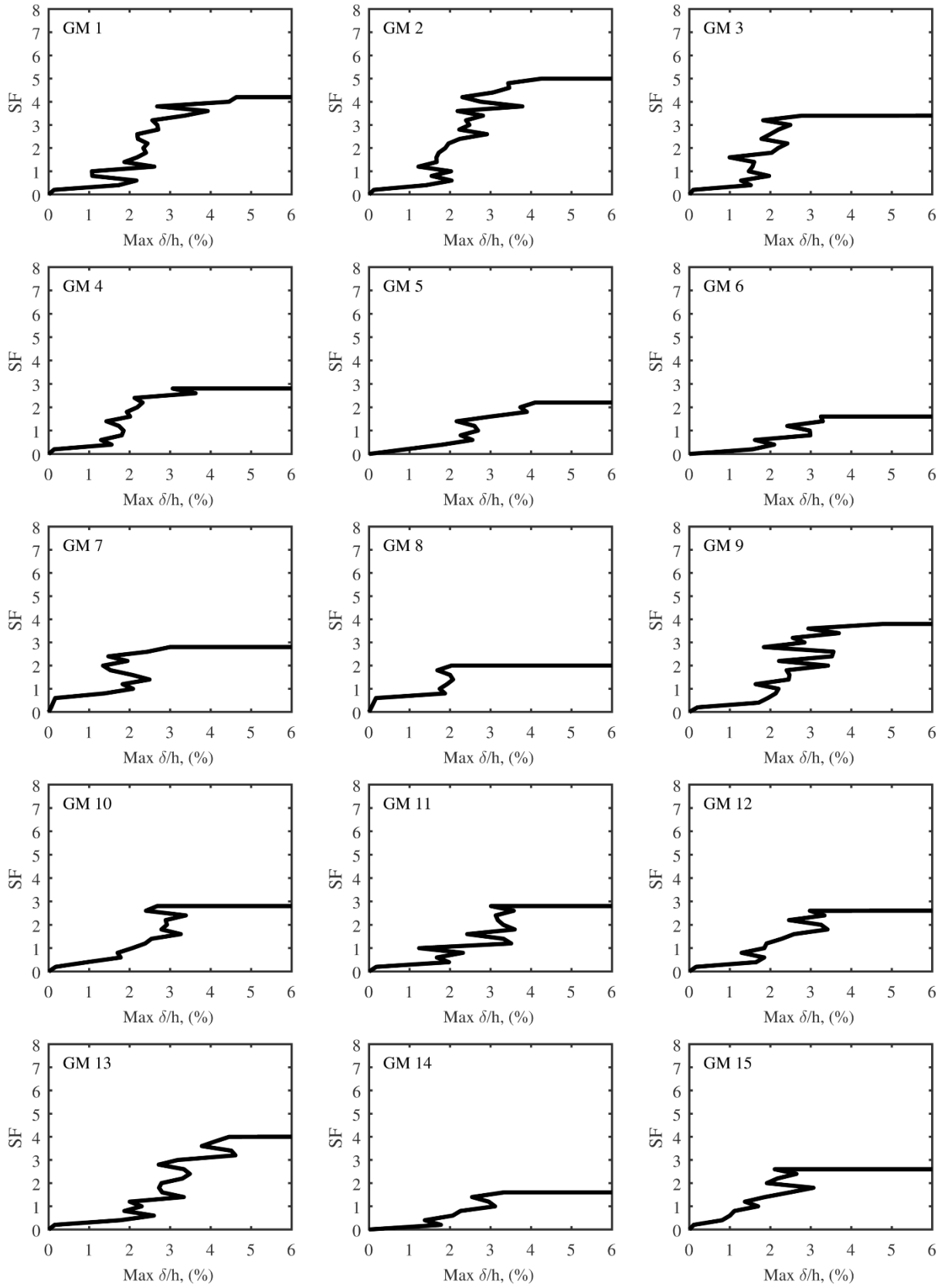

Figure A.26 – Individual IDA results for Ch. 8 building R4-SX-6-FIX (Pinned GBC).

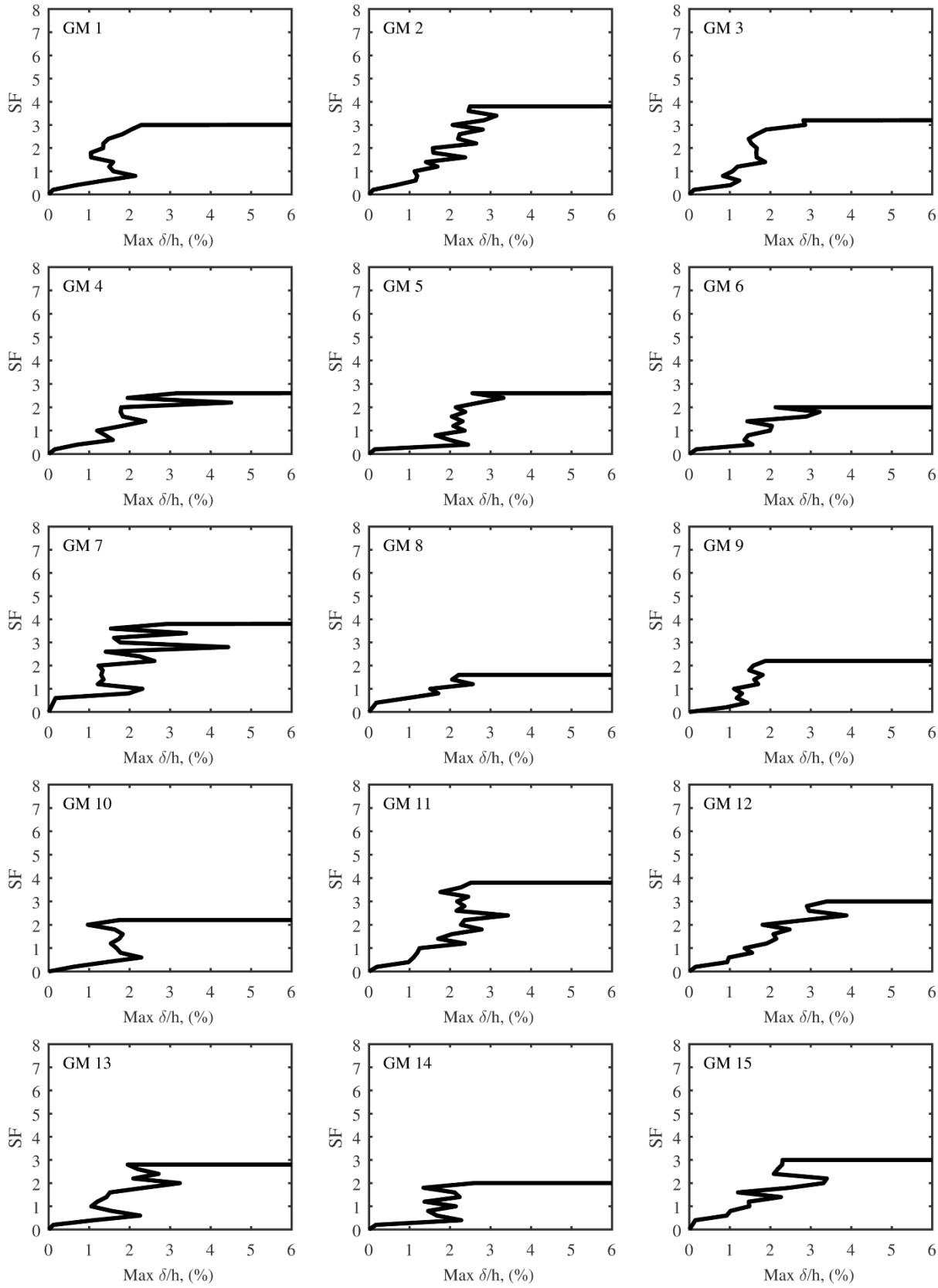

Figure A.27 – Individual IDA results for Ch. 8 building R4-SX-9-FIX (Pinned GBC).

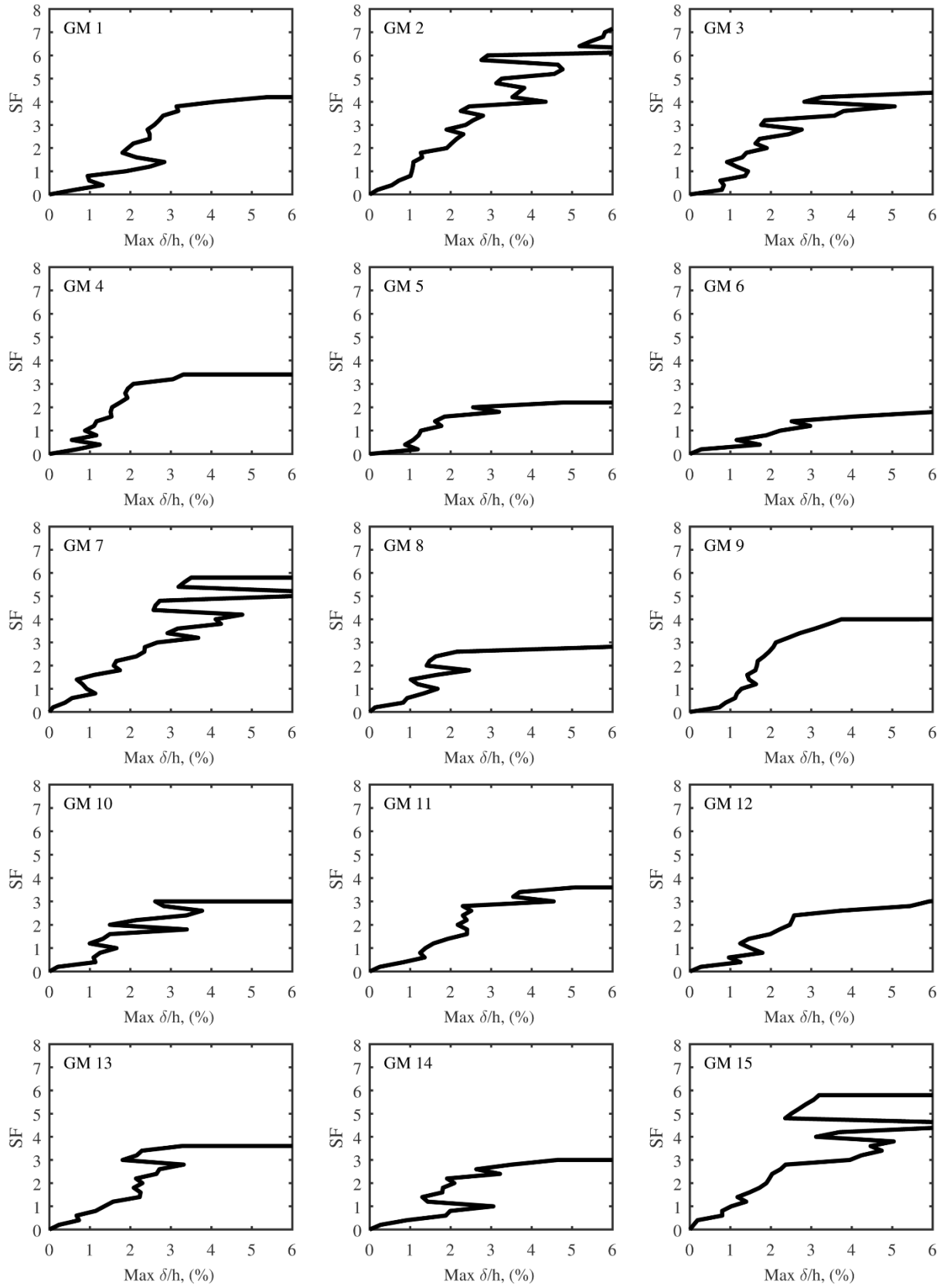

Figure A.28 – Individual IDA results for Ch. 8 building R3-CH-3 (Actual GBC).

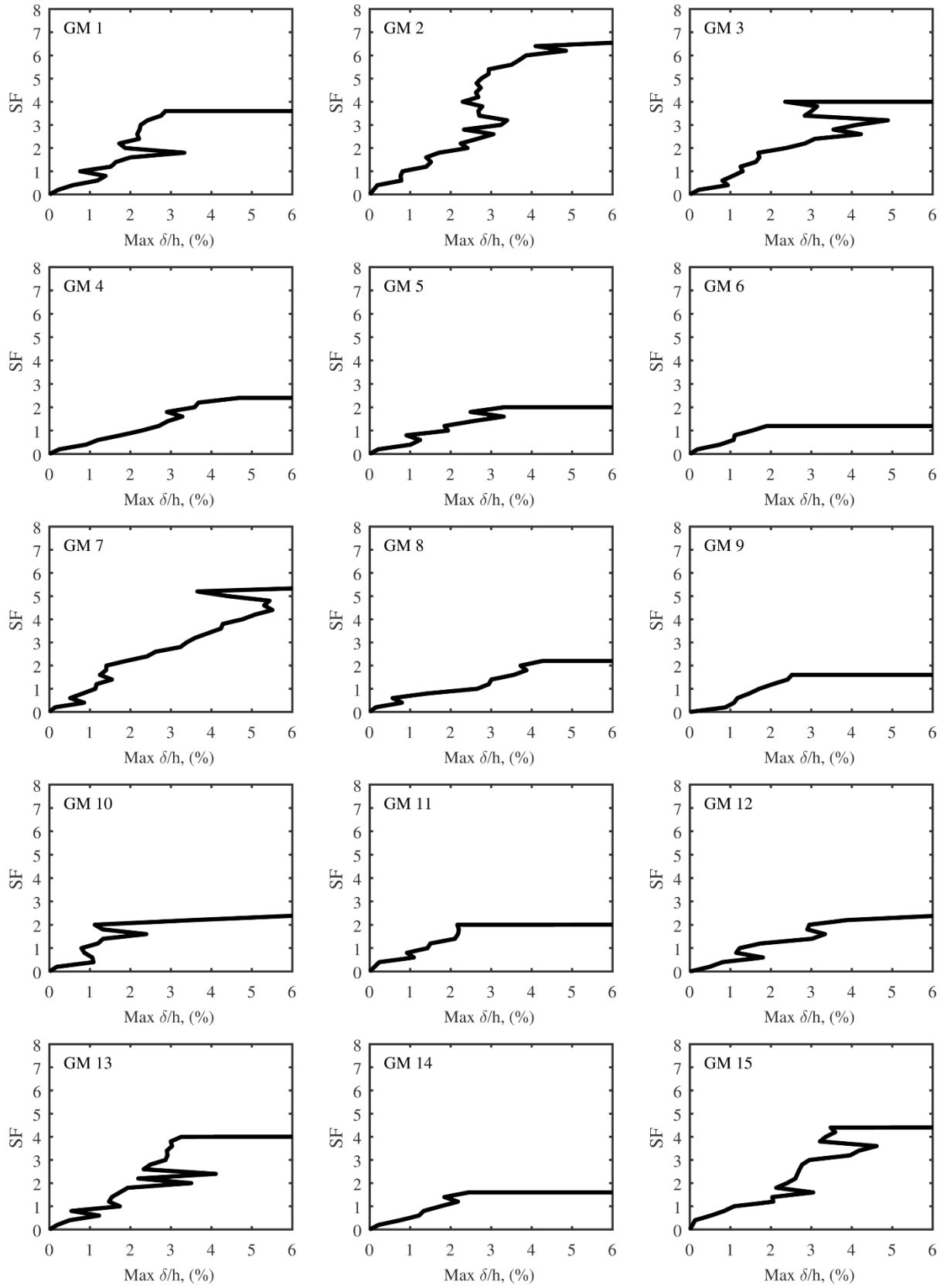

Figure A.29 – Individual IDA results for Ch. 8 building R3-SX-3 (Actual GBC).

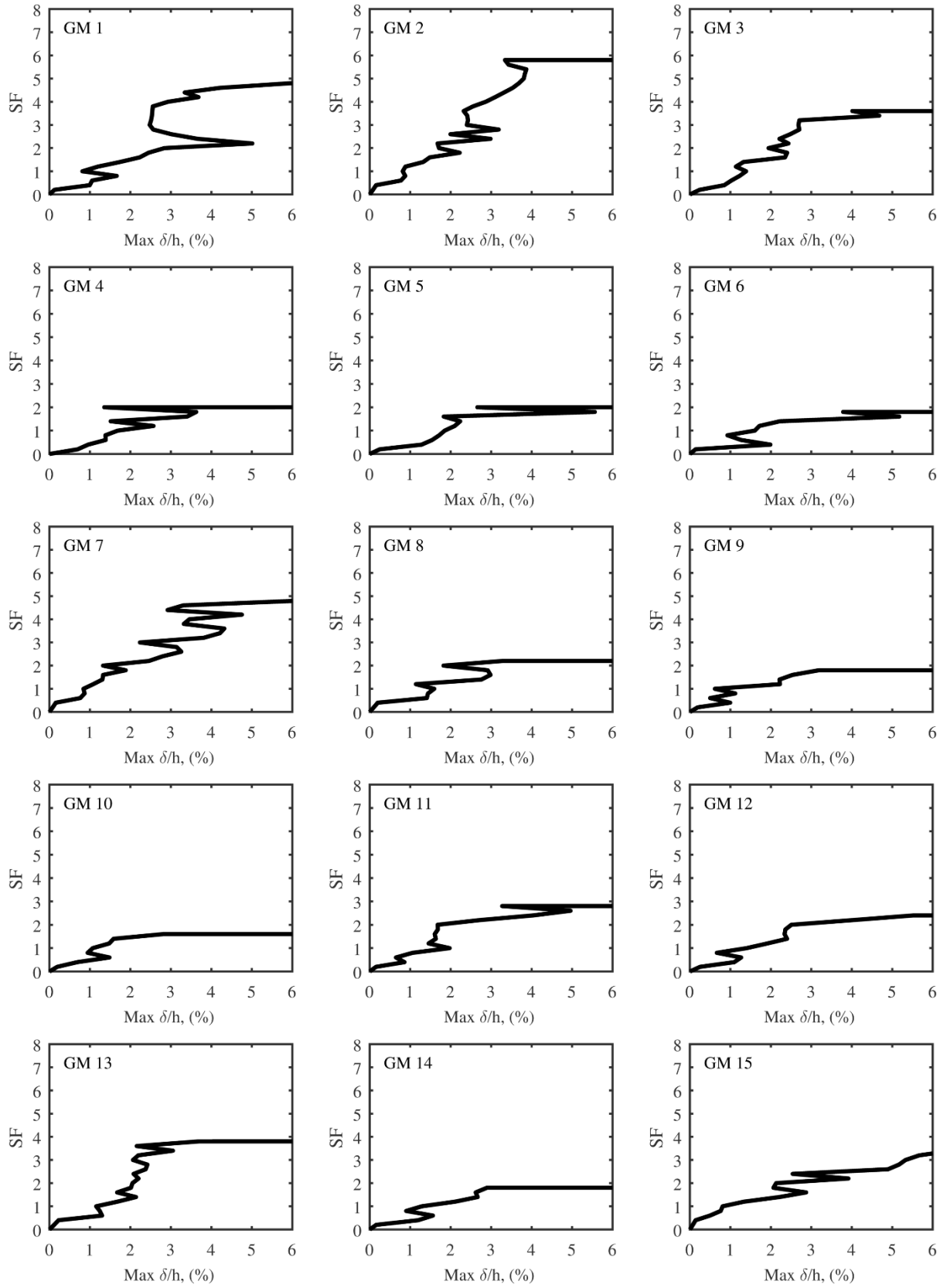

Figure A.30 – Individual IDA results for Ch. 8 building OC-SX-3 (Actual GBC).

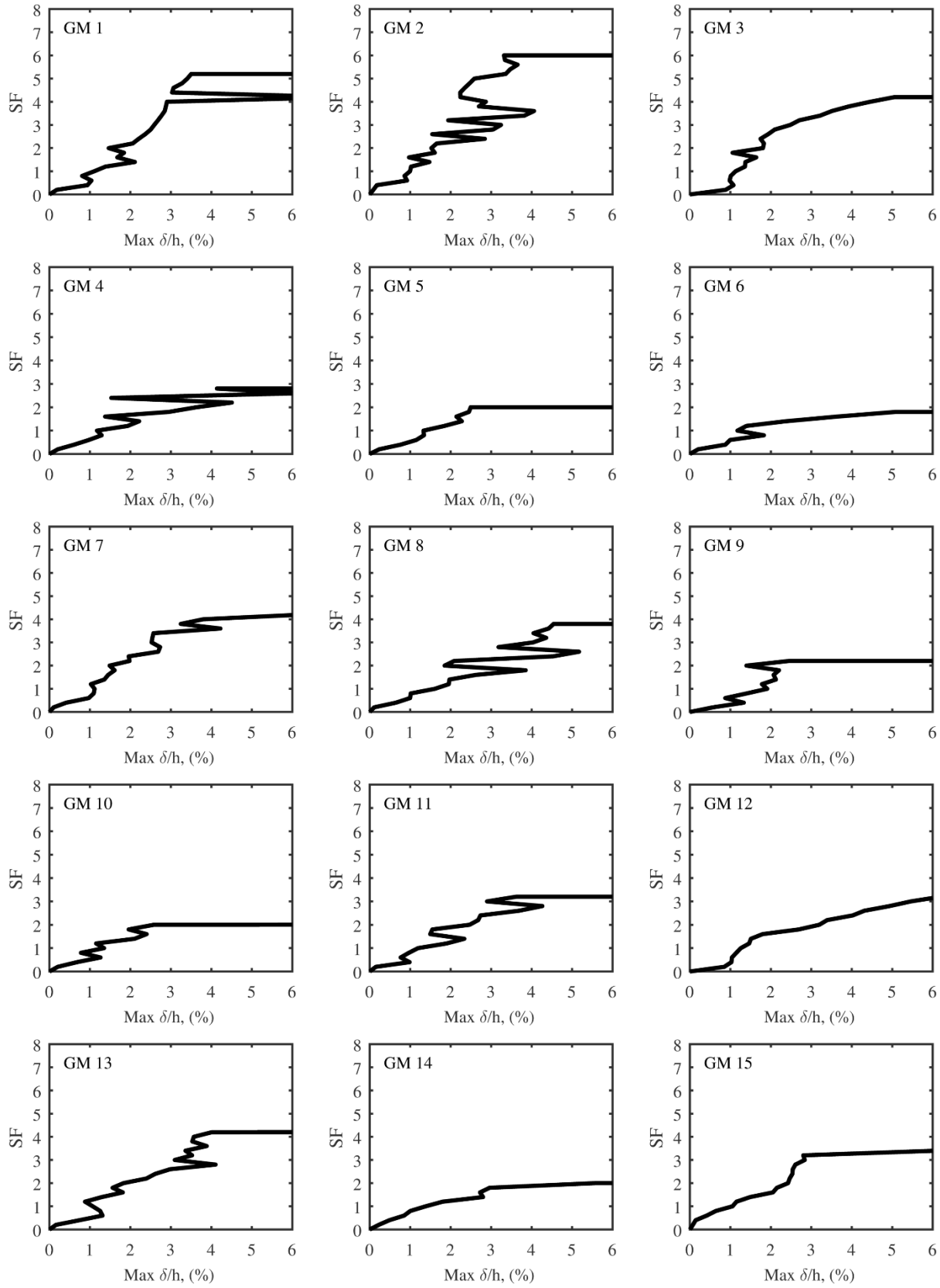

Figure A.31 – Individual IDA results for Ch. 8 building R4-SX-3 (Actual GBC).

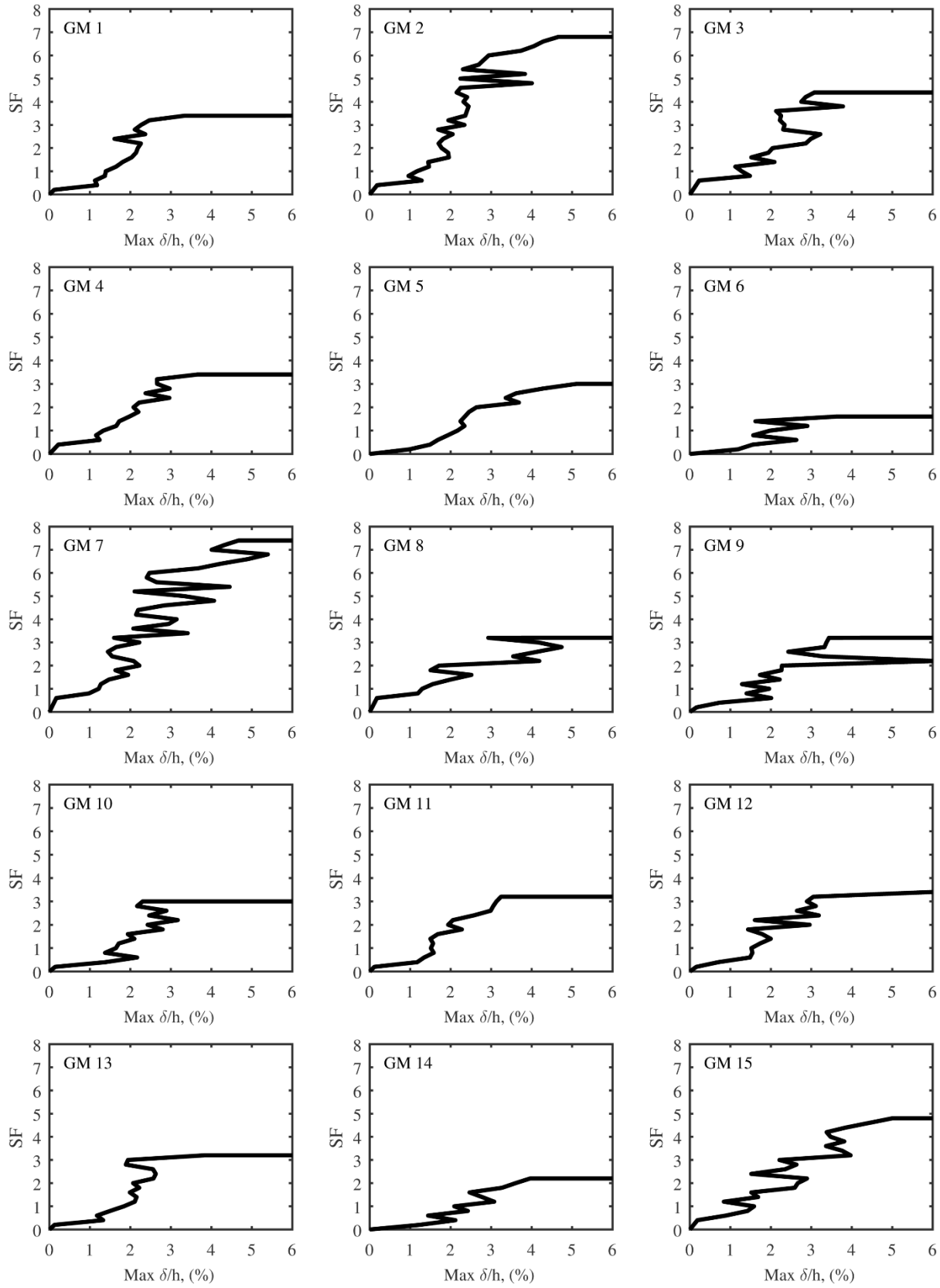

Figure A.32 – Individual IDA results for Ch. 8 building R3-CH-6 (Actual GBC).

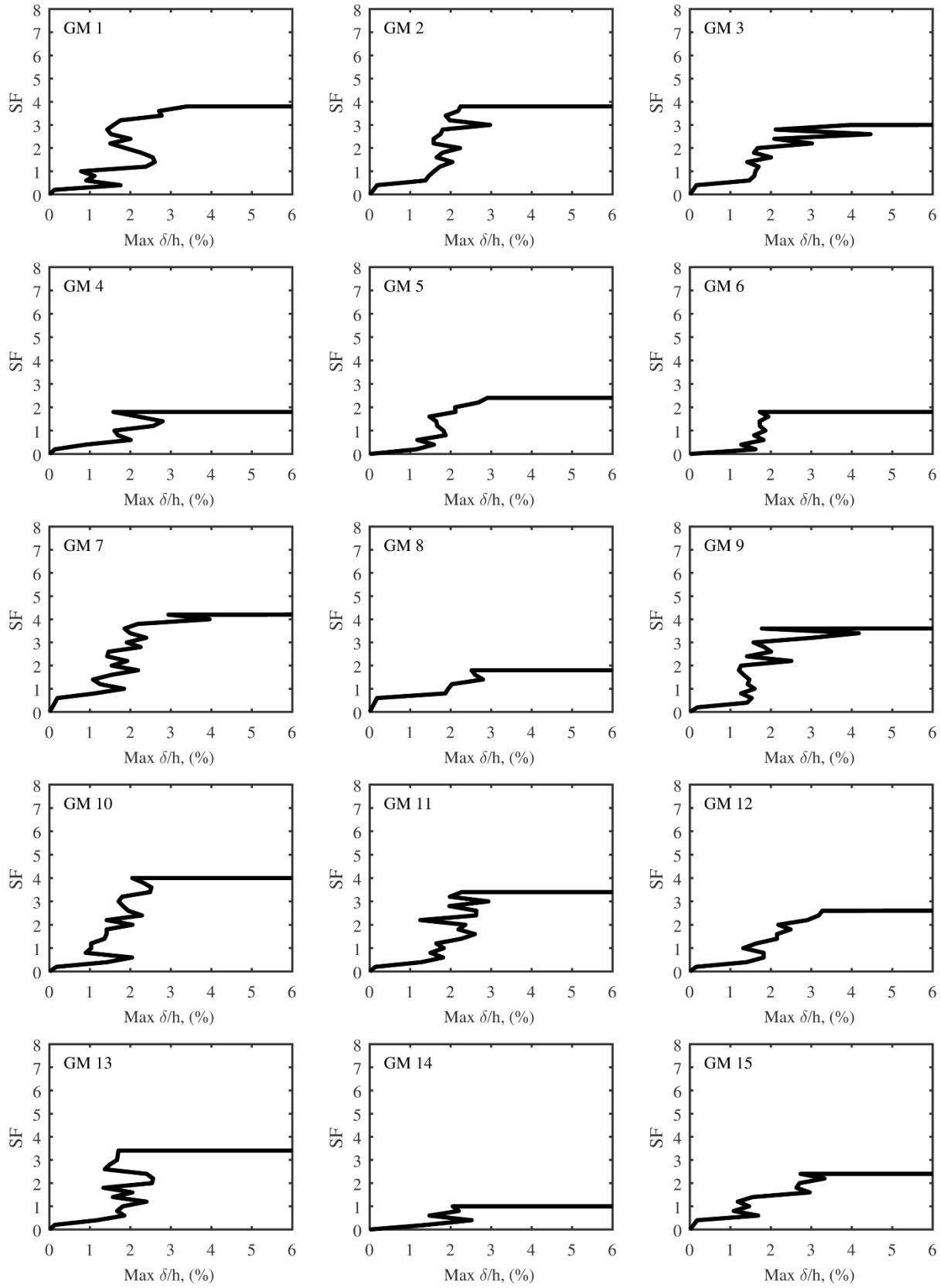

Figure A.33 – Individual IDA results for Ch. 8 building R3-SX-6 (Actual GBC).

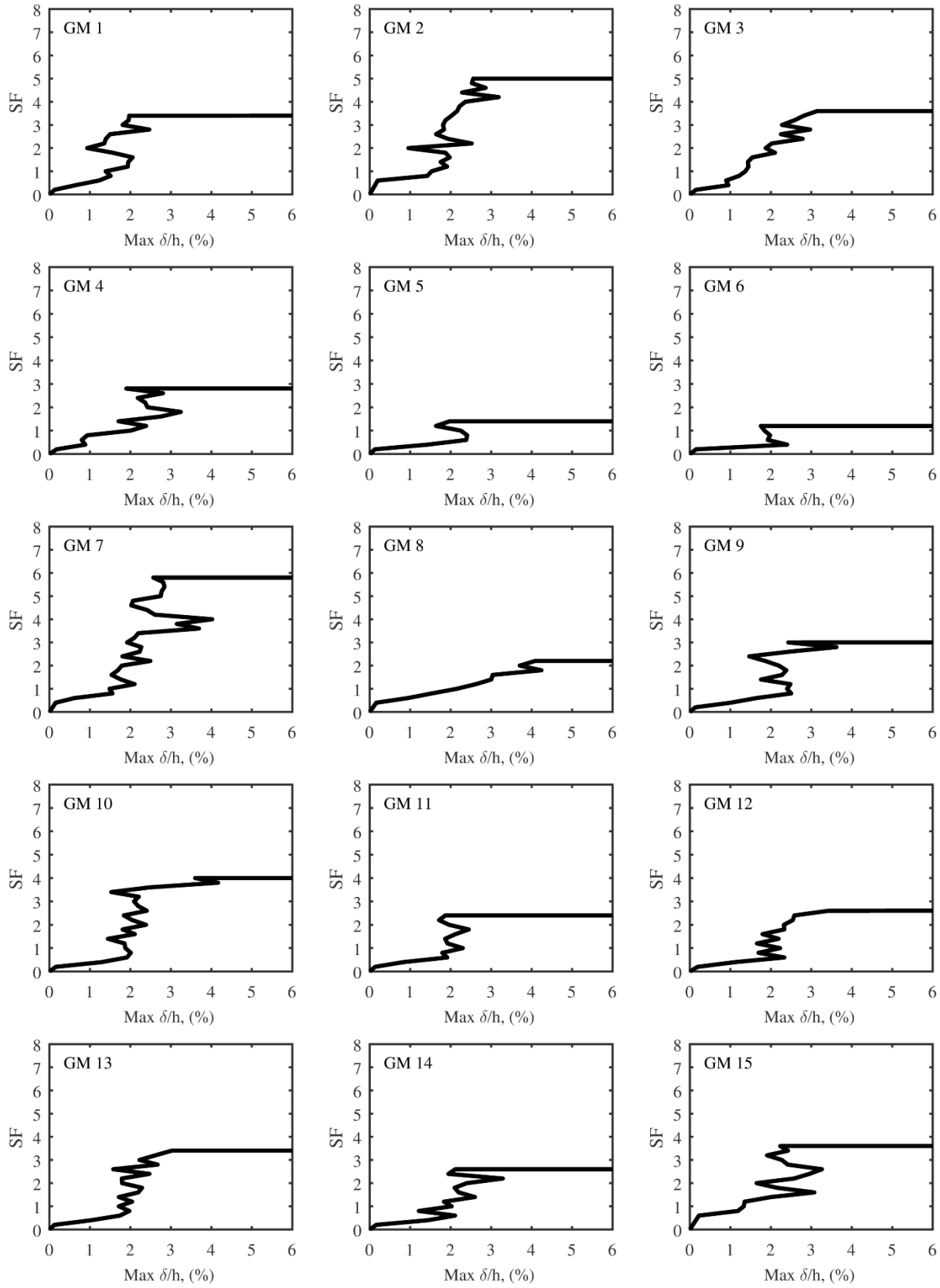

Figure A.34 – Individual IDA results for Ch. 8 building R3-CH-9 (Actual GBC).

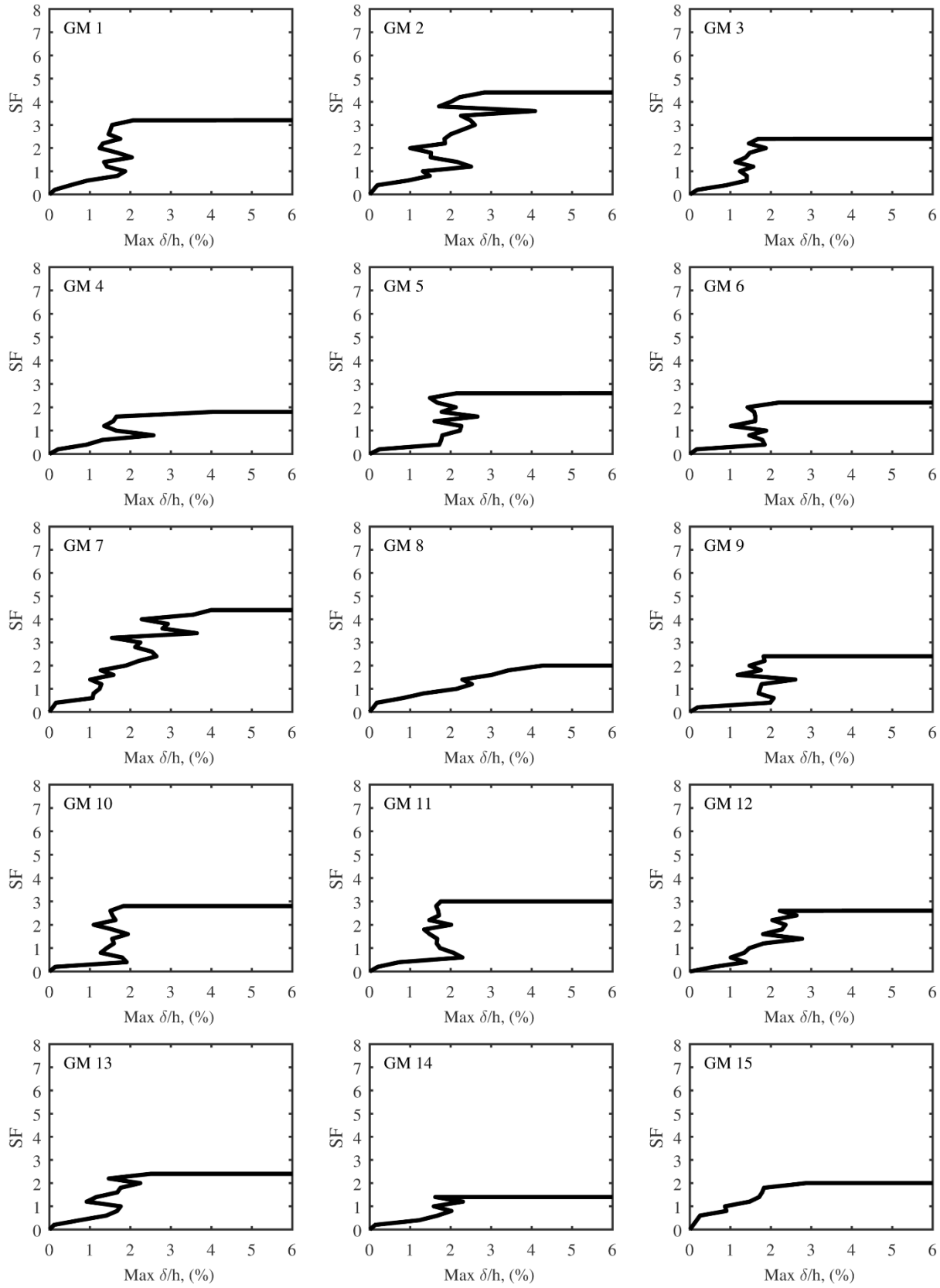

Figure A.35 – Individual IDA results for Ch. 8 building R3-SX-9 (Actual GBC).

A.2 MEDIAN IDA CURVES (16%, 50%, 84%)

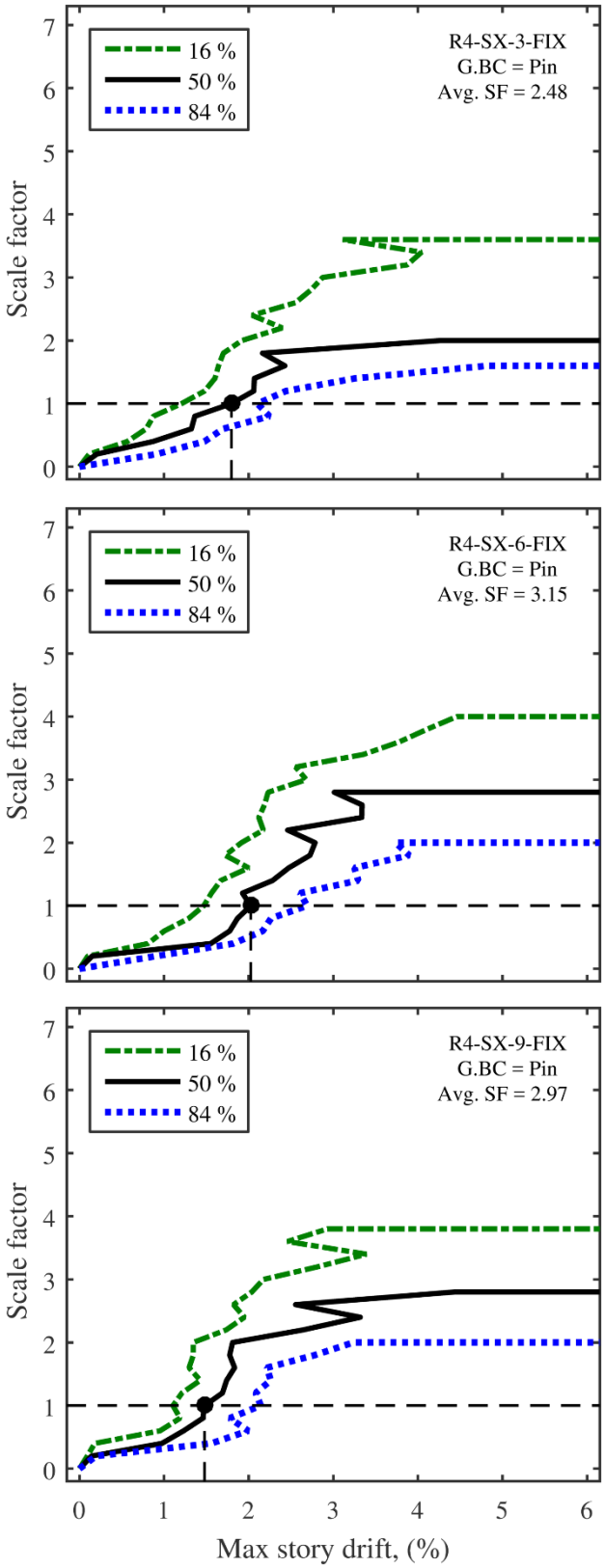

Figure A.36 – IDA results for Ch. 8 buildings R3-SX-3-FIX; R3-SX-6-FIX; and R3-SX-9-FIX. (Pinned GBC).

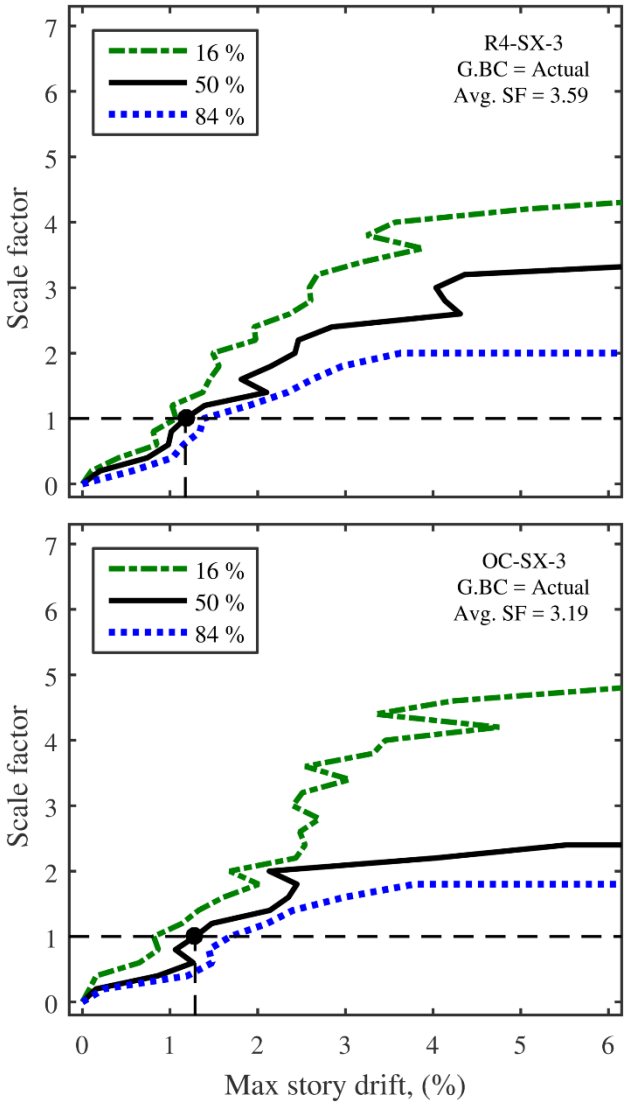

Figure A.37 – IDA results for Ch. 8 buildings R4-SX-3; and OC-SX-3. (Actual GBC).

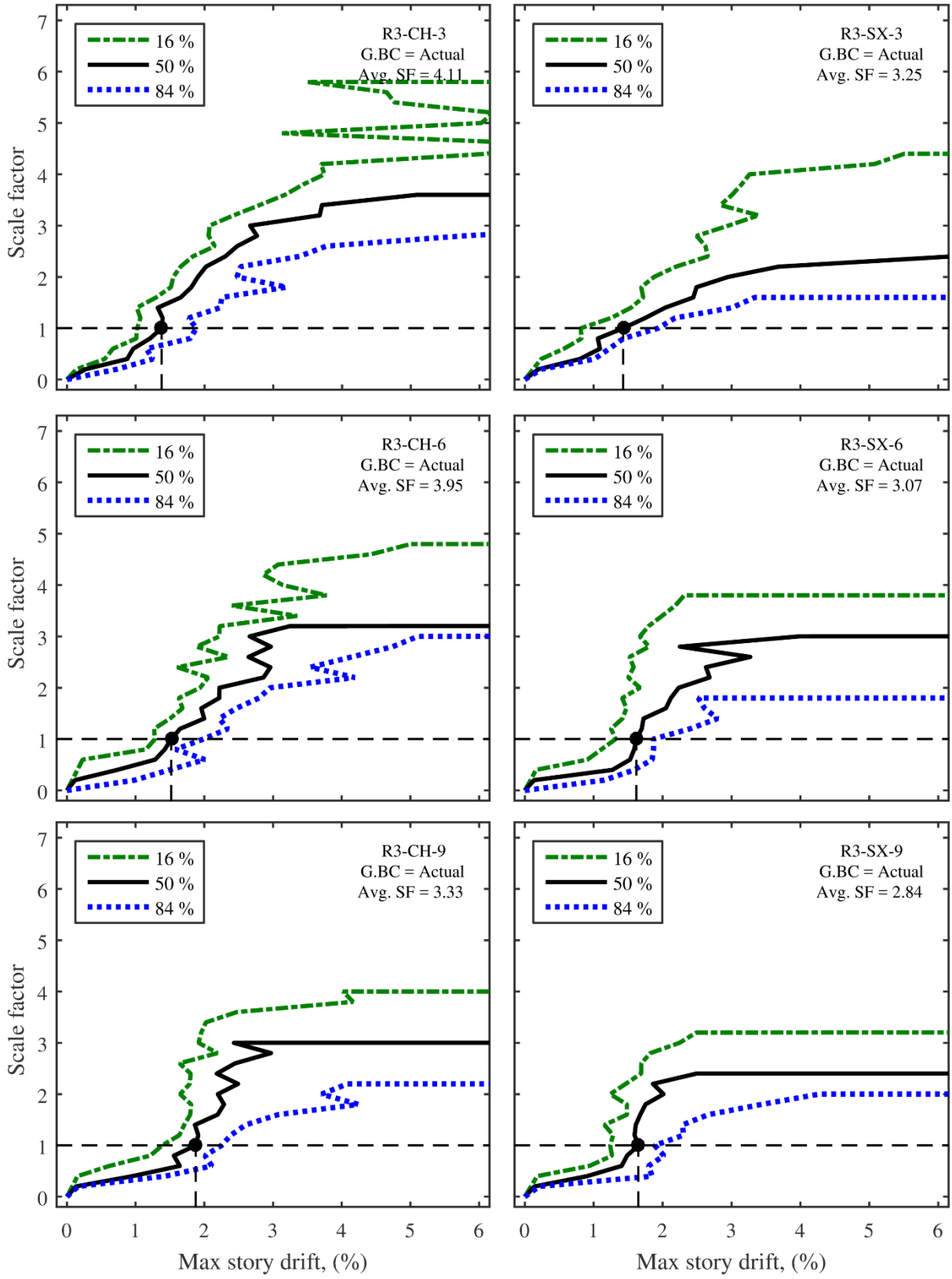

Figure A.38 – IDA results for Ch. 8 buildings R3-CH-3; R3-SX-3; R3-CH-6; R3-SX-6; R3-CH-9; and R3-SX-9. (Actual GBC).

A.3 INITIAL FRAGILITY CURVES

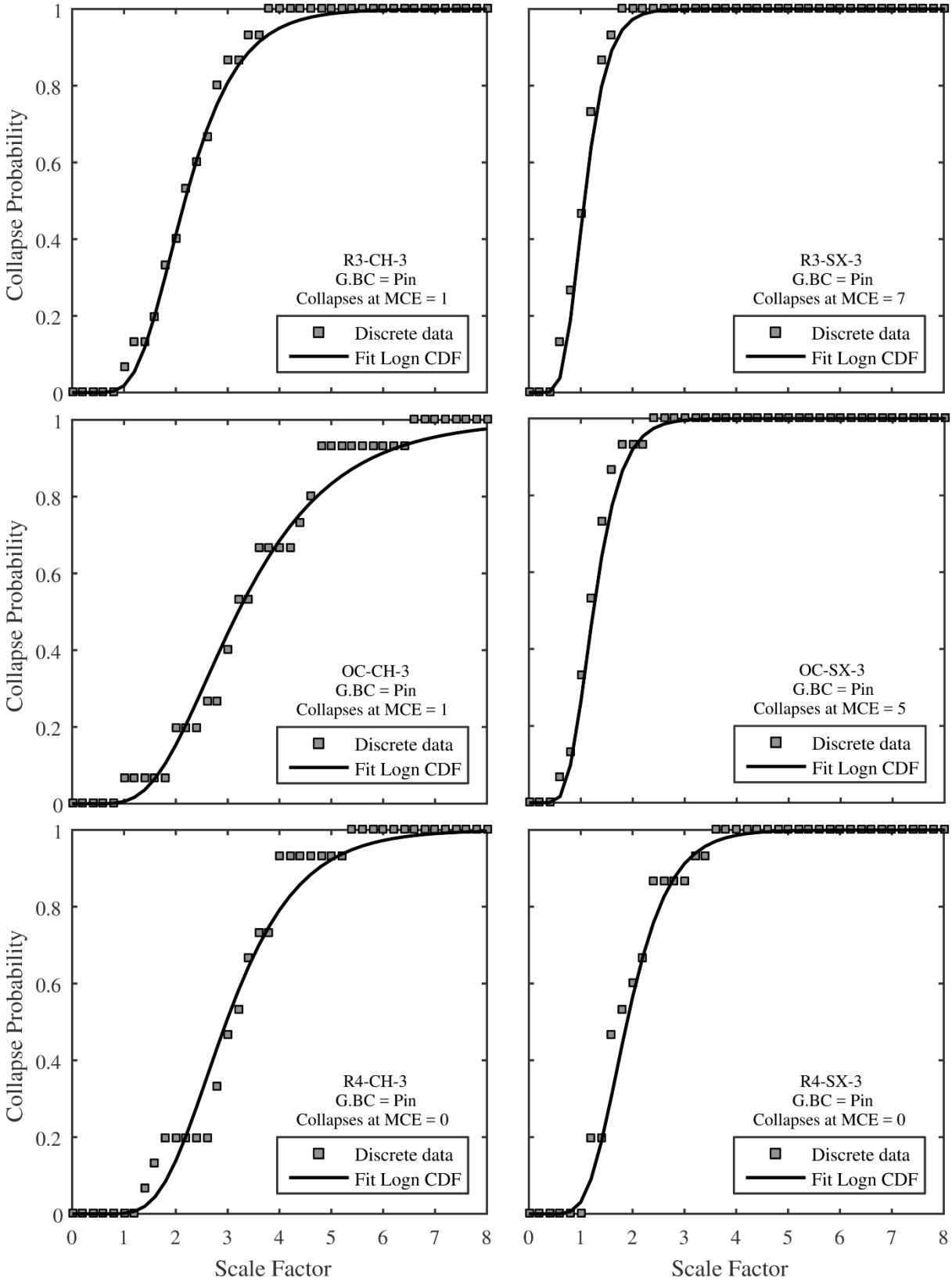

Figure A.39 – Initial fragility curves for Ch. 8 buildings R3-CH-3; R3-SX-3; OC-CH-3; OC-SX-3; R4-CH-3; and R4-SX-3 (Pinned GBC).

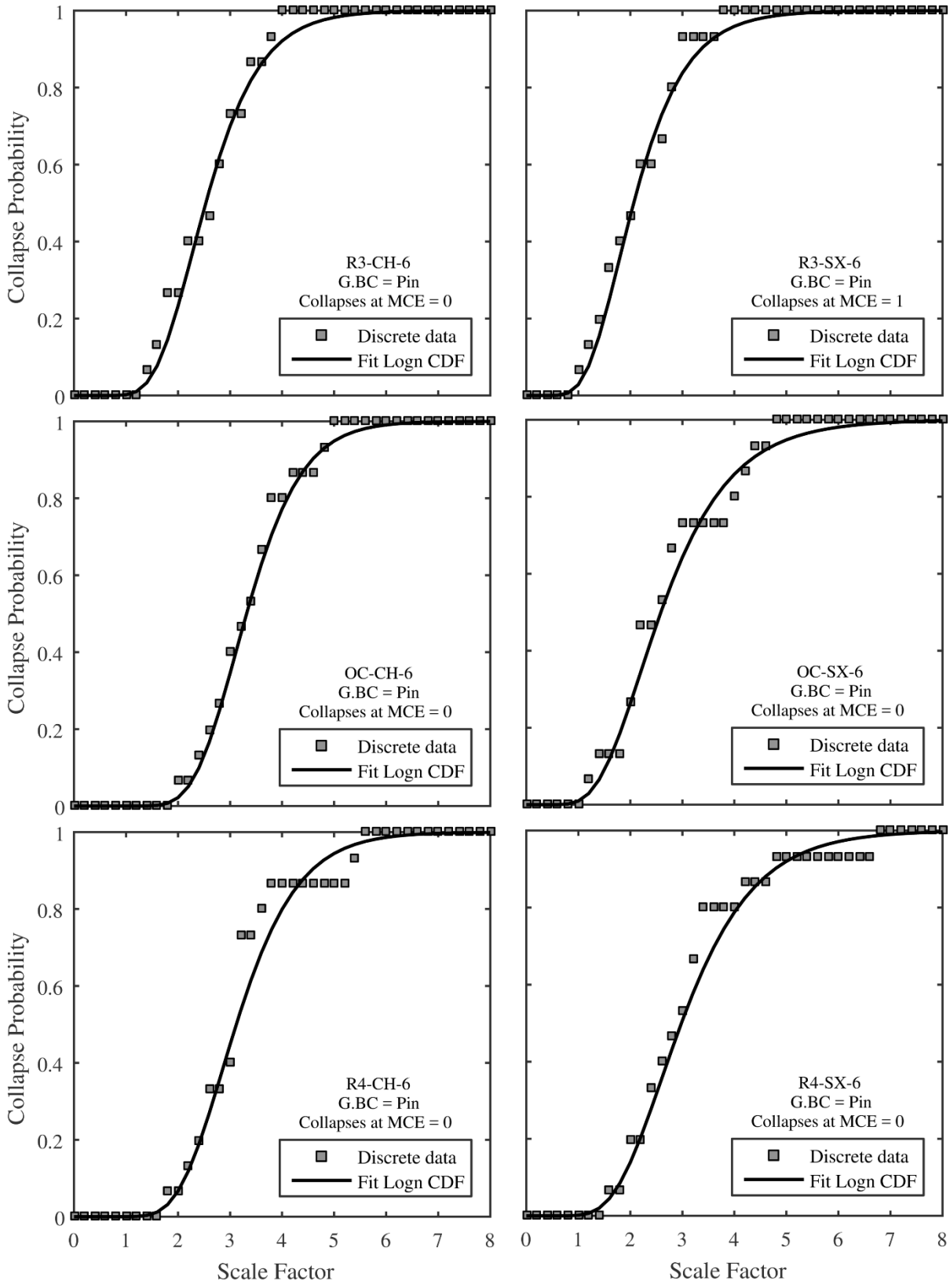

Figure A.40 – Initial fragility curves for Ch. 8 buildings R3-CH-6; R3-SX-6; OC-CH-6; OC-SX-6; R4-CH-6; and R4-SX-6 (Pinned GBC).

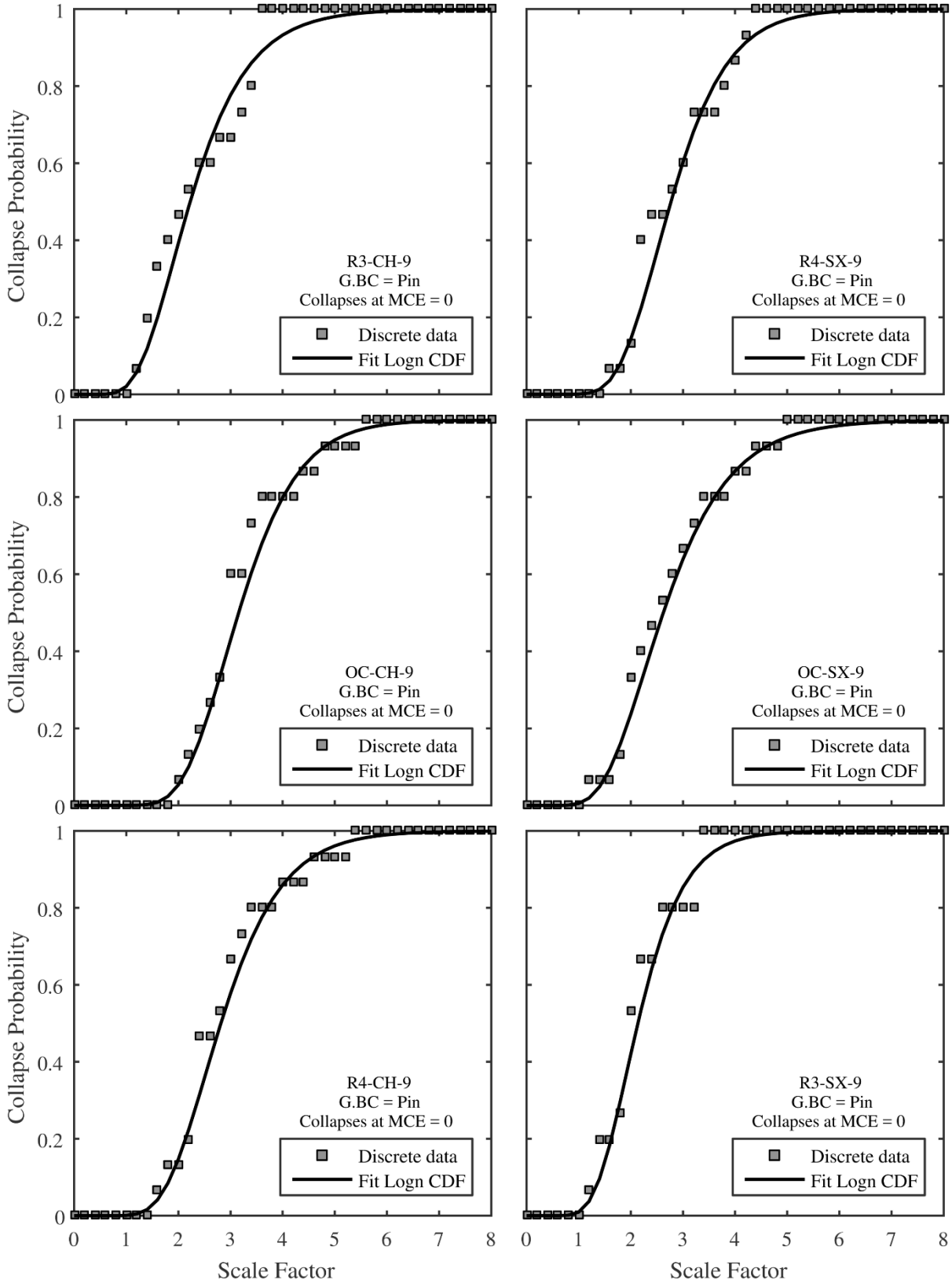

Figure A.41 – Initial fragility curves for Ch. 8 buildings R3-CH-9; R3-SX-9; OC-CH-9; OC-SX-9; R4-CH-9; and R4-SX-9 (Pinned GBC).

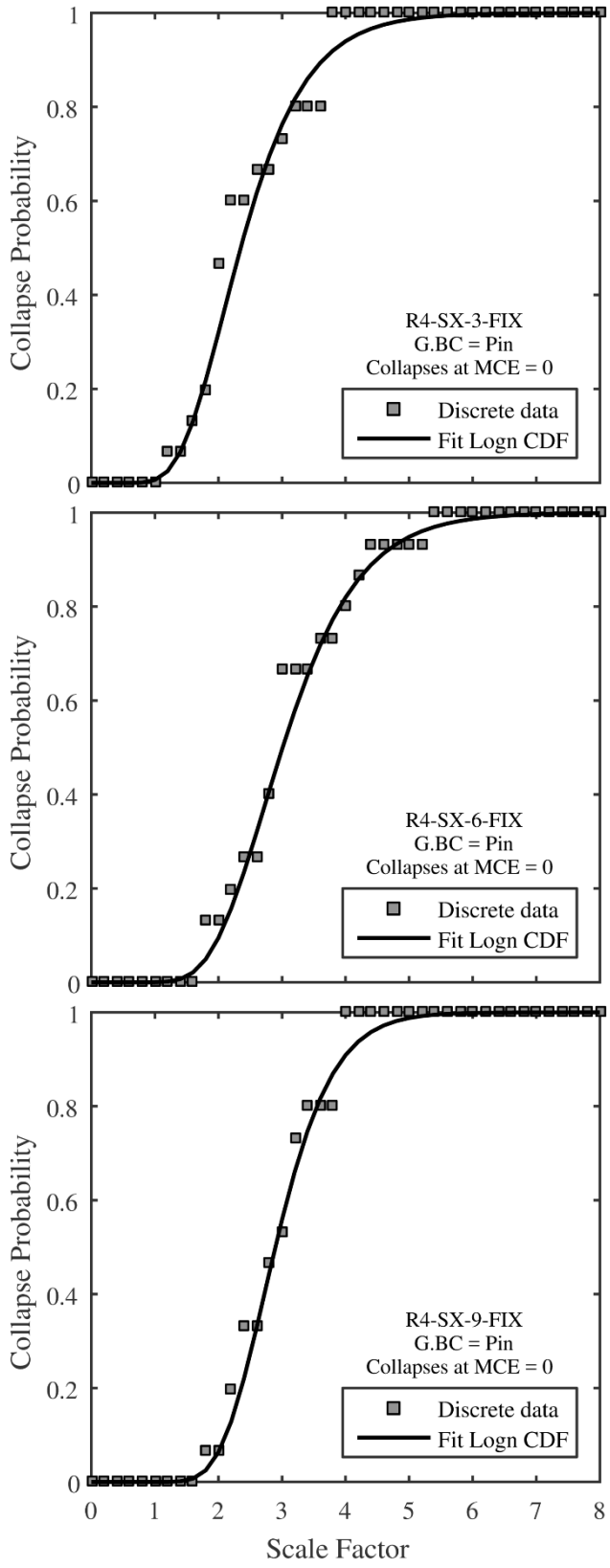

Figure A.42 – Initial fragility curves for Ch. 8 buildings R4-SX-3-FIX; R4-SX-6-FIX and R4-SX-9-FIX (Pinned GBC).

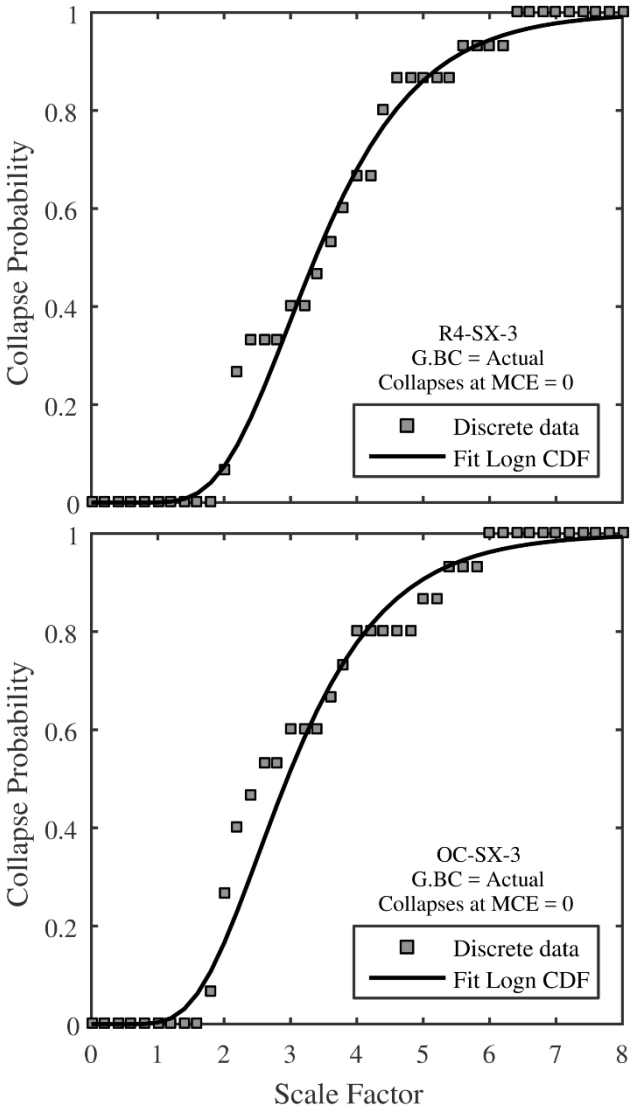

Figure A.43 – Initial fragility curves for Ch. 8 buildings R4-SX-3; and OC-SX-3 (Actual GBC).

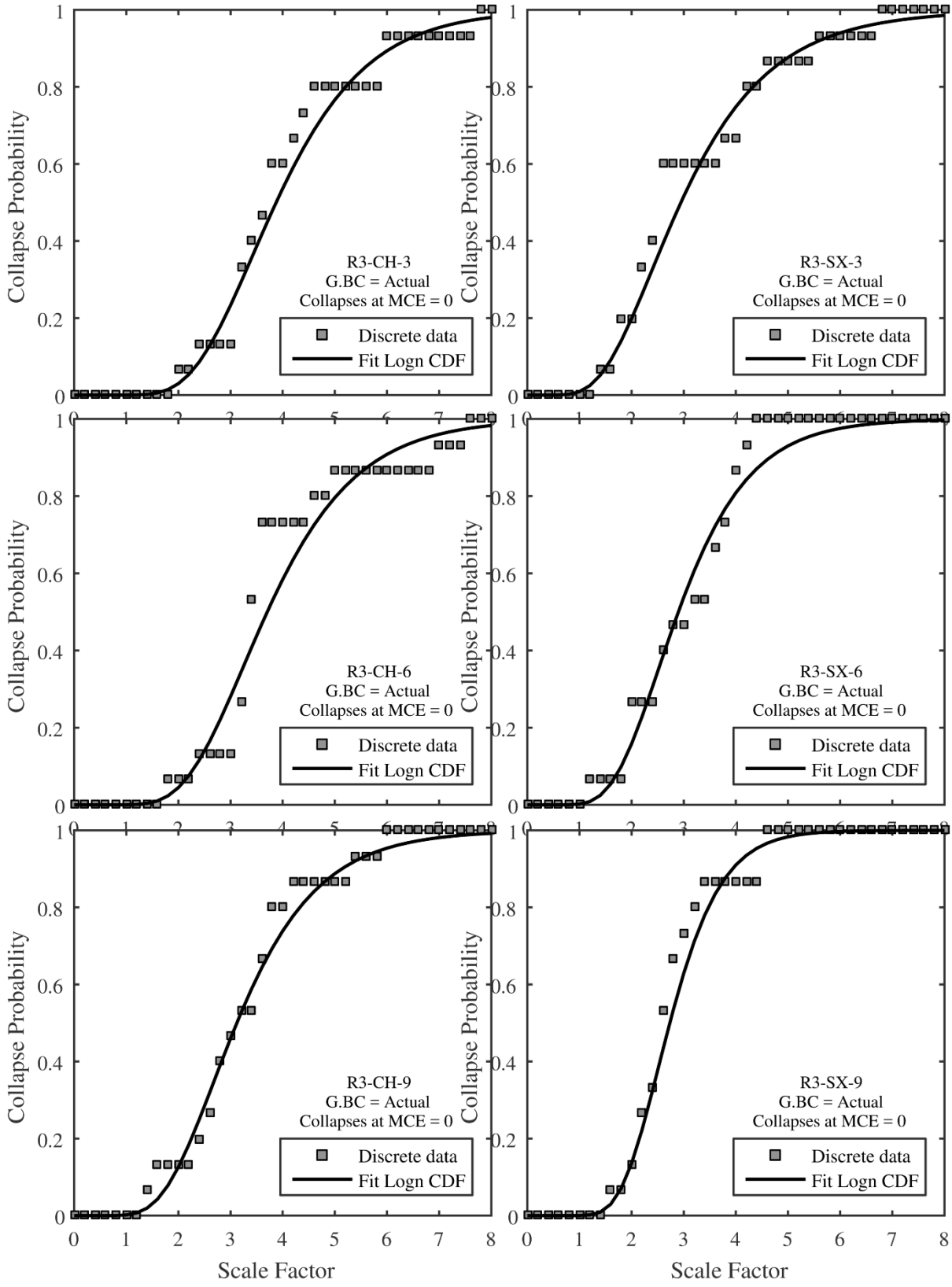

Figure A.44 – Initial fragility curves for Ch. 8 buildings R3-CH-3; R3-SX-3; R3-CH-6; R3-SX-6; R3-CH-9; and R3-SX-9 (Actual GBC).

A.4 ADJUSTED FRAGILITY CURVES

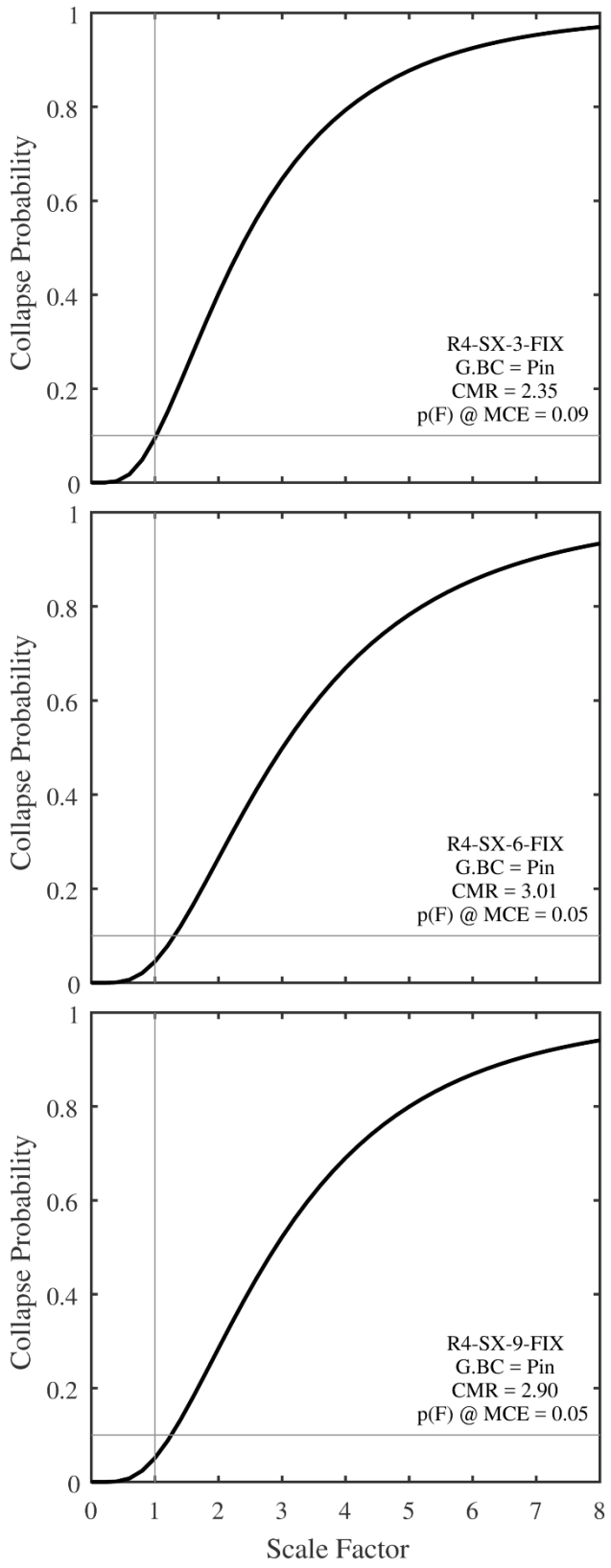

Figure A.45 – Adjusted fragility curves for Ch. 8 buildings R4-SX-3-FIX; R4-SX-6-FIX; and R4-SX-9-FIX (Pinned GBC).

APPENDIX B

COUPON TESTS FROM FULL-SCALE TEST UNITS

81 coupons were tested:

- 7 from each W-section from a unique heat (3 web, 4 flange)
  - (21) W12x40 – 3 heats
  - (21) W12x53 – 3 heats
  - (7) W12x26
  - Total = 49
- 8 from each HSS-section (2 from each tube wall)
  - (8) HSS8x8x1/4
  - (8) HSS8x8x3/8
  - (8) HSS6x6x3/8
  - (8) HSS6x6x1/2
  - Total = 32

Shop drawings for the coupons are provided on the following pages.

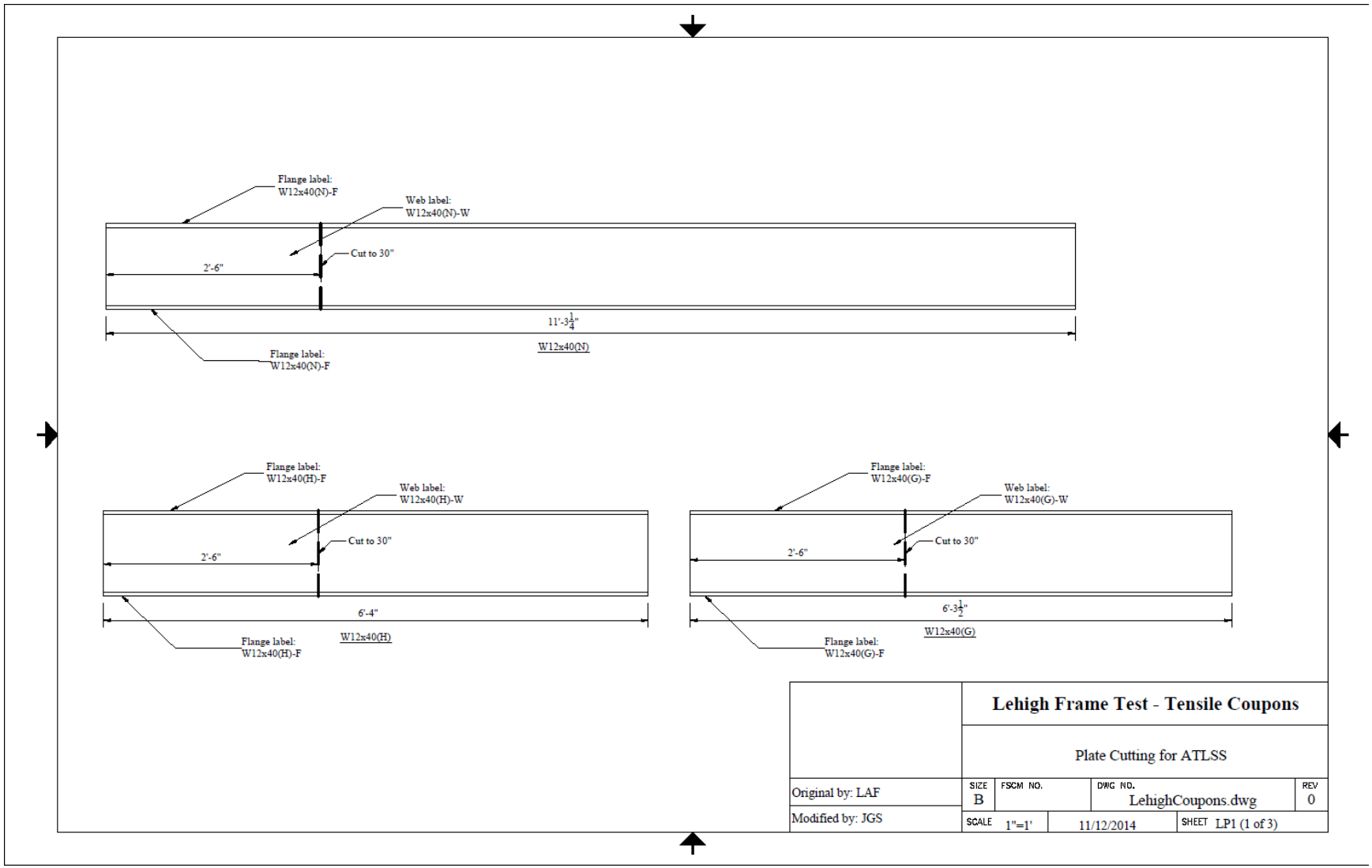

Figure B.1– Shop drawings for coupon testing (Page 1 of 5).

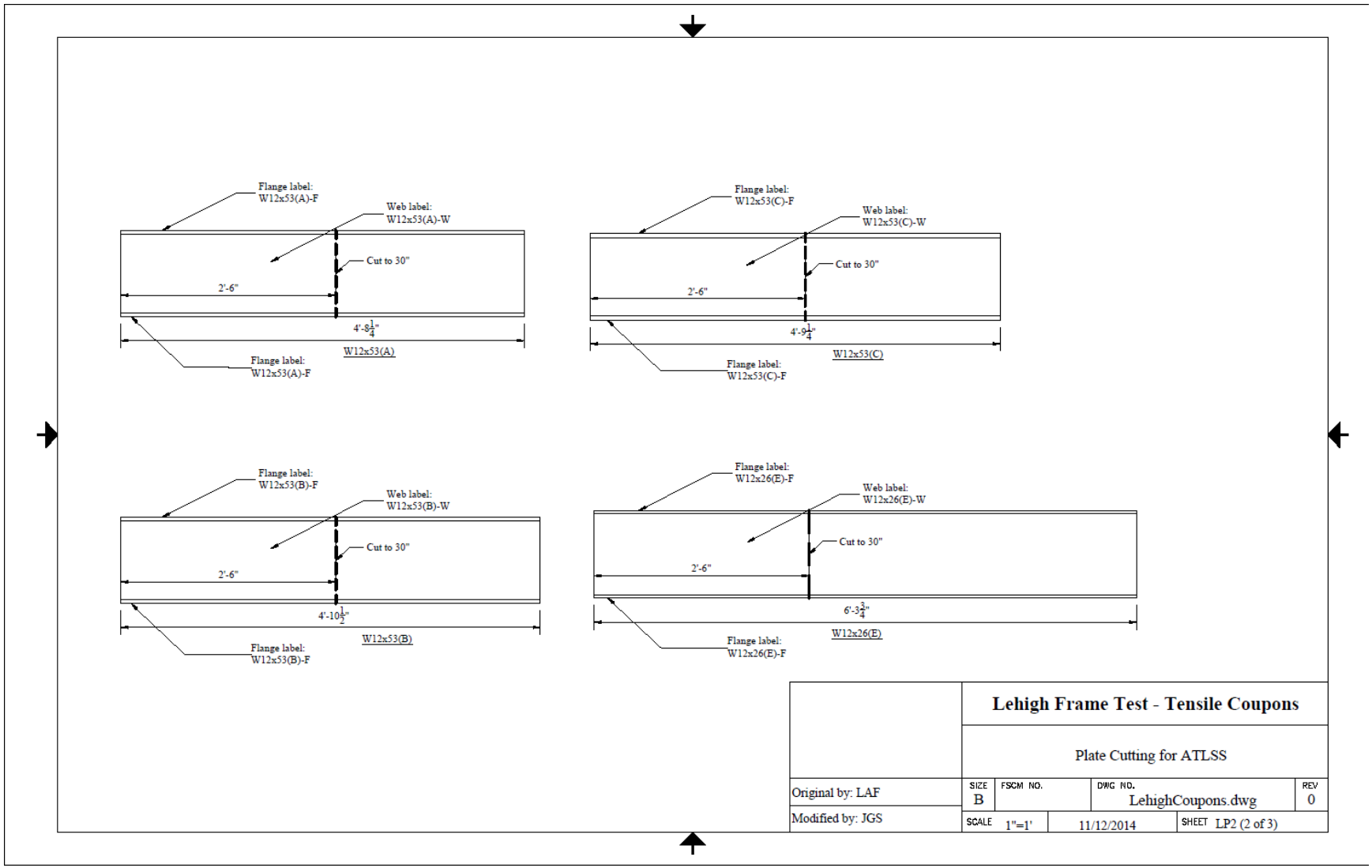

Figure B.1– Shop drawings for coupon testing (Page 2 of 5).

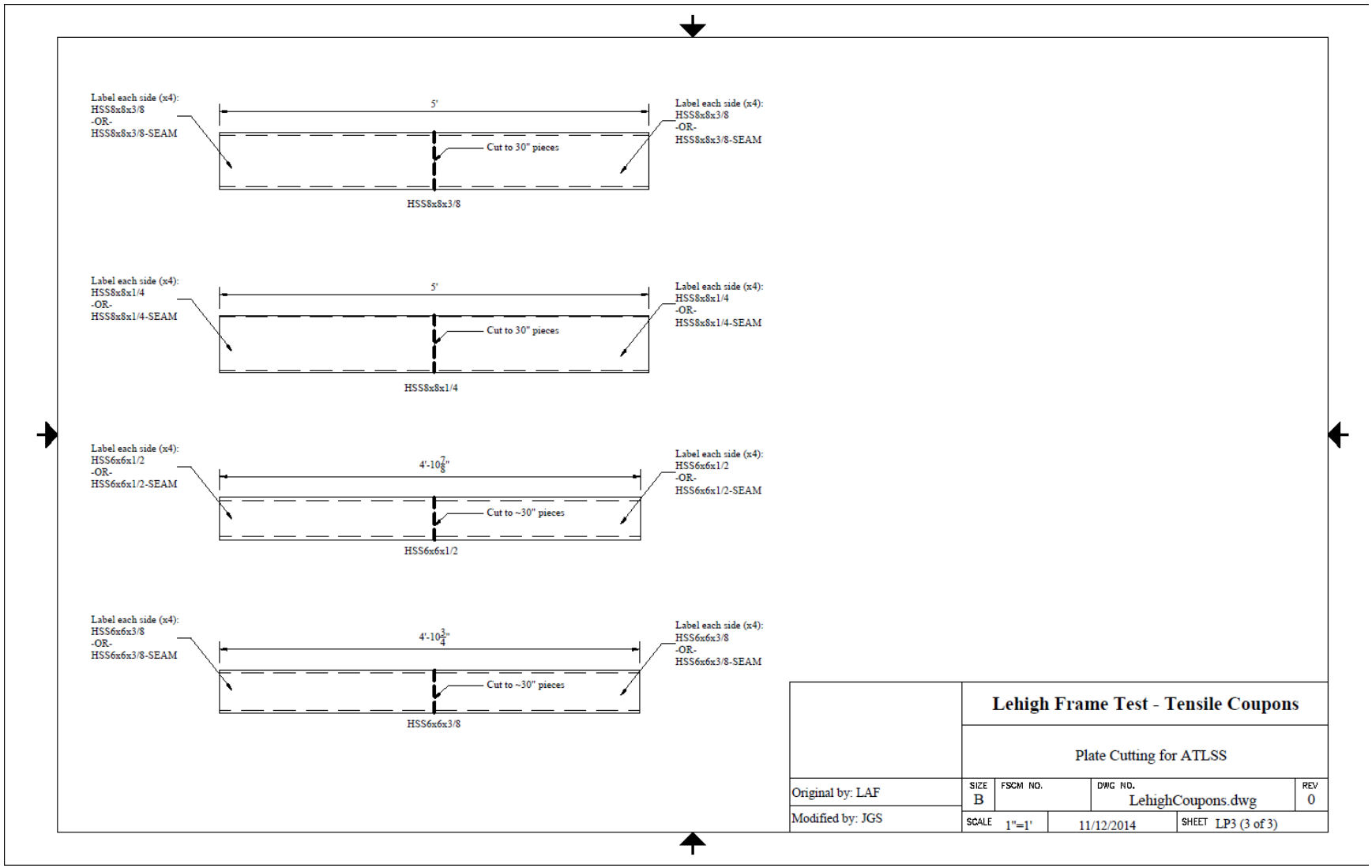

Figure B.1– Shop drawings for coupon testing (Page 3 of 5).

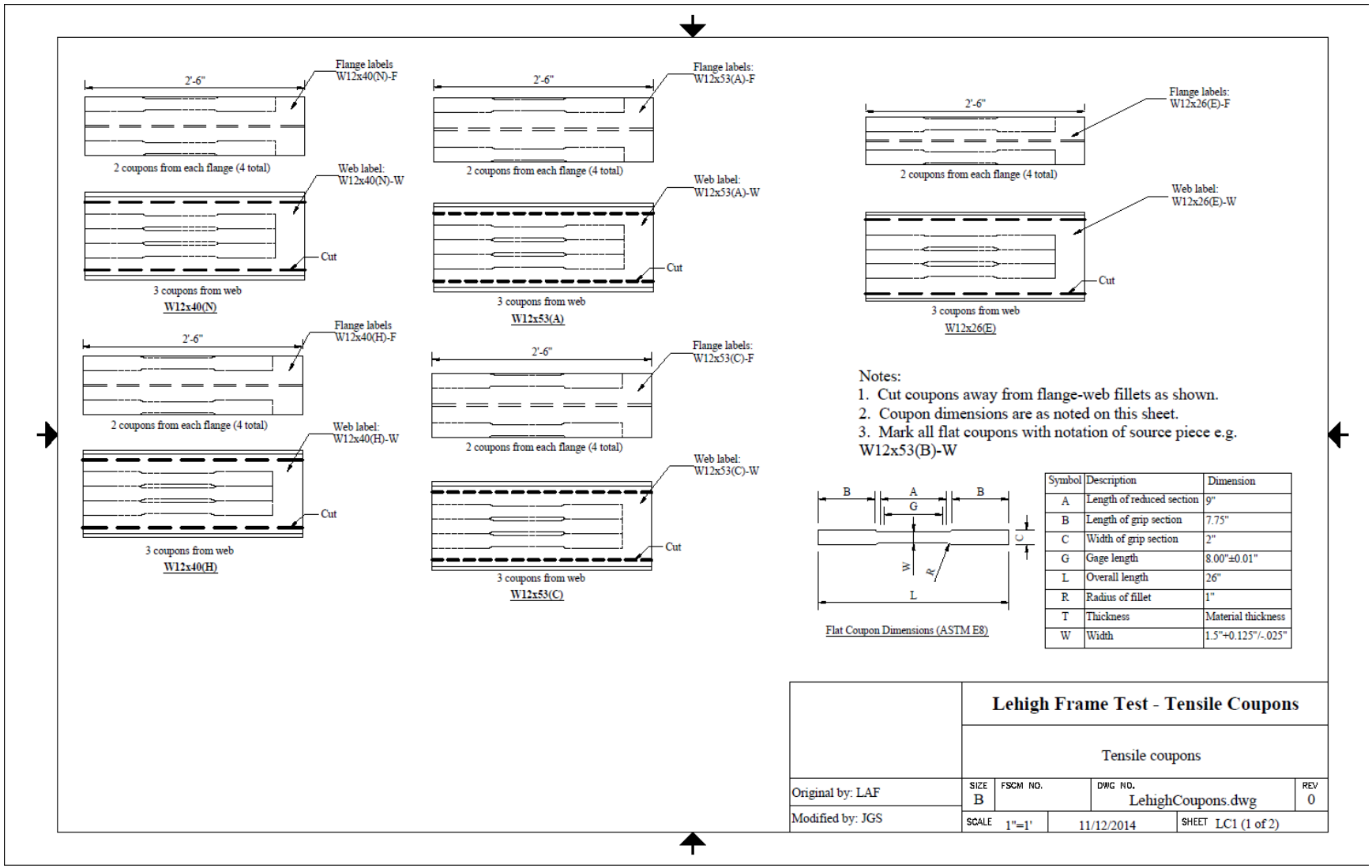

Figure B.1– Shop drawings for coupon testing (Page 4 of 5).

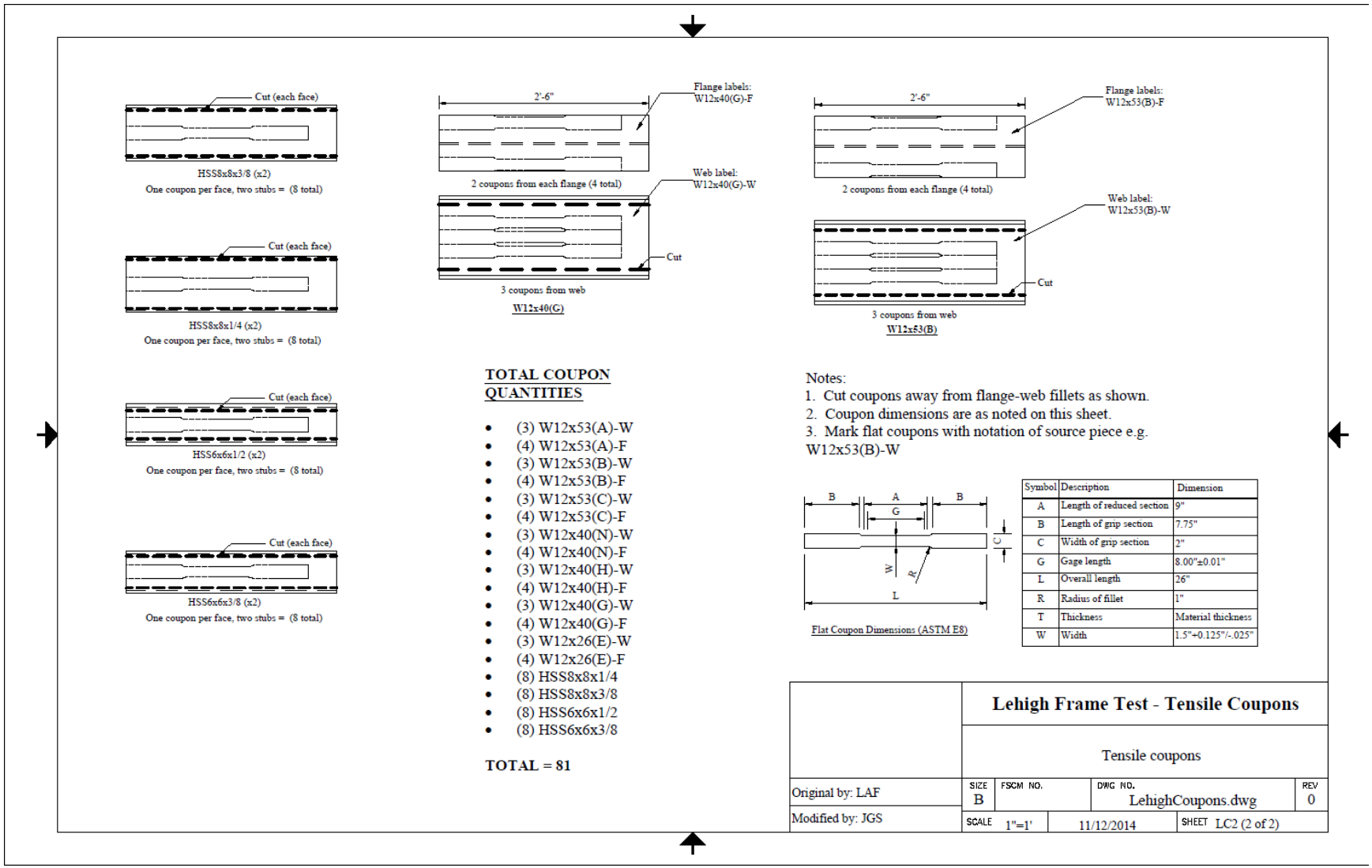

Figure B.1– Shop drawings for coupon testing (Page 5 of 5).

Coupon testing information:

- Control = crosshead rate
- Initial crosshead rate = 0.04 in/min
  - 0.005 in/in/min strain (8 in. gage)
- Hold at 0.004 strain for 2 minutes
- Resume with initial crosshead speed
- Hold at 0.008 strain for 2 minutes
- Resume with initial crosshead speed
- Hold at 0.012 strain for 2 minutes
- Resume with initial crosshead speed until 0.02 strain, then increase crosshead speed to 0.04 in/min (no pause here)

Calculation of yield values:

- For W-sections (hot rolled ASTM A992 steel)
  - Dynamic yield is peak yield stress
  - Static yield is average value of stress at the 3 holds during yield plateau.
- For HSS sections (cold rolled ASTM A1085 steel)
  - Dynamic yield – stress at intersection of stress-strain curve with a line with slope E offset at strain of 0.004.
  - Static yield – intersection between dynamic yield line and a line through the first two hold points.

Two plots are provided for each member: one zoomed in between a strain of 0 and 0.02 to better illustrate the yield and elastic regions, and one of the full stress-strain data for the coupon. Each plot contains all coupon curves from the member and the average curve.

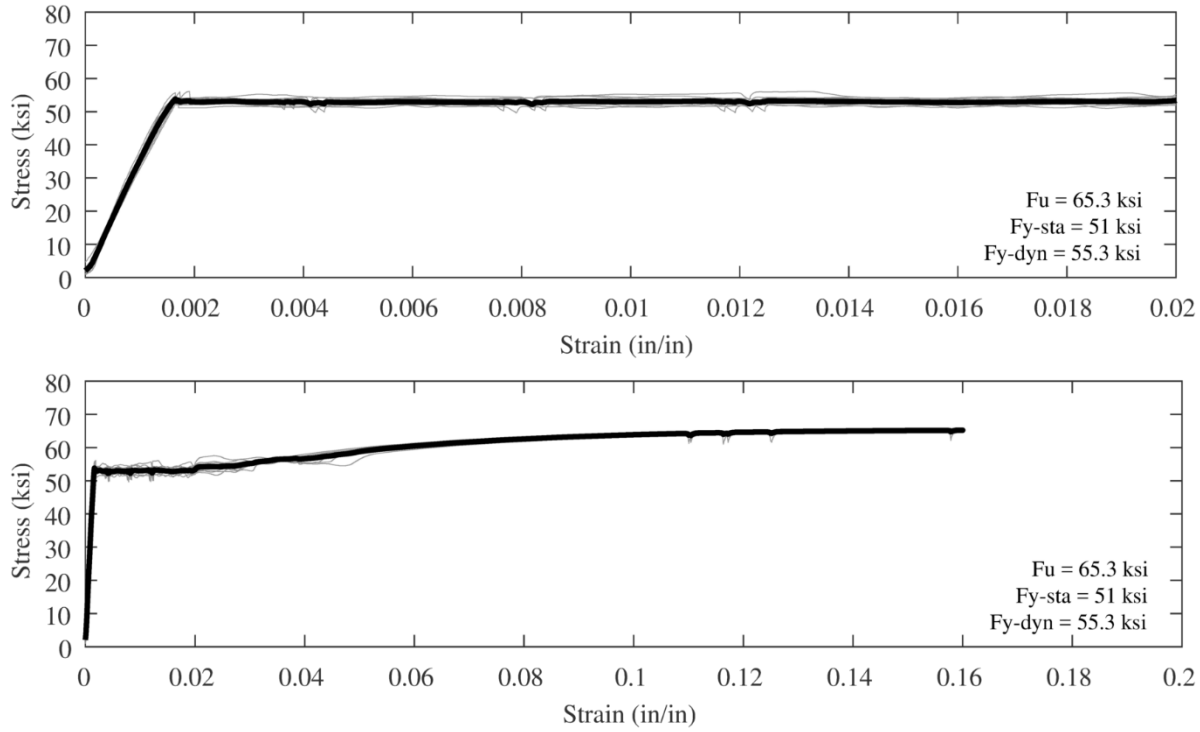

Figure B.2 – Coupon test data for OCBF test unit Level 2 beam (W12x26).

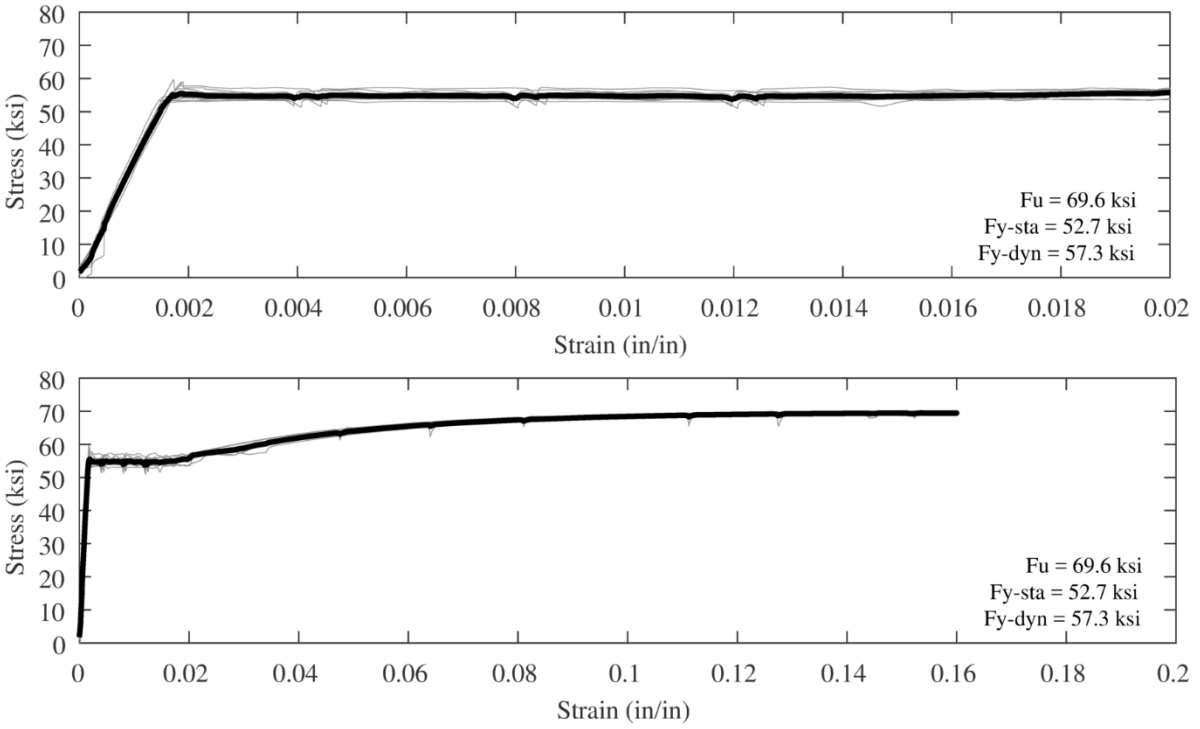

Figure B.3 – Coupon test data for OCBF test unit Level 3 beam (W12x40).

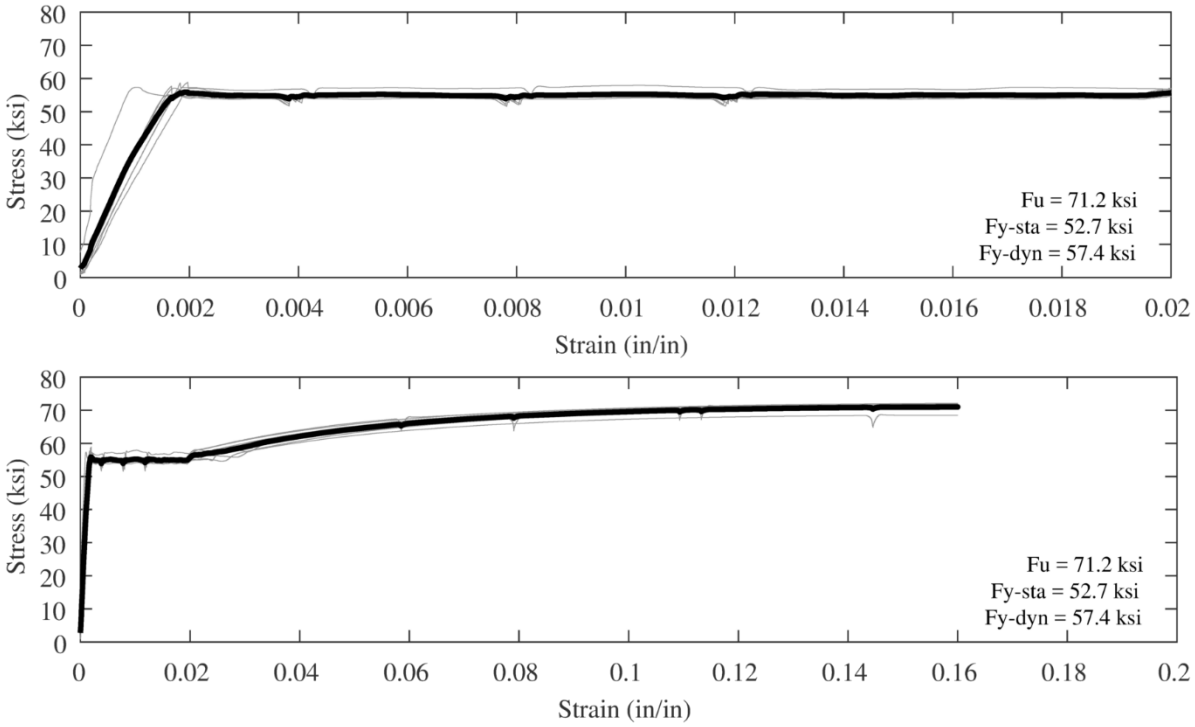

Figure B.4 – Coupon test data for R = 3 CBF test unit Level 2 beam (W12x40).

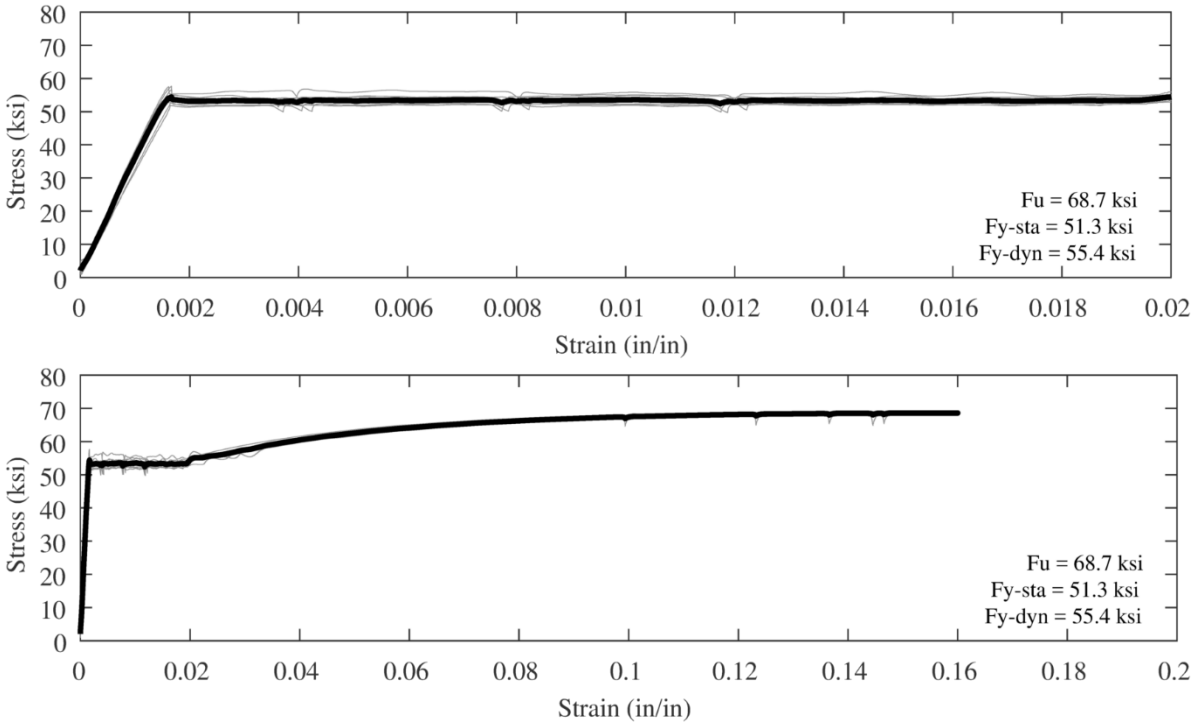

Figure B.5 – Coupon test data for R = 3 CBF test unit Level 3 beam (W12x40).

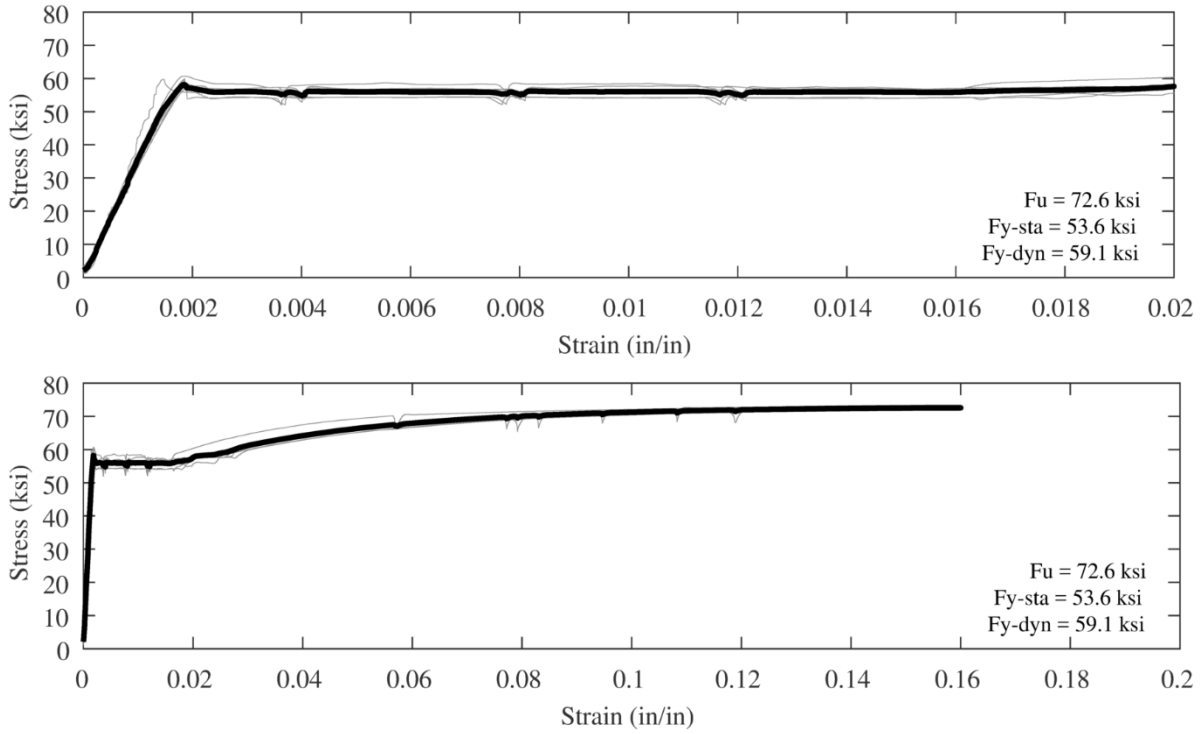

Figure B.6 – Coupon test data for OCBF test unit North and South columns (W12x53).

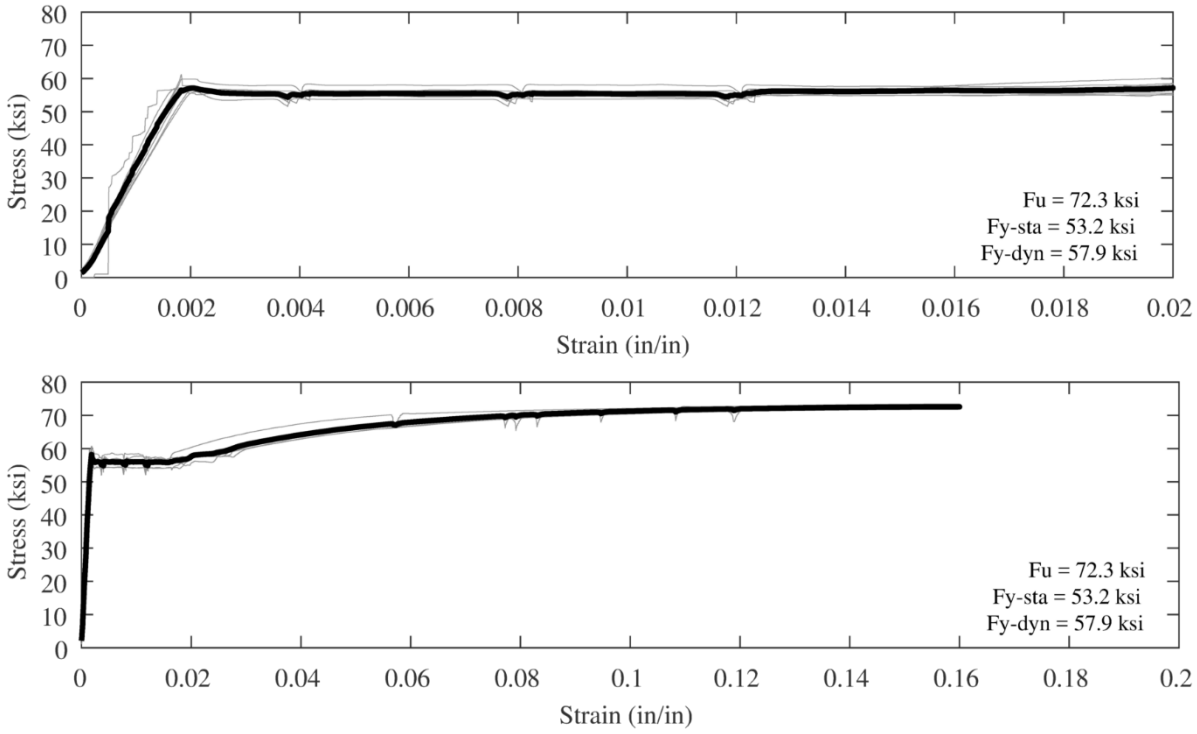

Figure B.7 – Coupon test data for R = 3 test unit South column (W12x53).

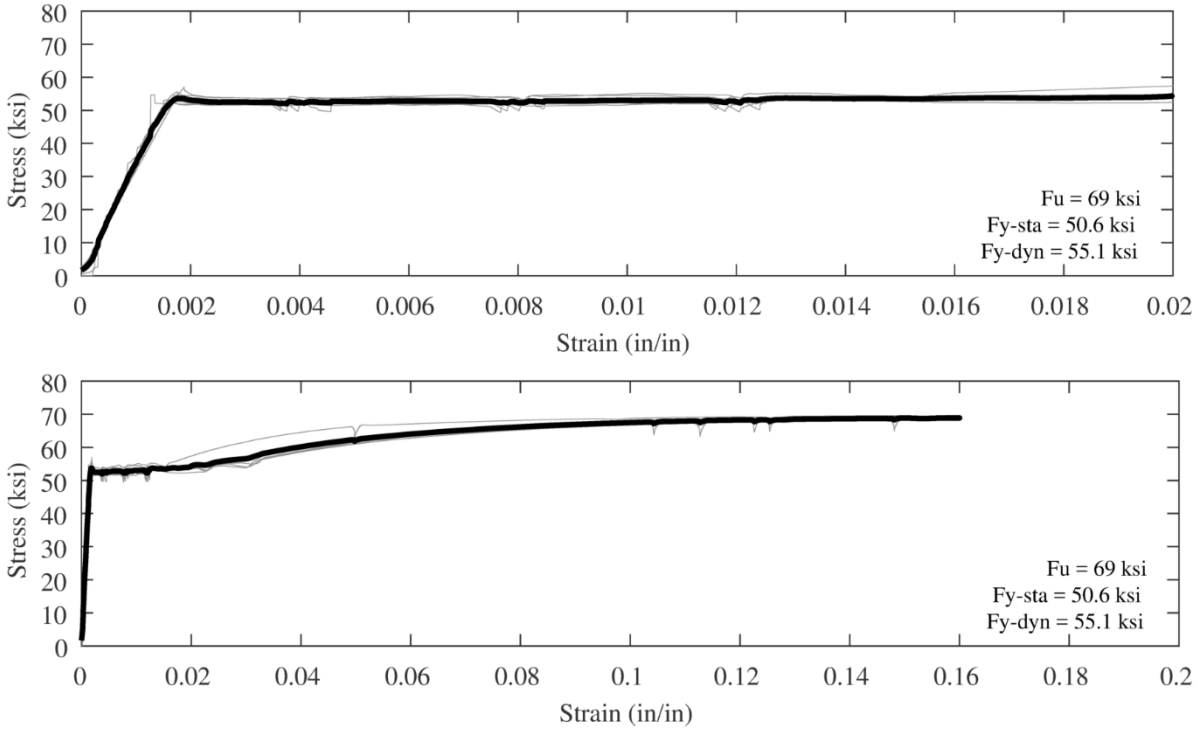

Figure B.8 – Coupon test data for R = 3 test unit North column (W12x53).

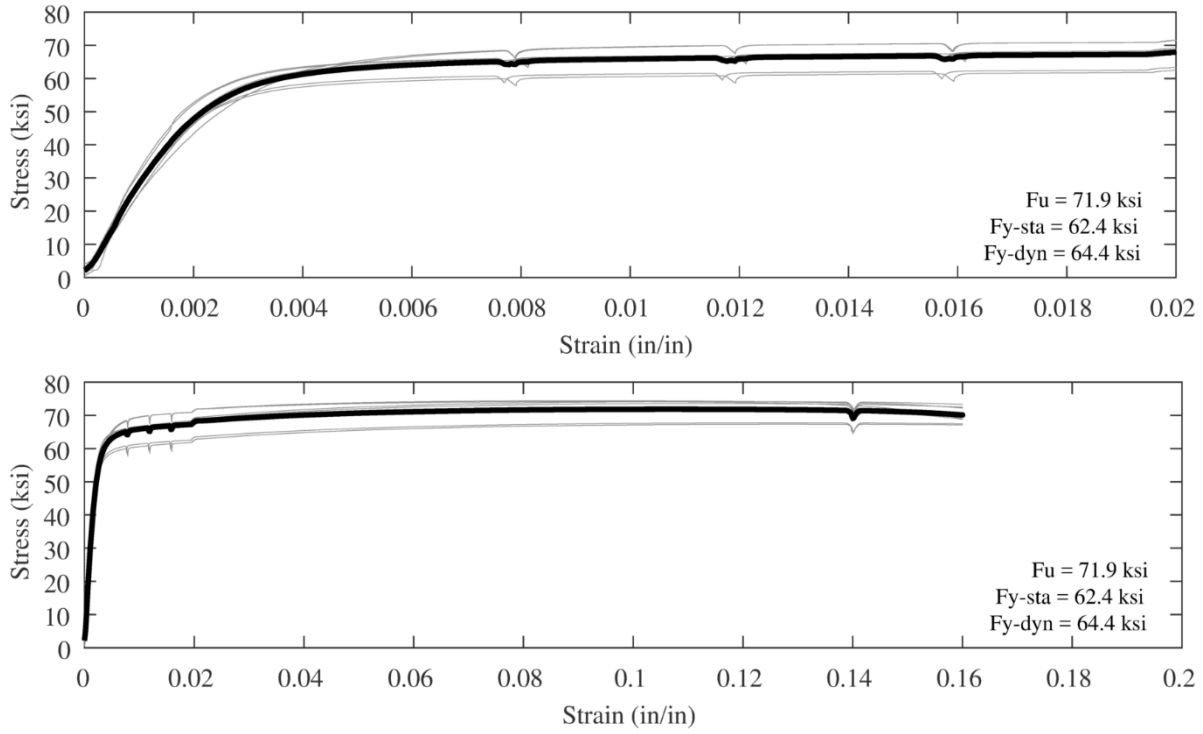

Figure B.9 – Coupon test data for OCBF test unit Story 2 braces (HSS6x6x3/8).

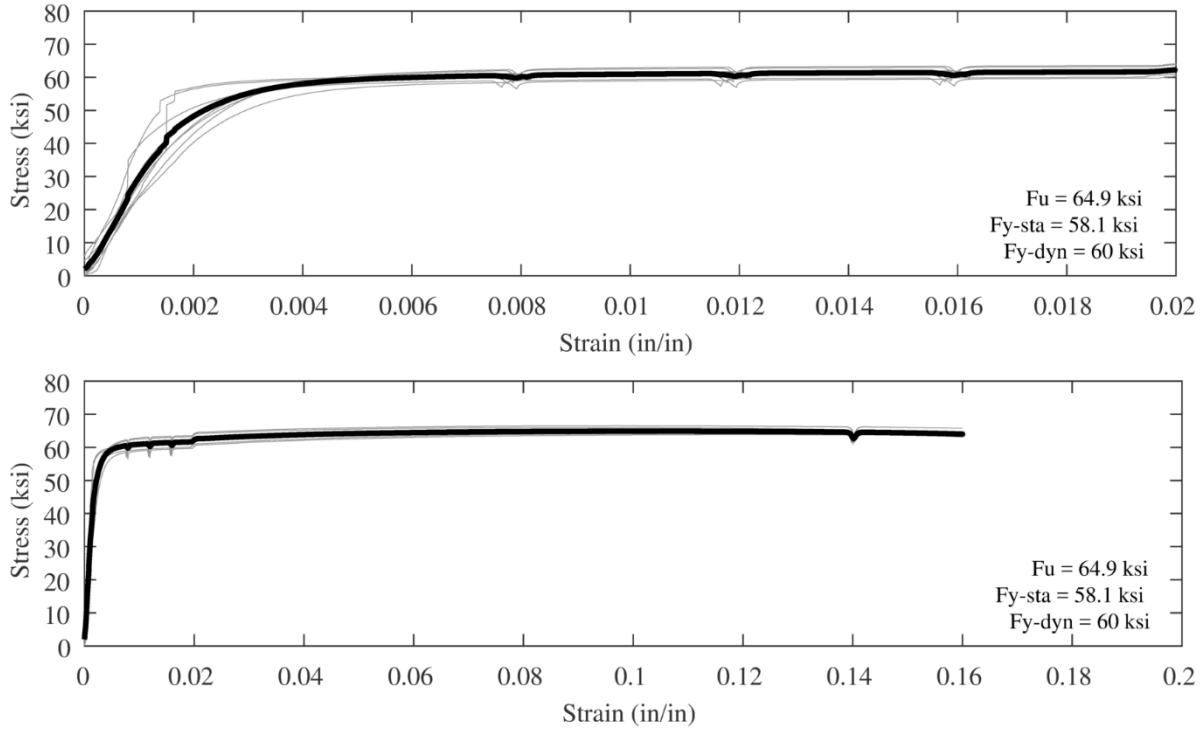

Figure B.10 – Coupon test data for OCBF test unit Story 1 braces (HSS6x6x1/2).

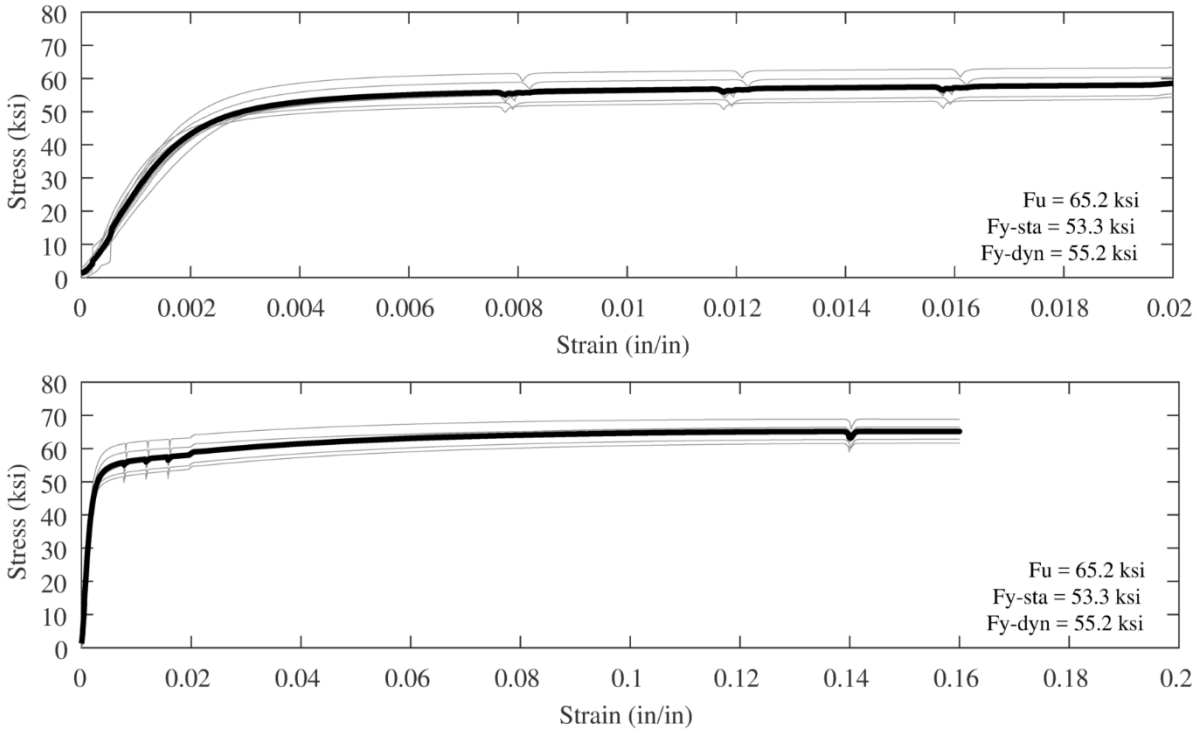

Figure B.11 – Coupon test data for *R* = 3 CBF test unit Story 2 braces (HSS8x8x1/4).

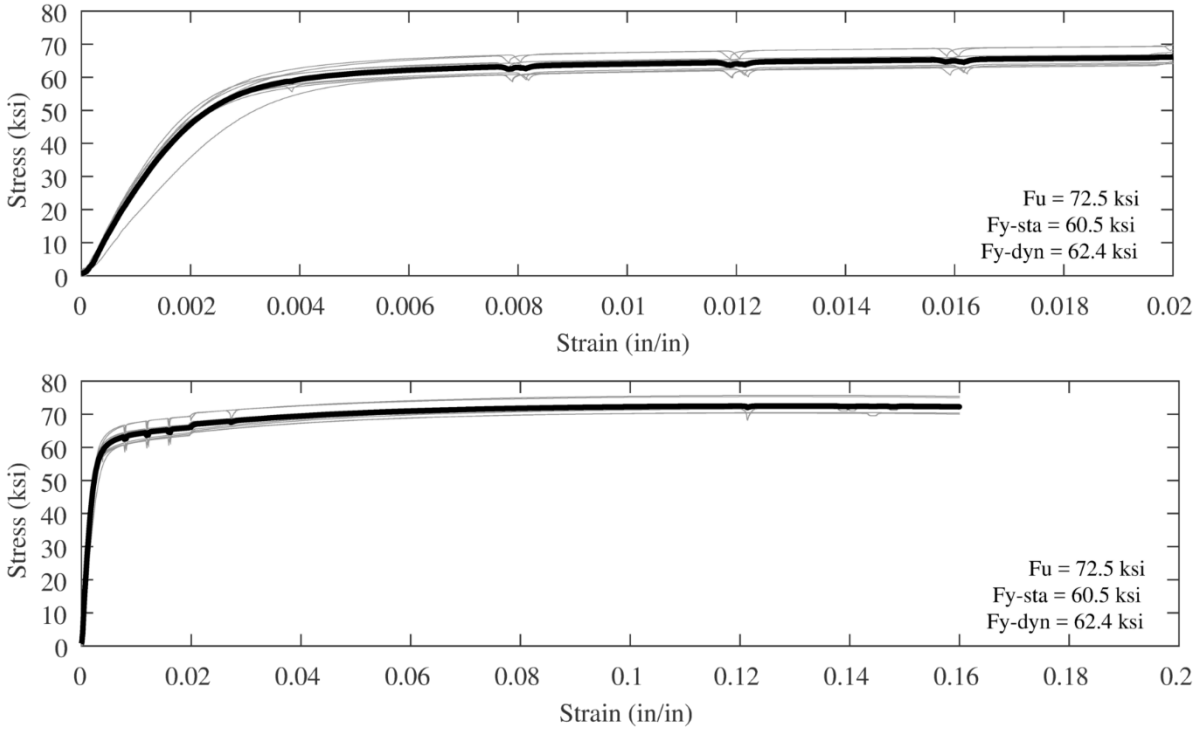

Figure B.12 – Coupon test data for *R* = 3 CBF test unit Story 1 braces (HSS8x8x3/8).

APPENDIX C

AISC 341 OCBF PROVISIONS

Three versions of the AISC 341 provisions for OCBFs are provided in this Appendix: (1) the then-current 2010 edition, which was used for the design of test units and prototype frames in this dissertation; (2) the now-current 2016 edition; and (3) the proposed 2022 edition incorporating the R = 4 OCBF. While technically included in the OCBF provisions, language on multi-tier braced frames and OCBFs above seismic isolation systems are not included in this Appendix so the comparison between aspects focused on in this dissertation are clearer.

C.1 AISC 341–10 OCBF

F1. ORDINARY CONCENTRICALLY BRACED FRAMES (OCBF)

1. Scope

Ordinary concentrically braced frames (OCBF) of structural steel shall be designed in conformance with this section. In seismically isolated structures, OCBF above the isolation system shall satisfy the requirements of Sections F1.4b, F1.5, F1.6 and F1.7 and need not satisfy the requirements of Section F1.4a.

2. Basis of Design

This section is applicable to braced frames that consist of concentrically connected members. Eccentricities less than the beam depth are permitted if they are accounted for in the member design by determination of eccentric moments using the *amplified seismic load*.

OCBF designed in accordance with these provisions are expected to provide limited inelastic deformation capacity in their members and connections.

3. Analysis

There are no additional analysis requirements.

4. System Requirements

4a. V-Braced and Inverted V-Braced Frames

Beams in V-type and inverted V-type OCBF shall be continuous at brace connections away from the beam-column connection and shall satisfy the following requirements:

(1) The *required strength* shall be determined based on the *load combinations* of the *applicable building code* assuming that the braces provide no support of dead and live

loads. For load combinations that include earthquake effects, the seismic load effect, *E*, on the member shall be determined as follows:

(i) The forces in braces in tension shall be assumed to be the least of the following:

(a) The *expected yield strength* of the brace in tension, $R_y F_y A_g$

(b) The load effect based upon the amplified seismic load

(c) The maximum force that can be developed by the system

(ii) The forces in braces in compression shall be assumed to be equal to $0.3P_n$.

(2) As a minimum, one set of lateral braces is required at the point of intersection of the braces, unless the member has sufficient out-of-plane strength and stiffness to ensure stability between adjacent brace points.

4b. K-Braced Frames

K-type braced frames are not permitted for OCBF.

5. Members

5a. Basic Requirements

Braces shall satisfy the requirements of Section D1.1 for *moderately ductile members*.

5b. Slenderness

Braces in V or inverted-V configurations shall have $KL/r \leq 4\sqrt{(E/Fy)}$.

6. Connections

6a. Diagonal Brace Connections

The required strength of *diagonal brace* connections is the load effect based upon the amplified seismic load.

Exception: The required strength of the brace connection need not exceed the following:

(1) In tension, the expected yield strength of the brace multiplied by 1.0 (LRFD) or divided by 1.5 (ASD), as appropriate. The expected yield strength shall be determined as $R_yF_yA_g$.

(2) In compression, the expected brace strength in compression multiplied by 1.0 (LRFD) or divided by 1.5 (ASD), as appropriate. The expected brace strength in compression is permitted to be taken as the lesser of $R_yF_yA_g$ and $1.14F_{cre}A_g$ where F_{cre} is determined from *Specification* Chapter E using the equations for F_{cr} except that the *expected yield stress* R_yF_y is used in lieu of F_y. The brace length used for the determination of F_{cre} shall not exceed the distance from brace end to brace end.

(3) When oversized holes are used, the required strength for the limit state of bolt slip need not exceed a *load effect* based upon using the load combinations stipulated by the applicable building code, not including the amplified seismic load.

C.2 AISC 341–16 OCBF

F1. ORDINARY CONCENTRICALLY BRACED FRAMES (OCBF)

1. Scope

Ordinary concentrically braced frames (OCBF) of structural steel shall be designed in conformance with this section.

2. Basis of Design

This section is applicable to braced frames that consist of concentrically connected members. Eccentricities less than the beam depth are permitted if they are accounted for in the member design by determination of eccentric moments using the overstrength seismic load.

OCBF designed in accordance with these provisions are expected to provide limited inelastic deformation capacity in their members and connections.

3. Analysis

There are no additional analysis requirements.

4. System Requirements

4a. V-Braced and Inverted V-Braced Frames

Beams in V-type and inverted V-type OCBF shall be continuous at brace connections away from the beam-column connection and shall satisfy the following requirements:

(a) The required strength of the beam shall be determined assuming that the braces provide no support of dead and live loads. For load combinations that include earthquake effects, the seismic load effect, *E*, on the beam shall be determined as follows:

(1) The forces in braces in tension shall be assumed to be the least of the following:

(i) The load effect based upon the overstrength seismic load

(ii) The maximum force that can be developed by the system

(2) The forces in braces in compression shall be assumed to be equal to $0.3P_n$ where

P_n = nominal axial compressive strength, kips (N)

(b) As a minimum, one set of lateral braces is required at the point of intersection of the braces, unless the member has sufficient out-of-plane strength and stiffness to ensure stability between adjacent brace points.

4b. K-Braced Frames

K-type braced frames shall not be used for OCBF.

4c. Multi-Tiered Braced Frames [OMITTED FOR BREVITY]

5. Members

5a. Basic Requirements

Braces shall satisfy the requirements of Section D1.1 for moderately ductile members.

Exception: Braces in tension-only frames with slenderness ratios greater than 200 need not comply with this requirement.

5b. Slenderness

Braces in V or inverted-V configurations shall have

$$\frac{L_c}{r} \leq 4\sqrt{E/F_y} \qquad \text{(F1-1)}$$

where

E = modulus of elasticity of steel, ksi (MPa)

L_c = effective length of brace = KL, in. (mm)

K = effective length factor

r = governing radius of gyration, in. (mm)

5c. Beams

The required strength of beams and their connections shall be determined using the overstrength seismic load.

6. Connections

6a. Brace Connections

The required strength of diagonal brace connections shall be determined using the overstrength seismic load.

Exception: The required strength of the brace connection need not exceed the following.

(a) In tension, the expected yield strength divided by α_s, which shall be determined as $R_y F_y A_g / \alpha_s$, where α_s = LRFD-ASD force level adjustment factor = 1.0 for LRFD and 1.5 for ASD.

(b) In compression, the expected brace strength in compression divided by α_s, which is permitted to be taken as the lesser of $R_y F_y A_g / \alpha_s$ and $1.1 F_{cre} A_g / \alpha_s$, where F_{cre} is determined from *Specification* Chapter E using the equations for F_{cr}, except that the expected yield stress, $R_y F_y$, is used in lieu of F_y. The brace length used for the determination of F_{cre} shall not exceed the distance from brace end to brace end.

(c) When oversized holes are used, the required strength for the limit state of bolt slip need not exceed the seismic load effect based upon the load combinations without overstrength as stipulated by the applicable building code

C.3 PROPOSED AISC 341–22 OCBF (R = 4)

F1. ORDINARY CONCENTRICALLY BRACED FRAMES (OCBF)

1. Scope

Ordinary concentrically braced frames (OCBF) of structural steel shall be designed in conformance with this section.

2. Basis of Design

This section is applicable to braced frames that consist of concentrically connected members. Eccentricities less than the beam depth are permitted if they are accounted for in the member design by determination of eccentric moments using the overstrength seismic load.

OCBF designed in accordance with these provisions are expected to provide limited inelastic deformation capacity in their members and connections.

3. Analysis

There are no additional analysis requirements.

4. System Requirements

Beams shall be continuous between columns. The required strength of the beams shall be determined assuming that the braces provide no support of dead and live loads.

4a. V-Braced and Inverted V-Braced Frames

Beams in V-type and inverted V-type OCBF shall as a minimum be provided with one set of lateral braces at the point of intersection of the braces, unless the member has sufficient out-of-plane strength and stiffness to ensure stability between adjacent brace points.

4b. K-Braced Frames

K-type braced frames shall not be used for OCBF.

4c. Multi-Tiered Braced Frames [OMITTED FOR BREVITY]

5. Members

5a. Basic Requirements

Braces and beams shall satisfy the requirements of Section D1.1 for moderately ductile members, assuming C_a = 1.0.

Exception: Braces in tension-only frames with slenderness ratios greater than 200 need not comply with this requirement.

5b. Beams

The required strength of beams and their connections shall be determined using the overstrength seismic load.

5c. Braces

All braces shall have $KL/r < 200$.

6. Connections

6a. Brace Connections

The required strength of diagonal brace connections shall be determined using the overstrength seismic load.

Exception: The required strength of the brace connection need not exceed the following.

(a) In tension, the expected yield strength divided by α_s, which shall be determined as $R_y F_y A_g / \alpha_s$, where α_s = LRFD-ASD force level adjustment factor = 1.0 for LRFD and 1.5 for ASD.

(b) In compression, the expected brace strength in compression divided by α_s, which is permitted to be taken as the lesser of $R_y F_y A_g / \alpha_s$ and $1.1 F_{cre} A_g / \alpha_s$, where F_{cre} is determined from *Specification* Chapter E using the equations for F_{cr}, except that the

expected yield stress, R_yF_y, is used in lieu of F_y. The brace length used for the determination of F_{cre} shall not exceed the distance from brace end to brace end.

(c) When oversized holes are used, the required strength for the limit state of bolt slip need not exceed the seismic load effect based upon the load combinations without overstrength as stipulated by the applicable building code.

6b. Beam-to-Column Connections

For a beam-to-column connection where a brace gusset plate does not connect to the beam and column, the connection shall be designed to resist a moment equal to 50% of the beam nominal flexural strength, M_p, divided by α_s.

6c. Column Splices

Column splices shall comply with the requirements of Section D2.5. Where groove welds are used to make the splice, they shall be complete-joint-penetration groove welds. Column splices shall be designed to develop at least 50% of the lesser plastic flexural strength, M_p, of the connected members, divided by α_s.

The required shear strength shall be $(\Sigma M_p/\alpha_s)/H_c$,

where

H_c = clear height of the column between beam connections, including a structural slab, if present, in. (mm)

ΣM_p = sum of the plastic flexural strengths, F_yZ, of the top and bottom ends of the column, kip-in. (N-mm)

APPENDIX D

BRACE FUSE SYSTEM

As shown through the numerical simulations, the experimental study, and the simple analytical model, brace re-engagement has potential to provide more reserve strength than any other part of the structure. However, as the experimental tests at Lehigh showed, this mechanism is unreliable in reality, both in the assurance that it will happen and in the assurance that it will prevail whilst the structure cycles back and forth under seismic demands.

Kassis and Tremblay (2008) presented the idea of using a brace fuse system to limit and control brace forces during inelastic frame response in seismic events. Although their idea does not transition perfectly over into insuring weld fracture in brittle $R = 3$ chevron frames, the idea of providing a detail which can be better controlled than brace-gusset weld fracture is a good one. Oftentimes in the field, there may be a misunderstanding of how much weld needs to be provided between the brace-gusset connections, or a welder could sacrifice precision for speed during erection of the frame. In addition, welding the brace-gusset connection in the field is a difficult task to begin with due to the tight clearances and the angle at which the welding gun must be held. All of these considered, it is extremely difficult to obtain a brace-gusset weld with the intended strength required (neither more nor less than the supplied weld size and length). Furthermore, even if weld fracture were to occur at this connection, there is a good possibility of the weld fracture being asymmetrical or the brace coming out of plane with the gusset plate, thus preventing brace re-engagement.

Building off the concept Kassis and Tremblay used in their brace fuse system, a detail for a modified "weld-fracture" mechanism is presented in Figure D.1. This detail incorporates an end-capped HSS brace section that is welded to two plates that form a clevis around the

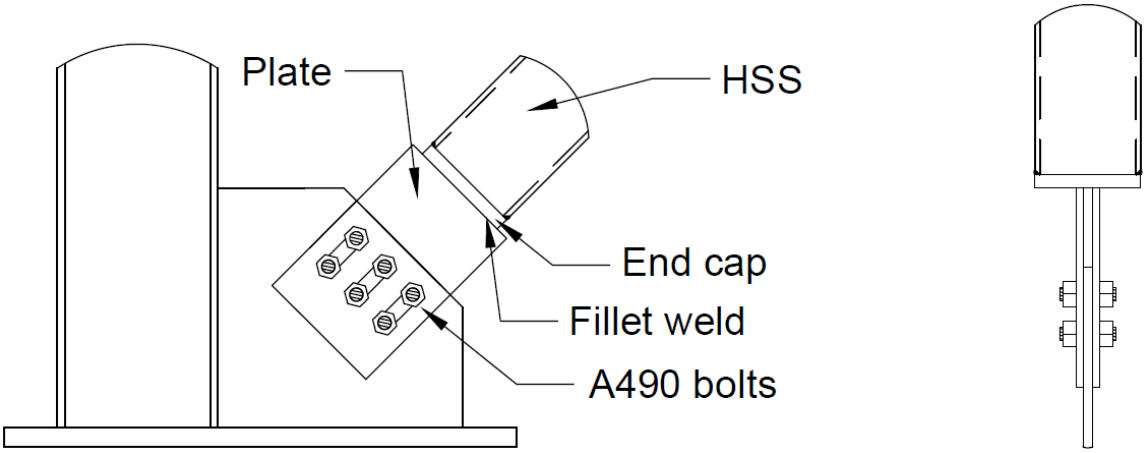

Figure D.1 – Modified brace-gusset connection to promote reliable brace reengagement.

gusset plate. The plates are attached using bolts. This detail would be "capacity designed" in such a way that bolt slip and bolt bearing capacities are lower than that of brace buckling. Rather than the braces buckling in compression and significantly reducing story strength to mostly column bending, the mechanism formed through this detail is one of bolt bearing in both tension and compression. As one brace has its slip-critical bolts reach their slip capacity, the bolts will begin to bear on the clevis plates, allowing for beneficial deformations that will result in additional strength from beam bending. By placing a bolt through both ends of the overly long-slotted holes, bearing will occur when the brace is in compression or tension. The overly long slot shown in Figure D.1 may be required as the bolt bearing strength is typically much higher than the bolt slip capacity, and it is undesirable and counterproductive to have the bolt bearing strength exceed the brace bucking capacity.

The failure mechanism is more controllable when using this detail, allowing for increased probability of post-damage reserve strength. In addition, this mechanism for post-damage reserve strength (bearing on bolt holes) is a more defined and quantifiable method than the brace slot bearing on the gusset plate. Accurate calculation of bearing on bolt holes allows for further insurance that this mechanism's capacity may be capped at a capacity lower than

that of the brace's buckling capacity, thus preventing the brace from buckling after bolt bearing occurs. By providing the "weak link" of the detail in the brace-gusset connection itself rather than along the brace length, the connection may easily be replaced or retrofitted if it is damaged during a seismic event.